IMPACT OF CROSS SECTION, WEB REINFORCEMENT AND LOAD HISTORY ON THE SEISMIC PERFORMANCE OF SLENDER CONCRETE WALLS

BY

ANAHID A. BEHROUZI

DISSERTATION

Submitted in partial fulfillment of the requirements
for the degree of Doctor of Philosophy in Civil Engineering
in the Graduate College of the
University of Illinois at Urbana-Champaign, 2016

Urbana, Illinois

Doctoral Committee:

Professor Bill F. Spencer, Chair
Professor Daniel A. Kuchma, Tufts University, Director of Research
Professor Dawn E. Lehman, University of Washington
Professor Daniel P. Abrams
Professor John S. Popovics

ABSTRACT

Many reinforced concrete buildings in seismic regions employ reinforced concrete shear walls as part of the lateral force resisting system and these walls often have non-planar cross-sectional geometries. To date, the majority of experimental tests on slender concrete walls have been conducted on planar walls which have been subject to low shear stress demands. An experimental program was developed to examine the response of flanged C-shaped walls with respect of load history and a computational parametric study was conducted to focus more specifically on the impact of web reinforcement for walls subject to a range of shear stress demands.

The experimental program investigated the impact of bi-directional loading on flanged C-shaped walls that were designed to meet the minimum *ACI 318-08* special structural wall requirements. The results indicate that irrespective of load history the C-shaped walls have a similar damage progression leading to a buckling-rupture failure and a nearly identical strong-axis load-deformation response up to the peak flexural strength. However, bi-directionally loaded walls exhibit earlier onset of critical damage limit states and reduced strong-axis drift capacity. Compared to experimentally-tested planar walls that tend to fail via crushing-buckling, the flanged C-shaped wall geometry has a more ductile failure mode despite being subject to higher shear stress demands. The improved response can be attributed to the ability to redistribute forces to the boundary elements and flanges after considerable web damage.

Damage to the unconfined web of the flanged C-shaped walls was substantial. Though walls developed distributed cracking, there was a single wide crack plane that developed near the wall base. Widening of this crack led to high tensile strains in web reinforcement and ultimately the widespread fracture of vertical web bars, limited fracture of horizontal web bars, as well as severe concrete degradation in the surrounding region. This performance suggests that the minimum web steel content required by *ACI 318* may be insufficient. As such, the current minimum web reinforcement requirements were studied using an experimentally-validated, high-resolution finite element modelling approach.

The computational parametric study examined the impact of the shear stress demand and web reinforcement ratio on wall deformation and ductility. The study results indicate that increased shear stress demand can significantly reduce wall deformation and ductility; however, designs with excess horizontal reinforcement, beyond what is required by *ACI 318-14* to meet shear demand, can improve ductility. The data suggest there are similar performance benefits of reducing the design

shear demand-to-capacity ratio. A second stage of the parametric study explored the combined effect of modifying the horizontal reinforcement ratio and increasing boundary element length from the *ACI 318-14* minimum to the full neutral axis depth. For walls with low-moderate shear stress demands, this combination results in even greater wall ductility than providing excess horizontal reinforcement alone.

The experimental tests provide critical data to developing performance-based design criteria for non-planar walls, since most prior efforts have been related to planar walls. The computational parametric study results are of value in developing new code recommendations for the minimum horizontal web reinforcement ratio which have essentially remained unchanged throughout the history of the *ACI 318* building code.

ACKNOWLEDGMENTS

The African proverb *"it takes a village to raise a child"* is the most accurate analogy that describes the support I have had along my journey from an enthusiastic, abet untrained, aficionada of structural design to an earthquake engineering researcher. I would like to take this opportunity to thank that *village* that raised this *child*.

First, I would like to express my love and gratitude for my family to whom this work is dedicated.

My mother and father, an educator and engineer duo, who were early to recognize my interest in the combination of math/science and the arts. They understood that this combination allowed me to interpret the beautifully complex world around me via a logic that was equally rooted in technical, emotional, and creative understanding. They took each day to nurture both my inquisitiveness through home science experiments; road trips to be explore the unique regional culture, environment, and vernacular architecture throughout the United States; and facilitating learn-by doing projects from designing and building a garden structure for our backyard, to soldiering electronics, to painting, baking, …the list goes on. I thank them for being my constant educator-guides and demonstrating that learning is exciting, knowledge is powerful, and that the greatest use of your education is sharing it with others. Moreover, I have blessed to have a family who has given me is the love, courage, and support to go down what would otherwise have been a challenging path. They have been and continue to be present at every life and academic milestone helping me make my way in the world and through the last five years of the doctoral degree.

My brother, and best friend, has been my adventurous companion through the last twenty-odd years. He has been a major player in most of life's best memories, a fellow Lego-builder, an engaging storyteller-teacher, and a role model. Among the many other hats he has worn, staunch advocate is probably the most important to my continued pursuit of engineering career and doctoral degree. When I was five, I have a clear recollection of asking him if should be more like other girls, and he said that I was uniquely different and that is what he loved about his little sister. He elaborated that I could do and become anything I wanted; it did not matter what others did. This message has been a common thread throughout the years with his words of encouragement when I faced doubt or difficulty with my engineering studies and his exclamations of pride when I weathered through those times. I am very fortunate to have such a kind and loving brother.

And so the story of "breaking walls", real and simulated, is for you. My family.

I would like to thank Dr. Dan Kuchma, who has served as my research advisor throughout the course of my graduate studies. His extensive knowledge of large-scale testing and non-linear finite element modelling of concrete structures has been critical to the experimental and computational portions of my doctoral research. Perhaps more than that, I appreciate that Dr. Kuchma recognized and nurtured my interests in engineering education by helping me seek out opportunities such as conducting STEM teaching workshops for K-12 educators and finding the resources to carry out human studies research related to how students learn. His enthusiasm and support of these extracurricular teaching endeavors helped me evolve as an educator-researcher.

I would also like to express my deep appreciation for my co-advisors Drs. Dawn Lehman and Laura Lowes at the University of Washington. They exemplify what it means to be strong, knowledgeable, female engineers. As such, I consider them respected mentors and role models. Both very versed in the research of structural concrete walls, their input and feedback was instrumental to the experimental project and computational parametric wall study portions of my research. Their visits to the University of Illinois during the first two years of my studies for our experimental tests, and the countless hours of web-conferencing since, have been opportunities to learn a great deal from some of the very best in the field. I would like to thank the rest of my doctoral committee: Drs. Bill Spencer, Dan Abrams, and John Popovics, who supported me in the research work described in this document as well as other academic, teaching, and study-abroad endeavors throughout the years.

My research partner, Andrew Mock, has been the most hard-working, knowledgeable, kind, and humble individual I have had the pleasure of working with for the past five years. I have been continually impressed by his creative problem-solving that I observed in the months working together preparing for tests, hundreds of hours on the lab floor running experiments, and many off-shoot writing projects ranging from sponsor reports to journal publications. He has also been a wonderful and motivating peer-advisor throughout my academic journey.

There are many people to acknowledge for their support in my doctoral research work:

I would like to thank Michael Bletzinger who served as a mentor and helped me feel a part of the small, but tight-knit research family at the large-scale lab at Illinois. Moreover, he authored a vast majority of the programming code we used for in our experiments to carry out complex load control and data collection. He also spent many hours helping us learn about and troubleshoot assorted instrumentation and control systems.

I would like to thank Tim Prunkard, our laboratory/shop manager, and the Civil & Environmental Engineering shop personnel who made our experimental research aspirations into reality. This team was critical in many of the fabrication, preparation, and instrumentation tasks necessary to carry out our tests. Furthermore, I am personally indebted to the shop for their willingness to collaborate on constructing several museum-quality teaching models for engineering education research I conducted during my doctoral studies. The type of shop support we had at Illinois has no parallel at any other large-scale lab I have worked at or visited, and that is special indeed.

Additionally, I would like to thank my research family comprised of lab staff that not only insured that our experiments were a success, but individuals that I worked with for multiple years and consider dear friends: Weslee Walton , Nathan Baker, Pete Smit, and Chia-Ming Chang. Thanks also to undergraduate students that provided significant assistance in fabrication, instrumentation, or data analysis for the projects: Yumen Cao, Zack Grabijas, Abby Mitchell and Rui Li. I also very much appreciate the support of past graduate students that stepped in to provide assistance with items ranging from data acquisition training to computational modelling to support our experimental tests, including: Drs. Chris Hart, Anna Birely, Thomas Frankie, and Ken Marley. With respect to the computational work, I would like to thank University of Washington students Kamal Ahmed and Zach Whitman for sharing their expertise of non-linear modelling with the ATENA 3D software tool. Finally, I would like to thank other members of Dr. Dan Kuchma's research group that provided research/ academic guidance and companionship through the years: Somashekar Viswanath, Anna Flessner, and Sihang Wei.

There are many other faculty, friends, and students who have positively impacted my learning, research, and teaching experiences over the years. It would be a very long list, and those individuals know who they are. Thank you for your motivational words, your insights, and your role in helping me grow as a researcher and educator.

I would like to express my appreciation for the external support on the experimental portion of this doctoral work including funding from the National Science Foundation through the Network for Earthquake Engineering Simulation Research Program, Grant CMS-042157 and CMMI-0927178 (Program Manager: Joy Pauschke), and the Charles Pankow Foundation through the CPF Research Grant 03-09 (Industry Champions: Ron Klemencic, Chairman & CEO of MKA and Neil Hawkins, Emeritus Professor of the University of Illinois at Urbana-Champaign).

With heartfelt thanks to my family and the *village* that raised this *child*.

TABLE OF CONTENTS

LIST OF FIGURES

LIST OF TABLES

LIST OF SYMBOLS

a depth of equivalent rectangular stress block used in determining flexural capacity of a member (=$\beta_1 c$), in

A_{ch} area of confined core for wall boundary element measured to outside edges of transverse reinforcement, in^2 (=$b_{c1} b_{c2}$)

A_{cv} shear area of a wall, or walls aligned in a plane (for rectangular walls, = bl_w), in^2

A_{cw} shear area of an individual wall/pier, in^2

A_g gross area of a concrete section, in^2

$A_{sh,i}$ total cross-sectional area of transverse reinforcement (including cross-ties) within a spacing s and perpendicular to the dimension b_c, in^2 (i=1,2 for A_{sh} perpendicular to b_{c1} and b_{c2})

A_{vh} total cross-sectional area of horizontal shear reinforcement within a spacing s_2, in^2

ALR axial load ratio calculated as $100 \times P_u / A_g f_c'$, %

b wall thickness, in (for non-planar walls this is replaced by t_w for web thickness and t_f for flange thickness)

b_{be} width of wall boundary element, in (for planar walls often b_{be} = b)

$b_{c,i}$ dimension of confined core for wall boundary element measured to outside edges of transverse reinforcement, in (i=1,2 for length and width)

b_{eff} effective flange width (measured in longitudinal direction of flange), in

b_f flange length (measured in longitudinal direction of flange), in

BE boundary element, can be “special” or “ordinary

c depth of compression zone in wall, in

$CSAR$ cross-sectional aspect ratio calculated as the wall length divided by the wall thickness or l_w / t_w

d distance from extreme compression fiber to centroid of longitudinal tension reinforcement or $0.8 l_w$ for walls, in

d_b diameter of longitudinal reinforcement, in

d_t diameter of transverse reinforcement, in

D dead loads, used in load combinations to determined factored load U

E effect of earthquake forces (vertical and horizontal), used in load combinations to determined factored load U

E_c elastic modulus of concrete, calculated as $w_c^{1.5}\sqrt{f_c'}$ for $w_c = 90 - 160$ lbs/ft^3, psi

$E_c I_{eff}$ effective flexural stiffness of a member

E_s elastic modulus of steel, commonly taken as 29,000$\times 10^3$ psi

f_c maximum extreme fiber compressive stress, psi

f_c' specified compressive strength of concrete, psi

f_r modulus of ruputure of concrete, calculated as $7.5\lambda\sqrt{f_c'}$, psi

f_y specified yield strength of steel reinforcement, psi

$f_{y,actual}$ actual, measured yield strength of steel reinforcement, psi

f_{yt} specified yield strength of transverse steel reinforcement, psi

f_u specified ultimate strength of steel reinforcement, psi

$f_{u,actual}$ actual, measured ultimate strength of steel reinforcement, psi

h_{be} vertical height of wall boundary element beyond critical section, in

h_{eff} effective height (=M_u/V_u), in

h_w height of wall, in

h_u laterally unsupported height of wall/pier at extreme compression fiber, in

h_x maximum center-to-center spacing of longitudinal bars laterally supported by hoops or cross-ties in wall boundary element, in

H loads due to soil or water within soil, used in load combinations to determined factored load U

I_g moment of inertia of gross concrete section taken about member centroid, in^4

I_{se} moment of inertia of steel reinforcement taken about member centroid, in^4

l_{be} length of wall boundary element, in (for nonplanar walls subscript denotes location: $l_{be,f}$ for boundary element at free-end of flange and $l_{be,w}$ for boundary element at web-flange intersection)

l_d development length in tension of reinforcement, in

l_w length of wall, in

L live loads, used in load combinations to determined factored load U

M_u factored flexural demand at section, lb-in

OBE “ordinary” boundary element

P_b axial load capacity of wall at balance point (where $\varepsilon_t = \varepsilon_y$ and $\varepsilon_c = \varepsilon_{cu}$ occur simultaneously)

P_e maximum design axial load on a wall due to earthquake forces, lb

P_u factored axial load demand on wall, lb

s vertical spacing of transverse reinforcement in wall boundary element, in

s_1 spacing of vertical shear reinforcement, in

s_2 spacing of horizontal shear reinforcement, in

S snow load, used in load combinations to determined factored load U

SBE "special" boundary element

t_f flange thickness (measured perpendicular to longitudinal direction of flange), in

t_w thickness of wall web for nonplanar walls, in (replaces b)

U required strength to resist factored loads related to internal moments and forces

V_c nominal shear capacity of member provided by concrete, lbs

V_n nominal shear capacity of member, lbs

V_s nominal shear capacity of member provided by steel reinforcement, lbs

V_u factored shear demand at section, lbs

w_c density (unit weight) of concrete, lbs/ft^3

α_c coefficient defining relative contribution of concrete to nominal shear strength of a wall

β_d ratio of maximum factored axial dead load to total load only considering gravity or lateral load effects where appropriate

β_1 factor relating a to c for equivalent rectangular stress block, based on f_c'

δ_u design displacement, in

ε_c strain in extreme concrete compression fiber

ε_{cu} condition where strain in extreme concrete compression fiber = 0.003

ε_t net tensile strain in extreme layer of longitudinal tension reinforcement

ε_y tensile strain at yield in longitudinal tension reinforcement

λ modification factor to account for differences in properties for lightweight concrete (value relative to normal-weight concrete)

$\rho_{BE,l}$ ratio of longitudinal reinforcement located in the wall boundary element

ρ_l ratio of gross longitudinal reinforcement in the wall

$\rho_{web,h}$ ratio of horizontal reinforcement located in the wall web (equivalent to horizontal shear reinforcement)

$\rho_{web,l}$ ratio of longitudinal reinforcement located in the wall web (equivalent to vertical shear reinforcement)

ϕ strength reduction factor (to distinguish different factors may be used: ϕ_f for flexure and axial, ϕ_v for shear)

LIST OF REFERENCE FIGURES

Distinction between Planar and Nonplanar Cross-Sections

- Planar Walls: Rectangular and Barbell

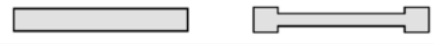

- Nonplanar Walls: T, L, C, U, I, H-Shaped Walls

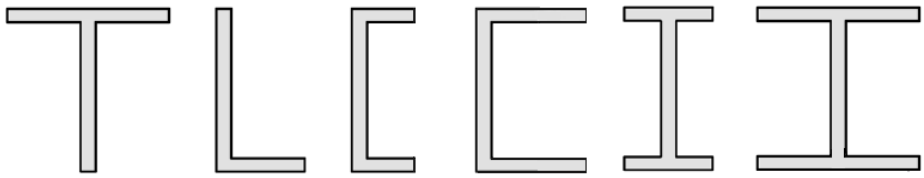

Overall Wall Details

- Planar Walls:

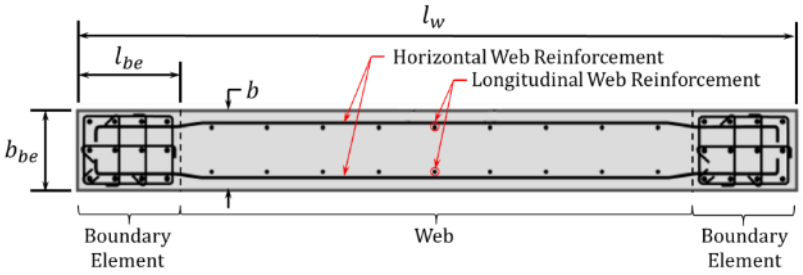

- Nonplanar Wall – C-Shaped (note: reinforcement notes are same as planar wall):

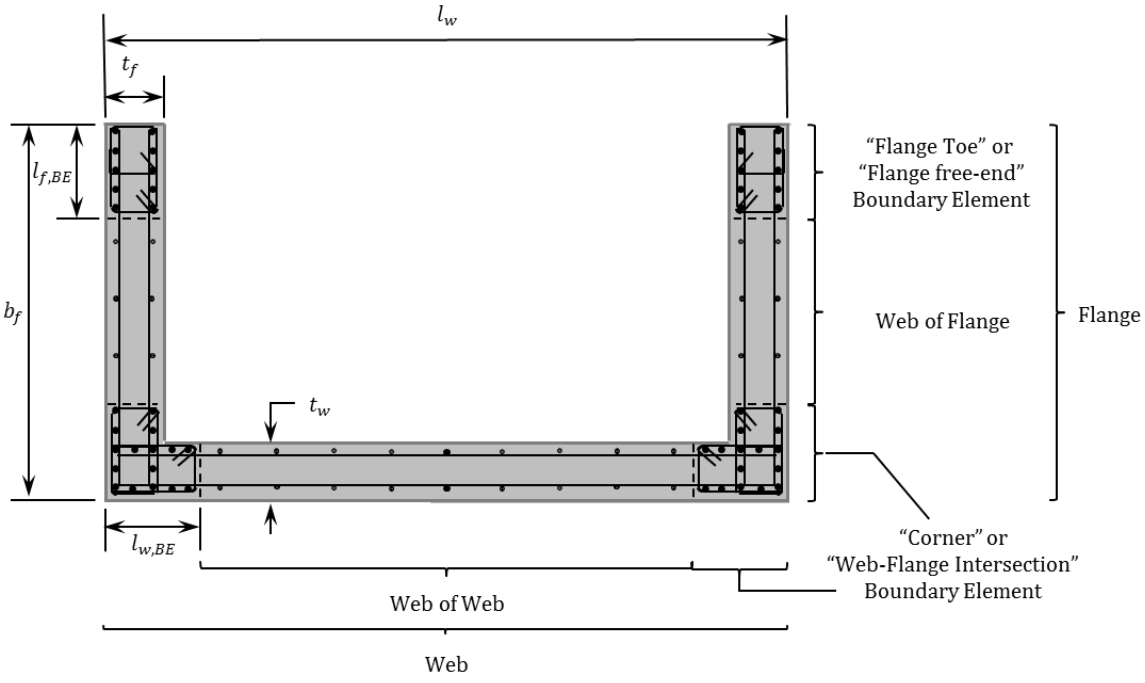

Boundary Element Details based on Planar Wall:

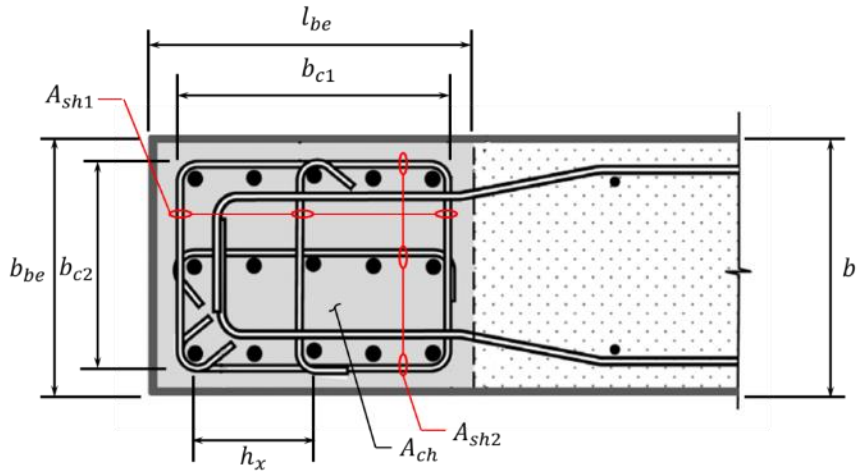

Wall Elevation based on Planar Wall:

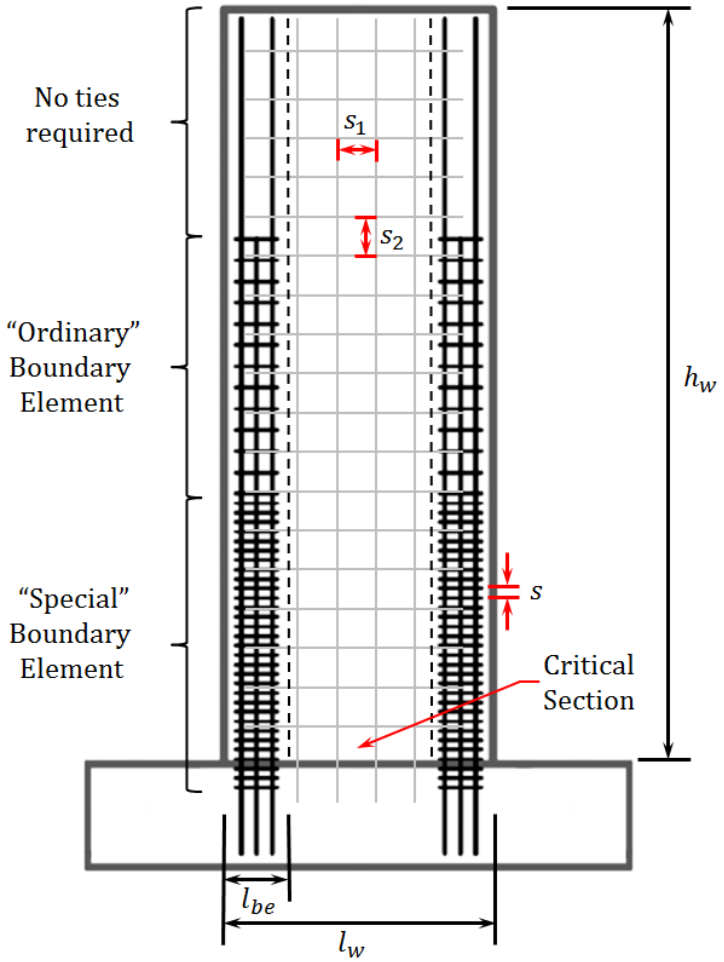

Note: List of Symbols were largely derived from *ACI318-71 to -14* versions [4-16,18] and Structural Wall Definition Figures were modified from [134]

1 INTRODUCTION

Many reinforced concrete buildings utilize reinforced concrete structural walls as a primary lateral-load resisting system for mid- to high-rise construction in seismic regions such as the West Coast of the United States, Chile, New Zealand, and Japan. Historically, these walls have performed well in that the damage was moderate (limited to cracking and cover spalling). However, there has been considerable damage to structural wall buildings in recent earthquakes. These more recent observations have, to some degree, eroded engineers' confidence in wall performance and current design provisions. There have been notable cases both in New Zealand and in the Maule, Chile 2010 earthquake of significant damage that exhibited undesirable flexural-compression type failures including web or boundary element crushing as well as out-of-plane buckling, especially in flanged walls with thin webs [18, 105].

Study of these earthquakes indicated that demand levels, cross-sectional shapes, boundary element detailing and other aspects of design should be studied [125]. This study was undertaken to investigate these issues, in particular cross-sectional shape, shear stress demand and web reinforcement. Specifically, these issues were studied in two phases using different research approaches. First, an experimental program was undertaken to examine the response of flanged C-shaped walls with respect to load history. Second, a computational parametric study (using experimentally validated finite element analyses) was conducted to study the impact of web reinforcement and shear stress demands on the deformability of walls.

The experimental phase examined the response of slender flanged C-shaped walls with respect of load history, specifically uni- vs. bi-directional loading of isolated walls. In addition, because C-shaped walls are commonly used as part of a coupled core wall system, a sophisticated loading algorithm was developed to simulate the simulated coupling action resulting from bi-directional loading (in terms both shear and axial demands) of a wall in a core-wall system. The three flanged C-shaped walls were approximately one-third scale and tested at the Network for Earthquake Engineering Simulation (NEES) "Multi-Axial Full-Scale Sub-Structured Testing and Simulation (MUST-SIM) facility at the University of Illinois at Urbana-Champaign utilizing unique, specialized equipment to simulate the complex multi-axial state of loading (shear, moment, and axial load). The walls were three stories high, but the demands at the top of the wall simulated loads expected in a regular, mid-rise building during an earthquake. Dense, high-resolution monitoring of local and global specimen response was provided to enable the types of investigations necessary to further the performance-based design of non-planar walls. These research efforts were a collaboration with the University of Washington and supported

by the National Science Foundation NEES program and the Charles Pankow Foundation (CPF). The experimental data were combined with prior test data to understand the impact of salient design parameters (e.g., shear stress) and bi-directional loading.

The experimental results were combined with prior work on non-planar walls (this database, and planar wall database as part of a prior research effort, were developed under the same funding). Using this work, it was observed that both the flanged and planar walls with moderate to high shear stress demands sustained significant damage in the lightly-reinforced unconfined web. This is also support by post-earthquake damage evaluation of walls in mid-rise buildings. Using this as motivation, a finite element model was developed in the reinforced concrete analysis software program ATENA to study the impact of web reinforcement and shear stress demand on ductility of walls. First a high-resolution, non-linear finite element modelling tool ATENA was validated using experimental results from slender reinforced concrete walls with high shear stress demands, after the work by *Whitman* [173]. Using this validated model, a parametric study was conducted to examine the impact that web reinforcement has on deformability and ductility for walls subject to varying shear stress demand levels. The results suggest a positive impact of larger horizontal reinforcement ratios for higher shear stress demands on the ductility of walls.

1.1 Research Objectives

The overall objective of this study is to study the performance of slender reinforced concrete structural walls with respect to loading, both shear stress demand and bi-directional effects. In particular, the design parameters of cross-sectional shape, web reinforcement, and load history were investigated to assess their impact on deformation, ductility, and strength response. The major research efforts are as follows:

1. To develop an improved understanding of slender non-planar wall response and the impact of bi-directional loading history.
2. To develop an improved understanding of the role that web reinforcement has on deformation and ductility for walls subject to range of shear stress demands.

1.1.1 Non-Planar Wall Response and Impact of Bi-Directional Loading

The assessment of non-planar wall response involved three major components: (i) a large-scale experimental program in which flanged C-shaped walls were subject to uni- and bi-directional loading, (ii) an evaluation of previous experimental non-planar wall test programs with varying

cross-sections and loading histories, and (iii) an examination of in-field earthquake response of non-planar wall s over the last fifty years. At present there are deficiencies in code/guide documents related to the design of non-planar walls, there are few explicit references to flanged walls in *ACI 318-14* [18] except for the definition of effective flange width. The remainder of provisions is generic for planar and non-planar walls despite the fact that experimental and in-field wall performance has demonstrated that planar and non-planar wall response is distinct. The new data available from the C-shaped wall tests along with data from previous non-planar wall experiments, permitted relationships and observations for the following wall categories to be investigated:

- Cross-sectional shape
- Failure Mode (buckling-rupture, crushing-buckling, and shear-compression)
- Loading in a Symmetric versus Asymmetric Direction
- Uni- versus Bi-directional Loading

For these wall categories, wall response in terms of drift capacity, displacement ductility was investigated with respect to the following parameters:

- Material Properties
- Overall Wall Geometric Properties
- Boundary Element Geometric Properties
- Reinforcement Ratios for Boundary Element and Unconfined Web Region
- Axial Load and Shear Span Ratio
- Shear Capacity-to-Demand and Shear Stress Demand

1.1.2 Impact of Web Reinforcement on Walls with Varying Shear Stress Demands

There was substantial damage noted to the unconfined, lightly-reinforced wall webs of the flanged C-shaped wall tests conducted as part of this research. The C-shaped wall tests exhibited fracture of a majority of vertical reinforcement in the unconfined web, occasional fracture of horizontal reinforcement in this region, and significant concrete degradation in the areas surrounding the damaged reinforcement. Moreover, the review of previous experimental work and in-field earthquake performance of non-planar walls show that this type of damage is more widespread than just the current experimental test program. These poorer-than-expected experimental and in-field results suggest that the minimum *ACI 318* requirements associated with web reinforcement may be insufficient. However, there have been few tests that have isolated vertical and/or

horizontal web reinforcement as the primary variable to investigate their effects on wall deformation and ductility, rather than strength. Furthermore, there are few prior tests where walls are subject to moderate-to-high shear stress demands that more closely represent the upper limit for shear stress allowed by *ACI 318*. As such, the current minimum web reinforcement requirements were studied using an experimentally-validated, high-resolution finite element modelling approach.

The computational parametric study examined the impact of the shear stress demand and web reinforcement ratio on wall deformation and ductility. This study was founded on a slender wall test specimen with a relatively large cross-sectional aspect ratio and high shear stress demand. The simulation wall matrix was parametrized in terms of shear stress demand by selecting values for: the area and steel strength of large-diameter vertical reinforcement located in the wall end-zones, shear span and axial load ratios. The simulation wall matrix was parametrized in terms of horizontal web reinforcement by designing for target shear demand-to-capacity ratios. From this study, wall deformation and ductility was explored to evaluate the impact of the following variables:

- Shear Stress Demand
- Shear Demand-to-Capacity Ratio
- Vertical Web Reinforcement
- Horizontal Web Reinforcement
- Horizontal-to-Vertical Web Reinforcement
- Excess Horizontal Web Reinforcement
- Axial Load Ratio

An additional parameter that was investigated in this parametric study was the influence of boundary element length on wall ductility. A recent investigation conducted on slender planar walls with varying shear stress demands indicated that though increasing shear stress demand negatively affects wall ductility, increasing the boundary element length could improve wall ductility (*Whitman* [173]). Therefore, the current parametric study also explored the difference in response for walls with a ACI compliant boundary element length and extended boundary elements that are the full neutral axis depth.

1.2 Thesis Chapters

Chapter 2 compiles a historic overview of *ACI 318* code-provisions related to structural wall design; presents research results from prior large-scale non-planar wall tests; and summarizes the observed earthquake damage seen in non-planar walls over the last five decades.

Chapter 3 examines results of prior non-planar wall tests and categorizes walls in terms of failure mode, loading in symmetric/asymmetric directions, and bi-directional loading to assess wall deformation, ductility, and response for specific design parameters. Furthermore, this chapter characterizes and assesses non-planar wall damage observed during post-earthquake reconnaissance. These efforts are intended to provide a comprehensive database of experimental and real performance that can inform engineers on the performance of non-planar walls, as they have distinct behavior from planar walls that are largely the basis for *ACI 318* design provisions.

Chapter 4 outlines the objectives and testing details for the three flanged C-shaped wall experiments conducted at the University of Illinois that concluded the testing on the "NEESR-SG Behavior, Analysis, and Design of Complex Wall Systems" project. These tests were conducted by the author and her co-workers. The summary includes specimen design, fabrication, load control and test protocols, as well as instrumentation.

Chapter 5 presents key observations related to damage progression, failure mechanism, and load-deformation response of the three flanged walls introduced in Chapter 4. Additional analysis of sensor data to evaluate differences in wall deformation, ductility, and strength were also conducted. The primary objective is to better understand how load history can impact C-shaped wall response, and more generally how C-shaped wall response compares to planar walls.

Chapter 6 provides a background into the non-linear, three-dimensional finite element modelling approach that was utilized to conduct the parametric study in Chapter 7. Additionally, this chapter introduces the slender wall test used to calibrate a baseline model, and the procedure that was used to calibrate this model.

Chapter 7 describes the parametric study investigating the impact of web reinforcement on the deformation and ductility of walls with varying shear stress demands. The chapter details the design process utilized to develop the simulation wall matrix as well as the simulation results used to assess the relationship between specific design parameters and wall response. This chapter concludes with

design recommendations related to design shear stress demand, shear demand-to-capacity ratio, and boundary element length.

Chapter 8 presents a summary of the research work conducted in this thesis; conclusions in regards to the experimental tests on flange C-shaped walls, the extensive review of prior non-planar wall tests and in-field performance, and the results of the parametric study investigating horizontal web reinforcement ratio and shear stress demand. The chapter concludes with a discussion of future work that would allow the structural wall research community to continue updates to the *ACI 318* structural wall provisions and the performance-based design of walls.

2 LITERATURE REVIEW

2.1 Introduction

Chapter 2 compiles a historic overview of code-provisions related to structural wall design; presents research results from prior large-scale non-planar wall tests; and summarizes the observed earthquake damage seen in non-planar walls over the last five decades. Section 2.2 examines the progression of seismic design provisions for structural walls in *ACI 318: Building Code Requirements for Structural Concrete*, a design standard that currently forms the basis of national building codes for more than twenty-two countries [17]. Section 2.3 introduces the performance-based seismic design philosophy and how this can be applied to reinforced concrete structural walls. Section 2.4 summarizes major experimental tests on slender, non-planar structural walls that have been conducted to date. Finally, Section 2.5 chronicles observed damage to non-planar structural walls in earthquakes ranging over the span of nearly fifty years. As a whole, this chapter is intended to provide a comprehensive basis for later work conducted in Chapter 3.

2.2 Code-Based Design

This section investigates the evolution of seismic design procedures for reinforced concrete shear walls as specified by the *ACI 318: Building Code Requirements for Structural Concrete*. Prior work by Welt [172] focused on the significant changes that have occurred between *ACI 318-11* [16] and *-14* [18] due to structural wall response in New Zealand (2010-2011) and Chile (2010) earthquakes. The current investigation aims to supplement this work by examining the complete historic arc of *ACI 318*. Specific attention will be given to the inception and modification of structural wall provisions as well as the associated rationale contained in *ACI 318R: Commentary* documents. Section 2.2.1 provides a timeline of general design and wall provision changes from codes dating from the early 1900s to the current 2014 standard; Section 2.2.2 contains in-depth examinations of structural wall provisions on a topic-by-topic basis focusing on codes from 1971-2014; and Section 2.2.3 consists of tables that summarize the textual discussion from Section 2.2.2 in a succinct and visual format.

2.2.1 Timeline of Major Design and Wall Provision Changes in ACI 318

The following timeline provides a general history of the *ACI 318* code with a particular focus on how the overall design methodology and structural wall provisions have changed:

- ***1908 National Association of Cement Users (NACU) Report*** [126]– considered the first of the predecessor documents to ACI 318, it did not contain any provisions explicitly for walls only for columns with an aspect ratio ≤ 12.
- ***1910 NACU Standard Building Regulations for the Use of Reinforced Concrete*** [127]– first appearance of provisions explicitly related to walls, including a few notable requirements on maximum spacing and minimum ratio of reinforcement that still remain in *ACI 318-14*.
- ***ACI 318-56 Building Code Requirements for Reinforced Concrete*** [2]– first appearance of ultimate strength design in an appendix. Also, first appearance of provision stating that design of columns/walls should consider stresses from earthquake forces.
- ***ACI 318-63 Building Code Requirements for Reinforced Concrete*** [3]– ultimate strength design was formally adopted into the body of the code, and could be used instead of working stress design. Also, a chapter for empirical design of walls was established; later versions of this chapter (in 1989-2014) were referenced by seismic provisions for shear design of structural walls with $V_u < A_{cv}\sqrt{f_c'}$.
- ***ACI 318-71 Building Code Requirements for Reinforced Concrete*** [4]– working stress design no longer appears in the body of the code; ultimate strength design is now primary design approach and continues to be used in *ACI 318-14*. The 1971 code marks the first appearance of "Special Provisions for Seismic Design" as an appendix. It contains a dedicated section for structural walls which includes requirements for (special) boundary elements. This code references lateral load analysis (equivalent lateral force, ELF, procedure) as the method for determining shear demand due to earthquake forces.
- ***ACI 318-83 Building Code Requirements for Reinforced Concrete*** [7]– as an addition to lateral load analysis (ELF) this code has the first appearance of a smaller reduction factor for V_n to account for shear demand resulting from plastic hinging of the wall. Also, this code contained the first seismic design provisions for calculating V_n of structural walls; the provisions have been consolidated, but otherwise remain unchanged in *ACI 318-14*.
- ***ACI 318(R)-89 Building Code Requirements for Reinforced Concrete and Commentary*** [9]- "Special Provisions for Seismic Design" was formally adopted into the body of the code.
- ***ACI 318(R)-99 Building Code Requirements for Structural Concrete and Commentary*** [12]-

  updates to structural wall provisions include significant changes in the triggers, length, width, and confinement of special boundary elements. Also, first appearance of provisions related to the colloquially-termed "ordinary" boundary elements.

- ***ACI 318(R)-14 Building Code Requirements for Structural Concrete and Commentary*** [18]- considerable re-organization of the code from analysis/design based on behavior to systems and members. Also, updates to structural wall provisions relate to triggers, width, and confinement of boundary elements to avoid failures seen in recent earthquakes.

2.2.2 Examination of Structural Wall Provisions

Section 2.2.2 provides a detailed explanation of the seismic design criteria for structural walls that currently exist in *ACI 318-14* [18] and insight into how these provisions have changed since the *ACI 318-71* [4] introduction of "Appendix A: Special Provisions for Seismic Design". The topics covered in this section include: load factors used to determine demand; strength reduction factors to calculate design strength; as well as requirements for distributed web reinforcement, "special" versus "ordinary" boundary elements, and flanged walls.

2.2.2.1 Load Factors

In *ACI 318-14* (Table 5.3.1) [18] the load combinations that include earthquake demands are: $1.2D + 1.0E + 1.0L + 0.2S$ and $0.9D + 1.0E$ which are taken from *ASCE7-10* (Section 2.3.2) [23]. In these expressions, *D* is dead load, *E* is earthquake load, *L* is live load, and *S* is snow load.

The changes that have occurred to the load factor combinations are as follows:

(1) In *ACI 318-11* (Section 9.2.1) [16] the variable representing loads due to soil or water in soil, *H*, was removed and incorporated into the calculated dead load, *D*.

(2) In *ACI 318-02* (Section 9.2.1) [13] nearly all the load factors changed from the previous code versions. The variable H was added to the load factors such that the two expressions were: $1.2D + 1.0E + 1.0L + 0.2S$ and $0.9D + 1.0E + 1.6H$. Also, an additional note was added in Section 9.2.1(c) that if service-level earthquake forces were utilized, the 1.0E value was to be replaced by 1.4E.

(3) From *ACI 318-71* (Section 9.3.3) [4] to *ACI 318-99* (Section 9.2.3) [12] the load combinations that included earthquake demands were: $1.05D + 1.40E + 1.28L$ or $0.9D + 1.43E$.

The value *E* utilized in *ACI 318-14* (Table 5.3.1) [18] comes from the *ASCE7-10* (Section 12.4) [23] definition of earthquake load as $E = E_h + E_v$ where the earthquake load effect is comprised of horizontal, E_h , and vertical components, E_v . The determination of E_h will be described in further depth in Section 2.2.2.10. In general the earthquake force, *E*, is determined by the *ASCE7-10* [23]

equivalent lateral force procedure, modal response spectrum, or linear/non-linear response history methods.

2.2.2.2 Strength Reduction Factors

2.2.2.2.1 Flexural/Axial Strength Reduction Factors

In *ACI 318-14* [18] the strength reduction factors, ϕ, for special structural walls can be found in Table 21.2.1. The reduction for moment, axial force, or combined moment and axial force has been essentially unchanged since *ACI 318-02* (Section 9.3.2) [13] and ranges from 0.65 to 0.90 for members with ties. These reduction values are based on the strain at the extreme layer of tension reinforcement, ε_t, at nominal flexural strength where the strain in the extreme concrete compression fiber is 0.003. For walls, tension-controlled sections have $\varepsilon_t \geq 0.005$ corresponding to $\phi = 0.90$ and compression-controlled sections have $\varepsilon_t \leq \varepsilon_y$ corresponding to $\phi = 0.65$ (note ε_y is the steel yield strength, which can be taken as 0.002 for Grade 60 rebar). Values of ε_t that fall between these bounds vary by a linear relationship (Table 21.2.2).

Between *ACI 318-77* [5] and *ACI 318-99* [12] (Section 9.3.2, for both), the reduction for axial force or combined moment and axial force ranged from 0.70 to 0.90 for members with ties. Walls with axial tension or no axial compression demand corresponded to $\phi = 0.90$ and walls with an axial compression demand equal to the minimum of $0.10A_g f_c'$ or ϕP_b corresponded to $\phi = 0.70$. Values of axial compression between these bounds vary by a linear relationship.

Despite the transition from calculating the reduction factor using the magnitude of axial load to strain conditions, both approaches described above provide a lower flexural/axial reduction factor for sections that would exhibit less ductility and have greater variability in strength.

2.2.2.2.2 Shear Strength Reduction Factors

In *ACI 318-14* [18], the shear strength reduction factor, ϕ, can be found in Table 21.2.1 and has a value of 0.75 which remains unchanged since *ACI 318-02* (Section 9.3.2.3) [13]. Between *ACI 318-71* (Section 9.3.1.3) [4] and *ACI 318-99* (Section 9.3.2.3) [12], the shear reduction factor had been higher at 0.85. There is no explicit statement in the commentary on the decrease in this reduction factor.

In *ACI 318-14* [18], the shear reduction factor for shear-critical structural walls is further decreased to 0.60 (Section 21.2.4.1); this provision first appeared in *ACI 318-83* (Appendix A.2.3.1) [7]. Shear critical is defined as the instance when the wall's nominal shear capacity is smaller than the shear

demand associated with its nominal moment capacity. This condition can also be thought of as the shear demand resulting from plastic hinging in the wall.

2.2.2.3 Material Properties

2.2.2.3.1 Concrete Material Properties

In *ACI 318-14* [18], the concrete strength requirements for the seismic design of structural walls can be found in Table 19.2.1.1. The specified compressive strength, f_c', of normal-weight concrete must be greater than 3000 psi, while lightweight concrete must be between 3000 and 5000 psi. The strength requirements for normal-weight concrete have remained the same since *ACI 318-71* (Appendix A.3.3) [4]. For light-weight concrete, the range of allowable strengths has been the same since *ACI 318-02* (Section 21.2.4.1) [13].

Between *ACI 318-83* [7] and *ACI 318-99* [12] (Section 21.2.4.1, for both), lightweight concrete had a reduced range from $3000 \leq f_c' \leq 4000$ psi. Starting in *ACI 318R-83* [8], the commentary has indicated that the upper bound on lightweight concrete strength exists since experimental/field data suggests deficiencies in its non-linear hysteretic response. The code does permit higher strength mixes to be used if experimental evidence supports its strength and robustness. Prior to *ACI 318-83* [7] there was no strength limits related to lightweight concrete.

2.2.2.3.2 Steel Material Properties

2.2.2.3.2.1 Flexural/Axial Steel Material Properties

In *ACI 318-14* [18], the material properties for steel reinforcement can be found in Section 20.2.2. Flexural, axial, and shrinkage/temperature steel must not exceed a yield strength, f_y, of 60 ksi and must also meet ASTM A706, Grade 60 or ASTM A625, Grades 40 and 60. With regards to ASTM A625, for Grade 40 items (i) & (ii) and for Grade 60 items (i) & (iii) must be met:

(i) the actual versus specified yield strength does not exceed 18 ksi,
(ii) that the ratio of actual to specified yield strength is greater than or equal to 1.25, and
(iii) a minimum elongation in 8 inches must be between 10-14% based on bar size.

These material property requirements for flexural and axial steel, except for item (iii) in the aforementioned list, have remained essentially unchanged since *ACI 318-83* (Appendix A.2.5.1) [7]. Starting in *ACI 318R-83* [8], the commentary indicated that these requirements exist to limit flexural reinforcement of strengths from being significantly higher than design, which would lead to high

shear/bond stresses and can result in brittle failures; and to ensure a sufficiently long yield region that allows the wall to deform in-elastically.

Prior to 1983, steel strength in the seismic design of structural walls could not exceed f_y of 60 ksi, and the first reference to the ASTM A706 standard appeared in *ACI 318R-77* [6].

2.2.2.3.2.2 Transverse Steel Material Properties

In *ACI 318-14* [18], the maximum specified yield strengths are 100 ksi for lateral support/confinement steel and 60 ksi for shear reinforcement as stated in Table 20.2.2.4a. These requirements have remained unchanged since *ACI 318-08* (Section 21.1.5) [15].

The *ACI 318-05* (Section 21.2.5) [14] code is more generic in its requirement that the yield strength of transverse reinforcement cannot exceed 60 ksi. Codes prior to 2005 indicate that all boundary element reinforcement used in the seismic design of structural walls must comply with the flexural/axial steel requirements described in the previously in Section 2.2.2.3.2.1.

2.2.2.4 Flexural and Shear Capacity

2.2.2.4.1 Calculation of Flexural Capacity

In *ACI 318-14* (Section 22.2) [18], the procedure for calculating nominal flexural capacity involves the plane-sections-remain-plane assumption where the extreme concrete compression fiber has a strain of 0.003. An equivalent rectangular concrete stress block can be used where the concrete compressive stress is $0.85f_c'$ and the height of the stress block is $a = \beta_1 c$. The definition for β_1 can be found in the Table 22.2.2.4.3. Also, concrete is assumed to have no tensile strength and that steel has an elastic, perfectly plastic behavior. Overall, the nominal flexural capacity calculation procedures have remained the same since *ACI 318-71* (Section 10.2) [4], except that the lower bound for $\beta_1 \geq 0.65$ was instated in *ACI 318-77* (Section 10.2) [5].

Also, relevant to the discussion of flexural capacity is the effective stiffness that can be utilized in the elastic analysis of walls. In *ACI 318-14* (Table 6.6.3.1.1(a)) [18] the effective un-cracked wall stiffness is defined as $0.70E_cI_g$ and for cracked as $0.35E_cI_g$. This provision has remained unchanged since *ACI 318-95* (Section 10.11.1) [11]. Prior to that, the effective stiffness was defined more generically (not specifically for walls). From *ACI 318-71* [4] to *ACI 318-92* [10] (Section 10.11.5.2, for both) this could be determined using either of the expressions in Table 2.3.

2.2.2.4.2 Calculation of Shear Capacity

In *ACI 318-14* (Section 18.10.4.1) [18], the nominal shear capacity for the seismic design of structural walls is calculated as $V_n = A_{cv}(\alpha_c \lambda \sqrt{f_c'} + \rho_{v,h} f_y)$, where $h_w/l_w \leq 1.5 \rightarrow \alpha_c = 3.0$, $h_w/l_w \geq 2.0 \rightarrow \alpha_c = 2.0$, and varies linearly in between these values. While the intent of this provision has not changed since *ACI 318-83* [7], there have been slight changes in wording and the fact that separate equations were provided for different wall slenderness values: $A_{cv}\left(\alpha_c \sqrt{f_c'} + \rho_{v,h} f_y\right)$ where $h_w/l_w < 2.0$ and $A_{cv}\left(2\sqrt{f_c'} + \rho_{v,h} f_y\right)$ where $h_w/l_w \geq 2.0$; the definition of α_c is essentially unchanged. In *ACI 318-99* (Section 21.6.4.1) [12], the two equations were consolidated into one.

In *ACI 318-71* (Section 11.6.1 & 11.16) [4] and *ACI 318-77* (Section 11.1.1 & 11.10.9) [5], shear capacity for walls (irrespective of regular or seismic applications) was based on $\phi V_n = \phi(V_c + V_s)$ where $V_c = 2\sqrt{f_c'} bd$ and $V_s = (A_{v,h} f_y d/s_2)$. In these expressions $A_{v,h}$ denotes area of horizontal shear reinforcement within the spacing s_2.

2.2.2.4.3 Shear Capacity Limits

In *ACI 318-14* (Section 18.10.4.4) [18], this shear capacity for multiple walls in a single plane cannot exceed $8A_{cv}\sqrt{f_c'}$, and for an individual wall $V_n \leq 10A_{cw}\sqrt{f_c'}$. This provision has remained unchanged since *ACI 318-83* (Appendix A.7.3.6) [7].

In *ACI 318-71* (Section 11.16.5) [4] and *ACI 318-77* (Section 11.10.3) [5], the shear capacity limit for walls (irrespective or regular or seismic applications) was $V_n \leq 10\sqrt{f_c'} hd$.

**Note: in Section 2.2.2.4.2 and 2.2.2.4.3 the shear capacity calculation procedures and shear capacity limits in *ACI 318-71* [4] were written in terms of stresses, while in *ACI 318-77* [5] they were in terms of force; however, the resultants were the same.

2.2.2.5 Distributed Web Reinforcement

2.2.2.5.1 Minimum Longitudinal and Horizontal Reinforcement Ratios

In general, the minimum distributed shear reinforcement in the web region of the wall is intended to control width of inclined cracking. In *ACI 318-14* (Section 18.10.2.1) [18], both the longitudinal and horizontal **web** reinforcement ratios for the seismic design of structural walls must exceed 0.0025; this language has remained unchanged since *ACI 318-99* [12]. From *ACI 318-83* (Section A.5.2.1) [7] to *ACI 318-95* (Section 21.6.2.1) [11], the provision was identical, but instead referenced **shear**

reinforcement ratios, and *ACI 318-71* [4] to *ACI 318-77* [5] (Appendix A.8.2, for both) more generically referenced **distributed** reinforcement ratios.

ACI 318-14 (Section 18.10.2.1) [18] allows that reinforcement ratios be reduced for low shear demands based on Section 11.6. A similar provision has existed since *ACI 318-89* (Section 21.5.2.1) [9] where the reduction is based on Sections 11.10.9 and 14.3. The reduction is as follows:

(1) If $V_u \leq A_{cv}\lambda\sqrt{f_c'}$ and $V_u \leq 0.5\phi V_c$:

- Longitudinal reinforcement ratio is ≥ 0.0012 for bars $\leq$ #5 bars with $f_y \geq 60$ ksi, and ≥ 0.0015 for all other bars.
- Horizontal reinforcement ratio is ≥ 0.0020 for bars $\leq$ #5 bars with $f_y \geq 60$ ksi, and ≥ 0.0025 for all other bars.

(2) If $V_u \leq A_{cv}\lambda\sqrt{f_c'}$ and $V_u > 0.5\phi V_c$: (for *ACI 318-89* [9] to *ACI 318-11* [16] can also be for $V_u \leq 0.5\phi V_c$)

- Longitudinal reinforcement ratio must be at least the maximum of:

  $$0.0025 + 0.5(2.5 - \frac{h_w}{l_w})(\rho_{v,h} - 0.0025) \text{ and } 0.0025$$

  but does not need to be greater than the horizontal reinforcement ratio except if the wall has $h_w/l_w \leq 2.0$ (where horizontal versus longitudinal reinforcement becomes less effective at carrying the shear demand).
- Horizontal reinforcement ratio should meet the shear strength required for the structural wall (refer to formula in Section 2.2.2.4.2), but be at least 0.0025.

For *ACI 318-71* (Section 11.16.4) [4] to the current *ACI 318-14* [18] code, one could use provisions described in item (2) for the **shear** design of structural walls since it enforces the minimum longitudinal and horizontal reinforcement ratios of 0.0025 from the seismic provisions, and accounts for the amount of horizontal reinforcement required to meet the shear demand. However, for **flexural** design additional requirements for longitudinal reinforcement must be considered.

2.2.2.5.2 Minimum Longitudinal and Horizontal Reinforcement Spacing

In *ACI 318-14* (Section 18.10.2.1), the seismic provisions for structural walls require that distributed longitudinal and horizontal reinforcement must be spaced at less than 18 inches, this requirement has been unchanged since *ACI 318-83* (Appendix A.5.2.1) [8].

Additional spacing requirements can be found in other code sections that address flexural/axial design and shear design of walls, these are summarized below:

(1) Related to flexural/axial design of walls, *ACI 318-71* (Section 10.16) [4] to *ACI 318-11* (Section 14.3.5) [16] has contained spacing requirements for longitudinal and horizontal reinforcement. These values have not changed since *ACI 318-77* (Section 10.15) [5] and are identical for both directions of reinforcement. The spacing must not exceed maximum of: $3b$ or 18 inches.

(2) For shear design of walls, *ACI 318-71* (Section 11.16.4) [4] to *ACI 318-11* (Section 11.9.9) [16] has contained spacing requirements for longitudinal and horizontal reinforcement. The spacing requirements have not changed over the code versions; longitudinal reinforcement spacing must not exceed the maximum of: $l_w/3$, $3b$, or 18 inches and horizontal reinforcement spacing must not exceed the maximum of: $l_w/5$, $3b$, or 18 inches.

It would seem appropriate where the spacing requirements from items (1) or (2) are more restrictive than that found in the seismic provisions, they should take precedence.

2.2.2.5.3 Minimum Layers of Longitudinal and Horizontal Reinforcement

In *ACI 318-14* (Section 18.10.2.2) [18], at least two curtains are required in the seismic design of structural walls if the shear demand is $V_u > 2A_{cv}\lambda\sqrt{f_c}'$ or slenderness ratio is $h_w/l_w \geq 2.0$. The shear demand requirement has remained unchanged since *ACI 318-83* (Appendix A.5.2.2) [7]. It was instated since it is difficult to maintain a single layer of reinforcement at the middle of a wall; furthermore, reinforcement near the wall surface can limit fragmentation of concrete in cases of extensive cracking. The slenderness requirement was added in *ACI 318-14* [18] due to concerns with lateral instability of the compression of slender walls after tensile yielding of longitudinal reinforcement.

From *ACI 318-71* (Section 14.2(g)) [4] to *ACI 318-11* (Section 14.3.4) [16] there was also a requirement for two curtains of reinforcement for walls with a thickness greater than or equal to 10 inches.

2.2.2.6 "Special" Boundary Elements

2.2.2.6.1 Trigger for "Special" Boundary Elements

In *ACI 318-14* (Sections 18.10.6.2-3) [18], the seismic design of structural walls requires a displacement or stress-based approach to determine if the compression zones of walls have to be reinforced with "special" boundary elements. The objective of these provisions is to improve the compressive strength and strain capacity of wall boundaries, so that the entire structural system can remain ductile under severe cyclic loading. The displacement-based approach, in Section 18.10.6.2 is triggered when $c \geq l_w/600(1.5\delta_u/h_w)$ where the ratio δ_u/h_w must exceed 0.005. In this expression, c is the largest neutral axis depth associated with the factored axial load-nominal moment capacity in the direction of the design displacement, δ_u. Note that the allowable drift for reinforced concrete shear wall or dual system structures from *ASCE7-10* (Table 12.12-1) [23] is 2%, which would equate to $0.020h_w$. Alternatively, the stress-based approach in *ACI 318-14* (Section 18.10.6.3) [18] can be utilized where a "special" boundary element is triggered when the maximum extreme concrete compression fiber stress exceeds $0.2f_c'$ for load combinations that consider earthquake effects. Stress should be determined based on E_cI_g (linear-elastic model and gross section properties of the wall).

The two trigger options – displacement and stress-based – for "special" boundary elements have existed since *ACI 318-99* (Section 21.6.6.2(a)) [12]. Of these, only the displacement trigger has changed. Previously it had been $c \geq l_w/600(\delta_u/h_w)$ where the ratio δ_u/h_w must exceed 0.007. The *ACI 318R-14* (R.18.10.6.2) [18] commentary indicates that the multiplier of 1.5 was added to the denominator of this expression to produce wall detailing consistent with a low probability of collapse in a Maximum Considered Earthquake. Furthermore, the δ_u/h_w value was lowered to 0.005 so "special" boundary elements would be required for walls where the boundary longitudinal reinforcement does not reach twice the strain limit associated with tension-controlled beams.

From *ACI 318-83* (Appendix A.5.3.1) [7] to *ACI 318-95* (21.6.6.1) [11], only the stress-based trigger existed and was identical to that found in *ACI 318-14* [18]. Prior to stress-based triggers, in *ACI 318-71* [4] and *ACI 318-77* [5] (Appendix A.8.5, for both), the need for "special" boundary element was determined based on the maximum design axial load on a wall considering earthquake forces, P_e, as a percentage of the axial load capacity of the wall at the balance point, P_b, calculated using E_cI_g. If $P_e > 0.4\phi P_b$ then a "special" boundary element was required (note: the reduction factor, ϕ, only appears in this expression for *ACI 318-77* [5]).

2.2.2.6.2 Dimensions for the Boundary Element

2.2.2.6.2.1 Minimum Height

Minimum height limits exist so that the "special" boundary element extends through the expected region of plastic hinging where there will be considerable tensile yielding of reinforcement and concrete spalling. In *ACI 318-14* [18], when using the displacement-based approach from Section 18.10.6.2, the boundary element must extend a distance from the critical section of the wall that is at least the greater of l_w and $M_u/4V_u$. With the stress-based approach from Section 18.10.6.3, the boundary element can be discontinued when the extreme concrete compressive fiber stress is less than $0.15f_c'$. The minimum height requirement for "special" boundary elements has remained unchanged since *ACI 318-99* (Sections 21.6.6.2-3) [12].

From *ACI 318-83* (Appendix A.5.3.1) [7] to *ACI 318-95* (21.6.6.1) [11], the minimum height was solely based on the stress value of $0.15f_c'$. Earlier code versions do not explicitly define a minimum height requirement.

2.2.2.6.2.2 Minimum Length

In *ACI 318-14* (Section 18.10.6.4(a)) [18], a minimum horizontal length for a "special" boundary element is defined to insure that this confined region extends at least to the location of critical concrete compressive strain. The horizontal length of the boundary element, l_{be} , must extend from the extreme compression fiber of the wall a distance at least the maximum of $c - 0.1l_w$ and $c/2$ (additional provisions for flanged walls are discussed in Section 2.2.2.9). As with the definition for "special" boundary element triggers described in Section 2.2.2.6.1, c is the largest neutral axis depth associated with the factored axial load-nominal moment capacity in the direction of the design displacement, δ_u. These provisions have remained unchanged since *ACI 318-99* (Section 21.6.6.4) [12]. Prior versions of the code did not have explicitly defined minimum length requirements for "special" boundary elements.

2.2.2.6.2.3 Minimum Width

In *ACI 318-14* (Section 18.10.6.4(b-c)) [18], new "special" boundary element width dimensions were defined to insure section stability after spalling of cover concrete in slender walls. This code addition was in response to recent poor earthquake performance of structural walls with slender boundaries. The wall width at the boundary element, b_{be}, should be at least $h_u/16$ and for slender walls ($h_w/l_w \geq 2.0$) that are not tension-controlled ($c/l_w \geq 3/8$) then this width must be greater than or

equal to 12 in. Prior to the current code version, there were no explicit requirements for boundary element width.

2.2.2.6.3 Transverse Reinforcement & Cross-ties

As a general note, the transverse reinforcement provisions for "special" boundary element in walls are consistent with requirements for the seismic design of columns. There are two notable exceptions: (i) omission of one equation related to the area of transverse reinforcement from *ACI 318-99* [12] to *ACI 318-2011* [16], and (ii) modification of one parameter for minimum vertical spacing between transverse reinforcement from *ACI 318-08* [15] to *ACI 318-14* [18]. These will be discussed in further detail in Sections 2.2.2.6.3.3 and 2.2.2.6.3.4, respectively.

2.2.2.6.3.1 Allowable Types

In *ACI 318-14* (Section 18.7.5.2) [18], transverse reinforcement is specified as including individual or overlapping spirals, circular hoops, or rectilinear hoops. For walls, rectilinear hoops are most common. These hoops are used with cross-ties with the same or smaller diameter to provide lateral support to longitudinal reinforcement in the boundary element. Additionally, when cross-ties are utilized they are alternated end-to-end. For the most part, the content of this provision has been consistent since *ACI 318-71* (Appendix A.6.4) [4].

From *ACI 318-89* (Section 21.1) [9] to *ACI 318-14* (Sections 2.2 and 25.7.4) [18] the definitions of seismic hoops and crossties have remained essentially unchanged with respect to hook angle and extension length. These provisions exist to insure that transverse reinforcement provides effective confinement and are sufficiently embedded into the concrete core to avoid unwinding/pop-out during severe loading of the wall. Hoops must have a 135-degree hook and extension of the greater of $6d_b$ and 3 inches. Cross-ties must have one end with ≥135-degree hook and extension that must not be less than the greater of $6d_b$ and 3 inches, while the other end has a ≥90-degree hook and extension that must not be less than $6d_b$. Prior codes required longer extensions for both hoops and cross-ties of $10d_b$, and 180-degree hooks for cross-ties.

2.2.2.6.3.2 Horizontal Position of Transverse Reinforcement

In *ACI 318-14* (Section 18.10.6.4(e)) [18], the horizontal position of laterally supported longitudinal bars, h_x, must not exceed the minimum of 2b/3 or 14 inches. Bars can be laterally supported using the allowable reinforcement types introduced in Section 2.2.2.6.3.1.

From *ACI 318-83* (Appendix A.4.4.3) [7] to *ACI 318-11* (Section 21.6.4.2) [16], the variable h_x had a slightly different definition as the maximum center-to-center horizontal spacing of cross-ties or hoop legs. It was required to be more than 14 inches. (Note: the actual variable name of h_x has also changed over time, here it is used to describe conceptually equivalent terms in various code versions.) Prior to *ACI 318-83* [7], there was no explicit requirement related to horizontal position for hoops/cross-ties in walls.

2.2.2.6.3.3 Area of Transverse Reinforcement

In *ACI 318-14* [18], the minimum amount of transverse reinforcement to avoid bar buckling and provide concrete core confinement is defined in Table 18.10.6.4(f). When using rectilinear hoops (with cross-ties) the area of transverse reinforcement, A_{sh}, in the "special" boundary element must be at least the maximum of: (i) $0.3sb_c\left(\frac{A_g}{A_{ch}}-1\right)\ \frac{f_c\prime}{f_{yt}}$ and (ii) $0.09sb_c\ \frac{f_c\prime}{f_{yt}}$ where $A_g = l_{be}b_{be}$. An important note is that this code version includes the re-instatement of the expression (i) that had been excluded from *ACI 318-99* [12] to *ACI 318-11* [16]. It was believed expression (ii), on its own, does not provide sufficient transverse reinforcement for thin walls that have large concrete cover.

Aside for the temporary omission of the expression (i) for a number of code versions, other relevant changes to be aware of when examining the progression of A_{sh} in Table 2.8, include:

(1) *ACI 318-71*(Appendix A.6.4.3) [4] and *ACI 318-77*(Appendix A.6.5.3) [5]:

- A_{sh} was defined as the area of ONE leg of transverse reinforcement, the expressions included in Table 2.8 reconcile this to be the total area of transverse reinforcement and therefore consistent with recent codes.
- Original expressions for A_{sh} included the variable l_h which was defined as the maximum unsupported length of rectangular hoop between perpendicular legs of hoop or cross-ties. Modifications have been made to the expression to use the current variable b_c associated with the overall cross-sectional dimension of the boundary element core.

(2) *ACI318-83* (Appendix A.4.4.1) [7] to *ACI 318-05* (Section 21.4.4.1(b)) [14]:

- Original expressions for A_{sh} included the variable h_c (or b_c) which was defined as the cross-sectional dimension of the boundary element core from **center-to-center** of the outer legs of transverse reinforcement. Modifications have been made to the expression(s) in Table 2.8 to use the current variable b_c which is measured from **outside edges** of the outer legs of transverse reinforcement.

2.2.2.6.3.4 Vertical Spacing of Transverse Reinforcement

In *ACI 318-14* (Section 18.7.5.3) [18], the vertical spacing between transverse reinforcement is specified for adequate concrete confinement and to restrain longitudinal bar buckling after cover spalling. The provisions require that the spacing not be greater than the minimum of: (i) b/3, (ii) $6d_b$ for the smallest longitudinal bar, and (iii) $4\ in \leq 4 + \left(\frac{14-h_x}{3}\right) \leq 6\ in.$

The current provisions have remained unchanged since *ACI 318-08* (Section 21.6.4.3) [15] when b/4 was replaced by b/3, and d_b was noted as the **smallest** longitudinal bar diameter. Prior to that, major changes occurred in *ACI 318-99* (Section 21.4.4.2) [12] when requirements (ii) and (iii) were added to the existing *ACI 318-83* (Appendix A.4.4.2) [7] provisions requiring that spacing be greater than the minimum of b/4 and 4 inches. From *ACI 318-71* [4] to *ACI 318-77* [5], the only requirement was that the vertical spacing be less than 4 inches.

2.2.2.6.3.5 Vertical Continuation of Transverse Reinforcement into Support

In *ACI 318-14* (Section 18.10.6.4(g)) [18] requires that transverse reinforcement be continued into the wall's support at least a distance of l_d associated with $1.25f_y$ for the largest diameter flexural reinforcement in the boundary element. For walls terminating on a footing or mat the transverse reinforcement must extend at least 12 inches. This provision has remained unchanged since *ACI 318-08* (Section 21.9.6.4(d)) [15]. From *ACI 318-99* (Section 21.6.6.4(d)) [12] and *ACI 318-05* (Section 21.7.6.4(d)) [14], the distance l_d associated with f_y rather than $1.25f_y$; otherwise the provision was the same. Prior to *ACI 318-99* (Section 21.6.6.4(d)) [12] there was no explicit mention of the vertical distance that the transverse reinforcement in the boundary element needed to extend into the wall's support or footing/mat.

2.2.2.6.4 Vertical Reinforcement

In *ACI 318-14 [18]*, there are no explicit requirements on the amount of flexural reinforcement that needs to be contained in the boundary element, so long as the wall as an overall member meets the imposed flexural demands.

However, a minimum vertical reinforcement requirement for the boundary element did exist in *ACI 318-71* [4] and *ACI 318-77* [5] (Appendix A.8.4, for both). If $P_e \leq 0.4\phi P_b$ and the extreme tensile stress in the concrete exceeded 15% of the concrete modulus of rupture ($0.15f_r$) calculated based on $E_c I_g$, then the area of vertical reinforcement had to be at least $\left(200/f_y\right)bd$. The *ACI 318R-77* (Appendix A.8.4) [6] commentary indicates that this provision was intended to prevent brittle

flexural failure in a wall with a low axial load, where the flexural cracking strength may exceed the post-cracking strength.

2.2.2.7 "Ordinary" Boundary Elements

2.2.2.7.1 Comparisons between "Ordinary" and "Special" Boundary Elements

ACI 318-14 (Section 18.10.6.5) [18] defines what is colloquially referred to as "ordinary" boundary element. These regions have a longitudinal reinforcement ratio at the wall boundary that is in excess of $400/f_y$ and where the need for "special" boundary elements was not triggered via the provisions described in Section 2.2.2.6.1. "Ordinary" boundary elements are intended for situations where there is a lower deformation demand on the wall, but ties are necessary to provide lateral support to the longitudinal reinforcement in the wall boundary.

The only condition the remains the same for an "ordinary" boundary element compared to its "special" counterpart is that the horizontal length of the boundary element must extend from the extreme compression fiber of the wall a distance at least the maximum of $c - 0.1l_w$ and $c/2$.

The following provisions are unique to "ordinary" boundary elements:

(1) The cut-off for "ordinary" boundary element height is when the longitudinal reinforcement ratio at the wall boundary is less than $400/f_y$. Above this height, ties are not required.

(2) The horizontal position of laterally supported longitudinal bars, h_x, must not exceed the minimum of 14 inches.

(3) No explicit minimum requirement for area of transverse reinforcement, A_{sh}, is provided.

(4) No explicit minimum requirement for boundary element width , b_{be}, is provided.

(5) The vertical spacing of transverse reinforcement, *s*, varies based on distance from the critical section:
   - Further than the maximum distance of l_w and $M_u/4V_u$ from the critical section: spacing less than the minimum of 8 inches or $8d_b$
   - Otherwise: spacing less than the minimum of 6 inches or $6d_b$

The concept of "ordinary" boundary element was first introduced in *ACI 318-99* (Section 21.6.6.5) [12]. All the aforementioned provisions have remained the same except the vertical spacing of

transverse reinforcement from *ACI 318-99* (Section 21.6.6.5(a)) [12] to *ACI 318-11* (Section 21.9.6.5(a)) [16] could not exceed 8 inches.

2.2.2.8 Axial Load Limits

The *NEHRP Seismic Design Technical Brief No. 6* [134] indicates that the *1997 Uniform Building Code* Section 1921.6.6.4(3) [98] provision limited the axial force to $0.35P_o$; the same axial load limitation is expressed in the *ASCE/SEI 41-06* document [22].

2.2.2.9 Provisions related to Flanged Walls

Considerations for flanged (or, non-planar) structural walls appeared in the *ACI 318-99* [12] code and for the most part have remained the same to the current code version of *ACI 318-14* [18]. The following section summarizes specific provisions that apply because of the presence of flanges, these are in addition to the requirements already described in Section 2.2.2.

2.2.2.9.1 Limitations on Wall Configuration/Shape

There are no explicit limitations on wall configuration/shape.

2.2.2.9.2 Effective Flange Width

In *ACI 318-14* (Section 18.10.5.2) [18], the effective flange width, b_{eff}, is defined as a distance equal to the minimum value of either one-half the distance to an adjacent wall web or 25% of the total wall height, $0.25h_w$. This code provision was first introduced in *ACI 318-99* (Section 21.6.5.2) [12] and has remained unchanged to the current code version.

2.2.2.9.3 Modifications to Boundary Element Dimensions

In *ACI 318-14* (Section 18.10.6.4(d)) [18], the boundary element length for flanged walls is modified such that it includes the thickness of the effective flange, t_f, and extends at least 12 in into the wall web. This code provision was first introduced in *ACI 318-99* (Section 21.6.6.4(b)) [12] and has remained unchanged to the current code version. Extending the boundary element beyond the web-flange intersection insures that this high-stressed region will be well-confined to avoid a local crushing failure.

2.2.2.9.4 Modifications to Vertical Reinforcement

In the *ACI 318-14* [18] code there are no requirements on the amount of flexural reinforcement in the "special" boundary element and consequently none for the "ordinary" boundary element. Though historically there have been requirements for this as described in Section 2.2.2.6.4.

In *ACI 318-14* (Section 18.10.5.1) [18], there is a note that reinforcement in the effective flange width, b_{eff}, is considered effective in resisting flexural demands. This provision has remained unchanged since the *ACI 318-99* (Section 21.6.5.1) [12].

2.2.2.9.5 Modifications to Calculated Wall Capacity

In *ACI 318-14* (Section 18.10) [18] related to special structural walls, there are no explicit indications that the calculated capacity for the wall should be modified based on flange slenderness. However, a sectional analysis considering the wall cross-section including the contribution of the effective width of the flange(s) should be conducted. This has been the consistent approach for determining capacity has existed since *ACI 318-99* (Section 21.6) [12].

2.2.2.10 Considerations for Multi-Directionally Loaded Walls

In *ACI 318R-14* (Section 18.10.6.4) [18] the commentary indicates that the design of "special" boundary elements requires that flanged sections utilize a lateral load consistent with the orthogonal combinations defined in ASCE7. The orthogonal components of the horizontal earthquake demands, E_h , in *ASCE7-10* (Section 12.5) [23] for Seismic Categories C-F, generally, can be designed using the following approaches:

(1) the orthogonal combination procedure where members are designed for 100% of forces for one direction and 30% in the other direction (using equivalent lateral force, model response spectrum or linear response history procedures); or

(2) simultaneous application of orthogonal ground motion where orthogonal pairs of ground motion accelerations are used in linear or non-linear response history procedure.

Prior codes do not explicitly reference the *ASCE7* for how lateral load should be applied to account for multi-directional loading. However, these documents are referenced for the appropriate load factors that accompany earthquake forces in lateral load analysis, as described in Section 2.2.2.1.

2.2.3 Summary Tables

This section contains tables that are intended to summarize the discussion from Section 2.2.2 in a concise and visual format. Including *ACI 318-71* [4], where seismic provisions first appeared, there have been 13 versions of the building code to date that have addressed the seismic design of structural walls. In addition to these, there were also 5 supplementary documents provided between 1973-1980. All 18 of these documents had been closely reviewed in the preparation of the discussion in Section 2.2.2. To condense this information for the reader, the 6 versions provided in the tables (1971, 1983, 1999, 2008, 2011, and 2014) [4, 7, 12, 15, 16, 18] represent the years where the greatest number of changes occurred for the seismic design of structural walls.

As a key to interpreting the following tables:

- Refer to the "List of Symbols" and "List of Reference Figures" located at the preface of this document for a definition of each of the variables or acronyms utilized in the tables.
- The use of inequality signs with a list of options should be interpreted as follows:
  "≤" means the value should be less than or equal to the minimum of the options
  "≥" means the value should be greater than or equal to the maximum of the options
- Red text is used to highlight a provision change from the previous code version.
- Italicized text in parenthesis is used to indicate if a provision change occurred in the years between the 6 versions presented in the tables. For example, "*(changed in 1977)*" might appear with red text in a cell associated with *ACI 318-83* [8] to indicate the change actually occurred in 1977.
- Any empty cell in the table indicates there is no provision associated with the item listed.
- Use of the terms "None", "REMOVED", "Qualifier Removed" indicates that a provision or clarification existed for an item in a previous version of the code and was removed.

Table 2.1: ACI 318 History for Seismic Design of Walls – Factored Load & Strength Reduction Factors (1971-2014)

Design Parameter	1971		1983		1999	
	Code Section	Provision	Code Section	Provision	Code Section	Provision
Factored Load, U	9.3.3	(1) $1.05D + 1.40E + 1.28L$ (2) $0.90D + 1.43E$	9.2.3	(1) $1.05D + 1.40E + 1.28L$ (2) $0.90D + 1.43E$	9.2.3	(1) $1.05D + 1.40E + 1.28L$ (2) $0.90D + 1.43E$
ϕ_f	9.2.1.1-2	$0.70 - 0.90$ increases linearly as P_u decreases from $0.10A_g f_c'$ or P_b (whichever is smaller) to zero	9.3.2	$0.70 - 0.90$ increases linearly as $\phi_f P_n$ decreases from $0.10A_g f_c'$ or $\phi_f P_b$ (whichever is smaller) to zero *(changed in 1977)*	9.3.2	$0.70 - 0.90$ increases linearly as $\phi_f P_n$ decreases from $0.10A_g f_c'$ or $\phi_f P_b$ (whichever is smaller) to zero
ϕ_v	9.3.1.3	0.85	9.3.2.3 and A.2.3.1	0.85 0.6 if $V_n < V_u$ based on M_n	9.3.2.3 and 9.3.4(a)	0.85 0.6 if $V_n < V_u$ based on M_n

Design Parameter	2008		2011		2014	
	Code Section	Provision	Code Section	Provision	Code Section	Provision
Factored Load, U	9.2.1	(1) $1.2D + 1.0E + 1.0L + 0.2S$ (2) $0.9D + 1.0E + 1.6H$ use 1.4E if based on service-level *(changed in 2002)*	9.2.1	(1) $1.2D + 1.0E + 1.0L + 0.2S$ (2) $0.9D + 1.0E +$ use 1.4E if based on service-level	T. 5.3.1	(1) $1.2D + 1.0E + 1.0L + 0.2S$ (2) $0.9D + 1.0E$ Qualifier Removed
ϕ_f	9.3.2	$0.65 - 0.90$ increases linearly as ε_t increases from yield strain to 0.005 *(changed in 2002)*	9.3.2	$0.65 - 0.90$ increases linearly as ε_t increases from yield strain to 0.005	T. 21.2.1	$0.65 - 0.90$ increases linearly as ε_t increases from yield strain to 0.005
ϕ_v	9.3.2.3 and 9.3.4(a)	0.75 0.6 if $V_n < V_u$ based on M_n *(changed in 2002)*	9.3.2.3 and 9.3.4(a)	0.75 0.6 if $V_n < V_u$ based on M_n	T 21.2.1(b) and 21.2.4	0.75 0.6 if $V_n < V_u$ based on M_n

Table 2.2: ACI 318 History for Seismic Design of Walls – Material Properties (1971-2014)

Design Parameter	1971		1983		1999	
	Code Section	Provision	Code Section	Provision	Code Section	Provision
Concrete	A.3.3	$f_c' \geq 3000\ psi$	A.2.4.1 and A.2.4.2	$f_c' \geq 3000\ psi$ and $f_c' \leq 4000\ psi$ for light-weight concrete	21.2.4.1 and 21.2.4.2	$f_c' \geq 3000\ psi$ and $f_c' \leq 4000\ psi$ for light-weight concrete
Flexural/ Axial Steel	A.3.3	$f_y \leq 60000\ psi$	A.2.5.1	1. ASTM A 706; or 2. ASTM A 615 (Gr. 40 and 60) if: (a) $f_{y,actual} \leq f_y + 18000psi$ (b) $f_{u,actual}/f_u \geq 1.25$	21.2.5	1. ASTM A 706; or 2. ASTM A 615 (Gr. 40 and 60) if: (a) $f_{y,actual} \leq f_y + 18000psi$ (b) $f_{u,actual}/f_u \geq 1.25$
Transverse Steel	implied by A.3.3	Reinf. in wall boundary elements should comply with the above listed axial/flexural steel reqm'ts	A.2.5.1	Reinf. in wall boundary elements should comply with the above listed axial/flexural steel reqm'ts	21.2.5	Reinf. in wall boundary elements should comply with the above listed axial/flexural steel reqm'ts

Design Parameter	2008		2011		2014	
	Code Section	Provision	Code Section	Provision	Code Section	Provision
Concrete	21.2.4.2 and 21.2.4.3	$f_c' \geq 3000\ psi$ and $f_c' \leq 5000\ psi$ light-weight conc *(changed in 2002)*	21.2.4.2 and 21.2.4.3	$f_c' \geq 3000\ psi$ and $f_c' \leq 5000\ psi$ for light-weight concrete	T. 19.2.1.1	$f_c' \geq 3000\ psi$ normal-weight and $3000 \leq f_c' \leq 5000\ psi$ for light-weight concrete
Flexural/ Axial Steel	21.2.5.2	1. ASTM A 706; or 2. ASTM A 615 (Gr. 40 and 60) if: (a) $f_{y,actual} \leq f_y + 18000psi$ (b) $f_{u,actual}/f_u \geq 1.25$	21.2.5.2	1. ASTM A 706 (Gr. 60) ; or 2. ASTM A 615 (Gr. 40 and 60) if: (a) $f_{y,actual} \leq f_y + 18000psi$ (b) $f_{u,actual}/f_u \geq 1.25$	20.2.2.5	1. ASTM A 706 (Gr. 60) ; or 2. ASTM A 615 (Gr. 40 if a&b met or Gr 60 if a & c met) : (a) $f_{y,actual} \leq f_y + 18000psi$ (b) $f_{u,actual}/f_{u,} \geq 1.25$ (c) Min. elong over 8 inches is 10-14% based on bar size
Transverse Steel	21.1.5.4 and 21.1.5.5	$f_{yt} \leq 100{,}000\ psi$ for confine. $f_{yt} \leq 60{,}000\ psi$ for shear bars *(in 2005, $f_{yt} \leq 60{,}000\ psi$ all bars)*	21.1.5.4 and 21.1.5.5	$f_{yt} \leq 100{,}000\ psi$ for confine. $f_{yt} \leq 60{,}000\ psi$ for shear bars	T. 20.2.2.4(a)	$f_{yt} \leq 100{,}000\ psi$ for confine. $f_{yt} \leq 60{,}000\ psi$ for shear bars

Table 2.3: ACI 318 History for Seismic Design of Walls – Flexural Analysis/Design (1971-2014)

Design Parameter	1971		1983		1999	
	Code Section	Provision	Code Section	Provision	Code Section	Provision
ε_{cu} & f_c	10.2.3 and 10.2.7	0.003 and $0.85f_c'$	10.2.3 and 10.2.7.1	0.003 and $0.85f_c'$	10.2.3 and 10.2.7.1	0.003 and $0.85f_c'$
β_1	10.2.7	$f_c' \le 4000psi, \beta_1 = 0.85$ otherwise $\beta_1 = 0.85 - \frac{(f_c' - 4000)}{1000} \times 0.05$	10.2.7.3	$f_c' \le 4000psi, \beta_1 = 0.85$ otherwise $\beta_1 = 0.85 - \frac{(f_c' - 4000)}{1000} \times 0.05$ where $\beta_1 \ge 0.65$ *(changed in 1977)*	10.2.7.3	$f_c' \le 4000psi, \beta_1 = 0.85$ otherwise $\beta_1 = 0.85 - \frac{(f_c' - 4000)}{1000} \times 0.05$ where $\beta_1 \ge 0.65$
EI_{eff}	10.11.5.2	$\frac{E_c I_g/5 + E_{se} I_{se}}{1 + \beta_d}$ or, $\frac{E_c I_g/2.5}{1 + \beta_d}$	10.11.5.2	$\frac{E_c I_g/5 + E_{se} I_{se}}{1 + \beta_d}$ or, $\frac{E_c I_g/2.5}{1 + \beta_d}$	10.11.1	Uncracked: $0.70E_c I_g$ Cracked: $0.35E_c I_g$ *(changed in 1995)*

Design Parameter	2008		2011		2014	
	Code Section	Provision	Code Section	Provision	Code Section	Provision
ε_{cu} & f_c	10.2.3 and 10.2.7.1	0.003 and $0.85f_c'$	10.2.3 and 10.2.7.1	0.003 and $0.85f_c'$	22.2.2.1 and 22.2.2.4.1	0.003 and $0.85f_c'$
β_1	10.2.7.3	$f_c' \le 4000psi, \beta_1 = 0.85$ otherwise $\beta_1 = 0.85 - \frac{(f_c' - 4000)}{1000} \times 0.05$ where $\beta_1 \ge 0.65$	10.2.7.3	$f_c' \le 4000psi, \beta_1 = 0.85$ otherwise $\beta_1 = 0.85 - \frac{(f_c' - 4000)}{1000} \times 0.05$ where $\beta_1 \ge 0.65$	10.2.7.3	$2500 \le f_c' \le 4000\ \ si, \beta_1 = 0.85$ $4000 < f_c' < 8000\ \ si,$ $\beta_1 = 0.85 - \frac{(f_c' - 4000)}{1000} \times 0.05$ $f_c' \ge 8000psi,\ \beta_1 \ge 0.65$
EI_{eff}	10.10.4.1	Uncracked: $0.70E_c I_g$ Cracked: $0.35E_c I_g$	10.10.4.1	Uncracked: $0.70E_c I_g$ Cracked: $0.35E_c I_g$	T. 6.6.3.1.1(a)	Uncracked: $0.70E_c I_g$ Cracked: $0.35E_c I_g$

Table 2.4: ACI 318 History for Seismic Design of Walls - General Shear Analysis/Design (1971-1999)

Design Parameter	1971		1983		1999	
	Code Section	Provision	Code Section	Provision	Code Section	Provision
Shear Design Basis	A.8.1 and A8.5.1	Not explicit. But seems to imply lateral load analysis with factored loads.	A.7.1.2	V_u should be obtained by lateral load analysis using factored loads and load combinations from Section 9.2-3	21.6.3	V_u should be obtained by lateral load analysis using factored loads and load combinations from Section 9.2-3
d	11.16.1	$= max$ { $0.8l_w$; d from PRSP }	11.10.4	$= max$ { $0.8l_w$; d from PRSP }	11.10.4	$= max$ { $0.8l_w$; d from PRSP }
α_c			A.7.3.3	varies linearly between: $h_w/l_w = 1.5, \alpha_c = 3.0$ $h_w/l_w = 2.0, \alpha_c = 2.0$	21.6.4.1	$h_w/l_w \leq 1.5, \alpha_c = 3.0$ $h_w/l_w \geq 2.0, \alpha_c = 2.0$ varies linearly between $h_w/l_w = 1.5 - 2.0$
V_n	implied by 11.6.1	$v_c + v_s$ where $v_s = \frac{A_{v,h} f_y}{bs_2}$ (stress)	A.7.3.2 or A.7.3.3	$A_{cv}\left(2\sqrt{f_c'} + \rho_{v,h} f_y\right)$ where $h_w/l_w \geq 2.0$ $A_{cv}\left(\alpha_c\sqrt{f_c'} + \rho_{v,h} f_y\right)$ where $h_w/l_w < 2.0$	21.6.4.1	REMOVED $A_{cv}\left(\alpha_c\sqrt{f_c'} + \rho_{v,h} f_y\right)$ Qualifier Removed
V_c	11.16.2	$2\sqrt{f_c'}$ (shear stress)	11.10.5	$2\sqrt{f_c'}bd$	11.10.5	$2\sqrt{f_c'}bd$
Shear Limit(s)	11.16.5	$v_n \leq 10\sqrt{f_c'}$ (stress on individual wall)	A.7.3.6	$V_n \leq 8A_{cv}\sqrt{f_c'}$ (all walls) $V_n \leq 10A_{cw}\sqrt{f_c'}$ (individual wall)	21.6.4.4	$V_n \leq 8A_{cv}\sqrt{f_c'}$ (all walls) $V_n \leq 10A_{cw}\sqrt{f_c'}$ (individual wall)
# of Reinf. Layers	14.2(g)	2 layers for each direction, if b ≥ 10 *in*	14.3.4 and/or A.5.2.2	2 layers for each direction, if b ≥ 10 *in* and/or ≥ 2 layers if $V_u > 2A_{cv}\sqrt{f_c'}$	14.3.4 and 21.6.2.2	2 layers for each direction, if b ≥ 10 *in* and/or ≥ 2 layers if $V_u > 2A_{cv}\sqrt{f_c'}$

Additional note: Provisions in *ACI 318-77* identical to *ACI 318-71* except they are expressed in force rather than stress.

Table 2.4 cont'd: ACI 318 History for Seismic Design of Walls - General Shear Analysis/Design (2008-2014)

Design Parameter	2008		2011		2014	
	Code Section	Provision	Code Section	Provision	Code Section	Provision
Shear Design Basis	21.9.3	V_u should be obtained by lateral load analysis using factored loads and load combinations from Section 9.2-3	21.9.3	V_u should be obtained by lateral load analysis using factored loads and load combinations from Section 9.2-3	18.10.3	V_u should be obtained by lateral load analysis using factored loads and load combinations from Chaps. 5 & 21
d	11.9.4	$= max$ { $0.8l_w$; d from PRSP }	11.9.4	$= max$ { $0.8l_w$; d from PRSP }	11.5.4.2	$= max$ { $0.8l_w$; d from PRSP }
α_c	21.9.4.1	$h_w/l_w \leq 1.5, \alpha_c = 3.0$ $h_w/l_w \geq 2.0, \alpha_c = 2.0$ varies linearly between $h_w/l_w = 1.5 - 2.0$	21.9.4.1	$h_w/l_w \leq 1.5, \alpha_c = 3.0$ $h_w/l_w \geq 2.0, \alpha_c = 2.0$ varies linearly between $h_w/l_w = 1.5 - 2.0$	18.10.4.1	$h_w/l_w \leq 1.5, \alpha_c = 3.0$ $h_w/l_w \geq 2.0, \alpha_c = 2.0$ varies linearly between $h_w/l_w = 1.5 - 2.0$
V_n	21.9.4.1	$A_{cv}\left(\alpha_c \lambda \sqrt{f_c'} + \rho_{v,h} f_y\right)$	21.9.4.1	$A_{cv}\left(\alpha_c \lambda \sqrt{f_c'} + \rho_{v,h} f_y\right)$	18.10.4.1	$A_{cv}\left(\alpha_c \lambda \sqrt{f_c'} + \rho_{v,h} f_y\right)$
V_c	11.9.5	$2\lambda\sqrt{f_c'}bd$	11.9.5	$2\lambda\sqrt{f_c'}bd$	11.5.4.5	$2\lambda\sqrt{f_c'}bd$
Shear Limit(s)	21.9.4.4	$V_n \leq 8A_{cv}\sqrt{f_c'}$ (all walls) $V_n \leq 10A_{cw}\sqrt{f_c'}$ (individual wall)	21.9.4.4	$V_n \leq 8A_{cv}\sqrt{f_c'}$ (all walls) $V_n \leq 10A_{cw}\sqrt{f_c'}$ (individual wall)	18.10.4.4	$V_n \leq 8A_{cv}\sqrt{f_c'}$ (all walls) $V_n \leq 10A_{cw}\sqrt{f_c'}$ (individual wall)
# of Reinf. Layers	14.3.4 and 21.9.2.2	2 layers for each direction, if b ≥ 10 *in* and/or ≥ 2 layers if $V_u > 2A_{cv}\sqrt{f_c'}$	14.3.4 and 21.9.2.2	2 layers for each direction, if b ≥ 10 *in* and/or ≥ 2 layers if $V_u > 2A_{cv}\sqrt{f_c'}$	18.10.2.2	REMOVED ≥ 2 layers if $V_u > 2A_{cv}\sqrt{f_c'}$ or $h_w/l_w \geq 2.0$

Additional note: Provisions in *ACI 318-77* identical to *ACI 318-71* except they are expressed in force rather than stress.

Table 2.5: ACI 318 History for Seismic Design of Walls – Shear Design for Low Shear Demand Level (1971-1999)

Provisions apply for $V_u < A_{cv}\lambda\sqrt{f_c'}$ AND $V_u < \frac{\phi_v V_c}{2}$

Design Parameter	1971		1983		1999	
	Code Section	Provision	Code Section	Provision	Code Section	Provision
$\rho_{web,l}$	A.8.2	≥ 0.0025	A.5.2.1	≥ 0.0025	14.3.2	≥ 0.0012 for $\leq$ #5 bar with $f_c' \geq 60ksi$ ≥ 0.0015 for other bars
$\rho_{web,h}$	A.8.2	≥ 0.0025	A.5.2.1	≥ 0.0025	14.3.3	≥ 0.0020 for $\leq$ #5 bar with $f_c' \geq 60ksi$ ≥ 0.0025 for other bars
s_1	10.16.3	$\leq$ min($3b$, 18")	14.3.5 and A.5.2.1*	$\leq$ min($3b$, 18"*)	14.3.5 and 21.6.2.1*	$\leq$ min($3b$, 18"*)
s_2	10.16.6	$\leq$ min($1.5b$, 18")	14.3.5 and A.5.2.1*	$\leq$ min($3b$, 18"*) *(changed in 1977)*	14.3.5 and 21.6.2.1*	$\leq$ min($3b$, 18"*)

Design Parameter	2008		2011		2014	
	Code Section	Provision	Code Section	Provision	Code Section	Provision
$\rho_{web,l}$	14.3.2	≥ 0.0012 for $\leq$ #5 bar with $f_c' \geq 60ksi$ ≥ 0.0015 for other bars	14.3.2	≥ 0.0012 for $\leq$ #5 bar with $f_c' \geq 60ksi$ ≥ 0.0015 for other bars	T 11.6.1	≥ 0.0012 for $\leq$ #5 bar with $f_c' \geq 60ksi$ ≥ 0.0015 for other bars
$\rho_{web,h}$	14.3.3	≥ 0.0020 for $\leq$ #5 bar with $f_c' \geq 60ksi$ ≥ 0.0025 for other bars	14.3.3	≥ 0.0020 for $\leq$ #5 bar with $f_c' \geq 60ksi$ ≥ 0.0025 for other bars	T 11.6.1	≥ 0.0020 for $\leq$ #5 bar with $f_c' \geq 60ksi$ ≥ 0.0025 for other bars
s_1	14.3.5 and 21.9.2.1*	$\leq$ min($3b$, 18"*)	14.3.5 and 21.9.2.1*	$\leq$ min($3b$, 18"*)	18.10.2.1*	$\leq$ 18"* Other reqs. not referenced
s_2	14.3.5 and 21.9.2.1*	$\leq$ min($3b$, 18"*)	14.3.5 and 21.9.2.1*	$\leq$ min($3b$, 18"*)	18.10.2.1*	$\leq$ 18"* Other reqs. not referenced

* = Spacing provision also found in Special Provision for the Seismic Design of Structural Walls

Table 2.6: ACI 318 History for Seismic Design of Walls – Shear Design for Higher Shear Demand Level (1971-1999)

Provisions apply for two cases: $V_u < A_{cv}\lambda\sqrt{f_c'}$ AND $V_u \geq \frac{\phi_v V_c}{2}$ **(OR)** $V_u \geq A_{cv}\lambda\sqrt{f_c'}$

Design Parameter	1971		1983		1999	
	Code Section	Provision	Code Section	Provision	Code Section	Provision
A_{vh}	11.6.1 and 11.16.1-2	$\geq \frac{(v_n - v_c)bs_2}{f_y}$ (in terms of shear stresses) where $v_n = \frac{V_u}{\phi_v bd}$ and $v_c = 2\sqrt{f_c'}$	7.3.2 or 3 and 11.1.1	$\geq \frac{V_s\, b\, s_2}{A_{cv} f_y}$ where $V_s = \frac{V}{\phi_v} - A_{cv}\alpha_c\sqrt{f_c'}$ (α_c replaced by 2.0 when $h_w/l_w \geq 2.0$)	21.6.4.1 and 11.1.1	$\geq \frac{V_s\, b\, s_2}{A_{cv} f_y}$ where $V_s = \frac{V_u}{\phi_v} - A_{cv}\alpha_c\sqrt{f_c'}$ Qualifier Removed
$\rho_{web,l}$	11.16.4.2	$\geq$ { $0.0025 + 0.5(2.5 - \frac{h_w}{l_w})(\rho_{v,h} - 0.0025)$; 0.0025** } and $\rho_{web,l} \leq \rho_{web,h}$	11.10.9.4 and A.7.3.5	$\geq$ { $0.0025 + 0.5(2.5 - \frac{h_w}{l_w})(\rho_{web,h} - 0.0025)$; 0.0025** } and $\rho_{web,l} \leq \rho_{web,h}$ except if $h_w/l_w \leq 2.0$ then $\rho_{web,l} \geq \rho_{web,h}$	11.10.9.4 and 21.6.4.3	$\geq$ { $0.0025 + 0.5(2.5 - \frac{h_w}{l_w})(\rho_{web,h} - 0.0025)$; 0.0025** } and $\rho_{web,l} \leq \rho_{web,h}$ except if $h_w/l_w \leq 2.0$ then $\rho_{web,l} \geq \rho_{web,h}$
$\rho_{web,h}$	11.6.1 and 11.16.4.1	$\geq$ { $\frac{A_{vh}}{bs_2}$; 0.0025** }	11.10.9.1 and 11.10.9.2	$\geq$ { $\frac{A_{vh}}{bs_2}$; 0.0025** }	11.10.9.1 and 11.10.9.2	$\geq$ { $\frac{A_{vh}}{bs_2}$; 0.0025** }
s_1	11.16.4.2	$\leq$ { $l_w/3$; $3b$; 18" }	11.10.9.5 and A.5.2.1*	$\leq$ { $l_w/3$; $3b$; 18"* }	11.10.9.5 and 21.6.2.1*	$\leq$ { $l_w/3$; $3b$; 18"* }
s_2	11.16.4.1	$\leq$ { $l_w/5$; $3b$; 18" }	11.10.9.3 and A.5.2.1*	$\leq$ { $l_w/5$; $3b$; 18"* }	11.10.9.3 and 21.6.2.1*	$\leq$ { $l_w/5$; $3b$; 18"* }

* = Spacing provision also found in Special Provision for the Seismic Design of Structural Walls

** = Minimum reinforcement provision also found in Special provision for the Seismic Design of Structural Walls

Additional note: Provisions in *ACI 318-77* identical to *ACI 318-71* except they are expressed in force rather than stress.

Table 2.6 cont'd: ACI 318 History for Seismic Design of Walls – Shear Design for Higher Shear Demand Level (2008-2014)

Provisions apply for two cases: $V_u < A_{cv}\lambda\sqrt{f_c'}$ AND $V_u \geq \frac{\phi_v V_c}{2}$ **(OR)** $V_u \geq A_{cv}\lambda\sqrt{f_c'}$

Design Parameter	2008		2011		2014	
	Code Section	Provision	Code Section	Provision	Code Section	Provision
A_{vh}	21.9.4.1 and 11.1.1	$\geq \frac{V_s\, b\, s_2}{A_{cv} f_y}$ where $V_s = \frac{V}{\phi_v} - A_{cv}\alpha_c\sqrt{f_c'}$	21.9.4.1 and 11.1.1	$\geq \frac{V_s\, b\, s_2}{A_{cv} f_y}$ where $V_s = \frac{V}{\phi_v} - A_{cv}\alpha_c\sqrt{f_c'}$	18.10.4.1 and 22.5.1.1	$\geq \frac{V_s\, b\, s_2}{A_{cv} f_y}$ where $V_s = \frac{V}{\phi_v} - A_{cv}\alpha_c\sqrt{f_c'}$
$\rho_{web,l}$	11.9.9.4 and 21.9.4.3	$\geq \begin{cases} 0.0025 + 0.5(2.5 - \frac{h_w}{l_w})(\rho_{web,h} - 0.0025) \\ 0.0025^{**} \end{cases}$ and $\rho_{web,l} \leq \rho_{web,h}$ except if $h_w/l_w \leq 2.0$ then $\rho_{web,l} \geq \rho_{web,h}$	11.9.9.4 and 21.9.4.3	$\geq \begin{cases} 0.0025 + 0.5(2.5 - \frac{h_w}{l_w})(\rho_{web,h} - 0.0025) \\ 0.0025^{**} \end{cases}$ and $\rho_{web,l} \leq \rho_{web,h}$ except if $h_w/l_w \leq 2.0$ then $\rho_{web,l} \geq \rho_{web,h}$	11.6.2(a) and 18.10.4.3	$\geq \begin{cases} 0.0025 + 0.5(2.5 - \frac{h_w}{l_w})(\rho_{web,h} - 0.0025) \\ 0.0025^{**} \end{cases}$ and $\rho_{web,l} \leq \rho_{web,h}$ except if $h_w/l_w \leq 2.0$ then $\rho_{web,l} \geq \rho_{web,h}$
$\rho_{web,h}$	11.9.9.1 and 11.9.9.2	$\geq \begin{cases} \frac{A_{vh}}{b s_2} \\ 0.0025^{**} \end{cases}$	11.9.9.1 and 11.9.9.2	$\geq \begin{cases} \frac{A_{vh}}{b s_2} \\ 0.0025^{**} \end{cases}$	11.6.2(b)	$\geq \begin{cases} \frac{A_{vh}}{b s_2} \\ 0.0025^{**} \end{cases}$
s_1	11.9.9.5 and 21.6.2.1*	$\leq \begin{cases} l_w/3 \\ 3b \\ 18"^{*} \end{cases}$	11.9.9.5 and 21.9.2.1*	$\leq \begin{cases} l_w/3 \\ 3b \\ 18"^{*} \end{cases}$	18.10.2.1*	$\leq$ 18"* Other reqs. not referenced
s_2	11.9.9.3 and 21.9.2.1*	$\leq \begin{cases} l_w/5 \\ 3b \\ 18"^{*} \end{cases}$	11.9.9.3 and 21.9.2.1*	$\leq \begin{cases} l_w/5 \\ 3b \\ 18"^{*} \end{cases}$	18.10.2.1*	$\leq$ 18"* Other reqs. not referenced

* = Spacing provision also found in Special Provision for the Seismic Design of Structural Walls

** = Minimum reinforcement provision also found in Special provision for the Seismic Design of Structural Walls

Table 2.7: ACI 318 History for Seismic Design of Walls – "Ordinary" Boundary Element (1971-1999)

Design Parameter	1971		1983		1999	
	Code Section	Provision	Code Section	Provision	Code Section	Provision
Trigger					21.6.6.5(a)	$\rho_{BE,l} > 400/f_y$ at wall boundary
l_{be}					21.6.6.4(a)	$\geq \begin{cases} c - 0.1l_w \\ c/2 \end{cases}$
b_{be}						
h_{be}					implied by 21.6.6.5(a)	BE discontinued at section where $\rho_{BE,l} \leq 400/f_y$ at wall boundary
A_{sh}						
s					21.6.6.5(a)	$\leq 8"$
h_x					21.4.4.3	$\leq 14"$

Table 2.7 cont'd: ACI 318 History for Seismic Design of Walls – "Ordinary" Boundary Element (2008-2014)

Design Parameter	2008		2011		2014	
	Code Section	Provision	Code Section	Provision	Code Section	Provision
Trigger	21.9.6.5(a)	$\rho_{BE,l} > 400/f_y$ at wall boundary	21.9.6.5(a)	$\rho_{BE,l} > 400/f_y$ at wall boundary	18.10.6.5.(a)	$\rho_{BE,l} > 400/f_y$ at wall boundary
l_{be}	21.9.6.4(a)	$\geq \begin{cases} c - 0.1l_w \\ c/2 \end{cases}$	21.9.6.4(a)	$\geq \begin{cases} c - 0.1l_w \\ c/2 \end{cases}$	18.10.6.4(a)	$\geq \begin{cases} c - 0.1l_w \\ c/2 \end{cases}$
b_{be}						
h_{be}	implied by 21.9.6.5(a)	BE discontinued at section where $\rho_{BE,l} \leq 400/f_y$ at wall boundary	implied by 21.9.6.5(a)	BE discontinued at section where $\rho_{BE,l} \leq 400/f_y$ at wall boundary	implied by 18.10.6.5(a)	BE discontinued at section where $\rho_{BE,l} \leq 400/f_y$ at wall boundary
A_{sh}						
s	21.9.6.5(a)	$\leq 8"$	21.9.6.5(a)	$\leq 8"$	18.10.6.5.(a)	$\leq \min(8", 8d_b)$ if above height for $\max(l_w, M_u/4V_u)$, otherwise use $\leq \min(6", 6d_b)$
h_x	21.6.4.2	$\leq 14"$	21.6.4.2	$\leq 14"$	18.7.5.2(e)	$\leq 14"$

Table 2.8: ACI 318 History for Seismic Design of Walls – "Special" Boundary Element (1971-1999)

Design Parameter	1971		1983		1999	
	Code Section	Provision	Code Section	Provision	Code Section	Provision
Trigger	A.8.5	$P_e > 0.4\phi P_b$ based on $E_c I_g$ varies from $\phi = 0.70$ - 0.90 *(red =changes in 1977)*	A.5.3.1	$f_c > 0.2 f_c'$ based on $E_c I_g$	21.6.6.2(a) OR 21.6.6.3	$c \geq l_w/600(\delta_u/h_w)$ where $\delta_u/h_w \geq 0.007$ OR $f_c > 0.2 f_c'$ based on $E_c I_g$
l_{be}					21.6.6.4(a)	$\geq \begin{cases} c - 0.1 l_w \\ c/2 \end{cases}$
b_{be}						
h_{be}			A.5.3.1	BE discontinued at section where $f < 0.15 f_c'$ based on $E_c I_g$	21.6.6.2(b) OR 21.6.6.3	BE discontinued at section for: 21.6.6.2(a): $\geq \max(l_w, M_u/4V_u)$ 21.6.6.3: $f_c < 0.15 f_c'$ based on $E_c I_g$
A_{sh} (rect. ties)	A.6.4.3	$\geq \begin{cases} 0.225 s(b_c + h_x)\left(\frac{A_g}{A_{ch}} - 1\right) \frac{f_c'}{f_{yt}} \\ 0.06 s(b_c + h_x) \frac{f_c'}{f_{yt}} \end{cases}$	A.4.4.1	$\geq \begin{cases} 0.3 s(b_c - d_t)\left(\frac{A_g}{A_{ch}} - 1\right) \frac{f_c'}{f_{yt}} \\ 0.12 s(b_c - d_t) \frac{f_c'}{f_{yt}} \end{cases}$	21.4.4.1(b)	$\geq \begin{cases} \text{Removed} \\ 0.09 s(b_c - d_t) \frac{f_c'}{f_{yt}} \end{cases}$ *(0.12 →0.09 changed in 1989)*
s	A.6.4.3	$\leq 4"$	A.4.4.2	$\leq \begin{cases} b/4 \\ 4" \end{cases}$	21.4.4.2	$\leq \begin{cases} b/4 \\ 6 d_b \\ 4" \leq 4 + \left(\frac{14 - h_x}{3}\right) \leq 6 \end{cases}$
h_x		None	A.4.4.3	$\leq 14"$	21.4.4.3	$\leq 14"$

Table 2.8 cont'd: ACI 318 History for Seismic Design of Walls – "Special" Boundary Element (2008-2014)

Design Parameter	2008		2011		2014	
	Code Section	Provision	Code Section	Provision	Code Section	Provision
Trigger	21.9.6.2(a) OR 21.9.6.3	$c \geq l_w/600(\delta_u/h_w)$ where $\delta_u/h_w \geq 0.007$ OR $f_c > 0.2f_c'$ based on E_cI_g	21.9.6.2(a) OR 21.9.6.3	$c \geq l_w/600(\delta_u/h_w)$ where $\delta_u/h_w \geq 0.007$ OR $f_c > 0.2f_c'$ based on E_cI_g	18.10.6.2(a) OR 18.10.6.3	$c \geq l_w/600(1.5\delta_u/h_w)$ where $\delta_u/h_w \geq 0.005$ OR $f_c > 0.2f_c'$ based on E_cI_g
l_{be}	21.9.6.4(a)	$\geq \begin{cases} c - 0.1l_w \\ c/2 \end{cases}$	21.9.6.4(a)	$\geq \begin{cases} c - 0.1l_w \\ c/2 \end{cases}$	18.10.6.4(a)	$\geq \begin{cases} c - 0.1l_w \\ c/2 \end{cases}$
b_{be}					18.10.6.4(b-c)	$\geq \begin{cases} h_u/16 \\ 12" \text{ if } h_w/l_w \geq 2.0 \ \& \ c/l_w \geq 3/8 \end{cases}$
h_{be}	21.9.6.2(b) OR 21.9.6.3	BE discontinued at section for: 21.9.6.2(a): $\geq \max(l_w, M_u/4V_u)$ 21.9.6.3: $f_c < 0.15f_c'$ based on E_cI_g	21.9.6.2(b) OR 21.9.6.3	BE discontinued at section for: 21.9.6.2(a): $\geq \max(l_w, M_u/4V_u)$ 21.9.6.3: $f_c < 0.15f_c'$ based on E_cI_g	18.10.6.2(b) OR 18.10.6.3	BE discontinued at section for: 18.10.6.2(a): $\geq \max(l_w, M_u/4V_u)$ * 18.10.6.3: $f_c < 0.15f_c'$ based on E_cI_g
A_{sh} (rect. ties)	21.6.4.4(b)	$\geq 0.09sb_c\frac{f_c'}{f_{yt}}$	21.6.4.4(b)	$\geq 0.09sb_c\frac{f_c'}{f_{yt}}$	18.10.6.4(f)	$\geq \begin{cases} 0.3sb_c\left(\frac{A_g}{A_{ch}} - 1\right)\frac{f_c'}{f_{yt}} \\ 0.09sb_c\frac{f_c'}{f_{yt}} \end{cases}$
s	21.6.4.3	$\leq \begin{cases} b/3 \\ 6d_b \text{ of smallest longitudinal bar} \\ 4" \leq 4 + \left(\frac{14 - h_x}{3}\right) \leq 6" \end{cases}$	21.6.4.3	$\leq \begin{cases} b/3 \\ 6d_b \text{ of smallest longitudinal bar} \\ 4" \leq 4 + \left(\frac{14 - h_x}{3}\right) \leq 6" \end{cases}$	18.7.5.3	$\leq \begin{cases} b/3 \\ 6d_b \text{ of smallest longitudinal bar} \\ 4" \leq 4 + \left(\frac{14 - h_x}{3}\right) \leq 6" \end{cases}$
h_x	21.6.4.2	$\leq 14"$	21.6.4.2	$\leq 14"$	18.7.5.2(e) and 18.10.6.4(e)	$\leq \begin{cases} 2b/3 \\ 14" \end{cases}$

Table 2.9: ACI 318 History for Seismic Design of Walls – Boundary Element (1971-2014)

Design Parameter	1971		1983		1999	
	Code Section	Provision	Code Section	Provision	Code Section	Provision
d_t	A.6.4.3	$\geq$ #3 for $d_b \leq$ #10 $\geq$ #4 for $d_b =$ #11, 14, 18		None		None
Crosstie, Hook Ext.'s	A.2	both ends semi-circular (180°) hook *(red =changes in 1977)*	A.1	one end 135° hook w. ext $\geq 10d_b$ other end 90° hook w. ext $\geq 6d_b$	21.1	one end $\geq$ 135° hook w. ext $\geq max(6d_b, 3")$ oth $\geq$ 90° hook w. ext $\geq 6d_b$ *(changed in 1989)*
Hoop, Hook Ext.'s	A.2	135° hook w. ext = $10d_b$	A.1	135° hook w. ext = $10d_b$	21.1	$\geq$ 135° hook w. ext = m x($6d_b$, 3") *(extension length changed in 1989 and hook angle changed 1995)*

Design Parameter	2008		2011		2014	
	Code Section	Provision	Code Section	Provision	Code Section	Provision
d_t		None		None	18.7.5.2(c)	$\geq$ #3 for $d_b \leq$ #10 $\geq$ #4 for $d_b \geq$ #11
Crosstie, Hook Ext.'s	2.2	one end $\geq$ 135° hook w. ext $\geq max(6d_b, 3")$ oth $\geq$ 90° hook w. ext $\geq 6d_b$	2.2	one end $\geq$ 135° hook w. ext $\geq max(6d_b, 3")$ oth $\geq$ 90° hook w. ext $\geq 6d_b$	2.2 and 25.7.4	one end $\geq$ 135° hook w. ext $\geq max(6d_b, 3")$ oth $\geq$ 90° hook w. ext $\geq 6d_b$
Hoop, Hook Ext.'s	2.2	$\geq$ 135° hook w. ext = m x($6d_b$, 3")	2.2	$\geq$ 135° hook w. ext = m x($6d_b$, 3")	2.2 and 25.3.5	$\geq$ 135° hook w. ext $\geq$ m x($6d_b$, 3")

Table 2.10: ACI 318 History for Seismic Design of Walls – Flanged Walls (1971-2014)

Design Parameter	1971		1983		1999	
	Code Section	Provision	Code Section	Provision	Code Section	Provision
b_{eff}					21.6.5.2	extend from face of wall web : $\min \begin{cases} 0.5 \times \text{dist. to next wall web} \\ 0.25h_w \end{cases}$
l_{be}					21.6.6.4(a) and 21.6.6.4(b)	$\geq \begin{cases} c - 0.1l_w \\ c/2 \end{cases}$ For flanged walls, $l_{be} \geq t_f +$ 12 *inches* into web where t_f is for the flangein compress.

Design Parameter	2008		2011		2014	
	Code Section	Provision	Code Section	Provision	Code Section	Provision
b_{eff}	21.9.5.2	extend from face of wall web : $\min \begin{cases} 0.5 \times \text{dist. to next wall web} \\ 0.25h_w \end{cases}$	21.9.5.2	extend from face of wall web : $\min \begin{cases} 0.5 \times \text{dist. to next wall web} \\ 0.25h_w \end{cases}$	18.10.5.2	extend from face of wall web : $\min \begin{cases} 0.5 \times \text{dist. to next wall web} \\ 0.25h_w \end{cases}$
l_{be}	21.9.6.4(a) and 21.9.6.4(b)	$\geq \begin{cases} c - 0.1l_w \\ c/2 \end{cases}$ For flanged walls, $l_{be} \geq t_f +$ 12 *inches* into web where t_f is for the flangein compress.	21.9.6.4(a) and 21.9.6.4(b)	$\geq \begin{cases} c - 0.1l_w \\ c/2 \end{cases}$ For flanged walls, $l_{be} \geq t_f +$ 12 *inches* into web where t_f is for the flangein compress.	18.10.6.4(a) and 18.10.6.4(b)	$\geq \begin{cases} c - 0.1l_w \\ c/2 \end{cases}$ For flanged walls, $l_{be} \geq t_f +$ 12 *inches* into web where t_f is for the flangein compress.

2.3 Performance-Based Design

2.3.1 Introduction

The previous section detailed prescriptive code-based provisions for reinforced concrete structural walls. As is evident from the summary tables presented at the end of the section, code-based design consists of fixed values that dictate wall geometry and reinforcement detailing, among other aspects. However, these codes do not require that engineers evaluate the performance of their code-compliant design solution for the anticipated hazard to determine if the predicted level of damage is acceptable for a given structure. Engineers are left to assume that by meeting the requirements of their prevailing reinforced concrete building and seismic design codes, that good structural performance can be expected. The 1994 Northridge, CA, USA and 1995 Kobe, Japan earthquakes were evidence that damage in code-compliant structures could be quite severe [56, 69, 122, 123, 132]. In many cases, this damage exceeded what the public or involved stakeholders perceived as acceptable performance for an engineered structure. Acknowledging these shortcomings, work began in the early 1990s to formalize the Performance Based Seismic Design (PBSD) philosophy that will be discussed in this section [30].

2.3.2 Definition of Performance-Based Seismic Design

On a fundamental level, PBSD differs from code-based design because it involves an iterative process that allows building owners and engineers to determine what constitutes an acceptable level of risk in terms of repair costs, downtime, or safety of property and occupants. The stages in the iterative process include: (i) development of performance objectives that defines the acceptable damage associated for a level of hazard, (ii) preliminary design (typically, this design just meets the minimum code requirements), (iii) analysis of performance for varying levels of hazard to examine if the performance objectives have been met, and if the performance objectives are not met then (iv) redesign and reassessment of the new design solution until the performance objectives are achieved [30]. In recent years, PBSD has become increasingly prevalent in practice as it provides a rational approach to designing buildings beyond code-specified limits to achieve a balance of economy and safety.

Paramount to effective implementation of PBSD is the accuracy of inelastic analysis techniques utilized to predict building response and characterize performance. On-going work in this area has included structural component testing to provide research results (Section 2.4 as well as Chapter 4

& 5) that can be utilized to validate models developed in research-oriented and commercial software (Chapter 6 &7). At both the experimental testing and computational modelling level the objective with PBSD is to correlate an engineering demand parameter (EDP) with a series of damage states (DS). The remainder of this section will focus on structural performance limit states and specifically the EDP and DS related to these performance limit states for reinforced concrete structural walls.

2.3.2.1 Definition of Structural Performance Levels

Structural performance levels are a broad manner of defining the desired building response for a given hazard level, these classifications can be utilized by the building owner to communicate their expectations for acceptable risk. As defined by ASCE/SEI 41 [22] these categories include:

- ***Immediate Occupancy*** is where a building is safe to re-occupy with essentially no impact to strength/stiffness and with very minor structural damage.
- ***Life Safety*** is where a building has significant structural damage but the risk of partial or total collapse is low; however, structural repairs are required prior to re-occupancy.
- ***Collapse Prevention*** is where the structure has substantial structural damage that results in a considerable reduction in strength/stiffness. While the buildings can still carry gravity loads, there is no margin against partial or total collapse.

The engineering demand parameters and damage states are associated with each of these structural performance levels.

Engineering demand parameters are a range of metrics that describe the earthquake demand on a structure, in many guide documents related to PBSD [20, 22, 28, 30]. The most prevalent EDPs are total drift or inter-story drift. Drift is a basic quantity recorded by essentially all researchers that conduct structural experiments; moreover, it is available as output from the most simple to refined structural models. There are other options for EDPs such as: dissipated hysteretic energy, a function of maximum drift and number of displacement cycles, and maximum shear stress or strain demand [39, 85]. These are often not as readily available from experiments and less straightforward to determine; consequently, they are used as EDP measures with much less frequency.

Damage states are defined using some combination of quantitative to qualitative measure of various damage measures (DM). These DMs include maximum and/or residual cracking widths; type of cracking (flexural/shear); extent of concrete spalling and crushing; extent of buckling or fracturing of reinforcement; and level of damage to wall boundary elements. In the most severe cases, the

"failure" damage state is assigned to structural walls that are no longer capable of supporting gravity loads [22, 39]. The costs associated with each of DS can be related to a Method of Repair (MoR) which can range from cosmetic/non-structural repairs, epoxy injecting cracks, patching or removal/replacement of spalled concrete, and replacement of reinforcement. The triggers for the different methods of repair are detailed in *Brown* [39]; also, *Gulec et al.* [85] summarizes the increasing severity of damage states from DS.1 to DS.4 (Table 2.11).

Table 2.11: Damage States and Associated Method of Repair for Structural Walls [85]

ID	Damage states	Method of Repair (MoR)
DS1	Maximum measured crack width less than 0.02 in. (0.5 mm)	Cosmetic repair (MoR-1)
DS2.1	Yielding in web and boundary element reinforcement	Epoxy-resin injection (MoR-2)
DS2.2	Maximum measured crack widths larger than 0.02 in. (0.5 mm) but less than 0.12 in. (3 mm)	
DS2.3	Maximum measured crack widths larger than 0.04 in. (1.0 mm) but less than 0.12 in. (3 mm)	
DS3.1	Concrete crushing at the compression toes/initiation of crushing in the wall web	Partial wall replacement (MoR-3)
DS3.2	Vertical cracking in the toe regions of the web	
DS3.3	Buckling of boundary element vertical reinforcement	
DS3.4	Flexural cracks with widths exceeding 0.12 in. (3 mm)	
DS4.1	Sliding at the base of the wall	Wall replacement (MoR-4)
DS4.2	Wide diagonal cracks	
DS4.3	Widespread crushing of concrete	
DS4.4	Reinforcement fracture	
DS4.5	Shear cracks with widths exceeding 0.12 in. (3 mm)	

In evaluating wall damage observed in experimental tests and actual earthquakes, it is important to have both semi-quantitative and qualitative measures where damage states and engineering demand parameters can be correlated and assigned to a structural performance level. An example of this is found in *ASCE/SEI 41* (Table 2.12); structural walls are classified primary structural components when they are necessary to resist lateral seismic loading to reach the target structural performance level, and secondary components if they are not [22]. An early, but possibly more descriptive, example is found in *ATC-40* (note: "Damage control" represents the range from "Immediate Occupancy" to "Life Safety", while "Structural Stability" is now "Collapse Prevention") [27].

Table 2.12: Structural Performance Level and Damage for Structural Walls [22]

Elements	Type	Structural Performance Levels: Collapse Prevention (S-5)	Life Safety (S-3)	Immediate Occupancy (S-1)
Concrete Walls	Primary	Major flexural and shear cracks and voids. Sliding at joints. Extensive crushing and buckling of reinforcement. Failure around openings. Severe boundary element damage. Coupling beams shattered and virtually disintegrated.	Some boundary element stress, including limited buckling of reinforcement. Some sliding at joints. Damage around openings. Some crushing and flexural cracking. Coupling beams: extensive shear and flexural cracks; some crushing, but concrete generally remains in place.	Minor hairline cracking of walls, < 1/16 in. wide. Coupling beams experience cracking < 1/8-in. width.
	Secondary	Panels shattered and virtually disintegrated.	Major flexural and shear cracks. Sliding at joints. Extensive crushing. Failure around openings. Severe boundary element damage. Coupling beams shattered and virtually disintegrated.	Minor hairline cracking of walls. Some evidence of sliding at construction joints. Coupling beams experience cracks < 1/8-in. width. Minor spalling.
	Drift	2% transient or permanent.	1% transient; 0.5% permanent.	0.5% transient; negligible permanent.

Table 2.13: Structural Performance Level and Damage for Structural Walls [27]

Element/ Component	Immediate Occupancy	Damage Control	Life Safety	Structrual Stability
Walls and Pilasters (Piers)	Very minor shear cracking in plane of wall. Very little or no cracking at end of wall or of pilasters. No permanent horizontal offset. Gravity capacity maintained.	Minor shear cracking in plane of wall. Little or no cracking at end of wall or of pilasters. No permanent horizontal offset. Gravity capacity maintained.	Extensive spalling and shear and flexural cracking, particularly at the ends and heels of shear walls. Evidence of sliding shear failures. Permanent horizontal offset approaching 2.0% interstory drift with other areas marginally higher. Gravity capacity maintained.	Extensive spalling and shear and flexural cracking throughout wall, particularly in areas with greatest permanent offset. Evidence of longitudinal rebar buckling. Evidence of sliding shear failures along construction joints and at base of wall. Permanent horizontal offset approaching 3.5% interstory drift with other areas marginally higher. Gravity capacity maintained throughout nearly all of structure.

When evaluating results from experimental wall tests and comparing these to computational models for the aforementioned tests, much more detailed quantitative measures are necessary to determine if the desired PBSD performance level has been achieved. The most basic of which is global performance comparisons where lateral deformation at the performance point (where capacity equals demand for a given hazard level) is evaluated against varying deformation limits such as maximum total drift (inter-story drift) and maximum inelastic drift (Table 2.14).

Table 2.14: Lateral Deformation Limits [27]

	Performance Level			
Interstory Drift Limit	Immediate Occupancy	Damage Control	Life Safety	Structural Stability
Maximum total drift	0.01	0.01 - 0.02	0.02	$0.33\frac{V_i}{P_i}$
Maximum inelastic drift	0.005	0.005 - 0.015	no limit	no limit

More specifically, key points from the experimental/computational load-deformation relationship can be extracted to use with the generalized load-deformation relationship found in *ASCE/SEI 41* (Fig. 2.1) [22]. In this plot, the region between A to B has a linear stiffness where B is the effective yield, there is a reduced stiffness from B to C, and significant strength loss at D, after which the strength is reduced until a final loss of strength occurs at E. Using this load-deformation relationship, and known results experimental/computational models then the structural performance level can be assessed using the *ASCE/SEI 41* table summarizing numerical acceptance criteria (Table 2.15) [22].

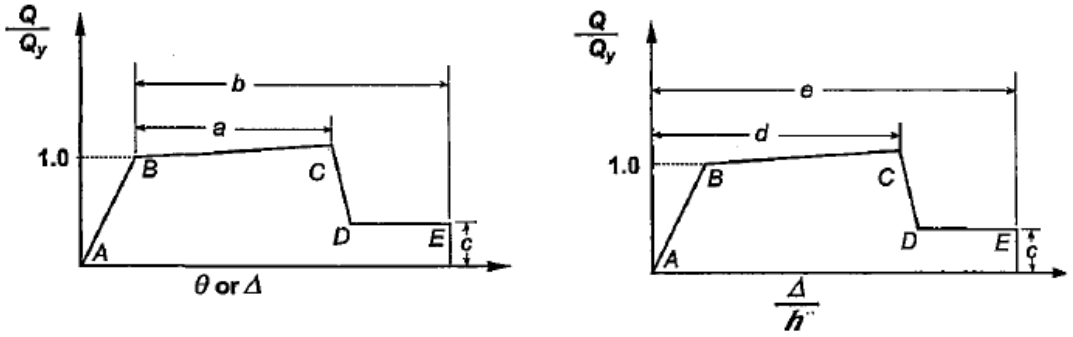

Figure 2.1: Generalized Load-Deformation for Reinforced Concrete Structural Components [22]

Table 2.15: Acceptance Criteria for Flexure-Controlled Reinforced Concrete Walls [22]

Conditions			Plastic Hinge Rotation (radians)		Residual Strength Ratio	Acceptable Plastic Hinge Rotation[1,2] (radians)				
						Performance Level				
							Component Type			
							Primary		Secondary	
			a	*b*	*c*	IO	LS	CP	LS	CP
i. Shear Walls and Wall Segments										
$\frac{(A_s - A_s')f_y + P}{t_w l_w f_c'}$	$\frac{V}{t_w l_w \sqrt{f_c'}}$	Confined Boundary[3]								
≤ 0.1	≤ 3	Yes	0.015	0.020	0.75	0.005	0.010	0.015	0.015	0.020
≤ 0.1	≥ 6	Yes	0.010	0.015	0.40	0.004	0.008	0.010	0.010	0.015
≥ 0.25	≤ 3	Yes	0.009	0.012	0.60	0.003	0.006	0.009	0.009	0.012
≥ 0.25	≥ 6	Yes	0.005	0.010	0.30	0.0015	0.003	0.005	0.005	0.010
≤ 0.1	≤ 3	No	0.008	0.015	0.60	0.002	0.004	0.008	0.008	0.015
≤ 0.1	≥ 6	No	0.006	0.010	0.30	0.002	0.004	0.006	0.006	0.010
≥ 0.25	≤ 3	No	0.003	0.005	0.25	0.001	0.002	0.003	0.003	0.00
≥ 0.25	≥ 6	No	0.002	0.004	0.20	0.001	0.001	0.002	0.002	0.004

[1]Primary and secondary component demands shall be within secondary component acceptance criteria where the full backbone curve is explicitly modeled including strength degradation and residual strength in accordance with Section 3.4.3.2.
[2]Linear interpolation between values listed in the table shall be permitted.
[3]Requirements for a confined boundary are the same as those given in ACI 318 (ACI 2002).

2.3.3 Probabilistic Nature of Performance-Based Seismic Design

Performance-based seismic design is, by nature, probabilistic. There is both uncertainty in determining the level of anticipated hazard and the expected performance of the structure. As a result, in their design, engineers have to consider the probability of exceeding a certain damage state or performance limit state (for example, 10% probability of exceeding DS.1 as defined in Table 2.11). Fragility functions graphically represent the probability of exceedance versus the engineering demand parameter for a particular performance point of interest. An example presented in *Gulec et al.* [85] draws on 28 low-aspect ratio, flanged wall tests where the experimental and theoretical fragilities is plotted for the damage states DS.1 to DS.4 in Fig. 2.2) Similarly, a series of computationally modelled walls can be utilized to develop fragility functions. This is a large portion of the work undertaken by *ATC-58* [29]. The discussion of fragility functions is relative as the current research intends to further the understanding of modelling slender non-planar reinforced concrete walls, and with improved simulation abilities the resulting fragility functions using these sorts of models can become more reliable.

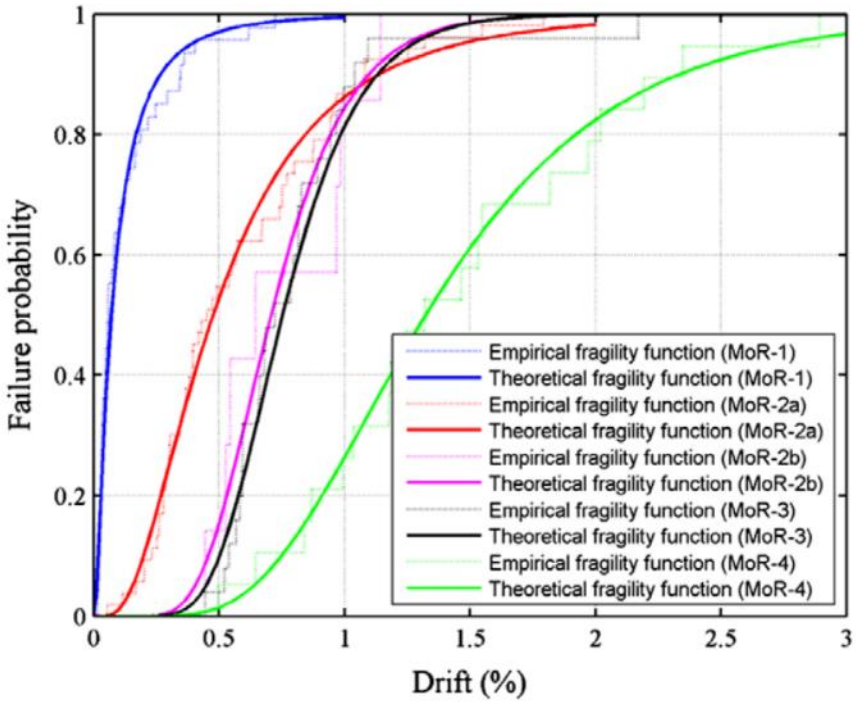

Figure 2.2: Fragility Functions for Damage States in Flanged Walls [85]

2.4 Experimental Performance of 3-D Walls

In an effort to examine previous experimental tests on non-planar walls, fifteen test programs consisting of a total of 36 slender, flexure-controlled (shear span ratio ≥ 2.0) specimens were reviewed. Wall cross-sections included C, U, I, L and T-Shaped configurations with at least one axis of symmetry. All specimens were subjected to cyclic lateral loading; a majority of walls were subjected to constant axial loading (generally less than $0.15A_g f_c'$), though some had variable axial loads. Most specimens were loaded uni-directionally; however, some C, U, and T-Shaped walls were subjected to bi-directional lateral loading, using a cruciform, clover leaf, or other displacement path and many of the L-Shaped walls were loaded on a 45-degree angle to the legs. Walls with penetrations and walls loaded on a 45-degree angle not corresponding to an axis of symmetry were excluded from the experimental database (i.e. U-shaped walls with asymmetric reinforcement configurations and L-shaped walls with legs of different lengths loaded at 45-degree angle).

Table 2.16 provides basic information for the test specimens reviewed in Sections 2.4.1-2.4.5. Each of the following sub-sections will provide: (i) overall objective of the wall test series, (ii) details on the test program including wall geometry and reinforcement, test set-up, and loading protocol, (iii) discussion of experimental results, and (iv) research conclusions for the test series. Tabulated information related to wall geometry and reinforcement as well as a detailed, aggregate analysis of damage observed in experimental wall tests can be found in Chapter 3.

Table 2.16: Summary of Non-planar Test Programs and Specimens

Researcher			Loading Direction	
			Unidirectional[1]	Bidirectional[2]
Sittipunt & Wood (1993)	CLS	C	WA	
	CMS	C	WA	
Lowes (2014)	CWall6	C	SA	
	CWall7	C		SA,WA
	CWall8	C		SA,WA
Ile & Reynouard (2005)	IleX	U	SA	
	IleY	U	WA	
	IleXY	U		CL
Beyer et al (2008)	TUA	U		SA,WA, 45, CL
	TUB	U		SA,WA, 45, CL
Oesterle et al. (1976/1979)	F1	I	SA	
	F2	I	SA	
Shouzhong (2002)	SW3	I	SA	
Paulay & Goodsir (1985)	Wall 3	T	SA	
Thomsen & Wallace (1995)	TW1	T	SA	
	TW2	T	SA	
Choi (2004), Ha et al. (2002)	TC	T	SA	
	TC-aw	T	SA	
	TC-b1	T	SA	
	TC-b2	T	SA	
Brueggen (2009)	NTW1	T		SA,WA,360
	NTW2	T		SA,WA,360
Nakachi (1996)	No1	L	45	
	No2	L	45	
	No3	L	45	
	No4	L	45	
Hu (2004)	No1	L	PL	
	No2	L	PL	
Hosaka et al. (2008)	L-1	L	45	
	L-2	L	45	
	L-5	L	45	
	L-6	L	45	
Inada (2008)	L00A	L	PL	
	L45A	L	45	
Kono (2011)	L45C	L	45	
	L45D	L	45	

[1] SA = strong axis loading, WA = weak axis loading, PL = loading parallel to leg

[2] 45 = loading 45° to leg, CL = cloverleaf or similar pattern, 360 = sweep of approx. circular displacement path

2.4.1 Tests on C-Shaped Wall Configurations

2.4.1.1 Sittipunt & Wood (1993) [158]

Research Objectives

A set of two C-Shaped walls were tested at the University of Illinois at Urbana-Champaign to better understand the inelastic behavior of flanged wall sections when subjected to cyclic loading. Specifically, for non-planar walls, there was still limited knowledge of the effects of flexural and shear reinforcement in the wall webs and confinement in the boundary elements. Moreover, the 1989 *ACI318 Building Code* [9] being employed at the time of this study gave no explicit guidance on how to determine the effective flange width necessary in evaluating the flexural capacity of these wall sections. Aside from developing a better understanding of C-Shaped wall performance, these experimental tests were part of a more extensive research program to develop finite element models capable of capturing material-level hysteretic behavior to predict the global inelastic response of slender reinforced concrete walls. The data collected from the tests at Illinois, along with results from thirteen wall tests at the Portland Cement Association by *Oesterle et al.* [140, 141], were utilized to validate the computational models developed in this study.

Test Program

The two isolated C-Shaped walls (Figure 2.3) that were tested are considered to be 1:4 scale specimens by the research team. The overall geometry of both walls are identical with a 5-ft wide web, 3-ft long flanges, and height of 9-ft. The specimen configuration is referred to as "C-shaped" as flange length is significantly shorter than web length (ratio of flange to web length is 0.6). The wall web dimension was selected such that it exceeds the effective width calculated using *ACI318-89* [9] for a T-beam with a 3-in flange, this was done in an effort to investigate the effective width of flanged walls.

Both the flange-web intersection (interior) and flange tip (exterior) wall zones have concentrated flexural and transverse reinforcement; the boundary element dimensions and reinforcing details are constant between the two specimens. The confinement provided in these regions is noted to be two-thirds of the required amount for walls with high axial stresses per *ACI318-89* [9]. The primary difference between the two wall specimens is the amount of reinforcement in the center "web" portions of the wall web and flanges. Specimen CLS has half of the flexural and horizontal shear

reinforcement as Specimen CMS to examine the impact of "web" reinforcement on overall wall strength, stiffness, and ductility. The difference in the reinforcement details are shown in Figure 2.3.

The specimens were subjected to cyclic lateral loading and a constant axial loading. The lateral load was applied in the weak-axis direction by a single actuator at the top of the wall that was attached with a 2-in steel plate. Note that positive displacement is when the wall web is compressed and negative displacement is when it is under tension. The gravity load of $0.06\text{-}0.07A_g f_c'$ (100 kips) was applied to the walls using eight center hole jacks mounted to the top steel plate to distribute the load uniformly over the wall cross-section. The test set up is shown in Figure 2.4.

The cyclic loading protocol is comprised of five intervals: one force-controlled followed by four displacement-controlled stages. The initial portion of testing is an elastic stiffness evaluation conducted at half of the predicted cracking load (±10 kips), the subsequent stage is a single cycle at a ±1 in top deflection, followed by two additional cycles at ±1 in, three cycles at ±1.5 in, and multiple cycles at a deflection greater than ±2 in until wall failure.

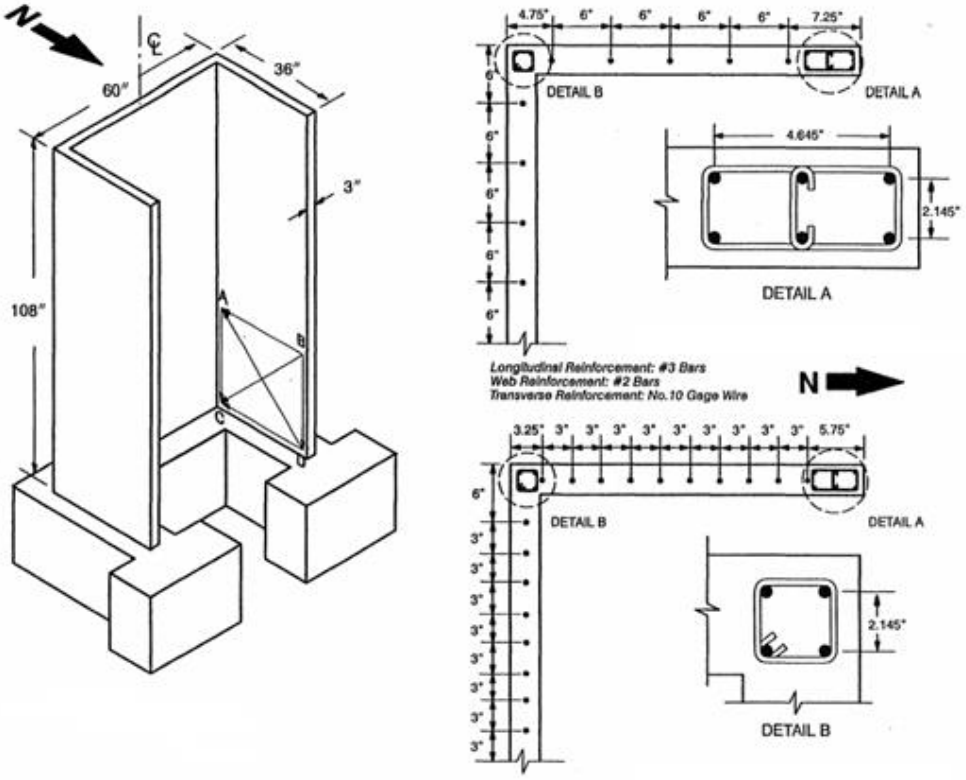

Figure 2.3: Test Specimen Geometry and Reinforcement Details for Sittipunt & Wood [158]
(Left) Overall Geometry, Reinforcement for (Right Top) Specimen CLS and (Right Bottom) CMS

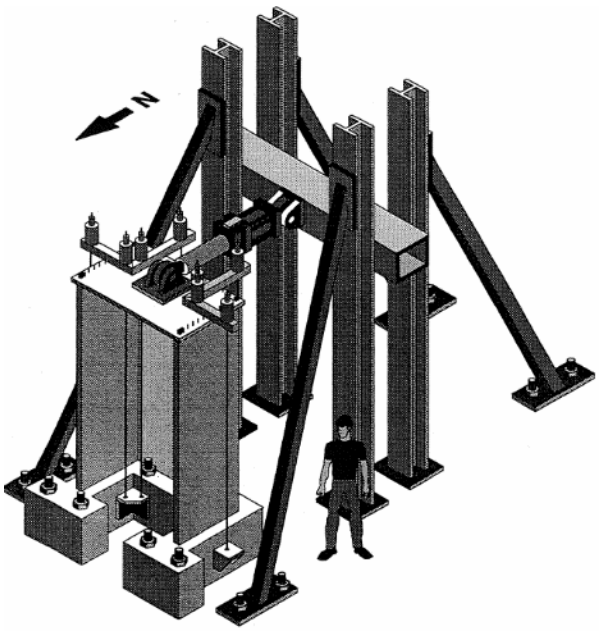

Figure 2.4: Test Set Up for Sittipunt & Wood [158]

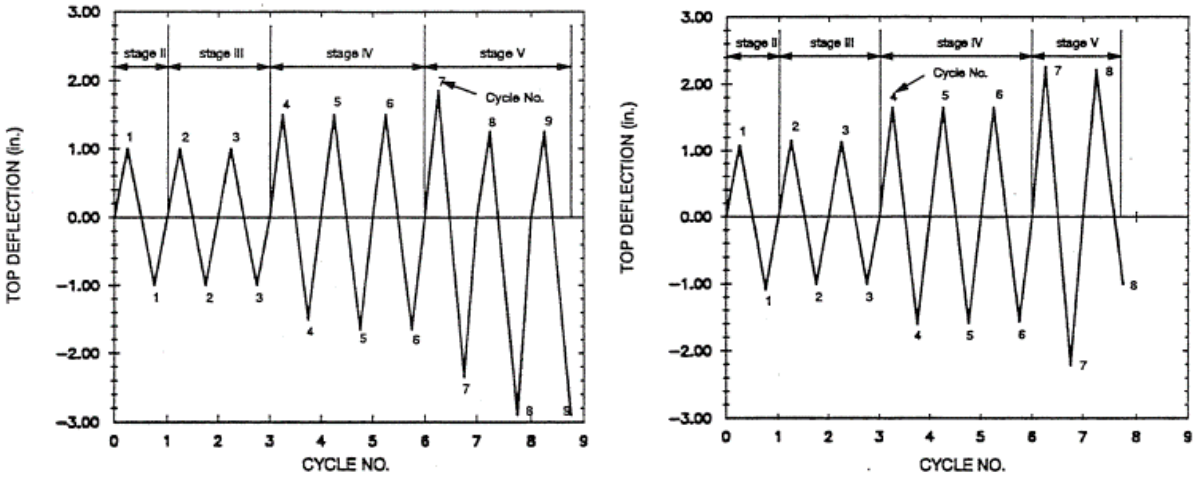

Figure 2.5: Displacement History for Sittipunt & Wood [158]
(Left) Specimen CLS and (Right) Specimen CMS

Experimental Test Results

For Specimen CLS the lateral load versus displacement response measured at the top of the specimen is shown in Figure 2.6. The following summarizes the major observations in the wall performance of Specimen CLS that experienced a flexural-compression (crushing-buckling) failure.

- During the ±1 in cycles (1% drift) the flexural reinforcement in both the boundary elements and the center portion of the wall web had yielded. There were horizontal and inclined cracks on the wall flanges and concrete spalling was observed at the exterior boundary elements at the flange tips.
- During ±1.65 in cycles (1.5% drift) there was complete cover loss at the exterior boundary elements and slight buckling of the flexural reinforcement in these regions (at this stage buckling was still mostly restrained by transverse reinforcement).
- During ±2 in cycles (2% drift) significant buckling occurred in the exterior boundary elements.
- After crushing of the exterior boundary elements, the wall failed in the third cycle beyond ±2 in when approaching -2.25 in. This occurred as a result of a transverse hoop fracturing in the west exterior boundary element and buckling of multiple flexural bars.

For Specimen CMS the lateral load versus displacement response measured at the top of the specimen is shown in Figure 2.6. The following summarizes the major observations in the wall performance of Specimen CMS that experienced a flexural-compression (crushing-buckling) failure.

- The damage progression is similar to that described for Specimen CLS through the ±2 in cycles.
- After crushing of the exterior boundary elements, the wall failed in the second cycle beyond ±2 in when approaching -2.50 in.
- No significant damage to transverse reinforcement was observed like in Specimen CLS.

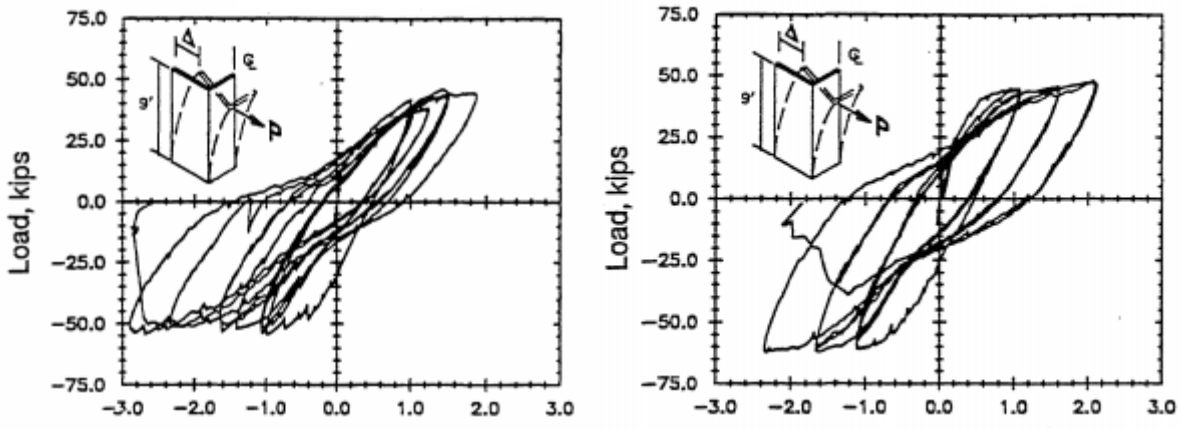

Figure 2.6: Force-displacement responses for Sittipunt & Wood [158]
(Left) Specimen CLS and (Right) Specimen CMS

Research Conclusions

Even considering that the C-shaped wall specimens were loaded about the weak axis, the performance of these walls is satisfactory for earthquake demands. The observed displacement capacity for the specimens is around 2% drift for positive loading (both walls) and around 2.3 and 2.9% (CMS and CLS, respectively) for negative loading. For both walls there is very little cyclic strength degradation as the applied displacement increased, and only after considerable compressive damage to the exterior boundary elements in the flanges do the walls fail. In terms of strength, stiffness, and ductility characteristics of the two specimens, where one has double the vertical and horizontal "web" (center region) reinforcement, the differences are not appreciable to indicate any benefit from increased reinforcement in these zones. The noted difference in onset of failure with the hoop fracture in Specimen CLS is attributed to the fact that the flexural bars in the west exterior boundary element buckled in opposite directions, straining the transverse reinforcement considerably, whereas in Specimen CMS all boundary element bars buckled in the same direction.

The major findings in this research study are related to results from computational modelling (validated with the C-shaped wall tests) that enable further parametric studies that, in part, examine effective flange width and reinforcement level in this type of flanged wall. As a result, there is limited experimental data beyond the lateral load-displacement response for the specimens. Despite this limitation, having C-shaped wall specimens loaded about the weak-axis only will provide a point of comparison for the U-shaped IleY test described in Section 2.4.2.1.

2.4.2 Tests on U-Shaped Wall Configurations

2.4.2.1 Ile & Reynouard (2005), Reynouard & Fardis (2001), Pegón et al. (2000) [101, 144, 145, 151]

Research Objectives

As part of the European Research Programs "Innovative Concepts for New and Existing Structures" focused on shear wall structures, three U-Shaped walls were designed and analyzed by *Reynouard and Fardis* [151] and tested under quasi-static cyclic loading by *Pegón et al.* [144, 145] at the European Laboratory for Structural Assessment (ELSA). At the time of the study, there was limited understanding of how the interaction of biaxial bending, shear, and axial force influence the behavior of non-planar walls. As a result, existing design procedures and detailing requirements in *Eurocode 8* [44]– as is true with the ACI318 code documents described in Section 2.2 – pertain to

rectangular walls and their extension to 3-D cross-sections were not well established. Additionally, the study also intended to explore local modelling approaches that incorporated material-level hysteretic behavior to more effectively capture non-linear response compared to existing frame or wide-column analogy models. The data collected through the uni- and bi-directional experimental tests in this study demonstrated how code-compliant non-planar walls would perform under earthquake loading; furthermore, these results served as a basis to verify and refine 3-D thin shell computational models. The findings had implications both for design and analysis of this wall type.

Test Program

The three isolated U-shaped walls (Figure 2.7) that were tested were considered to be full (0.82:1) scale specimens where a full-scale wall has a thickness of 12-in. The overall geometry and reinforcement configuration of the walls were identical with a 1.5-m (4.92-ft) wide web, 1.25-m (4.10-ft) long flanges, height of 3.6-m (11.81-ft), and wall thickness of 0.25-m (0.82-ft). The specimen configuration was referred to as "U-shaped" as the flange length is nearly the same as the web length (ratio of flange to web length is 0.83). Both the flange-web intersection (interior) and flange tip (exterior) wall zones had concentrated flexural and transverse reinforcement; the boundary element dimensions and reinforcing details were constant between the specimens. These reinforcement details are shown in Figure 2.8. These specimens were designed in accordance with *ENV1998:1994* [43] and are compliant with the proposed revision in prEN1998: 2003, which as mentioned previously are provisions more appropriate for rectangular wall sections.

The specimens were subjected to cyclic lateral loading and a constant axial loading. The primary difference between the three wall tests was the directionality of the lateral loading. The first two wall tests were each subject to a unidirectional cyclic lateral loading protocol: Wall 1 was tested in the Y-direction (weak axis) and Wall 2 in the X-direction (strong axis). The third test examined the effects of bi-directional loading by employing a butterfly loading pattern with both X and Y components. The test setup was comprised of four actuators aligned with the mid-height of the top wall cap. Two of these actuators were parallel to the wall flanges and two were parallel to the wall web. For the uni-directional tests, the two actuators positioned in line with the desired lateral loading direction were employed using displacement-control and a zero-torsion target for the pair. For the bi-directional test all four actuators were used, three of which are operated under displacement-control while the forth in the X-direction maintains the same force as the other X-direction actuator. The gravity load of $0.1\text{-}0.12A_g f_c'$ (2120 kN) was applied to the walls using six vertical post-tensioned bars that are

located so the resultant force acts nearly at the centroid of the cross-section to limit unintended moment in the wall specimen. The test set up is shown in Figure 2.9.

The cyclic loading protocol for the uni-directional tests was comprised of four distinguishable intervals. The initial portion of testing consisted of a single low-level displacement cycle in the cracking region prior to yielding, the subsequent stages were three-cycle sets at increasing displacement levels 4 cm (1.57 in), 8 cm (2.36 in), and 12 cm (4.72 in) associated with drift levels of 1%, 2%, and 3%, respectively. The 3% drift cycles were repeated until failure, where failure is defined as two-thirds of peak strength. The bi-directional test was comprised of two cycles at the inner loop followed by two cycles at the outer loop of the butterfly shaped displacement history shown in Figure 2.10. The inner loop corresponded to a maximum displacement of 4 cm (1.57 in) in both the X- and Y-directions, while the outer loop was 8 cm (2.36 in).

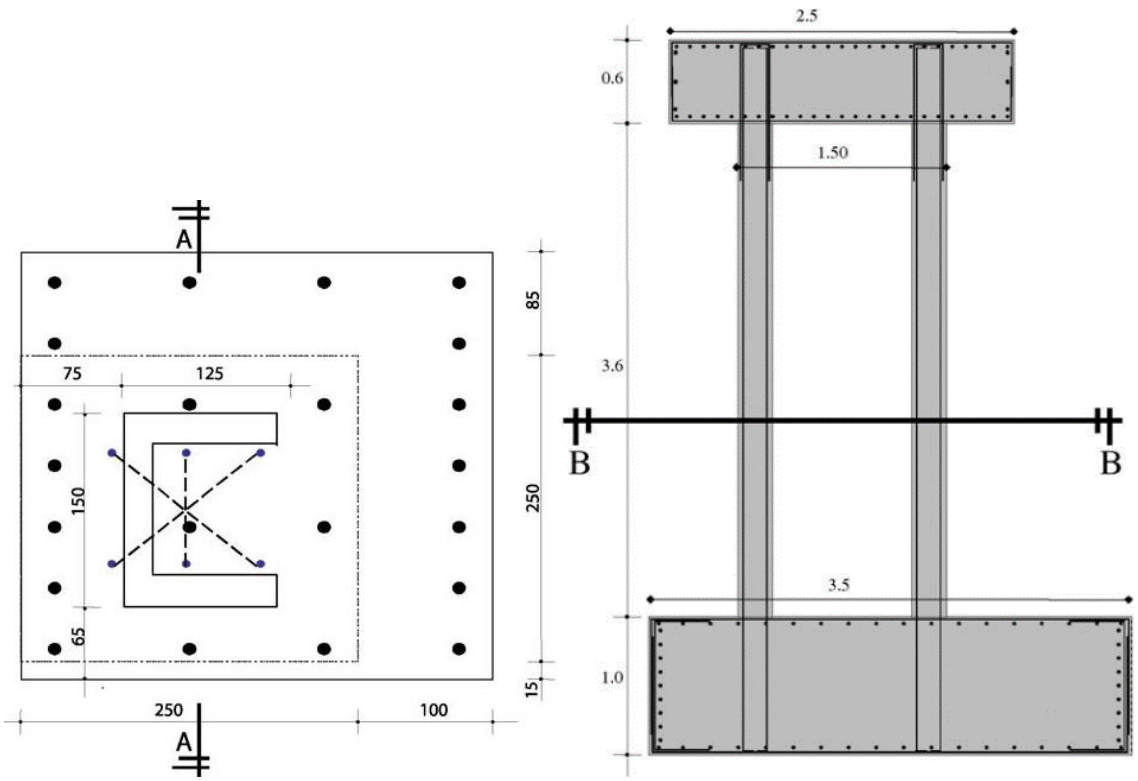

Figure 2.7: Test Specimen Geometry for Ile & Reynouard [101]

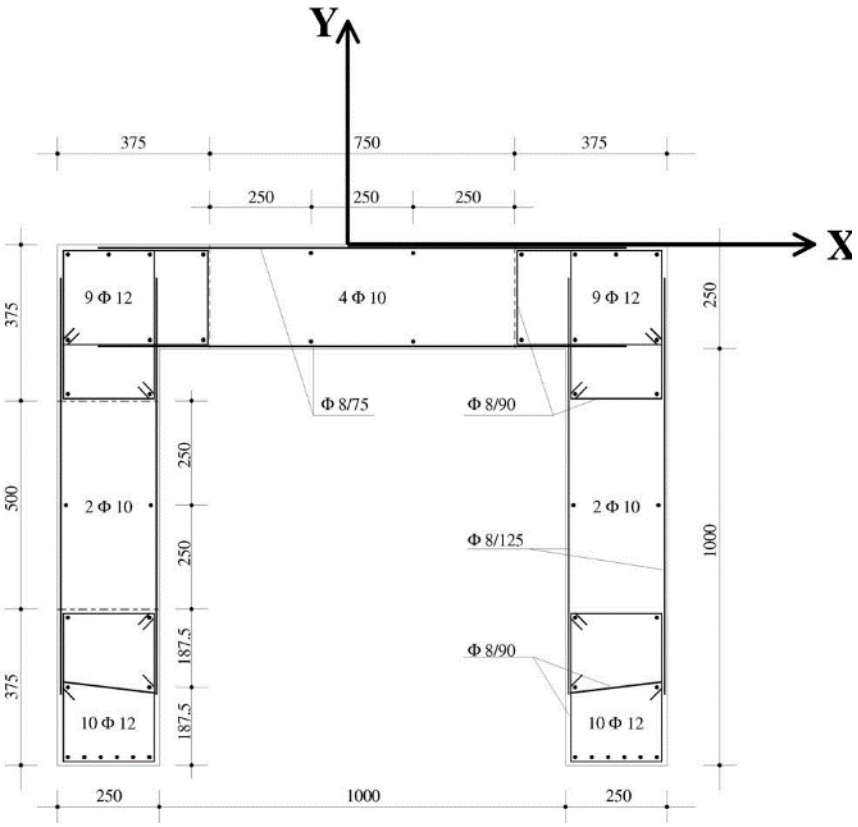

Figure 2.8: Test Specimen Reinforcement Details for Ile & Reynouard [101]

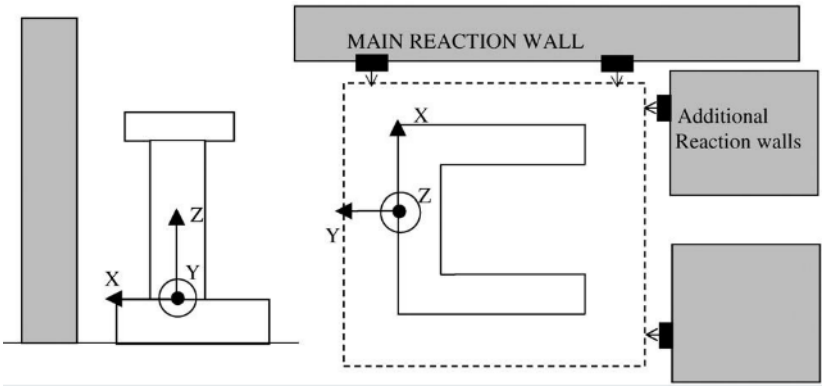

Figure 2.9: Test Set Up for Ile & Reynouard [101]

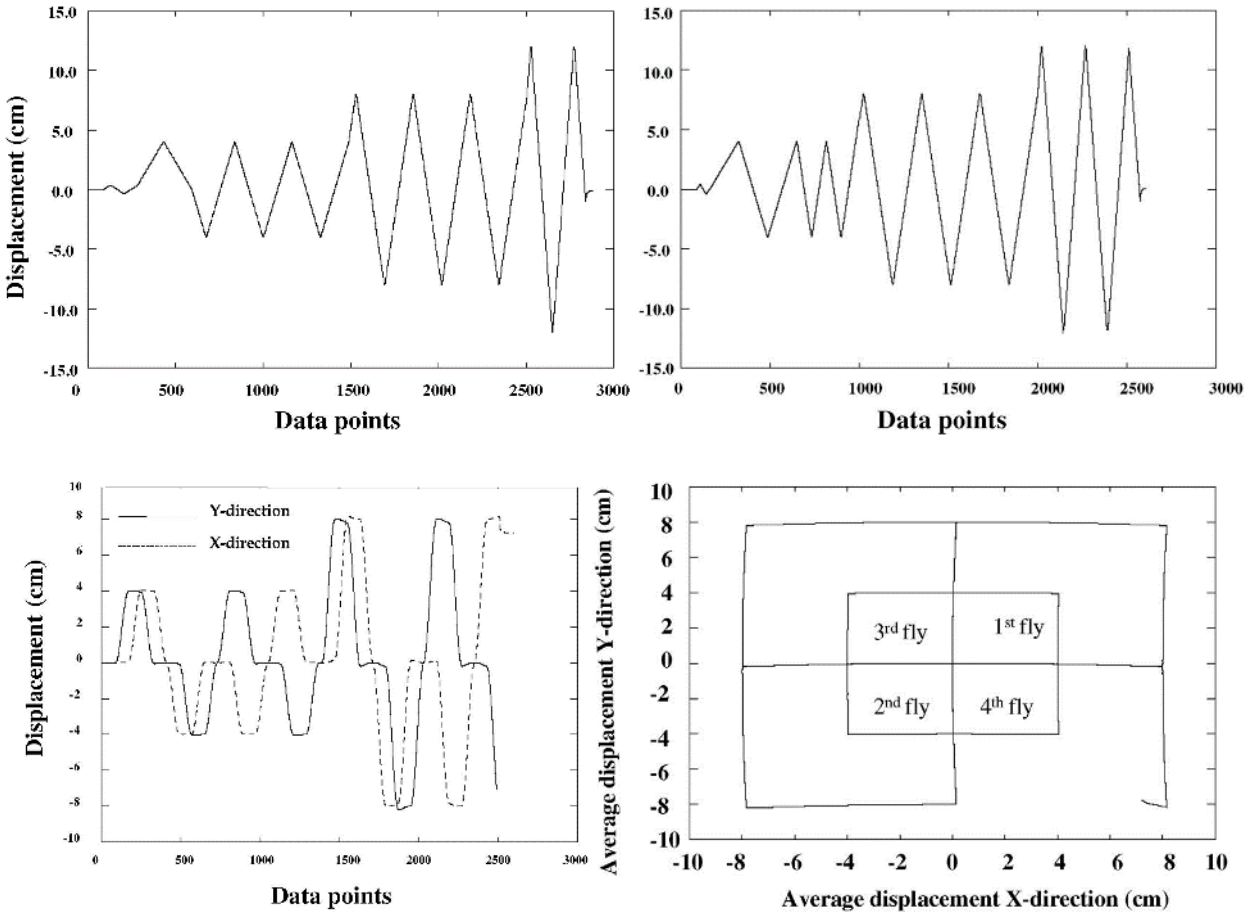

Figure 2.10: Uni- and Bi-directional Displacement Histories for Ile & Reynouard [101]
(Top Left) IleY: Y-Direction only, (Top Right) IleX: X-Direction only, (Bottom) IleXY: Bi-directional (Butterfly)

Experimental Test Results

For Specimen IleY (USW1) the lateral load versus drift response measured at the top of the specimen is shown in Figure 2.11. Note that positive motion in the Y-direction was when the wall web is in compression. The following summarizes the major observations in the wall performance of Specimen IleY (USW1) that experienced a flexure-tension (buckling-rupture) failure.

- At 2 cm displacement (0.5% drift) inclined cracks appeared at the base of the flanges, and significant horizontal cracks in the wall web occurred at -2 cm displacement (-0.5% drift).
- During the ±4 cm cycles (1% drift) the wall web was heavily cracked and the flexural bars at the flange tips began buckling.
- During ±8 cm cycles (2% drift) significant damage was observed at base of boundary elements of the flange tips in the form of heavy spalling and buckling of flexural rebar.

- The wall exhibited good performance until failing during the second excursion to -12 cm (3% drift) as a result of simultaneous bar buckling and concrete crushing in one of the flange tips (where a stirrup was missing due to a construction error). This was followed by a stirrup fracture and bar buckling in the other flange. These buckled flexural bars subsequently fractured in tension upon load reversal.

For Specimen IleX (USW2) the lateral load versus drift response measured at the top of the specimen is shown in Figure 2.11. The following summarizes the major observations in the wall performance of Specimen IleY (USW1) that experienced a flexure-tension (buckling-rupture) failure.

- The onset of cracking was noted at 1 cm displacement (0.25% drift). The considerable inclination of these cracks suggests shear-dominated behavior.
- During the ±4 cm cycles (1% drift) web and flange cracks distributed cracking continues.
- During ±8 cm cycles (2% drift) moderate buckling observed in flange tips.
- After two cycles of ±12 cm (3% drift) wall damage included severe bar buckling, fracture of several stirrups as well as of flexural rebar at the base of flange tips and web corners. The wall failure is attributed to the fracture of previously buckled flexural rebar in the flange.
- Researchers observed shear-dominated behavior in the web and flanges; this is attributed to significant warping that occurred while loading this cross-section in the X-direction.

For Specimen IleXY (USW3) the lateral load versus drift response measured at the top of the specimen is shown in Figure 2.11. The following summarizes the major observations in the wall performance of Specimen IleY (USW1) that experienced a flexure-tension (buckling-rupture) failure.

- During the ±4 cm (1% drift) loop of the butterfly loading scheme significant inclined cracking was observed. Unlike previous uni-directional tests, where strength was maintained nearly until failure at 3% drift, there is already apparent cyclic strength degradation at the 1% drift level that continues through the remainder of the test. Therefore, the strength achieved in the bi-directional test was noted to be lower than the Y and X tests, individually.
- During the ±8 cm (2% drift) loop of the butterfly loading scheme there was severe buckling and rupture of flexural reinforcement in addition to spalling of concrete.
- The wall failed at +2% drift for strong and -2% drift for the weak axis, the failure in each direction was attributed to the fracture of previously buckled flexural rebar in the flange (Fig. 2.12).

- Similar to the specimen loaded about the strong-axis only, researchers observed shear-dominated behavior in the web and flanges and noted that following the flexure-tension failure of the wall, one of the flanges experienced a shear failure.

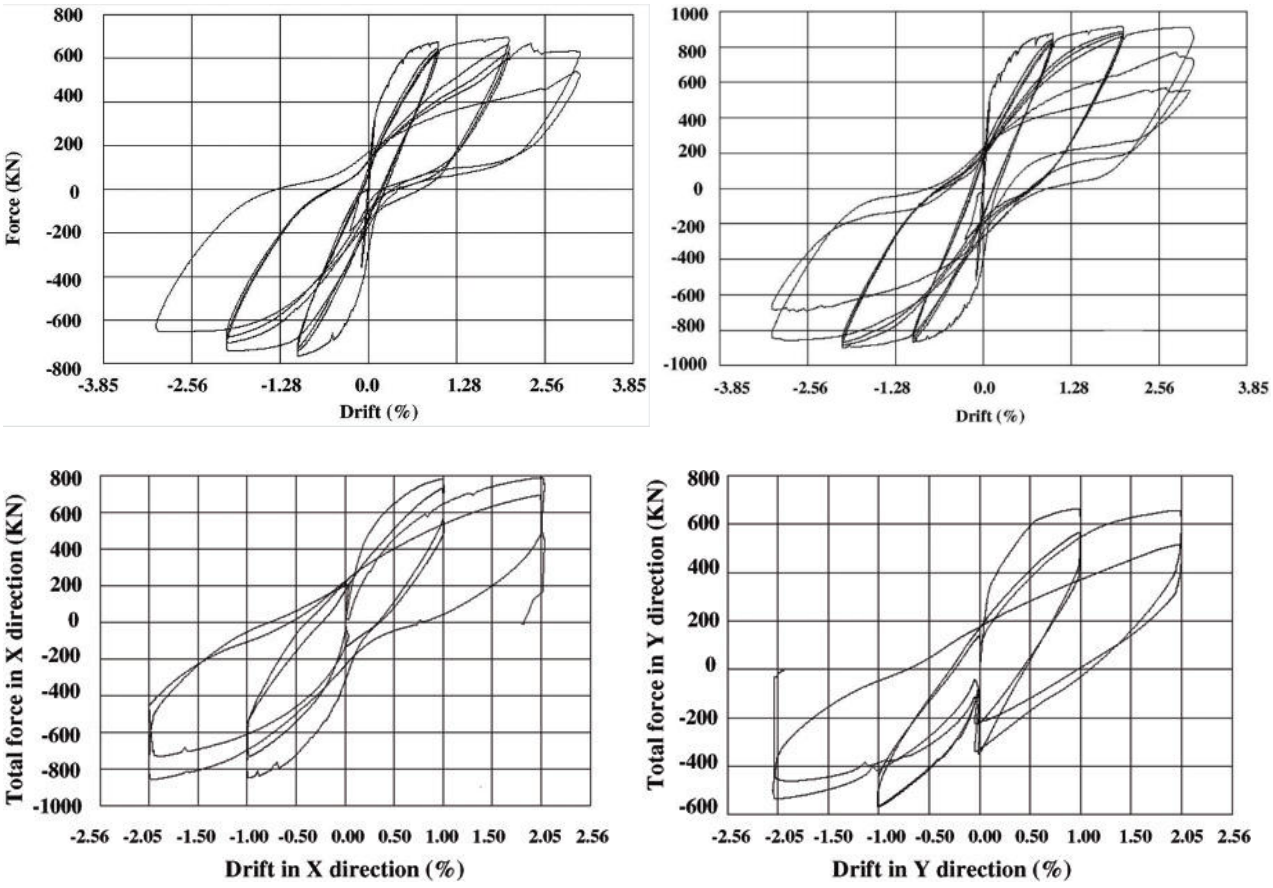

Figure 2.11: Force-displacement responses for Ile & Reynouard [101]
(Top Left) IleY: Y-Direction only, (Top Right) IleX: X-Direction only, (Bottom) IleXY: Bi-directional

Research Conclusions

The experimental results of this U-Shaped wall test series indicated that both uni- and bi-directional loading demands can be met by implementing the design procedure and detailing requirements of *ENV1998:1994* [43] and the proposed revision in *prEN1998* [44]. The uni-directional specimens were both able to achieve at least one cycle at 3% drift without considerable strength loss, while the bi-directionally loaded wall was able to very nearly able to achieve the previous peak strength seen at 1% drift loop of the butterfly loading pattern, on the first loop at 2% drift. The research team indicated that the wall design for these specimens was adequate to perform in a stable manner at a ductility level of 6 (considered to be medium ductility). However, there was evidence of the

detrimental impact of bi-directional loading where cyclic strength degradation occurs at each drift level.

In addition to verifying that the current *Eurocode 8* [44] provisions were sufficient, the researchers made an important observation in regards to shear resistance in this type of flanged wall. During a majority of the IleX test, it was noted that shear force was concentrated in the compression flange. The observation was confirmed by force measurements taken during the IleXY test, which show on various occasions that the total applied shear in the Y-direction was concentrated in the compression flange. Understanding the shear transfer mechanism is particularly critical when secondary shear forces due to bending in the perpendicular direction are combined with the primary shear demand. The research team indicated that this shear behavior requires designers to provide the total required shear capacity parallel to an axis of symmetry only in one flange or portion of the wall, rather than assuming both flanges are actively engaged in shear resistance.

Figure 2.12: Damage to Specimen IleXY at end of test [101]

2.4.2.2 Beyer et al. (2008) [34]

Research Objectives

At the time of the *Beyer et al.* [34] study the most comprehensive investigation of U-Shaped core walls under uni- and bi-directional loading was the *Ile & Reynouard* [101] test series described in Section 2.4.2.1. This research program provided limited insight into the bi-directional response of U-Shaped walls via the IleXY (USW3) specimen test that was subjected to a butterfly pattern loading at two ductility levels. These experimental observations highlighted concerns that arise with bi-directional loading of these non-planar wall types, including: (i) undesirable failure mechanisms including shear and sliding shear; (ii) degradation of stiffness, strength, and ductility; as well as (iii) influence on the

relative contributions of flexure, shear, and sliding to overall wall deformations. To further investigate these areas, the *Beyer et al.* [101] study conducted at ETHZ (Swiss Federative Institute of Technology – Zurich) examined two U-Shaped wall specimens designed for high ductility with variable cross-section geometry and reinforcement configurations. In particular, the research team was interested in U-shaped wall behavior for different directions of loading and how certain wall parameters might affect the wall response.

Test Program

The two U-shaped walls (Figure 2.13) that were tested are considered to be a half-scale (TUA) and one-third scale (TUB) specimens of a prototype elevator shaft of a 6-story reference building, where full-scale specimens have a thickness of 12-in. The primary difference between the two specimens is the wall thickness since this parameter was anticipated to impact the walls' shear capacity, compression zone depth, and stability, among other effects. The walls have a 1.3-m (4.27-ft) wide web and 1.05-m (3.44-ft) long flanges; the wall thickness of Test Unit A (TUA) is 0.15-m (0.49-ft) and TUB is 0.10-m (0.33-ft). These specimens are considered "U-shaped" as the ratio of flange to web length is close to unity, at 0.81. Both the flange-web intersection (interior) and flange tip (exterior) wall zones have concentrated flexural and transverse reinforcement. The walls have nearly identical amounts of flexural reinforcement, which leads to higher reinforcement ratios for the thinner TUB specimen; however, the horizontal reinforcement is identical for the two specimens. These reinforcement details are shown in Figure 2.13. It is relevant to note that the design of these specimens does not adhere to any particular code document; rather the research team was interested in achieving a high level of ductility while still avoiding over-conservatism in the shear/shear-sliding. To limit sliding failure, shear keys consisting of unreinforced concrete studs were employed at the wall-foundation interface.

The specimens were subjected to cyclic lateral loading and a constant axial loading. The test setup is comprised of three actuators: two of these actuators was parallel to the wall flanges and loaded the wall 2.95-m (9.68-ft) above the foundation, and one actuator was parallel to the wall web that loaded the wall at 3.35-m (10.99-ft). These actuators controlled the two translational degrees of freedom and restrained torsion at the wall top cap. The gravity load was applied to the walls using a pre-tensioned tendon that was moderated by a hollow core jack located on the transfer beam at the top of the wall specimens, the total gravity load including specimen self-weight was of 0.02 $A_g f_c'$ for TUA and $0.04A_g f_c'$ for TUB (780kN). The test set up is shown in Figure 2.14.

The cyclic loading protocol subjected the test specimens to five directions of loading: (1) parallel to the wall web (strong axis bending in +/- directions), (2&3) parallel to the flanges (weak axis bending in +/- directions), (4) along diagonal such that one flange tip is compressed, and (5) along diagonal such that one web corner is compressed. The characteristic that distinguishes the "sweep" pattern of this loading protocol from the butterfly (or, rectangular cloverleaf) seen in *Ile & Reynouard* [101] is that the yield displacement is explicitly defined for the diagonal direction and does not result in higher ductility demands than the principal strong or weak axis directions. The bi-directional displacement history with a description of the load path is provided in Figure 2.15. Each test began with four force-controlled cycles of the load path at 25, 50, 75, and 100% of predicted first yield to determine the nominal yield in each direction. Then displacement-controlled cycles at the ductility levels 1, 2, 3, 4, 6, and 8 were carried out until specimen failure. It is relevant to note that this loading protocol is considered more extreme than that from *Ile & Reynouard* [101] due to the greater number of plastic excursions and sum of normalized plastic deformation ranges.

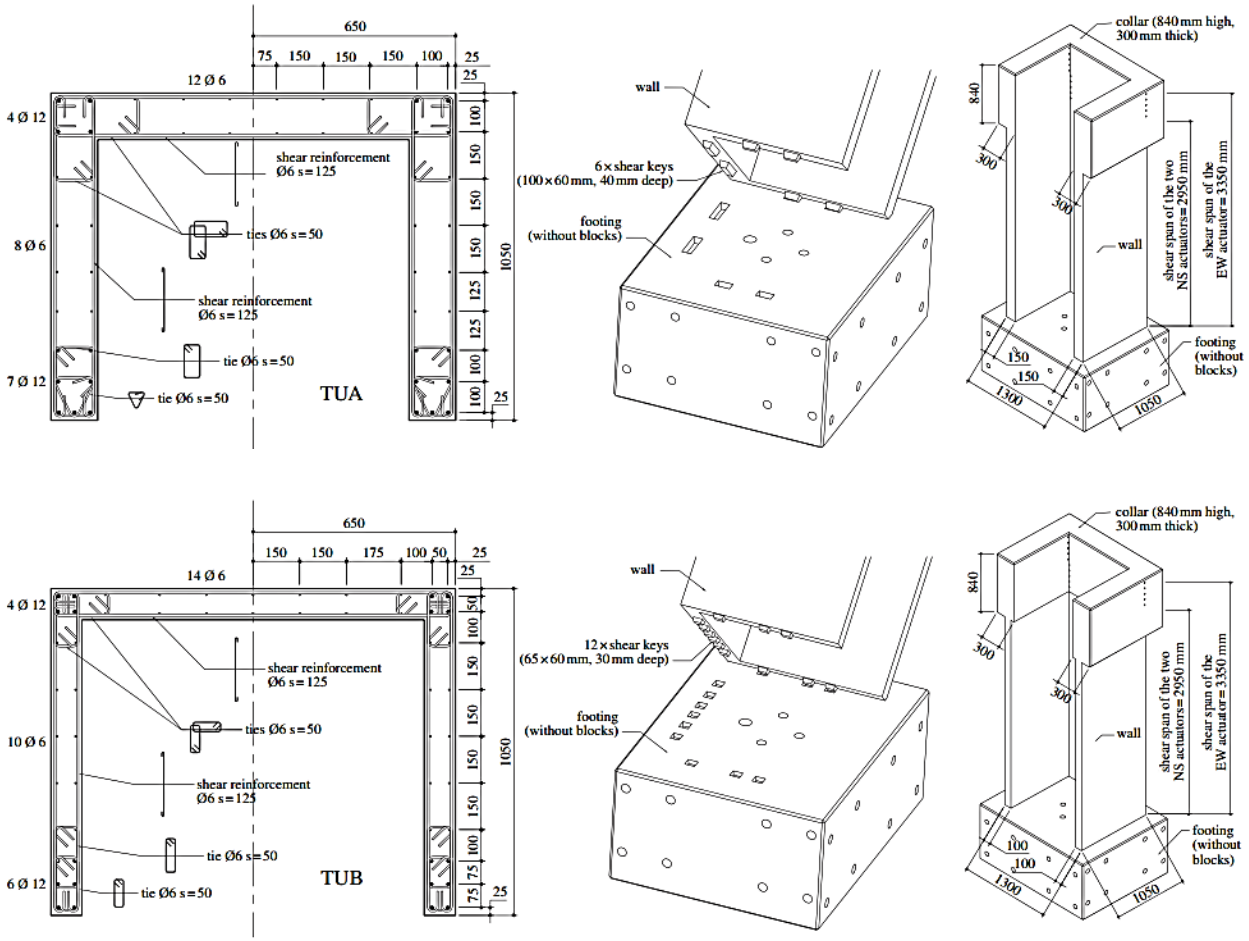

Figure 2.13: Test Specimen Geometry and Reinforcement Details for Beyer et al. [34]
(Top - Previous Page) Specimen TUA, (Bottom – Current Page) Specimen TUB

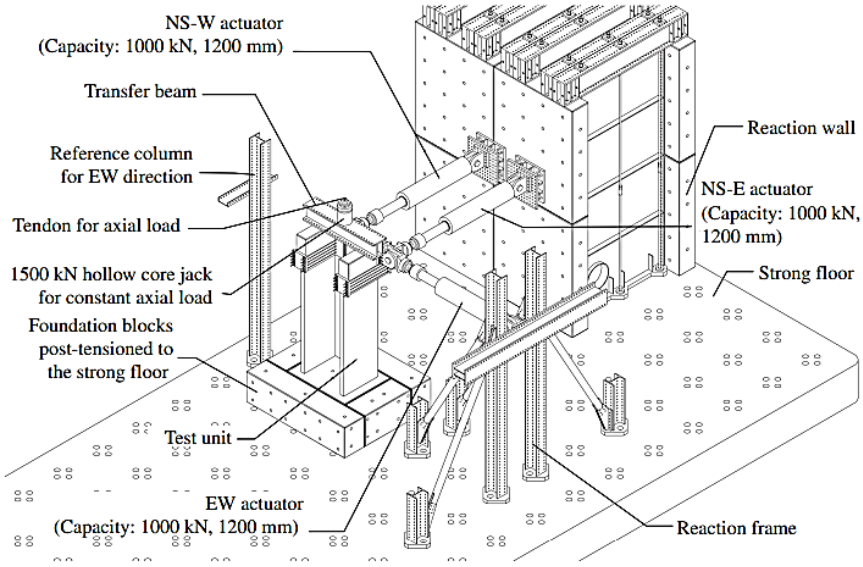

Figure 2.14: Test Set Up for Beyer et al. [34]

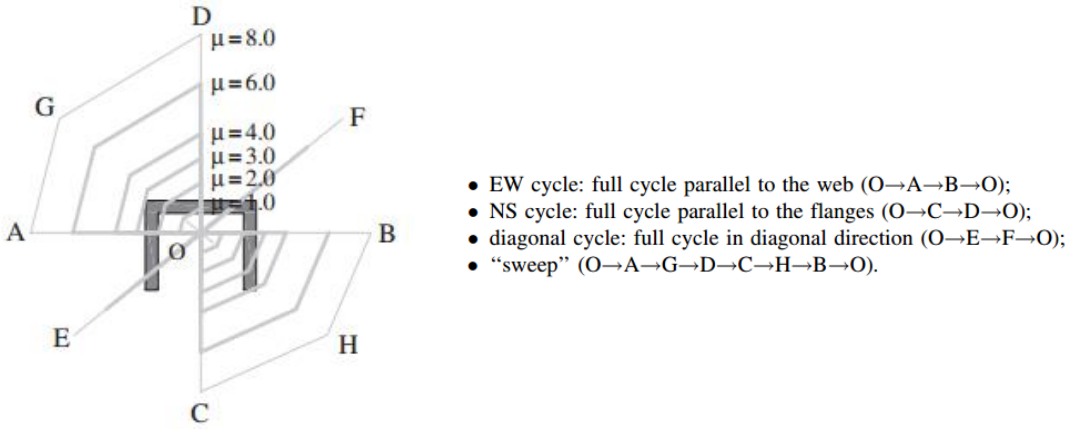

Figure 2.15: Bi-directional Displacement History and Description for Beyer et al. [34]

Experimental Test Results

For Specimen TUA, with the thicker cross-section, the normalized base moment versus drift response for the different loading directions measured at the locations of applied loading is shown in Figure 2.16. The following summarizes the major observations in the wall performance of Specimen TUA that experienced a flexural-tension (buckling-rupture) failure.

- The specimen yielded in the various directions between 0.88 cm - 1.3 cm (0.30-0.44% drift), this was determined based on average strain of flexural reinforcement at the wall base and pre-test predictions of first yield.
- The first instance of flexural bar buckling was observed during the 1.8% drift (ductility 6) cycle along the diagonal where the west flange tip was compressed. This was a larger diameter rebar located in the outer corner of the west flange tip boundary element.
- Bar fracturing was first observed approaching +2.4% drift (ductility 8) in the strong axis, when two smaller, previously buckled flexural bars ruptured. The continued load reversal to continue the cycle at this ductility level was marked by rupture of previously buckled bars primarily in the west flange tip and limited bars in the opposite wall web corner.
- Ultimately, the wall failure resulted from the loss of two larger and all the smaller flexural bars in the west flange tip.
- During this test, damage to concrete in compression was limited to spalling (which initiated at around 1% drift during the "sweep" portion of the loading protocol). By the end of the test, concrete in the confined boundary elements remained mostly intact.
- Though the research team indicated that shear sliding was minor at 4.4% of total wall deformation at a maximum at ductility 6, it was observed that sliding was significant enough to cause at that least one of the shear keys to shear off. No other significant shear behavior, like that seen in the flange of the IleXY specimen [101], was observed.

For Specimen TUB, with the thinner cross-section, normalized base moment versus drift response for the different loading directions measured at the locations of applied loading is shown in Figure 2.17. The following summarizes the major observations in the wall performance of Specimen TUB that experienced a web-crushing (shear-compression) failure; also, a number of notable differences between test specimens TUA and TUB are included.

- The TUB specimen yielded in the various directions between 1.21 cm - 1.5 cm (0.40-0.51% drift), these yield values were obtained in a similar fashion to the previous test. This suggests that the onset of yielding is slightly later in TUB compared to TUA.
- The first instances of flexural bar buckling were observed at the same 1.8% drift (ductility 6) cycle at TUA, along the diagonal where the west flange tip was compressed. These were seen in two of the larger diameter rebar located in the west flange tip boundary element.

- Concrete compression ended up playing a more critical role in the TUB wall failure than rebar performance. Spalling initiated in the boundary elements as early as cycles to 1.25% drift and began exposing flexural reinforcement during cycles approaching 1.65% drift.
- In subsequent cycles, spalling propagated towards the unconfined region of the wall web that led to considerable reduction in the wall thickness. The damaged web had insufficient capacity to carry the compression, and the diagonal compression struts failed at the 2.5% drift cycles in the strong axis.
- Though the web-crushing failure led to more than a 20% loss of strong axis strength, the failure of the wall was not as brittle as is typical of this failure mode. This was due to the fact that a portion of the lateral load was transferred to the boundary elements in the wall web corners, resulting in a "frame mechanism" where the confined regions act as short columns.
- No bar fracturing was observed during the TUB test. This is in stark contrast to TUA that failed as a result of previously-buckled flexural bars that ruptured during load reversals (particularly those in the west flange tip boundary element).
- The shear sliding in TUB was smaller than that observed in TUA (based on absolute displacement measured); however, this still led to the same magnitude contribution of 4.4% to total wall deformation at a maximum at ductility 6. There was no observation of visible damage to the shear keys or any other significant shear behavior.

Note: Images of damage to Specimens TUA and TUB can be found in Figs. 3.1 and 3.36.

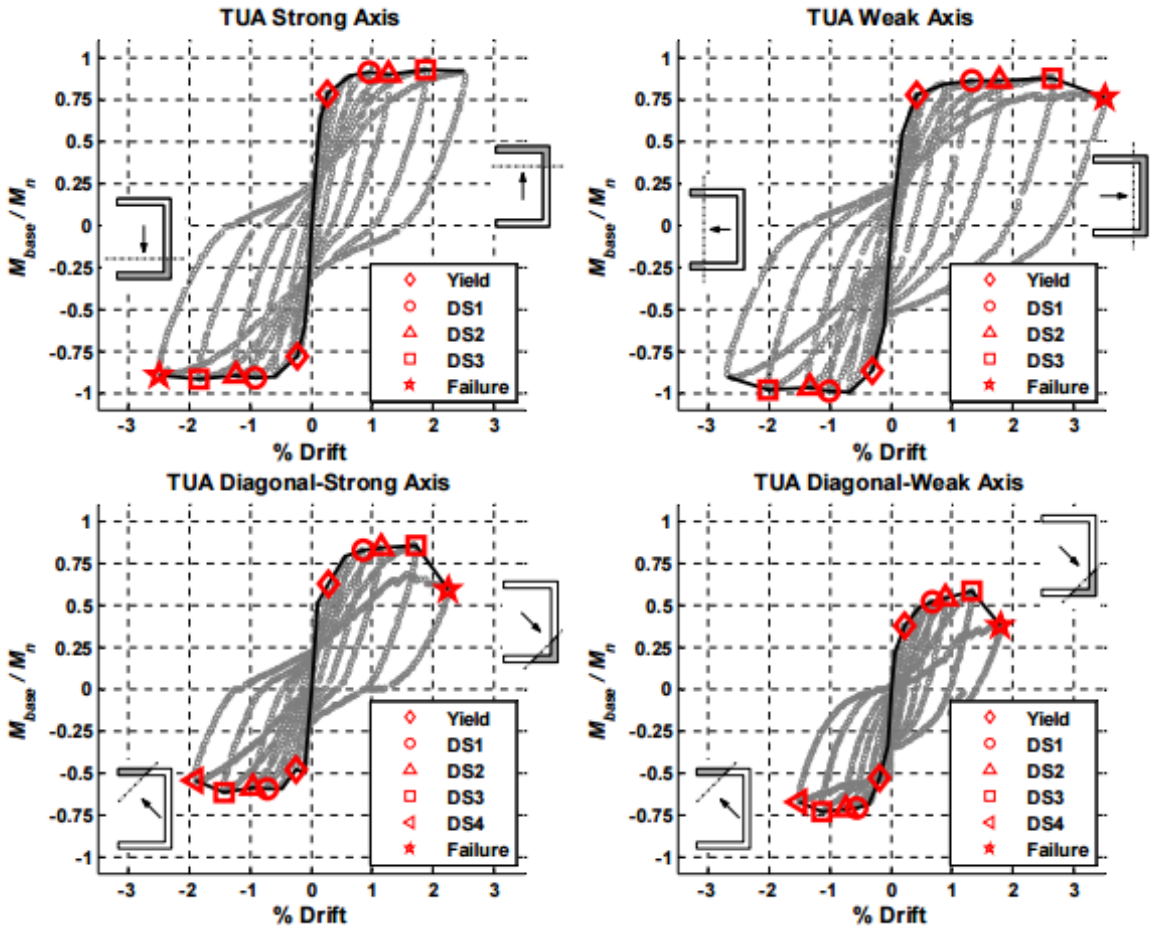

Figure 2.16: Force-displacement response for Specimen TUA from Beyer et al. ([34] as modified in [33])

(Note: Yield = theoretical first yield of longitudinal steel, DS1 = initial spalling, DS2 = significant spalling exposing steel, DS3 = buckling of longitudinal bars, and DS4 = fracture of longitudinal bars, and Failure = significant loss in load carrying capacity)

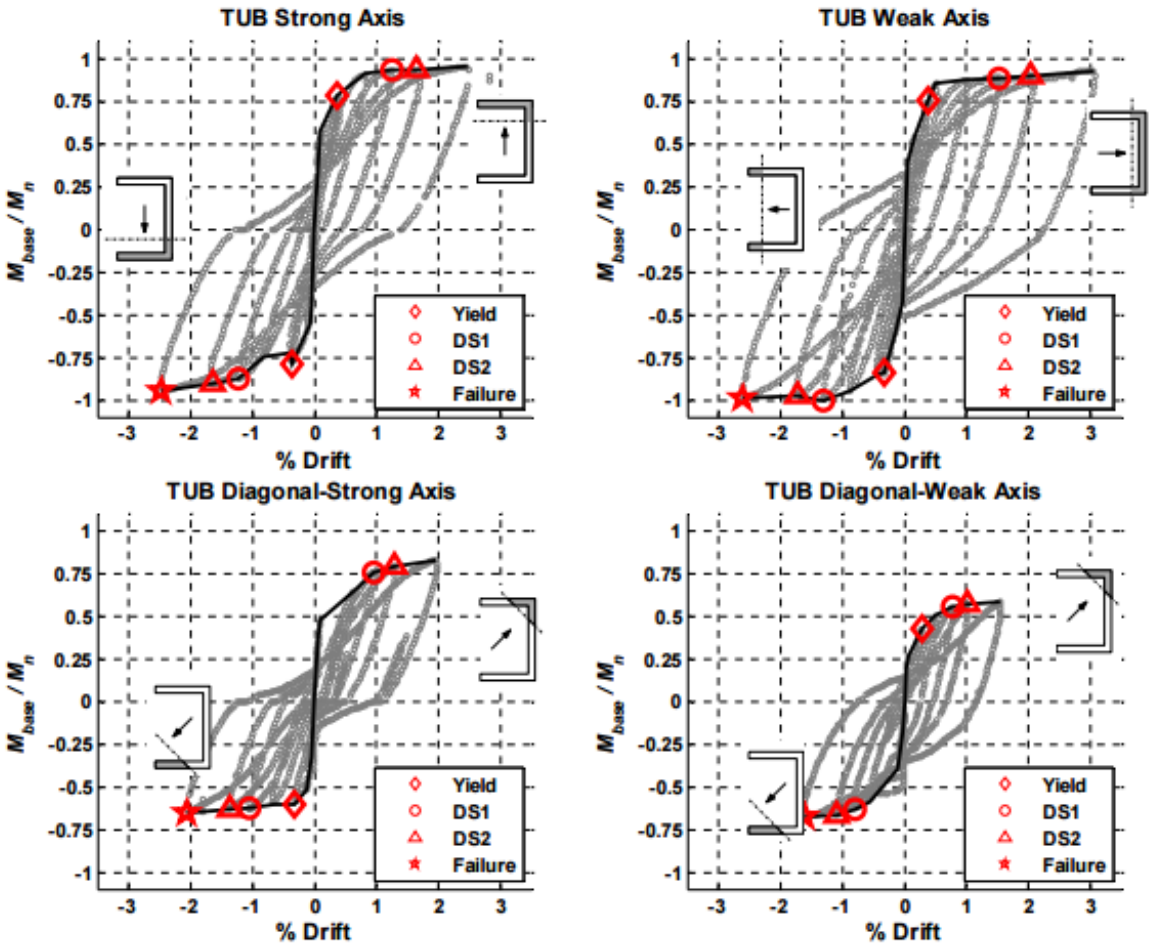

Figure 2.17: Force-displacement response for Specimen TUB from Beyer et al. ([34] as modified in [33])
(See note provided with Figure 2.16)

Research Conclusions

There were several important lessons derived from these two bi-directional U-Shaped wall tests. The first was that the diagonal loading condition where one flange tip is compressed is the most critical out of the five directions investigated in the loading protocol. Plastic hinge models overestimate flexural capacity of the wall for this diagonal condition, despite providing reasonable results for wall capacity in the primary strong and weak axis directions. The discrepancy in the prediction can be that the force distribution to the various wall elements – web and flanges – is complex and is effected by differences in stiffness between the compression and tension flanges that result from cracking from previous loading. The researchers expressed concern at this finding since many engineers do not consider the diagonal loading case for non-planar walls nor the effects of cyclic loading history, in part, because most sectional analysis tools do not easily accommodate these functions. At the same

time, researchers indicate that the diagonal moment capacities reached in the test were not ultimate moment capacities of the wall and so this may affect the predicted versus observed response.

These tests also demonstrated whether detailing procedures consistent with high ductility (non-code specific) design was effective. The thicker TUA wall specimen was able to achieve a large displacement ductility of 8 and experienced a buckling-rupture failure consistent with a tension-controlled flexure response. This failure mechanism is often observed in well-detailed, capacity-design walls. However, despite employing a similar logic with the design of the thinner TUB wall specimen, the displacement ductility was lower and the web-crushing failure is dominated by the compression capacity of the wall web. Fortunately, the wall does not experience the brittle failure since the lateral load was transferred to well-detailed boundary elements that were engaged through frame action. The research team notes that future design of thin non-planar walls should account for considerable spalling in the unconfined wall web that occurs due to bi-directional loading as this can severely limit the compression capacity and trigger wall failure.

The final observations from the test program are related to shear behavior. The research team notes that, in general, the shear contribution to overall wall deformation is higher in the non-planar test specimens compared to previous rectangular walls. This may necessitate modifications to code provisions for shear design of rectangular cross-sections compared to non-planar walls. Furthermore, test results indicate that shear deformation is largest when the section is under net tension (specifically for diagonal loading); it is hypothesized that this shear deformation is significant since large crack widths lead to a small shear stiffness. Other observations include that, the ratio of shear to total wall displacement is notably larger for the thinner TUB wall than for TUA; that the formation of a large base crack along nearly the entire wall-foundation interface limits the transfer of shear forces to the foundation; and that the sliding shear mechanism did not trigger failure as predicted by Eurocode 8 [44] as these deformations were relatively small (although it is likely that the use of shear keys limited this undesirable response).

2.4.3 Tests on I-Shaped Wall Configurations

2.4.3.1 Oesterle et al. (1976), Oesterle et al. (1979) [140, 141]

Research Objectives

At the time of the *Oesterle et al.* [140, 141] two-part study conducted at the Portland Cement Association, there was limited experimental data for walls subjected to cyclic lateral loading since a majority of prior large-scale tests had monotonic loading schemes. A variety of structural wall geometries were investigated, including two flanged I-Shaped specimens, in an effort to better understand the inelastic performance of these structural components. All the wall specimens were designed for flexure and shear in accordance with ACI318-1971 [4], and the particular parameters of interest for the I-Shaped walls were the amount of flexural reinforcement, presence of confinement in the boundary elements, and application of axial load. Both walls were subjected to high nominal shear stresses (greater than $7.0\sqrt{f_c'}$) which ultimately played a critical role in the wall failures. Researchers examined the global hysteretic response of the specimens to evaluate strength, energy dissipation capabilities, and ductility resulting from the differing design choices. The overarching objective was to evaluate the current state of the ACI318 code provisions and develop design procedures that would insure adequate strength and energy dissipation for these lateral load resisting wall systems. It is relevant to note that despite the passage of nearly four decades, this extensive experimental work is regarded as a standard which modern wall test programs still use as a measure.

Test Program

The two isolated I-shaped walls (Figure 2.18) that were tested are considered to be a one-third (1:3) scale specimens by the researchers. The walls have a 75-in wide web, 36-in long flanges, height of 15-ft; and wall thickness of 4-in. These specimens are considered "I-shaped" as flange length is significantly shorter than web length (ratio of flange to web length is 0.48). The first wall specimen (F1) has uniformly distributed flexural reinforcement in the flange bounded by horizontal reinforcement; these flanges were considered were detailed as compression columns. In contrast, F2 was designed to have "special boundary elements" consisting of concentrated flexural steel and closely spaced confining reinforcement at the web-flange intersection only. These reinforcement details are shown in Figure 2.18. Other than reinforcement configuration, the primary difference between the two specimens was that F1 only had a lateral loading, while F2 also has an applied axial load.

The specimens were subjected to cyclic lateral loading and a constant axial loading. The setup for the wall tests was comprised of two or four actuators (based on predicted wall strength). Actuators were positioned at each side of the specimen parallel to the wall web and are joined via a link assembly, since each of these actuators functioned in a "push-only" direction. The gravity load was applied to the walls using two hydraulic jacks on a steel transfer beam at top of the wall, the applied axial load to Specimen F2 was 0.07 $A_g f_c'$ which was moderated throughout the test. The test set up is shown in Figure 2.19.

The uni-directional cyclic loading protocol was applied parallel to the web (strong axis bending) and was applied as in an incrementally increasing fashion. The displacement history for each of the wall specimens is provided in Figure 2.20.

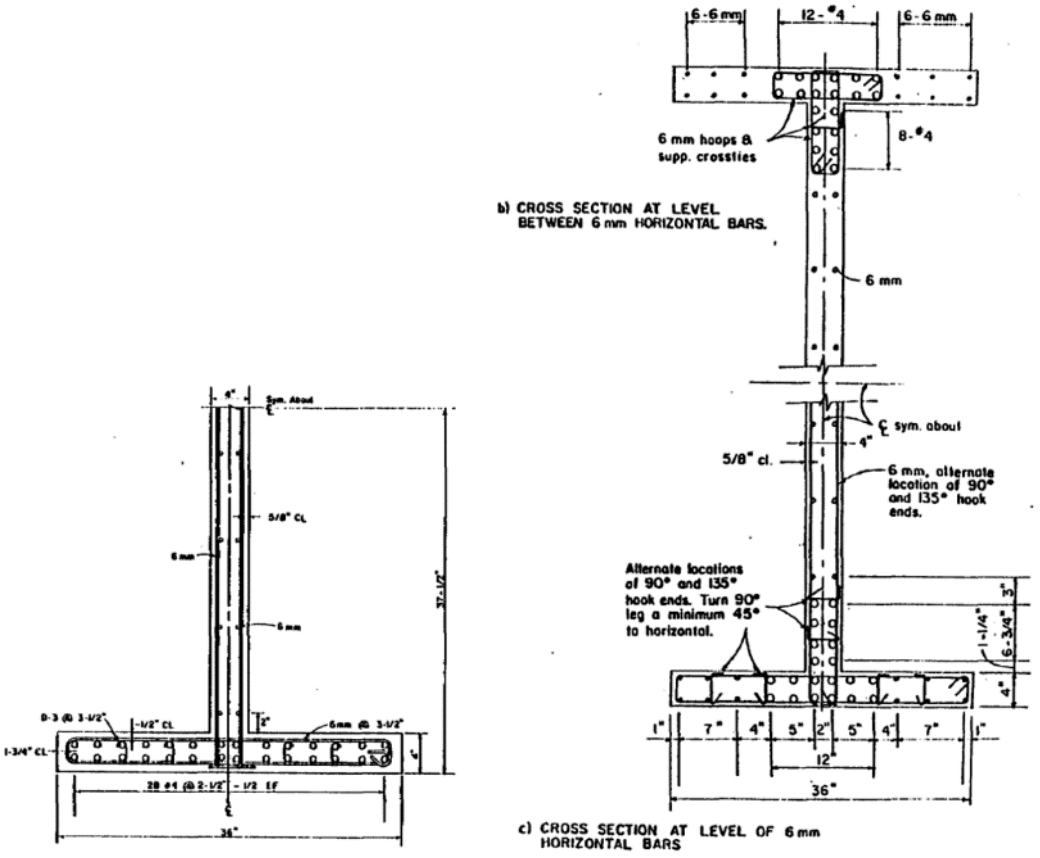

(a) Specimen F1 (b) Specimen F2

Figure 2.18: Test Specimen Geometry and Reinforcement Details for Oesterle et al. [140, 141]

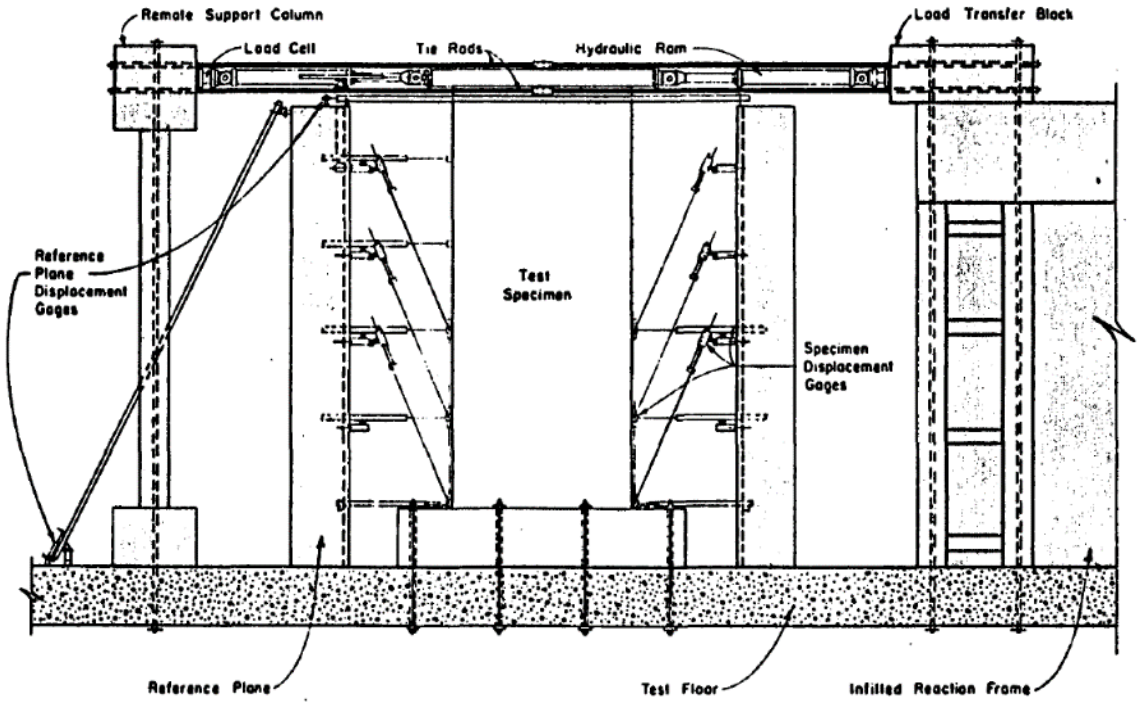

Figure 2.19: Test Set Up for Oesterle et al. [140, 141]

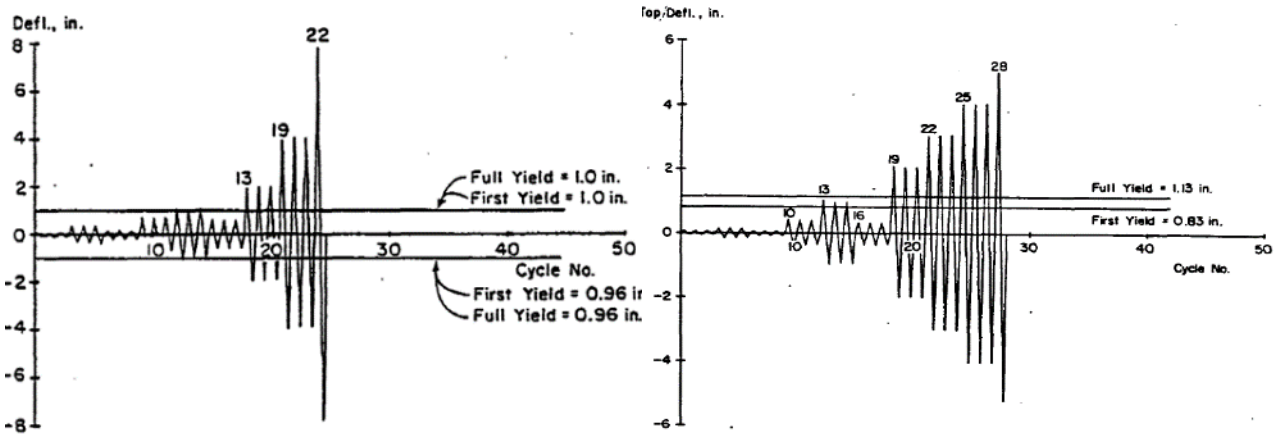

(a) Specimen F1 (b) Specimen F2

Figure 2.20: Displacement History for Oesterle et al. [140, 141]

Experimental Test Results

For Specimen F1, the lateral load versus displacement response is shown in Figure 2.21(a). The following summarizes the major observations in the wall performance of Specimen F1 that experienced a web-crushing (shear-compression) failure.

- During the first cycle at 1 in (0.5% drift) the onset of flexural reinforcement was noted. Inclined cracking in the web formed a fan that terminated in the web 4-in above the wall base. It is believed that the flexible boundary element caused the crack pattern to converge in this small region above the wall base.
- During the third cycle at 2 in (1% drift) spalling had initiated along the construction joints and inclined web cracks. Also, during this cycle notable bowing of the flanges was observed due to horizontal movement of the wall web. This resulted in cracking of the flange.
- During the cycle when approaching -4 in (-2.25% drift), multiple compression struts sequentially crushed and slipped along adjacent cracks in a direction opposite of loading at 1-ft above the wall base. This led to a rather significant reduction in capacity; however, the research team believes the wall could have sustained cycles at ±3in (1.67% drift) with less than 20% capacity loss. Damage at the end of the test is shown in Fig. 2.22(a).

For Specimen F2, the lateral load versus displacement response is shown in Figure 2.21(b). The following summarizes the major observations in the wall performance of Specimen F2 that experienced a web-crushing (shear-compression) failure.

- During the cycle at 0.5 in (0.25% drift) the onset of yielding in flexural reinforcement was noted. Also, horizontal cracking in the boundary elements and inclined cracking in the web was observed.
- During the cycle at 2 in (1% drift) spalling had initiated along the inclined web cracks. Spalling was also observed due to opening of cross-tie hooks in the confined region at the first cycle at 3 in (1.67% drift). During the first cycle at 4 in (2.25% drift), crushing was noted in the lower-left, confined portion of the web near the flange interface.
- When approaching +5 in (2.75% drift), significant crushing of the unconfined region of the web occurred; however, the boundary elements were intact and only a 2% reduction in wall capacity occurred.
- Upon load reversal to -5 in (-2.75% drift) the wall failed when multiple compression struts terminating at the lower-left corner of the wall crushed followed by shearing of the compression flange. This created a horizontal failure plane through the web and led to a horizontal bar fracture. Damage at the end of the test is shown in Fig. 2.22(b).

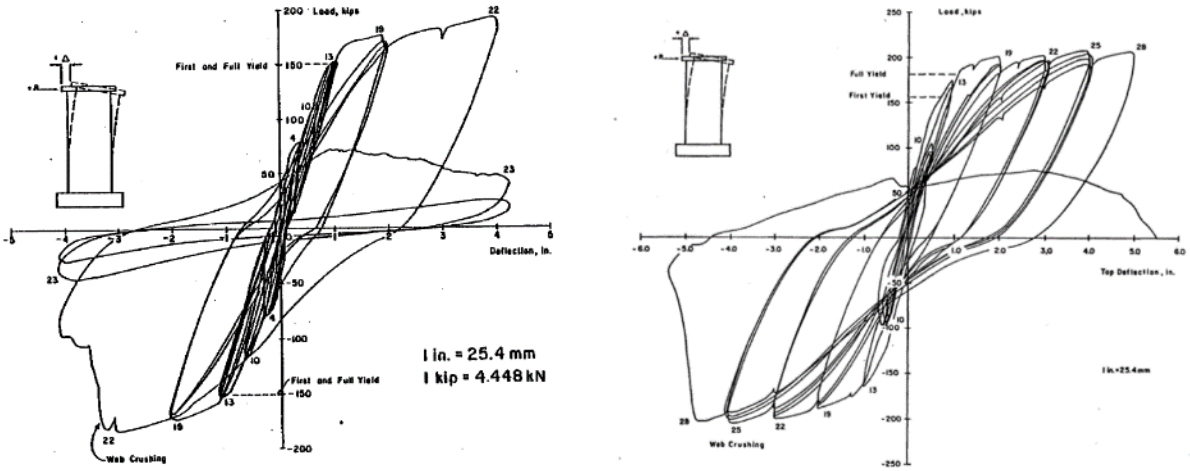

(a) Specimen F1 (b) Specimen F2

Figure 2.21: Force-displacement responses for Oesterle et al. [140, 141]

Research Conclusions

There were many learning gains from this test program reflated to reinforcing configuration for boundary elements in flanged walls, the benefits or drawbacks of using a flanged wall geometry, and the web crushing failure mechanism observed in specimens subjected to high shear stresses. First, there is notably improved inelastic performance for the I-Shaped wall with a stiff boundary element consisting of concentrated flexural steel since the reinforcement can be engaged in dowel action that limits shear deformations near that base of the wall as well as slippage at wall-foundation interface. Furthermore, confined boundary elements (particularly extending along the height of the plastic hinge region) improves wall performance since it delays flexural bar buckling; helps maintain core concrete; in addition to increasing the stiffness, shear resistance, and compressive stress capacity of the boundary element. Second, the use of flanges instead of a rectangular cross-section provides a relatively large out-of-plane stiffness that is expected to prevent global instability in the wall, yet unlike a barbell boundary element a flange provides lower in-plane stiffness and is thought to be vulnerable to shear sliding (though not observed in either F1 or F2 tests). The flange also may result in a design with high shear stresses. Lastly, high shear stresses result in steep inclined cracking in the web that leads to the formation of compression struts that deteriorate due to abrasion upon load reversal and ultimately fail in a sudden manner. This web crushing failure mechanism is an important to consider as limits ductility. The research team indicated that web crushing depends on both shear stress and deformation, and a truss analogy model with appropriate modifications can be utilized to predict web crushing strength using the axial compressive load and concrete strength values.

As a general observation, irrespective of wall geometry, the researchers noted that for wall specimens subject to cyclic lateral loading, shear deformations (particularly in the plastic hinge region) make up a significant portion of the total wall deformation which should be considered in inelastic analyses. That is to say that there is coupling between flexural-shear deformations. Related, shear stiffness degrades through load reversals due to the hysteretic behavior of flexural reinforcement and deterioration of concrete. Current researchers continue to work on methods to account for this flexure-shear interaction as this is a rather critical but complex issue.

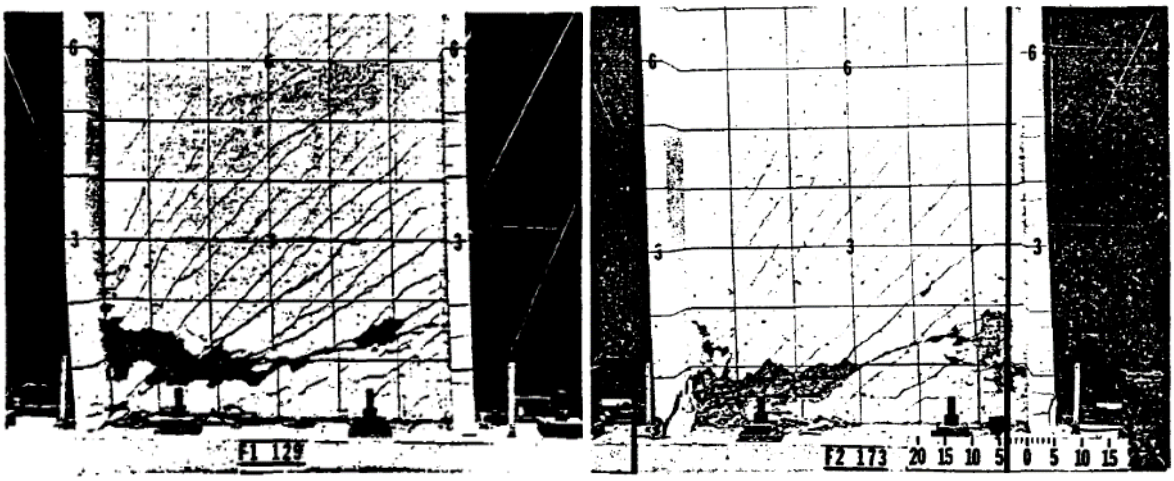

(a) Specimen F1 (b) Specimen F2

Figure 2.22: Damage to the specimens at end of test from Oesterle et al. [140, 141]

2.4.3.2 Shouzhong (2002) [157]

Research Objectives

In this wall test program, a single I-shaped wall was tested at the State Key Laboratory of Disaster Reduction in Civil Engineering (SLDRCE) at Tongji University. This experiment is part of a much more extensive database of seismic structural tests funded under a grant from the National Basic Research of China that involved over 250 individual specimen tests conducted between 1996 and 2008. The objective of this particular shear wall investigation was to examine how the shape of a wall boundary element can impact earthquake performance. In practice engineers employ different boundary elements based on architectural constraints that result in rectangular, barbell, or flanged wall configurations; therefore, it is critical to understand the differences in failure mechanisms, strength capacity, ductility, and energy dissipation of these wall types. Additionally, researchers were

interested how the increased restraint provided by the boundary element would impact out-of-plane wall instability.

Test Program

The single I-shaped wall (Figure 2.23) was tested was considered to be a one-fifth (1:5) scale specimen where a full-scale specimen has a thickness of 12-in. The wall had a 1000-mm (39.37-in) wide web, 420-mm (16.54-in) long flanges, a wall thickness of 60-mm (2.36-in) and an overall height of 3000-mm (118.11-in) as it is comprised of four floors at 750-mm (29.53-in). These specimens are considered "I-shaped" as the flange to web length ratio is rather low at 0.42. Only the flange-web intersection (interior) wall zone had concentrated flexural and transverse reinforcement. These reinforcement details are shown in Figure 2.23. A notable difference between this particular test specimen and all the previously described non-planar walls is that each floor a portion of the slab diaphragm is included. This slab is 30-mm (1.18-in) thick and extends 180-mm (7.09-in) from each side of the wall face.

The specimen was subjected to cyclic lateral loading and a constant axial loading. The lateral load was applied using a single actuator through the center of the wall top cap. The gravity load was applied to the wall using two, symmetrically placed hydraulic jacks at the top of the wall; this applied axial load was 0.1 $A_g f_c'$ which was moderated throughout the test. The test set up is shown in Figure 2.24.

The uni-directional cyclic loading protocol was applied parallel to the web (strong axis bending). During the first stage of loading, force control was utilized to progressive load the specimen to cracking and then yield, once the wall began behaving inelastically, displacement control was implemented. The second stage of lateral loading involved incrementally increasing displacements that were a set ratio of the yield displacement, and three cycles were executed at each of these displacement levels until the wall's strength dropped to 85% of the maximum measured capacity.

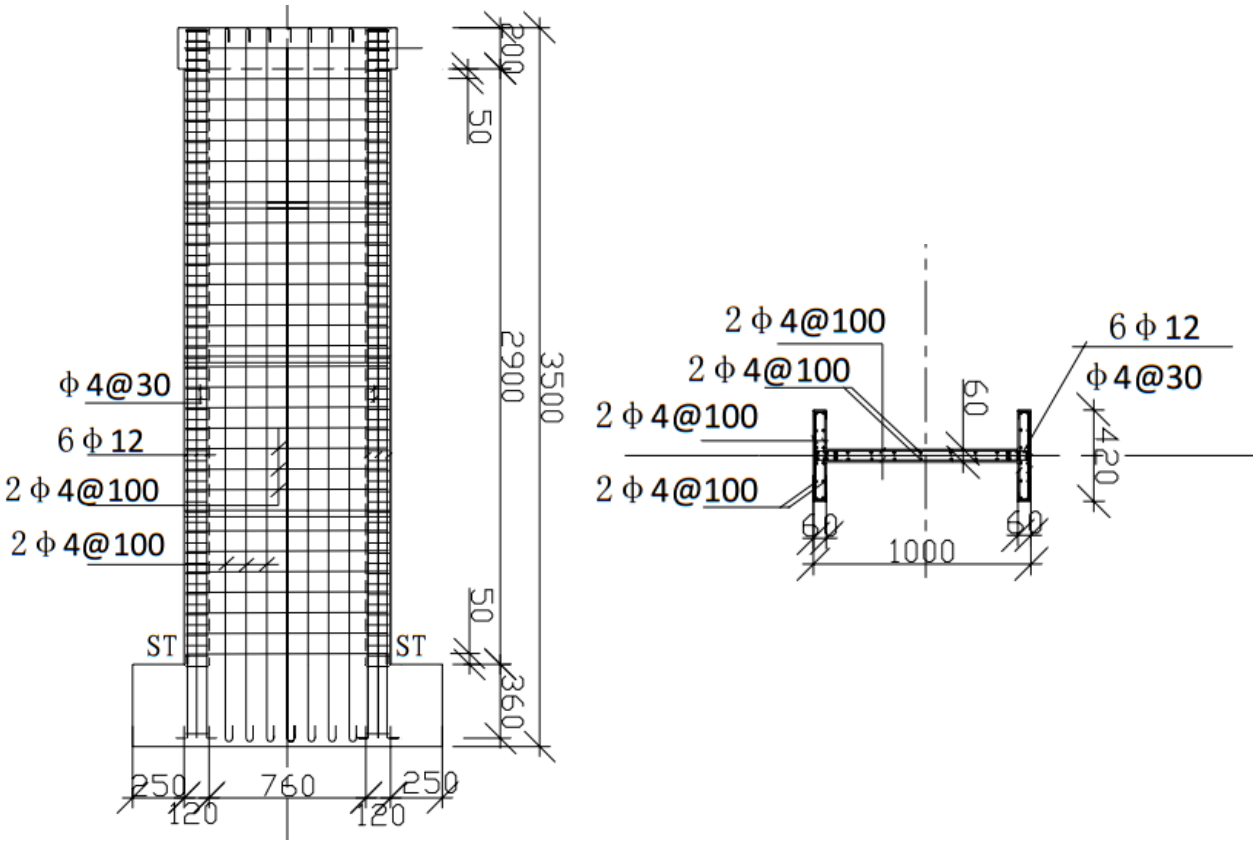

Figure 2.23: Test Specimen Geometry and Reinforcement Details for Shouzhong [157]

Figure 2.24: Test Set Up for Shouzhong [157]

Experimental Test Results

For the flanged I-Shaped specimen SW-3, the lateral load versus displacement response is shown in Figure 2.25. The following summarizes the major observations in the wall performance of Specimen SW-3 that experienced a crushing-buckling failure.

- At a lateral load of 50 kN, associated with displacement of 0.6 cm (0.24 in, 0.2% drift), horizontal cracking at the flange base and inclined cracking at the center of wall at the first and second floors of the specimen was observed.
- During the cycle at 2.5 cm (1 in, 0.83% drift) the onset of yielding in flexural reinforcement was noted.
- During the first cycle at 4 cm (1.57 in, 1.33% drift) spalling was first observed, and after two additional cycles at this drift level there appeared to be shear slip occurring at the wall-foundation interface.
- There was significant reduction in wall capacity by the first cycle at 4.5 cm (1.77 in, 1.5% drift) due to core crushing in the flange region (and later in boundary elements) and increased levels of shear slip. By the 5.5 cm cycle (2.17 in, 1.83 %drift) the lower portions of both flanges began buckling and there was severe core damage.
- At the end of the test, researchers noted that out-of-plane buckling made have contributed to the final failure. Damage at the end of the test is shown in Fig. 2.26.

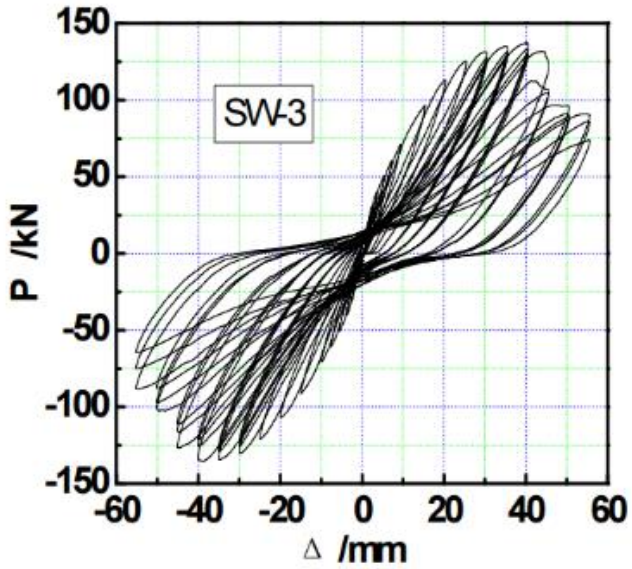

Figure 2.25: Force-displacement response for Specimen SW-3 from Shouzhong [157]

Research Conclusions

This test series led to important observations about the impact of the restraint provided by a flanged boundary element that can be related to the findings of *Oesterle et al* [140, 141]. The results from the PCA I-Shaped wall tests suggested that shear deformations near the wall base were limited by dowel action of flexural steel in the boundary element; however, the *Shuozhong* [157] research team indicated observations suggesting that the flange boundary element shape restrains the wall web in a way that shear deformations (especially after the specimen has yielded) dominated the overall wall deformation. With flanged walls, the varying contribution of shear deformation through progressive cyclic lateral loading cycles is a concern that warrants further investigation. Another observation related to the *Oesterle et al* [140, 141] tests is that researchers anticipated shear slip at the web-foundation interface for flanged walls, and though this was not seen in Specimens F1 and F2, it was observed in SW-3. Shear slip has been credited as a factor that greatly reduces wall ductility, and it would be important to identify why it appears in some instances and not in others with non-planar wall configurations. A final comment related to the three I-Shaped walls tested in the two test programs *Oesterle et al* [140, 141] and *Shuozhong* [157] is that they all experienced undesirable compression-type failures (F1 and F2 failing due to web crushing and SW-3 due to boundary element crushing) despite the use of concentrated flexural reinforcement and what is considered adequate confinement steel in the boundary element to ensure wall ductility. More investigation is likely necessary to determine what is driving these compression-dominated failure mechanisms and how design might be modified to avoid them.

Figure 2.26: Damage to the specimen at end of test from Shouzhong [157]

2.4.4 Tests on T-Shaped Wall Configurations

2.4.4.1 Paulay & Goodsir (1985) [143]

Research Objectives

This wall test program at the University of Canterbury was conducted to address two major gaps in technical knowledge identified during drafting of the New Zealand concrete design code document NZS 3101:1982 [138] that provided guidelines for the seismic design of ductile structural walls. The researchers wanted to evaluate whether existing design provisions were sufficient, first, to prevent inelastic instability in the plastic hinge region of slender walls, and second, to provide necessary confinement via transverse reinforcement of wall flexural-compression zones to insure ductility under large displacements. In addition to these explicit objectives, researchers were able to investigate the load-deformation response of cyclically loaded, thin-walled sections to understand the damage progression and ultimate failure mechanisms of these structural components.

Test Program

The researchers designed the single T-shaped wall (Figure 2.27) to be a one-third (1:3) scale specimen representing the bottom few floors of a wall in a prototype medium-rise building, where full-scale walls have a thickness of 12-in. The wall had a 1300-mm (51.18-in) wide web, a 700-mm (27.56-in) long flange, a wall thickness of 100-mm (3.94-in) and is comprised of two floors for a total height of 2400-mm (94.49-in). Both the flange and web-end (exterior) wall zones had concentrated flexural and transverse reinforcement, though this was not the case at the flange-web interface. It is relevant to note that the confinement steel in the boundary elements only extend 1300 mm (51.18 in) from the wall base, and more widely spaced hoops are used above this region. These reinforcement details are shown in Figure 2.27. Similar to the *Shouzhong* [157] I-shaped wall specimen, a portion of the slab diaphragm is included. This slab is located 1000-mm (39.37-in) above the wall foundation; it is 100-mm (3.94-in) thick and extends 300-mm (11.81-in) from each side of the web wall face.

The specimen was subjected to cyclic lateral loading with variable axial loading. The lateral load was applied using an actuator connected to the top of the wall top cap that is part of a steel reaction frame. The axial load was applied incrementally to the wall using a test machine ram, this value ranged from $0.02A_gf_c'$ for negative displacement (flange under compression) to $0.12\ A_gf_c'$ (web tip under compression). The test set up is shown in Figure 2.28.

The uni-directional cyclic loading protocol was applied parallel to the web (strong axis bending). Researchers intentionally developed a loading scheme that would initiate a lateral instability in the wall by applying a larger axial compressive load during the positive displacement portion of each cycle (web tip in compression), such that the combined compression from bending and axial load are exerted on the thin, unbraced wall web tip. The objective of the negative direction of loading was to soften the critical buckling region by subjecting it to plastic tensile excursions. During the test there were initially two force-controlled cycles at 75% of the predicted wall strength. This was followed by two displacement-controlled cycles at each of μ_{Δ}=2, 4, 6 until specimen failure. The incremental loading in terms of ductility levels is given in Figure 2.29.

Experimental Test Results

For the T-Shaped specimen Wall 3, the lateral load versus displacement response is shown in Figure 2.30. The following summarizes the major observations in the wall performance of Wall 3 that experienced a web-crushing (shear-compression) failure initiated by an instability in the wall web.

- At +3.8 cm (+1.5 in, +1.6% drift) vertical splitting cracks were noted in the cover concrete of the web tip, and by +7.6 cm (+3 in, +3.2% drift) spalling had extended from the wall base to 700 mm (27.56 in).
- Over subsequent the cycles, cracks across the center of the flange widened and there were notably few inclined shear cracks in the wall web.
- During the nominal ductility cycle approaching +11.4 cm (+4.49 in, +4.75% drift) a global instability was observed as the bottom 800 mm (31.5 in) of the wall web moved out-of-plane (northward). In later load steps the wall web re-stabilized with an opposite (southward) movement.
- During a pause for data acquisition immediately following the re-stabilization the wall experienced a concrete crushing failure primarily in the unconfined region of the wall web. The research team notes that this material compression failure was likely due to a shift in the compression zone depth due to the lateral movement of the web. Damage at the end of the test is shown in Fig. 2.31.

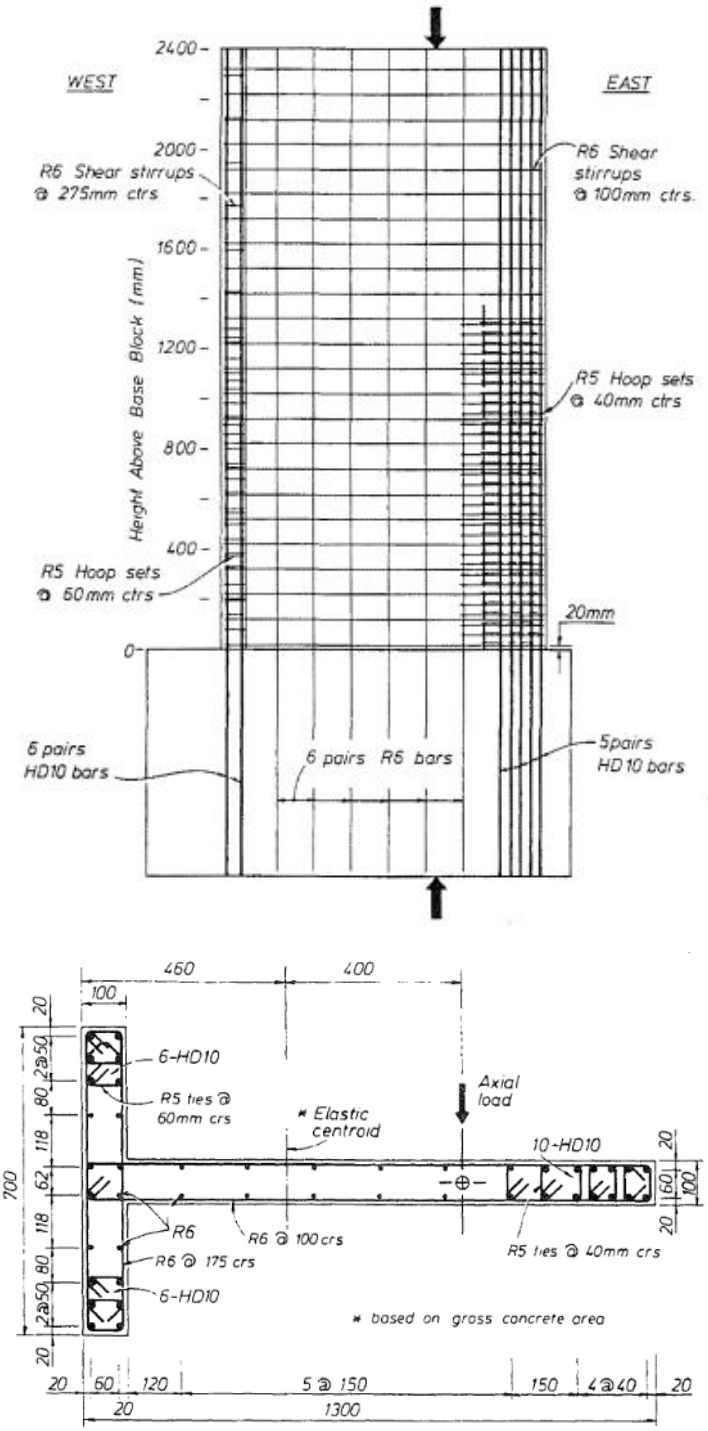

Figure 2.27: Test Specimen Geometry and Reinforcement Details for Paulay & Goodsir [143]

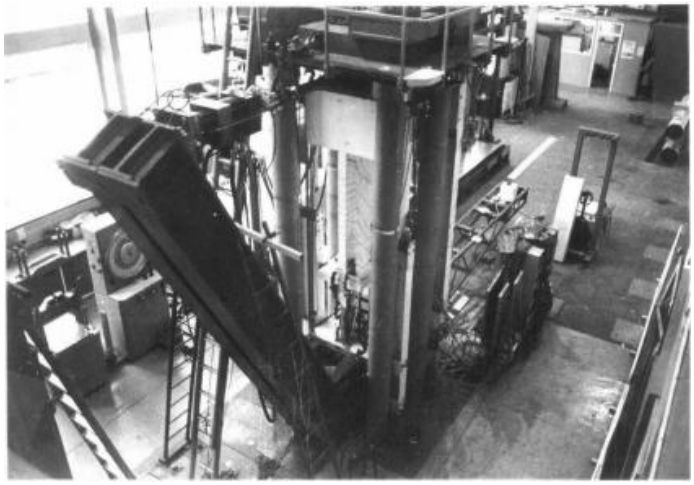

Figure 2.28: Test Set Up for Paulay & Goodsir [143]

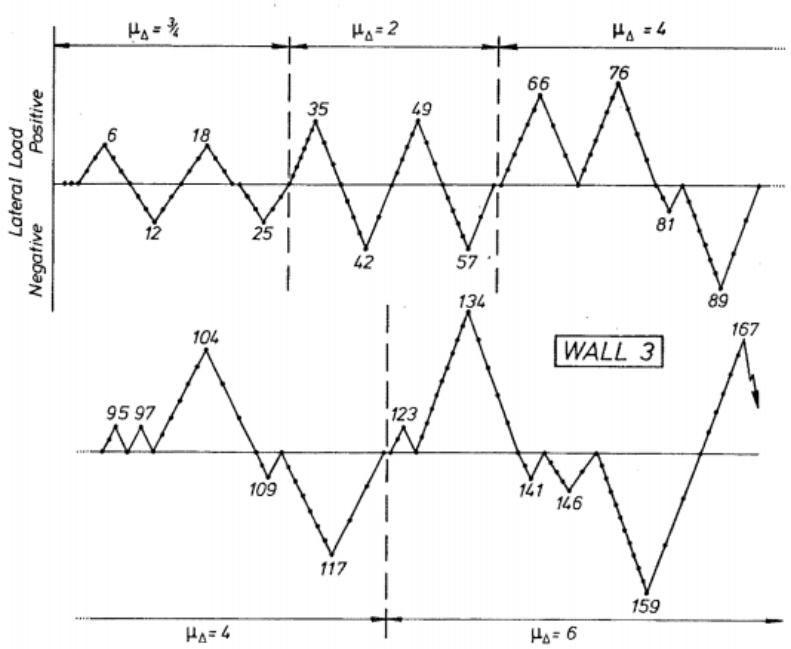

Figure 2.29: Displacement History for Paulay & Goodsir [143]

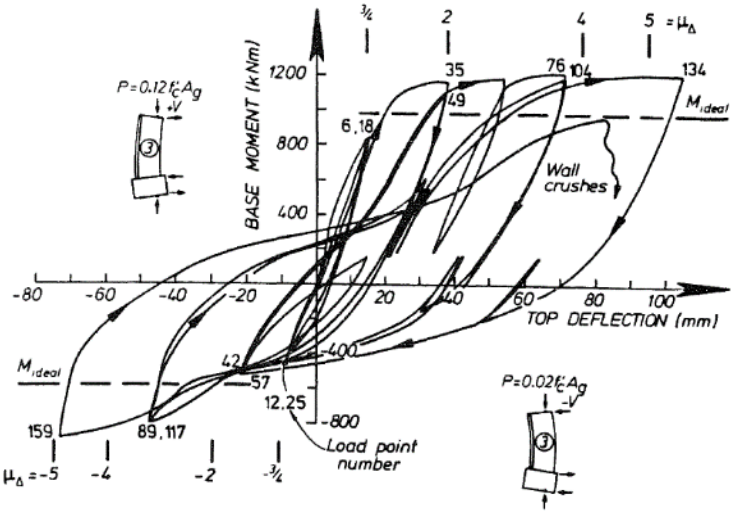

Figure 2.30: Force-displacement response for Specimen Wall 3 from Paulay & Goodsir [143]

Research Conclusions

This test series enabled researchers to make critical observations that clarify the onset of global instability in a thin-wall section. In brief summary, their findings indicate that at large displacement demands, wide cracks open in the portion of the wall subjected to tension. If, upon load reversal, these cracks remain open due to residual tensile strain in the reinforcement, then the reinforcement alone has to resist the compression forces on the section. The wall is susceptible to buckling as the rebar, responsible for carrying the compressive load, has already been subject to various inelastic cycles. In the T-Shaped Wall 3 specimen, researchers observed it is possible that the wall exhibits an instability followed by a redistribution of internal forces so the wall can regain stability and maintain its load carrying capacity. However, the negative outcome of this out-of-plane motion is an increase in the compression depth, which with increasing ductility demands results in high compressive strains in the unconfined region of the wall inducing cover loss and ultimately concrete crushing in this region. The research team indicates one method of avoiding this type of instability failure is to provide boundary elements in the form of flanges or barbells at the critical free-end to provide out-of-plane stiffness.

In addition to lessons learned about instability in thin-wall sections, researchers were able to evaluate the existing design procedures related to confinement of boundary elements to ensure wall ductility. An important observation was that a confinement length half the theoretical compression depth was insufficient since compressive strains measured in the unconfined region near the boundary element were rather high at greater ductility demands. Instead of having a fixed value for

this length, the researchers suggest that it vary based on the desired displacement ductility of the wall. An examination of the quantity and placement of transverse reinforcement to provide confinement indicated that the code provisions were sufficient, measured strains for the hoop reinforcement was generally below yield even at high ductility values.

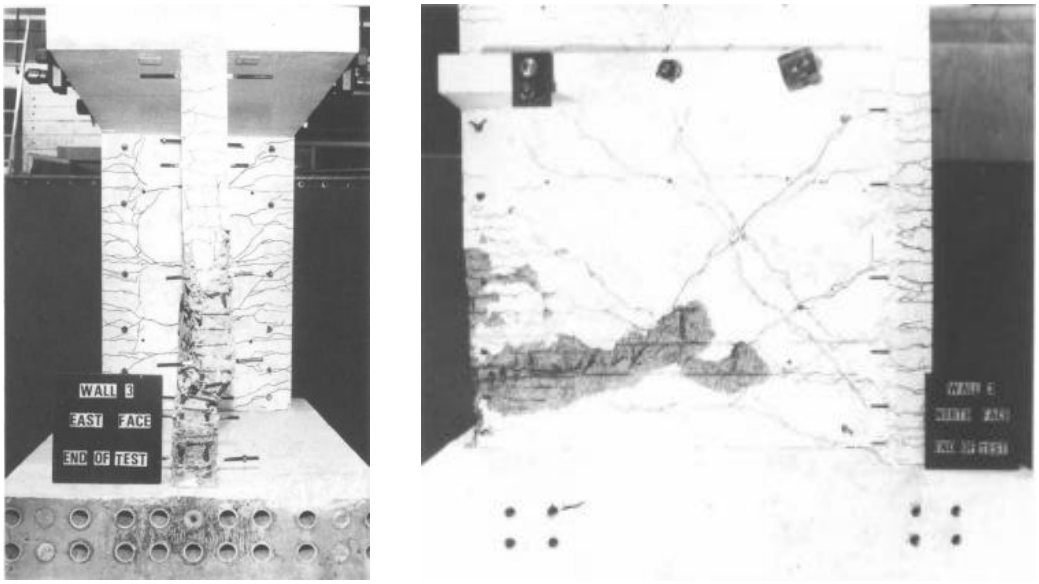

Figure 2.31: Damage to the specimen at end of test Paulay & Goodsir [143]

2.4.4.2 Thomsen & Wallace (1995); Thomsen & Wallace (2004) [161, 162]

Research Objectives

Prior to 1994, the design of special confined boundary elements in structural walls was based on a stress-based approach described in the *ACI318-89* [9] and *UBC-91* [95] codes. However, this method was determined to be overly conservative for most wall systems and a displacement-based design procedure was developed, in part, by one of the researchers in this study. An experimental program including two T-shaped walls was undertaken at Clarkson University to validate this new design approach. At the time of the test program there were also very little experimental data available for asymmetrical cross-sections; in the absence of test data, existing codes did not include recommendations for these non-planar wall configurations and engineers typically designed them as if the web and flange(s) were independent rectangular walls that were joined together. To address this shortcoming in the code, one of the study's objectives was to develop appropriate procedures for detailing and adequately predicting the effective flange width of the wall.

Test Program

The two T-shaped walls (Figure 2.32) that were tested are considered to be a one-third (1:3) scale specimens where full-scale walls have a thickness of 12-in. They were designed to be part of a lateral load resisting system in a six-story prototype building. The walls have a 48-in wide web, a 48-in long flange, height of 12-ft, and wall thickness of 4-in; there is a floor slab every 3ft. The flange and web-end (exterior) as well as the flange-web interface (interior) wall zones had concentrated flexural and transverse reinforcement. However, the reinforcement configurations for these boundary elements vary. The first wall specimen (TW1) is designed as two independent rectangular walls such that all the exterior and interior boundary elements have identical reinforcement and ignore the interaction between the flange and web (this is considered intentionally poor detailing). The second wall specimen (TW2) takes into account this interaction which produces a design with lower confinement ratio for the flange-web boundary element, and a longer boundary element with higher confinement ratio at the web-end. These reinforcement details are shown in Figure 2.32.

The specimens were subjected to cyclic lateral loading and a constant axial loading. The lateral load was applied by a single horizontal actuator positioned at the mid-height of a beam placed at the top of the specimen. Out-of-plane support was provided to restrain torsional effects. The gravity load was applied to the walls using two hydraulic jacks on transfer beam at top of the wall that were connected to high-strength post-tensioned cables anchored to the laboratory floor, the applied axial load was for TW1 was 0.09 $A_g f_c'$ and for TW2 0.075 $A_g f_c'$ which was moderated throughout the test. The test set up is shown in Figure 2.33.

The uni-directional cyclic loading protocol was applied parallel to the web of the T-Shaped section. These consisted of two cycle sets at incrementally increasing displacements. The displacement history for each test specimen is provided in Figure 2.34.

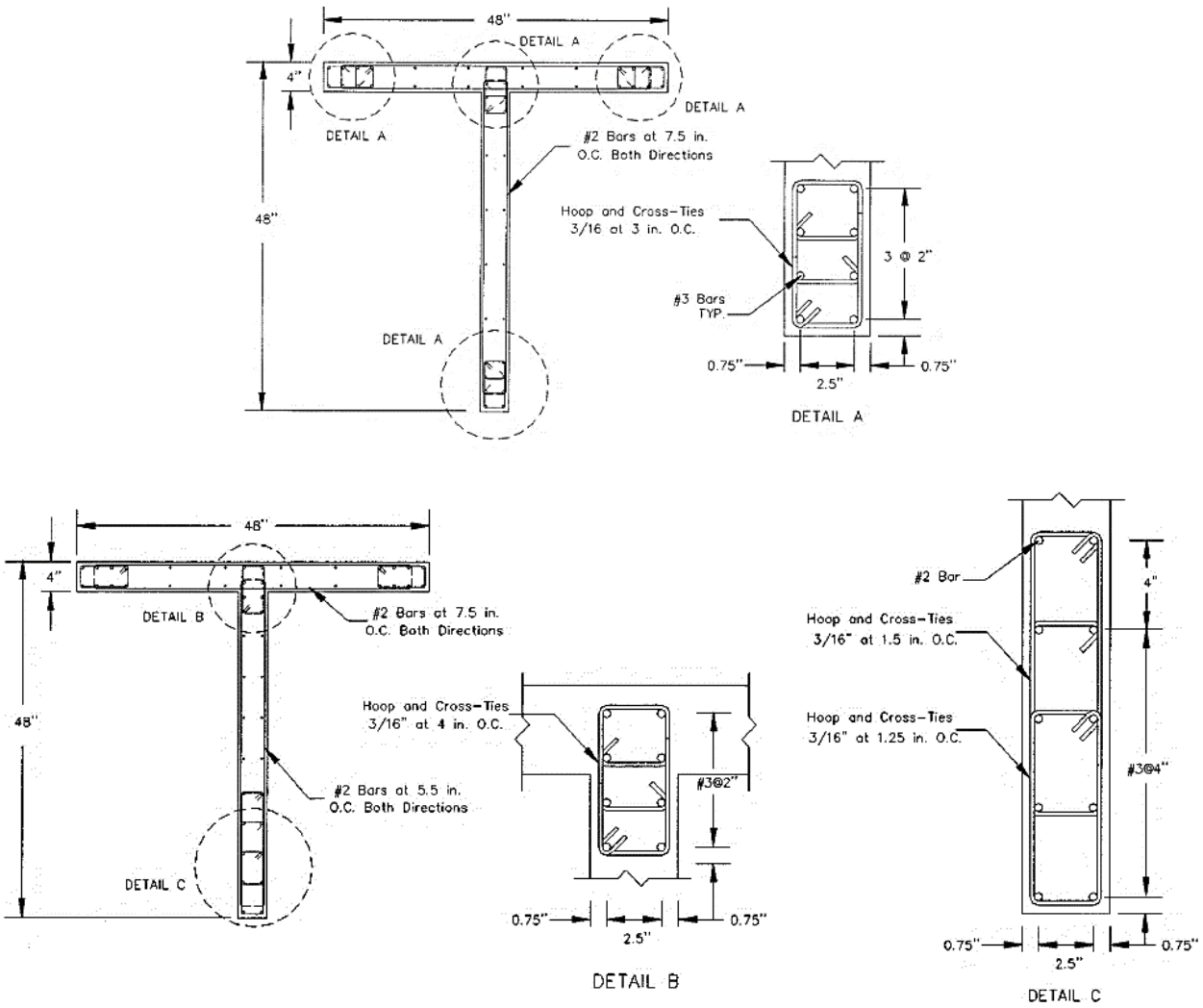

Figure 2.32: Test Specimen Geometry and Reinforcement Details for Thomsen & Wallace [161]
(Top) Specimen TW1 and (Bottom) Specimen TW2

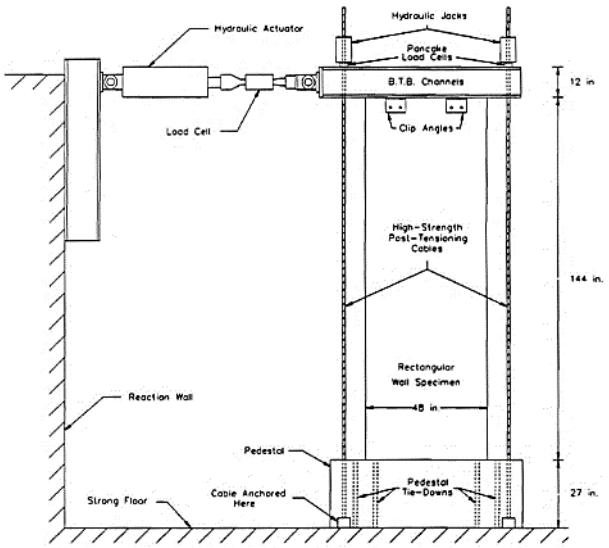

Figure 2.33: Test Set Up for Thomsen & Wallace [161]

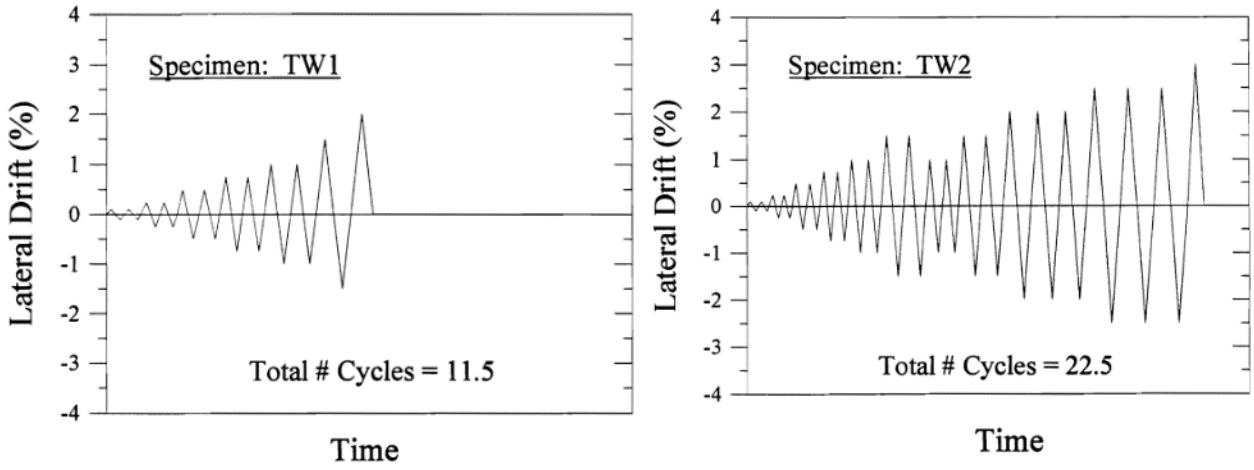

Figure 2.34: Displacement History for Thomsen & Wallace [161]

Experimental Test Results

For Specimen TW1, the lateral load versus displacement response is shown in Figure 2.35(a). The following summarizes the major observations in the wall performance of Specimen TW1 that experienced a flexural-compression (crushing-buckling) failure.

- During the first cycle at 0.75% drift the flexural steel in the web-end boundary element yielded in tension. Following subsequent cycles at this drift level there was widespread

inclined cracking across the web for the full height of the specimen and flexural cracking in the flange of the bottom half of the specimen.

- During the first cycle at 1% drift inclined cracks had propagated into the flange; also, significant vertical splitting and the onset of crushing at the bottom 1-ft of the web-end boundary element was observed.
- During the first cycle approaching at 1.5% drift, at around 1.25% drift with the web in compression, the wall suffered a brittle failure when all flexural bars in the wall-end boundary element and some additional bars along nearly half the unconfined web region buckled under high compressive demands. This failure was described as explosive and was accompanied by a sudden drop in wall capacity. Damage at the end of the test is shown in Fig. 2.36(a).

For Specimen TW2, the lateral load versus displacement response is shown in Figure 2.35(b). The following summarizes the major observations in the wall performance of Specimen TW2 that experienced a failure characterized by crushing-buckling accompanied by an instability of the compression zone (out-of-plane buckling).

- During the first cycle at 0.5% drift the flexural steel in the web-end boundary element had reached tensile yield. Following the cycles at this drift level, flexural and shear cracking was only noted in the lower half of the wall specimen. By the end of the 0.75% drift cycles, these had extended the full wall height.
- During the 1% drift cycle where the web was under compression, vertical splitting was observed in the web-end boundary element and the flexural reinforcement in this region where at four times compressive yield. The second cycle at this drift level led to some crushing of the web-end boundary element.
- During the 1.5% drift cycles the vertical splitting spread, concrete cover continued to crush, and extensive spalling was noted in the web-end boundary element. Researchers indicate the confined concrete core was still in good condition.
- During the first 2% drift cycle, a large crack at the wall-foundation interface was noted, suggesting there was slippage of the flexural reinforcement (this was considered minor).
- During the 2.5% cycle the confined core began to crush. In the cycle approaching 3% drift, with the web in compression, the web-end boundary element began to experience an out-of-plane instability at which point the test was halted. Damage at the end of the test is shown in Fig. 2.36(b).

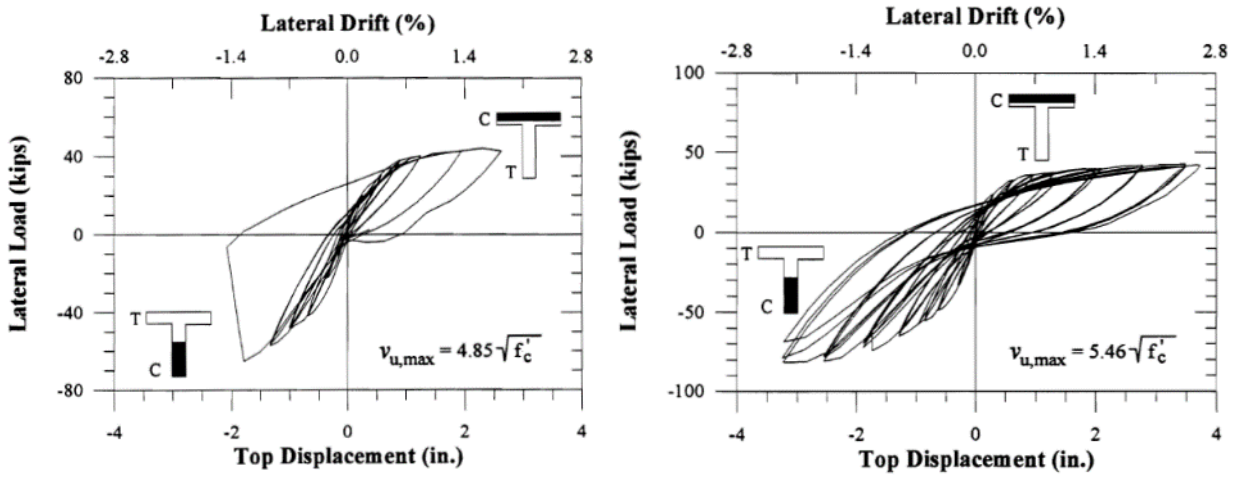

(a) Specimen TW1 (b) Specimen TW2

Figure 2.35: Force-displacement responses from Thomsen & Wallace [161]

Research Conclusions

The research study led to several important findings beyond the fact that the proposed displacement-based design procedure was effective as it led to flexure-dominated behavior in all of the wall tests. In respect to non-planar walls with asymmetric cross-sections, it is clear that designing the boundary elements based on the wall shape rather than two independent rectangular walls results in superior performance (when loaded so the web is under compression). The researchers suggest that the web-end boundary element is the critical region of the wall and transverse reinforcement for this location should be designed using the proposed displacement-based design procedure. However, they indicate that confinement in boundary elements at the flange tip and web-flange interface are of less consequence. The experimental results seem to support this claim as the confinement provided in the flange tips was less than current code provisions and the wall performed well for loading where the flange was under compression. Other observations from the research study included that: (i) shear demands in T-Shaped sections were notably higher than symmetric wall sections, likely due to the increase in flexural strength when the flange is subjected to tension; and (ii) that the effective flange width defined in *ACI318-89* [9] for T-beams provided an upper-bound estimate for T-shaped walls while *UBC-94* [96] provided an gross underestimate.

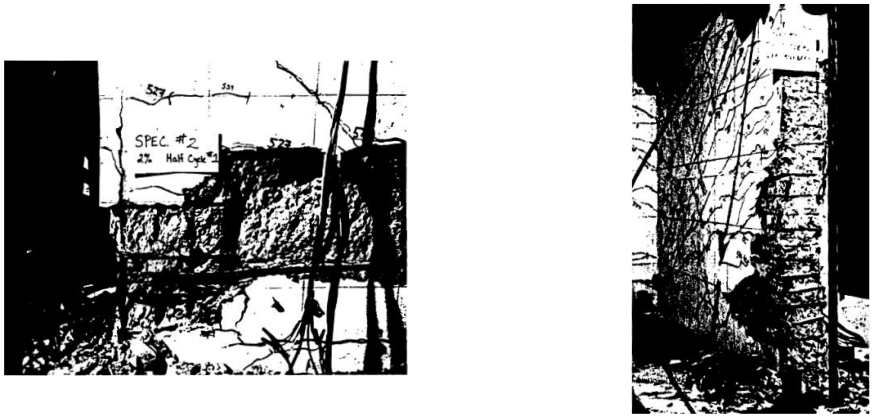

(a) Specimen TW1 – Web BE damage (b) Specimen TW2– Web BE instability

Figure 2.36: Damage to the specimens at end of test from Thomsen & Wallace [161]

2.4.4.3 Choi et al. (2004); Ha et al. (2002) [47, 86]

Research Objectives

A set of four T-shaped walls were tested at Hanyang University to better understand the deformation capacity of this type of asymmetric non-planar wall. For architectural or functionality reasons, engineers often choose to join multiple symmetric rectangular walls into asymmetric configurations (such as T-Shaped cross-sections); yet, there is still a limited understanding of how the wall shape and lateral loading direction impacts strength, stiffness, and ductility of the wall. The research team designed the wall specimens in accordance with UBC-97 [97]and ACI318-99 [12], with variances in the length and confinement ratio of the boundary elements. In addition to experimental tests that focused on transverse reinforcement configuration, the research program included sectional analyses to investigate the effects of parameters including axial load, flexural reinforcement ratio and distribution. The overall objective was to evaluate existing code provisions for special boundary elements (particularly spacing of confining reinforcement) and make recommendations that are appropriate for asymmetric wall sections, since existing code documents are directed at rectangular wall cross-sections.

Test Program

The isolated T-shaped walls (Figure 2.37) that were tested are considered to be a one-half (1:2) scale specimens based on the wall thickness. The walls have 85-cm (33.46-in) wide web, an 85-cm (33.46-in) long flange, height of 1.6-m (5.25-ft), and wall thickness of 15-cm (5.91-in). The flange and web-end (exterior) as well as the flange-web interface (interior) wall zones had concentrated flexural and

transverse reinforcement. The length of the confinement zone varies for the interior wall zone between the specimens: $0.15l_w$ for Specimens TC, TC-b1, and TC-b2, and when the compressive strain at the ultimate limit state exceeds 0.004 for Specimen TC-aw. Another difference between the specimens is the spacing of the boundary elements above 45-cm (17.72-in) from the wall base. These specific reinforcement details are shown for Specimen TC in Figure 2.37(a) and the variations made to this design for Specimens TC-aw, TC-b1, and TC-b2 is illustrated in Figure 2.38.

The specimens were subjected to cyclic lateral loading and a constant axial loading. The lateral load was applied by a single horizontal actuator positioned at the mid-height of the specimen's top cap. The axial load was applied to the walls using a loading frame at the top of the wall with two symmetrically placed actuators, the applied axial load for all the specimens was 0.06 $A_g f_c'$. The test set up is shown in Figure 2.39.

The uni-directional cyclic loading protocol was applied parallel to the web of the T-Shaped section. These consisted of three cycle sets at incrementally increasing drift angle values.

It should be noted that in many regards the research team tried to maintain similar practices as those seen in the *Thomsen & Wallace* [161] test protocol.

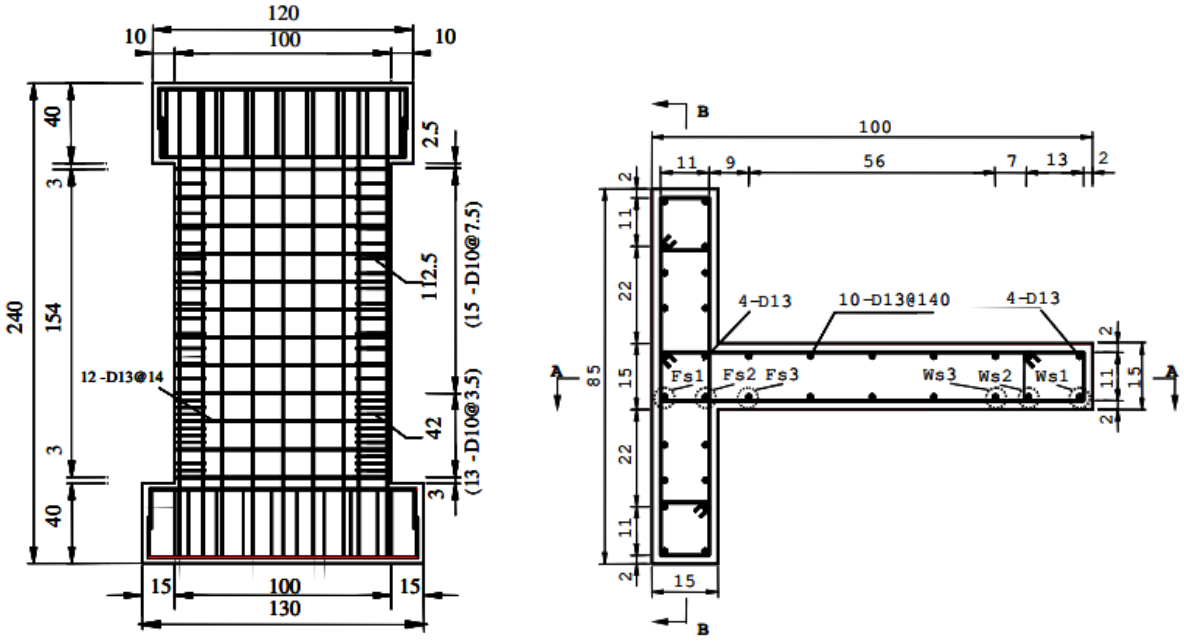

Figure 2.37: Test Specimen Geometry and Reinforcement Details for Specimen TC for Choi et al. [47, 86]

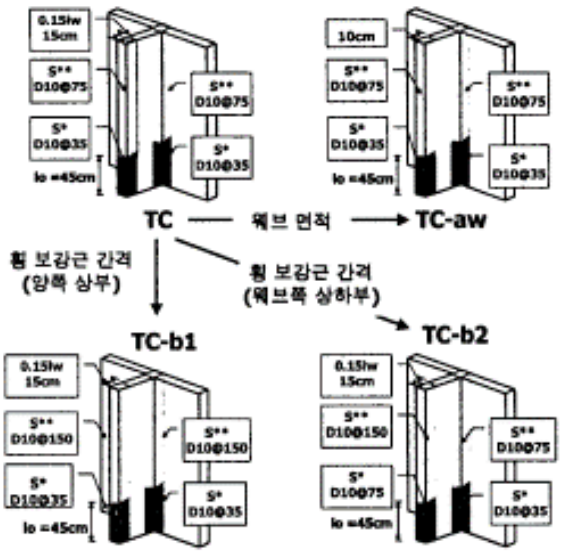

Figure 2.38: Test Specimen Reinforcement Details for Specimens TC-aw, TC-b1, and TC-b2 Choi et al. [47, 86]

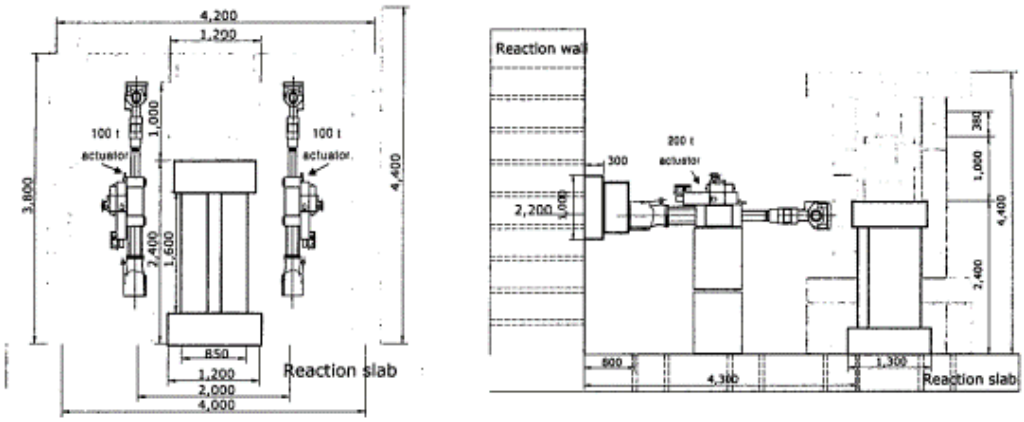

Figure 2.39: Test Set Up for Choi et al. [47, 86]

Experimental Test Results

For Specimens TC, TC-aw, TC-b1, and TC-b2, the lateral load versus displacement response plots are shown in Figure 2.40. The following summarizes the major observations (similarities and differences) in the wall performance of Specimens TC, TC-aw, TC-b1, and TC-b2 that experienced a web crushing (shear-compression) failure.

- Flexural cracking was first observed at the bottom of the web, around 15-20cm (5.91-7.87 in) above the wall base, at the 0.25% drift cycle for all specimens. Flexural cracking in the flange occurred slightly later at the 0.33% drift cycle.

- After this point, there was a progression of flexural cracking and onset of shear cracking to the point where web and flange cracks were intersecting.
- Concrete crushing of the web occurred in Specimen TC at 2% drift, TC-aw at 1.33% drift, TC-b1 and TC-b2 at 1% drift. No flange crushing or vertical splitting cracks were noted.
- All of the specimens ultimately failed from due web crushing resulting from high compressive demands.

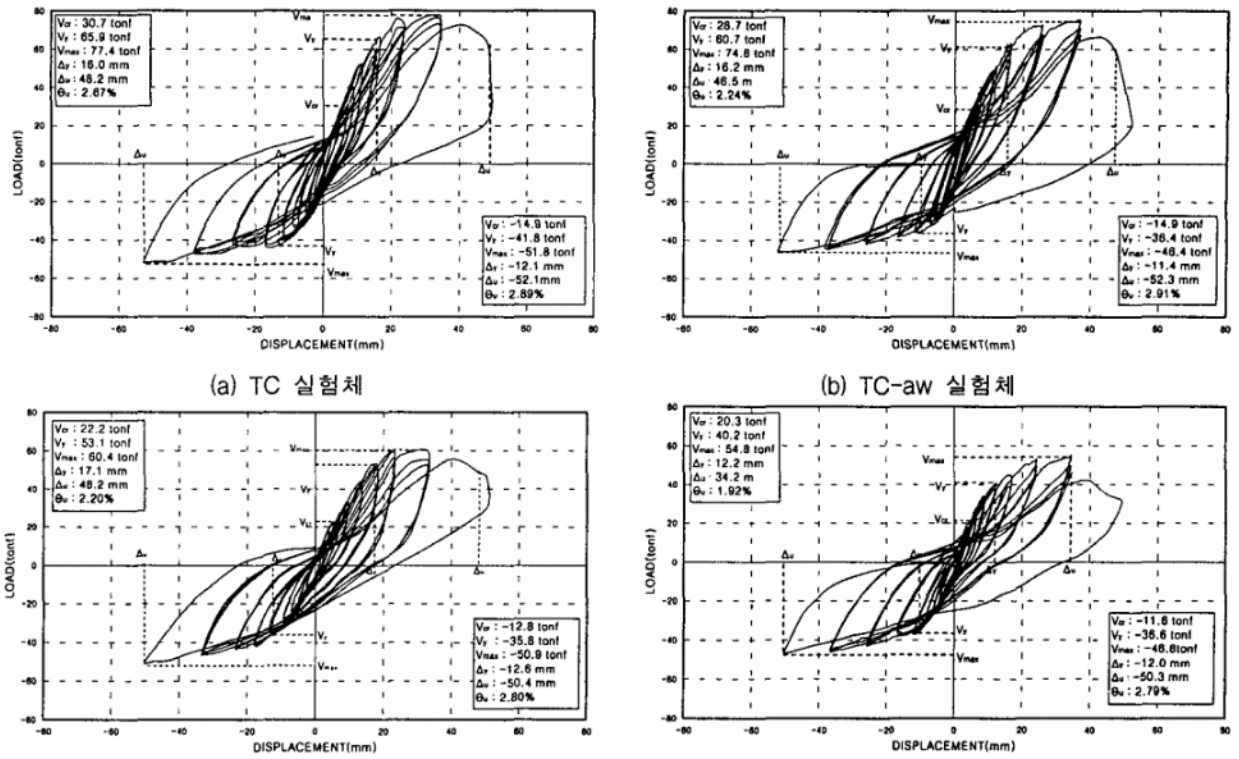

Figure 2.40: Force-displacement responses for Choi et al. [47, 86]

Research Conclusions

One of the primary lessons from this investigation was that the capacity/ductility of the web of a T-Shaped wall is more critical than that of the flange to the overall wall performance. Researchers indicated that the UBC-97 [97] minimum $0.15l_w$ for confinement length was insufficient to achieve the desired deformation capacity of 2% drift when the web was in compression. They suggest that a length associated with a strain of 0.003 at the ultimate limit state would be appropriate, which for amount to $0.4l_w$ for Specimen TC. It was observed in the tests that as the confined area increases, the energy dissipation capacity of the wall section is improved. In a similar sense, when the web is in compression (due to direction of lateral load) and also subject to axial load less than 0.1 $A_g f_c'$, special transverse reinforcement is necessary for ductile response; while this is not the case with the flange.

A suggestion, in addition to changing the length of the confinement region, is investigating the impact of reducing the flexural reinforcement in flange region to reduce the depth of compression in the web, and perhaps avoiding the compressive-controlled web crushing type failure seen in the test specimens for this study.

2.4.4.4 Brueggen (2009) [40]

Research Objectives

This test program at the University of Minnesota was undertaken to explore the interaction between the flange and web elements of the non-planar cross-sections, particularly T-shaped configurations. Previous tests on this wall type had involved only uni-directional lateral loading, and there was a need to understand the multi-directional response of these specimens that would be more representative of an actual earthquake scenario. The researchers intended to use the experimental results to examine the displacement-based design method that was mentioned earlier in *Thomsen & Wallace* [161], since preliminary computational results indicated that the compression zone in a skew-loading condition for a T-shaped wall could be much larger than orthogonal loading considered in the design method. The research team also wanted to investigate the effects of flexural reinforcement splices, distributed versus concentrated flexural reinforcement layouts for the wall flange, flange shear reinforcement ratios, and length of the confined boundary element at the web-end. Ultimately, the objective was to develop a simplified modeling procedure that incorporates flexural, shear, and strain penetration deformation components (F-S-SP Integration Model) along with other design recommendations that would improve the performance-based design of T-Shaped wall members.

Test Program

The two T-shaped walls (Figure 2.41) were designed to be one-half (1:2) scale specimens of wall sub-assemblages from a six-story prototype building with a special reinforced concrete structural wall system. The walls have a 90-in wide web, a 72-in long flange, and wall thickness of 6-in; there is a floor slab every 6-ft that is 3.5-in thick. The flange and web-end (exterior) boundary elements had concentrated flexural and transverse reinforcement, yet the web-flange interface does not. The first wall specimen (NTW1) was a four-story model based on the prototype structure designed in accordance with *ACI318-02* [13] and *IBC 2003* [99]. The second two-story wall specimen (NTW2) incorporated changes to the reinforcement configuration of NTW1, based on results of the first test, to examine certain parameters of interest. These primary differences are the distribution of flexural

reinforcement in the flange and length of the confined region in the web-end. The reinforcement details are shown in Figure 2.41.

The specimens were subjected to cyclic lateral loading and a constant axial loading. The lateral displacement, desired moment to shear ratio, and axial load are applied using the MAST crosshead system comprised of four vertical and four horizontal actuators. The applied axial load was for NTW1 was $0.03A_g f_c'$ (186.5 kips) and for NTW2 $0.03A_g f_c'$ (initially 186.5 kips and 201.2 kips for majority of test) which was moderated throughout the test. The test set up is shown in Figure 2.42.

The bi-directional cyclic loading protocol involved: one displacement cycle each parallel and perpendicular to the stem of the T-wall, one displacement cycle each at a 45-degree and a 135-degree angle to the stem of the T-wall, and 360-degree bidirectional displacement path that traced the shape of the yield envelope; these generally consisted of three cycle sets. There was an effort to apply the same displacement to the top of NTW2 that was experienced at the second story of NWT1 (recall the height difference in the specimens). The displacement history for each of the specimens is provided in Figure 2.43.

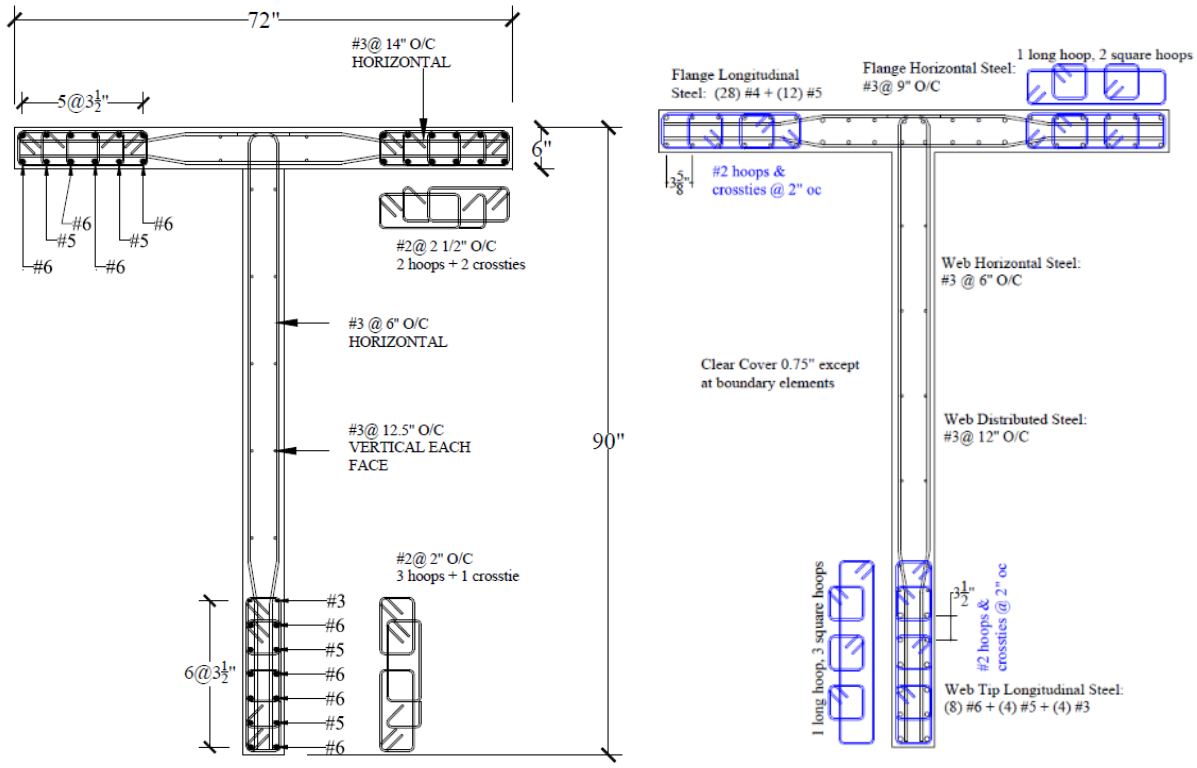

(a) Specimen NTW1 (b) Specimen NTW2

Figure 2.41: Test Specimen Geometry and Reinforcement Details for Brueggen [40]

Figure 2.42: Test Set Up for Brueggen [40]

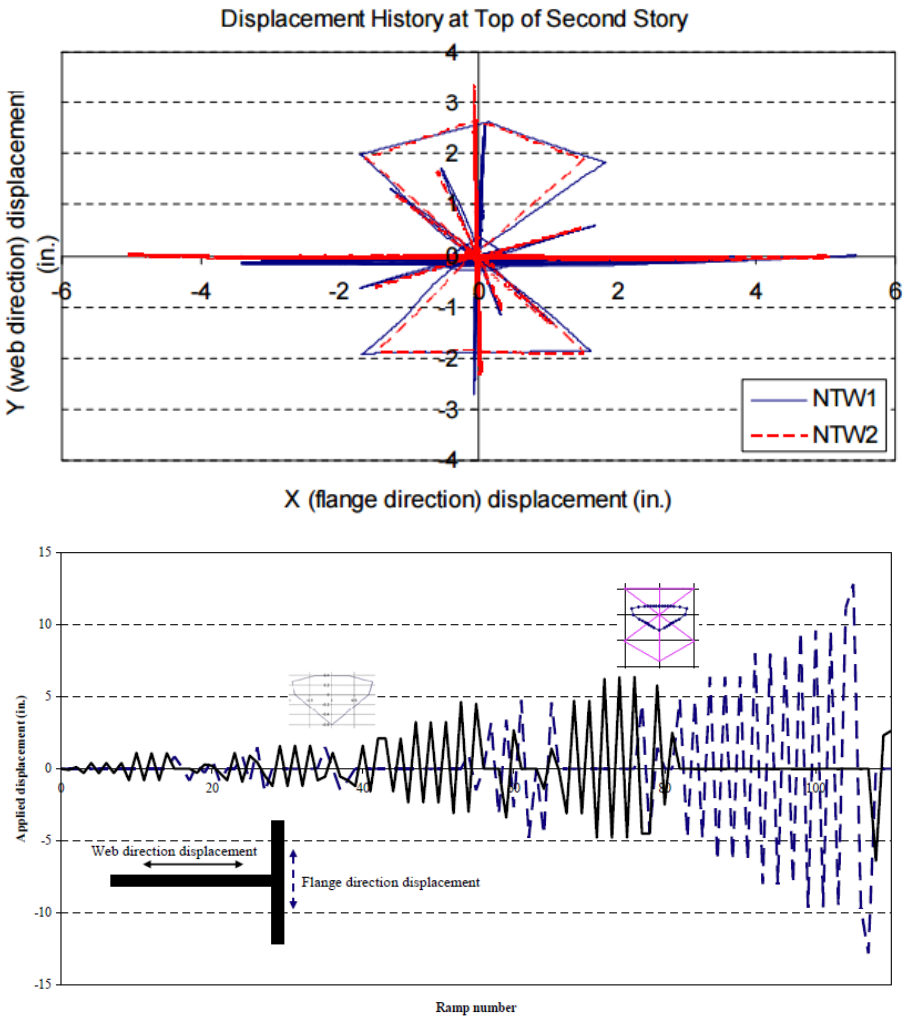

Figure 2.43: Displacement History for Brueggen [40]
(Top) X vs. Y-Displacement for Specimens NTW1 and NTW2 (Bottom) Displacement History for NTW1

Experimental Test Results

For Specimen NTW1, the lateral load versus displacement response is shown in Figure 2.44. The following summarizes the major observations in the wall performance of Specimen NTW1 that experienced a crushing-buckling (boundary element crushing) failure.

- During the cycle at predicted ductility level 0.25 with loading parallel to the wall web, researchers observed the onset of shear (in the web) and flexural cracking (in the web-end) in the first two stories of the wall.
- At the predicted ductility level 1, the closely spaced flexural cracks in the boundary elements and widely spaced shear cracks in the unconfined portions of the wall. Additionally, a crack at the wall-to-foundation interface had opened.
- When approaching 1.5% drift with loading parallel to the wall web and the web-end in compression, spalling of cover concrete at the web-end boundary element was noted.
- On load reversal to 1.5% drift with the flange in compression, there was shear sliding across web cracks on the first story of the wall.
- During the 2% cycle with web-end in compression, there was additional spalling and core crushing in the web-end boundary element. Subsequent sweeps along the hourglass portion of the loading curve led to multiple bars buckling in the web-end. Testing with the web-end in compression was halted at this point.
- The test continued with loading parallel to the flange. During in the second cycle to 3%, spalling of the flange tips was observed without significant capacity loss. During the approach to 4% drift the flange tips crushed and there was a substantial reduction in strength.
- Past this point there was additional loading cycles that resulted in previously buckled bars to rupture and buckling of additional bars. After web crushing, the wall was no longer able to carry the applied axial load. Damage at the end of the test is shown in Fig. 2.46.
- A post-test specimen autopsy indicated that multiple transverse hoops had fractured or unwound.

For Specimen NTW2, the lateral load versus displacement response is shown in Figure 2.45. The following summarizes the major observations in the wall performance of Specimen NTW2 that experienced a flexural-compression (crushing-buckling) failure.

- Similar to NTW1, flexure and shear cracking was observed at predicted ductility level 0.25.
- When approaching 1.5% drift with loading parallel to the wall web and the web-end in compression, spalling of cover concrete at the web-end boundary element was noted.
- On the skew loading at 1.5%, horizontal shear sliding was measured along a horizontal web crack. This sliding continued on subsequent cycles of loading parallel to the wall web (up to 1/8-in of motion). Also, a crack at the wall-to-foundation interface began widening.
- During the 2.5% cycle with web-end in compression, the web-end failed in compression with rupture of transverse hoops and buckling of the four flexural bars closest to the web tip. Load reversals at this drift led to fracturing of previously buckled flexural bars and additional bar buckling.
- The test continued with the loading parallel to the flange. During the approach to 4% drift significant spalling of the south flange tip was noted with no noted buckling, on load reversal a flexural bar fractured in this region and two bars buckled in the opposite flange tip. Additional cycles led to similar buckling and fracture of flexural bars
- Past this point there was additional loading cycles that resulted in previously buckled bars to rupture and buckling of additional bars. After web crushing, the wall was no longer able to carry the applied axial load. Damage at the end of the test is shown in Fig. 2.46.
- A post-test specimen autopsy indicated that while several confining hoops had fractured or deformed, the core was largely intact.

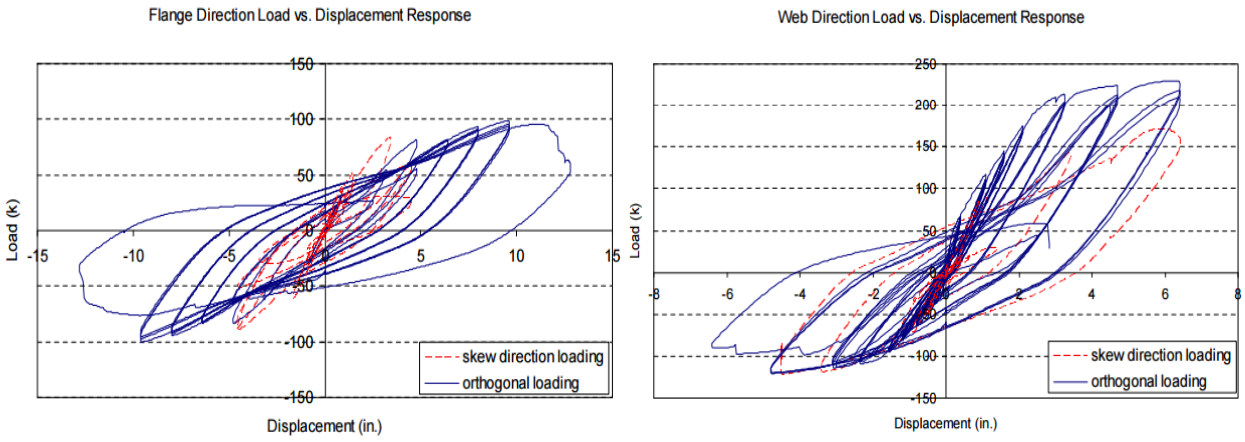

Figure 2.44: Force-displacement response for Specimen NTW1 from Brueggen [40]

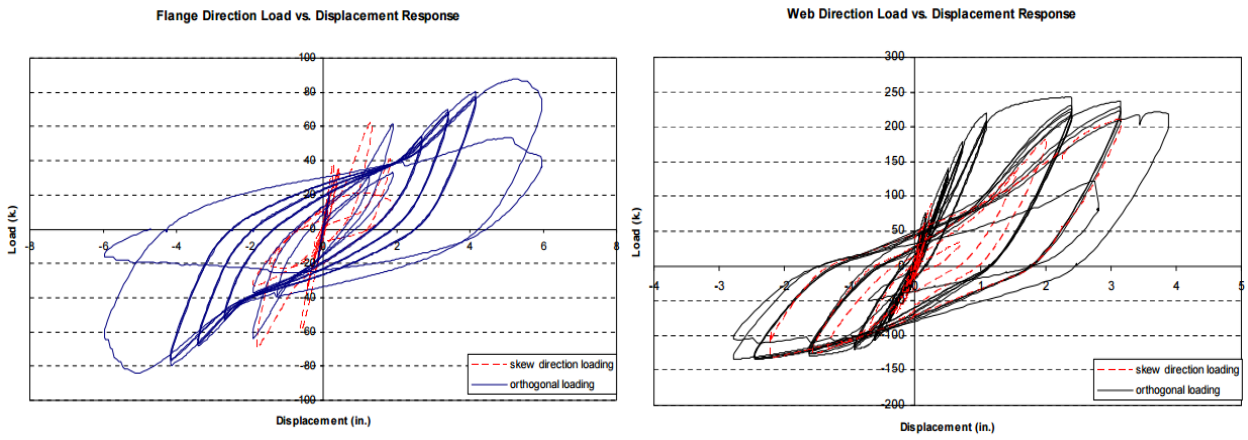

Figure 2.45: Force-displacement response for Specimen NTW2 from Brueggen [40]

Research Conclusions

One of the major findings of this test program related to the design of non-planar, T-Shaped walls is that the displacement-based design procedure described in *Thomsen and Wallace* [161] and introduced in *ACI 318-02* [13] is appropriate for walls subject to multi-directional loading. However, it was noted that T-Shaped walls (and other asymmetric non-planar walls) may not meet the requirements for a tension-controlled section due to a large compression zone depth when the wall flange is in tension; in that case, the ACI 318 displacement-based design procedure would be insufficient. Another important observation was that shear lag effects can be quite pronounced especially in walls with concentrated flexural reinforcement at the boundary elements. In this situation for at lower displacement cycles, the strain in the flexural steel at the flange tips is approximately half the strain at the center of the flange, and only at higher displacement demands does the entire flange exhibit a more uniform straining pattern. The simplified modelling procedure the research team proposed and verified using the two T-Shaped wall specimens is promising as it is based on a rather straightforward sectional analysis of the wall and captures the effects of multiple deformation components.

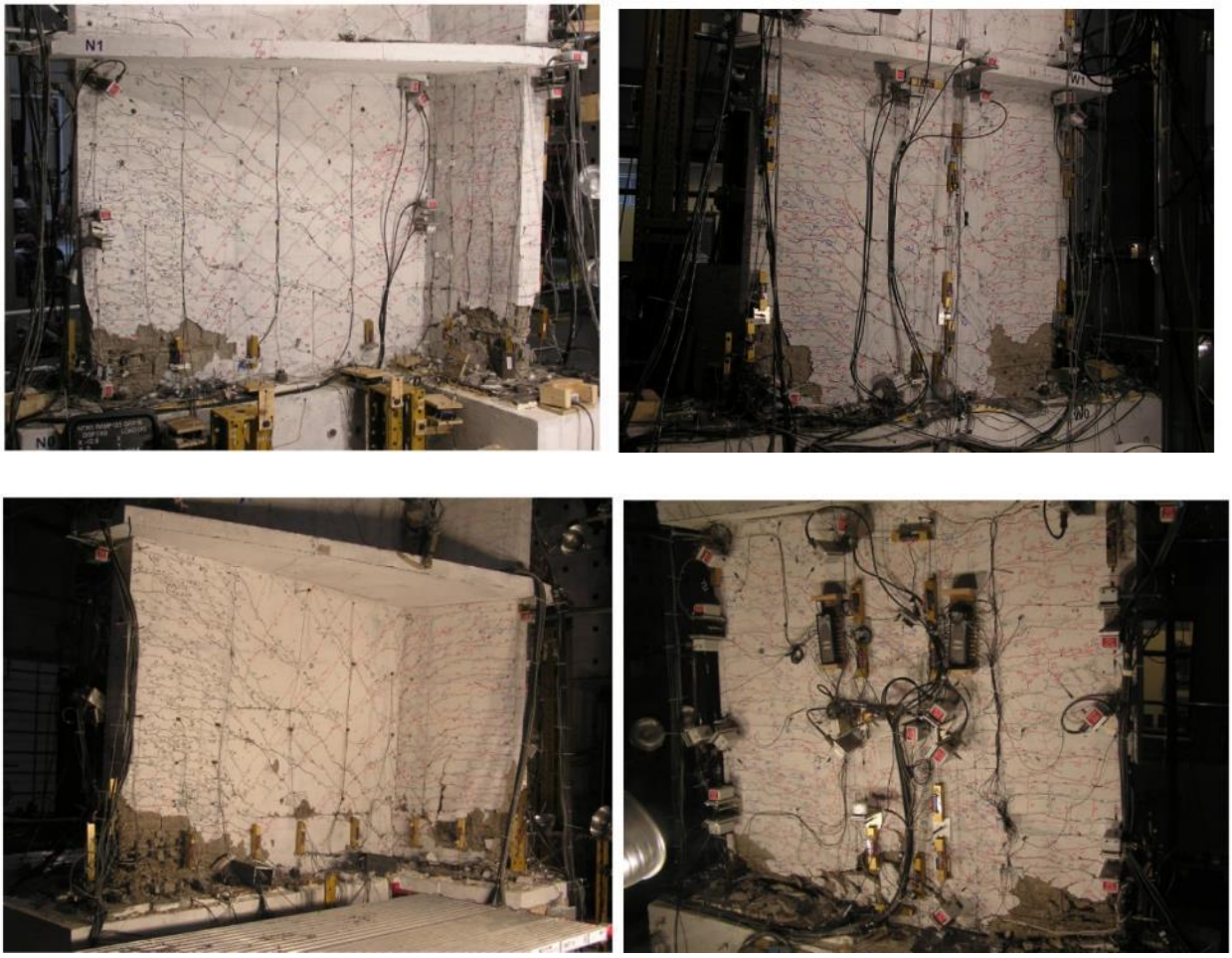

Figure 2.46: Damage to the specimens at end of test from Brueggen [40]
(Top) Specimen NTW1, web and flange damage (Bottom) NTW2, web and flange damage

2.4.5 Tests on L-Shaped Wall Configurations

2.4.5.1 Nakachi et al. (1996) [128]

Research Objectives

This test program was conducted by the Technical Research Institute of the Hazama (now Hazama Ando) Corporation. The firm was involved in the construction of such high-rise structures as the Petronas Towers, which contained a reinforced concrete box-shaped core wall system. To investigate the response of similar building cores comprised of L-Shaped walls, four specimens with varying boundary element lengths and confinement ratios were tested. In particular, the researchers were interested in the ductility of L-Shaped walls when subjected to diagonal loading with high axial loads where the wall corner and adjacent zones are under significant compressive stress. The study

included additional experimental tests in the study that focused on isolated boundary element columns of varying overall dimension as well as shear and confinement reinforcement scheme. The overall objective was to evaluate different options for confinement of the corner boundary element, and provide design recommendations based on the study findings.

Test Program

The research team considers the four L-shaped walls (Figure 2.47) to be a three-tenths (0.3:1) scale specimens that represent the bottom three stories of a 25-story building, where full-scale walls have a thickness of 12-in. The walls have equilateral flanges that are each 900-mm (35.4-in) long and wall thickness of 90-mm (3.54-in); the walls have a height of 1700-mm (66.96-in). The flexural reinforcement is uniformly distributed across the wall section (not concentrated in the boundary elements) and the layout is identical for each of the walls. The boundary elements vary in length and the confinement configuration. The first wall specimen (No1) has no confined boundary element, while the subsequent specimens have increasingly larger and/or more heavily confined boundary elements at the web-end and web-flange interface. The confinement reinforcement does not seem to extend the full height of the wall specimen, but this is not clearly noted in the specimen drawings. These reinforcement details are shown in Figure 2.47.

The specimens were subjected to cyclic lateral loading and a constant axial loading (value for axial load is a different value for positive and negative loading). The lateral load was applied by a single horizontal actuator connected to a frame affixed to the top of the specimen. The applied axial load was applied to the walls using a hydraulic jack centered at top of the wall, the axial load for all specimens was $0.6A_gf_c'$ under positive loading when the wall corner was under compression and 78.5kN ($0.0071\text{-}0.01A_gf_c'$) for negative loading. It is important to note that this axial load ratio is much greater than that applied to walls in the previously described tests which range from zero to $0.15 A_gf_c'$. The test set up is shown in Figure 2.48.

The uni-directional cyclic loading protocol was applied at a 45-degree angle to the corner of L-Shaped wall specimen. These consisted of typically one cycle at incrementally increasing displacements that corresponded to set drift angles (1/1000 rad (1 cycle), 2/1000 rad (2 cycles), 5/1000, 7.5/1000, 10/1000 (1 cycle each)) at the second story level at 615-mm (24.21-in).

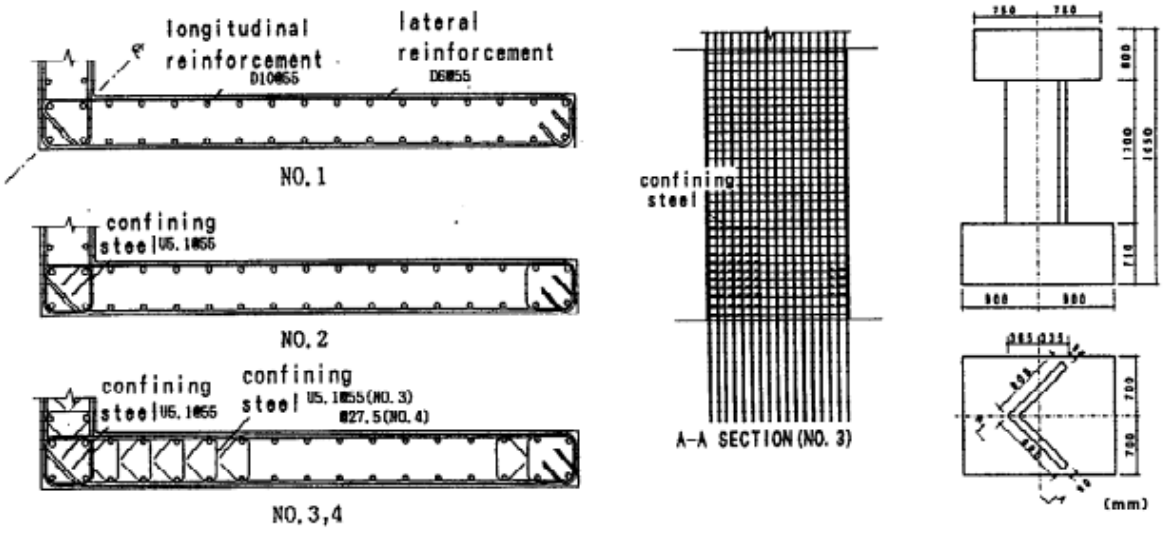

Figure 2.47: Test Specimen Geometry and Reinforcement Details for Nakachi [128]

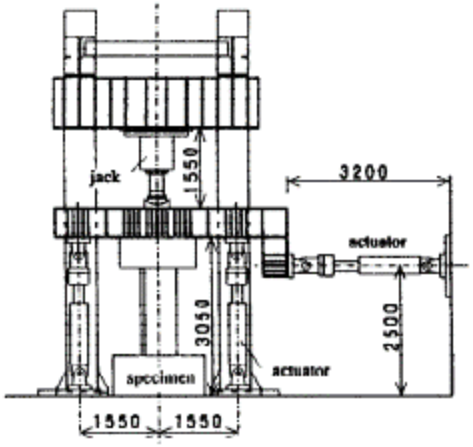

Figure 2.48: Test Set Up for Nakachi [128]

Experimental Test Results

For Specimens No1-No4, the lateral load versus drift angle response plots are shown in Figure 2.49. The following summarizes the major observations (similarities and differences) in the wall performance of Specimens No1-No4 that experienced a crushing-buckling (boundary element crushing) failure in the web corner.

- During the cycle at 0.1% drift where the wall corner was compressed, the flexural reinforcement in this region yielded in compression. At the same drift level, when the wall corner is subjected to tension, flexural cracking was noted in the wall corner.

- During the cycle at 0.2% drift, the wall corner showed signs of vertical cracking and began spalling/crushing.
- All specimens failed due to crushing in the web corner and experienced a rather severe drop in strength. In general, the specimens with longer boundary elements and higher confinement ratios had superior strength capacity and ductility (except for No2 that under-performed based on researchers' predictions). The limiting drift associated with 80% of peak strength for Specimens No1-No4 are 0.46%, 0.31%, 0.6%, and 0.96%, respectively.
- Both Specimens No1 and No2 had very limited energy dissipation, but this improves with better confinement of the critical wall corner region as observed in Specimens No3 and No4.

As a note, the drift levels at which cracking, compressive yielding, and crushing occur appear to be much lower than the other walls described in Section 2.4 regarding experimental performance of non-planar walls. This can likely be attributed to the very high axial load ratio applied to the specimen when the wall corner is in compression. Researchers also note that the lower axial load on Specimen No1 (4825 kN), due to low measured concrete cylinder strength had a greater impact than the absence of confined boundary elements.

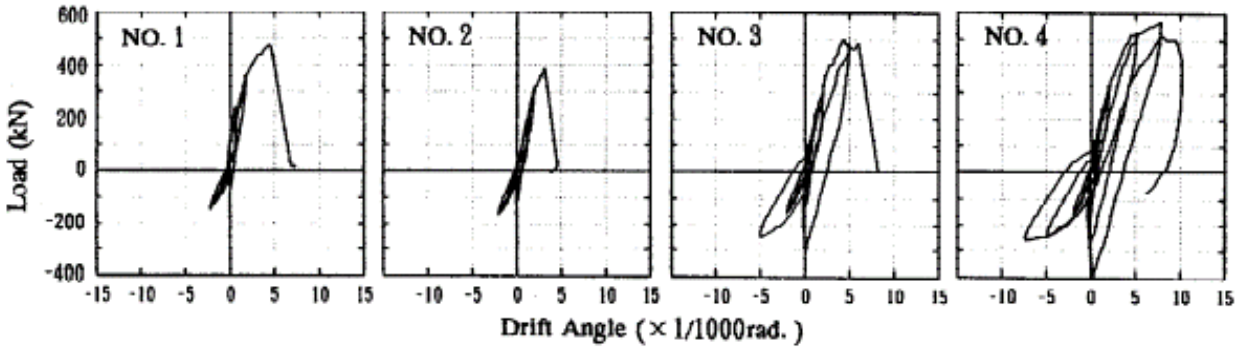

Figure 2.49: Force-drift angle response for Specimen No1-No4 from Nakachi [128]

Research Conclusions

Examining both the L-Shaped wall results and the boundary element columns that were tested as part of the study, it is clear that using closed transverse hoops/ties to achieve higher confinement ratios in the boundary element improves its compressive ductility, and therefore, overall deformation capacity of the wall. This conclusion is based partly on strain measurements taken during the wall tests; researchers indicate that the confining force per unit area of the wall cross-section is greater for the specimen with tighter confinement spacing. Another observation derived from these strain measurements is that with larger lateral displacement demands, the strain in the

transverse reinforcement increases and becomes more non-linear across the wall section. Perhaps an unintended lesson derived from the experiments was that modifying the axial load may have a greater impact on compressive ductility than extent or amount of confinement reinforcement. The relationship between the two parameters is likely worth investigating for L-Shaped walls with some additional detail.

2.4.5.2 Hu (2004) [93]

Research Objectives

In this wall test program, a two short limbed, L-Shaped walls were tested at the State Key Laboratory of Disaster Reduction in Civil Engineering (SLDRCE) at Tongji University. This experiment, like *Shouzhong* [157], is part of a database of seismic structural tests funded by the National Basic Research of China grant. Based on the definition provided in the Professional Standard of P.R. China [160], short-limbed L-Shaped walls would have a flange length-to thickness ratios ranging from 5 to 8 where the thickness exceeds 200-mm (7.87-in). At the time of the test program, there had been limited data regarding this wall type. It is important wall configuration to investigate as it has been implemented in high-rise residential structures since they occupy less floor area than traditional shear walls, while providing lateral stiffness that is superior to a frame system. This study examined the seismic performance of two short-limbed walls with varying flexural and horizontal shear reinforcement to evaluate strength capacity, ductility, energy dissipation, and failure mechanism. The outcome from these investigations was to determine if the short limbed L-Shaped wall type was effective in resisting earthquake forces and to compare the effect of reinforcement configuration on wall behavior.

Test Program

The two L-Shaped walls (Figure 2.50) that were tested were considered to be nearly two-fifths (2:5) scale specimen where a full-scale wall has a thickness of 12-in. The geometry of both walls are identical and are comprised of unequal flanges of 700-mm (27.56-in) wide web, 325-mm (12.8-in) long flanges, a wall thickness of 125-mm (4.92-in) and an overall height of 1525-mm (60.04-in). Based on the confinement that is used in this specimen, the wall corner (interior) boundary element will be considered the full length of the short flange and partly into the long flange; there is also a boundary element with concentrated flexural and confining reinforcement as the tip of the longer flange (exterior). These reinforcement details are shown in Figure 2.50.

The specimens were subjected to cyclic lateral loading and a constant axial loading. The lateral load was applied using a single actuator through the center of the wall top cap. The gravity load was applied to the wall using two, symmetrically placed hydraulic jacks at the top of the wall; this applied axial load was 0.13 $A_g f_c'$ (400kN, or 89.92 kips) which was moderated throughout the test. The test set up is shown in Figure 2.51.

The uni-directional cyclic loading protocol was applied parallel to the longer flange of the specimens. Initially the loading was force-controlled at 10kN (2.25 k) increments until yielding, and afterward displacement control was implemented. This lateral loading involved incrementally increasing displacements that were a set ratio of the yield displacement, and three cycles were executed at each of these displacement levels until wall failure.

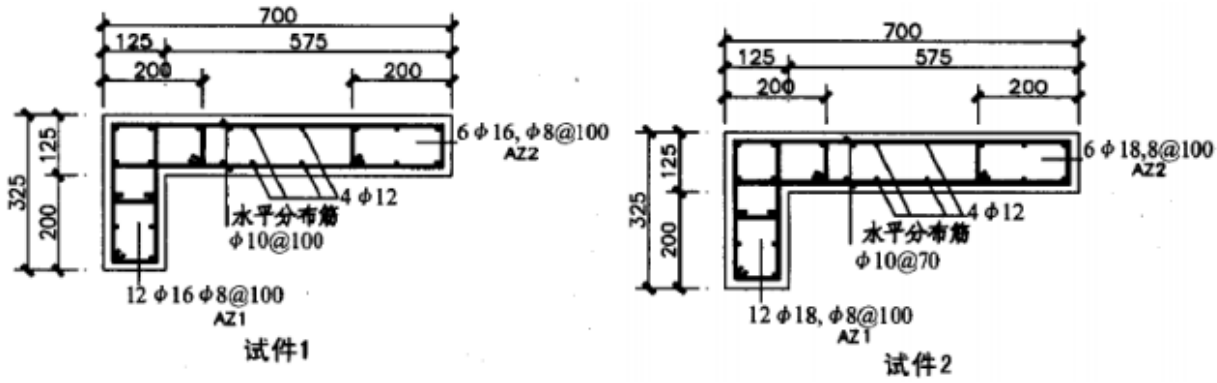

(a) Specimen No1 (b) Specimen No2

Figure 2.50: Test Specimen Geometry and Reinforcement Details for Hu [93]

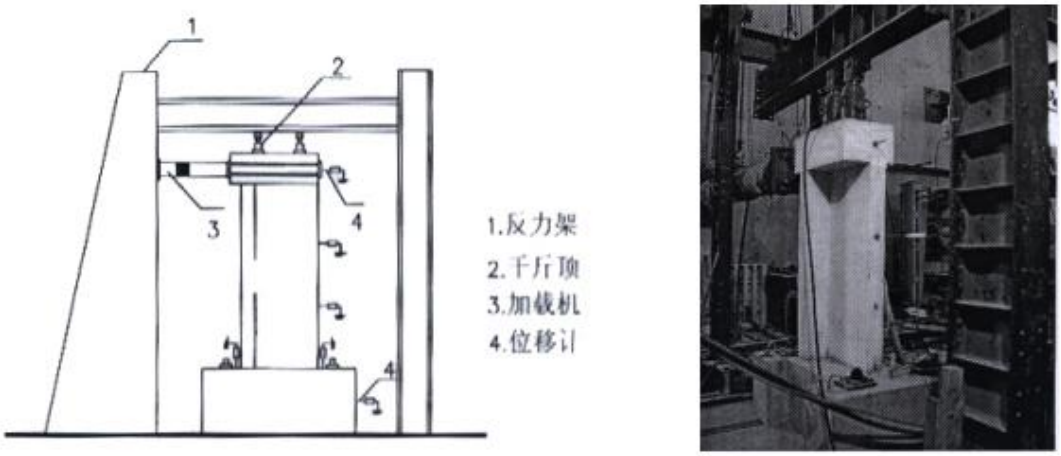

Figure 2.51: Test Set Up for Hu [93]

Experimental Test Results

For Specimens No1 and No2, the lateral load versus displacement response plots are shown in Figure 2.52. The following summarizes the major observations (similarities and differences) in the wall performance of Specimens No1 and No2 that experienced a crushing-buckling (boundary element crushing) failure. Damage at the end of each test is shown in Fig. 2.53.

- Flexural and inclined cracking was first observed in the bottom one-third of the walls
- With increased loading the flexural cracks extended into the compression zone decreasing the depth of compression.
- Ultimately the flexural reinforcement yielded and concrete crushed in the compression zone.
    - For Specimen No1, rebar yield occurred after the specimen reaching its peak strength. The observed crushing appeared to be more severe in the free-end of the longer leg. Recall that the transverse reinforcement had a greater spacing and the flexural reinforcement in the boundary elements was less than that in Specimen No2.
    - In comparison, for Specimen No2, rebar yield occurred prior to the specimen reaching its peak strength. The observed crushing appeared to be more severe in wall corner. The failure was considered shear-compression in nature.

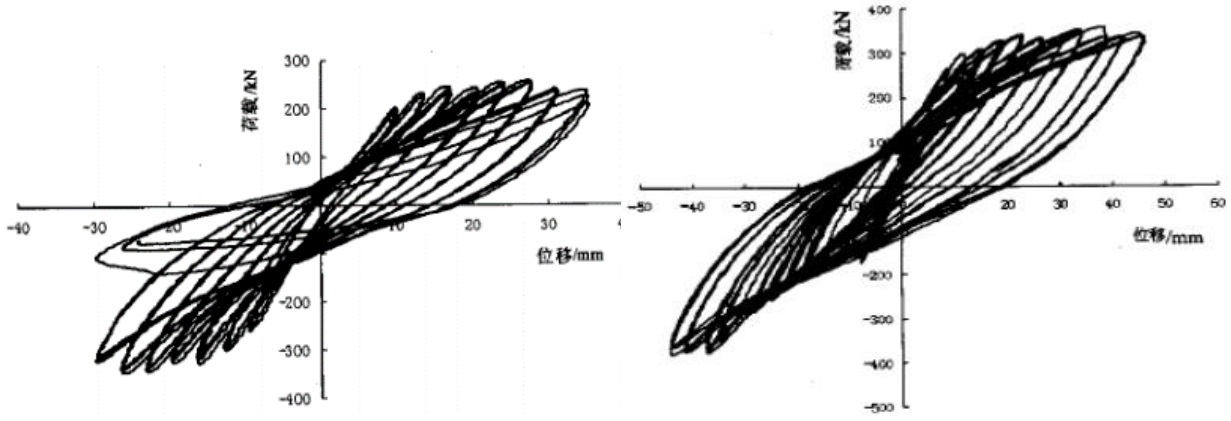

(a) Specimen No1 (b) Specimen No2

Figure 2.52: Force-displacement responses for Hu [93]

Research Conclusions

The general observations made by the research team were that the seismic performance of both walls was adequate with considerable ductility following global yielding. The stiffness degradation was gradual in both specimens except for the negative loading direction of Specimen No2, where it

appears that stiffness was essentially constant post-yield. Specimen No2 (with the more closely spaced horizontal reinforcement and greater area of reinforcement in the boundary elements) had both greater strength and ductility. The researchers indicate that use of the plane sections assumption led to rather accurate estimates for strength based on applying methodologies from GB 50010-2002 [160]. However, review of the provided strain distributions indicates that they are non-linear. It may be appropriate to try to predict the entire hysteretic behavior with the plane sections assumptions rather than just the nominal moment to assess whether this assumption is appropriate. This is of particular interest since many other researchers investigating L-Shaped walls indicate that the plane sections assumption is violated.

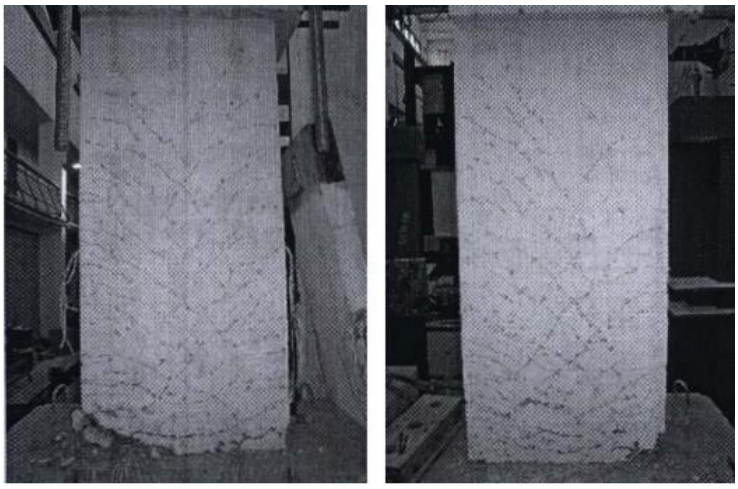

(a) Specimen No1 (b) Specimen No2

Figure 2.53: Damage to the specimen at end of test from Hu [93]

2.4.5.3 Hosaka et al. (2008) [92]

Research Objectives

In this wall test program, four L-Shaped walls were tested by researchers at the University of Tsukuba and Okumura Corporation. At the time of the study, engineers had begun using of core wall systems using high strength L-Shaped walls with more frequency. There was particular concern with the compression ductility of the wall corner based on the confinement ratio and configuration, as well as evaluate parameters such as concrete strength, flexural/confinement steel strength, applied axial stress, and confinement length/ratio of the flange-end boundary elements. The researchers were interested in the diagonal loading condition that leads to large localized compression demands. Beyond investigating methods to improve resistance to compressive-controlled flexural failure,

researchers also utilized the experimental results to evaluate the accuracy of a fiber-type section analysis in predicting overall load-deformation behavior.

Test Program

The four L-Shaped walls (Figure 2.54) that were tested was considered to be a four-ninths (4:9) scale models of the bottom portion of a 30-story prototype building specimen, where a full-scale walls have a thickness of 12-in. The walls had equilateral flanges that are both 670-mm (26.34-in) long, a wall thickness of 134-mm (5.28-in) and an overall height of 1940-mm (76.38-in). Both the wall corner (interior) and flange-end (exterior) wall zones had concentrated flexural and transverse reinforcement; although the length and reinforcement configuration of these boundary zones vary between the first set of two specimens (L-1, L-2) and the second set (L-5, L-6). Although it appears that the confinement reinforcement is consistent up the full height of the walls, the horizontal shear rebar varies with height; it is spaced more widely apart in the top portion of the wall, starting 1005-mm (39.57-in) and 670-mm (26.38-in) above the base of the wall for the first and second set of wall specimens, respectively. These reinforcement details are shown in Figure 2.54.

The specimens were subjected to cyclic lateral loading and a linearly variable axial loading. The lateral load was applied using an actuator connected to the top of the wall top cap via a frame. The gravity load was applied to the wall using multiple, distributed vertical actuators at the top of the wall; the axial-to-shear load ratios that ranged from zero when the flange ends were in compression to $0.4\ A_g f_c'$ (L-1, L-2, L-5) and $0.45 A_g f_c'$ (L-6) when the wall corner was in compression. Again, like the *Nakachi* [82] wall tests, these axial load ratios are quite high. The test set up is shown in Figure 2.55.

The uni-directional cyclic loading protocol was applied at a 45-degree angle to the corner of L-Shaped wall specimen. The loading is displacement-controlled using drift angle values (which can be related to drift percentage); there is no explicit indication of the displacement level and number of cycles at each displacement level that comprise the loading protocol.

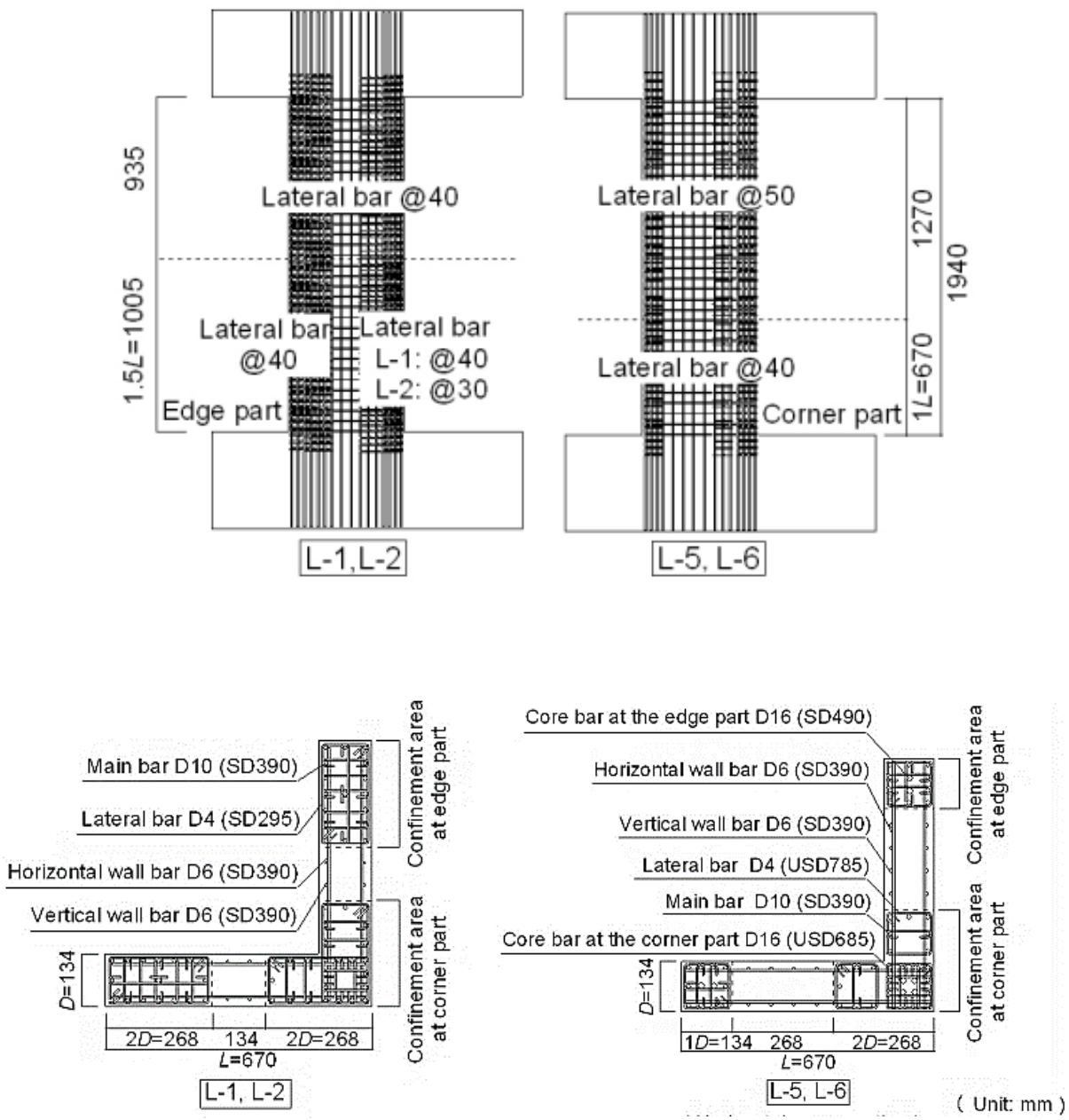

Figure 2.54: Test Specimen Geometry and Reinforcement Details for Hosaka [92]

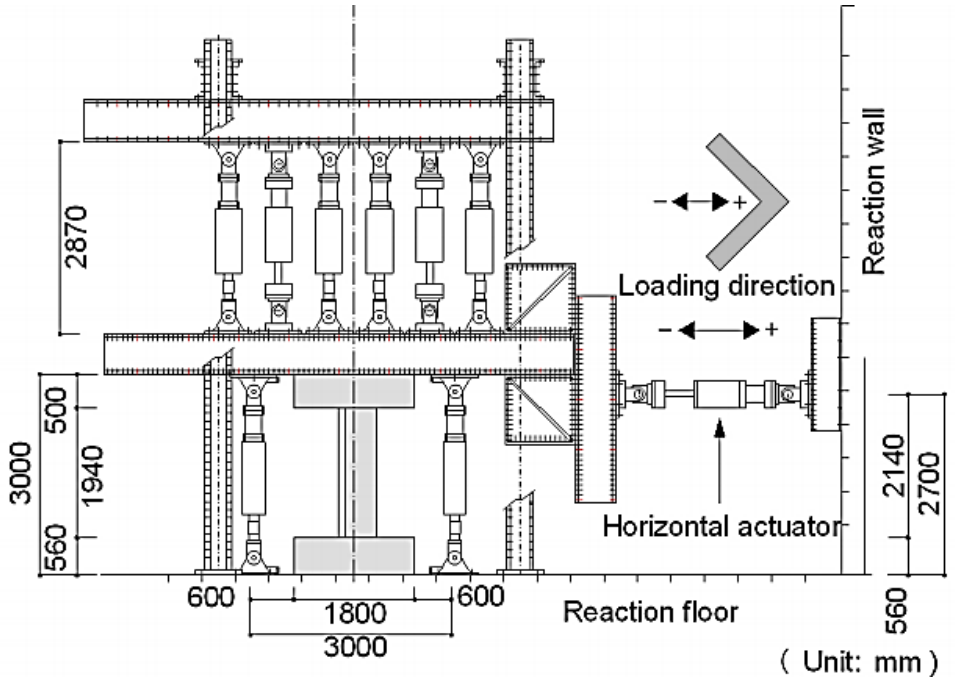

Figure 2.55: Test Set Up for Hosaka [92]

Experimental Test Results

For Specimens L-1, L-2, L-5, and L-6, the lateral load versus displacement response plots are shown in Figure 2.56. The following summarizes the major observations (similarities and differences) in the wall performance of Specimens L-1, L-2, L-5, and L-6 that experienced a crushing-buckling (boundary element crushing) failure. Damage at the end of each test is shown in Fig. 2.57.

- Flexural cracking at the wall corner was observed at -0.25% drift in the L-1 and L-2 Specimens, and at 0.125% drift for the L-5 and L-6 Specimens.
- For all walls, during the cycle approaching +0.5% drift where the wall corner was compressed, the flexural reinforcement in the wall corner yielded in compression. This was accompanied by spalling/crushing of concrete in the same region.
- During the cycle approaching +1.5% drift, crushing progressed in L-1 and L-2 to the unconfined portions of the flanges. Upon load reversal to -1.5%, flexural bars in the flange-end region of L-5 and L-6 yielded in tension.
- The strength capacity of the walls in the positive loading direction (web corner in compression) are approximately the same irrespective of concrete strength and differences in reinforcement configuration. However, the strength in the negative loading is improved quite significantly.

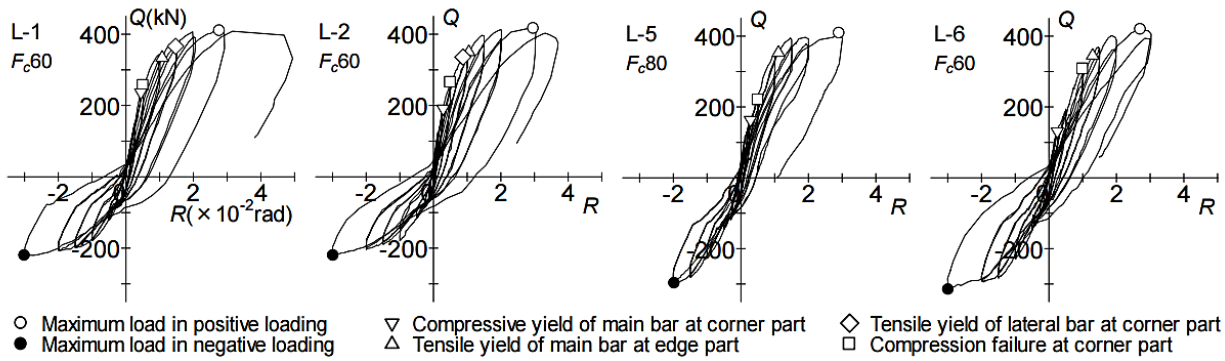

Figure 2.56: Force-drift angle responses for Hosaka [92]

Research Conclusions

All the L-Shaped wall specimens in this test series exhibited compression-controlled failures, characterized by simultaneous crushing of confined concrete and compression yielding of longitudinal reinforcement in the corner of the wall. Despite this undesirable failure mechanism, the experimental results helped researchers evaluate the impact on performance of various test parameters. Related to confinement configuration, the walls L-2 and L-2 exhibited greater ductility than L-5 and L-6 in both loading directions as overlapping rectangular hoops provided better confinement than abutting independent square hoops. The addition of high-strength, large diameter "core" reinforcing bars in the boundary elements of L-5 and L-6 increased wall strength when the flange-ends were under compression, but had no appreciable effect in the opposite direction of loading. Also, researchers observed that vertical strain distribution near the base of all the walls was linear prior to concrete crushing and nonlinear once concrete damage was observed. Related to this finding, the fiber-type section model (which involves a linear strain assumption) does not provide accurate prediction of the moment-curvature response near the base of the wall. Similar to other non-planar wall tests, researchers indicate that at higher displacement demands the plane sections do not remain plane and strain must be better understood and incorporated to models to more accurately model wall performance.

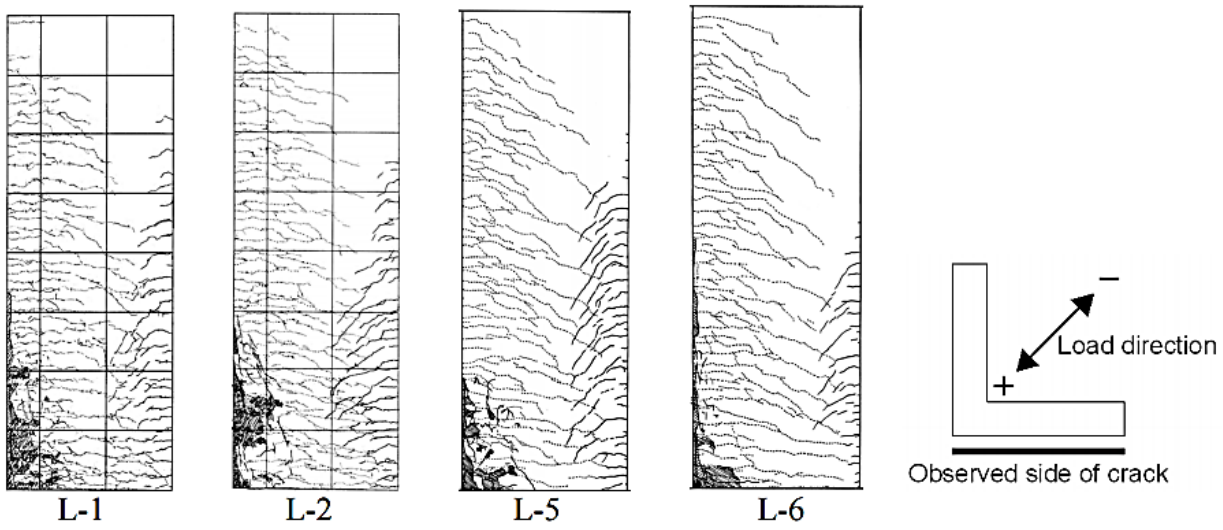

Figure 2.57: Damage to the specimen at end of test Hosaka [92]

2.4.5.4 Inada (2008); Kono (2011) [102, 107]

Research Objectives

As indicated in previous tests, there is increasing frequency of high-rise building design that involves core wall systems comprised of multiple L-Shaped walls. Based on records of experimental tests, it appears that this particular wall configuration is most popular in China and Japan. Designers have begun moving away from designs that involve supplementary moment frames since core walls can provide significant lateral load resistance with ductile performance while allowing greater architectural flexibility for the building floor plan that a frame system. However, the major concern with these L-Shaped wall sections is providing sufficient compression ductility in the boundary element regions at the wall corner and flange ends to sustain high compression demands, especially when loaded in the diagonal direction. The research team from Kyoto University was interested in investigating the effect of axial load, flange length, boundary element length and confinement ratio on wall response. Furthermore, prior test programs including *Nakachi* [128] had already indicated that the plane-sections-remain-plane assumption did not apply at higher deformation levels. In light of this, researchers utilized experimental results to better understand the strain behavior and to validate non-linear finite element analyses of select test specimens.

Test Program

Five L-Shaped walls were tested in two stages: three two-thirds scale (2:3) walls (L00A, L45A, L45B) that represented the bottom three floors of a 40-story building, followed by two walls at nearly two-

fifths (2:5) scale (L45C, L45D) of the bottom six floor of a 40-story building. Note that the scale is determined based on a full-scale wall having a 12-in thickness. Specimens L00A and L45A had equilateral flanges that are both 1200-mm (47.24-in) long, a wall thickness of 200-mm (7.87-in) and an overall height of 2480-mm (97.64-in). Specimen L45B was the only wall out of the test program that had unequal flange lengths at 1600-mm (62.99-in) and 1200-mm (47.24-in) and is excluded from the evaluation conducted in Chapter 3 and discussions below; otherwise the dimensions were the same as L00A and L45A. The second set of Specimens L45C and L45D had equilateral flanges of 720-mm (28.35-in) long, a wall thickness of 120-mm (4.72-in) and an overall height of 2540-mm (100-in). In all the tests, the wall corner (interior) and flange-end (exterior) wall zones had concentrated flexural and transverse reinforcement. These reinforcement details are shown in Figure 2.58 and Figure 2.59.

The specimens were subjected to cyclic lateral loading and a linearly variable axial loading. In the first set of tests, the lateral load was applied using an actuator connected to the top of the wall top cap via a wall top cap, and four hydraulic jacks (two placed above and two below the wall top cap) were used to apply the axial load; out-of-plane rotations were moderated using three laterally mounted actuators. In the second set of tests, a single actuator was also used for axial load thought this time it was connected to a loading frame; axial load was applied using two hydraulic jacks placed below the wall top cap. The out-of-plane motion was restrained by rollers placed on either side of the loading frame. The axial-to-shear load ratios ranged from zero when the flange ends were in compression to a maximum value of 0.31 $A_g f_c'$ (L00A), 0.20 $A_g f_c'$ (L45A=), 0.35 $A_g f_c'$ (L45C), and 0.5 $A_g f_c'$ (L45D) when the wall corner was in compression. Like many of the previous L-Shaped wall tests the axial load tends to be rather large and applied as a variable of the applied shear. This is intended to simulate the level and variation of vertical loading that is expected in high-rise buildings located in seismic areas that use multiple core wall systems as the lateral load resisting system. The two test set ups are shown in Figure 2.60 and Figure 2.61.

The uni-directional cyclic loading protocol was applied at a 45-degree angle to the corner of L-Shaped wall specimen (for all specimens except L00A, which was loaded parallel to one of the equilateral flanges). The loading is displacement-controlled using drift values (Figure 2.62); two cycles at each displacement level were conducted. The control point (location where this displacement was measured to determine the drift) was at 2130-mm (83.86-in) above the wall base for the first set of tests and 2905-mm (114.37-in) above the wall based for the second set.

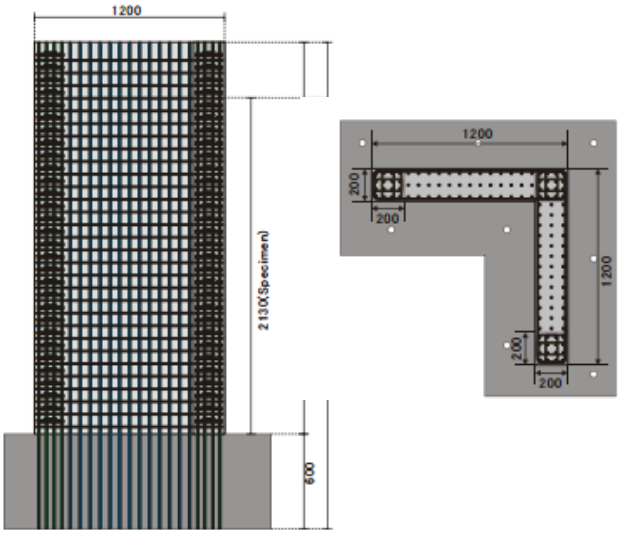

Figure 2.58: Test Specimen Reinforcement Details for Inada [102]

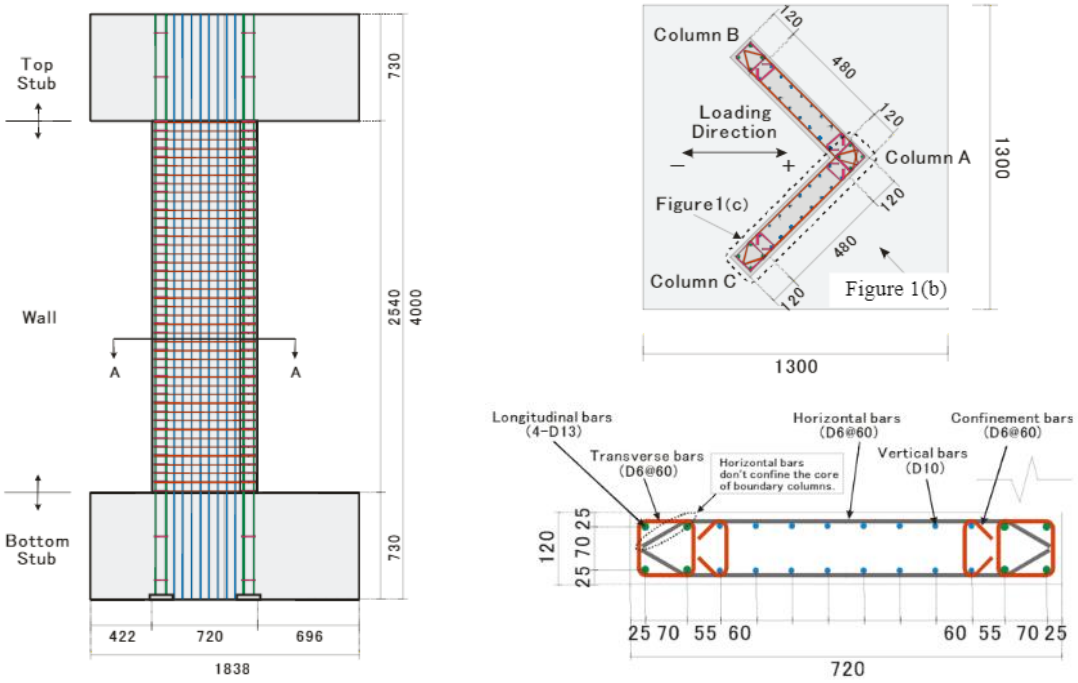

Figure 2.59: Test Specimen Reinforcement Details for Kono [107]

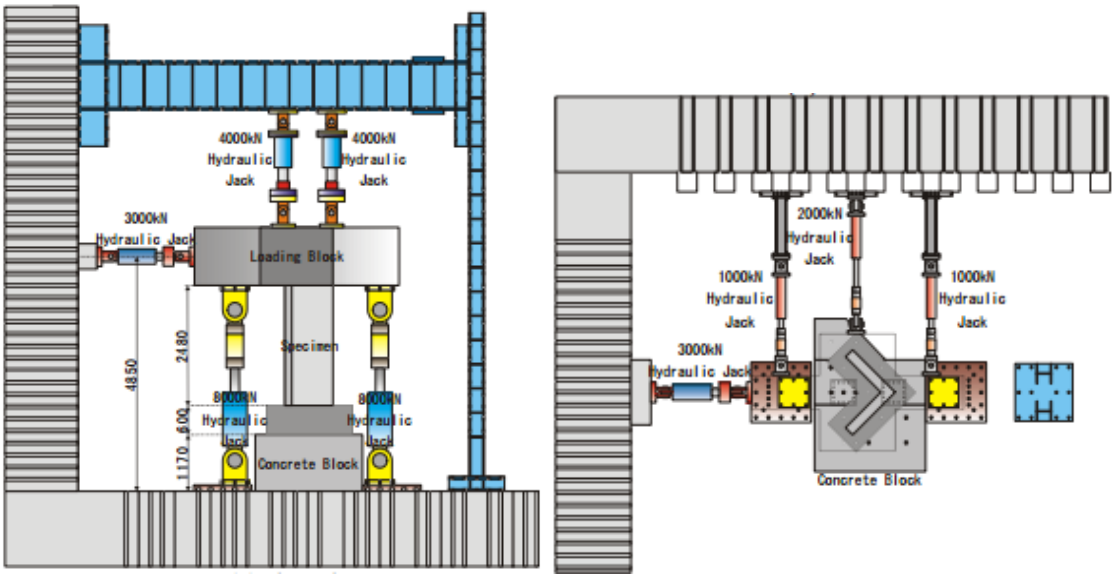

Figure 2.60: Test Set Up for Inada [102]

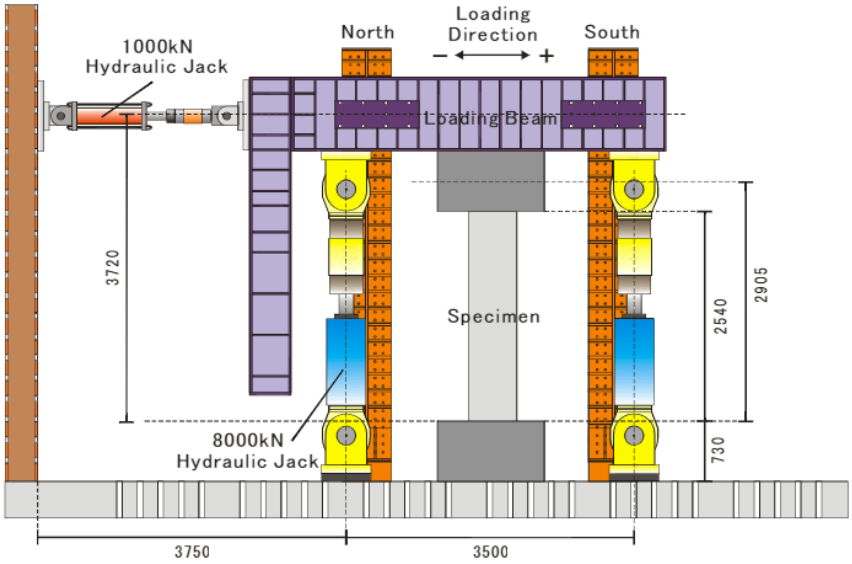

Figure 2.61: Test Set Up for Kono [107]

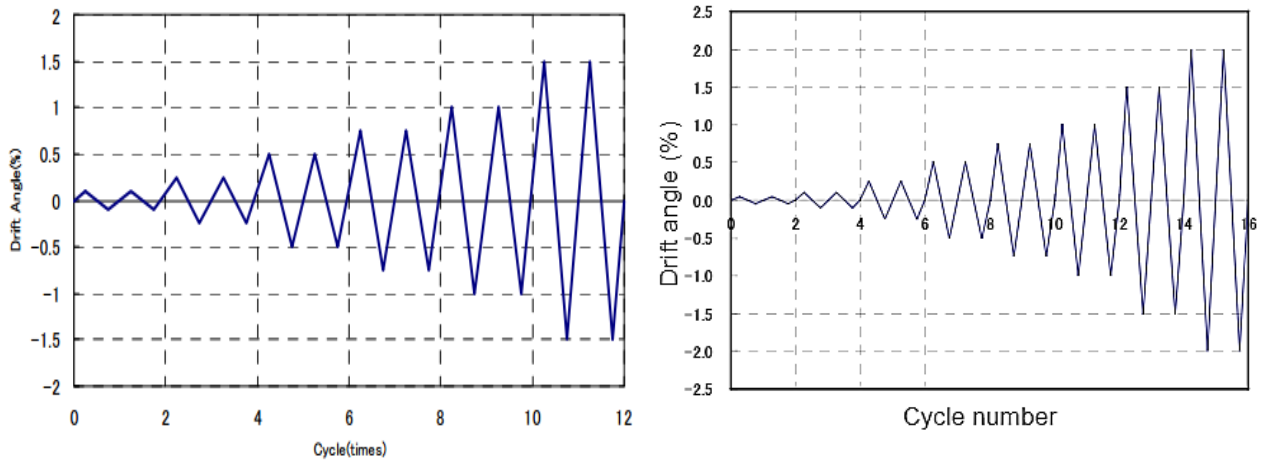

Figure 2.62: Displacement History for Inada and Kono [102, 107]

Experimental Test Results

For Specimens L00A and L45A, the lateral load versus displacement response plots are shown in Figure 2.63; L45C and L45D are shown in Figure 2.64. The following summarizes the major observations in the wall performance of Specimens L00A, L45A, L45C, and L45D. Final damage state is shown for L00A and L45A in Fig 2.65 and for L45C and L45D in Fig. 2.66.

L00A (loaded parallel to one of the equilateral flanges) experienced a crushing-buckling behavior that resulted in a shear failure.

- Flexural cracking at the end of the flange (parallel to loading) was observed at +0.1% drift.
- At +0.25% drift, flexural reinforcement in the wall corner yielded in compression, and rebar in the flange ends yielded later in tension at +0.5%.
- At -0.5% drift with the flange end in compression, researchers noted the onset of concrete crushing. The narrow compression zone is trying to balance tension force from the reinforcement in the flange oriented perpendicular to loading. At this drift level, there was no noted spalling/crushing in the flange perpendicular to loading.
- At +1% drift, the specimen reaches its maximum strength prior to sudden compressive damage the resulted in a shear failure (consistent with web crushing) of the flange perpendicular to the direction of loading.

L45A experienced a web-crushing (shear-compression) failure.

- Flexural cracking at the flange ends was observed at +0.16% drift.

- During the 0.34% drift cycle, flexural reinforcement in the wall corner yielded in compression, and flexural cracking began in the web corner region. Flexural rebar in the web corner yielded in compression at a +0.5% drift.
- Specimens L45A and L45B exhibit the same behavior until the maximum strength is reached at 1% drift.
- For L45A, at -1.5% drift, concrete crushing began in the compressed flange ends. Specimen failure occurs at +2.5% when the unconfined region of both flanges crushed. Afterwards, upon load reversal, a shear sliding failure occurred at the wall-foundation interface.
- For L45B, failure is considered to be 1.5% drift when concrete in (primarily) the unconfined region of the shorter leg occurred.

L45C and L45D experienced a crushing-buckling (boundary element crushing combined with web-crushing) failure.

- Flexural cracking at the web corner was observed at -0.25% and in the flange ends at +0.5% drift.
- At -0.75% drift, flexural reinforcement in the wall corner yielded in tension, and later at +1% drift, they subsequently yielded in compression accompanied by concrete crushing in the same region.
- At +1.5% (L45C) and +2% (L45D) drift cycle, flexural rebar in the flange ends yielded in tension.
- After the maximum strength was reached at 2.4% (L45C) and 2.3% (L45D) drift, the web corner boundary element crushed simultaneously with web crushing.

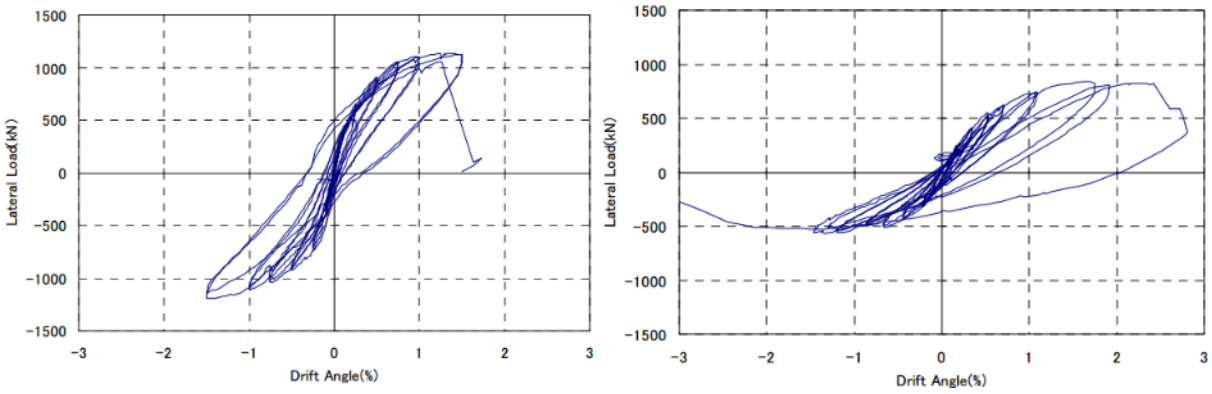

Figure 2.63: Force-drift angle responses for Inada [102]
(Left) Specimen L00A. (Right) Specimen L45A

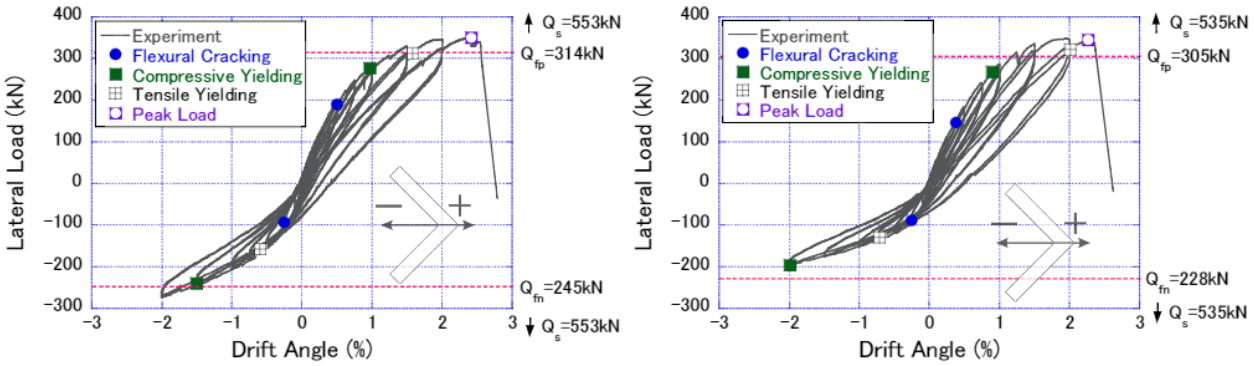

Figure 2.64: Force-drift angle responses for Kono [107]
(Left) Specimen L45C. (Right) Specimen L45D

Research Conclusions

All the walls exhibited compression-controlled flexural failures. Focusing on the results from the diagonally loaded specimens, the experimental data corroborates the same observations made in other L-Shaped research studies where the strain was linear at low deformation demands (up to reinforcement yielding) and became non-linear during the onset of concrete crushing. A direct result of the evolving strain distribution is that both fiber (first set of wall tests) and shell (second set of wall tests) models used to predict wall behavior exhibit higher stiffness than what was experimentally observed as damage progresses. This is believed to be the case since the model maintains the plane-section-remains-plane assumption which ignores local crushing and pull-out of flexural reinforcement near the wall base. Efforts to account for this inelasticity in the fiber models involved introducing springs at the wall base, while this improves the results for the initial cycles of loading additional work is still needed to develop a more accurate prediction method that captures the full response of the wall.

Figure 2.65: Damage to the specimen at end of test from Inada [102]
(Left) Specimen L00A. (Right) Specimen L45A

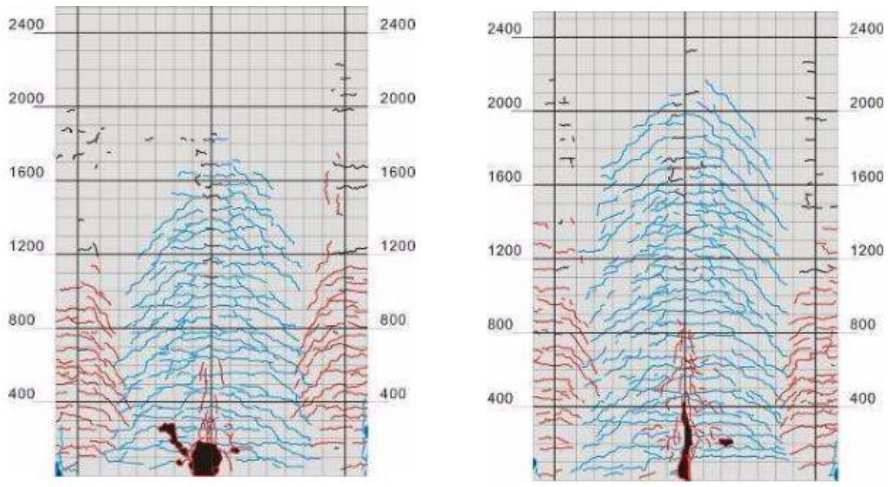

Figure 2.66: Damage to the specimen at end of test from Kono [107]
(Left) Specimen L45C. (Right) Specimen L45D

2.5 Earthquake Performance of Non-planar Walls

2.5.1 Introduction

The experimental test programs discussed in the previous section do not provide sufficient information to evaluate all code-of-practice provisions and develop reliably accurate models for performance-based design of non-planar walls. A detailed list of some of the shortcomings of experimental tests with respect to in-field performance is described in Chapter 6. It is therefore important to investigate in-field performance of these wall types since design and construction practices for these structural components varies nation to nation; moreover, realistic earthquake loading conditions are far more unpredictable in both duration and demand level than what researchers have modelled in experiments.

While there are earthquake reconnaissance documents and publications that focus on either the performance of reinforced concrete structures [51, 79, 105, 106, 122, 123, 153, 156, 176, 178] or shear walls in particular [37, 135, 159, 170, 176] perhaps the most comprehensive review of reinforced concrete structural wall behavior in earthquakes was carried out in the dissertation of *Birely* [35]. However, this document includes a more general investigation that does not distinguish non-planar from planar wall geometries, which one would expect might exhibit different types of damage. Moreover, the timing of its publication did not permit much discussion of the outcome of the Tohuku, Japan (2011), Christchurch, NZ (2010 & 2011) and Maule, Chile (2010) earthquakes; events that resulted in significant learning opportunities to better understand shear wall performance.

The following section is a summary of an investigation specifically on the earthquake behavior of non-planar reinforced concrete structural walls. This involved an extensive review of the available reconnaissance reports and photographs from (i) the Earthquake Engineering Research Institute (EERI) Learning from Earthquakes Archive [80], (ii) the EERI Concrete Coalition project database [79], (iii) the Institution of Structural Engineers, Earthquake Engineering Field Investigation Team (EEFIT) reports, and (iv) other sources when information from references (i)-(iii) indicated that further investigation was warranted for non-planar wall performance in a particular earthquake.

In identifying walls that qualify as part of this study, there were certain parameters that had to be met which are listed below. It is important to note that these had to be ascertained, oftentimes from limited descriptions in reconnaissance documents. Where possible there was an effort to cross-reference reports from different sources about the performance of shear wall(s) in a particular building; however, most cases the inclusion of wall(s) was a judgement call of the author.

In selection of walls for the study, they must:

- Have a three-dimensional cross-sectional geometry, which means that there are at least two intersecting orthogonal rectangular wall sections (where the shortest orthogonal section is at least 20% of the longest section). This is determined by one or more of the following:
  (i) explicit statements in reports of walls forming corners, serving as a "core wall", or surrounding multiple, adjacent sides of stairwell/elevator shafts;
  (ii) sketches or engineering drawings clearly indicating wall configuration and locations;
  (iii) photographs that either visually show the wall is non-planar or an accompanying caption that suggests a non-planar geometry.
- Have some level of flexure and/or shear reinforcement that is intended to resist lateral loads, rather than serve as a bearing wall for vertical loads only. Whether a wall is a shear or bearing wall is typically based on what is reported as the observed reinforcement configuration and connectivity of the wall into the building's lateral load resisting system.
- Have engaged in some degree in lateral load resistance for the building. There are instances where elevator/stairway wall systems are intended to contribute to resisting earthquake demands, but as a result of poor connectivity they experience limited damage while the remainder of the building is severely impacted or even collapses.
- Have been cast-in-place and considered permanent (rather than temporary) structural elements. Walls that are referenced as precast or tilt-up in nature are not considered in this

study as the design and connection detailing of these walls tends to vary. Again, this depends on the structural wall type indicated in reference reports.

- Have been damaged as a result of earthquake motion, as opposed to effects of tsunami, landslides, or extensive liquefaction that may accompany earthquakes.
- Do ***not*** consist of steel sections encased in concrete as boundary elements, or within the wall cross-section, to provide flexural capacity.

As one might presume, the process of positively identifying non-planar walls using the aforementioned criteria to access their performance after earthquakes became quite difficult. Some of the major obstacles included: the exactness of language used to describe structural systems used in reporting damage, availability of photographs of the wall(s) in question (and from multiple angles), access to engineering plans for buildings, and in the case of collapsed reinforced concrete buildings – visibility into the damage to affirm if the building contained shear walls and how they were distributed in the floorplan. This uncertainty, of course, is due to the rapid nature of conducting widespread reconnaissance after an earthquake event and the following section aims to be as thorough as possible considering the stated limitations.

2.5.2 Earthquakes with Notable Non-Planar Wall Damage

Each of the following sub-sections will provide: (i) brief details on an earthquake of interest (dates and magnitudes correspond to [136]), (ii) general performance description of reinforced concrete shear wall buildings, (iii) discussion of specific buildings that utilize non-planar shear wall(s), and (iv)damage details for the identified non-planar shear wall(s). An effort will be made to categorize the observed damage when possible. A more detailed, aggregate analysis of damage observed in the earthquakes can be found in Chapter 3. Table 2.17 provides an overview of number of wall damage records located for past earthquake events.

Table 2.17: Summary of Buildings with Non-Planar Wall Damage in Earthquakes

Earthquake	Date	# of Wall Damage Records
Erçis-Van, Turkey	10-23-2011	2
Tohoku, Japan	3-11-2011	1
Christchurch, New Zealand	2-21-2011	8*
Canterbury, New Zealand	9-3-2010	8*
Maule, Chile	3-27-2010	7
Bingöl, Turkey	5-1-2003	1#
Nisqually, WA, USA	2-28-2001	1#
Chi-Chi, Taiwan	9-20-1999	1#
Kocaeli, Turkey	8-17-1999	2
Cariaco, Venezuela	7-9-1997	1
Kobe, Japan	1-16-1995	1
Northridge, CA, USA	1-17-1994	3
Guam, USA Territory	8-8-1993	5
Erzincan, Turkey	3-13-1992	0
Loma Prieta, CA, USA	8-18-1989	2
Spitak, Armenia	12-7-1988	2
San Salvador, El Salvador	8-10-1986	1
Mexico City, Mexico	9-19-1985	1
Llolleo, Chile	3-3-1985	9
Miyagi, Japan	6-12-1978	1
San Fernando, CA, USA	4-9-1971	3
Anchorage, AK, USA	3-28-1964	5

* Damage inChristchurch & Canterbury EQs are grouped together into Canterbury EQ Series
# Building Heights Unknown

2.5.2.1 Erçis-Van, Turkey (2011)

The 7.1 (moment magnitude scale) Erçis-Van earthquake on October 23, 2011 struck the Van Province of Turkey near the eastern border with Iran. The ensuing damage rekindled concerns of reinforced concrete construction quality in Turkey seen in the Bingöl (2003) and Kocaeli (1999) earthquakes; where numerous partial and full collapses of structures were attributed to use of substandard concrete, insufficient confinement reinforcement, smooth rebar, and improper splicing among other shortcomings. The Turkish government attempted to instate the "Building Control Law" as early as 2000 to control private construction, yet these were not nationally adopted until the beginning of 2011 [77]. Following the Erçis-Van earthquake, the EERI Reconnaissance team report notes that there are few reinforced concrete buildings that employ structural walls aside from newer construction taller than five stories and schools. These walls tend to be inadequately proportioned and poorly positioned resulting in building torsion. However, it appeared that shear walls positioned around elevator shafts were generally effective in reducing overall building damage, though they did experience high levels of damage themselves [77].

There was heavy damage to a C-Shaped wall surrounding an elevator shaft in a six-story moment-frame/structural wall building in Erçis (Fig. 2.67). The building was under construction, but the structural system was essentially complete. The damage consisted of distributed diagonal cracking throughout the lower stories of the wall and, predominantly above the mezzanine floor, significant spalling that exposed reinforcement both in the web and flange. The reconnaissance team indicated that mezzanine floor slabs around the core created a stiffness discontinuity that made the wall system particularly vulnerable [77].

Figure 2.67: Erçis-Van: 6-story commercial building in Erçis [77]

Additionally, the three-story Gedikbulak Primary School collapsed. This 1980's vintage building had an asymmetric structural wall layout that included an L-Shaped wall in one of the corners (Fig. 2.68 (a)) [31]. In particular, the damage to the L-Shaped wall (Fig. 2.68(b)) consists of:

- Apparent twisting of the entire wall section;
- Heavy spalling/crushing along the wall corner which becomes more extensive and exposes reinforcement closer to the wall base;
- Possible buckling of flexural reinforcement, appears transverse reinforcement may be widely spaced apart;
- Cracking/spalling along the wall-foundation interface, which may indicate shear sliding; cracking/spalling along the horizontal construction joints.

Bal et al. [31] modelled the lateral load resisting system of the school to study its failure and concluded that bi-directional loading was necessary to achieve the pancake collapse of the far wing of the building. They attribute this to the "unbalanced" configuration of the lateral system.

(a) Floorplan (b) Structural Damage

Figure 2.68: Erçis-Van: 3-story Gedikbulak Primary School [31]

2.5.2.2 Tohoku, Japan (2011)

The 9.0 (moment magnitude scale) Tohoku, Japan earthquake on March 11, 2011 occurred near the east coast of Honshu, Japan triggering a tsunami. The cumulative damage amounted to what was considered to be costliest natural catastrophe in known history [136]. A summary report by the Building Research Institute (BRI) in Japan [38] indicates that the level of damage to reinforced concrete buildings was low considering the measured seismic excitation. The report also notes that building damage was primarily concentrated in areas with soft soil and structures designed in accordance with the 1981 seismic code or earlier. Moment-frame/shear wall construction is typically used for four to ten-story buildings and in modern schools [59]. Damage in multi-story shear walls was characterized by compression-controlled flexural failures at the base of boundary elements. The most notable case was a planar shear wall at the Tohoku University Civil Engineering & Architecture Building that experienced crushing-buckling of the barbell boundary elements [38, 78]; also, various steel reinforced concrete (SRC) buildings in Koriyama and Shirakawa cities showed similar crushing-buckling at the base of multi-story walls [38]. There were also several shear failures noted in more squat, planar walls found in various school buildings [19].

In terms of non-planar walls, there was severe damage to a core wall in the S Municipal Office Building, a four-story moment-frame/structural wall building of 1970's vintage located in Fukushima prefecture. AIJ and BRI reports [19, 38] noted that the second story of the wall failed in shear in both orthogonal directions. There was widespread spalling/crushing, and considerable buckling of flexural reinforcement in the lower portion of the wall (Fig. 2.69).

Figure 2.69: Tohoku 2011: 4-story Building [38]

2.5.2.3 Canterbury Earthquake Series (2010 & 2011)

The first 7.0 (moment magnitude scale) Darfield, New Zealand earthquake on September 3, 2010 had an epicenter located 50km (31.1 mi) from Christchurch, and the second 6.1 Christchurch, New Zealand earthquake on February 21, 2011 was 6km (3.7 mi) from the city center. The February event was considered to be part of the aftershock sequence, but more costly in terms of damage and lives lost [76, 136]. The overall performance of reinforced concrete buildings with shear walls was deemed satisfactory [76]. However, the report prepared by *Kam et al.* [105] on reinforced concrete building performance following the Christchurch earthquake pointed out major shortcomings with both pre-1970s and modern shear walls. The pre-1970's walls were lightly reinforced and not detailed for ductility, making them susceptible to shear and compressive buckling failures. Modern walls are significantly thinner, utilize minimal levels of reinforcing, and have higher axial load ratios and were vulnerable to shear-compression or premature tensile/compression fracture. In particular, the severe damage observed in modern buildings that have irregular shaped shear wall systems, such as boundary element crushing-buckling and compression zone failure, highlights the need to investigate the performance of non-planar wall configurations.

The Pyne Gould Corp (PGC) Building was a six-story, early 1960's structure that had three short wall segments in the EW direction that intersected with two long NS walls to form a core wall system intended to provide a majority of the lateral load resistance (Fig. 2.70(a)). Consistent with buildings of this era, the wall system was not a ductile design, it was very lightly reinforced with only a single layer of flexural steel and there were no cross-ties or hoops to confine the boundary region. Following the September 2010 earthquake and subsequent aftershocks there was only minor diagonal cracking of the core walls and a notable decrease in building stiffness based on occupant perception. During the February 2011 event, the core walls failed in what was presumed to be flexural compressive

buckling, and collapsed between the 1st and 2nd floors. Consequently the upper five stories of the building experienced a pancake-collapse (Fig. 2.70(b)) [105].

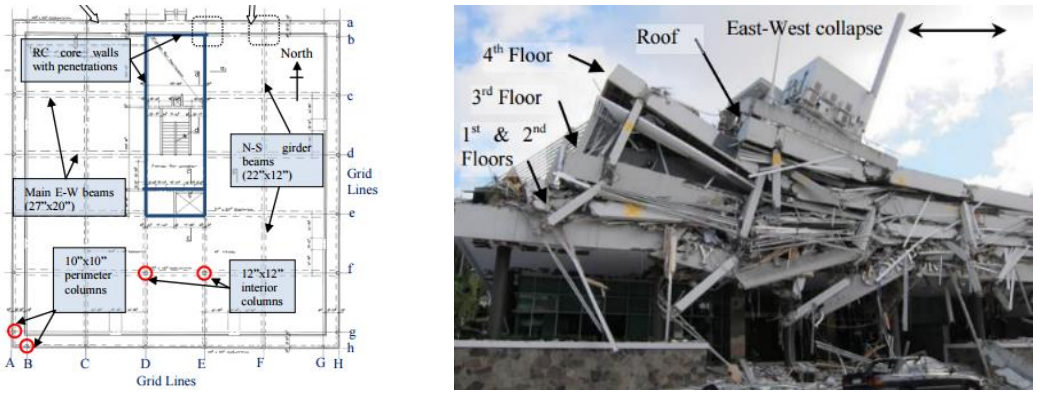

(a) Floorplan (b) Structural Damage

Figure 2.70: Canterbury 2010/2011: 6-story Pyne Gould Corp Building [105]

The Pacific Brands House was a seven–story, 1980's vintage building with a lateral load resisting system comprised primarily of two slender L-Shaped shear walls (Fig. 2.71(a)). One leg of the north wall suffered from an out-of-plane buckling failure in the bottom 1-m (3.3-ft) of the boundary element. This was likely exacerbated by cyclic strength degradation of the flexural reinforcement where the steel yielded and then high strains in compression region led to a global instability. Concrete crushing extended 3-m (9.8-ft) into the lightly reinforced web. Above the spalled regions, in the first story, flexural cracking was noted near the free end of the damaged leg while inclined cracks were observed in the web of the leg (Fig. 2.71(b)). The south wall of the building experienced very little damage, likely due to limited connectivity to the diaphragm as a result of voids created by the stairway/elevator shafts. The building, overall, experienced limited damage [88, 105, 159].

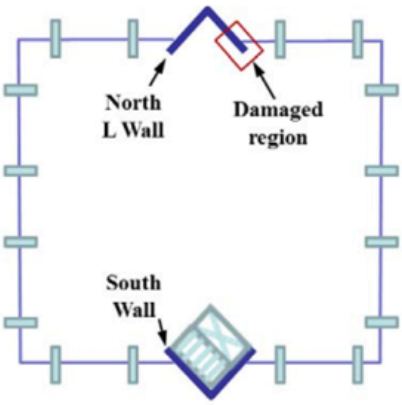

(a) Approximate Floorplan [159]

(b) Structural Damage: shown from (Left) exterior [79], (Right) interior [88]

Figure 2.71: Canterbury 2010/2011: 7-story Pacific Brands House Building

The Terrace on the Park Apartment Building was an 8-story plus basement structure built in 1999-2000. The lateral load resisting system included coupled planar walls and a C-Shaped wall with an opening; the strong-axis of these wall systems was oriented in orthogonal directions (Fig. 2.72(a)). The C-Shaped wall (considered L-Shaped in nature by *Bonelli et al.* [37] due to the opening) developed a diagonal compression strut with extensive crushing of the wall web. Exposed flexural reinforcement buckled over the height of the crushed region [37]. The shear-compression failure in this wall (Fig. 2.72(b)) and the severe damage to the coupled planar walls was attributed to the fact that the lateral system had limited redundancy, an issue that has been seen in various modern high-rise buildings. The structure was ultimately demolished [37, 105].

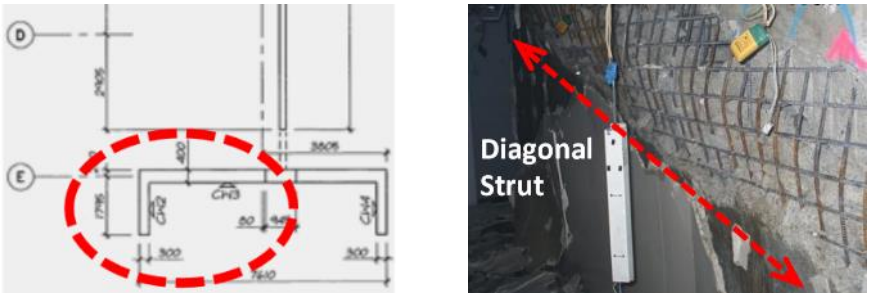

(a) Wall Configuration (b) Structural Damage (to circled portion in (a))

Figure 2.72: Canterbury 2010/2011: 8+-story Park Terrace Apartment Building [37]

There was damage to a shear wall system along the perimeter of a stairwell in the TVNZ building. *Kam et al.* [105] reports that this four-story moment-frame/structural wall building was of pre-1970's vintage and characterized by plan stiffness eccentricity; also, the reinforced concrete members were constructed with smooth bars and limited transverse reinforcement. The stairwell had a C-Shaped wall on the interior and L-Shaped wall on the exterior (Fig. 2.73(a)). There was diagonal cracking and minor spalling along primarily one leg of the L-Shaped wall, and working of construction joints in both the L- and C-Shaped walls (Fig. 2.73(b)) [79].

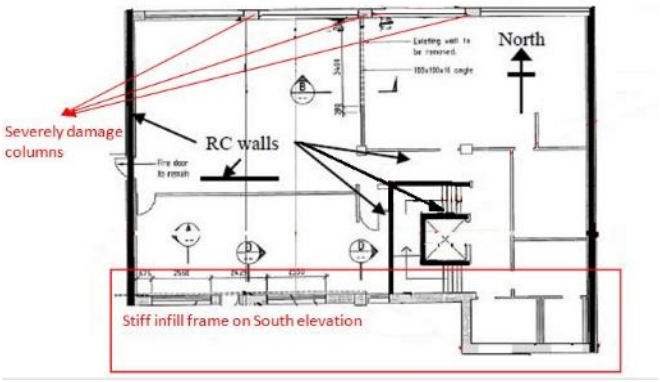

(a) Floorplan

(b) Structural Damage

Figure 2.73: Canterbury 2010/2011: 4-story TVNZ Building [79]

There was also damage observed in:

(i) the Grand Chancellor Hotel, a 22- story moment-frame/shear wall building of the late 1980's had L-and I-Shaped walls in the bottom fourteen stories. Failure at the base of a planar wall and subsequent column failures due to load redistribution resulted in a 1.3-m (4.3-ft) residual lean of the building. The only note of damage in non-failure critical shear walls is hairline flexural cracking [52].

(ii) a pre-1970's five-story moment-frame/shear wall building with multiple intersecting walls and elevator core shaft. These walls settled due to the liquefaction during the February 2011 earthquake, and the structure ultimately collapsed in the June 2011 aftershock [105].

(iii) the Copthorne Hotel, a 11-story moment-frame/shear wall building constructed in the mid-1980's with a post-September 2010 retrofit. This building had two sets of vertically discontinuous L-Shaped walls on the north and south sides, and two core walls (C-Shaped and box-shaped) on the south side. The effects on load path/stiffness eccentricity of these walls led to severe damage in the columns which led to a building lean of 0.2-0.4m (0.7-1.3 ft); no damage description was provided for the walls [79, 105].

There were also notable instances, detailed in *Kam et al.* [105], where core wall systems appeared essentially undamaged despite what appears to significant deformation demands on the remainder of the structure. These cases include:

(i) the mid-1980's six-story Canterbury Television (CTV) Building with a core wall system that remained standing despite a complete collapse of rest of the structure; and

(ii) a 1973 eight-story moment-frame/shear wall building containing a C-Shaped core wall with only minor cracking while perimeter columns failed in shear.

On the whole, the Canterbury earthquake series was extremely informative in regards to structural wall performance particularly since the nature of seismic design and quality of construction are held to very high standards.

2.5.2.4 Maule, Chile (2010)

The 8.8 (moment magnitude scale) Maule, Chile earthquake on March 27, 2010 struck the central south region of Chile. The EERI report [75] indicates that a majority of buildings performed in the elastic range, but there were 31 reinforced concrete buildings with significant damage and four of those collapsed. In terms of reinforced concrete walls there were several cases of brittle failures that included spalling, concrete core crushing, bar buckling, and infrequently, out-of-plane instabilities

and/or bar fracture [135]. Much of this poor performance is attributed to the fact that walls tend to have insufficient confining reinforcement in the wall boundary elements for the expected seismic demands. The amount of confinement ranges from not having hoops or ties with horizontal reinforcement extending into the boundary element, to having excessively large spacings for confining reinforcement. Confinement of boundary elements was not part of the Chilean concrete building code as a result of the generally good outcome seen with shear walls in the 1985 Llolleo, Chile earthquake (discussed in Section 2.3.2.17) [37, 75, 135, 170]. One critical difference between older design and modern structures is that those buildings had redundant, stiff shear-walls systems consisting of 2-3% wall area to floor area; however, modern buildings have fewer, more slender walls that make up 1% or less of wall area to floor area leading to more flexible systems. The earthquake was seen as a warning signal and led to revision of the Chilean code as well as extensive studies by NEHRP [133, 135] to evaluate the state of ACI318 provisions.

The Festival Apartment Building in Viña del Mar is a fourteen-story shear wall structure designed in 1978 (Fig. 2.74(a)). It experienced moderate damage in the Llolleo, Chile (1985) earthquake as described in Section 2.3.2.17. After the Maule, Chile Earthquake there was significant documentation of damage to L-Shaped walls in this particular building that highlights the type of brittle failures to which these walls are susceptible. In the interior L-Shaped wall of this structure there was a diagonal compression strut across this wall where significant web crushing. Crushing continued into the boundary elements, and buckling of flexural reinforcement can be seen at the base of the leg end (Fig. 2.74(b)). There appears to be no confining hoops or ties in the boundary element and the small diameter, smooth horizontal reinforcement that continued to the wall edge did a poor job of providing lateral restraint to the longitudinal bars. The exterior L-Shaped wall has a high concentration of flexural reinforcement with widely spaced horizontal rebar, again there was significant crushing-buckling at the base of the leg end (Fig. 2.74(b)) [58].

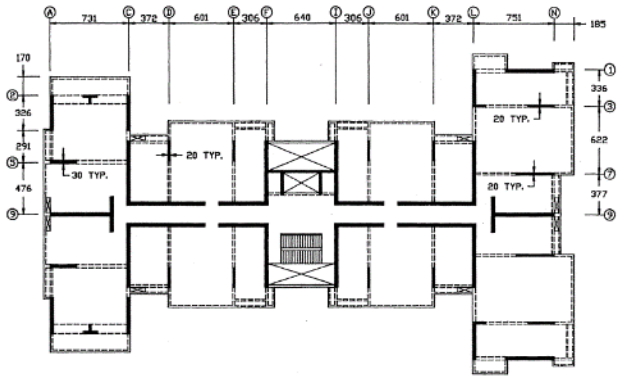

(a) Floorplan [177]

(b) Structural Damage: (Top) Interior L-Shaped Wall (Left to Right: [50, 149]), (Bottom) Exterior L-Shaped Wall (Left to Right: [36, 58])

Figure 2.74: Maule 2010: 14-story Festival Building

The Edificio Emerald Apartment Building in Santiago is a twenty-story shear-wall structure with four underground basement levels that was completed in 2008 (Fig. 2.75(a)). Some design concerns include that the wall system has vertical discontinuities over the height; also, boundary elements did not contain hoops, rather they had horizontal bars were hooked with 90-degree angles around the edge of the wall. There were many rectangular and non-planar walls in the first basement level of the

building that experienced severe crushing-buckling damage [74, 135]. The T-Shaped wall experienced crushing-buckling of the web in addition to out-of-plane buckling primarily at the top of the wall in the exterior web boundary element (Fig. 2.75(b)) [74, 135, 170]. Analyses of this particular wall in the NIST document [135] indicates crushing likely proceeded the out-of-plane buckling based on the necessary strain level necessary to cause the respective types of damage. Furthermore, the significant difference in damage to the web versus the flange of this wall is expected since crushing with the web under compression was predicted to occur at half the drift ratio for flange crushing.

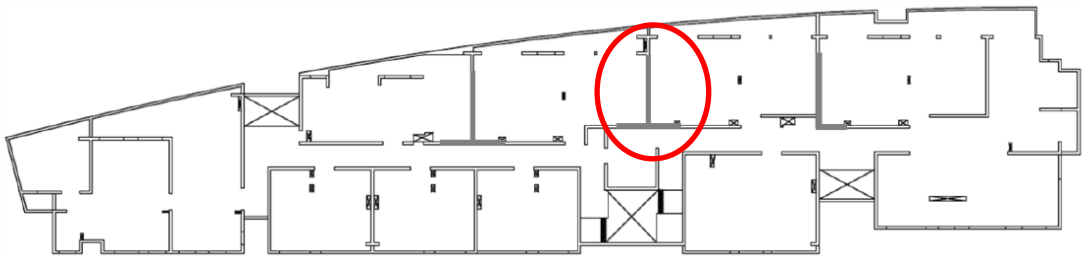

(a) Floorplan [135]

(b) Structural Damage (Left to Right: [74, 100])

Figure 2.75: Maule 2010: 20+-story Edificio Emerald Building

The Alto Huerto Building is a fifteen story shear-wall structure with two basement levels located in Concepción that was built in 2009. The T-Shaped wall experienced wall crushing, bar buckling, and out-of-plane global buckling in the wall web, it appears there is very little damage to the flange (Fig. 2.76). It is unclear if this image was taken after excavation of some core concrete and removal of transverse reinforcement, but there appears to missing horizontal bars near the base of the wall. Regardless, the boundary element does not appear to have additional flexural reinforcement compared to the web, nor are there confining hoops or ties (the latter is consistent with the Festival and Emerald buildings described above) [135].

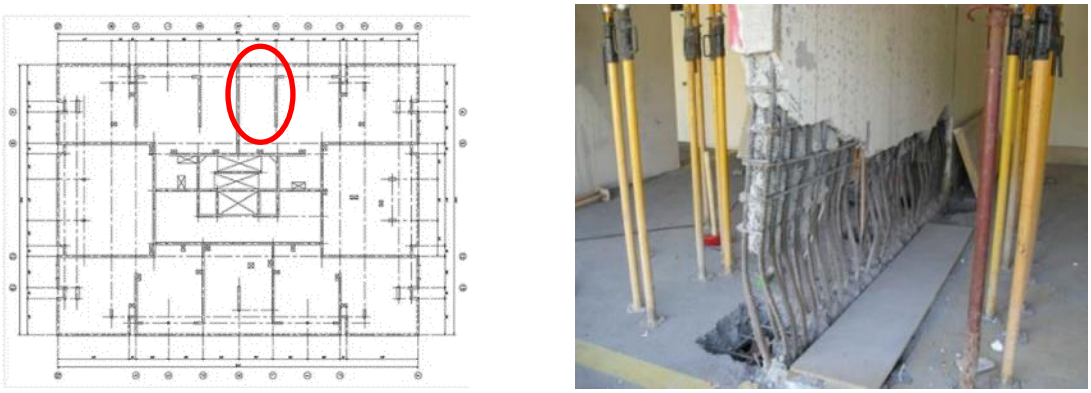

(a) Floorplan (b) Structural Damage

Figure 2.76: Maule 2010: 15+-story Alto Huerto Building [135]

The Edificio Toledo is a ten-story shear-wall building with one basement level in Viña del Mar that was built in 1996 (Fig. 2.77(a)). There was considerable crushing-buckling damage to all of the transverse walls at the ground story. The T-Shaped wall (second from the front in the image) appeared to develop a diagonal compression strut from the exterior boundary element and continuing across the entire web (Fig. 2.77(b)). Again, there were no hoops or ties in the boundary elements to confine concrete [37, 135].

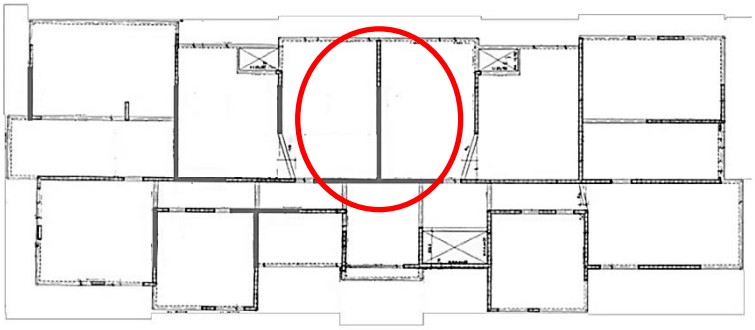

(a) Floorplan [135]

(b) Structural Damage [36]

Figure 2.77: Maule 2010: 10+-story Edificio Toledo Building

Damage to an unidentified twelve-story shear-wall structure in Viña del Mar included extensive crushing-buckling damage to a C-Shaped wall (Fig. 2.78) [16]. This failure appears to occur across a horizontal plane on the wall web. The flexural reinforcement buckled over the spacing between horizontal bars likely due to lack of restraint, and in the right flange it is possible to observe multiple transverse bars have been pushed together. It also is possible to observe that one bar in the left flange has fractured.

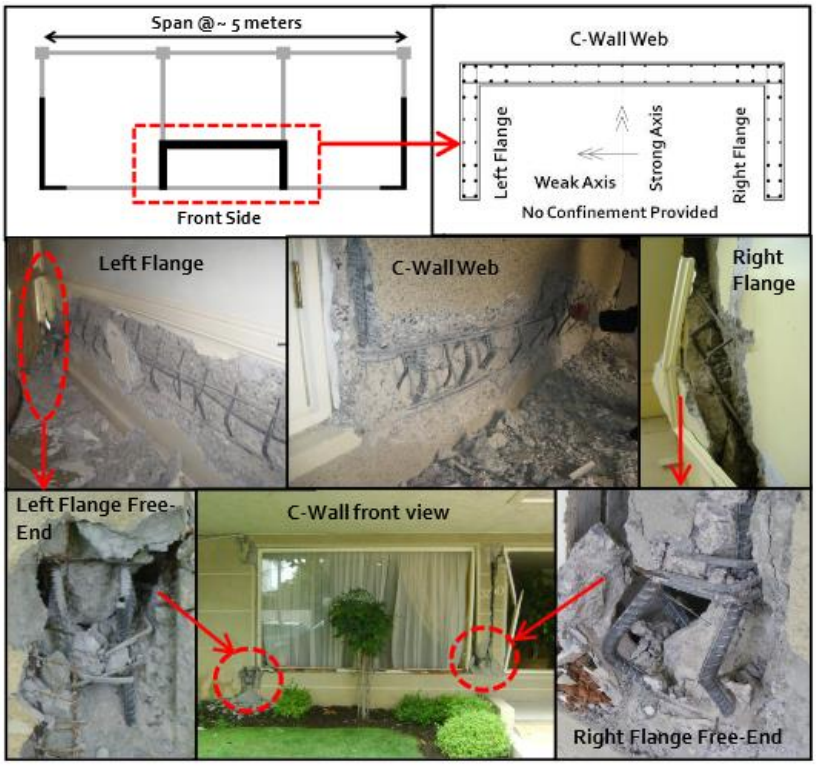

Figure 2.78: Maule 2010: 12-story Unidentified Building [37]

Other buildings with non-planar walls that were damaged based on the NIST report on concrete shear walls [135] (this list excludes severely damaged buildings attributed to the presence of discontinuity regions):

- Plaza del Rio, Building A (12 story from 2004 with T-Shaped and other non-planar walls) – damage was concentrated in first two levels and included spalling/crushing, bar buckling and fracture, and global buckling of walls. The most severe damage was in non-planar wall geometries.

- Undisclosed Building A (12 +2 story from 2005 with T- and L-Shaped walls)- one of the L-Shaped walls experienced some spalling at the exterior web boundary element, while the other had significant crushing-buckling over the entire web length

The Maule, Chile earthquake was a very costly event that provided one of the most robust datasets regarding in-field performance of reinforced concrete shear walls (and a number of non-planar walls, in particular) that is a valuable to furthering design of these structural components.

2.5.2.5 Bingöl, Turkey (2003)

The 6.4 (moment magnitude scale) Bingöl earthquake on May 1, 2003 struck the Bingöl Province in the eastern part of Turkey. As mentioned previously with the Erçis-Van, Turkey (2011) earthquake, poor construction quality and shortcomings with ductile design of lateral load resisting systems are major concerns [51, 82, 106]. In the Bingöl city center there were around 1200 buildings that were severely damaged or collapsed. While reinforced concrete moment-frame/shear wall buildings make up a rather small portion of the overall building stock, a report by *Doğangün* [51] and *Erdik et al.* [82] indicated that most modern reinforced concrete buildings that utilized shear walls tended to perform quite well, noting only instance of poor performance in one structural plan used at multiple high school campuses.

An L-Shaped shear wall in Building B of both Bingöl Liesi (C-14-08) and Bingöl Imam Hatip Lisesi (C-14-09) high schools was damaged. Building B is a four-story template structure that is part of a three-building complex that followed the standard design of high school buildings used by the Turkish Ministry of National Education. The floorplan for C-14-08 (Fig. 2.79(a)) is identical to C-14-09, except C-14-09 has two fewer bays in the long direction [139]. The shear wall in C-14-08 experienced significant crushing of concrete in a diagonal configuration; there was loss of core integrity leading to through voids in the wall (Fig. 2.79(b)). The web-crushing type failure observed in this wall is attributed to insufficient transverse reinforcement, poor concrete quality, and smooth reinforcing bars [51, 79, 82, 139]. In C-14-09 there was working along a construction joint evident by a horizontal crack at this location [139].

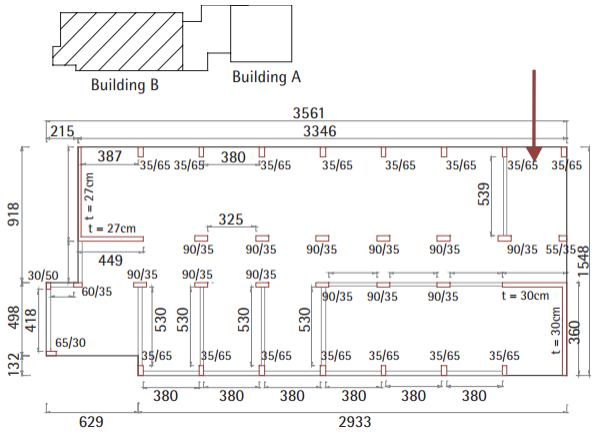

(a) Floorplan (RC shear walls are shown with solid red lines) [139]

(b) Structural Damage [79]

Figure 2.79: Bingol 2003: 4-story Bingöl Liesi Building B

2.5.2.6 Nisqually, WA, USA (2001)

The 6.8 (moment magnitude scale) Nisqually, Washington, USA earthquake on February 28, 2001 had an epicenter 11 mi northeast of Olympia, WA. A reconnaissance report prepared by the Nisqually Earthquake Clearinghouse Group at the University of Washington [130] indicated that damage to reinforced concrete structures was limited, especially in the case of newer construction. In general, the most severe effects on shear walls were diagonal cracking and cracking at construction joints, such as that seen in the planar walls in the five-story General Administration Building in Olympia [83, 130].

There was damage to the corner wall of red-tagged concrete building that includes spalling in the wall boundaries and cracking across the base (Fig. 2.80).

Figure 2.80: Nisqually 2001: Red-tagged Concrete Building [166]

2.5.2.7 Chi-Chi, Taiwan (1999)

The 7.7 (moment magnitude scale) Chi-Chi, Taiwan earthquake on September 20, 1999 had an epicenter near the center of the island. A large portion of the mid-rise (12-15 stories) residential structures in urban areas of Taiwan had reinforced concrete moment-frames. Although many contained lightly-reinforced concrete exterior walls and elevator shafts these were not designed for seismic load resistance. There were several cases of collapse of these mid-rise structures where columns suffered severe damage and non-structural walls failed in a brittle manner, but otherwise this building type performed well with limited shear cracking in the exterior, non-structural walls. The major shortcomings of these 5-10 year old buildings seemed to be the use of an open first story and inadequate lateral load resisting system that could have benefited from seismic design of the reinforced concrete walls [71, 73, 114, 131].

There was damage to a building under construction that had a structural core wall at the corner of the floorplan. The wall exhibited diagonal cracking across the first floor in both orthogonal wall directions; there was also minor spalling at the intersection of these cracks (Fig. 2.81) [115].

Figure 2.81: Chi-Chi 1999: Unknown Concrete Building [115]

2.5.2.8 Kocaeli, Turkey (1999)

The 7.6 (moment magnitude scale) Kocaeli, Turkey earthquake on August 17, 1999 had an epicenter 80 km (49.7 mi) southeast of Istanbul. Earlier statements about poor construction and non-ductile design of lateral load systems in Turkey pertain to this earthquake as well [51, 82, 106]. Dual-system buildings with moment-frame and shear wall or only shear wall systems represent a small number of reinforced concrete buildings in the effected region; though there are some instances where C- or U-Shaped elevator shafts are utilized [57]. Generally, buildings with shear walls did perform quite well and there were no noted story collapses in this structure type. Most walls are rectangular with small cross-sectional aspect ratios, and systems comprised of these walls are often provide insufficient stiffness to allow the non-ductile frames to remain elastic [155]. Older shear walls showed significant diagonal cracking and spalling that exposed flexural reinforcement, but for the most part maintained core integrity and exhibited very little crushing-buckling behavior; modern walls tended to experience limited diagonal cracking and minor spalling [154].

The main tower of the Sopali Hospital in Derince is comprised of three nine-story rectangular dual moment-frame and shear wall structures (construction date is not clear since structures on the hospital campus range from 1978-1991). Spalling was noted in the core walls surrounding the stairwells in the buildings [72]. Additionally, a building on the Golcuk Naval Base that was positioned over the fault suffered significant diagonal cracking and spalling damage to a corner L-Shaped wall (Fig. 2.82) [131, 155].

Figure 2.82: Kocaeli 1999: Golcuk Naval Base Building [111]

2.5.2.9 Cariaco, Venezuela (1997)

The 7.0 (moment magnitude scale) Cariaco, Venezuela earthquake on July 9, 1997 struck near the northeastern coast of the country. The EERI report [70] indicates that there was considerable

damage to several reinforced concrete structures in Cumana and Cariaco, including a few notable collapses (generally moment-frame only systems). Other multi-story concrete structures located nearby had minor to no structural damage. The more heavily damaged buildings exhibited insufficient transverse reinforcement in the lateral load resisting elements, plan stiffness eccentricity, or inadequate stiffness in one of the building's main orthogonal directions.

The Miramar Building was a six-story dual moment-frame and shear wall building constructed in 1979. A shear wall core was positioned in the corner of the building and surrounded the stairway/elevator shafts. A majority of the wall core system failed and the building collapsed, only the bottom two floors of the core remained standing after the earthquake (Fig. 2.83). Torsion due to asymmetric layout of walls as well as inadequate stirrups and poor anchoring of these stirrups in concrete leading to a non-ductile response of the structure [70, 150].

Figure 2.83: Cariaco 1997: 6-story Miramar Building [150]

2.5.2.10 Kobe, Japan (1995)

The 6.9 (moment magnitude scale) Kobe, Japan earthquake on January 16, 1995 had an epicenter located 20 km (12.5 mi) from this major port city. The EEFIT report [56] indicates that the dual moment-frame and shear wall system is the most prevalent concrete system in Japan for buildings of 4-10 stories. There were no collapses of structures with shear-walls as the primary lateral load resisting system; however, there were partial soft-story type collapses in dual system buildings [122, 132]. These failures were primarily from plan stiffness eccentricities or vertical stiffness discontinuities that led to high shear demands on the walls, often precipitating shear failures in these structural elements [132]. More commonly, though, damage to shear walls was moderate to significant diagonal and flexural cracking, and on a few occasions, out-of-plane failures of rectangular walls in the absence of sufficient shear walls positioned in the orthogonal building direction [122, 132]. In addition to previously mentioned items, some design shortcomings observed in reinforced

concrete dual system buildings include insufficient flexural and confining reinforcement of lateral system components, as well as inadequate stiffness in one of the building's main orthogonal directions [132].

The German Consulate Building is a predominantly shear-wall structure built in 1955, comprised of three buildings: an eight-story main block, eleven-story tower along one side, and a five-story building on the east-side. The tower has a 3-sided wall system (most similar to a C- or U-Shaped configuration) around the stairway that had varied damage across the height. There was considerable spalling and cracking at the lower level (Fig. 2.84) and higher up one of the walls displaced out-of-plane towards the center of the shaft. The particular lesson from this wall damage was the importance to provide restraint that stabilizes the free-ends of the C-/U-Shaped wall geometry [132].

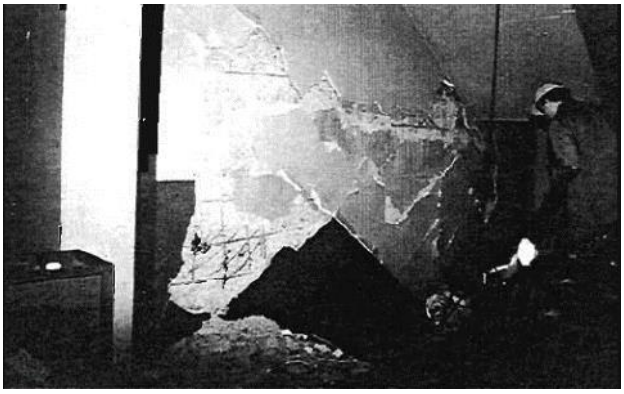

Figure 2.84: Kobe 1995: 11-story tower of German Consulate Building [132]

2.5.2.11 Northridge, CA, USA (1994)

The 6.7 (moment magnitude scale) Northridge, CA, USA earthquake on January 17, 1994 had an epicenter located in the Northridge area of Los Angeles. In general, reinforced concrete buildings that consisted of shear walls as the primary lateral load resisting system performed well, especially in buildings with a well-distributed wall layouts and adequate connections between walls and diaphragms. Damage observed in pre-1976 structures included shear cracking in walls and significant damage in other lateral system elements, more modern buildings tended to have less damage throughout the lateral load resisting system with only some instances where walls experienced minor cracking or sliding along construction joints [69, 123].

Notable structures that included non-planar wall systems in the form of shear wall cores included the dual moment-frame and shear wall buildings: Sherman Oaks Towers (12-story built 1965) and

the Barrington Medical Building (6-story built in 1968); and shear-wall building St. John's Hospital (7-story built 1966). Based on damage reports, these buildings all saw very limited damage to the wall cores despite considerable damage on exterior, planar shear walls or frame columns [69, 79]. This seems to suggest the effectiveness of non-planar wall systems, but also the necessity for detailing secondary lateral load resisting elements to have a high level of ductility.

2.5.2.12 Guam, USA Territory (1993)

The 7.8 (moment magnitude scale) Guam earthquake on August 8, 1993 struck about 50 mi off this US island territory. Reinforced concrete dual moment-frame and shear wall buildings are common in the taller hotel structures found on Agana and Tumon Bays. There were partial collapses of two moment-frame hotels and one entrance canopy, but the damage in shear walls ranged from minor to extensive diagonal cracking and spalling; no wall failures were noted [67]. The generally good performance of structural systems is attributed to the fact that they are designed for high wind speeds experienced in typhoons [68].

A brief overview of damage seen to non-planar wall systems described in the EERI report [67]:

- Guam Hilton Hotel – spalling/cracking at horizontal construction joints of core walls, often in locations of poorly consolidated concrete
- Hotel Nikko Guam & Pia Resort– extensive cracking in concrete stairway/elevator shafts
- Onward Agana Beach Hotel – diagonal cracking in concrete stairway/elevator shafts
- Pacific Star Hotel– minor to moderate cracking in stairway shafts

As a note, some of the spalling from concrete structural members is partly attributed to the corrosion from exposure to the salt-water environment in Guam, which exacerbated damage seen in the earthquake [67].

2.5.2.13 Erzincan, Turkey (1992)

The 6.9 (Richter magnitude scale) Erzincan, Turkey earthquake on March 13, 1992 struck eastern Turkey. There was complete or partial collapse of over 200 mid-rise reinforced concrete moment-frame structures. The reasons for collapse are consistent with observations previously made in Turkey related to non-ductile design, poor material quality [51, 82, 106], as well as asymmetrical floorplans, and orientation of all columns with the strong axis in only one of the building's orthogonal directions [65]. Very few buildings in the effected region contained concrete shear walls, but those examples seemed to survive the earthquake with little, if any, signs of structural distress [66, 153]. Reconnaissance teams noted that shear walls were able to limit inter-story drift in buildings and reduce the ductility demands on the moment-frame members; that led to an overall improved global

performance of the structures [66]. This earthquake is relevant as an example of good outcomes for the few shear wall buildings amidst otherwise catastrophic losses.

2.5.2.14 Loma Prieta, CA, USA (1989)

The 6.9 (moment magnitude scale) Loma Prieta, CA, USA earthquake on October 18, 1989 had an epicenter located 15 km (9.3 mi) northeast of Santa Cruz. This earthquake had a rather short duration of strong ground motion; so many engineers warn against drawing too much confidence from the generally good performance of engineered buildings. Most damage to modern reinforced concrete buildings appears to be cosmetic to minor structural damage where shear walls experienced diagonal and flexural cracking as well as horizontal cracking along construction joints [63]. However, there are some cases of more severe damage observed in several pre-1976 buildings that have non-ductile detailing, which included severe spalling/crushing [81].

The lightweight-concrete, corner wall of a sixteen-story reinforced concrete building in Oakland shattered (Fig. 2.85). This example of older non-ductile design exhibits: crushing of the wall in both orthogonal segments across an entire horizontal plane, exposure of reinforcement, and some signs of loss of concrete core integrity [81].

Figure 2.85: Loma Prieta 1989: 16-story Unknown Building [81]

Escondido Village at Stanford University was a complex of five structurally-identical buildings that served as residential housing. These eight-story reinforced concrete shear-wall buildings were constructed in the early 1960s. There were multiple non-planar wall configurations including corner L-Shaped walls and stairway cores (Fig. 2.86). The walls experienced distributed diagonal cracking and horizontal flexural cracking near wall bases; damage to interior core walls was noted to be most severe [79].

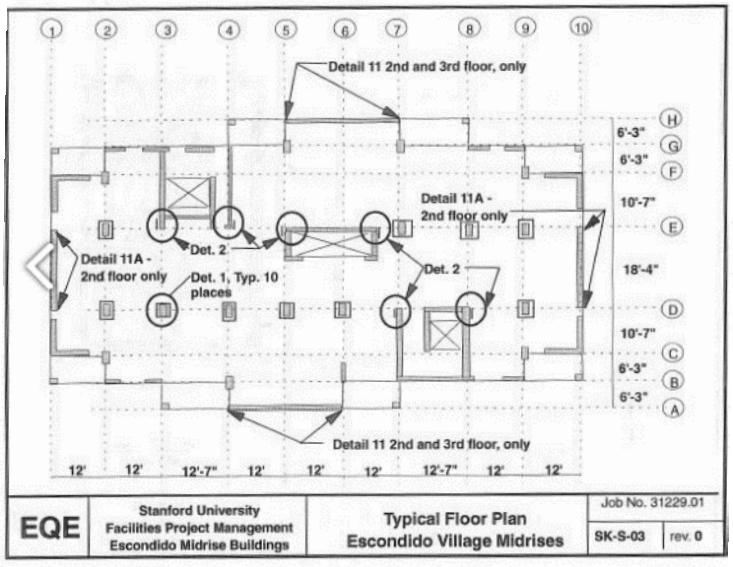

Figure 2.86: Loma Prieta 1989: 8-story Escondido Village Buildings [79]

2.5.2.15 Spitak, Armenia (1988)

The 6.8 (Richter magnitude scale) Spitak, Armenia earthquake on December 7, 1988 struck the northern part of this republic in the Soviet Union. Damage was widespread and highlighted concerns with construction quality and seismic design of engineered structures [61]. The design atmosphere in Armenia was unique in that there were four template structural systems generated by Soviet government design institutes and modified by another body for site-specific seismic demands [62]. The vast majority of reinforced concrete buildings in the affected area were precast moment-frame structures many of which collapsed or were heavily damaged; there were a small number of precast large-panel buildings that only had minor damage; and two lift-slab buildings that consisted of precast columns and cast-in-place concrete cores – one which collapsed and other was heavily damaged.

The lift-slab apartment buildings had circular concrete core walls systems surrounding the stairway/elevator shafts (Fig. 2.87(a-b)). These walls did not have confined boundary elements near any of the three wall openings; they consisted of uniformly spaced flexural and horizontal reinforcement (both with rather large spacing). The ten-story building collapsed and reconnaissance teams were unable to access the mode of failure. The sixteen-story building experienced a crushing-buckling failure of the entire wall core at the first floor near a horizontal construction joint. Based on the direction of vertical bar buckling it appears this damage resulted from torsion of the core (Fig. 2.87(c)). There was diagonal cracking noted in the core throughout the height of building, and

following the earthquake the building had a 4-ft residual lean. The damage of these shear-wall structures highlights the need for adequate spacing of horizontal reinforcement, confined boundary elements to provide ductility, properly roughened construction joints, and more complete connection between the core and diaphragm system [62, 178].

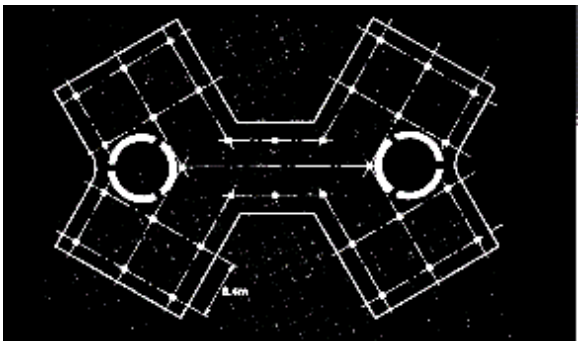

(a) 10-story Building Floorplan [62]

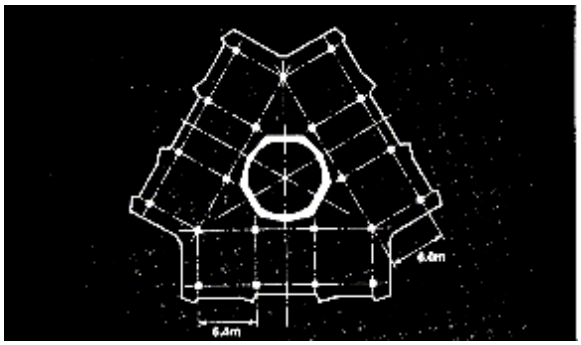

(b) 16-story Building Floorplan [62]

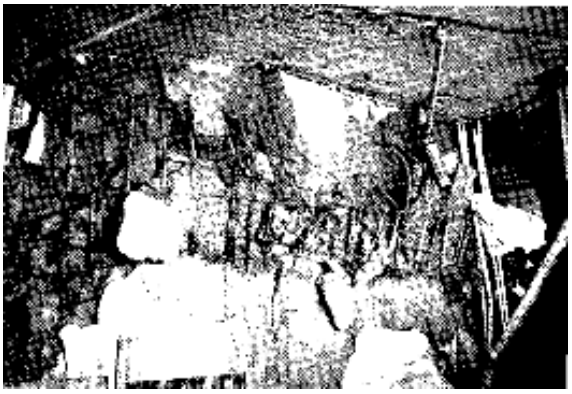

(c) 16-story Building Structural Damage (Left to Right: [62, 178])

Figure 2.87: Spitak 1988: Lift-Slab Apartment Buildings

2.5.2.16 San Salvador, El Salvador (1986)

The 5.4 (Richter magnitude scale) San Salvador, El Salvador earthquake on October 10. 1986 struck in close proximity to the capital city. Damage to low to mid-rise engineered buildings was more severe, including several complete and partial collapses, while high-rise structures experienced very little impact. This was attributed to the short-period ground motion making shorter buildings more vulnerable [60]. Reinforced concrete shear walls were rarely used in San Salvador; however, the few buildings that did contain these systems had performance ranging from minor to moderate structural damage to shear walls [54]. There was one case of complete collapse with the Ministry of Planning

Building, but the core walls were still fully intact and standing after the earthquake, indicating they were poorly tied into the rest of the lateral system and did not engage [60].

The U.S. Embassy Building, a five-story building comprised of a two-story base and three-story tower, was designed in 1963 and constructed in the late 1960s, with an addition in the late 1970s. The tower experienced considerable overall damage including cracking of core shear walls surrounding the stairway/elevator and restrooms. Noted issues with the lateral system included plan stiffness eccentricity due to core wall placement and limited confining reinforcement in reinforced concrete members that led to non-ductile response [60].

2.5.2.17 Mexico City, Mexico (1985)

The 8.1 (Richter magnitude scale) Mexico City, Mexico on September 19, 1985 struck 400 km (248.5 mi) from this capital city. Reinforced concrete use for high-rise, engineered structures is prevalent; moment-frame only buildings that suffered from extreme damage or collapse were isolated to pockets of the central city zone. There are few dual moment-frame and shear wall structures, and it is even rarer to find primarily shear-wall lateral systems. Dual and shear-wall buildings had good seismic performance with very little damage to the overall structural system though shear walls experienced flexural and shear cracking [42, 53].

The fifteen-story plus basement building is one tower in a three office complex designed using 1976 code. The dual moment-frame and shear wall structure contained two core walls (both are C-Shaped, but one has rather short flanges) as shown in Fig. 2.88. Damage was limited at the lower floors and became more significant at levels 4-12, particularly in regions close to the shear walls, likely due to settlement of the core system. Reconnaissance notes indicate that damage to the shear walls included diagonal cracking in wall webs, spalling at the top of the fifth floor extensive enough to expose reinforcement, and vertical cracking at the top floor [64, 79].

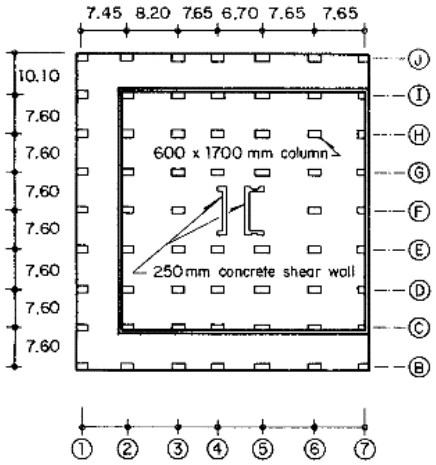

Figure 2.88: Mexico 1985: 15+-story Office Building [64]

2.5.2.18 Llolleo, Chile (1985)

The 8.0 (moment magnitude scale) Llolleo, Chile on March 3, 1985 occurred near the coast of central Chile. Chile is rather unique in the fact that shear walls are commonly used as a primary lateral load resisting system; in the effected city of Viña del Mar about 97% of reinforced concrete buildings are of this type, and an 80% of those buildings sustained essentially no structural damage. While Chilean structural walls lacked ductile detailing with almost no confinement of boundary elements, the comparatively large ratio of wall area to floor area led to rather stiff buildings that performed elastically [177]. However, there were some notable cases of severe damage to shear walls that correspond to that seen in Acapulco and Hanga Roa, described below.

The Acapulco Condominium Building was a fifteen-story shear wall structure constructed in 1964. Parallel transverse walls were arranged on an angle and intersected with other walls flanking the corridors to form irregular non-planar configurations (Fig. 2.89(a)). Wall webs were reinforced with smooth rebar, and twisted bars were used in the boundary regions; also, diagonal reinforcement in addition to horizontal and vertical reinforcement was present in the walls. The most extensive damage was seen in the L-Shaped wall on gridline M', this consisted of: wide shear cracks, slip/spalling along construction joints, and crushing-buckling of the wall boundary (Fig. 2.89(b)). Additionally, crushing-buckling of another boundary element was observed (Fig. 2.89(c)) and diagonal cracking was quite common in the other shear walls. Other instances of distress at construction joints and boundary regions in walls was noted [131, 152, 176, 177].

Hanga Roa is another fifteen-story condominium located directly north of the Acapulco. This shear-wall structure with curving floorplan was constructed in 1970. Two curved shear walls follow the

corridors in this building and transverse walls between rooms intersect with these central walls at 90-degree angles (Fig. 2.90(a)). Based on reports it seems that the location of transverse walls was staggered every other floor. A wide vertical crack in the shear wall between door openings progressed up the entire height of the structure from minor in width at the first floor to nearly 1-ft wide at the fourteenth floor (Fig. 2.90(b)). Investigators attribute this to high shear stresses induced in the wall [176]. There was notably heavy damage at the intersection of walls that form an inverted "Y" at the western side of the structure [177].

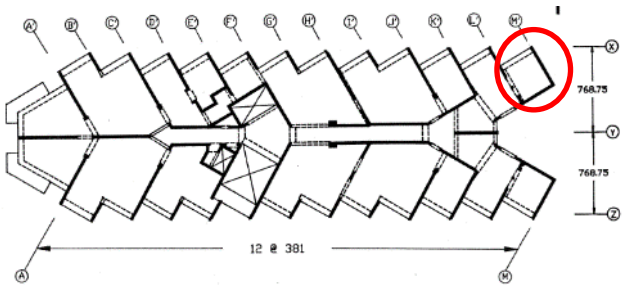

(a) Floorplan [177]

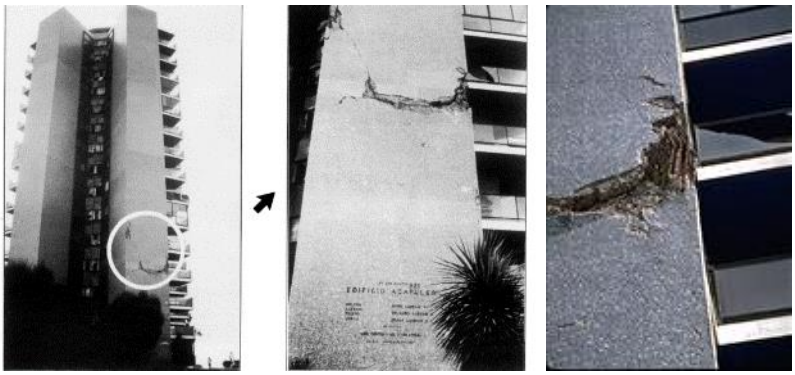

(b) Building Structural Damage for Gridline M' (Left & Center:[55], Right: [131])

(c) Boundary Element Crushing-Buckling Damage [131]

Figure 2.89: Llolleo 1985: 15-story Acapulco Building

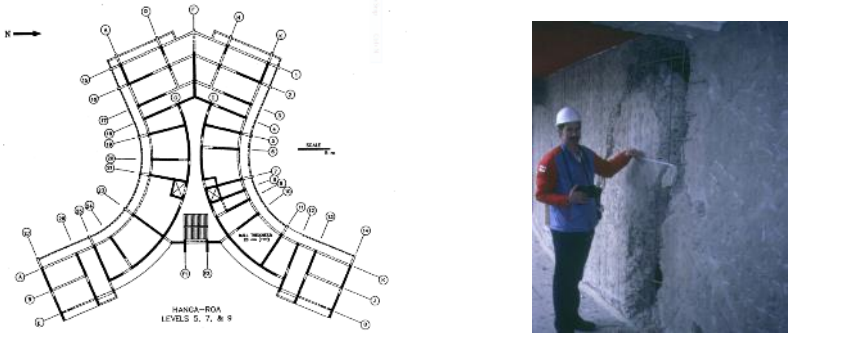

(a) Floorplan [177] (b) Structural Damage [??]

Figure 2.90: Llolleo 1985: 15-story Hanga Roa Building

Another example of significant damage to a structure with non-planar walls was Edificio El Faro. This eight-story plus basement building built in the early 1980s had an asymmetrical wall layout creating a stiffness eccentricity that led to torsion (Fig. 2.91(a)). The lower portion of the T-shaped wall, formed by intersecting wall segments at gridlines M and D, collapsed. The walls in this structural were under-reinforced for flexure, and it was determined that the brittle failure was triggered by bar fracture in the segment on gridline M. After the earthquake, the building had a residual lean and was immediately demolished due to safety concerns (Fig. 2.91(b)) [152].

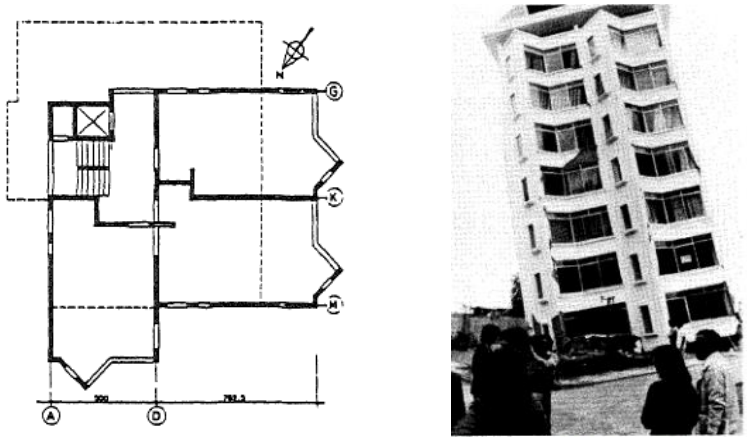

(a) Floorplan (b) Structural Damage

Figure 2.91: Llolleo 1985: 15-story Edificio El Faro [152]

Other residential structures with damaged non-planar walls from *Wood et al.* [177] (unless otherwise noted):

- Plaza del Mar (23-story with L- walls) – minor hairline cracking [176]

- Coral (12-story with L-, T-, C-walls) – cracks observed throughout walls
- Festival (14-story with L-, T-, C-walls) – diagonal cracks in several shear walls and crushing of a wall boundary at intersection with retaining wall (this building was more severely damaged in the Maule, Chile 2010 earthquake as noted in Section 2.3.2.4)
- Villa Real (10-story with irregular configurations) – diagonal cracking in floors 1-3
- Torres de Sol (22-story with C-, L-walls) – diagonal cracking
- Barrios Edificio (5-story with core walls) – reopening of patched cracks [55]

There were at least three other structures reported by Wood et al. [177] with non-planar walls that showed no structural damage to the shear wall systems.

2.5.2.19 Miyagi, Japan (1978)

The 7.7 (Richter magnitude scale) Miyagi, Japan on June 12, 1978 had an epicenter that was 100 km (62.1 mi) from Sendai. The building performance in Sendai city was generally very good with few pockets of damage. The most severe damage to buildings with planar shear walls included extensive diagonal cracking ranging to shear failures that led to a partial collapse; however, structures with core (non-planar) wall systems tended to exhibit better performance [164].

The Sumitomo Insurance Building was an eighteen-story steel and reinforced concrete system (moment-frame using columns of steel encased sections) that had C-Shaped walls surrounding the elevator shaft and exterior walls of non-planar configurations (Fig. 2.92). The core wall system exhibited minor diagonal cracking; most other lateral system elements appeared undamaged [164].

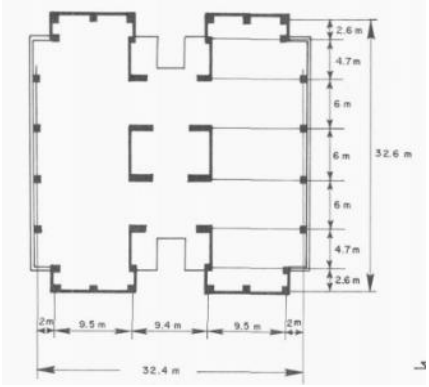

Figure 2.92: Miyagi 1978: 18-story Sumitomo Insurance Building v

2.5.2.20 San Fernando, CA, USA (1971)

The 6.5 (moment magnitude scale) San Fernando Valley, CA, USA earthquake on March 9, 1971 had an epicenter north of the Los Angeles metropolis area. While not a strong earthquake in terms of

ground motion, the location made it a significant earthquake as a test of engineered structures. The performance of modern reinforced concrete structures ranged from little to severe damage in areas of strong ground motion. Buildings with shear walls tended to have damage limited to diagonal cracking/spalling and working at construction joints; there were instances of more considerable damage including bar buckling, fracture, and base crushing in planar walls [103].

The Holy Cross Hospital includes a main building that is seven stories tall and was completed in the early 1960s (Fig. 2.93(a)). The most significant observed damage was to the non-planar wall surrounding the west stairway, this included cracking/spalling along the horizontal construction joint, as well as diagonal cracking and spalling that exposed reinforcement at the wall corner (Fig. 2.93(b)) [165]. Additionally, all the walls from floors 2-4 exhibited diagonal cracking and at some locations spalling that exposed reinforcement; there was decreasing levels of cracking at the higher stories [103]. Excessive deformation in the shear walls put lateral demands on the gravity column system, and many of the exterior column members crushed in flexural compression [165].

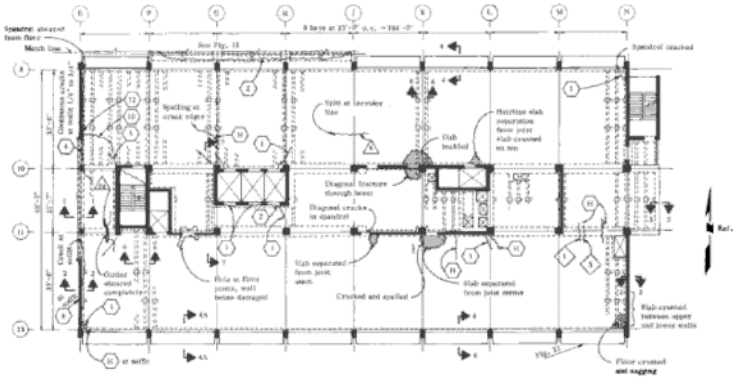

(a) Typical Shear Wall Configuration [165]

(b) Structural Damage [131]

Figure 2.93: San Fernando 1971: 7-story Holy Cross Hospital Building

The main unit at the Olive View Hospital is a five-story structure with a moment-frame lateral system for the bottom two floors and shear wall for higher floors; as such, a majority of the walls were discontinuous (Fig. 2.94(a)). Most walls in the building had some non-planar configuration (as is believed of the wall shown in Fig. 2.94(b)). This structure was heavily stressed in shear and there was significant crushing/spalling and buckling in columns, shear walls also experienced moderate to severe diagonal cracking and spalling that exposed reinforcement [165].

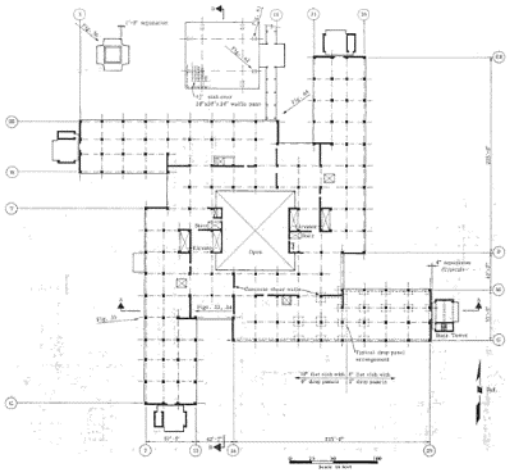

(a) Typical Shear Wall Configuration

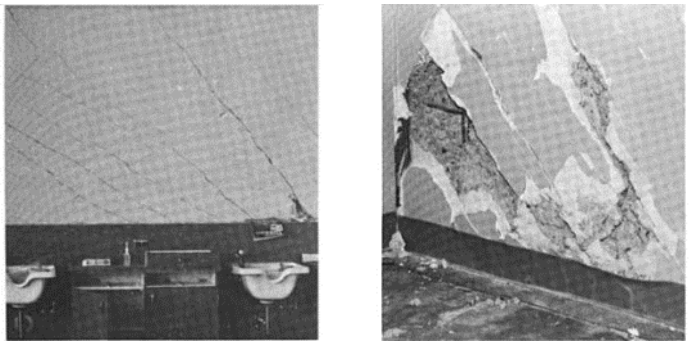

(b) Structural Damage

Figure 2.94: San Fernando 1971: 5-story Olive View Hospital Building [165]

The Museum for Antique Cars was a five-story building under construction at the time of the earthquake; however, all the concrete lateral system elements were complete to that level. Exterior walls were cast integrally with columns and core walls were positioned around stairway/elevator shafts (Fig. 2.95(a)). On exterior walls of three sides of the building, there was a shear failure/slip along the horizontal construction joint above the first floor; this was accompanied by spalling and

fracture of smaller diameter flexural reinforcement (Fig. 2.95(b)). The lateral motion at this location resulted in residual displacement of the upper portion of the building. Exterior walls had diagonal cracking up to 0.75 in width, and interior core walls also exhibited cracking between floors 1-3 [165].

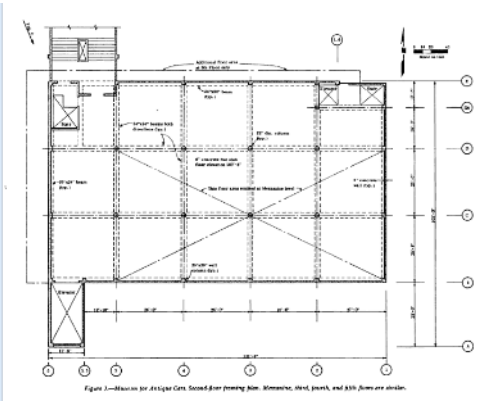

(a) Floorplan

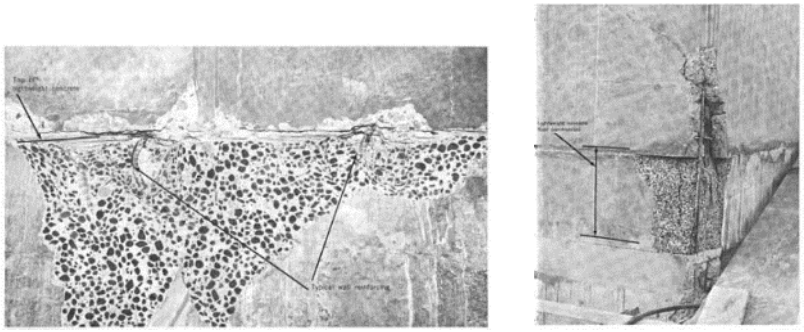

(b) Structural Damage

Figure 2.95: San Fernando 1971: 5-story Museum for Antique Cars Building [165]

2.5.2.21 Anchorage, AK, USA (1964)

The 9.2 (moment magnitude scale) Anchorage, AK, USA earthquake on March 28, 1964 had an epicenter 120 km (74.6 mi) away from this city. The earthquake had a relatively long duration of strong ground motion and while there were relatively few partial or complete collapses of engineered structures, there were many severely damaged buildings that were costly to repair. One concern highlighted by the Anchorage earthquake was the Four Seasons building (described below) that was compliant with the seismic code of the time and collapsed, while other non-compliant structures survived with little to no damage. The use of shear walls, both planar and core systems, seems to be used rather frequently in schools and mid-rise buildings. However, they seem to lack adequate confinement reinforcement and suffer from poor connections to the rest of the rest of the lateral system [137].

The Cordova building was a six-story building with steel moment-frame and reinforced concrete core wall system around the stairway/elevator shafts (Fig. 2.96(a)). The walls experienced a shear failure at the bottom of the first floor and loss of concrete core integrity (Fig. 2.96(b)). It does not appear that these walls have additional transverse reinforcement at the corner boundary elements that would have been able to confine the concrete [137].

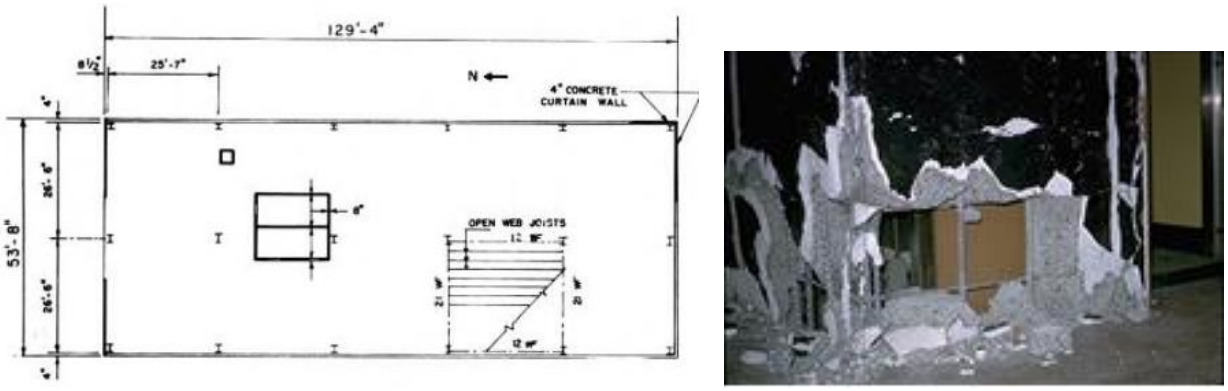

(a) Floorplan [137] (b) Structural Damage [131]

Figure 2.96: Anchorage 1964: 6-story Cordova Building

The Hill Building was an eight-story building with steel frame and two conjoined reinforced concrete core wall systems (Fig. 2.97(a)). The cores were intended to take the entire lateral load and this is where the most significant damage was seen in the building. The walls experienced an uneven vertical displacement at the base because of concrete crushing (noted as concrete disintegration due to poor material properties) (Fig. 2.97(b)); there was also cracking observed throughout the lower levels of the walls [137].

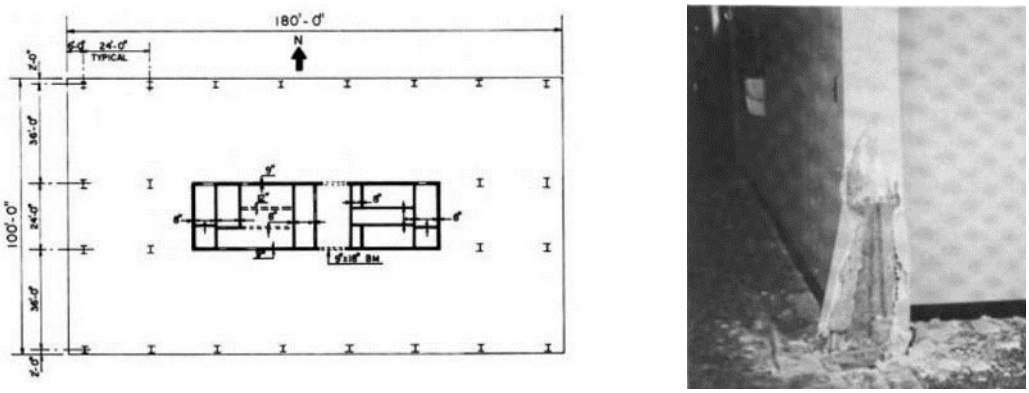

(a) Floorplan (b) Structural Damage

Figure 2.97: Anchorage 1964: 8-story Hill Building [137]

Other damage reported to non-planar walls in [137] included:

- Four Seasons Apartment (structural system constructed in 1963) contained two concrete core shafts; the collapse of this building was attributed to inadequate lap length of flexural reinforcement.
- Mt. McKinley & 1200 L Street Buildings (nearly identical buildings) contained core walls around stairway/elevator shafts; these experienced only hairline diagonal cracking and horizontal cracks at construction joints, which were most pronounced at floors 3-6. The 1200 L Street Building had less severe damage than the Mt. McKinley Building.

3 ASSESSMENT OF EXPERIMENTAL AND IN-FIELD WALL PERFORMANCE

Chapter 3 further examines the non-planar wall tests and in-field observations that were presented in the literature review in Chapter 2. The combination of laboratory results and records of earthquake response forms a more comprehensive dataset that can be evaluated to better understand structural wall behavior. On the one hand, physical testing of isolated, large-scale wall specimens may only be an approximation of actual seismic performance. Yet physical tests allow researchers to investigate a wide range of specific design parameters and assess how these parameters impact the onset of damage states, as well as strength, stiffness, and ductility of non-planar walls. On the other hand, reconnaissance efforts to gather wall damage data provides insights into the complexity of the real earthquake response of structural walls that is difficult to capture in the laboratory. However, in-field data is often insufficient to make a detailed assessment of specific wall parameters. For these reasons, Chapter 3 evaluates both types of data: Section 3.1 examines prior experimental tests, while Section 3.2 focuses on in-field response of non-planar walls. Finally, Section 3.3 summarizes the outcomes of both assessments and the implications of these findings on future non-planar wall research and design.

3.1 Examination of Experimental Response of Non-planar Walls

In an effort to examine previous laboratory tests on non-planar walls, a database of fifteen test programs consisting of a total of 36 slender wall specimens was compiled and analyzed from walls described in Chapter 2. Section 3.1.1 provides tabulated design parameters and experimental results for each of the test specimens in the database. Section 3.1.2 analyzes the experimental response of the wall dataset to examine the impact of various wall design parameters on non-planar wall performance; specifically, drift capacity and displacement ductility.

3.1.1 Summary of Design Parameters and Test Results for Experimental Wall Database

This section summarizes the design and response of each of the non-planar walls tests in the experimental database. Chapter 2 includes a detailed description for each of the non-planar walls and their respective test program. This includes: (i) the overall objective of the wall test series, (ii) details on the individual specimens including wall geometry and reinforcement, test set-up, and loading protocol, (iii) discussion of experimental results, and (iv) research conclusions for the test series.

3.1.1.1 Design Parameters for Experimental Wall Database

Table 3.1 describes the loading parameters for each test; Table 3.2, the geometric and material parameters; and Table 3.3, the reinforcement ratios in the boundary elements (BE) and web regions of the walls.

Additional notes on the tables:

- Table 3.1: A majority of the walls in the experimental database have a constant axial load throughout the loading protocol; however, there are some walls where the axial load varies: (i) to account for the effect of coupling in the weak-axis direction, (ii) based on the direction of lateral load, or (iii) linearly with respect to the magnitude of lateral load.
- Table 3.3: A few walls are not reported to have vertical boundary element or web reinforcement ($\rho_{BE,l}$ and $\rho_{web,l}$, respectively). The former is true when light reinforcement is distributed across the entire web or flange region and there is no concentrated steel in the wall end zones, and the latter is the case when the entire flange contains heavy reinforcement and is confined as a boundary element.

3.1.1.2 Test Results for Experimental Wall Database

Tables 3.4-3.6 provide experimental results related to strength and deformation capacity of all the walls in database, which include: normalized maximum peak shear stress ($V_u/A_{cv}\sqrt{f_c'}$), shear demand-to-capacity (V_u/V_n), drift capacity, displacement ductility (Δ_u/Δ_y). Additionally, the primary failure mechanism is classified as compression-buckling (CB), buckling-rupture (BR), and shear-compression (SC). The results are organized by wall shape where Table 3.4 includes C, U, and I-shaped walls; Table 3.5, T-shaped walls; and Table 3.6, L-shaped walls. The direction of loading associated with the strength/deformation results is shown above each column of data in the tables.

Section 3.1.1.2.1 provides a description of wall failure classifications (CB, BR, SC) used to determine the primary failure mechanism of laboratory tests in Chapter 2. Section 3.1.1.2.2 summarizes the approach used to determine the yield and ultimate drift from experimental load-deformation data in order to calculate the displacement ductility (Δ_u/Δ_y) of each wall specimen.

Note: To calculate shear capacity of a wall, V_n, the shear area is taken as the wall segment carrying in-plane lateral load (e.g. for a C-shaped wall with weak-axis loading the shear area is the area of the flanges). For walls loaded at an angle, shear area is determined with respect to loading (e.g. for a L-shaped wall with 45^0 loading the shear area is the gross wall area multiplied by $\sqrt{2}$).

Table 3.1: Loading Parameters for Experimental Wall Specimens

Researcher	Name	Shape	Loading					Shear Span	
			Direction		Axial Load Ratio			Strong	Weak
			Unidirectional[1]	Bidirectional[2]	Constant %	Min %	Max %	/l	/l
Sittipunt & Wood (1993)	CLS	C	WA		5.9				3.0
	CMS	C	WA		6.5				3.0
Lowes (2014)	CWall6	C	SA		5.0			2.84	
	CWall7	C		SA,WA	5.0			2.84	7.1
	CWall8	C		SA,WA	5.0	-6.4	16.0	2.84	varies
Ile & Reynouard (2005)	IleX	U	SA		10.3			2.60	
	IleY	U	WA		10.3				3.12
	IleXY	U		CL	11.7			2.60	3.12
Beyer et al (2008)	TUA	U		SA,WA, 45, CL	2.2			2.58	2.81
	TUB	U		SA,WA, 45, CL	4.4			2.58	2.81
Oesterle et al. (1976/1979)	F1	I	SA		0.0			2.40	
	F2	I	SA		7.3			2.40	
Shouzhong (2002)	SW3	I	SA		10.0			3.00	
Paulay & Goodsir (1985)	Wall 3	T	SA			2.0	12.0	1.85	
Thomsen & Wallace (1995)	TW1	T	SA		9.0			3.00	
	TW2	T	SA		7.5			3.00	
Choi (2004), Ha et al. (2002)	TC	T	SA		6.0			2.20	
	TC-aw	T	SA		6.0			2.20	
	TC-b1	T	SA		6.0			2.20	
	TC-b2	T	SA		6.0			2.20	
Brueggen (2009)	NTW1	T		SA,WA,360	2.8			3.47	4.33
	NTW2	T		SA,WA,360		3.0	3.3	3.47	4.33
Nakachi (1996)	No1	L	45			1.0	59.6	2.78	2.78
	No2	L	45			0.7	59.7	2.78	2.78
	No3	L	45			0.7	59.7	2.78	2.78
	No4	L	45			0.8	59.7	2.78	2.78
Hu (2004)	No1	L	PL		24.8			2.36	
	No2	L	PL		24.8			2.36	
Hosaka et al. (2008)	L-1	L	45			0.0	45.0	3.19	3.19
	L-2	L	45			0.0	45.0	3.19	3.19
	L-5	L	45			0.0	45.0	3.19	3.19
	L-6	L	45			0.0	40.0	3.19	3.19
Inada (2008)	L00A	L	PL		21.0	0.0	31.0	2.57	
	L45A	L	45		17.5	0.0	26.0	2.57	2.57
Kono (2011)	L45C	L	45			20.0	35.0	5.17	5.17
	L45D	L	45			20.0	50.0	5.17	5.17

[1] SA = strong axis loading, WA = weak axis loading, PL = loading parallel to leg

[2] 45 = loading 45° to leg, CL = cloverleaf or similar pattern, 360 = sweep of approx. circular displacement path

Table 3.2: Geometric and Material Parameters for Experimental Wall Specimens

Researcher	Name	Shape	$/t$	$/t$	$/l$	Scale /12 in	$'$ ksi	[1] ksi
Sittipunt & Wood (1993)	CLS	C	20.00	12.00	0.60	0.25	4.5	62
	CMS	C	20.00	12.00	0.60	0.25	4.1	62
Lowes (2014)	CWall6	C	20.00	8.00	0.40	0.50	4.9	64
	CWall7	C	20.00	8.00	0.40	0.50	5.3	64
	CWall8	C	20.00	8.00	0.40	0.50	5.1	64
Ile & Reynouard (2005)	IleX	U	6.00	5.00	0.83	0.82	3.4	75
	IleY	U	6.00	5.00	0.83	0.82	3.4	75
	IleXY	U	6.00	5.00	0.83	0.82	3.0	75
Beyer et al (2008)	TUA	U	8.67	7.00	0.81	0.49	11.3	71
	TUB	U	13.00	10.50	0.81	0.33	7.9	68
Oesterle et al. (1976/1979)	F1	I	18.75	9.00	0.48	0.33	5.6	65
	F2	I	18.75	9.00	0.48	0.33	6.6	62
Shouzhong (2002)	SW3	I	16.67	7.00	0.42	0.20	2.2	54
Paulay & Goodsir (1985)	Wall 3	T	13.00	7.00	0.54	0.33	4.9	58
Thomsen & Wallace (1995)	TW1	T	12.00	12.00	1.00	0.33	4.9	63
	TW2	T	12.00	12.00	1.00	0.33	6.0	63
Choi (2004), Ha et al. (2002)	TC	T	6.67	5.67	0.85	0.49	5.6	52
	TC-aw	T	6.67	5.67	0.85	0.49	5.6	52
	TC-b1	T	6.67	5.67	0.85	0.49	5.6	52
	TC-b2	T	6.67	5.67	0.85	0.49	5.6	52
Brueggen (2009)	NTW1	T	15.00	12.00	0.80	0.50	7.3	64
	NTW2	T	15.00	12.00	0.80	0.50	6.6	69
Nakachi (1996)	No1	L	10.00	10.00	1.00	0.30	7.6	52
	No2	L	10.00	10.00	1.00	0.30	10.4	52
	No3	L	10.00	10.00	1.00	0.30	10.3	52
	No4	L	10.00	10.00	1.00	0.30	9.6	52
Hu (2004)	No1	L	5.60	2.60	0.46	0.41	4.1	49
	No2	L	5.60	2.60	0.46	0.41	4.1	50
Hosaka et al. (2008)	L-1	L	5.00	5.00	1.00	0.44	8.5	63
	L-2	L	5.00	5.00	1.00	0.44	9.7	59
	L-5	L	5.00	5.00	1.00	0.44	13.0	73
	L-6	L	5.00	5.00	1.00	0.44	9.5	73
Inada (2008)	L00A	L	6.00	6.00	1.00	0.66	12.9	64
	L45A	L	6.00	6.00	1.00	0.66	11.1	64
Kono (2011)	L45C	L	6.00	6.00	1.00	0.39	11.1	107
	L45D	L	6.00	6.00	1.00	0.39	11.1	107

[1] Strength given is for primary vertical steel reinforcement located in the wall boundary element

Table 3.3: Reinforcement Ratios for Experimental Wall Specimens

Researcher	Name	Shape	Web				Flange				Web Free-End	
			BE[1]		Web		BE[2]		Web		BE[3]	
			$\rho_{BE,l}$	$_{E,}$	$\rho_{web,l}$	$\rho_{web,h}$	$\rho_{BE,l}$	$_{E,c}$	$\rho_{web,l}$	$_{eb,h}$	$_{E,}$	$_{E,c}$
Sittipunt & Wood (1993)	CLS	C	4.89	0.87	0.27	0.27	4.00	0.80	0.30	0.27		
	CMS	C	4.89	0.87	0.51	0.54	4.00	0.80	0.59	0.54		
Lowes (2014)	CWall6	C	3.81	1.45	0.28	0.73	3.33	1.02	0.23	0.73		
	CWall7	C	3.81	1.45	0.28	0.73	3.33	1.20	0.23	0.73		
	CWall8	C	3.81	1.45	0.28	0.73	3.33	1.20	0.23	0.73		
Ile & Reynouard (2005)	IleX	U	0.81	0.89	0.17	0.54	1.20	0.71	0.13	0.32		
	IleY	U	0.81	0.89	0.17	0.54	1.20	0.71	0.13	0.32		
	IleXY	U	0.81	0.89	0.17	0.54	1.20	0.71	0.13	0.32		
Beyer et al (2008)	TUA	U	0.84	1.33	0.22	0.30	2.11	1.58	0.23	0.30		
	TUB	U	1.88	1.85	0.41	0.45	2.45	1.96	0.31	0.45		
Oesterle et al. (1976/1979)	F1	I	3.89	0.69	0.30	0.71	3.89	0.69				
	F2	I	4.35	2.65	0.30	0.63			0.67	0.63		
Shouzhong (2002)	SW3	I	9.43	1.89	0.39	0.43			0.71	0.43		
Paulay & Goodsir (1985)	Wall 3	T			0.33	0.57	3.37	1.11	0.54	0.34	3.15	2.12
Thomsen & Wallace (1995)	TW1	T	2.93	0.81	0.30	0.33	2.93	0.81	0.35	0.33	2.93	0.81
	TW2	T	2.93	0.46	0.44	0.46	2.93	0.46	0.35	0.33	1.40	1.68
Choi (2004), Ha et al. (2002)	TC	T	2.36	5.72	1.30	1.27	2.36	5.72	1.77	1.27	2.09	5.40
	TC-aw	T	2.36	5.72	1.30	1.27	2.36	5.72	1.77	1.27	2.95	6.40
	TC-b1	T	2.36	5.72	1.30	1.27	2.36	5.72	1.77	1.27	2.09	5.40
	TC-b2	T	2.36	5.72	1.30	1.27	2.36	5.72	1.77	1.27	2.09	2.52
Brueggen (2009)	NTW1	T			0.30	0.61	4.09	1.82	0.22	0.26	3.64	1.82
	NTW2	T			0.25	0.61	2.37	1.85	1.89	0.41	3.29	1.92
Nakachi (1996)	No1	L			2.92	1.29			2.92	1.29		
	No2	L	3.51	1.44	2.85	1.29	3.51	1.44	2.85	1.29		
	No3	L	3.00	0.74	2.76	1.29	3.37	1.16	2.76	1.29		
	No4	L	3.00	1.26	2.76	1.29	3.37	1.40	2.76	1.29		
Hu (2004)	No1	L	4.54	1.46	1.46	1.26	4.28	1.11				
	No2	L	5.72	1.46	1.47	1.80	5.38	1.11				
Hosaka et al. (2008)	L-1	L	3.43	1.38	0.71	1.19	3.36	1.53	0.71	1.19		
	L-2	L	3.43	1.84	0.71	1.19	3.36	1.53	0.71	1.19		
	L-5	L	5.29	1.11	0.71	0.96	6.63	1.40	0.71	0.96		
	L-6	L	5.29	1.11	0.71	0.96	6.63	1.40	0.71	0.96		
Inada (2008)	L00A	L	5.08	1.65	3.10	0.89	5.08	1.65	3.10	0.89		
	L45A	L	5.08	1.65	3.10	0.89	5.08	1.65	3.10	0.89		
Kono (2011)	L45C	L	2.87	1.11	1.92	0.89	3.10	1.21	1.92	0.89		
	L45D	L	2.87	1.11	1.92	0.89	3.10	1.21	1.92	0.89		

[1]Refers to boundary element at web-flange intersection

[2]Refers to boundary element at free-end of flange

[3]Refers to boundary element at free-end of web (only applies for T-shaped walls where free-end flange/web boundary elements vary)

Table 3.4: Strength and Deformation Response of C, U, and I-Shaped Walls from Experimental Database

Researcher	Name	Shape	Strength							
			$/A\sqrt{'}$				$/V$			
			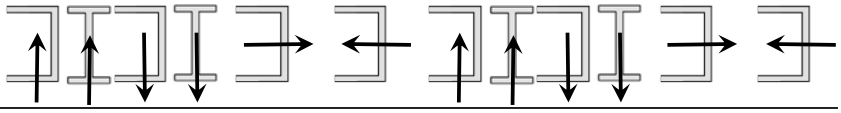							
Sittipunt & Wood (1993)	CLS	C			3.16	3.71			0.75	0.88
	CMS	C			3.49	4.50			0.52	0.67
Lowes (2014)	CWall6	C	4.26	4.15			0.43	0.42		
	CWall7	C	3.98	3.97	1.31	2.18	0.41	0.41	0.14	0.22
	CWall8	C	4.01	3.94	4.07	2.76	0.41	0.40	0.41	0.28
Ile & Reynouard (2005)	IleX	U	6.01	5.96			0.64	0.63		
	IleY	U			2.75	2.97			0.43	0.46
	IleXY	U	5.53	6.05	2.81	2.37	0.56	0.61	0.42	0.35
Beyer et al (2008)	TUA	U	3.19	3.23	1.70	1.91	0.77	0.78	0.41	0.46
	TUB	U	5.65	5.76	2.80	3.35	0.97	0.99	0.48	0.58
Oesterle et al. (1976/1979)	F1	I	8.56	8.16			0.92	0.88		
	F2	I	8.43	8.31			1.18	1.16		
Shouzhong (2002)	SW3	I	6.99	6.84			0.88	0.86		

Researcher	Name	Deformation								Failure Mode
		Drift Capacity, %				Displacement Ductility, $/\Delta$				
		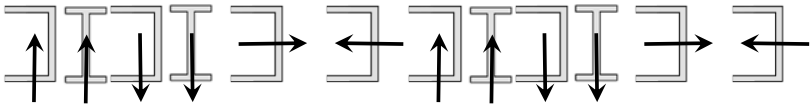								
Sittipunt & Wood (1993)	CLS			1.72	2.71			2.39	8.12	CB
	CMS			1.95	2.15			3.50	4.24	CB
Lowes (2014)	CWall6	2.26	1.86			5.86	5.00			BR
	CWall7	1.48	1.33	2.23	1.48	3.83	3.24	2.87	2.02	BR
	CWall8	1.76	1.79	2.00	2.10	4.79	4.97	4.92	3.87	BR
Ile & Reynouard (2005)	IleX	3.07	3.08			7.45	8.71			BR
	IleY			3.08	3.11			6.90	8.85	BR
	IleXY	2.07	2.05	2.07	2.07	4.24	4.00	4.64	2.87	BR
Beyer et al (2008)	TUA	2.52	2.49	3.52	2.68	9.40	10.88	7.41	9.66	BR
	TUB	2.49	2.48	3.07	2.59	7.04	6.74	6.50	8.12	SC
Oesterle et al. (1976/197	F1	2.26	1.89			3.32	2.97			SC
	F2	2.77	2.70			5.17	4.54			SC
Shouzhong (2002)	SW3	1.52	1.54			1.87	1.90			CB

Table 3.5: Strength and Deformation Response of T-Shaped Walls from Experimental Database

Researcher	Name	Shape	Strength							
			$/A\sqrt{f'}$				$/V$			
			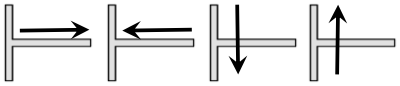							
Paulay & Goodsir (1985)	Wall 3	T	8.07	5.88			1.19	0.87		
Thomsen & Wallace (1995)	TW1	T	4.77	3.22			0.94	0.63		
	TW2	T	5.48	2.82			0.94	0.49		
Choi (2004), Ha et al. (2002)	TC	T	9.79	6.55			0.91	0.61		
	TC-aw	T	9.49	5.83			0.88	0.54		
	TC-b1	T	7.68	6.44			0.71	0.60		
	TC-b2	T	6.83	5.96			0.63	0.55		
Brueggen (2009)	NTW1	T	4.98	2.55	2.69	2.69	0.69	0.35	0.63	0.63
	NTW2	T	5.63	3.05	2.51	2.38	0.75	0.41	0.44	0.42

Researcher	Name	Deformation								Failure Mode
		Drift Capacity, %				Displacement Ductility, $/\Delta$				
		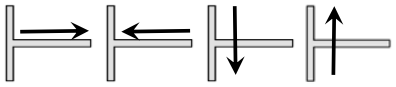								
Paulay & Goodsir (1985)	Wall 3	4.33	3.02			4.28	1.60			SC
Thomsen & Wallace (1995)	TW1	1.30	1.79			1.42	2.62			CB
	TW2	2.24	2.59			2.16	4.42			CB
Choi (2004), Ha et al. (2002)	TC	3.07	3.31			2.67	3.59			SC
	TC-aw	2.90	3.18			2.35	4.19			SC
	TC-b1	3.04	3.15			2.46	2.56			SC
	TC-b2	2.38	3.10			2.04	3.82			SC
Brueggen (2009)	NTW1	2.21	2.00	4.22	3.39	2.24	3.00	2.11	1.77	CB
	NTW2	2.69	1.93	4.14	4.08	3.96	4.72	1.42	1.92	CB

Table 3.6: Strength and Deformation Response of L-Shaped Walls from Experimental Database

Researcher	Name	Shape	Strength							
			/A √′				/V			
			→	←	→	←	→	←	→	←
Nakachi (1996)	No1	L	6.99				0.69			
	No2	L	4.83				0.54			
	No3	L	6.42				0.71			
	No4	L	7.56				0.81			
Hu (2004)	No1	L			6.49	8.82			0.54	0.73
	No2	L			9.11	9.70			0.56	0.60
Hosaka et al. (2008)	L-1	L	5.67	3.17			0.57	0.32		
	L-2	L	5.38	2.81			0.51	0.27		
	L-5	L	4.46	3.31			0.60	0.45		
	L-6	L	5.47	4.01			0.66	0.48		
Inada (2008)	L00A	L			6.04	6.30			0.86	0.89
	L45A	L	3.74	2.46			0.50	0.33		
Kono (2011)	L45C	L	4.32	3.30			0.62	0.47		
	L45D	L	4.27	2.35			0.61	0.34		

Researcher	Name	Deformation								Failure Mode
		Drift Capacity, %				Displacement Ductility, /Δ				
		→	←	→	←	→	←	→	←	
Nakachi (1996)	No1	0.50				2.21				CB
	No2	0.34				1.37				CB
	No3	0.59				1.74				CB
	No4	0.99				2.26				CB
Hu (2004)	No1			2.14	1.77			2.86	2.43	CB
	No2			2.78	2.66			3.51	1.16	CB
Hosaka et al. (2008)	L-1	4.94	3.11			4.92	2.38			CB
	L-2	3.71	3.00			3.48	2.56			CB
	L-5	2.97	1.99			3.08	1.55			CB
	L-6	3.02	3.00			2.21	2.10			CB
Inada (2008)	L00A			1.50	1.48			2.38	2.40	CB
	L45A	2.53	2.48			2.55	6.48			SC
Kono (2011)	L45C	2.58	2.02			2.12	1.63			CB
	L45D	2.39	1.99			2.14	1.62			CB

3.1.1.2.1 Experimental Wall Failure Classifications

***Note: Portions of Section 3.1.1.2.1 were taken from a sponsor report written for the Charles Pankow Foundation, titled "Summary of Large-Scale Nonplanar Reinforced Concrete Wall Tests" (Behrouzi et al. 2015 [33]). I was a primary author of the content included in this report. ***

The primary damage mechanism classifications used to categorize the experiments in the non-planar wall database include: buckling-rupture (BR), buckling-crushing (BC), and shear-compression (SC) as defined in the following paragraphs.

3.1.1.2.1.1 Buckling-rupture (BR)

The buckling-rupture failure is characterized by fracture of previously-buckled flexural reinforcement in the boundary element. This failure mechanism begins with concrete cover loss and outward buckling of vertical reinforcing bars when subjected to compression, leading to strength degradation of the rebar. Upon load reversal, bars straighten and the significant tension strain demands lead to bar rupture. The BR failure can be accompanied by crushing of confined boundary element concrete. The detailing of boundary element stirrups and the buckling length of the vertical bars were observed to be important factors in the onset of this failure mechanism. This failure mechanism was observed primarily in C- and U-shaped wall configurations (Fig 3.1).

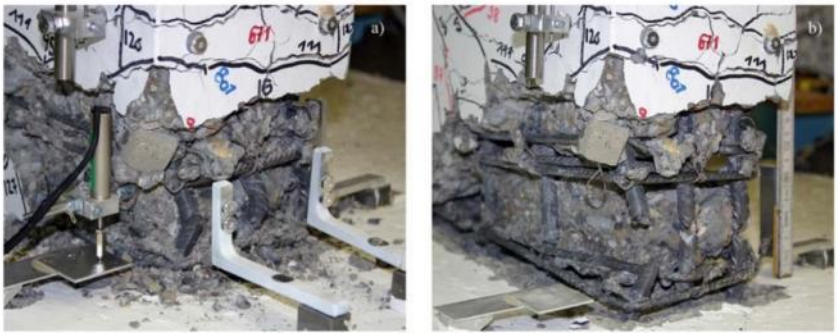

Figure 3.1: Example of buckling-rupture failures, Specimen TUA from *Beyer et al.* [34]

3.1.1.2.1.2 Crushing-buckling (CB)

The crushing-buckling failure is characterized by crushing of the concrete in the boundary element core as well as buckling of the flexural reinforcement in this region. Similar to buckling-rupture, this mechanism initiates with spalling of cover concrete. The spalling is often severe and extends a significant distance up the height of the wall and into the unconfined web of the wall, which is followed by a loss of confinement in the boundary element. After loss of core integrity, some wall

specimens with CB failures exhibited a sudden loss of strength due an instability failure of the compression zone, while other specimens progressively lost capacity as the core concrete crushed. This failure mechanism was observed primarily in L- and T- shaped wall types (Fig. 3.2).

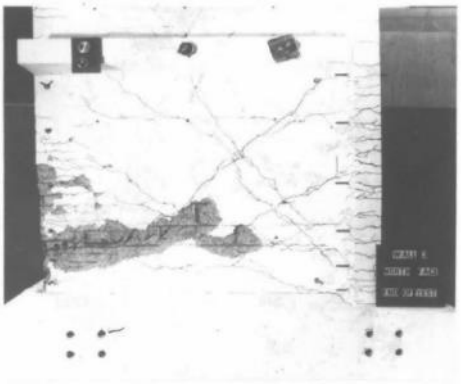

(a) Wall 3 from *Paulay & Goodsir* [143]

(b) Specimen NTW2 from *Brueggen* [40]

Figure 3.2: Examples of crushing-buckling failures

3.1.1.2.1.3 Shear-compression (SC)

The shear compression failure is characterized by crushing of the concrete between the boundary element zones of a wall (often considered web crushing). For walls with significant shear demand, this mechanism occurs when a diagonal compression strut crossing the web spalls and experiences significant crushing. This is a result of the lack of confining reinforcement and wide spacing of horizontal and vertical bars in the web. In addition, the cyclic loading of walls causes sliding along the diagonal cracks of the wall that further degrades the web's ability to transfer compression. This failure mechanism was observed primarily in I- and T-shaped wall configurations (Fig. 3.3).

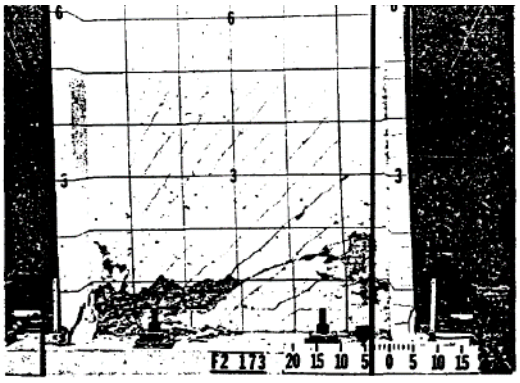

(a) Specimen F2 from *Oesterle et al.* [140]

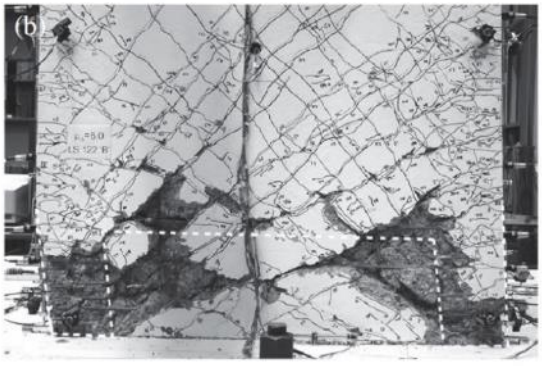

(b) Specimen TUB from *Beyer et al.* [34]

Figure 3.3: Examples of shear-compression failures

3.1.1.2.2 Determination of Ductility from Experimental Load-Deformation Response

*** Refer to note in Section 3.1.1.2.1. ***

Two methods for computing non-planar displacement ductility from experimental load-deformation data were considered. Both calculation approaches employed a bi-linear (elastic-perfectly plastic) model to represent the load-deformation envelope response as shown in Fig. 3.4.

Approach #1: 75% Method

- Initial Linear Elastic Stiffness: Defined as secant to the load-deformation response, starting at the point of zero load and terminating at the drift level corresponding to 75% of the maximum experimental load (marked as Pt. A on Fig. 3.4(a)).
- Horizontal/Perfectly Plastic Response: Defined as tangent to the load deformation response, starting at Pt. A and passing through the point of maximum load.

Approach #2: Energy Equivalence Method

- Initial Linear Elastic Stiffness: Defined as the line that results in zero energy error. Using Fig. 3.4(b) as a reference, zero energy error means the area in Region 1 and Region 2 are equal. Solving for the slope of this line requires an iterative solution.
- Horizontal/Perfectly Plastic Response: Similar to the 75% Method this is defined as tangent to the load-deformation response, starting at Pt. A on Fig. 3.4(b) and passing through the point of maximum load.

The two methods were found to provide similar results, and both methods were found to predict yield drifts that were in good agreement with the experimental yield drift (the measured drift at which the computed yield moment was reached). Due to its relative efficiency and accuracy, the 75% method was used to calculate yield drift, Δ_y (%). The drift capacity, Δ_u (%), of each specimen was calculated as the displacement at which there was a 20% loss in lateral load carrying capacity, or the maximum experimental drift, if the test was terminated prior to a 20% strength loss. Finally, the displacement ductility was calculated as the ratio of the drift capacity to yield drift, Δ_u,/ Δ_y.

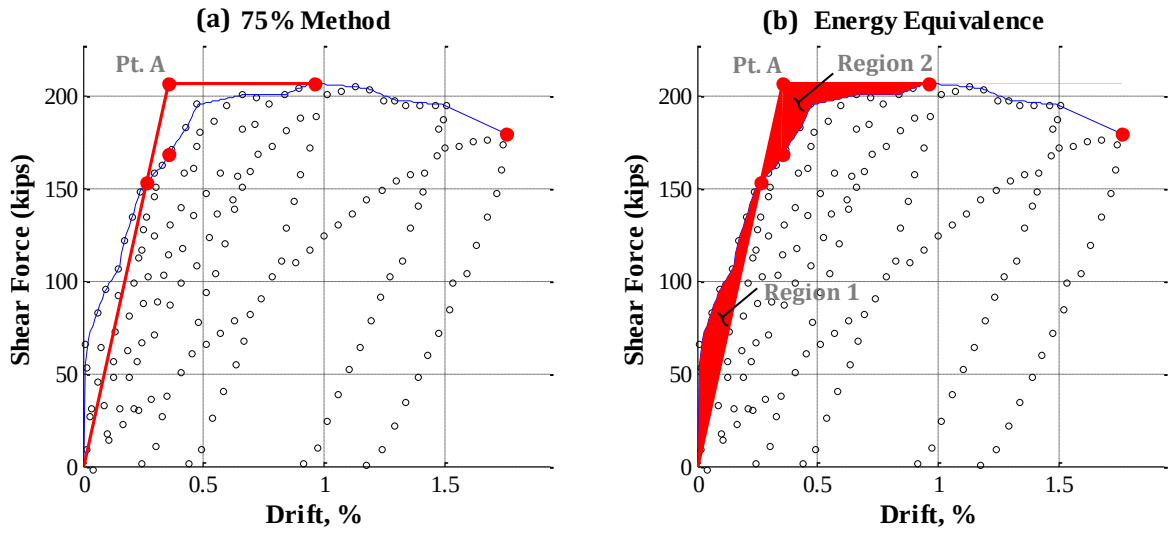

Figure 3.4: Approaches to Determine Yield and Ultimate Drift
(Red line: Calculated bi-linear response model, Blue line: experimental load-deformation envelope)

3.1.2 Examination of Design Parameters on Experimental Wall Response

This section investigates the influence that design parameters have on non-planar wall response, where wall response is captured using the metrics of drift capacity and displacement ductility (Δ_u/Δ_y). In Fig. 3.6-3.20, each of the design parameters is plotted against drift capacity and displacement ductility, where different markers indicate the failure mechanism classification (CB, BR, SC). Due to space considerations, only plots examining select design parameter effects on deformability (drift capacity and displacement ductility) are included in Section 3.1.2; additional plots can be found in Appendix A.

3.1.2.1 Summary of Relationship between Design Parameters and Response Metrics

The relationship between a design parameter and each of the deformation response metrics is assessed by calculating the coefficient of determination (R^2) and the sign of the correlation coefficient (R). The results shown in Tables 3.7-3.8 are determined from sub-sets of the experimental wall database based on: wall failure mode, wall shapes with loading in a symmetric versus asymmetric direction, and uni- versus bi-directional loading. Finally, the full wall database is examined as a whole.

The relationship between a design parameter and a response metric is deemed significant when the calculated coefficient of determination (R^2) is larger than 0.20. Significance is indicated in Tables 3.7-3.8 with a grey color. However, there are some instances where a data sub-set may meet the R^2 criteria, but has an extremely limited range of values to establish a valid correlation for a design

parameter (i.e. when parameters are clustered around ≤2 distinct design values). These cells are still marked in grey, but the numerical values are shown in red suggesting that the classification as "significant" is unsubstantiated. This issue results from the limited number of non-planar slender wall tests that have been conducted to date, such that there are only 10 C/U-shaped walls, 3 I-shaped walls, 9 T-shaped walls, and 14 L-shaped walls that met the criteria to be included in the experimental wall database.

Additional notes on the tables:

- Loading in a symmetric direction refers to strong axis loading for C, U, and I-shaped walls; and loading parallel to a T-shaped wall flange as shown in Fig. 3.5(a).
- Loading in an asymmetric direction corresponds to weak axis loading for C and U-shaped walls; loading parallel to a T-shaped wall web or leg of an L-shaped wall; or, loading at a 45° angle to a L-shaped wall as shown in Fig. 3.5(b).

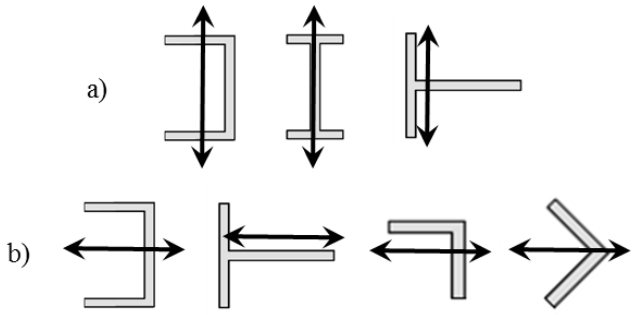

Figure 3.5: Definition of Loading in an Asymmetric vs. Symmetric Direction

In addition to Tables 3.7-3.8 indicating the correlation between design parameters and the response metrics of drift and displacement ductility, Table 3.9 provides the mean and standard deviation of the response parameters (drift, displacement ductility, maximum shear stress, and shear demand-to-capacity ratio) for each of the wall sub-sets.

Table 3.7: Correlation of design parameters and drift capacity

Parameter	Failure Mode						Symmetric Loading							Asymmetric Loading								Loading Direction				Full Dataset	
	BR		CB		SC		C/U		I		T		All	C/U		T		L -Parallel		L-45^0		All		Uni-direct		Bi-direct		
	R^2	+/–	R^2	+/–	R^2	+/–	R^2	+/–	R^2	+/–	R^2	+/–	R^2 +/–	R^2	+/–	R^2	+/–	R^2	+/–	R^2	+/–	R^2	+/–	R^2	+/–	R^2	+/–	R^2	+/–
f_c'	0.06	+	0.00	–	0.14	–	0.02	+	0.84	+	0.20	–	0.13 +	0.22	+	0.10	–	0.59	–	0.00	–	0.01	–	0.04	–	0.02	+	0.00	+
f_y[1]	0.40	+	0.03	+	0.22	–	0.49	+	0.49	+	0.20	+	0.12 +	0.26	+	0.34	–	0.55	–	0.02	+	0.00	+	0.00	–	0.01	+	0.00	+
$t_w/12$ in	0.14	+	0.16	+	0.00	+	0.09	+	0.67	+	0.00		0.04 +	0.03	+	0.01	+	0.59	–	0.28	+	0.03	+	0.11	+	0.01	+	0.03	+
l_w/t_w	0.45	–	0.01	–	0.09	–	0.53	–	0.67	+	0.00		0.09 –	0.33	–	0.18	–	0.59	–	0.75	–	0.08	–	0.12	–	0.04	–	0.06	–
l_f/t_f	0.28	–	0.01	–	0.14	–	0.08	–	0.67	+	0.00		0.31 +	0.06	–	0.52	–	0.59	–	0.75	–	0.16	–	0.11	–	0.00	–	0.03	–
l_f/l_w	0.48	+	0.00	+	0.00	+	0.58	+	0.67	+	0.00		0.44 +	0.40	+	0.36	–	0.59	–	0.35	+	0.00	–	0.01	+	0.04	+	0.02	+
$l_{w,BE-w}/l_w$	0.47	+	0.18	+	0.19	–	0.51	+	1.00	+	0.00		0.65 +	0.32	+	0.66	–	0.59	+	0.15	+	0.05	+	0.06	+	0.16	+	0.10	+
$l_{w,BE-w}/t_w$	0.02	+	0.01	–	0.01	–	0.01	+	0.34	+	0.00		0.66 +	0.18	+	0.66	–	0.59	+	0.07	–	0.04	–	0.01	–	0.02	–	0.02	–
$l_{w,BE-f}/l_f$	0.46	+	0.06	+	0.02	–	0.28	+	1.00	+	0.00		0.65 +	0.16	+	0.66	+	0.59	+	0.15	+	0.01	+	0.01	+	0.14	+	0.02	+
$l_{w,BE-f}/t_f$	0.02	+	0.00	+	0.45	–	0.01	+	0.06	+	0.00		0.65 +	0.18	+	0.00		0.59	+	0.07	–	0.02	–	0.01	–	0.02	–	0.01	–
$l_{f,BE}/l_f$	0.28	+	0.08	+	0.05	–	0.47	+	0.00		0.20	+	0.06 –	0.21	+	0.02	–	0.59	+	0.56	+	0.04	+	0.00	–	0.37	+	0.04	+
$l_{f,BE}/t_f$	0.15	–	0.18	+	0.32	–	0.02	+	0.00		0.20	+	0.00 +	0.04	+	0.29	–	0.59	+	0.14	+	0.00	–	0.06	–	0.14	+	0.00	+
$\rho_{BE,l}$	0.47	–	0.00	–	0.08	–	0.54	–	0.60	–	0.20	–	0.11 –	0.33	–	0.06	–	0.31	+	0.15	+	0.00	–	0.31	–	0.02	+	0.03	–
$\rho_{BE,conf}$	0.10	–	0.15	+	0.14	+	0.03	–	0.18	+	0.20	+	0.08 +	0.05	+	0.25	+	0.59	–	0.29	+	0.12	+	0.18	+	0.25	+	0.10	+
$\rho_{tot,l}$	0.42	–	0.00	–	0.00	–	0.38	–	0.00	–	0.20	–	0.08 +	0.18	–	0.10	+	0.81	+	0.00	+	0.01	–	0.04	–	0.00	+	0.00	–
$\rho_{tot,h}$	0.51	–	0.01	–	0.04	+	0.54	–	0.79	+	0.20	–	0.14 –	0.25	–	0.24	+	0.95	+	0.10	–	0.00	+	0.05	+	0.06	–	0.00	–
$\rho_{tot,l}/\rho_{tot,l}$	0.13	+	0.00	+	0.02	–	0.09	+	0.32	–	0.20	–	0.15 +	0.03	+	0.36	–	0.79	–	0.04	+	0.03	–	0.37	–	0.15	+	0.00	–
ALR	0.01	+	0.06	–	0.01	+	0.06	+	0.04	–	0.00		0.02 –	0.01	–	0.06	–	0.59	+	0.00		0.07	–	0.04	–	0.04	–	0.03	–
h_{eff}/l_w	0.46	–	0.03	+	0.44	–	0.57	–	0.67	–	0.00		0.25 +	0.44	–	0.55	–	0.59	–	0.01	+	0.02	–	0.49	–	0.02	+	0.00	–
h_{eff}/l_f	0.48	–	0.06	+	0.12	+	0.88	–	0.00		0.00		0.12 –	0.20	–	0.00		0.00	+	0.01	+	0.02	–	0.69	+	0.02	–	0.01	–
V_u/V_n	0.13	+	0.14	–	0.01	+	0.40	+	0.85	+	0.20	–	0.00 +	0.02	+	0.12	+	0.78	–	0.12	–	0.00	+	0.00	–	0.00	–	0.00	+
$V_u/A_{cv}\sqrt{f_c'}$	0.00	–	0.10	–	0.02	+	0.23	+	0.71	+	0.16	–	0.13 –	0.04	–	0.41	+	0.58	+	0.09	–	0.01	+	0.04	+	0.09	–	0.00	–

[1] Strength given is for primary vertical steel reinforcement located in the wall boundary element

Table 3.8: Correlation of design parameters and displacement ductility

Parameter	Failure Mode						Symmetric Loading							Asymmetric Loading								Loading Direction				Full Dataset	
	BR		CB		SC		C/U		I		T		All	C/U		T		L -Parallel		L-45^0		All		Uni-direct		Bi-direct		
	R^2	+/–	R^2	+/–	R^2	+/–	R^2	+/–	R^2	+/–	R^2	+/–	R^2 +/–	R^2	+/–	R^2	+/–	R^2	+/–	R^2	+/–	R^2	+/–	R^2	+/–	R^2	+/–	R^2	+/–
f_c'	0.32	+	0.05	–	0.28	+	0.44	+	0.84	+	0.29	+	0.21 +	0.26	+	0.06	+	0.00	–	0.01	–	0.01	–	0.05	–	0.01	+	0.00	–
f_y[1]	0.19	+	0.02	–	0.50	+	0.17	+	0.47	+	0.29	–	0.28 +	0.18	+	0.03	+	0.01	–	0.06	–	0.00	+	0.45	+	0.01	–	0.02	+
t_w/12 in	0.00	+	0.01	–	0.11	–	0.01	–	0.65	+	0.00		0.08 +	0.01	+	0.04	+	0.00	–	0.37	+	0.06	+	0.28	+	0.00	+	0.08	+
l_w/t_w	0.27	–	0.09	+	0.08	+	0.26	–	0.65	+	0.00		0.24 –	0.25	–	0.01	+	0.00	–	0.08	–	0.02	+	0.00	+	0.00	+	0.00	+
l_f/t_f	0.07	–	0.04	+	0.51	+	0.00	–	0.65	+	0.00		0.20 –	0.02	–	0.00	+	0.00	–	0.08	–	0.01	+	0.00	–	0.00	–	0.00	–
l_f/l_w	0.33	+	0.03	–	0.01	+	0.34	+	0.65	+	0.00		0.09 +	0.35	+	0.01	–	0.00	–	0.05	+	0.02	–	0.00	+	0.03	–	0.01	–
$l_{w,BE-w}/l_w$	0.31	+	0.05	–	0.06	+	0.29	+	0.98	+	0.00		0.31 –	0.23	+	0.03	–	0.00	+	0.00	–	0.03	–	0.00	+	0.07	–	0.02	–
$l_{w,BE-w}/t_w$	0.23	+	0.05	–	0.30	+	0.28	+	0.38	+	0.00		0.26 –	0.15	+	0.03	–	0.00	+	0.04	–	0.00	–	0.00	+	0.00	+	0.00	+
$l_{w,BE-f}/l_f$	0.29	+	0.01	–	0.02	+	0.16	+	0.98	+	0.00		0.31 –	0.10	+	0.03	+	0.00	+	0.00	–	0.02	–	0.01	–	0.05	–	0.01	–
$l_{w,BE-f}/t_f$	0.23	+	0.03	–	0.00	–	0.28	+	0.05	+	0.00		0.29 –	0.15	+	0.00		0.00	+	0.04	–	0.00	–	0.00	–	0.00	+	0.00	–
$l_{f,BE}/l_f$	0.07	+	0.00	–	0.62	+	0.07	+	0.00		0.29	–	0.11 –	0.14	+	0.08	+	0.00	+	0.06	+	0.00	–	0.00	–	0.01	+	0.00	–
$l_{f,BE}/t_f$	0.00	–	0.02	+	0.01	+	0.02	+	0.00		0.29	–	0.14 –	0.06	+	0.04	+	0.00	+	0.01	+	0.06	+	0.00	–	0.01	+	0.00	+
$\rho_{BE,l}$	0.30	–	0.01	–	0.01	–	0.30	–	0.58	–	0.29	+	0.34 –	0.25	–	0.03	–	0.03	–	0.04	+	0.13	–	0.20	–	0.20	–	0.19	–
$\rho_{BE,conf}$	0.00	+	0.02	–	0.17	–	0.02	+	0.21	+	0.29	–	0.04 –	0.06	+	0.00	+	0.00	–	0.14	+	0.01	–	0.07	–	0.04	+	0.01	–
$\rho_{tot,l}$	0.23	–	0.08	–	0.04	–	0.16	–	0.00	+	0.29	+	0.48 –	0.14	–	0.02	+	0.02	–	0.13	+	0.22	–	0.25	–	0.28	–	0.26	–
$\rho_{tot,h}$	0.47	–	0.04	–	0.33	–	0.50	–	0.78	+	0.29	+	0.09 –	0.30	–	0.00	–	0.00	–	0.01	–	0.21	–	0.13	–	0.30	–	0.20	–
$\rho_{tot,l}/\rho_{tot,h}$	0.42	+	0.02	–	0.09	+	0.45	+	0.30	–	0.29	+	0.24 –	0.08	+	0.00	+	0.00	–	0.10	+	0.03	–	0.17	–	0.05	–	0.09	–
ALR	0.05	–	0.03	–	0.00	+	0.10	–	0.03	–	0.00		0.00 –	0.04	–	0.01	–	0.00	+	0.00		0.08	–	0.04	–	0.06	–	0.07	–
h_{eff}/l_w	0.36	–	0.02	–	0.44	+	0.39	–	0.65	–	0.00		0.34 –	0.45	–	0.02	+	0.00	–	0.11	–	0.05	–	0.00	+	0.24	–	0.08	–
h_{eff}/l_f	0.42	–	0.06	–	0.49	+	0.38	–	0.00		0.00		0.08 –	0.28	–	0.00		0.00		0.11	–	0.06	–	0.42	+	0.14	–	0.14	–
V_u/V_n	0.51	+	0.00	+	0.00	–	0.39	+	0.87	+	0.23	+	0.03 +	0.11	+	0.13	–	0.03	–	0.04	–	0.03	–	0.07	–	0.07	+	0.00	+
$V_u/A_{cv}\sqrt{f_c'}$	0.00	+	0.01	–	0.30	–	0.01	–	0.67	+	0.07	+	0.00 –	0.00	+	0.05	–	0.05	–	0.01	–	0.14	–	0.16	–	0.02	–	0.05	–

[1] Strength given is for primary vertical steel reinforcement located in the wall boundary element

Table 3.9: Mean and standard deviation of response parameters for non-planar wall database

Response Parameter	Failure Mode						Symmetric Loading				Asymmetric Loading					Loading Direction		Full Dataset	
	BR		CB		SC		C/U	I	T	All	C/U	T	L -Parallel	L-45^0	All	Uni-direct	Bi-direct		
Drift, %	2.28	0.6	2.34	1.0	2.84	0.5	2.20	2.11	3.96	2.47	2.41	2.68	2.06	2.34	2.44	2.48	2.41	2.45	0.8
	0.6	0.5	0.62	0.2	0.77	0.3	0.60	0.98	0.53	0.68	0.47	0.71	0.70	0.53	0.58	0.73	0.52	0.61	0.2
Disp. Ductility Δ_y/Δ_u	5.74	2.5	2.65	1.3	4.15	1.9	6.15	3.29	1.81	4.71	5.43	3.00	2.46	2.58	3.48	3.77	3.90	3.84	2.2
	1.4	2.3	1.1	0.8	0.3	2.6	2.5	0.9	0.2	2.0	2.87	5.83	7.74	4.47	4.79	6.21	3.86	4.89	2.1
$V_u/A_{cv}\sqrt{f'_c}$	3.60	1.4	4.81	2.0	6.49	2.1	4.69	7.88	2.57	5.14	2.87	0.9	0.2	1.5	2.2	2.1	1.5	4.89	2.1
	0.46	0.2	0.62	0.2	0.77	0.3	0.60	0.98	0.53	0.68	0.47	0.2	0.70	0.53	0.58	0.73	0.52	0.61	0.2
V_u/V_n	2.28	0.6	2.34	1.0	2.84	0.5	2.20	2.11	3.96	2.47	2.41	0.6	2.06	2.34	2.44	2.48	2.41	2.45	0.8
	0.6	0.5	0.62	0.2	0.77	0.3	0.60	0.98	0.53	0.68	0.47	0.2	0.70	0.53	0.58	0.73	0.52	0.61	0.2
	5.74	2.5	2.65	1.3	4.15	1.9	6.15	3.29	1.81	4.71	5.43	2.5	2.46	2.58	3.48	3.77	3.90	3.84	2.2
	1.4	2.3	1.1	0.8	0.3	2.6	2.5	0.9	0.2	2.0	2.87	5.83	7.74	4.47	4.79	6.21	3.86	4.89	2.1
	3.60	1.4	4.81	2.0	6.49	2.1	4.69	7.88	2.57	5.14	2.87	0.9	0.2	1.5	2.2	2.1	1.5	4.89	2.1
	0.46	0.2	0.62	0.2	0.77	0.3	0.60	0.98	0.53	0.68	0.47	0.2	0.70	0.53	0.58	0.73	0.52	0.61	0.2

3.1.2.2 Discussion of Relationship between Design Parameters and Response Metrics

3.1.2.2.1 Material Properties

Table 3.10 presents the mean and standard deviation for the concrete strength and yield strength of primary vertical reinforcement in the non-planar wall database.

Table 3.10: Mean and standard deviation of material properties in non-planar wall database

Design Parameter	f_c'	$f_{y,BE}$
Mean,	6.83	65.19
St. Dev.,	2.89	12.15

Concrete strength: Only one experimental study explicitly examined the impact of compressive concrete strength on wall response, *Hosaka et al.* [92]. Two identically configured L-shaped wall specimens were tested; however, one wall had a slightly higher applied axial load range (0-0.45 $A_g f_c'$ versus 0-0.40 $A_g f_c'$). The drift capacity is slightly lower for the wall with the higher concrete compressive strength, yet these results are inconclusive with respect to concrete strength as this wall also had the higher axial demand.

The full experimental database consists of walls with concrete compressive strengths ranging from 2.2-13 ksi. Fig. 3.6 shows the drift capacity and displacement ductility as a function of concrete compressive strength. Table 3.8 indicates that with respect to displacement ductility: (i) walls with buckling-rupture and shear-compression failure modes, (ii) walls that are loaded in a symmetric direction (regardless of shape), (iii) and C-/U-shaped walls loaded in an asymmetric direction have greater displacement ductility with increased concrete compression strength. In terms of drift capacity, I-shaped walls loaded in a symmetric direction and C/U-shaped walls loaded in an asymmetric direction exhibit improved drift capacity with increased concrete compressive strength.

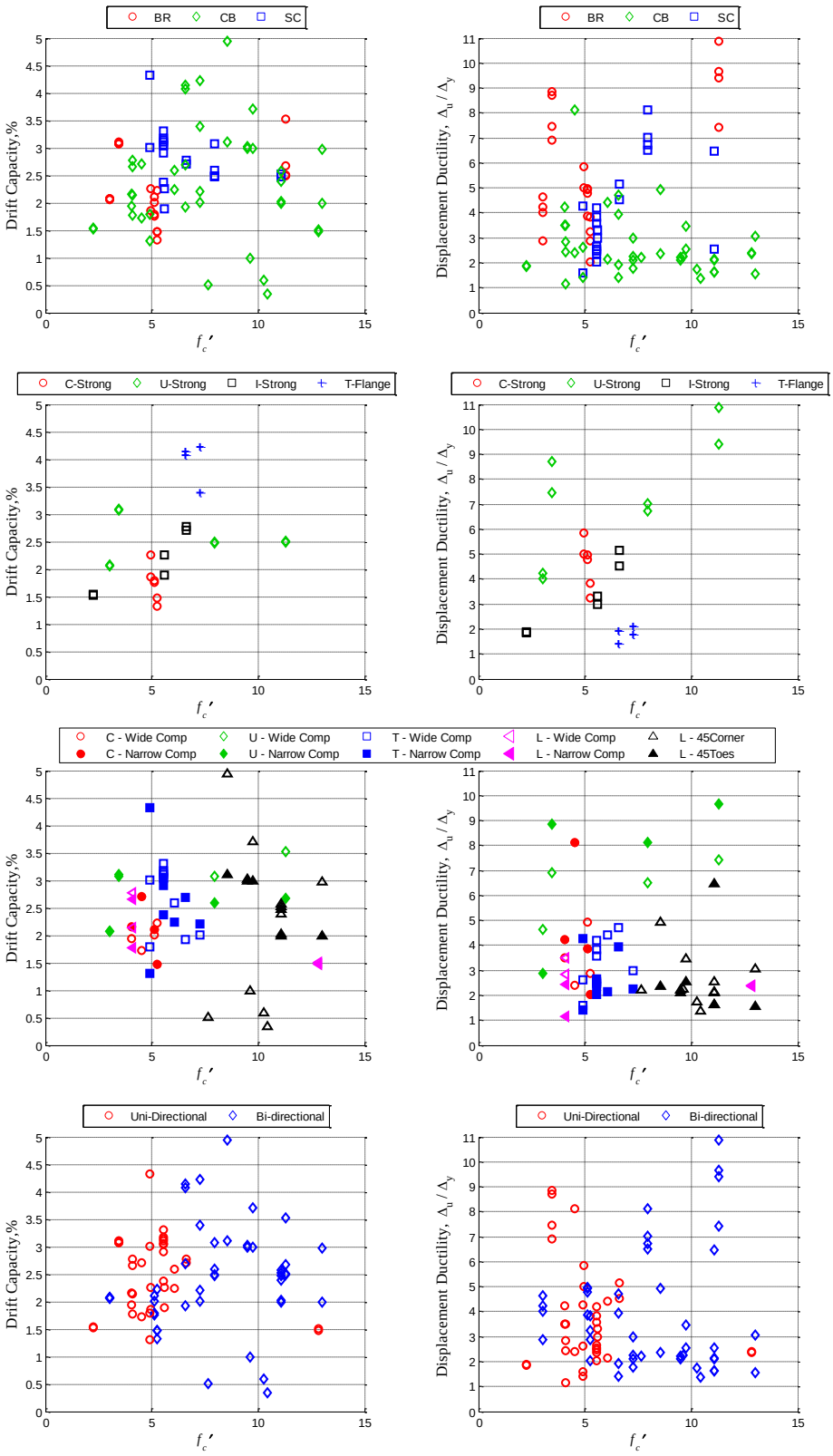

Figure 3.6: Relationship between Concrete Strength vs. Drift and Displacement Ductility
(Wall sub-sets examine failure mode, symmetric/asymmetric direction and uni-/bi-directional loading)

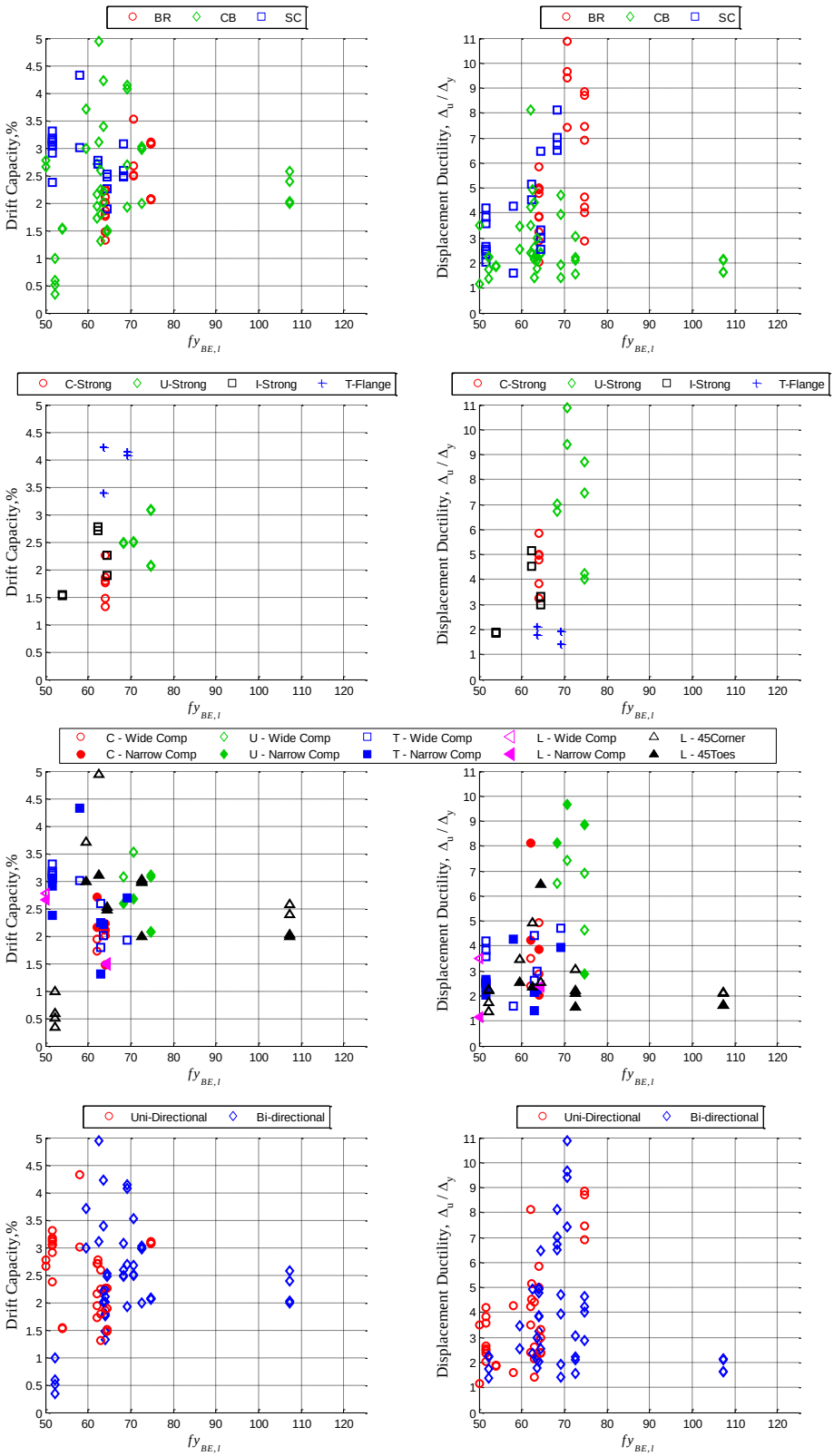

Figure 3.7: Relationship between Yield Strength of Primary Vertical Reinf. vs. Drift and Displacement Ductility (Wall sub-sets examine failure mode, symmetric/asymmetric direction and uni-/bi-directional loading)

Yield Strength of Primary Vertical Reinforcement: None of the experimental tests explicitly investigated the impact of steel strength (specifically, primary longitudinal reinforcement in the boundary element) on wall response. The full experimental database consists of walls with primary vertical reinforcement with yield strengths from 50-107 ksi. Fig. 3.7 shows the drift capacity and displacement ductility as a function of steel yield. Table 3.8 indicates that in terms of displacement ductility: (i) walls with buckling-rupture and shear-compression failure modes, (ii) walls that are loaded in a symmetric direction (regardless of shape), (iii) and uni-directionally loaded walls have greater displacement ductility with increased steel yield strength. For drift capacity, walls with shear-compression failures and symmetric loadings exhibit increased drift capacity with larger yield strengths.

3.1.2.2.2 Geometric Properties

Table 3.11 presents the mean and standard deviation of all geometric properties in the non-planar wall database.

Table 3.11: Mean and standard deviation of geometric properties in non-planar wall database

Design Parameter	Scale $t_w/12$ in	l_w/t_w	l_f/t_f
Mean,	0.46	11.23	7.68
St. Dev.,	0.15	5.63	2.80

None of the wall tests in the experimental database varied the length of the wall web, l_w, or wall flange, l_f. One study did investigate the impact of wall thickness, t_w, in U-shaped walls with bi-directional loading (*Beyer et al.* [34]). The thicker wall specimen was able to achieve a larger displacement ductility than the thinner wall. Moreover, the thicker wall exhibited a flexural-tension failure whereas the thinner wall experienced a web-crushing failure resulting from considerable spalling and loss of cross-section in the unconfined web region.

Figs. 3.8-3.10 show the drift capacity and displacement ductility as a function of a selection of overall geometric properties. Discussion of each of these properties is included in the subsequent paragraphs.

Scale: Researchers use different measures to calculate the scale of their test specimens. Therefore, comparison of researcher reported scale values are not meaningful, and it is necessary to set a baseline metric. This study adopts the approach from *Birely* [35] that assumes a full-scale wall has a

thickness of 12-in, such that scale is determined by dividing a wall specimen's thickness by 12-in. Tables 3.7 and 3.8 suggests that the increase in scale for L-shaped walls loaded at a 45-degree angle results in increased drift capacity and displacement ductility. Also, uni-directionally loaded walls show increased displacement ductility with increased scale.

Cross-sectional web aspect ratio: The cross-sectional web aspect ratio is calculated as the wall web length divided by wall thickness, l_w/t_w. While the experimental wall database represents a range of cross-sectional web aspect ratios; these values tend to be segregated by wall shape. L-shaped walls are primarily at the lower end of the spectrum with l_w/t_w values of 5-10, U- and T-shaped walls have values of 5-15, and C-shaped walls are concentrated at 20. The building inventory summarized in *Birely* [35] suggests that thin walls are common in modern mid-rise structures, and so there is a likely need to conduct wall tests of thin (l_w/t_w > 15) T and L-shaped walls. These wall shapes are particularly vulnerable to web instability, a failure mechanism in which the cross-sectional web aspect ratio plays a significant role.

The data in Table 3.7 indicates that increased cross-sectional web aspect ratio results in lower drift capacities for buckling-rupture failures, C and U-shaped walls (irrespective of loading type), and L-shaped walls loaded at a 45-degree angle. Similar relationships are observed in displacement ductility among the same wall sub-sets.

Cross-sectional flange aspect ratio: The cross-sectional flange aspect ratio is calculated as the wall flange length divided by flange thickness, l_f/t_f. Increased cross-sectional flange aspect ratio results in reduced drift capacity for walls with buckling-rupture failures and loading in an asymmetric direction. In the case of walls loaded in an asymmetric direction, thin flanges provide a very narrow compression region to balance large tensile forces in web reinforcement, which can lead to significant damage of the flange free-end boundary element (this applies to C- and U-shaped walls loaded in the weak-axis direction and L-shaped walls loaded parallel to one leg).

The relationship between cross-sectional flange aspect ratio and displacement ductility is not as clear. Table 3.8 indicates walls with shear-compression failures exhibit increased ductility with increasing l_f/t_f, whereas walls loaded in a symmetric direction see decreasing ductility with increased l_f/t_f. This suggests cross-sectional flange aspect ratio is a design parameter that merits further experimental investigation to understand how it drives the behavior of non-planar walls.

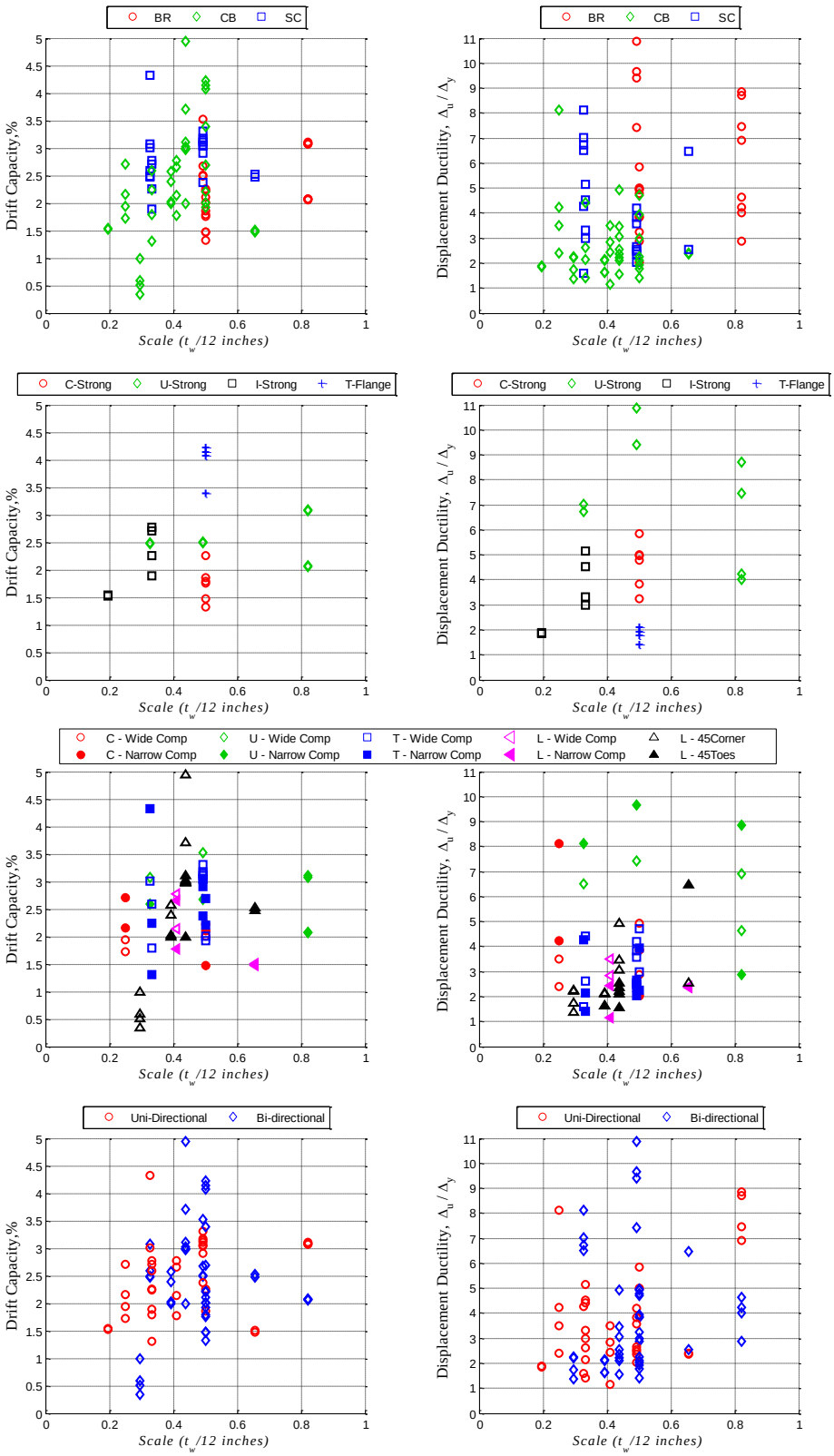

Figure 3.8: Relationship between Test Specimen Scale vs. Drift and Displacement Ductility
(Wall sub-sets examine failure mode, symmetric/asymmetric direction and uni-/bi-directional loading)

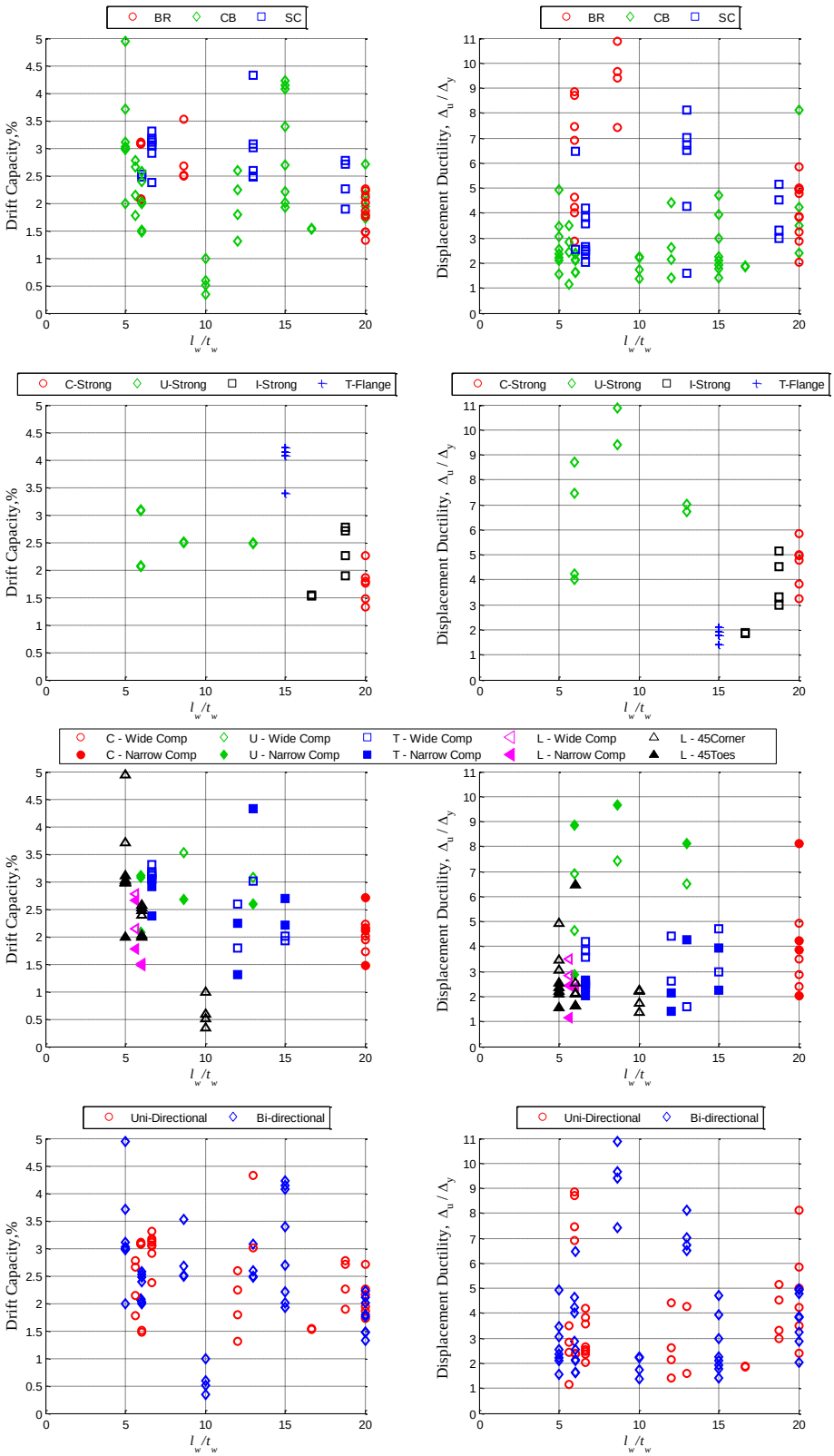

Figure 3.9: Relationship between Web Cross-sectional Aspect Ratio vs. Drift and Displacement Ductility (Wall sub-sets examine failure mode, symmetric/asymmetric direction and uni-/bi-directional loading)

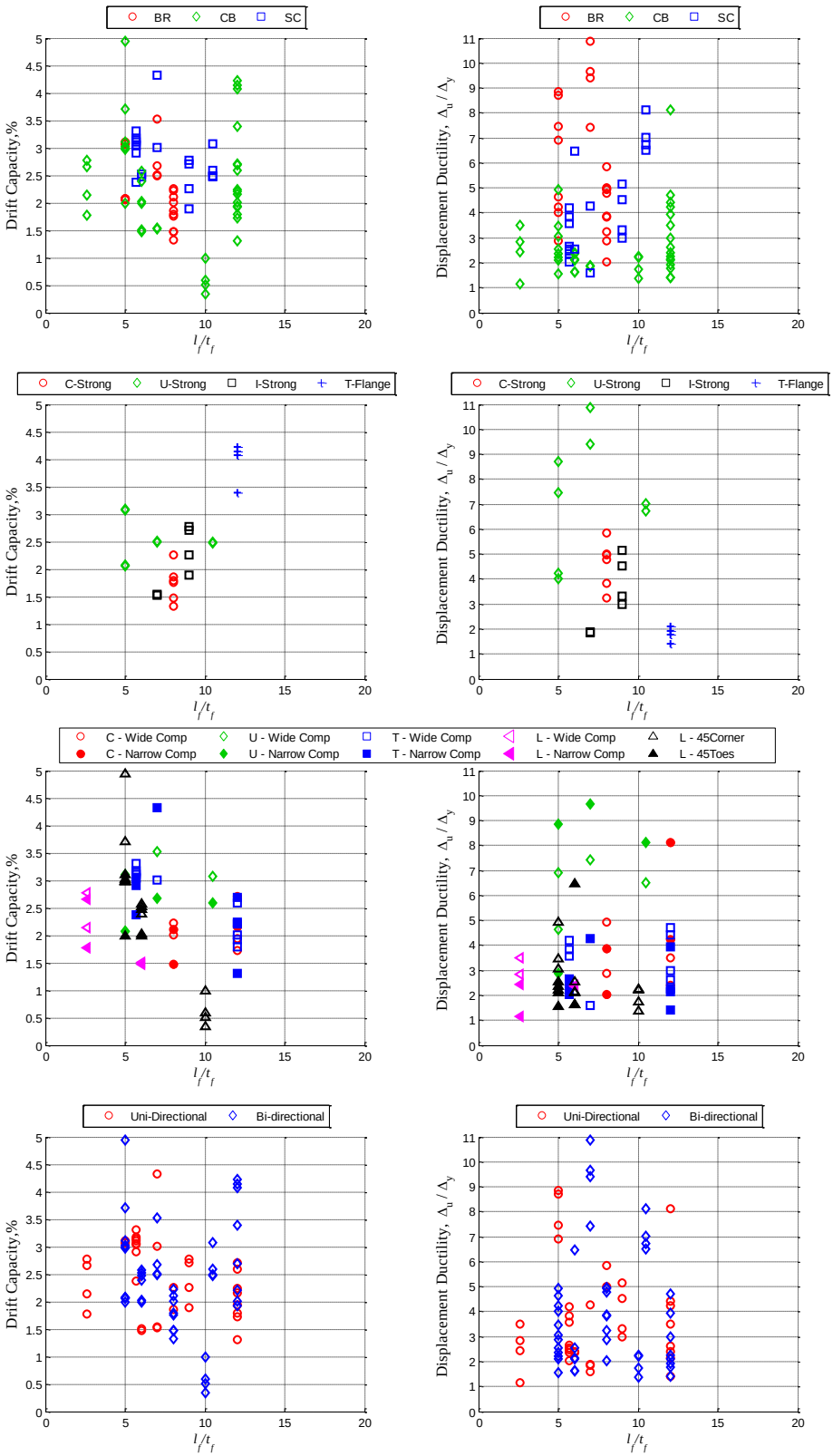

Figure 3.10: Relationship between Flange Cross-sectional Aspect Ratio vs. Drift and Displacement Ductility (Wall sub-sets examine failure mode, symmetric/asymmetric direction and uni-/bi-directional loading)

3.1.2.2.3 Boundary Element Geometry

Typically, non-planar walls have boundary elements located at the web-flange intersection, flange-free end, and web free-end (in the case of T-shaped walls); it is not uncommon for each of these boundary elements to have differing geometries. Table 3.12 presents the mean and standard deviation of all boundary element geometric properties in the non-planar wall database.

Table 3.12: Mean and standard deviation of boundary element geometry in non-planar wall database

Design Parameter	$l_{w,BE-w}/l_w$	$l_{w,BE-w}/t_w$	$l_{w,BE-f}/l_f$	$l_{w,BE-f}/t_f$	$l_{f,BE}/l_f$	$l_{f,BE}/t_f$
Mean,	0.20	1.67	0.28	1.87	0.25	1.95
St. Dev.,	0.11	0.62	0.20	1.40	0.12	1.35

Only one study has walls with different boundary element widths (*Beyer et al.* [34]); however, the lengths of the web-flange and flange free-end boundary elements also vary between the specimens. Therefore, the results are inconclusive as to the impact of boundary element width alone. There are also a number of studies that investigated boundary element length and its impact on wall ductility. These include T-shaped wall tests by *Brueggen, Choi et al.*, and *Thomsen & Wallace* [40, 47, 161]; and L-shaped wall tests by *Hosaka et al.* and *Nakachi et al.* [92, 128]. Many of these wall tests also concurrently examined the effect of changing vertical and/or transverse reinforcement ratios in the boundary element; these results are discussed in Section 3.1.2.2.4.

In the following discussion, the length of the boundary element at the web-flange intersection that extends into the web is designated by $l_{w,BE-w}$, while the portion that extends into the flange is $l_{w,BE-f}$; the length of the flange free-end boundary element is denoted by $l_{f,BE}$. Table 3.7 indicates that both the normalized lengths ($l_{w,BE-w}/l_w$, $l_{w,BE-f}/l_f$) and aspect ratios ($l_{w,BE-w}/t_w$, $l_{w,BE-f}/t_f$) for the boundary element at the web-flange intersection exhibit a positive correlation with drift capacity for walls loaded in a symmetric direction. As individual sub-sets, C/U-shaped and I-shaped walls loaded in a symmetric direction show positive correlation between the aforementioned boundary element parameters and displacement ductility. For the flange free-end boundary element, an increase in normalized length ($l_{f,BE}/l_f$) corresponds to increased drift capacity for (i) walls with buckling-rupture failures, (ii) C- and U-shaped walls (irrespective of loading), and (iii) L-shaped walls loaded at 45-degrees. An increase in aspect ratio ($l_{f,BE}/t_f$) seems to exhibit a negative correlation with drift capacity for walls with shear-compression failures and T-

shaped walls subject to loading in an asymmetric direction. These findings indicate that increasing boundary element length generally leads to improved drift capacity in walls loaded in a symmetric direction; however, results from walls loaded in an asymmetric direction suggests that length should be increased ***with*** consideration for the boundary element width since long, thin boundary elements do not seem as effective.

3.1.2.2.4 Reinforcement Ratios

Table 3.13 presents the mean and standard deviation of all reinforcement ratios in the non-planar wall database.

Table 3.13: Mean and standard deviation of reinforcement ratios in non-planar wall database

Design Parameter	$\rho_{BE,l}$	$\rho_{BE,conf}$	$\rho_{tot,l}$	$\rho_{tot,h}$	$\rho_{tot,l}/\rho_{tot,}$
Mean,	3.29	1.73	1.79	0.76	2.43
St. Dev.,	1.63	1.29	1.03	0.37	0.89

Fig. 3.11-3.15 show the relationship between wall reinforcement ratios and the response metrics of drift capacity and displacement ductility. The remainder of this section discusses the impact of boundary element vertical ($\rho_{BE,l}$) and confinement reinforcement ($\rho_{BE,conf}$) ratios, total vertical ($\rho_{tot,l}$) and horizontal ($\rho_{tot,h}$) reinforcement ratios.

Boundary Element Vertical Reinforcement Ratio: Boundary element vertical reinforcement ratio ($\rho_{BE,l}$) was a test variable for studies on I-shaped walls by *Oesterle et al.* [140, 141]; T-shaped walls by *Brueggen* and *Thomsen & Wallace* [40, 161]; as well as L-shaped walls by *Hosaka et al.* [92]. For *Oesterle et al.* [140, 141] and *Brueggen* [40] test specimens were designed to study the difference between heavy, concentrated reinforcement in the boundary element (fewer, large bars) versus lighter, more distributed reinforcement closer to size and spacing of reinforcement in the unconfined region of the wall. In the case of *Hosaka et al.* [92] and *Thomsen & Wallace* [40, 161], boundary element length and boundary element vertical reinforcement ratio were varied simultaneously. Some findings from these tests related to $\rho_{BE,l}$ are:

- *Brueggen* [40]: Concentrated boundary element reinforcement in T-shaped walls can lead to significant shear lag effects. At low displacement demands, the strain at concentrated

reinforcement is considerably higher than in other bars and the strain distribution only becomes more uniform at higher displacement demands.

- *Hosaka et al.* [92]: Use of high-strength, large bars placed in the center of corner and flange-end boundary elements in L-shaped walls loaded at a 45-degree angle increased wall strength when the flange-ends were under compression, but little effect the opposite loading direction. This response was in spite of the fact that the flange-end boundary element length, $l_{f,BE}$, for these walls was half the length of other wall specimens from the same test program with a lower $\rho_{BE,l}$.

Most of the walls in the experimental test database have boundary element vertical reinforcement ratios ranging from 1-6%. Based on the building inventory presented in *Birely* [35], modern wall construction generally consists of $\rho_{BE,l}$ between 0-4%. Walls in the experimental database presented with $\rho_{BE,l} \geq 5\%$ are primarily L-shaped, with one I-shaped wall; all other walls fall in the range consistent with modern design practice.

For nearly all walls, Tables 3.7 and 3.8 shows that $\rho_{BE,l}$ has a negative correlation with drift capacity and displacement ductility; the notable exception are L-shaped walls loaded at a 45-degree angle. Significant negative correlations with respect to drift capacity are observed in C/U-shaped walls (irrespective of loading) and uni-directionally loaded walls; with respect to displacement ductility, a significant negative correlation is also seen in bi-directionally loaded walls.

Boundary Element Confinement Reinforcement: The non-planar experimental database contains a number of test programs that explore boundary element confinement spacing/configuration including: I- shaped walls by *Oesterle et al.* [140, 141]; T-shaped walls by and *Choi et al.* and *Thomsen & Wallace* [47, 161]; as well as L-shaped walls by *Nakachi et al.* [128]. Conclusions from a selection of these studies, with respect to confinement reinforcement, are:

- *Oesterle et al.* [140, 141]: The first I-shaped wall specimen (F1) had flanges detailed as compression columns, while second wall (F2) had detailing consistent with special boundary elements (seismic ties and hoops) at the web-flange intersections. The confined boundary element was noted to delay flexural bar buckling and help maintain concrete; in addition to increasing the stiffness, shear resistance, and compressive stress capacity of the boundary element. The global wall performance of F2 was improved with significantly higher drift capacity and energy dissipation, as well as a modest increase in shear strength.

- *Thomsen & Wallace* [47, 161]: The first T-shaped wall specimen (TW1) had boundary element detailing based on a design approach where the web and flange were treated as two independent rectangular walls. The second specimen (TW2) was designed using a displacement-based design procedure that accounted for the non-planar wall shape, and resulted in boundary element at the web free-end that was longer and had more closely spaced seismic hoops. The global response of TW2 was characterized by significantly higher drift capacity and energy dissipation.
- *Nakachi et al.* [128]: Two L-shaped wall specimens in this test program had varying seismic tie spacing in the corner boundary element. The specimen with closer spacing had increased drift capacity and energy dissipation. Strain measurements indicate the specimen with tighter confinement spacing had greater confining force per unit area and the boundary element exhibited improved compressive ductility. However, the impact of confining reinforcement may not be conclusive, as the researchers believe that varying axial load (in the negative loading direction) may also have an impact on boundary element compressive ductility.

A majority of walls in the experimental test database have boundary element confinement reinforcement ratios ($\rho_{BE,conf}$) ranging from 0-2%, with a limited number of T-shaped walls having ratios $\rho_{BE,l} \geq 4\%$. Based on the building inventory presented in *Birely* [35], modern wall construction generally consists of $\rho_{BE,conf}$ between 0-2%; therefore, the walls in the experimental database are considered to be representative of modern design practice.

Assessment of the full experimental test database in Table 3.7 indicates that there is a positive correlation between boundary element confinement reinforcement ratio and drift capacity. The positive correlation holds for sub-sets of walls loaded in symmetric and asymmetric directions as well as uni- and bi-directionally loaded walls; although some correlations are weak ($R^2 < 20$).

Total Vertical and Horizontal Reinforcement: The total vertical reinforcement ratio ($\rho_{tot,l}$) is calculated as the area of vertical boundary element ***and*** web reinforcement divided by the total cross-sectional area of the wall. The total horizontal reinforcement ratio ($\rho_{tot,h}$) accounts for horizontal reinforcement in web and flanges of a wall. It is calculated using a weighted average of the horizontal reinforcement ratios in the web and flange/(s) region based on the cross-sectional area of the regions; for most walls $\rho_{tot,h}$ is equal to the web horizontal reinforcement ratio ($\rho_{web,h}$).

Sittipunt and Wood [158] was the only study that examined the impact of both vertical and horizontal reinforcement ratios, specifically in C-shaped walls loaded in the weak-axis direction. The first C-shaped wall specimen (CLS) had approximately half of the web vertical and horizontal reinforcement ratio as the second specimen (CMS). For both walls, the ratio of web vertical-to-horizontal reinforcement was approximately one. While there is a notable difference in displacement ductility for negative loading (when the flange-ends are in compression), researchers attributed this to a hoop fracture in the boundary element of CLS rather than a result of the varying web vertical or horizontal reinforcement ratios between the two walls. Therefore, this study is inconclusive with respect to web reinforcement ratios for non-planar walls.

The walls in the experimental test database have total vertical reinforcement ratios ($\rho_{tot,l}$) ranging from 0.5-4.5%. These values tend to be segregated by wall shape where C- and U- shaped walls have $\rho_{tot,l} \leq 1\%$, T-shaped walls have $1\% \leq \rho_{tot,l} \leq 2\%$, and L-shaped walls have $\rho_{tot,l} > 2\%$. The narrow band of vertical reinforcement ratios for a specific wall shape should be taken into account in the subsequent discussion on correlation. Examination of the experimental database in Table 3.8 indicates that there is a strong negative correlation between total vertical reinforcement ratio and displacement ductility for the full dataset. Additionally, a strong negative correlation is observed in sub-sets of walls with symmetric and asymmetric loading direction, as well as uni- and bi-directional loaded walls. A further observation is that buckling-rupture failures occur in walls with $\rho_{tot,l} \leq 1\%$ that are C/U-shaped, and shear-compression or crushing-buckling failures occur in walls with $\rho_{tot,l} > 1\%$ with other wall shapes.

The walls in the dataset have total horizontal reinforcement ratios ($\rho_{tot,h}$) ranging from 0.25-2%. Walls that exhibit both buckling-rupture failures and are C-/U-shaped (irrespective of loading direction) show a significant negative correlation between $\rho_{tot,h}$ and drift capacity/ductility. Additional negative correlations are observed for displacement ductility in with loading in an asymmetric direction, bi-directionally loaded walls, and the wall dataset as a whole. In contrast, there is a positive correlation between $\rho_{tot,h}$ and drift capacity for I-shaped walls and T- and L-shaped walls loaded in an asymmetric direction.

In some respects this negative correlation between increased reinforcement ratio ($\rho_{BE,l}, \rho_{tot,l}, \rho_{tot,h}$) and decreasing deformation capacity may be counter-intuitive; Section 3.1.2.2.8 provides some insight into the fact that increasing these reinforcement values leads to greater shear demands.

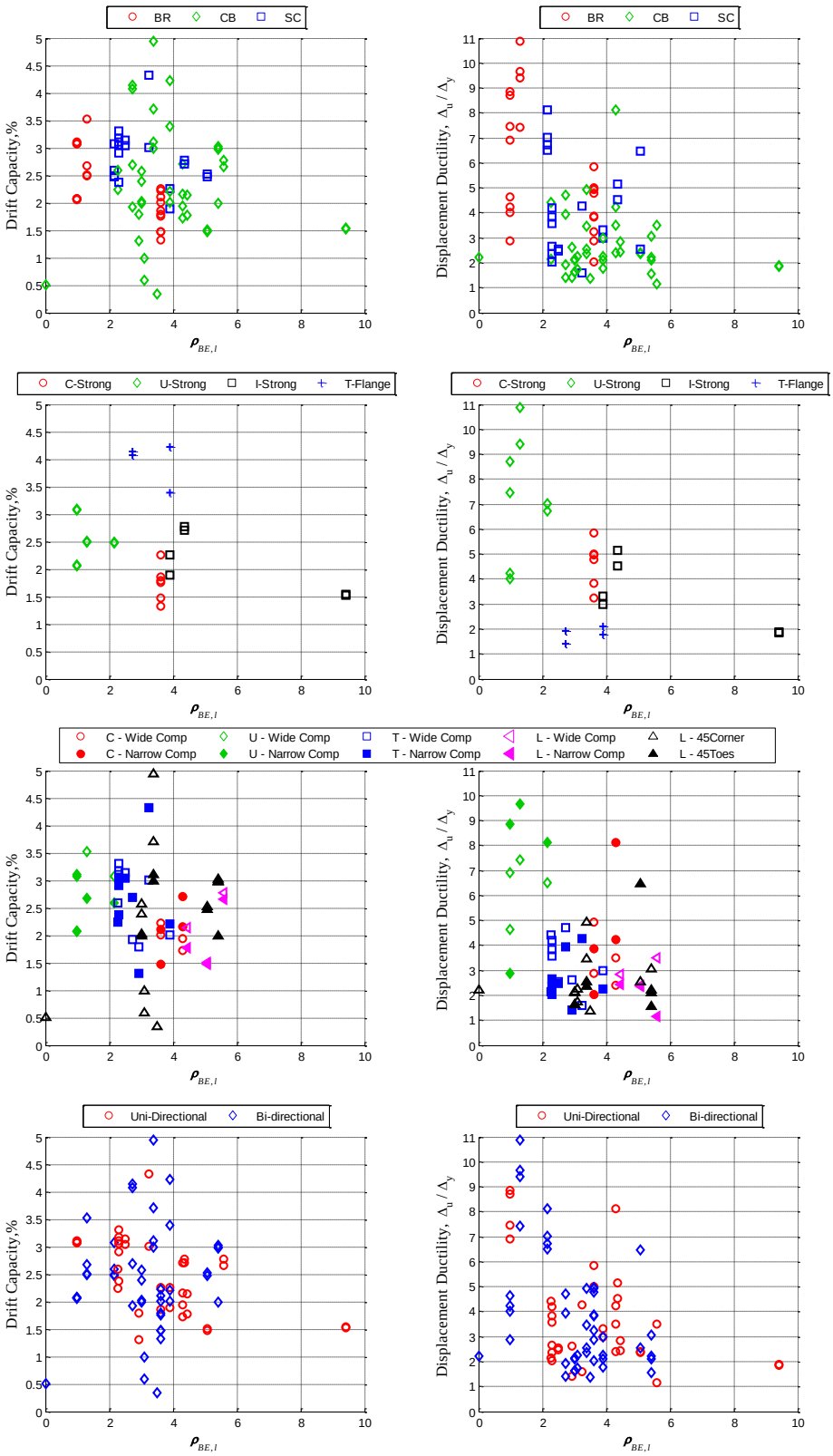

Figure 3.11: Relationship between BE Vertical Reinforcement Ratio vs. Drift and Displacement Ductility (Wall sub-sets examine failure mode, symmetric/asymmetric direction and uni-/bi-directional loading)

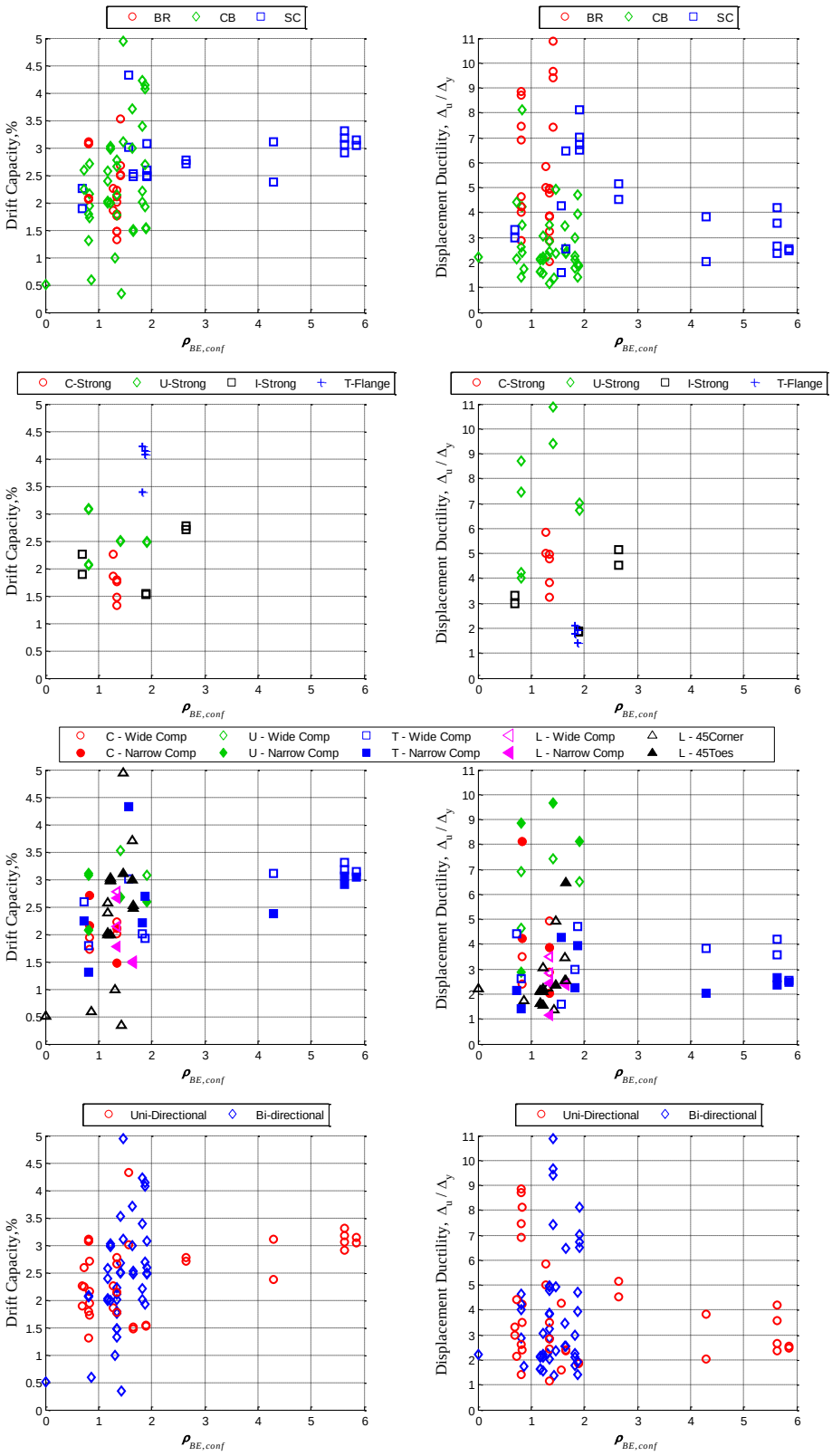

Figure 3.12: Relationship between BE Confining Reinforcement Ratio vs. Drift and Displacement Ductility (Wall sub-sets examine failure mode, symmetric/asymmetric direction and uni-/bi-directional loading)

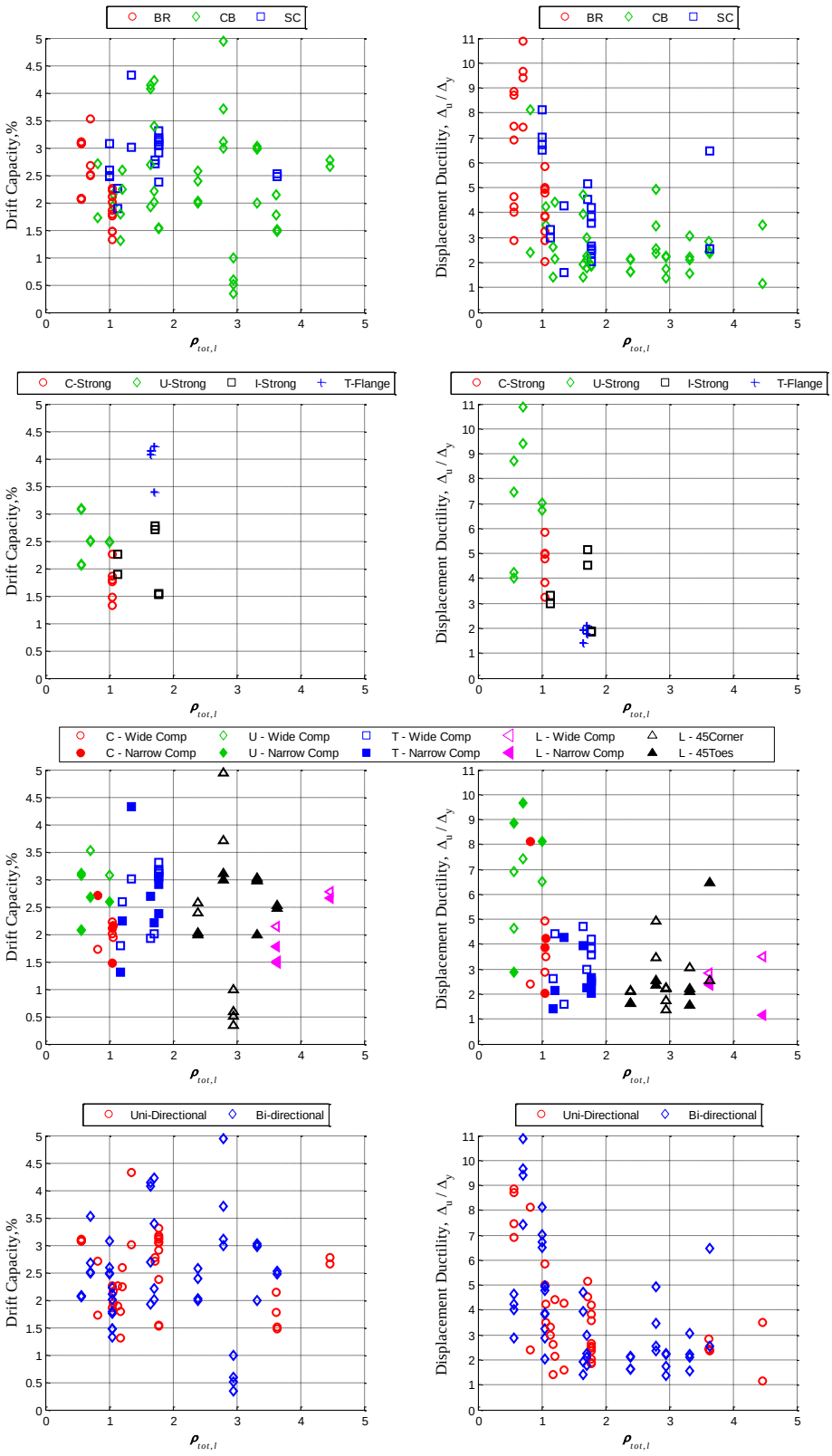

Figure 3.13: Relationship between Total Vertical Reinforcement Ratio vs. Drift and Displacement Ductility (Wall sub-sets examine failure mode, symmetric/asymmetric direction and uni-/bi-directional loading)

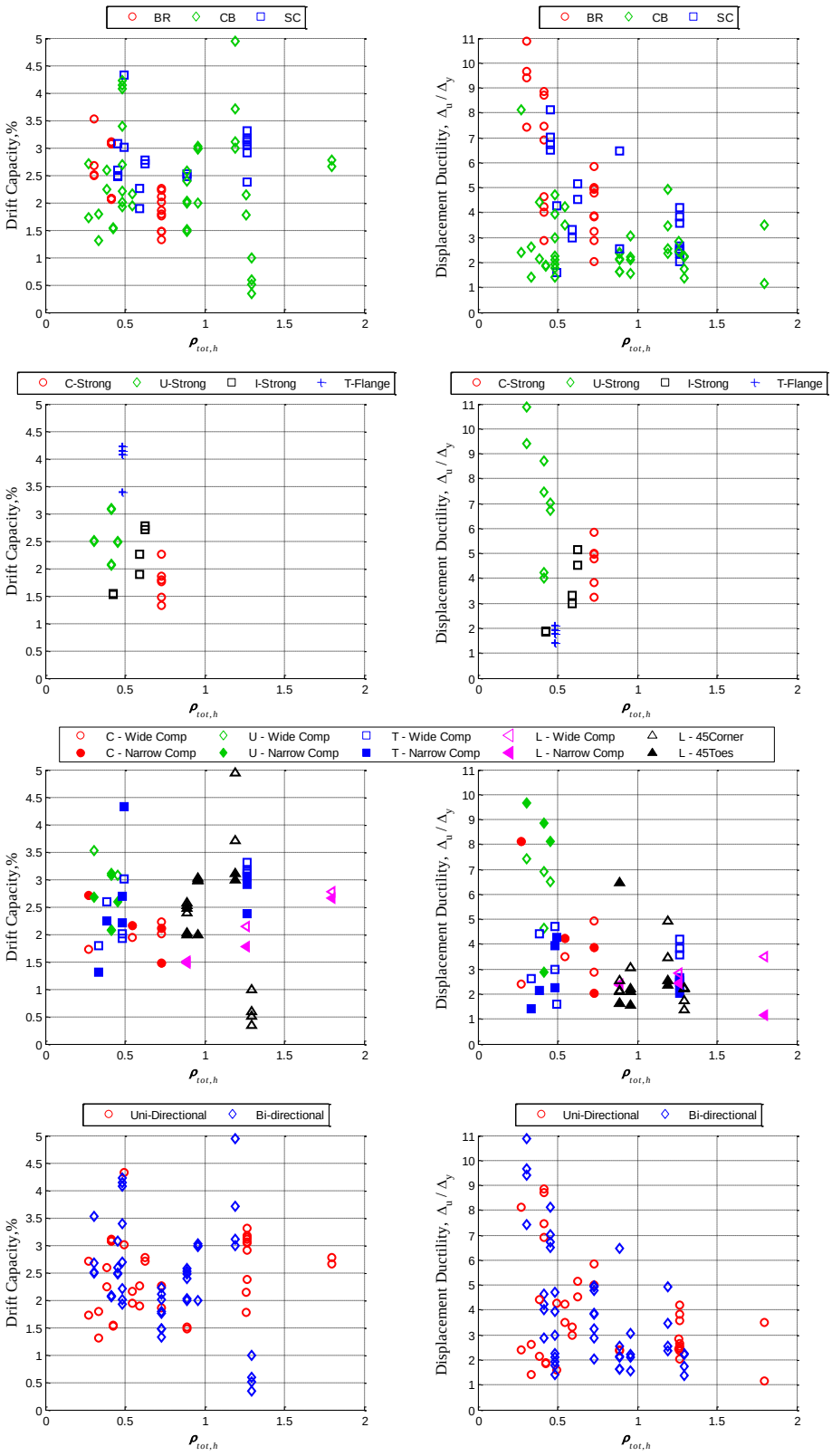

Figure 3.14: Relationship between Total Horizontal Reinforcement Ratio vs. Drift and Displacement Ductility (Wall sub-sets examine failure mode, symmetric/asymmetric direction and uni-/bi-directional loading)

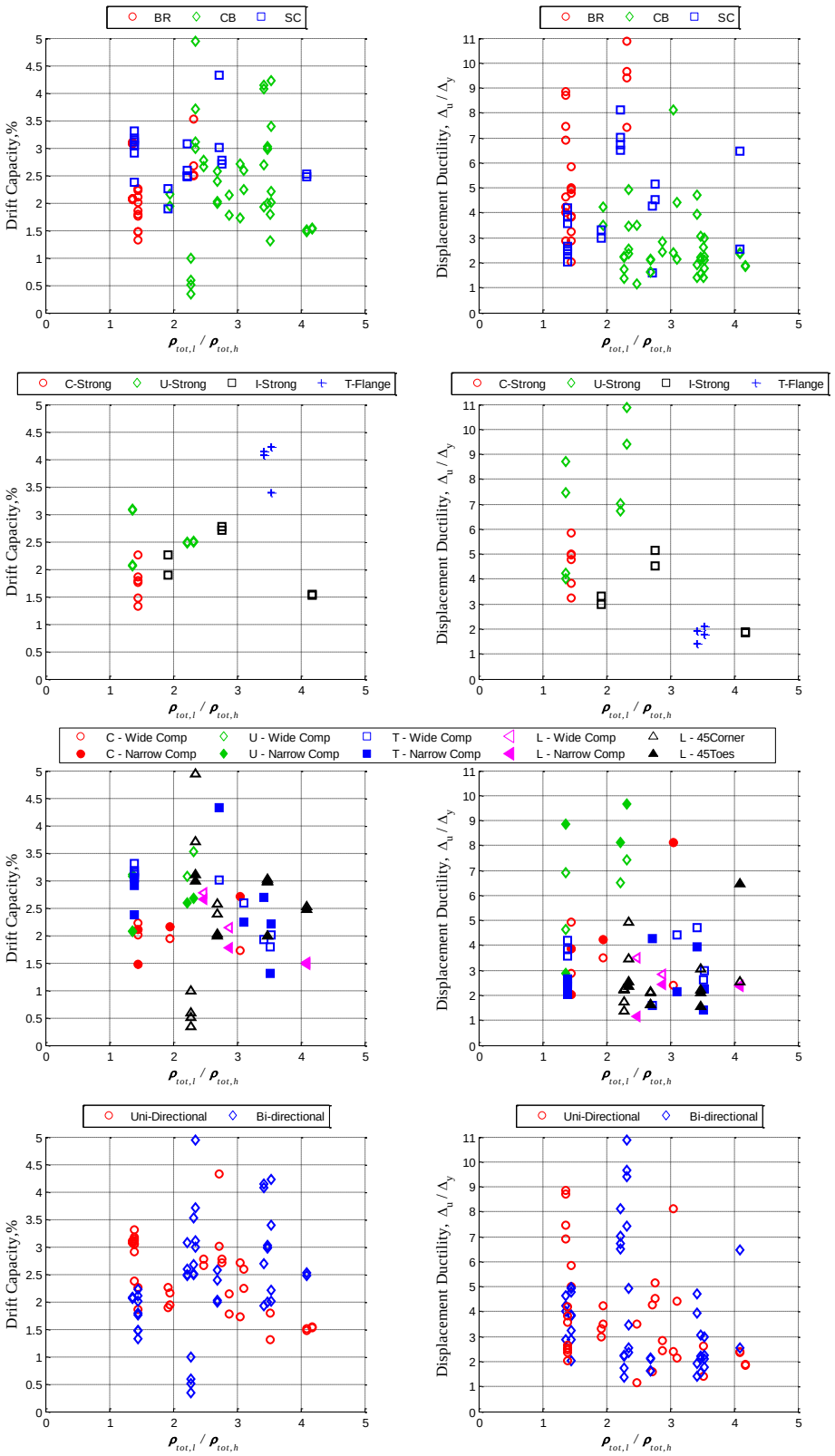

Figure 3.15: Relationship between Total Horizontal Vertical to Horizontal Reinforcement Ratio vs. Drift and Displacement Ductility
(Wall sub-sets examine failure mode, symmetric/asymmetric direction and uni-/bi-directional loading)

3.1.2.2.5 Axial Load Ratio

Table 3.14 presents the mean and standard deviation of the constant axial load ratio, $P/A_g f'_c$, applied to the specimens in the non-planar wall database. Fig. 3.16 shows the relationship between constant axial load ratio and the response metrics of drift capacity and displacement ductility.

Table 3.14: Mean and standard deviation of axial load ratio and wall shear spans in non-planar wall database

Design Parameter	ALR	h_{eff}/l_w	h_{eff}/l_f
Mean,	8.20	2.87	3.72
St. Dev.,	6.23	0.67	1.28

There are no experimental test programs in the non-planar wall database that explicitly investigate the effect of the magnitude of ***constant*** axial load ratio. There are a few cases where specimens in a single test program have different ***constant*** axial load ratios (*Beyer* et al. [48] and *Oesterle* [140, 141]); however, there are other major differences in the wall design such as a flange boundary element confinement or wall thickness, which may have a greater impact on response than the axial load ratio. Examination of Tables 3.7 and 3.8 indicates that there is no significant correlation between ***constant*** axial load ratio and drift capacity or displacement ductility for any of the wall sub-sets.

3.1.2.2.6 Shear Span Ratio

The shear span ratio, h_{eff}/l_w and h_{eff}/l_f, is the effective height of the applied lateral load divided by the web or flange length as appropriate for the direction of loading. Table 3.14 presents the mean and standard deviation of all the wall shear span ratios in the non-planar wall database. Figs. 3.17-3.18 shows the relationship between shear span ratios and drift capacity/ displacement ductility.

None of the tests in the experimental test database examine the effect of shear span ratio, though the *Lowes et al.* [119] test does employ a varying shear span ratio in the weak-axis loading of a C-shaped wall to simulate wall coupling. However, it cannot be used to independently assess the effect of the shear span ratio as a constant design parameter.

The shear span ratios associated with loading parallel to the wall web, h_{eff}/l_w, for the test specimens are mostly between 2 to 3.5. Based on a relatively narrow range of shear span ratios

available in the experimental test database, Table 3.7 shows a strong negative correlation between h_{eff}/l_w and drift capacity for walls with buckling-rupture and shear-compression failures, as well as uni-directionally loaded walls. The negative correlation holds for displacement ductility for buckling-rupture failures, walls with loading in a symmetric direction and bi-directionally loaded walls.

The shear span ratios for loading parallel to the wall flange, h_{eff}/l_f, range from 2 to 5 with the greatest concentration around 3. It is difficult to establish correlations between h_{eff}/l_f and drift capacity since many of the wall sub-sets in the database have a narrow band of values. The overall dataset and bi-directionally loaded walls in particular exhibit a weak negative correlation.

3.1.2.2.7 Shear Response

Two shear response metrics were investigated for each of the tests in the non-planar wall database, the shear demand-to-capacity ratio (V_u/V_n) and maximum shear stress ($V_u/A_{cv}\sqrt{f'_c}$) as shown in Figs. 3.19-3.20. Table 3.15 presents the mean and standard deviation of shear response metrics.

Table 3.15: Mean and standard deviation of shear response metrics

Design Parameter	V_u/V_n	$V_u/A_{cv}\sqrt{f_c'}$
Mean,	0.61	4.89
St. Dev.,	0.22	2.13

There are no test programs that are explicitly intended to examine walls with specific, distinct shear demand-to-capacity and/or maximum shear stress values. However, most tests in a single experimental program exhibit differences these shear response metrics as a result of the design parameter being investigated (length or confinement configuration of a boundary element, web and/or horizontal vertical reinforcement ratio, wall thickness, etc.).

In terms of the overall non-planar wall data set, it appears that the large number of crushing-buckling wall failures that have low ductility values irrespective of the magnitude V_u/V_n and $V_u/A_{cv}\sqrt{f'_c}$ seem to be obscuring the overall trend for these parameters. It appears that if walls with buckling-rupture and shear-compression only failures are considered then there is a clear negative correlation for both V_u/V_n and $V_u/A_{cv}\sqrt{f'_c}$ with respect to wall ductility.

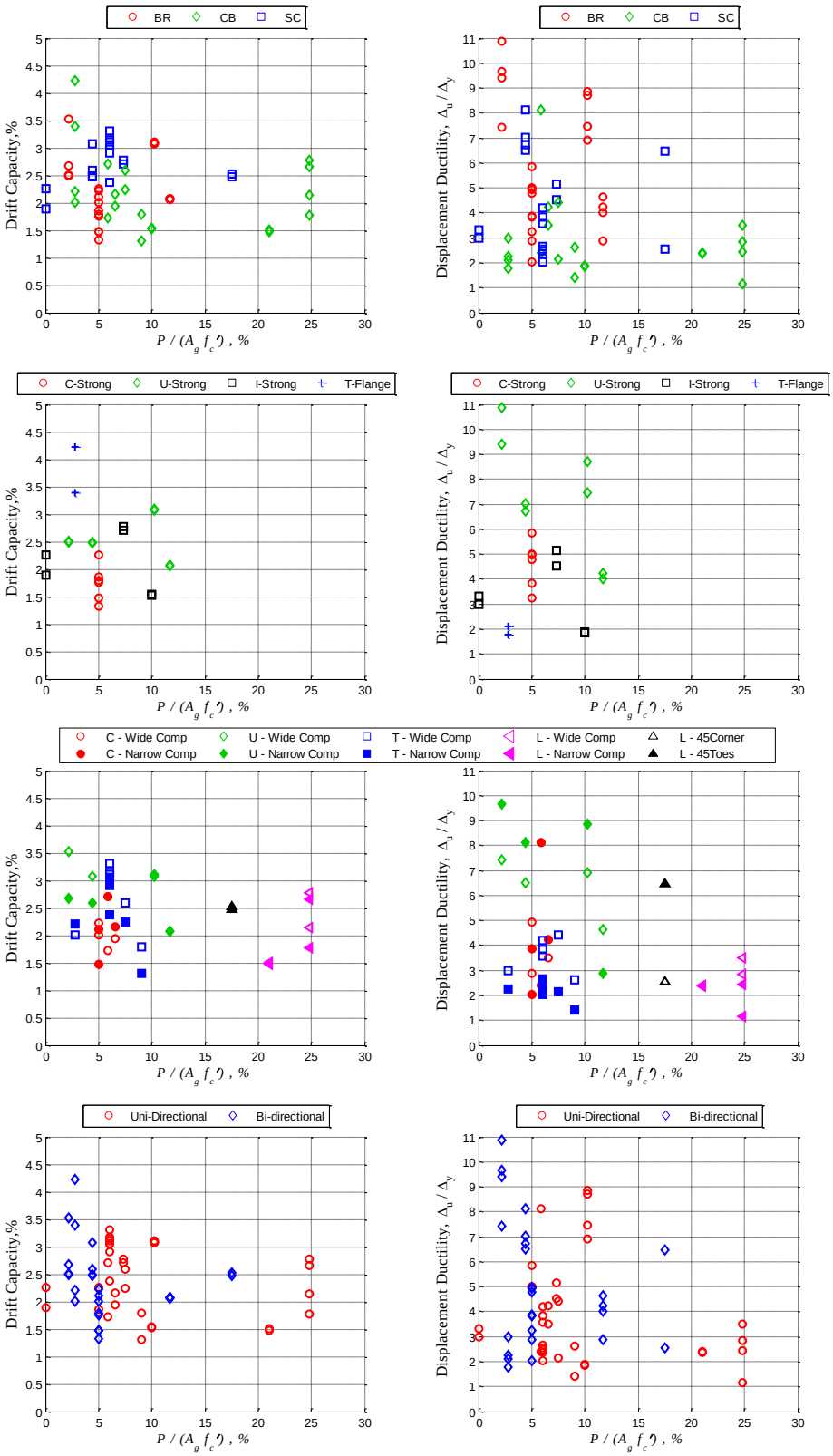

Figure 3.16: Relationship between Axial Load Ratio vs. Drift and Displacement Ductility
(Wall sub-sets examine failure mode, symmetric/asymmetric direction and uni-/bi-directional loading)

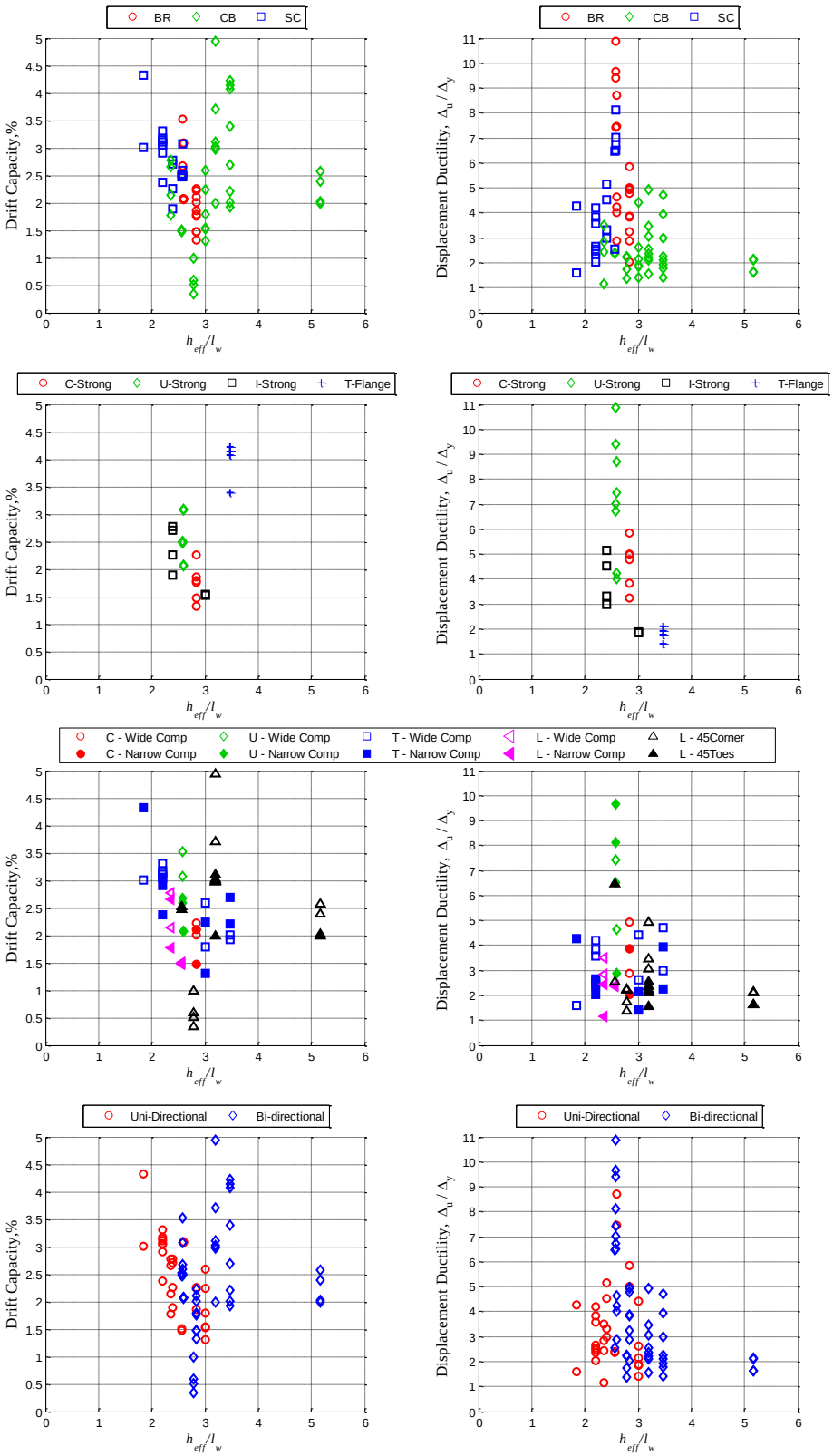

Figure 3.17: Relationship between Shear Span (Loading Parallel to Web) vs. Drift and Displacement Ductility (Wall sub-sets examine failure mode, symmetric/asymmetric direction and uni-/bi-directional loading)

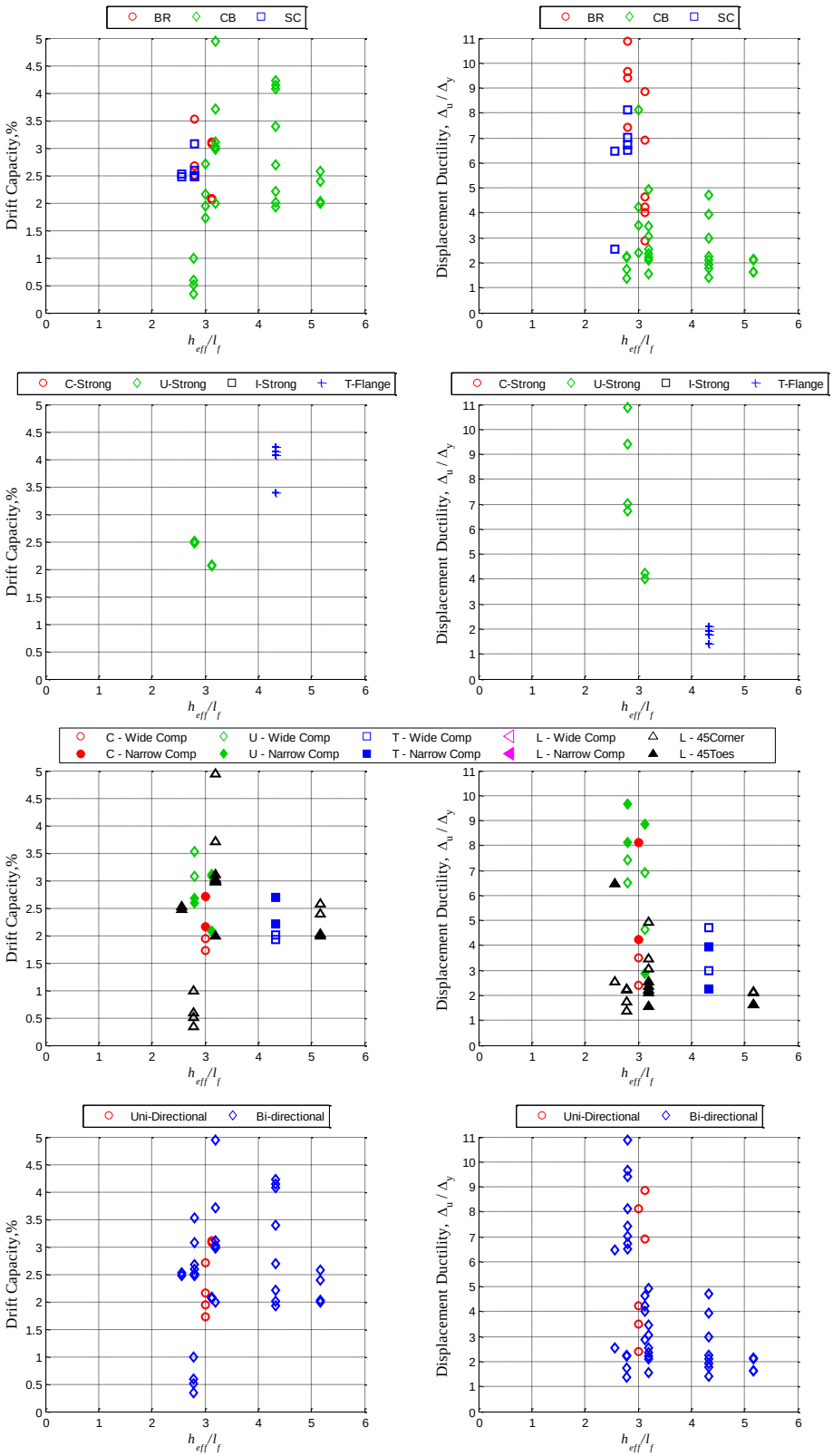

Figure 3.18: Relationship between (Shear Span Loading Parallel to Flange) vs. Drift and Displacement Ductility
(Wall sub-sets examine failure mode, symmetric/asymmetric direction and uni-/bi-directional loading)

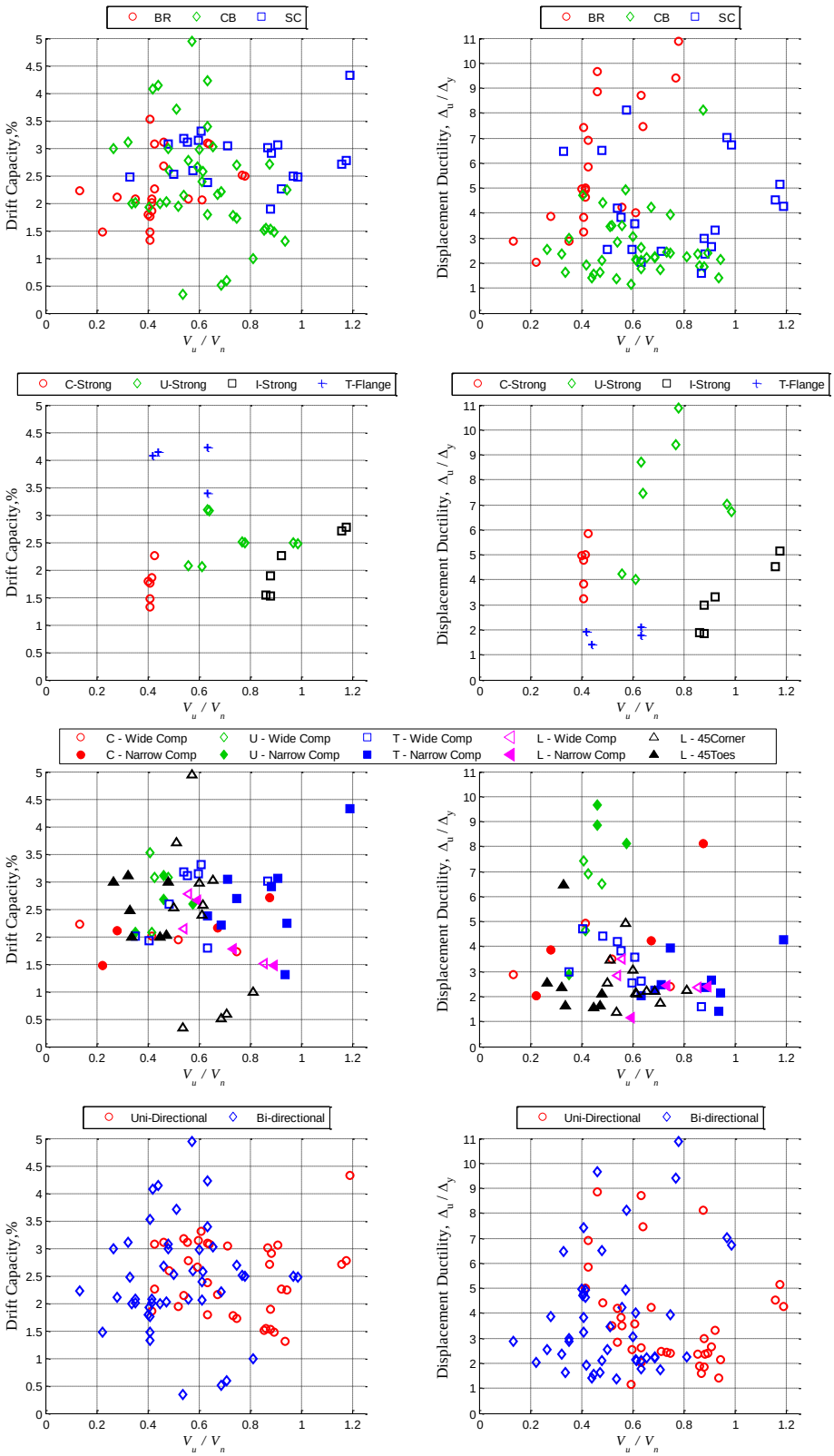

Figure 3.19: Relationship between Shear Demand-to Capacity Ratio vs. Drift and Displacement Ductility (Wall sub-sets examine failure mode, symmetric/asymmetric direction and uni-/bi-directional loading)

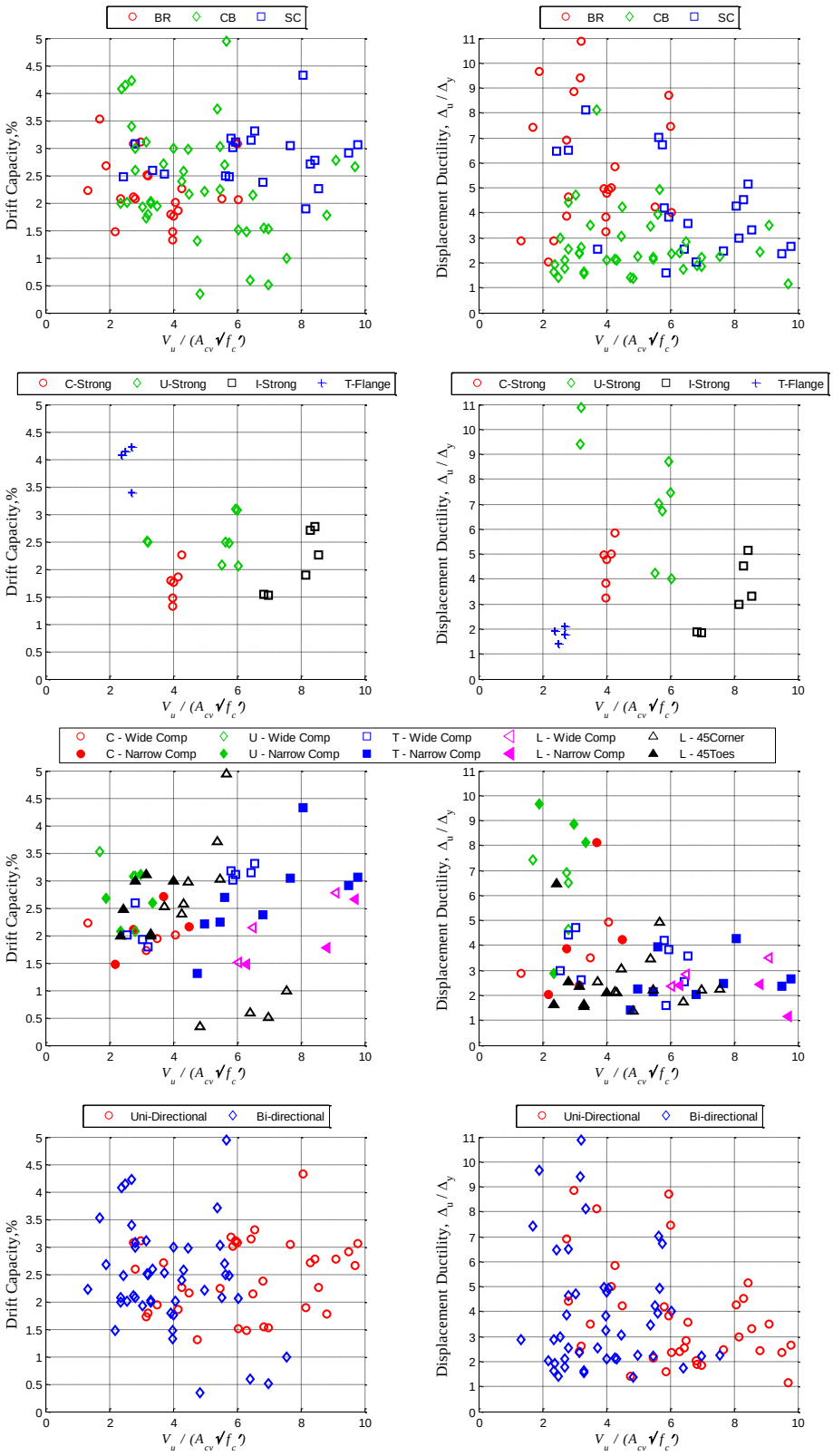

Figure 3.20: Relationship between Normalized Maximum Shear Stress vs. Drift and Displacement Ductility (Wall sub-sets examine failure mode, symmetric/asymmetric direction and uni-/bi-directional loading)

C/U- and I- shaped walls with loading in a symmetric direction show a strong positive correlation between V_u/V_n and drift capacity; the strong positive trends for these walls also hold for displacement ductility along with walls with buckling-rupture failures. Similarly for maximum shear stress, C/U- and I- shaped walls with loading in a symmetric direction show a strong positive correlation between $V_u/A_{cv}\sqrt{f'_c}$ and drift capacity; the distinction is that only I-shaped walls show a strong positive trend between $V_u/A_{cv}\sqrt{f'_c}$ and displacement ductility, and walls that exhibit a shear-compression failure exhibit a strong negative correlation between the parameters.

3.1.2.2.8 Commentary on Interaction between Reinforcement Ratios and Shear Response

Section 3.1.2.2.4 indicates there are negative correlations between $\rho_{BE,l}$, $\rho_{tot,l}$, and $\rho_{tot,h}$ and the deformation measures as increasing $\rho_{BE,l}$, $\rho_{tot,l}$, and/or $\rho_{tot,h}$ results in higher observed maximum shear stress on the wall (Fig. 3.21). The positive correlation between reinforcement ratio and shear demand is most notable for uni-directionally loaded walls with a crushing-buckling type failure. For these walls, as shear stress demand increases, displacement ductility decreases (refer to Section 3.1.2.2.7). Therefore, it would be important to study a range of $\rho_{BE,l}$, $\rho_{tot,l}$, and $\rho_{tot,h}$ for varying design shear demand-to-capacity (V_u/V_n) ratios and target shear stress demands ($V_u/A_{cv}\sqrt{f'_c}$).

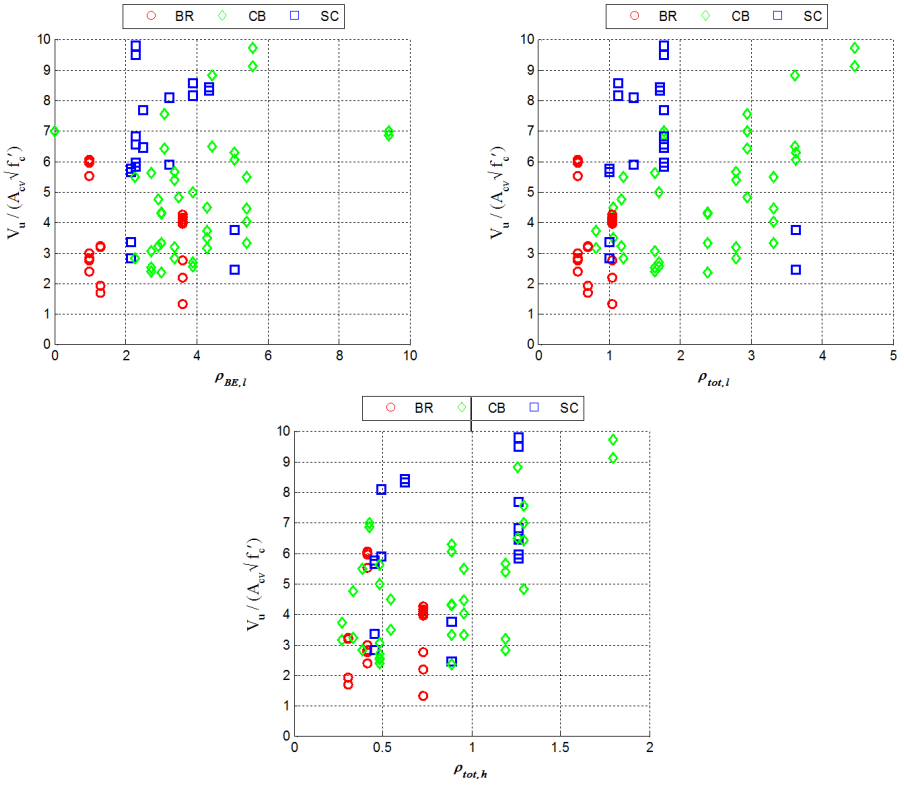

Figure 3.21: Relationship between Reinforcement Ratios and Normalized Maximum Shear Stress (Only showing walls classified by failure mode)

3.2 Examination of Post-Earthquake Damage Observations

This section assesses non-planar wall performance in historic earthquakes. As mentioned previously in Chapter 2, the Earthquake Engineering Research Institute "Learning from Earthquakes" (EERI-LFE) repository [80] was reviewed for major earthquakes in the last fifty years. From the reconnaissance literature 58 buildings were identified as containing non-planar walls with some level of damage. Section 3.2.1 describes the approach used to classify the damage mechanism for each wall based on descriptions and photographs provided in reconnaissance documents/archives. Section 3.2.2 provides an earthquake damage summary and investigation of building characteristics that impact wall response.

3.2.1 Damage Mechanism Classifications for Earthquakes

Earthquake damage to non-planar wall systems in buildings was generally grouped into light versus moderate-severe (Table 3.16). Light damage included hairline to more pronounced cracking (or working of construction joints) and limited spalling; this damage was only slightly more significant that something that would be deemed non-structural in nature. Moderate-severe damage was grouped into seven categories listed below, which are generally consistent with those used in *Birely* [35]. Note that these failure classifications are distinct from those provided for experimental tests in Section 3.1.1.2.1. The categories are described in further detail in this section:

- Compressive boundary element damage
- Diagonal shear
- Web crushing
- Horizontal failure plane
- Global instability
- Building residual displacement
- Collapse

Fig. 3.22 includes a set of reference images, one for each of the damage classifications, to supplement the definitions provided in Sections 3.2.1.1-3.2.1.7.

Figure 3.22: Reference Images for Earthquake Damage Classifications
(Images from: [74, 77, 79, 131])

3.2.1.2 Compressive boundary element damage

Compressive boundary element damage can include spalling, inelastic bar buckling, and/or crushing of the concrete core where damage is *primarily isolated to the boundary element region*. There were very few instances where compressive damage was *primary limited to* the boundary element. Of these, perhaps the most minor was in the red-tagged building in the Nisqually earthquake (Figure 2.80) that had moderate spalling at the base of the boundary element region. The most severe was in the Acapulco Building in the 1985 Chile earthquake with buckling of flexural reinforcement in the boundary element accompanied by core crushing (Figure 2.89(c)); as a note there were other, but less severe forms of wall damage in the Acapulco building.

Despite the low numbers of compressive boundary element damage in Table 3.16, this type of damage occurred frequently with web crushing. Cases of damage where there is both boundary element compression and web crushing were generally classified as horizontal plane failure.

3.2.1.3 Diagonal shear

Diagonal shear damage typically occurs as pronounced diagonal cracks that form in opposite directions of the wall due to the cyclic nature of loading. Where there are high tensile demands this can be accompanied by bar fracture across the crack plane. More significant compression-type damage along diagonal shear struts is classified as web crushing (or, when combined with boundary element compression damage, then it is often considered a horizontal failure plane). Some examples of diagonal shear damage such as that seen in a building under construction that was damaged in Erçis-Van earthquake (Figure 2.67) and in the TVNZ Building in the Canterbury earthquake series (Figure 2.73(b)). Both of these walls had minor amounts of spalling along or at intersections of cracks. Diagonal shear cracking and associated spalling was frequently mentioned in various reconnaissance reports, without accompanying photographs, these are summarized in Table 3.16.

3.2.1.4 Web crushing

Web crushing applies to cases where there are high shear demands on a wall and a diagonal shear strut suffers from a compression failure characterized by bar buckling and core crushing (this fits into the category of shear-compression failure described in Section 3.1.1.2.1.3). Web crushing is used to describe crushing failures that occur *primarily* in the web region of the wall, outside of boundary elements regions. Web crushing can be seen in the Terrace on the Park Apartment Building (Figure 2.72(b)) damaged in the Canterbury earthquake series. Another extreme case of web crushing, where locations of complete concrete core loss was observed, was in the Bingöl Liesi Building B (Figure 2.79(b)). The damage in Bingöl Liesi was attributed to wide spacing of horizontal reinforcement, and potentially concrete quality. A majority of cases that exhibited web crushing also had some amount of boundary element compression damage, and are often classified as a horizontal failure plane.

3.2.1.5 Horizontal Failure Plane

The horizontal failure plane is a designation developed in *Birely* [35] to capture compression-type failures that extend from the web into the boundary element. This is a combination of boundary element compression damage and web crushing where some amount of spalling, bar buckling, and core crushing occur *primarily* on a horizontal plane. This designation also captures occurrences of sliding shear and more severe working at construction joints. Also, on very rare occasions this failure type is used in Table 3.16 to describe damage that is not wholly horizontal, simply because it best captures boundary element and web compression damage. Nearly every building in the 2010 Chilean earthquake described in Chapter 2 falls into this failure category (Figure 2.74 - Figure 2.78). Other prominent occurrences are seen in the Pacific Brands House (Figure 2.71(b)) during the Canterbury earthquake series and a non-ductile building in the Loma Prieta earthquake (Figure 2.85).

3.2.1.6 Global Instability

Global wall instabilities occur when a portion of a wall experiences significant out-of-plane displacement or more commonly, buckling. Many times this occurs in slender compression zones in L- or T-Shaped walls after these walls have already been subjected to numerous cycles of loading and the strength of the flexural reinforcement has begun degrading and/or the cover concrete has spalled leading to a significant reduction in wall cross-section. The most notable examples of wall instability can be seen in the L-Shaped wall in the Pacific Brands House (Figure 2.71(b)) in the Canterbury earthquake series, and T-Shaped walls in Edificio Emerald (Figure 2.75(a)) and the Alto Huerto buildings (Figure 2.76(b)) in the 2010 Chile earthquake. Instances where reconnaissance reports

note walls with out-of-plane displacement, rather than a more pronounced buckling failure, are included in Table 3.16.

3.2.1.7 Building Residual Displacement

This classification is intended to serve as an overall building performance measure. There are occasions were reconnaissance reports either do not report damage specifically for the non-planar wall system(s) or that damage was rather insignificant, but that building has large residual displacement. Both examples are from the Canterbury earthquake series: the Grand Chancellor Hotel with a 4.3-ft residual drift and only hairline flexural cracking in non-planar walls (there was a wall failure of a planar wall); and the Copthorne Hotel with a lean of 0.7-1.3 ft with no description of damage to the L-Shaped and core walls.

3.2.1.8 Collapse

Collapse is used as either a wall or overall building performance measure (which can consist of partial or complete collapse of a building). An example where a building experienced a wall collapse is Edificio El Faro in the 1985 Chilean earthquake (Figure 2.91(b)) where a T-Shaped wall in this structure experienced a brittle failure due to bar fracture. A partial building collapse was seen in Gedikbulak Primary School in the Erçis-Van earthquake (Figure 2.68), and full building collapses in the Pyne Gould (Figure 2.70(b)) and an unidentified building in the Canterbury earthquake series.

3.2.2 Earthquake Damage Summary

Table 3.16 includes summarizes damage to buildings with non-planar shear wall systems. These buildings contain some combination of walls shapes that fall into: C-/U-Shaped; core (box, irregular, or undefined shape usually around stairway or elevator shafts); L-Shaped; T-Shaped; or other (irregular cross-sections, but not a core wall). The buildings are each described in Chapter 2.5 and are listed in the table in order of their appearance in the text. The damage states are associated with the definitions provided in Section 3.2.1. As a note, more than one damage type can be selected for a structure when different damage patterns are observed in multiple wall systems in one building; the exception is that a building cannot be specified as both “building lean” and “collapse”.

Table 3.16: Summary of Observed Earthquake Damage for Buildings with Non-planar Walls

Earthquake	Building Wall Details			Light Damage		Moderate to Severe Damage/Failure Type						
	Vintage	Stories	Wall Shape(s)	Minor Cracking	Limited Spalling	B.E. Compression	Diagonal Shear	Web Crushing	Horizontal plane	Instability	Building Lean	Collapse (wall/blg)
Erçis-Van, Turkey	2010	6	C/U				X					
Erçis-Van, Turkey	1980	3	L									X
Tohoku, Japan	1970	4	Core					X				
Christchurch, New Zealand	1960	6	Core									X
Christchurch, New Zealand	1980	7	L						X	X		
Christchurch, New Zealand	2000	8	C/U					X				
Christchurch, New Zealand	pre-1970	4	C/U, L	X			X					
Christchurch, New Zealand	1980	22	L, Other	X							X	
Christchurch, New Zealand	pre-1970	5	Core									X
Christchurch, New Zealand	1980	11	C/U. Core, L								X	
Christchurch, New Zealand	1970	8	C/U	X								
Maule, Chile	1970	14	L						X			
Maule, Chile	2000	20	T						X	X		
Maule, Chile	2000	15	T						X	X		
Maule, Chile	1990	10	T, Other						X			
Maule, Chile	-	12	C/U						X			
Maule, Chile	2000	12	T, Other						X	X		
Maule, Chile	2000	12	T, L			X			X			
Bingöl, Turkey	-	4	L					X				
Bingöl, Turkey	-	4	L	X								
Nisqually, WA, USA	-	-	L			X						
Chi-Chi, Taiwan	1990	-	Core				X					
Kocaeli, Turkey	-	9	Core		X		X					
Kocaeli, Turkey	-	-	L				X					
Cariaco, Venezuela	1970	6	Core									X
Kobe, Japan	1950	11	C/U	X			X			X		
Northridge, CA, USA	1960	12	Core	X								
Northridge, CA, USA	1960	6	Core	X								
Northridge, CA, USA	1960	7	Core	X								
Guam, USA Territory	1970	7	Core	X	X							
Guam, USA Territory	1990	15	Core				X					
Guam, USA Territory	-	12	Core	X	X							
Guam, USA Territory		16	Core				X					
Guam, USA Territory	-	19	Core	X								
Loma Prieta, CA, USA	-	16	L						X			
Loma Prieta, CA, USA	1960	8	Core, L				X					
Spitak, Armenia	-	10	Core									X
Spitak, Armenia	1970	16	Core				X	X				
San Salvador, El Salvador	1960	5	Core				X					
Mexico City, Mexico	1970	15	C/U	X	X							

Table 3.16 cont'd: Summary of Observed Earthquake Damage for Buildings with Non-planar Walls

Earthquake	Building Wall Details			Light Damage		Moderate to Severe Damage/Failure Type						
	Vintage	Stories	Wall Shape(s)	Minor Cracking	Limited Spalling	B.E. Compression	Diagonal Shear	Web Crushing	Horizontal plane	Instability	Building Lean	Collapse (wall/blg)
Llolleo, Chile	1960	15	L, Other			X			X			
Llolleo, Chile	1970	15	Other				X					
Llolleo, Chile	1980	8	T									X
Llolleo, Chile	1980	23	L	X								
Llolleo, Chile	1960	12	C/U, T, L	X								
Llolleo, Chile	1970	14	C/U, T, L			X	X					
Llolleo, Chile	1980	10	Other				X					
Llolleo, Chile	1980	22	C/U, L				X					
Llolleo, Chile	-	5	Core	X								
Miyagi, Japan	-	18	C/U	X								
San Fernando, CA, USA	1960	7	Other				X					
San Fernando, CA, USA	1970	5	Other				X					
San Fernando, CA, USA	1970	5	Core, Other				X					
Anchorage, AK, USA	-	6	Core					X				
Anchorage, AK, USA	-	8	Core			X						
Anchorage, AK, USA	1960	6	Core									X
Anchorage, AK, USA	-	14	Core	X								
Anchorage, AK, USA	-	14	Core	X								

Fig. 3.23 summarizes building damage type by non-planar wall shape; in a single building there may be more than one non-planar wall with damage. Each wall shape in a building constitutes an individual data point for this assessment. Similarly, a single wall or wall type can exhibit several damage types; these also constitute individual data points. For these reasons there are more cases of damage reported than there are buildings in the dataset. The results in Fig. 3.23 show that diagonal shear failures are most common in C-/U-shaped walls, core walls, and "other" geometries; note the diagonal shear failure is similar to, but less extreme than, web crushing. Horizontal plane and instability failures are most common in T- and L-shaped walls as well as "other" geometries. In particular, the instability failures tend to occur with slender walls where there is an unsupported wall segment (e.g. in a T-shaped wall the stem is unsupported and has limited out-of-plane stiffness). Examining the full dataset, it appears that there are almost as many horizontal plane failures as web crushing and boundary element compression failures combined. This suggests that in many cases that compression damage is widespread and not just present in the lightly-reinforced web or the heavily stressed boundary elements.

Table 3.17 and Fig. 3.24 examine the relationship between building damage type and building height (number of stories). There were three instances where building height was unknown as indicated previously in Table 3.16; these have been excluded from the dataset. Table 3.17 indicates that the non-planar wall damage database consists of buildings that are less than fifteen stories tall (84% of the 55 buildings with known height). Notably all the buildings with non-planar walls that are noted to have collapsed were 10 stories or less.

Table 3.17: Damage Types by Building Height (No. of Stories)

Region	# Blgs	# Minor Damage		# Significant Damage						
		Minor Cracking	Limited Spalling	B.E. Comp	Diagonal Shear	Web Crushing	Horiz plane	Instab.	Building Lean	Collapse
All	55*	18	4	4	16	5	10	5	2	7
$0 < H \leq 5$	10	3	0	0	4	2	0	0	0	1
$5 < H \leq 10$	19	4	2	1	5	2	2	1	0	6
$10 < H \leq 15$	17	7	2	3	4	0	6	3	1	0
$15 < H \leq 20$	6	2	0	0	2	1	2	1	0	0
$H > 20$	3	2	0	0	1	0	0	0	1	0

* Three buildings were excluded from the data set as number of stories was unknown.
Note: A building can have >1 damage classification due to the presence of multiple damaged walls.

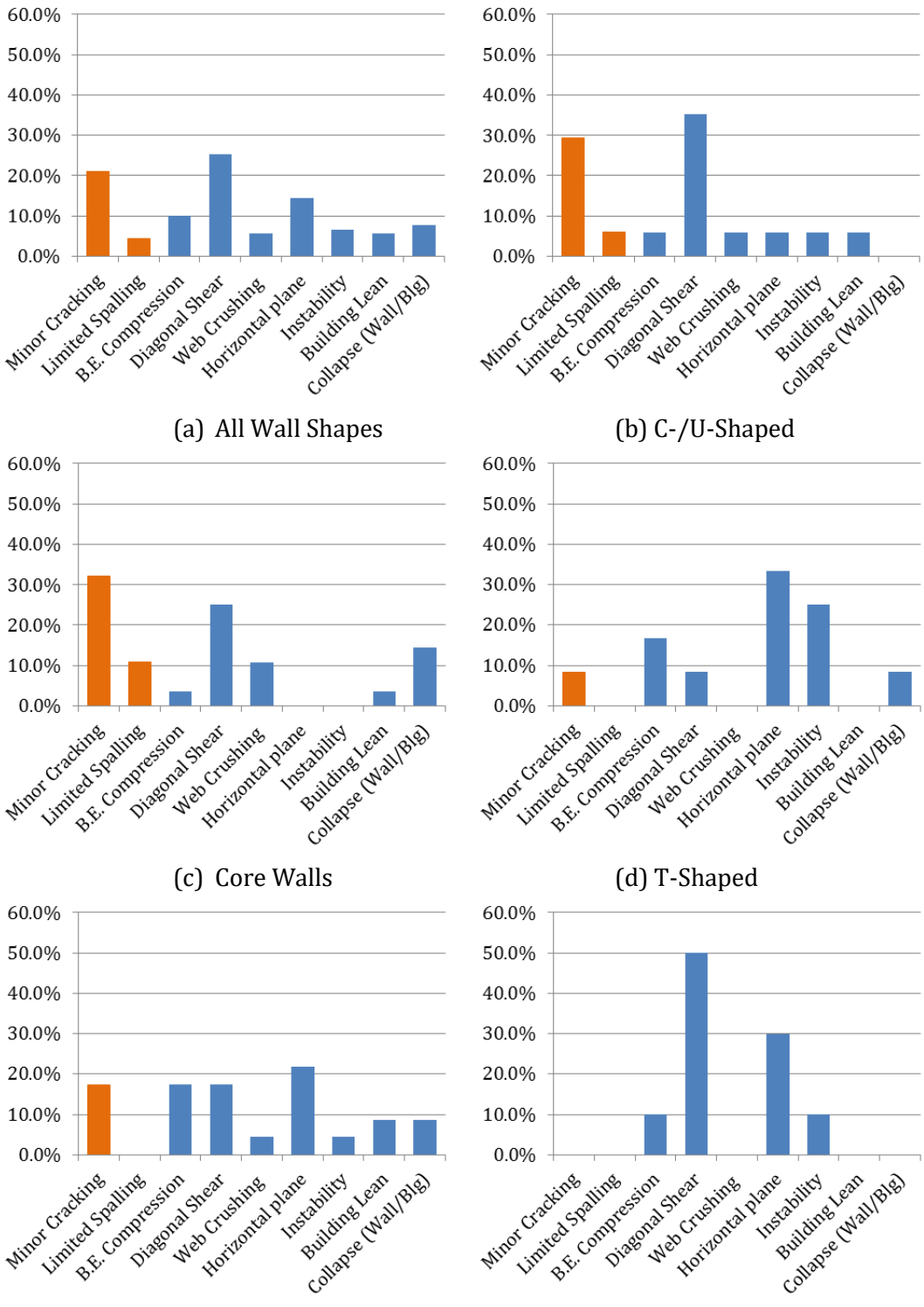

Figure 3.23: Percentage of buildings with a particular damage type, by wall shape
(Orange indicates minor damage and blue significant damage)

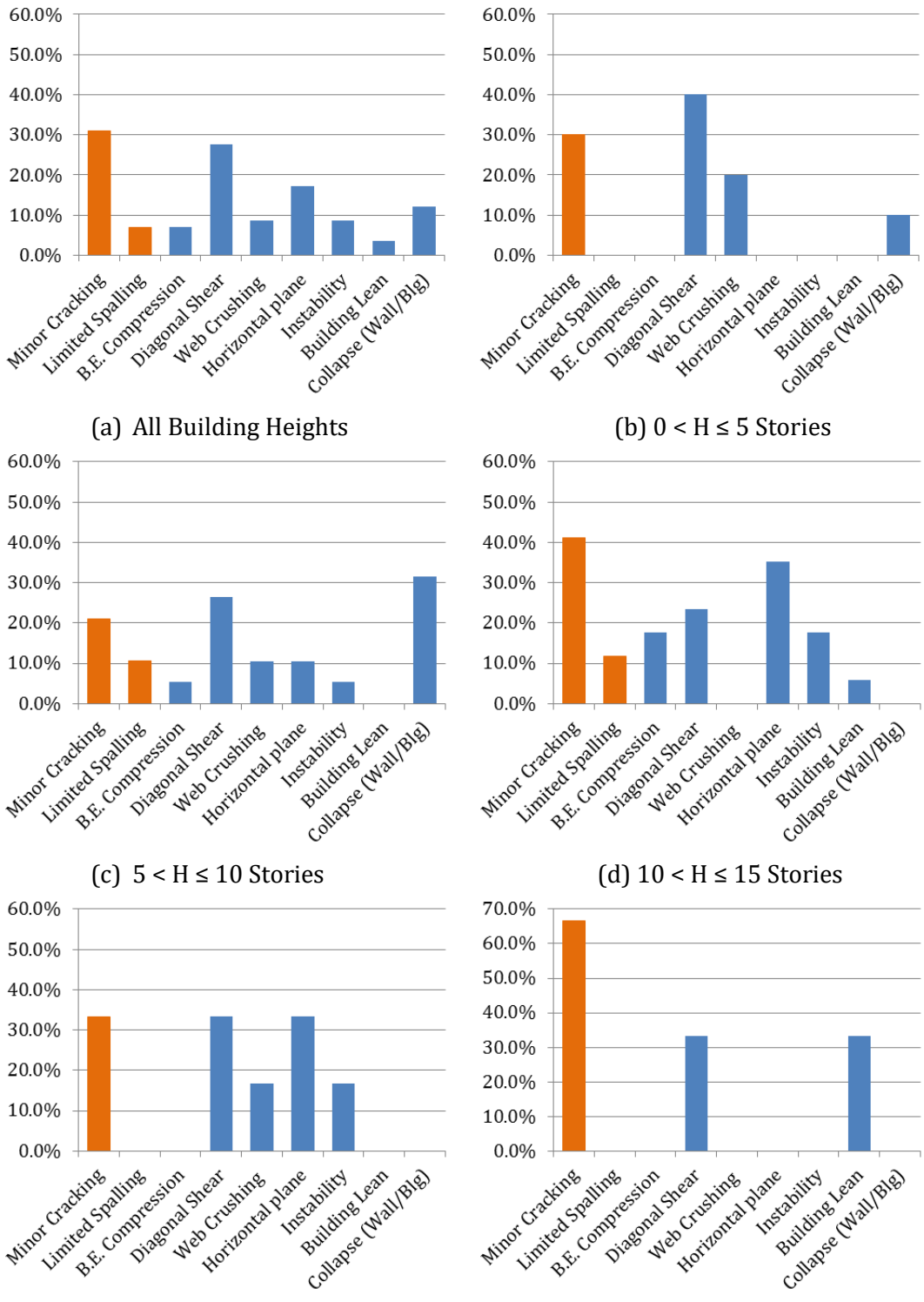

Figure 3.24: Percentage of buildings with a particular damage type, by building height in stories (Orange indicates minor damage and blue significant damage)

Note percentages can sum to >100% if there are multiple damaged walls in a single building.

The buildings with non-planar walls were also categorized by geographic location using a similar approach as *Birely* [35] in examining in-field planar wall response. In the categorizations of wall response geographic regions/countries are defined as: (i) United States (excluding territories), (ii) Chile, (iii) New Zealand, (iv) Asia (Japan, Taiwan), (v) Other (Armenia, El Salvador, Mexico, Turkey, US Territory of Guam, Venezuela). Fig. 3.25 provides a map that shows the geographical distribution of the earthquake events where non-planar wall damage was identified.

Figure 3.25: Geographic Distribution of Earthquake Events associated with Non-planar Wall Damage

Table 3.18 and Fig. 3.26 summarize building damage type by geographic region/country. Note that it is possible for the sum of percentages in Fig. 3.26 to exceed one-hundred percent since some buildings are associated with multiple damage types, as indicated previously in Table 3.16.

Table 3.18: Building Damage Types by Geographic Region/Country

Region	# Blgs	# Minor Damage		# Significant Damage						
		Minor Cracking	Limited Spalling	B.E. Comp	Diagonal Shear	Web Crushing	Horiz plane	Instab.	Building Lean	Collapse
All	58	18	0	5	18	5	10	0	2	7
United States	14	8	2	2	6	1	1	0	0	1
Chile	16	3	0	3	4	0	8	3	0	1
New Zealand	8	3	0	0	1	1	1	1	2	2
Japan/Taiwan	4	2	0	0	2	1	0	1	0	0
Other	16	2	2	0	5	2	0	0	0	3

Note: A building can have >1 damage classification due to the presence of multiple damaged walls.

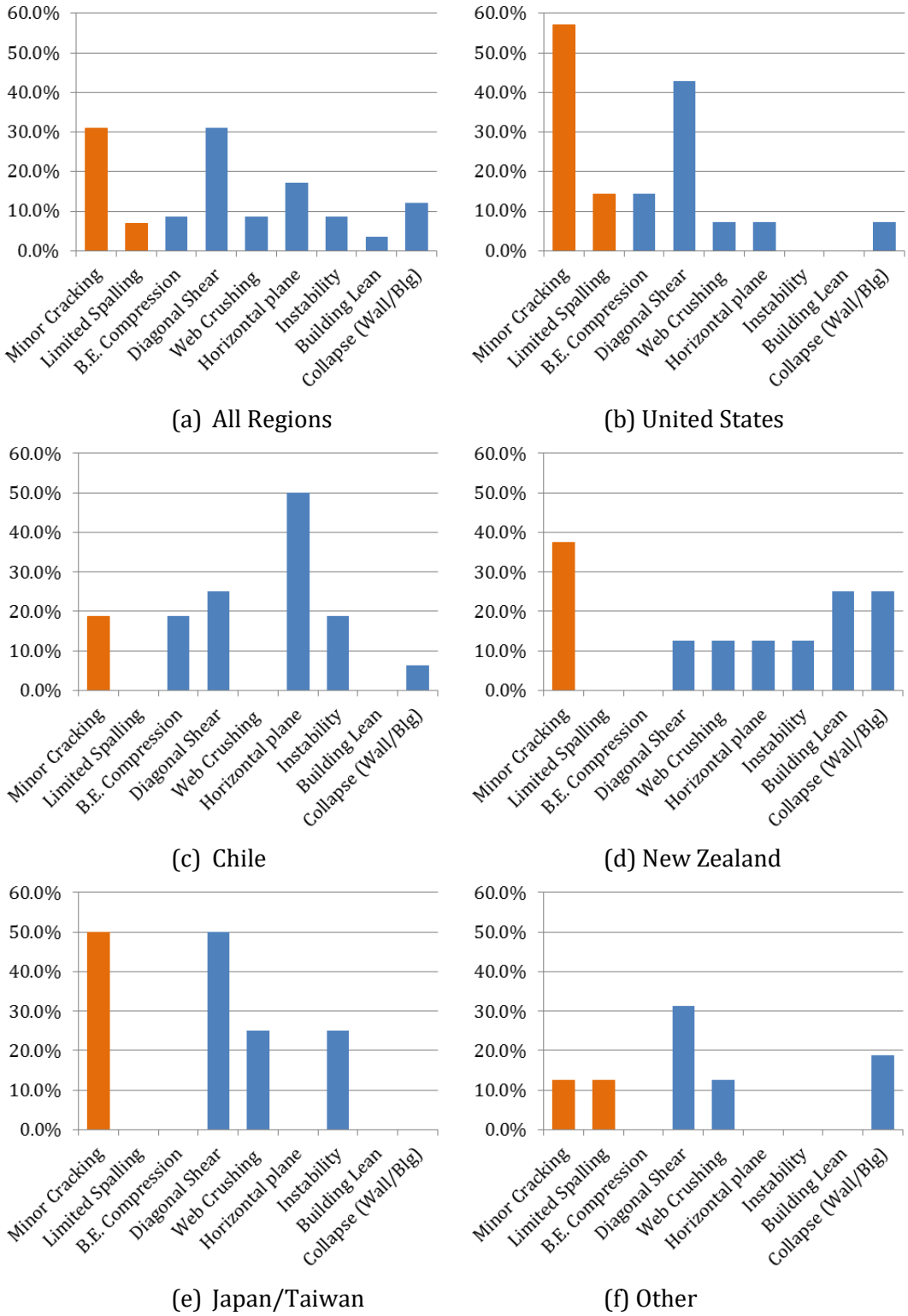

Figure 3.26: Percentage of buildings with a particular damage type, by geographic region/country (Orange indicates minor damage and blue significant damage)

Note percentages can sum to >100% if there are multiple damaged walls in a single building.

3.3 Summary of Experimental and In-Field Earthquake Response of Non-planar Walls

The major observations that can be taken from the **experimental non-planar wall database** are the following:

- **Materials:**

  Higher material strengths, both concrete compression strength and steel yield strength for primary longitudinal reinforcement, tend to result in improved drift capacity and displacement ductility for walls that are walls loaded in a symmetric direction or have buckling-rupture failures.

- **Wall geometry:**

  Increasing the web cross-sectional aspect ratio (l_w/t_w) results in lower drift capacity and displacement ductility for walls with C-/U-shaped geometries (irrespective of loading direction) or walls with buckling-rupture failures. Correlations were not as clear with other wall shapes or failure modes. Modern wall design seems to be trending towards thinner walls (higher l_w/t_w); therefore, this parameter likely merits further investigation.

  Evaluation of the flange cross-sectional aspect ratio (l_f/t_f) did not yield conclusive results across the wall types, failure modes, or loading; this design parameter will also require further study.

- **Boundary Element Geometry**:

  For C-,U-,I-Shaped walls loaded parallel to the web, increasing the length of the corner boundary element into the web, $l_{w,BE-w}$, led to improved drift capacity and ductility.

  The impact of the length of flange-end boundary elements, $l_{f,BE}$, is not as clear for the full non-planar wall database. However, the data suggests that increased slenderness of the flange-end boundary element ($l_{f,BE}/t_f$) at the stem tip for the T-shaped walls led to lower drift capacity often associated with instability failures. For T-shaped walls, it may be necessary to increase both the length AND width of the boundary element (i.e. reduce boundary element slenderness, $l_{f,BE}/t_f$) to improve T-stem compression response and overall wall ductility.

- **Reinforcement Ratios:**

  Examining the overall non-planar wall dataset, increasing the ratio of confinement in the boundary element ($\rho_{BE,conf}$) leads to improvements in drift capacity.

  Increasing the vertical reinforcement ratio in the boundary element or the total vertical/horizontal reinforcement ($\rho_{BE,l}, \rho_{tot,l}, \rho_{tot,h}$), results in reduced drift capacity and displacement ductility. Further exploration showed that walls that have higher values for these reinforcement ratios also have higher shear demands. A more complete understanding of the interaction between reinforcement ratio and shear demand may be gained through wall studies where a set of specimens have a similar target shear demand but varying reinforcement ratios.

- **Shear Stress Demand & Shear Demand-to-Capacity Ratio:** If walls with buckling-rupture and shear-compression only failures are considered then there is a clear negative correlation for both V_u/V_n and $V_u/A_{cv}\sqrt{f'_c}$ with respect to wall ductility. As a note: walls with crushing-buckling failures exhibit low ductility irrespective of V_u/V_n and $V_u/A_{cv}\sqrt{f'_c}$. A limited group of walls exhibit a positive correlation between V_u/V_n and $V_u/A_{cv}\sqrt{f'_c}$ with respect to deformation/ductility; these are C-/U and I-shaped walls loaded in a symmetric direction (strong-axis loading) that fail via buckling-rupture. This may have to do with the ability for shear demand to effectively transfer from the damaged web to flange and boundary elements which enables the wall to maintain its lateral strength at higher drift demands.

The major observations that can be taken from the **in-field earthquake non-planar wall database** are the following:

- **New Zealand (2010-11):**
  Damage observed in this earthquake series highlighted concerns with vintage walls (pre-1970s) that were lightly reinforced, as well as modern walls with thin cross-sections and also lightly reinforced. For both vintage and modern walls there were many observed cases of shear-compression failures and instabilities in the compression boundary element (generally in buildings of 4-8 stories). Significant wall damage also led to a number of cases of building collapse (5-6 story building) or building lean (variable height).

- **Chile (2010):**
  Significant damage in this earthquake was largely attributed to insufficient confinement of wall boundary elements (no seismic ties/hoops or too large of vertical spacing between ties/hoops) leading to brittle failures. This was particularly problematic in modern buildings with fewer and thinner walls than older structures which had higher stiffness and greater redundancy.

- **Other events (e.g. Turkey 2003; Venezuela 1997; Armenia 1988; El Salvador 1986)**
  Issues with wall construction included inadequate seismic hoops and/or transverse reinforcement, poor anchoring of hoops, poor material quality.

These observations indicate that some critical areas for future study are: (i) overall wall web/flange cross-sectional aspect ratio (l_w/t_w and l_f/t_f) , (ii) boundary element slenderness ($l_{w,BE-w}/t_w$, $l_{w,BE-f}/t_f$, and $l_{BE,f}/t_f$) , specifically for flange free-end boundary elements; and (iii) vertical and horizontal reinforcement ratios considering the interaction of these design parameters with shear demand. These investigations must examine the impact of each of the design parameters on deformation capacity and the occurrence of brittle failures (crushing-buckling, shear-compression, instability).

4 C-SHAPED WALL TEST PROGRAM

Note: Portions of this chapter are from a project report submitted to the Charles Pankow Foundation that was updated and resubmitted in mid-2015 (Behrouzi et al. [32] which is an update to Lowes et al. [119]). I was the primary author of content from both versions of the report which is presented below.

4.1 Project Motivation

Based on investigations undertaken in Chapter 2 of this study, post-earthquake reconnaissance of mid- to high-rise reinforced concrete buildings has demonstrated the effectiveness of structural walls that exhibit ductile detailing and are well-connected to the remainder of the structural system. These wall members have sufficient stiffness in low-level seismic events such that damage is limited to minor flexural and/or diagonal cracking that can be repaired, and damage to the rest of the building is predominantly non-structural. In more severe earthquakes, walls will undergo rather significant deformations; however, their success can be noted in the very few instances of catastrophic, collapse-type failures observed in well-engineered buildings with structural wall or dual frame-wall systems.

That being said, recent earthquakes, including the 2010 Maule, Chile and 2010-2011 Canterbury series, have brought into question whether current codes of practice: (i) require sufficient ductile detailing of walls to avoid brittle failure mechanisms such as web and/or boundary element crushing, global instabilities, etc., and (ii) adequately inform engineers how to approach the design of non-planar wall configurations that tend to exhibit a distinct damage progression and failure mechanisms compared to planar walls (especially considering bi-directional loading). These are significant concerns to the structural engineering community, because of the now-common implementation of reinforced concrete structural walls to achieve desired levels of stiffness, strength, and ductility for the overall lateral load resisting system. Furthermore, architectural constraints and, perhaps misplaced, confidence in current structural analysis and design techniques have led to buildings with lower wall-to-floor area ratios (i.e. fewer and more slender walls) and irregular non-planar configurations to accommodate service shafts or other building features.

A major factor that limits understanding of slender non-planar structural walls is the simple scarcity of the experimental data for these members. This is evident in Chapter 2 where a comprehensive effort was made to describe prominent research studies on C-, U-, I-, T-, and L-Shaped walls. The research described in Chapter 4 aims to contribute to this data-set by exploring uni- and bi-

directionally C-Shaped walls designed in accordance with *ACI318-08* [15]and *ASCE 7-05* [21] codes as well as input from an industry advisory panel.

4.2 Project Background

In 2004, a grant was awarded by the National Science Foundation (NSF) through the Network for Earthquake Engineering Simulation (NEES) program to conduct a series of large-scale experimental tests on reinforced concrete shear walls under the project title "NEESR-G: Seismic Behavior, Analysis, and Design of Complex Wall Systems" (CMMI Award # 0421577) [117]. Later in 2009, additional funding was provided by the Charles Pankow Foundation (CPF) [116] to extend the scope of the study to include bi-directional loading of isolated and coupled C-Shaped walls. The overarching objective of this study was to further performance-based design methods specifically for structural walls with varying geometric configurations. The University of Illinois at Urbana-Champaign Multi-Axial Full-Scale Sub-Structured Testing and Simulations Facility (UIUC MUST-SIM) was named a partner in the study to enable testing using axial, shear, and moment demands representative of earthquake loading, and to provide high-resolution, dense instrumentation capabilities that could be used to validate computational simulations. These unique characteristics of UIUC MUST-SIM represent the state-of-the art for experimental testing and monitoring.

This collaborative test program between the University of Washington and the University of Illinois was comprised of four planar, one coupled, and three C-Shaped wall specimens with the intent of examining the effects of wall configuration, reinforcement detailing, and loading protocol/direction on wall response (Table 4.1). Each of these wall specimens represent the lower three stories of a ten-story prototype wall at one-third scale. Descriptions of the planar walls can be found in *Birely* [35], *Hart* [87], and *Lowes et al.* [118] and the coupled wall in *Hart* [87], *Lehman et al*. [111], and *Turgeon* [163]. More details on the specifics of wall design, testing, and instrumentation for the C-Shaped walls (labelled as UW-1,2,3 in Table 4.1, but more commonly referred to as CWall6,7,8 in this document) can be found in subsequent sections in Chapter 4.

Table 4.1: NEESR-SG Complex Walls Testing Plan (modified from Hart [60])

Shape	Specimen ID	Loading			Reinforcement	
		Effective Height Ratio (h_{eff})	Axial Load	Loading Direction	Lap Splice Provided	Boundary Elements
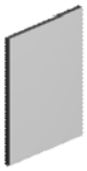	PW-1	0.71	$0.1f'_cA_g$	In Plane	Yes	Yes
	PW-2	0.525	$0.15f'_cA_g$	In Plane	Yes	Yes
	PW-3	0.5	$0.1f'_cA_g$	In Plane	Yes	Uniform
	PW-4	0.5	$0.1f'_cA_g$	In Plane	No	Yes
	CW-1	0.5	$0.1f'_cA_g$	In Plane	No	Yes
	UW-1	0.71	$0.05f'_cA_g$	Strong Axis	No	Yes
	UW-2	0.71	$0.05f'_cA_g$	Bi-Directional	No	Yes
	UW-3	0.71	$0.05f'_cA_g$	Strong Axis	No	Yes
		Variable	Variable	Weak Axis		

4.3 Specimen Design

The design of the C-Shaped walls was determined based on a West Coast shear wall building inventory of mid- to high-rise buildings (described in *Turgeon* [163]), recommendations from a panel of design practitioners, and the loading/geometry constraints of the UIUC MUST-SIM facility. Once the wall geometry was established based on these criteria, the horizontal reinforcement design was determined using the assumption walls would carry the maximum shear stress permitted by *ACI318-08* $\left(V_n = 8\sqrt{f_c}A_{cv}\right)$ [15]. The flexural design was carried out using the *ASCE 7-05* [21]. Equivalent Lateral Force (ELF) distribution to determine the base moment demand using the previously determined shear demand, and this resulted in the longitudinal reinforcement design. Consistent with modern wall design practice, the wall longitudinal reinforcement was concentrated in the boundary elements; also, *ACI318-08* [15] was used as the basis for confinement/buckling-resistance reinforcement in the boundary element regions. The target design strength for concrete was 5 ksi and yield strength for steel reinforcement was 60 ksi. A more detailed discussion of the C-Shaped wall design can be found in *Behrouzi et al.* [32].

The C-Shaped walls have an identical geometry with a wall height of 144-in, web width of 120-in, two flanges with a length of 48-in, and wall thickness of 6-in. The reinforcement layout is nominally

identical between the three specimens (Figure 4.1). The flexural reinforcement is continuous from the base of the footing into the wall top cap with no splices, and horizontal reinforcement was anchored 9-in into the boundary elements. During fabrication of CWall6 an error resulted in the absence of a 135-degree hook in the boundary element that was resolved in CWall7 and 8 (Figure 4.2). It is expected that this does not affect the response of CWall6 significantly, as this boundary element is not as heavily stressed in the uni-directional, strong-axis loading protocol. An additional error involved placement of confining reinforcement in CWall6 at a 2.25-in spacing rather than the *ACI318-08* [15] code minimum of 2-in (for the one-third scale). For consistency this spacing was maintained for CWall7 and 8 as it is not anticipated to significantly impact response.

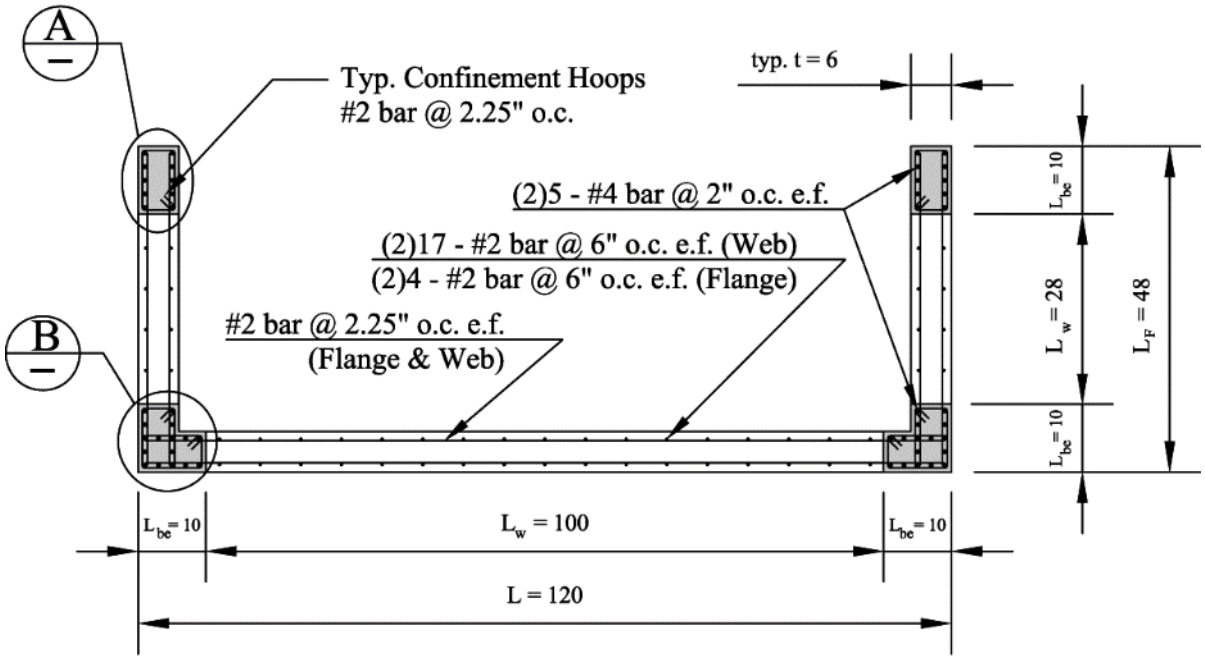

Figure 4.1: CWall6,7,8 Overall Wall Geometry and Reinforcement Layout (Units: inches)

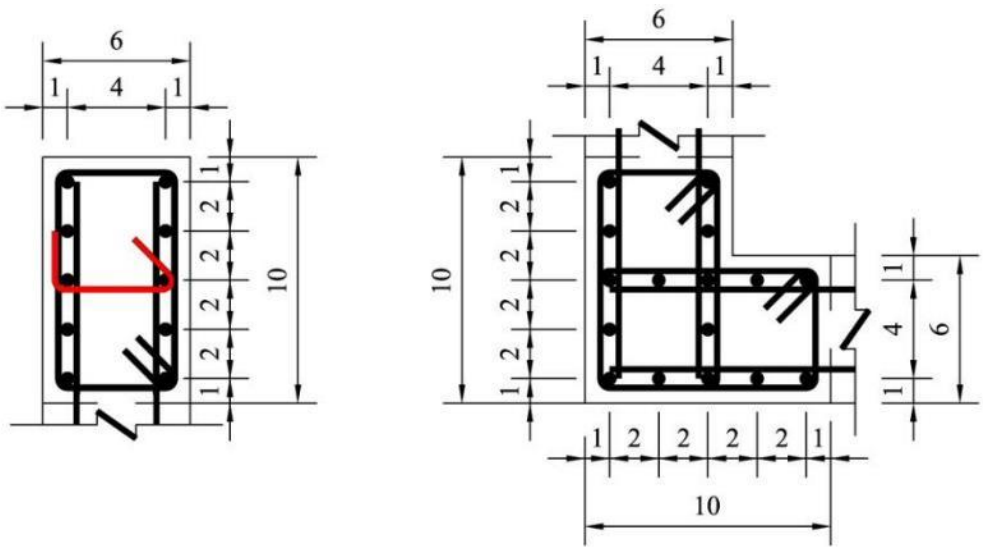

Figure 4.2: CWall Boundary Element Reinforcement Details (Units: inches)
Note: CWall6 is missing 135-degree hook noted in red

4.4 Fabrication of Wall Specimens

All of the C-Shaped wall specimens were constructed at UIUC using three stages of fabrication for the foundation, wall, and cap beam. The foundation and cap beam formwork, tied rebar mats, and PVC piping ducts were built by laboratory machine shop personnel; the heavy duty plate-girder wall formwork was purchased from EFCO Forms and the wall rebar cages were tied by students. Description of the design and construction of each of these components is described in the following subsections.

4.4.1 Wall Foundation Fabrication

The wall foundation is a concrete block of dimensions 14-ft by 8.75-ft by 2-ft (Figure 4.3) intended to serve two primary purposes: (i) allow for anchorage of the wall specimen to the laboratory strong floor using twelve 2-in rods each post-tensioned at approximately 100 kips of clamping force, and (ii) provide sufficient concrete for full development of the longitudinal steel reinforcement. The foundation contains a top and bottom horizontal mat of #4 bars and vertical hooked #4 stirrups. Each of the 3-in ducts for post-tensioning rods was surrounded by a #3 spiral to resist the concentrated loads that would occur at these locations. There are also two PVC ducts running through the foundation to be able to lift and maneuver the wall specimen from the construction and testing locations in the laboratory. The wall foundation was poured prior to the wall; it is relevant to note as there is a cold joint at the wall-foundation interface.

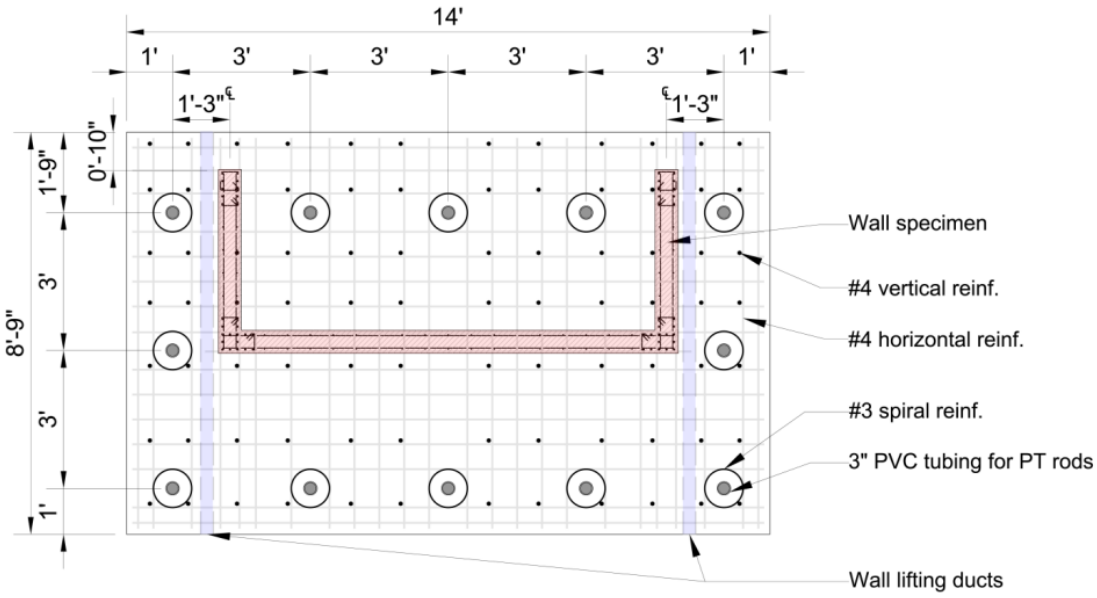

Figure 4.3: Footing Construction Drawing

4.4.2 Wall Fabrication

The wall rebar cage was tied after the foundation was cast. To provide a vertical guide during fabrication, the outside of the formwork was erected. This insured that the necessary wall thickness of 6-in, and the appropriate cover distance would be maintained. Students constructed the cage from bottom up placing confinement hoops over the vertical steel, and then tying them into position using a wooden spacer block (Figure 4.4). When this task was completed, the formwork was assembled and concrete was poured using a concrete pumping truck where concrete was pumped through rigid 3-in diameter steel tube (Figure 4.5). Despite using self-consolidating concrete for high workability around the tight rebar cages, on occasion it was chosen to use of a large rubber mallet at the bottom of the forms to reduce the potential for honeycombing, especially around the boundary element at the web-flange intersection.

Figure 4.4: Construction of CWall8 reinforcement cage

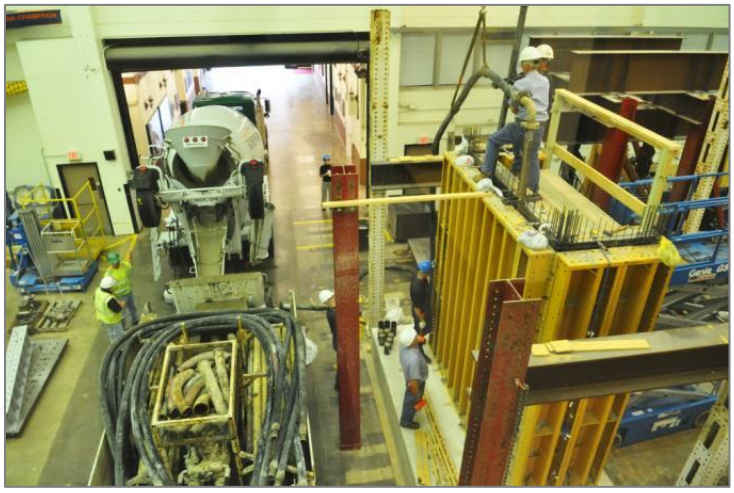

Figure 4.5: Casting of CWall8 specimen

4.4.3 Wall Cap Beam Fabrication

The wall cap beam was constructed after the wall formwork was removed (Figure 4.6). This had a similar design to the foundation with wooden formwork, tied rebar mats, and PVC tubing. This constituted the third and last concrete pour for each wall specimen. The wall cap beam served as a stiff collar at the top of the wall section where the connection plate/beam could be attached to mate the specimen to the loading apparatus. This is described in further detail in Section 4.6.2.

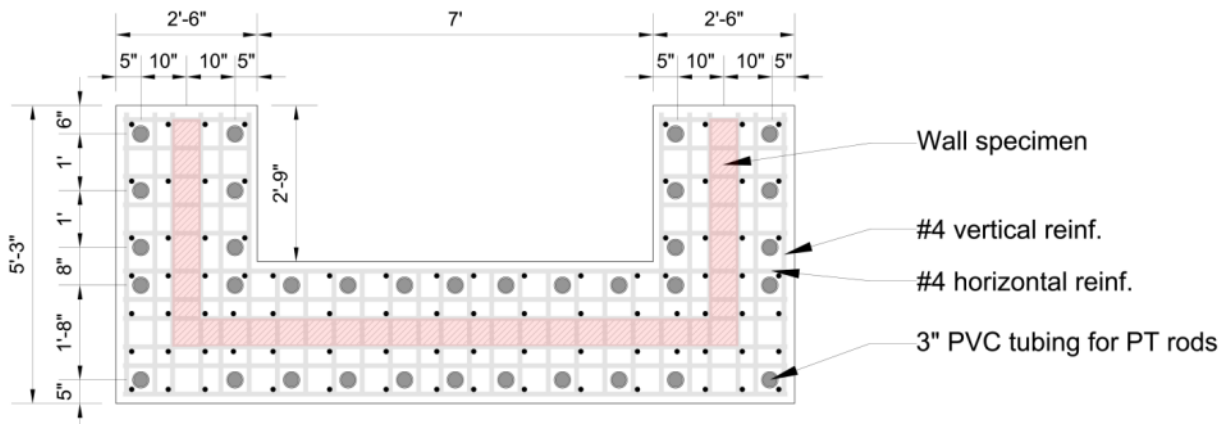

Figure 4.6: Wall Cap Beam Construction Drawing

4.5 Material Properties

4.5.1 Concrete Properties

The concrete mix design used to cast all the C-shaped wall specimens, inclusive of the foundation and cap, was a highly fluid self-consolidating concrete (SCC) with a maximum aggregate size limited to 0.375-in that could be poured around a tight rebar cage. Since more cement, flyash, and fines were substituted for typical coarse aggregate, reaching the 5000 psi target compressive strength required a water-to-cement ratio (w/c) of 0.50. The batch weights for the concrete mix design are shown in Table 4.2.

Table 4.2: SCC Mix Design (1 cubic yard)

Sand (FA-01)	1383	lb
Coarse (Chips CM-16)	1340	lb
Cement	450	lb
Water	36.7	gal
Flyash	150	lb
Admixtures		
Air	15	oz
WRDA 82	4-6oz/100	cwt
Properties		
w/c	0.50	

Each wall pour was accompanied with casting of 4 inch by 8 inch (4x8) cylinders and modulus of rupture (MOR) beams. All compressive cylinder tests were conducted in a Forney testing machine according to ASTM C39 specification [26], and MOR tests per the ASTM C78 specification [25]. The concrete material properties are summarized in Table 4.3.

Table 4.3: Summary of Concrete Compressive Strength

	CWall 6	CWall 7	CWall 8
Compression Strength (f'_c):	4937 psi	5254 psi	5119 psi
Age on day of test:	513 days	296 days	101 days
Ultimate Compression Strain (ε_{cu}):	0.0024	0.0022	0.0028
Modulus of Rupture (f_r):	700 psi	711 psi	1009 psi
Modulus of Elasticity (E_c):	4000 ksi	4100 ksi	4100 ksi
Poisson's Ratio (ν):	0.2	0.2	0.2

4.5.2 Steel Properties

The primary longitudinal reinforcement used to construct the three C-shaped walls was standard #4 grade 60 (ASTM A706 [24]) deformed bars. This type of steel is frequently used in seismic regions on the West Coast and must meet both minimum and maximum yield stress as well as ultimate stress criteria. To maintain similitude in the construction of a one-third scale specimen, it was necessary to use 0.25-in. diameter bars or "#2 bar" which is not commonly fabricated. To achieve the desired strength and ductility, the research team had to stamp a round bar with a helical pattern to provide the desired deformations and subject it to heat treatment to obtain a hot-rolled response.

Standard tension tests were carried out for the steel used in the C-shaped walls to determine the as-built properties of the reinforcement. These were performed using a MTS uniaxial testing frame with hydraulic grips. A calibrated extensometer with 4 or 8-inch gauge length was attached to each side of the specimen to measure strain in the bars; only if the specimen ruptured within the gauge length was the measured stress-strain response considered valid (Figure 4.7).

The measured parameters that correspond to the plots in Fig.4.7 are summarized in Table 4.4, where F_y is the yield stress, ε_y is the yield strain, ε_h is the strain at the onset of strain hardening, F_u is the ultimate stress, and ε_u is the strain at ultimate stress.

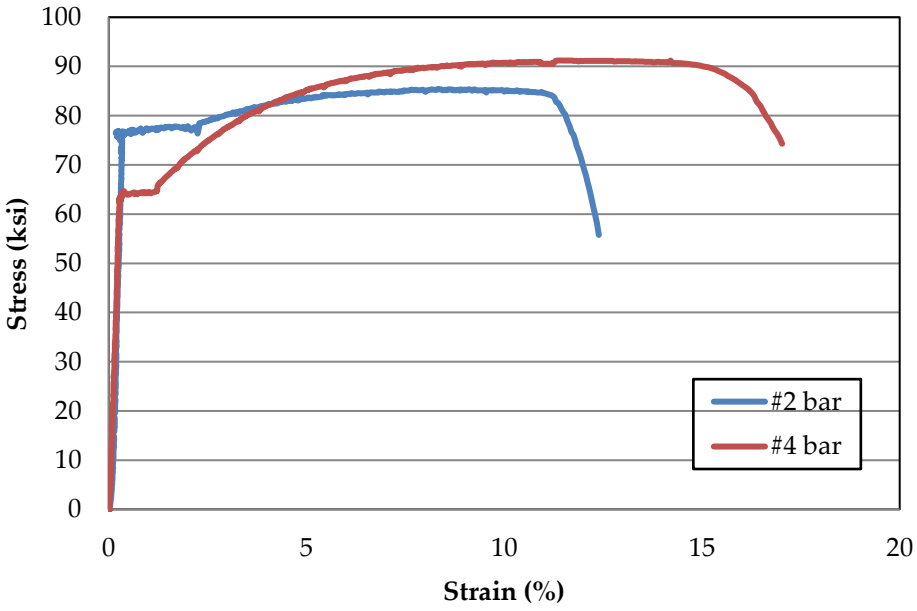

Figure 4.7: Stress-strain plot for Steel Reinforcement

Table 4.4: Summary of Steel Reinforcement Properties

Wall ID	Bar Size	F_y ksi	ε_y %	ε_h %	F_u ksi	ε_u %
CWall 6 CWall 7 CWall 8	#2	77	0.27	2.3	85.9	11.6
CWall 6 CWall 7 CWall 8	#4	64	0.22	1.17	91.3	17.2

4.6 Experimental Setup

4.6.1 Description of Test Setup

The experimental testing for the NEESR-SG Complex Walls Project was conducted at the UIUC MUST-SIM facility that contains a strong floor-wall system. The strong floor is comprised of 17-ft deep reinforced concrete box girder with the capacity of providing approximately 100 kips of clamping force 3-ft o.c.. The 50-ft x 30-ft L-shaped strong wall is 28-ft tall and 5-ft thick; it is heavily reinforced and post-tensioned with anchorage points 2-ft o.c.. The C-Shaped wall specimens were placed parallel to the long leg of the strong wall in the East-West direction (Figure 4.8 and Figure 4.9). As a note, the cardinal directions of the lab serve a naming convention for loading direction as well as referencing locations on the wall specimens. To apply the six degree-of-freedom (DOF)

loading, two "Load and Boundary Condition Boxes" (LBCB) were post-tensioned to the strong wall 22-ft above the strong floor and approximately 3-ft apart. The test specimen was placed beneath the LBCBs and a series of steel connection plates and beams were utilized to attach the LBCB and wall specimen. Details about this connection are included in the next section.

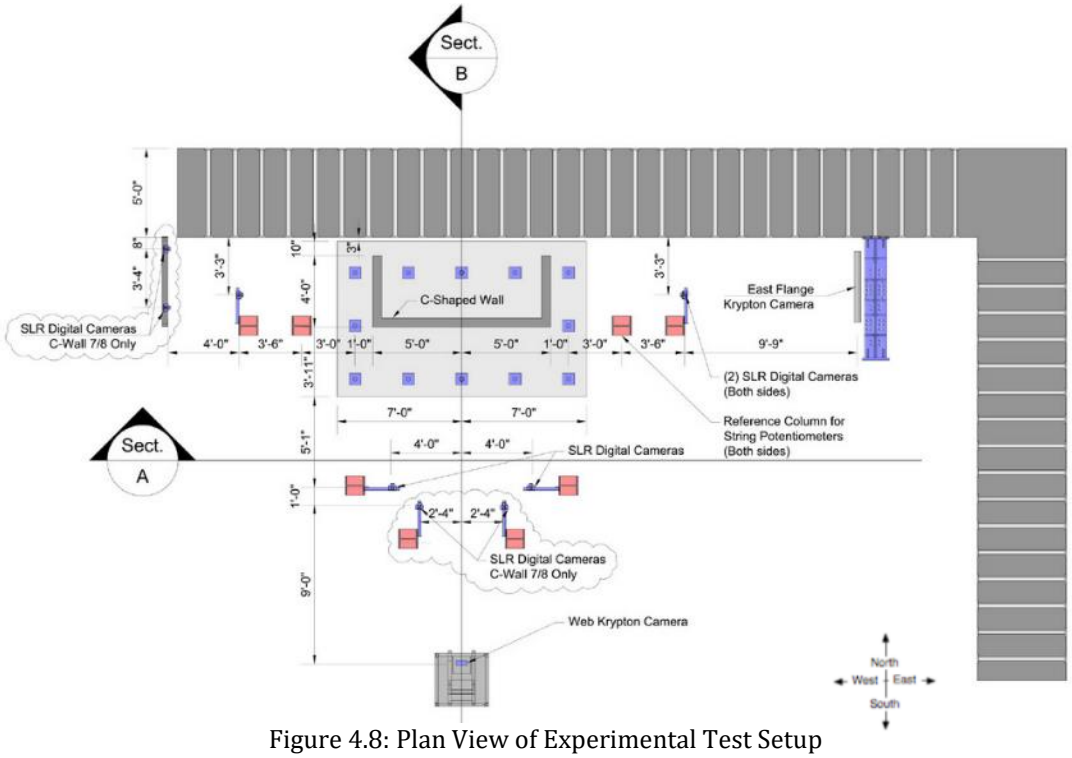

Figure 4.8: Plan View of Experimental Test Setup

4.6.2 Connection of Wall Specimen to Loading Apparatus

An assembly of steel beams and plates are used to mate the wall specimen cap to the LBCB platens (Fig. 4.9 and Fig. 4.10). The specimen wall cap (described in Section 4.4.3) has (34) 1.5-in diameter steel rods that are clamped to 2-in thick steel plates with a clamping force of nearly 45 kips. Attached atop these plates are three wide flange beams (W14x211) which are connected at (60) 1-in diameter high-strength bolts, each with a clamping force of approximately 40 kips. Finally, the beams are connected to the LBCB platens using (84) 1-in diameter high-strength bolts, each with a clamping force of approximately 40 kips.

The connection assembly first is attached to the LBCB platens and then lowered down onto a mixture of Hydrocal/grout on specimen wall cap to create a uniform surface for load transfer between the steel plates and wall cap (Figure 4.11). Hydrocal is a gypsum cement and was used for connection of CWall6 and CWall7; a high-strength grout was used in CWall8 to allow more working

time in making the connection. In all cases, the Hydrocal/grout mix was allowed to cure prior to connecting and post-tensioning the 1.5-in diameter steel rods between the steel plates and the wall cap.

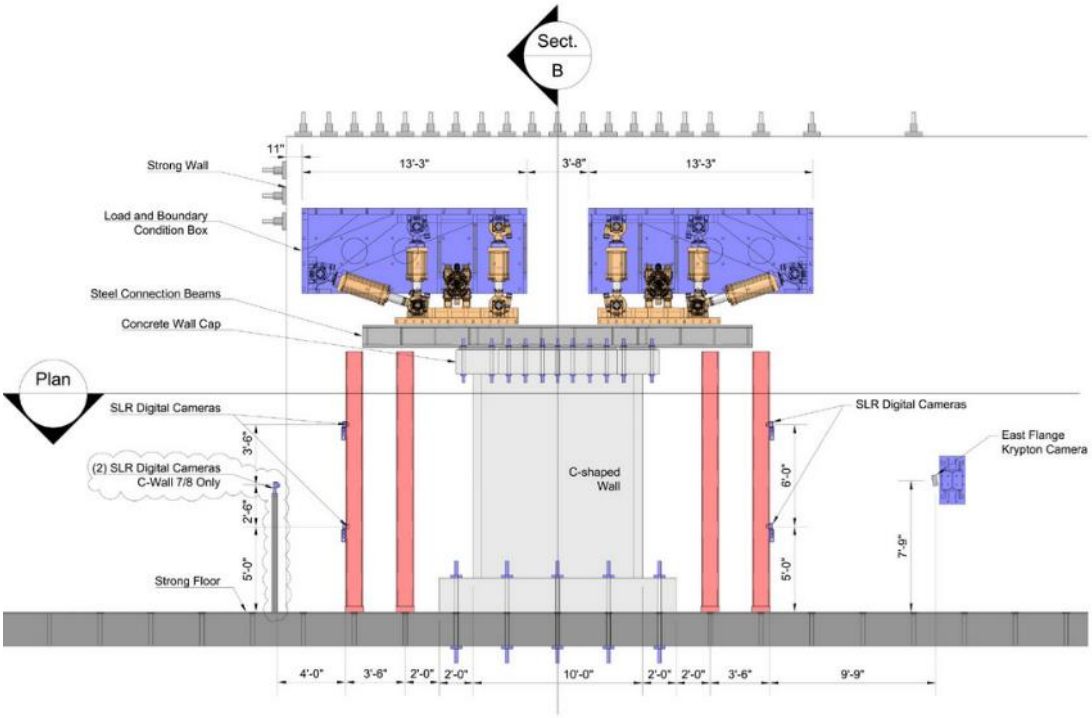

Figure 4.9: Elevation View of Experimental Test Setup

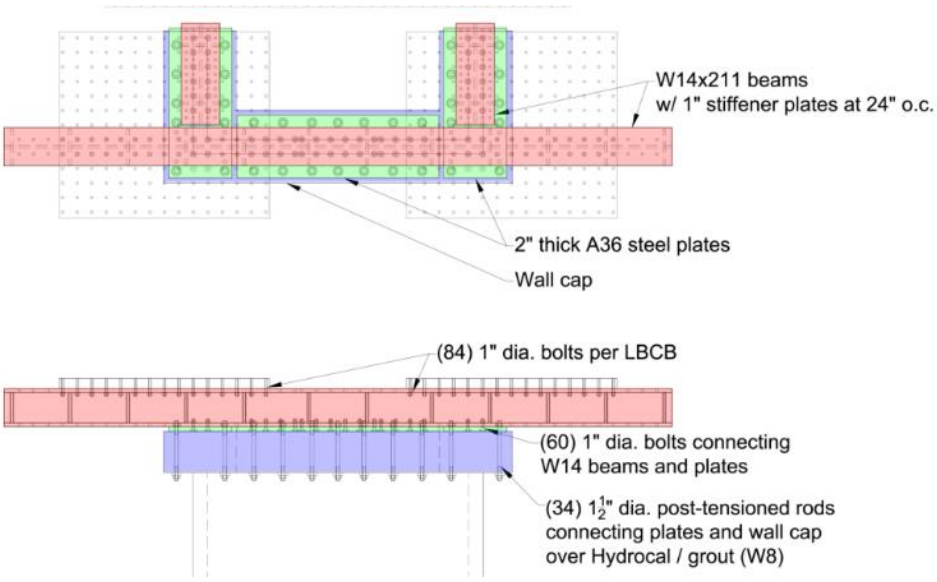

Figure 4.10: Wall Specimen-to-LBCB Connection Assembly Drawing

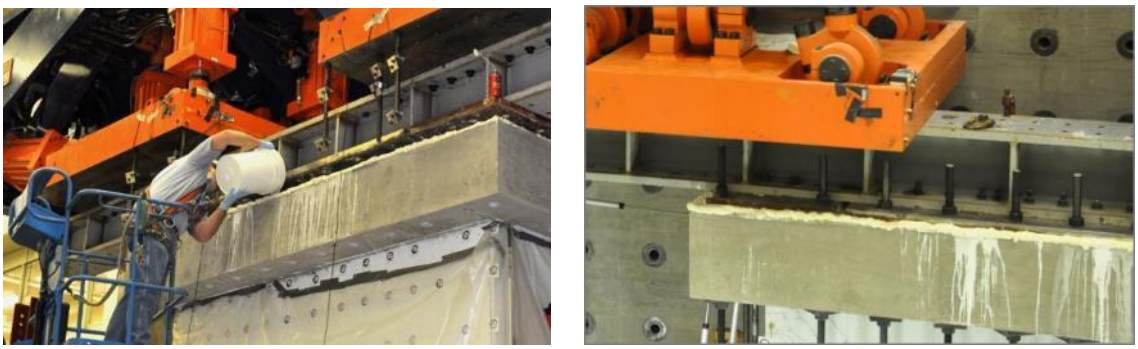

Figure 4.11: CWall 7 Hydrocal Pour/Rod Post-Tensioning

4.7 Load Control & Protocols

4.7.1 Load Control at UIUC MUST-SIM

The LBCB apparatus introduced in Section 4.6.1 is a self-contained six DOF loading unit with six actuators inside a reaction frame (shown in blue in Figure 4.12) that are attached to a steel loading platen (shown in orange in Figure 4.12). The LBCB is able to carry out any combination of six actions (three forces and three moments) and six displacements (three translations and three rotations). Each actuator has a linear displacement transducer and load cell that provides that position and force carried in each of the six actuators, and with mathematical transformation the six DOF Cartesian coordinates for displacement or load can be calculated. Every actuator has a capacity of 225 kips in tension and 311 kips in compression; they are individually identified as "X1" and "X2" for the X-direction, "Y1" for the Y-direction, and "Z1","Z2", and "Z3" for the Z-direction (Figure 4.12).

The LBCB "Mixed-mode" control software allows the LBCBs to be controlled in both displacement and force simultaneously. This enables the control a selection of the six DOFs to be in displacement control and other DOFs in force control, which as implemented during the C-Shaped wall tests.

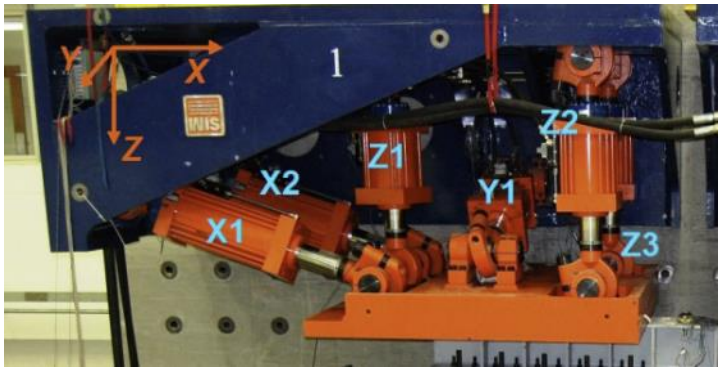

Figure 4.12: LBCB Apparatus

4.7.2 Loading Protocols

4.7.2.1 Introduction

As indicated in Table 4.1 the primary difference between the three C-Shaped wall tests was displacement history. CWall6 was subjected to cyclic uni-directional loading about the strong axis with constant axial load of $0.05f'_cA_g$; CWall7 had a cyclic bi-directional cruciform loading with the same constant axial load; and CWall8 had a cyclic bi-directional cruciform loading again with the same constant axial load under strong axis motion and variable axial load under weak motion to account for coupling action with an identical, simulated C-Shaped wall.

The loading protocol for all three C-shaped wall specimens was based on the prototype ten-story core-wall system subjected to the *ASCE 7-05* [21] equivalent lateral force (ELF) distribution. The test specimens represent the bottom three stories of this ten-story prototype structure as the performance of the upper stories of the wall was assumed non-critical to the global system behavior. The effects of the gravity and lateral loads acting on the upper seven stories of the wall were simulated through application of an overturning moment, shear force, and axial force at the top of the test specimen.

To achieve the quasi-static cyclic displacement history described previously, each step of the displacement history consisted of the application of a lateral translation as well as an axial force and overturning moment. The target axial force and overturning moment were a function of the measured lateral shear from the applied displacement, thus requiring an incremental-iterative approach for determining the converged state of the wall at the end of each step. The applied and measured motions/actions for the two principal axes of the test specimen are conducted about the control point, which corresponds to the geometric centroid of un-cracked wall specimen at the top of the third story (Figure 4.13). The following sections provide an overview of each test's loading protocol; additional details can be found in *Behrouzi et al.* [32].

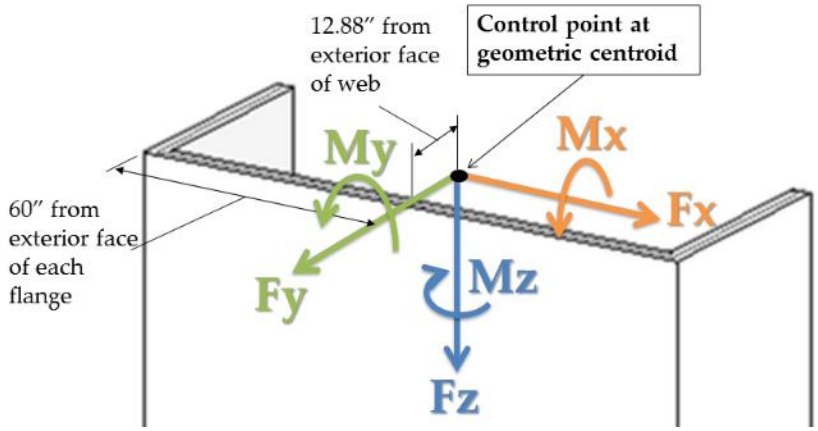

Figure 4.13: Definition of Control Point & Coordinate Axes

4.7.2.2 CWall6 Loading Protocol

The first C-shaped wall test investigated wall behavior under cyclic uni-directional, strong-axis loading with constant axial load of $0.05f'_cA_g$ (306 kips) and moment representative of the prototype structure. The overturning moment to shear (M/V) ratio was held constant at 196.8-in in accordance with the *ASCE 7-05* [21] ELF distribution. Two cycles of displacement were completed at each drift level in the X-direction (Figure 4.14). Maximum displacement demands for displacement cycles were intended to target performance limit states of concrete cracking, yielding of longitudinal reinforcement, nominal flexural strength, concrete spalling and subsequent damage states. The displacement history is shown in Figure 4.15 and Table 4.5

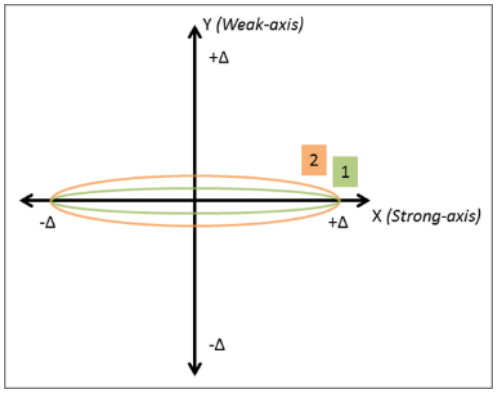

Figure 4.14: CWall6 Uni-directional Loading Pattern

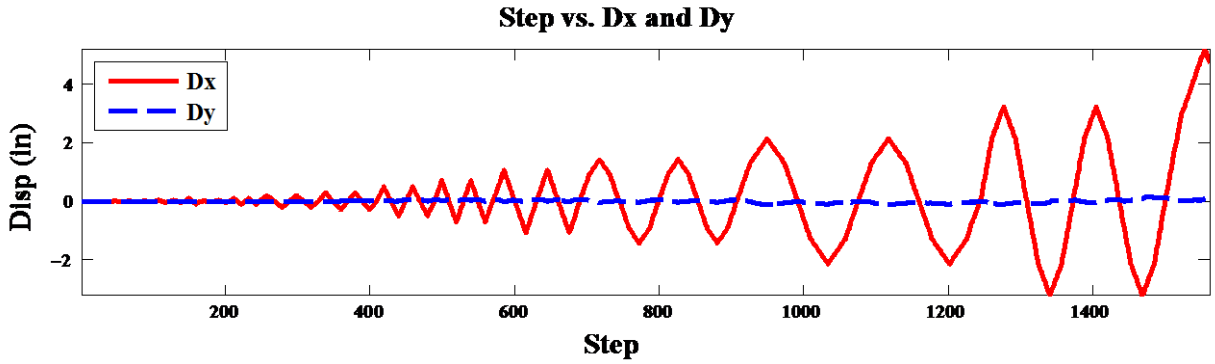

Figure 4.15: CWall6 Plot of Displacement History

Table 4.5: CWall6 Displacement History

Target Limit State	Disp(in)	Drift (%)	# of Cycles
Elastic	0.02	0.014%	1
Cracking	0.04	0.028%	1
25% Yield	0.1	0.069%	2
50% Yield	0.2	0.139%	2
75% Yield	0.3	0.208%	2
100% Yield	0.5	0.347%	2
150% Yield	0.72	0.5%	2
Nominal	1.08	0.75%	2
Damage	1.44	1%	2
Damage	2.16	1.5%	2
Damage	3.24	2.25%	2
Pushover	5.057	3.512%	+X only

4.7.2.3 CWall7 Loading Protocol

The second C-shaped wall test investigated performance under a cyclic bi-directional cruciform loading with axial load of $0.05f'_cA_g$ (306 kips) and M/V ratio of 198.6-in, consistent with CWall6. For the majority of the test, two displacement cycles were completed in each direction at each drift level following the cruciform history, where cycles 1 and 3 are in the strong-axis, X-direction while cycles 2 and 4 are in the weak-axis, Y-direction (Figure 4.16). Towards the end of the test, the displacement capacity of the loading apparatus was reached in the ±Y-direction. To apply increasing demand on the boundary elements of the wall, which are severely loaded under weak-axis Y-direction loading, the cruciform displacement history was replaced with the bi-directional

axis Y-direction loading, the cruciform displacement history was replaced with the bi-directional displacement history where a full displacement cycle in X-direction was conducted while maintaining a constant Y-direction displacement (Figure 4.16). As with CWall6, maximum displacement demands for displacement cycles in both the X- and Y-directions were intended to target performance limit states of concrete cracking, yielding of longitudinal reinforcement, nominal flexural strength, concrete spalling and subsequent damage states. The displacement history is shown in Figure 4.17 and Table 4.6.

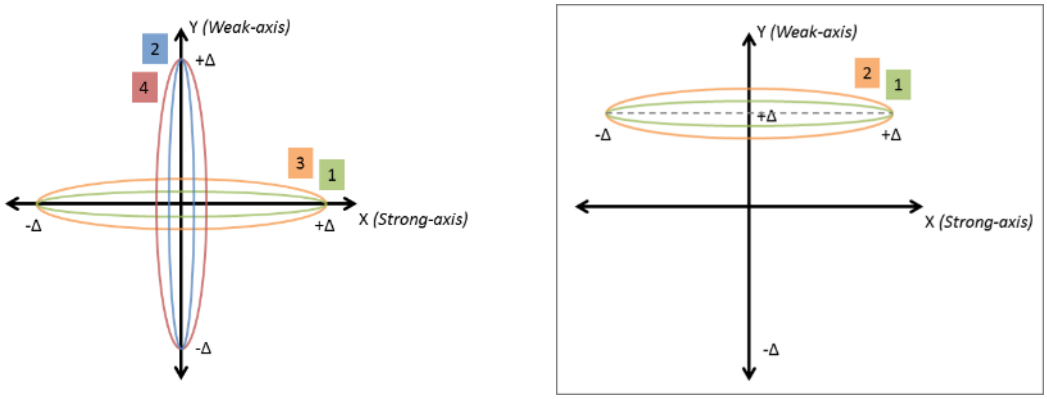

Figure 4.16: CWall7 Bi-directional Loading Patterns

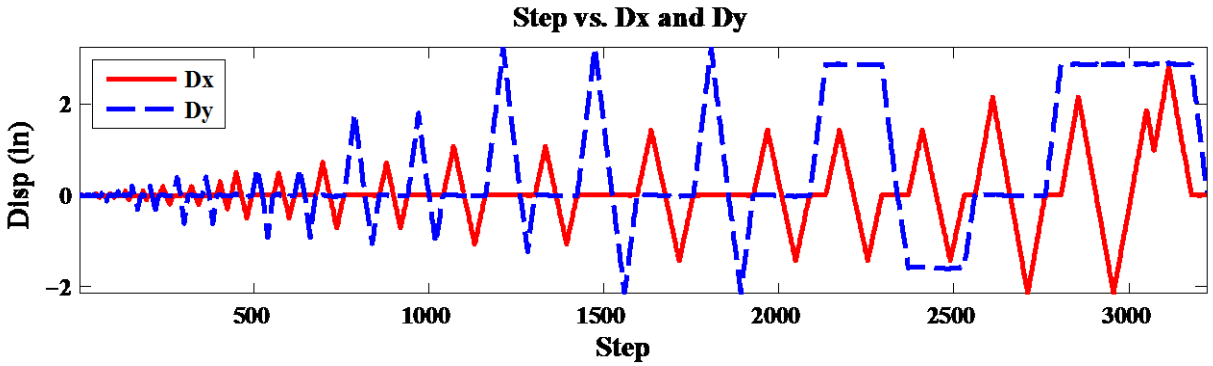

Figure 4.17: CWall7 Plot of Displacement History

Table 4.6: CWall7 Displacement History

Target Limit State	Loading Pattern	Dx (in)	+Dy (in)	-Dy (in)	Dx (%)	+Dy (%)	-Dy (%)	# of Cycles
Elastic	Cruciform	±0.02	0.02	-0.02	0.014%	0.014%	-0.014%	1
Cracking	Cruciform	±0.04	0.08	-0.12	0.028%	0.056%	-0.083%	2
	Cruciform	±0.1	0.2	-0.3	0.069%	0.14%	-0.21%	2
50% Yield	Cruciform	±0.2	0.4	-0.6	0.14%	0.28%	-0.42%	2
75% Yield	Strong Axis	±0.3	---	---	0.21%	---	---	1
100% Yield	Cruciform	±0.5	0.6	-0.9	0.35%	0.42%	-0.63%	2
1/2 Nominal	Cruciform	±0.72	1.8	-1.05	0.50%	1.25%	-0.73%	2
Nominal	Cruciform	±1.08	3.24	-1.22	0.75%	2.25%	-0.85%	1
	Cruciform	±1.08	3.24	-2.14	0.75%	2.25%	-1.49%	1
Damage 1	Cruciform	±1.44	3.24	-2.14	1%	2.25%	-1.49%	1
	Strong Axis	±1.44	---	---	1%	---	---	1
Damage 2	Constant Dy	±1.44	2.88	---	1%	2%	---	1
	Constant Dy	±1.44	---	-1.584	1%	---	-1.1%	1
Damage 3	Strong Axis	±2.16	---	---	1.5%	---	---	1
Damage 4	Constant Dy	±2.16	2.88	---	1.5%	2%	---	1
Pushover +X	Constant Dy	2.81	2.88	---	1.95%	2%	---	1

4.7.2.4 CWall8 Loading Protocol

The third C-shaped wall test investigated the wall performance when considered as part of a bi-directionally loaded coupled core wall system. A cyclic cruciform displacement history was executed with axial load and moment applied at the top of the specimen determined from the *ASCE 7-05* [21] ELF and gravity loads applied to the *complete* coupled core-wall. For displacement cycles in the strong axis, X-direction coupling beams are not activated and the coupled wall response is essentially identical that of an isolated C-shaped wall. Thus, for displacement cycles in the X-direction, a constant axial load equal to $0.05f'_cA_g$ (306 kips) and constant M/V ratio of 196.8-in was applied.

Lateral loading of the core wall system in the weak-axis, Y-direction activates coupling beams resulting in "coupling" of the C-shaped walls which results in tensile loads being applied to one of the C-shaped walls (tension pier) and compression loads being applied to the other C-shaped wall (compression pier). These tension/compression loads affect the flexural stiffness and strength of

the C-shaped walls where individual wall piers develop very different internal story moments and shears. To simulate this in the laboratory test, for displacement cycles in the Y-direction, axial load and moment applied to the top of the specimen were varied. A detailed discussion of the process employed to determine an appropriate protocol for Y-direction loading of the test specimen is described in *Behrouzi et al.* [32], only a general overview will be provided in the following section.

4.7.2.4.1 Determination of Weak-Axis Loading

In order to establish appropriate demand ratios (i.e. ratio of shear, axial and moment demand) for use Y-direction loading for the tension/compression pier, numerical analyses of the ten-story prototype core-wall system subjected to the increasing lateral load and constant gravity load were conducted. The resulting demand ratio versus roof drift histories were simplified for use in testing and ultimately seven different ratios were used at different stages of the test. Demand ratios were varied during the test on the basis of measured response quantities and observed damage. Since the laboratory test specimen represents the bottom three stories of one C-shaped wall pier *without coupling beams* demands were applied at the top of the laboratory specimen to achieve representative demands in the critical first story of the specimen.

Initially, displacement demands in the ±Y-directions were applied at equal magnitudes; however, as testing progressed and the stiffness of the specimen under positive Y-direction loading (compression pier) began to differ substantially from the stiffness of the specimen under negative Y-direction loading (tension pier), it was observed that the loads applied at the maximum ±Y-direction displacement demands did not, when combined, represent an equilibrium state for the core-wall system. In the core-wall system, loads applied to the specimen under ± Y-direction loading would be applied simultaneously to the individual wall piers; thus, applied loads, when combined, should approximately represent an equilibrium state for the core-wall system.

Thus, for subsequent displacement cycles, a force-based approach was used to determine maximum displacements in the ±Y-directions where: (i) the test specimen was first loaded to a target drift demand in the positive Y-direction, such that it became the compression pier, (ii) the axial force and moment demands at the target drift demand were recorded, and (iii) the specimen was loaded in the negative Y-direction until the axial force and moments required for equilibrium of the core-wall system were achieved. The specific load application logic can be found in *Behrouzi et al.* [32]. An outcome of this loading methodology is that the M/V ratio did not remain constant at the value associated with the *ASCE 7-05* [21] ELF distribution for the core-wall system.

The displacement history for CWall8 is given in Figure 4.18 and Table 4.7, where:

$V_{base,CompRatio}$ = Portion of system base shear to the compression pier

$V_{base,TensRatio}$ = Portion of system base shear to the tension pier

$M_{base,CompRatio}$ = Portion of system moment to the compression pier

$M_{base,TensRatio}$ = Portion of system moment to the tension pier

$M_{base,CoupleRatio}$ = Portion of system moment to coupling

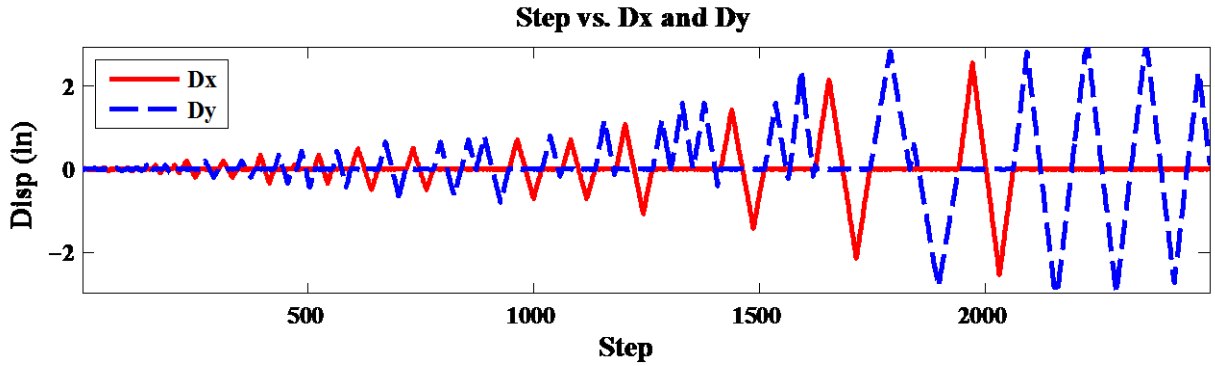

Figure 4.18: CWall8 Plot of Displacement History

Table 4.7 CWall8 Displacement History

Target Limit State	Loading Pattern	Dx (in)	Dy (in)	Dx (%)	Dy (%)	# of Cycles	Mbase Cpl Ratio	Mbase Comp Ratio	Mbase Tens Ratio	Vbase Tens Ratio	Vbase Comp Ratio
Elastic	Cruciform	±0.02	±0.02	0.014%	0.014%	1	0.65	0.25	0.1	0.35	0.65
Cracking	Cruciform	±0.04	±0.04	0.028%	0.028%	2	""	""	""	""	""
	Cruciform	±0.1	±0.1	0.069%	0.069%	2	0.65	0.25	0.1	0.2	0.8
50% Yield	Cruciform	±0.2	±0.2	0.14%	0.14%	2	""	""	""	""	""
75% Yield	Cruciform	±0.35	±0.35	0.24%	0.24%	1	""	""	""	""	""
	Weak axis	0	±0.44	0%	0.30%	2	""	""	""	""	""
100% Yield	Cruciform	±0.5	±0.65	0.35%	0.35%	2	""	""	""	""	""
	+Y only	0	0.711	0%	0.49%	1	""	""	""	""	""
	Weak axis	0	±0.8	0%	0.55%	1	0.6	0.32	0.08	0.3	0.7
Logic change to force target for tension pier											
1/2 Nominal	Strong Axis	±0.72	0	0.50%	0%	1	0.6	0.33	0.07	0.15	0.65
	Comp. Pier	0	0.8	0%	0.55%	1	""	""	""	""	""
	Tension Pier	0	-0.178	0%	-0.12%	1	""	""	""	""	""
	Strong Axis	±0.72	0	0.50%	0%	1	""	""	""	""	""
	Comp. Pier	0	1.2	0%	0.83%	1	""	""	""	""	""
	Tension Pier	0	-0.14	0%	-0.09%	1	""	""	""	""	""
Nominal	Strong Axis	±1.08	0	0.75%	0%	1	""	""	""	""	""
	Comp. Pier	0	1.2	0%	0.83%	1	""	""	""	""	""
	Comp. Pier	0	1.6	0%	1.11%	1	0.6	0.28	0.12	0.25	0.65
	Tension Pier	0	0.067	0%	0.05%	1	""	""	""	""	""
	Comp. Pier	0	1.6	0%	1.11%	1	""	""	""	""	""
	Tension Pier	0	-0.4	0%	-0.28%	1	""	""	""	""	""
Damage 1	Strong Axis	±1.44	0	1.0%	0%	1	""	""	""	""	""
	Comp. Pier	0	1.6	0%	1.11%	1	""	""	""	""	""
	Tension Pier	0	-0.223	0%	-0.16%	1	""	""	""	""	""
	Comp. Pier	0	2.4	0%	1.67%	1	""	""	""	""	""
	Tension Pier	0	-0.168	0%	-0.11%	1	""	""	""	""	""
Damage 2	Strong Axis	±2.16	0	1.5%	0%	1	""	""	""	""	""
	Comp. Pier	0	2.84	0%	1.94%	1	""	""	""	""	""
	Tension Pier		-2.84	0%	1.94%	1	0.6	0.28	0.26	0.6	0.65
Damage 3	Strong Axis	±2.56	0	1.777%	0%	1	""	""	""	""	""
	Comp. Pier	0	2.84	0%	1.97%	1	""	""	""	""	""
	Tension Pier	0	-3.01	0%	-2.09%	1	0.6	0.28	0.24	0.6	0.65
Damage 4	Comp. Pier	0	2.95	0%	2.05%	1	0.6	0.2	0.24	0.6	0.8
	Tension Pier	0	-3	0%	-2.08%	1	0.6	0.2	0.23	0.6	0.8
Damage 5	Comp. Pier	0	2.95	0%	2.05%	1	Fz = 1,000 kips				
	Tension Pier	0	-2.745	0%	-1.91%	1	Fz = -250 kips				
	Comp. Pier	0	2.33	0%	1.62%	1	Fz = 1,000 kips				

4.8 Instrumentation

4.8.1 Instrumentation Overview

A unique feature of the C-Shaped wall tests is the variety and density of instrumentation used to monitor specimen behavior. The instrumentation consisted of traditional and non-contact systems that capture displacement and strain. The traditional sensors consisted of strain gauges applied externally to the concrete and directly to the steel reinforcement within the specimen as well as displacement transducers such as linear variable displacement transducers (LVDTs) and string potentiometers to measure relative and absolute displacements. To gather full-field deformation data, advanced instrumentation methods were utilized including the Nikon Metrology/Krypton 600 Optical CMM system and photographs from high resolution still cameras to be used with photogrammetric techniques. Throughout the tests, a variety of other documentation equipment was employed to record the progression of damage including the use of a roaming camera as well as video and web cameras.

As a note, all of the strain gauges and traditional displacement transducers are utilized with National Instruments data acquisition hardware/software, and the Krypton systems has its own separate data acquisition system.

4.8.2 Strain Gauges

4.8.2.1 Introduction

During testing, strain gauge readings can be used as a verification method that the intended loading is being properly applied as the research team intends, and strain readings serve as one of the primary indicators that certain limit states have been reached such as concrete cracking, steel yield, and progression of plastic behavior. Furthermore, straining in the boundary element reinforcement at displacement peaks became particularly important in the bidirectional tests. These observed strains played a role in determining any modifications that needed for the displacement level and/or load ratios selected for future test cycles to achieve the desired benchmarks along the path to target limit states (i.e. selected percentage of yield or predicted nominal capacity).

Following testing, the data collected from the wide array of longitudinal, horizontal, and stirrup strain gauges distributed throughout the C-Shaped wall specimens provides many analysis opportunities including: strain distributions along vertical or horizontal cross-section; calculation

of variation in curvature over the height of wall; or to evaluate the moment being carried by each wall region.

4.8.2.2 Strain Gauge Types

Each C-shaped wall was heavily instrumented with quarter bridge strain gauges. Two types of Texas Measurements Inc (TML) gauges were utilized: high-elongation 5mm gauges were affixed to the reinforcing bars before tying the rebar cage and casting the concrete, and large general purpose 30mm gauges were applied to the concrete surface after curing.

4.8.2.3 Concrete Strain Gauge Layout

Each wall had 16 (CWall6) to 18 (CWall7 and 8) vertically oriented concrete gauges on the wall surface (Figure 4.19).

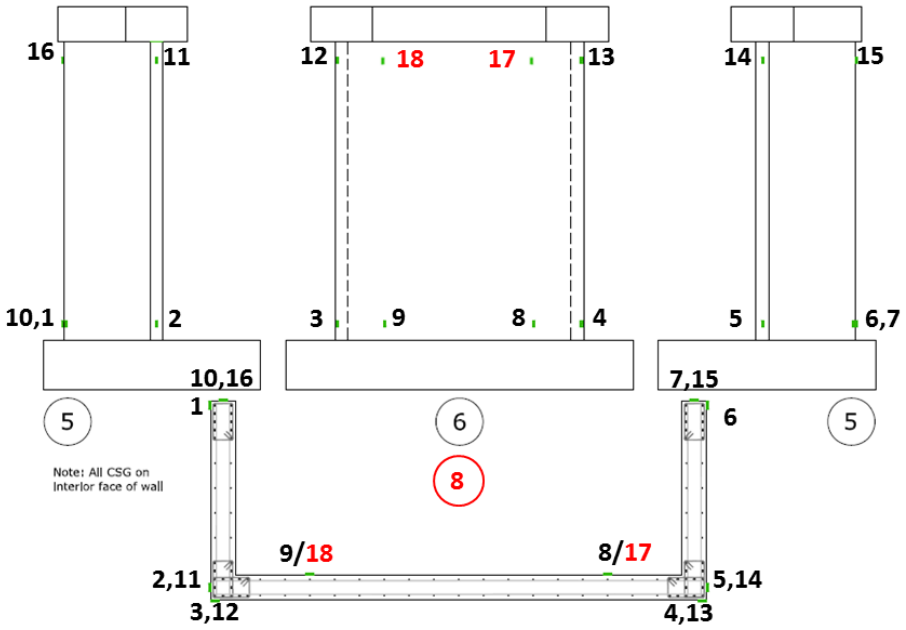

Figure 4.19: Concrete surface gauges (red indicates additions for CWall7 & 8)

4.8.2.4 Steel Strain Gauge Layout

The internal steel gauges are applied at select locations to the longitudinal, horizontal, and stirrup reinforcement (Figure 4.20, Figure 4.21, and Figure 4.22, respectively). A majority of the strain gauges are located in the first floor region where the most wall deformation is anticipated; also, horizontal and stirrup reinforcement only appears in one of the flanges as it is anticipated that there will be symmetric behavior between the two flanges.

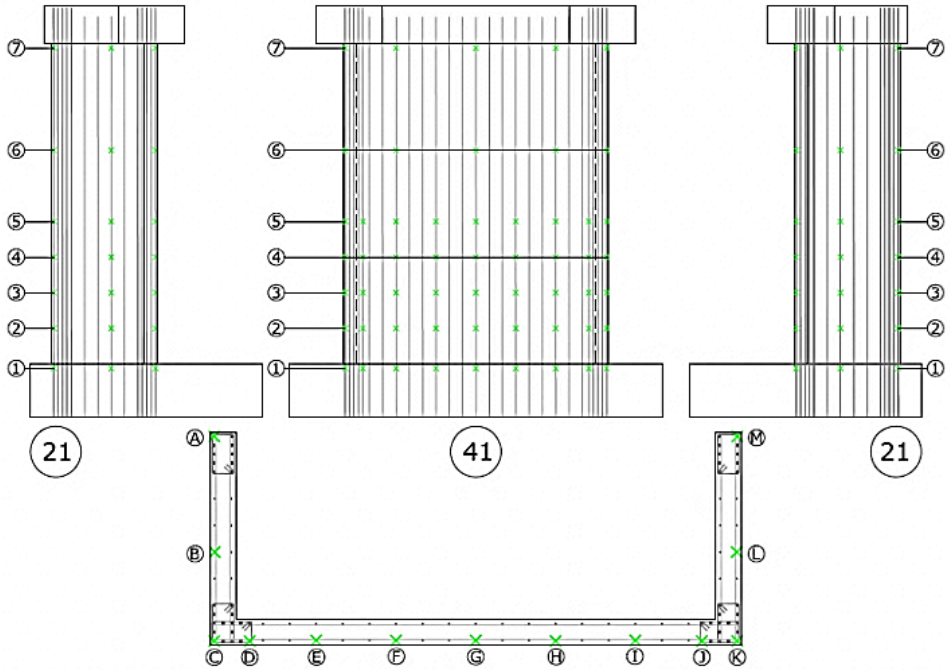

Figure 4.20: Steel gauges on longitudinal reinforcement

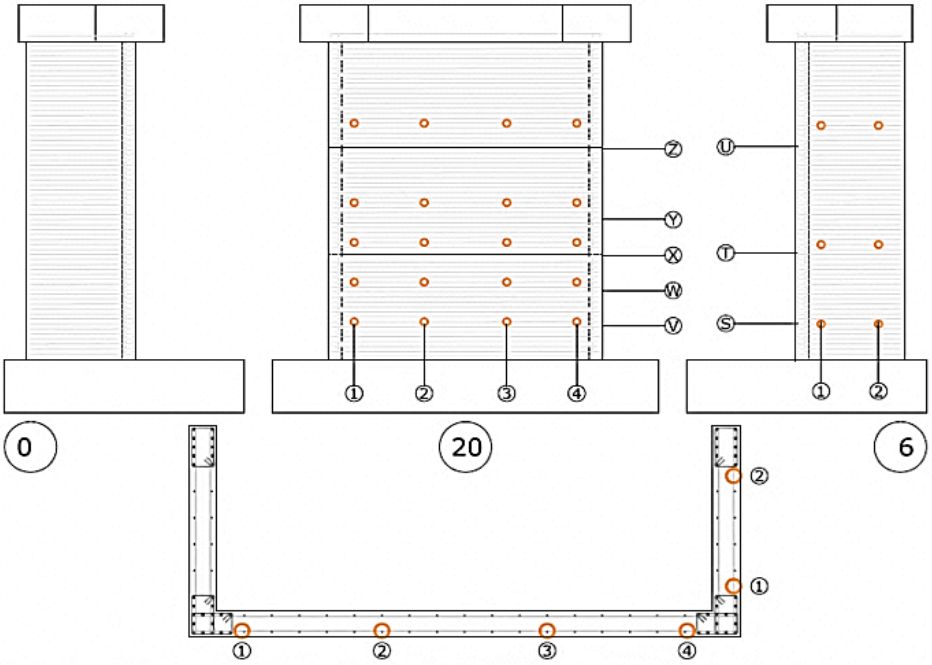

Figure 4.21: Steel gauges on horizontal reinforcement

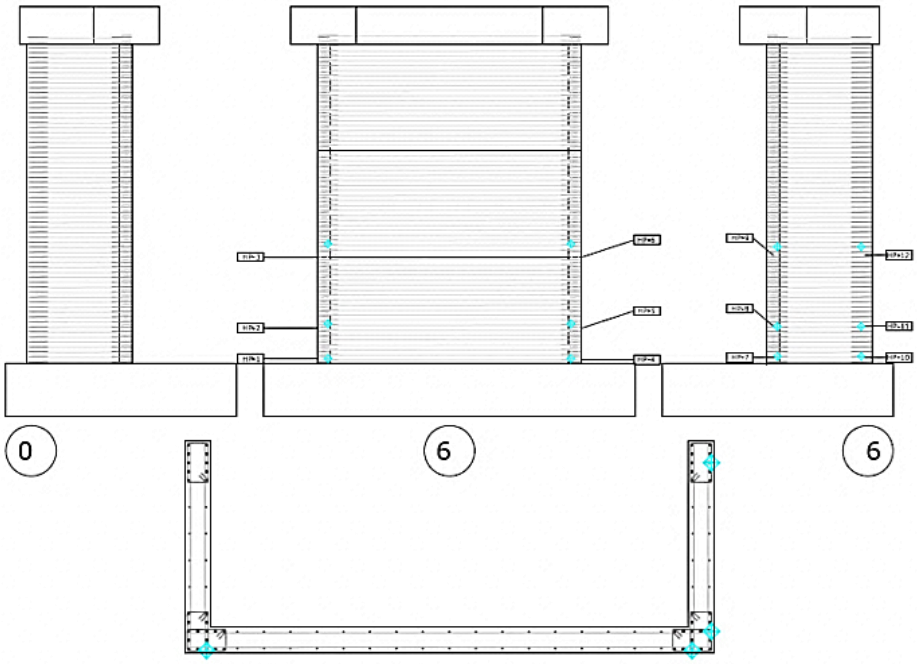

Figure 4.22: Steel gauges on stirrup reinforcement

4.8.3 Traditional Displacement Transducers

4.8.3.1 Introduction

A variety of traditional displacement transducers including linear variable displacement transducers (LVDTs) and string potentiometers are utilized to measure absolute and relative displacement of the test specimen. Perhaps the most critical application of this sensor type is the high-resolution linear potentiometers –referred to as control sensors – that provide information about specimen movement that can be used to determine elastic deformation in the system and is incorporated into the load control algorithm to reach a displacement target. Other absolute displacements are measured along the height of the wall in the in-plane (strong-axis) and out-of-plane (weak-axis) directions using string potentiometers. Also, LVDTs are applied to the foundation to monitor any occurrences of specimen base slip and rotation. Aside from absolute displacement measurements, relative deformation of the specimen is captured by a grid of linear potentiometers affixed to the rear face of the C-Shaped walls at all three floors.

4.8.3.2 High-Resolution Linear Potentiometers for Load Control

The deformations measured in the LBCB boxes may include a component of deformation in the steel reaction frame of the loading unit that is not being realized on the test specimen. A series of high-resolution linear potentiometers are placed on the specimen to measure the actual

deformation of the test structure (Figure 4.23). A mathematical transformation of the change in lengths of all sensors can be used to determine the Cartesian six DOF position. The control sensors are strategically located to be able to capture each DOF. This six DOF position is part of an external control loop ensuring the commanded displacement history is realized on the test structure.

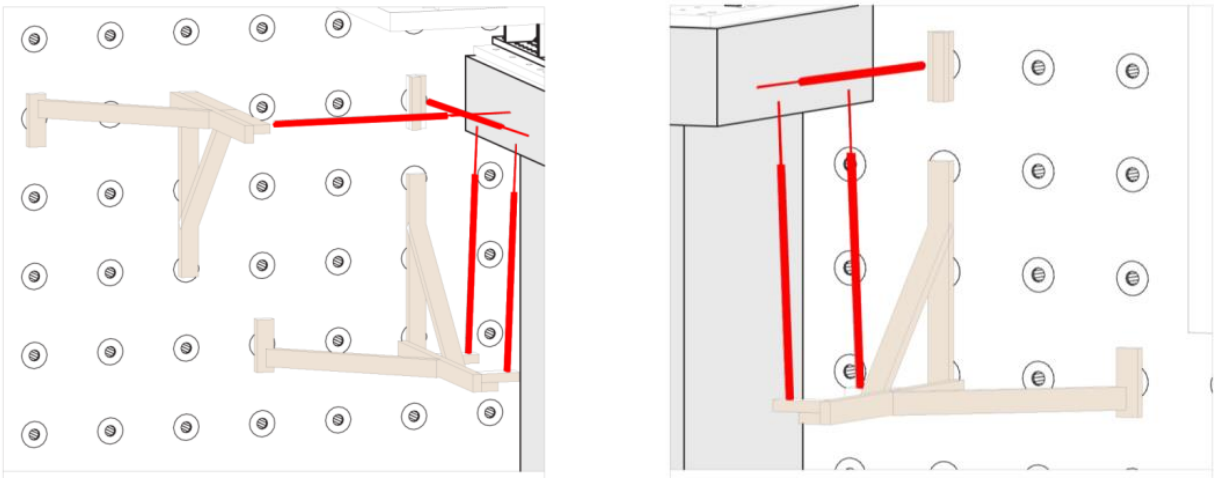

(a) West flange sensors **(b) East flange sensors**

Figure 4.23: Control sensor diagrams

4.8.3.3 Absolute Displacement Measurements

4.8.3.3.1 String Potentiometers

A total of (20) string potentiometers were employed in each of the C-Shaped wall tests, these have standard tension cables and have a full stroke of either 5 or 25-in. Five were installed along a vertical line at each flange/web interface and were oriented to measure strong-axis displacement, while five were attached to the back of each flange to monitor weak-axis motion (Figure 4.24).

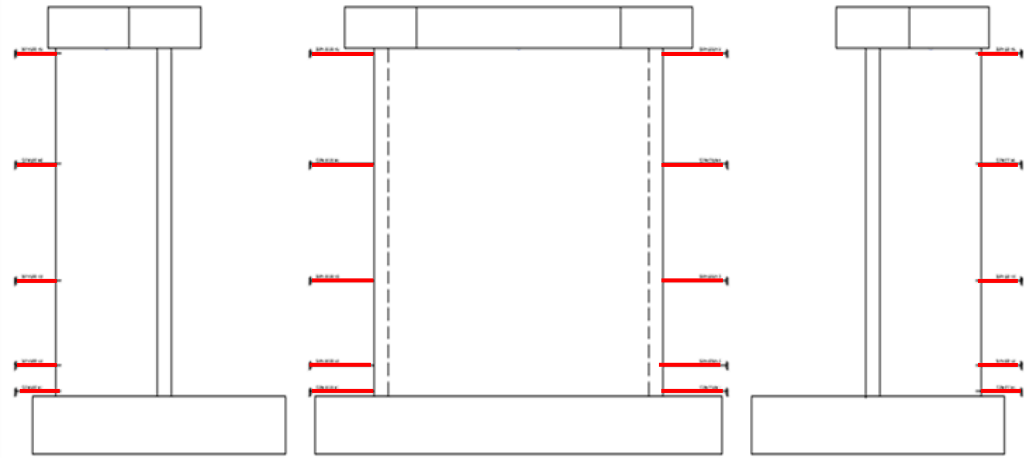

Figure 4.24: String Potentiometers

Absolute measurements from string potentiometers are useful in understanding global response of the wall specimens during testing including rotation of the specimen. Following testing, absolute displacements from these sensors can provide insight about displacement distributions or for flexural stiffness evaluations.

4.8.3.3.2 LVDTs to Monitor Foundation Slip/Rotation

In total there are (4) LVDTs mounted to the foundation block, one vertical and one horizontal on each flange side. These sensors have a stroke of 2 or 4-in and are used to monitor any slippage at the specimen connection to the strong floor, and to ensure that base fixity is maintained.

4.8.3.4 Relative Displacement Measurements

On the reverse of the C-Shaped wall, a grid of linear potentiometers was used to measure relative displacements, generally over large gauge lengths. The measurement system was able to capture deformation data for both flanges and the wall web at all three floor levels. Gauges had a 1, 2, 6 or 8-in stroke length and were primarily oriented in vertical and diagonal directions (Figure 4.25). The gauges were mounted to threaded posts anchored in the wall; in many cases the full pin-to-pin location between threaded rods was achieved by fabricating aluminum extensions for the linear potentiometers.

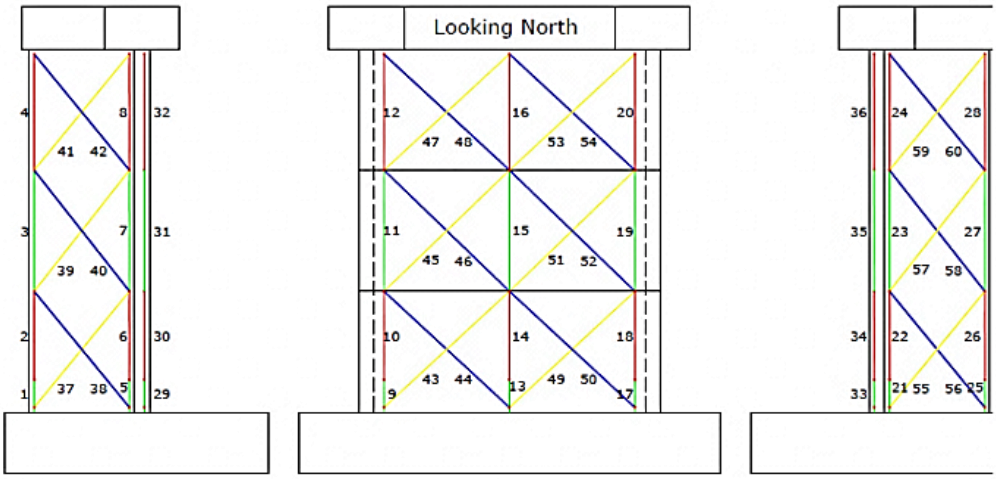

Figure 4.25: Linear Potentiometers for Relative Displacement Measurement

The diagonally oriented sensors provide a measure of average shear deformation for the wall specimens, while the vertically oriented linear potentiometers can provide vertical strain and rotation about the x- or y-axis.

4.8.4 Advanced Instrumentation Methods

4.8.4.1 Introduction

There are two non-contact measurement techniques employed in the C-Shaped wall tests: the Nikon Metrology/Krypton Optical CMM system and close-range digital photogrammetry (the latter is used in CWall7 & 8 only). These are both employed to capture full-field displacement data that would not be possible using the traditional systems mentioned previously. By developing a grid pattern on the specimen using either LED emitters or coded photogrammetric targets, the X, Y, and Z coordinates of these points can be determined for each load step along the test history. Each of these targets can be treated as a node of a quadrilateral finite element where the absolute displacement measurements can be used to determine principal tension, compression, and shear strains. These instrumentation methods have even helped researchers evaluate crack widths and angles by coupling strain information with crack map data.

4.8.4.2 Nikon Metrology/Krypton Optical CMM System

The Krypton system has three cameras mounted to a fixed unit and uses triangulation principles to measure the position of infrared signals emitted by light emitting diodes (LED) mounted to the wall specimen (Figure 4.26).

Figure 4.26: Nikon Metrology/Krypton K600 Optical CMM System

On each C-Shaped wall two of these camera units were utilized, one that captured the bottom two floors for the wall web and another for the east flange side. LEDs are laid out in a typical grid on each of this faces (Figure 4.27) where the coordinate systems for the two Krypton cameras are independent of one another.

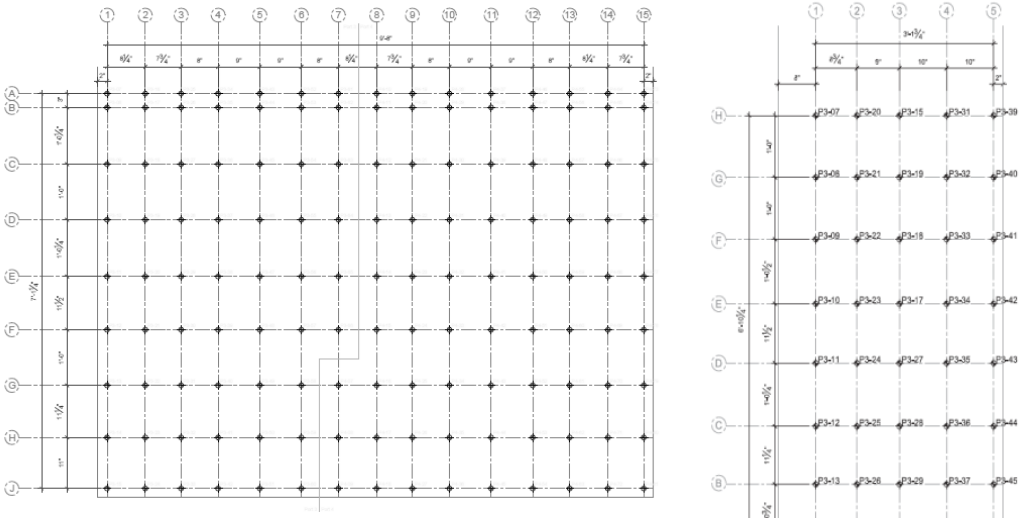

Figure 4.27: Typical Layout of Nikon Metrology/Krypton LEDs (left) web (right) east flange

The Krypton system enables real-time evaluation of displacement profiles and rotations, among other applications.

4.8.4.3 Close-range Digital Photogrammetry

Photogrammetry involves extracting three-dimensional coordinates of specific points on the wall specimen's surface. This technique works based upon the principles of feature recognition and triangulation. The procedure involves obtaining several digital photographs of the specimen at the completion of each load step which are stored for later processing through a photogrammetric

software package. These programs first recognize the special features (targets) in images, then cross-reference photographs to create relationships between corresponding features in at least three images to be able to finally solve spatial locations for points on the wall. Aside from providing three-dimensional displacement data, photogrammetry enables the vital task of creating crack maps. Cracking is an important indicator of the flow of forces in reinforced concrete structures; when reaching new displacement levels researchers manually mark these cracks on the wall. The photogrammetric targets serve as reference points so that a collection of photographs can be stitched together for a particular load step.

For C-shaped wall tests CWall7 & 8 a photogrammetric technique that utilizes a software packaged called PhotoModeler was implemented. Researchers applied ringed automatically detected (RAD) targets on the wall specimen, this target type which allows for a large number of unique targets and exhibits robustness in the solution process. Both the west flange and web were instrumented with a grid of these 2.75-in by 3-in targets that were generally spaced at 9-in horizontally and 11-12 inches vertically along the height of the wall, resulting in a total of 260+ measurement locations (Figure 4.28- 4.29). The target itself consists of a 12mm diameter high contrast dot that has a distinct ring pattern around it which can be automatically detected and referenced between photos by PhotoModeler. To capture the movement of these targets throughout the test required eleven calibrated high-resolution still cameras. Also critical to the photogrammetric project is the use of reference targets, both for the web and flange a fixed bracket is set up with three targets oriented perpendicularly to establish the x- and y-axis of the target coordinate system. These targets remain stationary throughout the duration of the test and are utilized in the solution process to determine the motion of the measurement points on the wall specimen.

4.8.5 Other Documentation Methods

Aside from the previously mentioned instrumentation techniques that collect quantitative data, the research team has also taken advantage of array of photography (roaming and still cameras) and video equipment (standard and web cameras) to monitor and document changes in specimen behavior. These methods are used to track global and local progression of cracking including location, orientation, and width; onset and progression of spalling/delamination; separation of the wall-foundation interface; and reinforcement buckling or fracture. These records of damage over the loading history allow comparisons between current and prior C-shaped wall tests and can contribute to decisions regarding the loading protocol during testing.

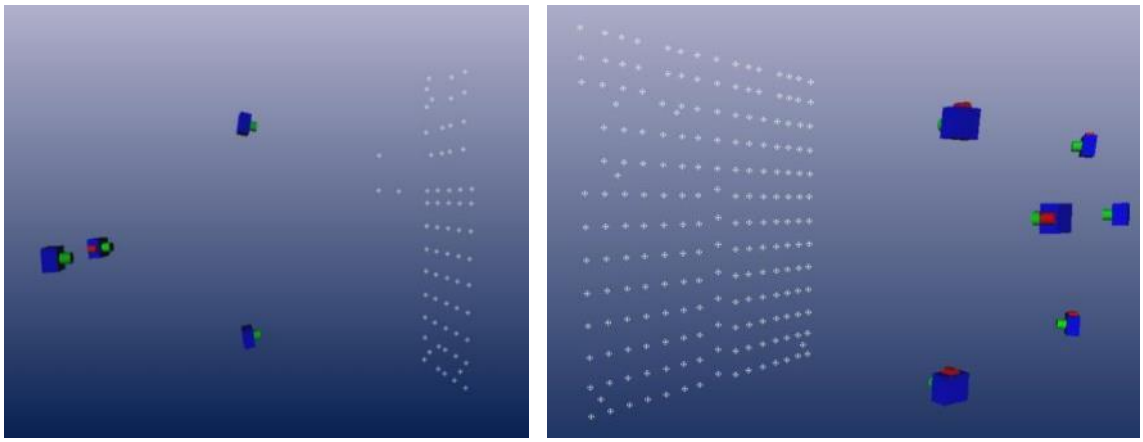

Figure 4.28: PhotoModeler Solution for camera stations and targets (left) west flange, (right) web

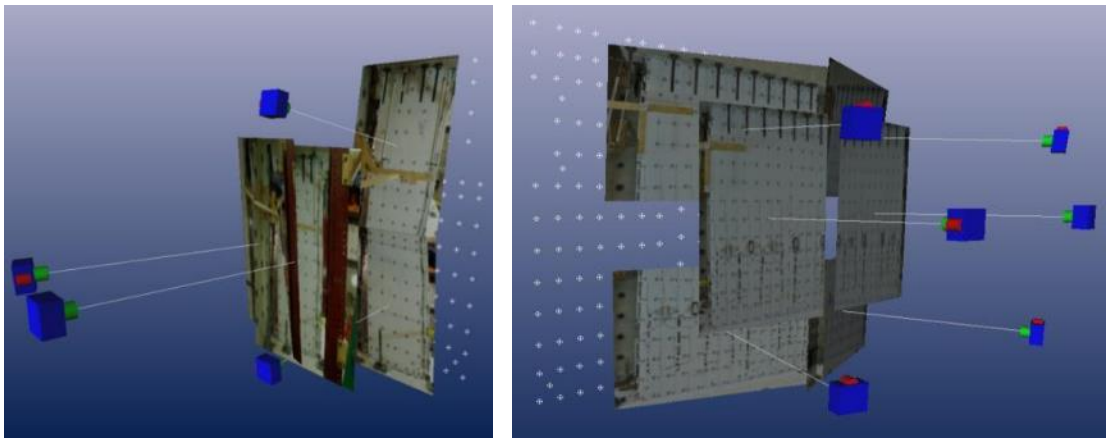

Figure 4.29: PhotoModeler Solution showing individual image contribution (left) west flange, (right) web

4.8.6 Data Acquisition System

With the multiple forms of instrumentation described in Section 4.8, it is relevant to note that the UIUC MUST-SIM software architecture was developed so the entire project is overseen by the Simulation Coordinator (SimCor) which takes a researcher's loading protocol and breaks it up into discrete load steps. At the completion of each load step, SimCor sends trigger messages to collect to each data acquisition program to collect data. This includes the in-house Labview program IlliDAQ that works with the National Instruments software (NiMAX); the Camera Plugin that triggers all the still cameras; and the Krypton Plugin that triggers both Krypton cameras.

5 SUMMARY OF KEY EXPERIMENTAL OBSERVATIONS FROM THE THREE C-SHAPED WALL EXPERIMENTS

5.1 Introduction

Chapter 5 provides a summary of key observations from the three reinforced concrete C-Shaped wall tests that were introduced in Chapter 4 (CWall6, CWall7, and CWall8). A more complete dataset for each of these experiments can be found at the NEES Project Warehouse referenced under the title "NEESR-SG Behavior, Analysis, and Design of Complex Wall Systems" (hereafter referred to as the "Complex Walls Project") [117]. Section 5.2 serves as an introduction to the experimental wall response by tabulating the strong-axis drift level associated with damage limit states. Section 5.3 outlines the general response of each wall test with respect to damage progression. Section 5.4 compares global wall behavior by examining similarities and differences in failure mechanism, shear and flexural demand/capacity, and load-deformation response. Section 5.5 presents the results of more detailed data analysis including displacement profiles, strain gauge yield maps, and strain fields that provide additional insight into the walls' performance. Section 5.6 highlights the most important conclusions from the experimental observation, global wall behavior, and detailed data analyses.

5.2 Summary of Experimental Wall Response

The C-shaped wall experiments were conducted to advance current knowledge of slender, non-planar wall performance. Complex wall configurations are frequently used in the design of modern buildings, yet the code has a limited treatment of this category of structural members. Specifically, the experiments were developed to examine the response of C-shaped wall configurations and the impact of uni- versus bi-directional loading, and bi-directional loading with coupling.

Table 5.1 summarizes the maximum positive historic strong-axis drift associated with each damage limit state for the three C-shaped wall specimens. It is important to note that CWall7 is subject to higher weak-axis drift demands than CWall8 for a majority of the loading protocol; this impacts the occurrence of damage limit states.

Table 5.1: Summary of Strong-Axis Drift Associated with Damage Limit States

	CWall6	CWall7	CWall8
	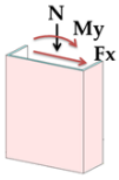	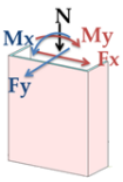	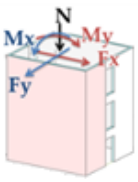
0.50% X-Drift	Cracking	Cracking	Cracking
0.75% X-Drift	Cracking - -	Cracking Cosmetic Spalling Exposed Rebar	Cracking Cosmetic Spalling -
1.00% X-Drift	Cracking - - - -	Cracking Cosmetic Spalling Exposed Rebar Bar Buckling Web Bar Fracture	Cracking Cosmetic Spalling - Bar Buckling Web Bar Fracture
1.50% X-Drift	Cracking Cosmetic Spalling Exposed Rebar Bar Buckling Web Bar Fracture - -	Cracking Cosmetic Spalling Exposed Rebar Bar Buckling Web Bar Fracture BE Bar Fracture Core Crushing	Cracking Cosmetic Spalling Exposed Rebar Bar Buckling Web Bar Fracture - Core Crushing

5.3 General Response of Walls

5.3.1 CWall6 Test Results

The CWall6 test was conducted to inform researchers about the behavior of the C-shaped wall configuration when subject to uni-directional, strong-axis loading and serve as a baseline for comparison when evaluating the subsequent bi-directionally loaded tests, CWall7 and CWall8. In terms of cross-section and loading protocol, there was only one similar wall test (IleX specimen from *Ile & Reynouard* [101]) found during the review of prior experimental programs in Chapters 2-3. In comparison the CWall6 specimen is likely more representative of modern design in two regards: (i) the vertical web reinforcement ratio is compliant with *ACI 318-14* [18], and (ii) the more slender cross-sectional aspect ratio (l_w/t_w) is consistent with current West Coast seismic design.

The damage progression for CWall6 is as follows:

Flexural cracking initiated in the bottom two stories of the wall flanges at 0.02% X-drift, followed by diagonal shear cracking in the web at -0.10% X-drift. Additional flexural cracking was observed in the web boundary element at a uniform spacing coinciding with confining hoop locations.

- Strain gauges on longitudinal reinforcement indicated the yielding of multiple No. 4 bars in the boundary elements and No. 2 bars in the flanges during the 0.35% X-drift cycle.
- During the 0.75% X-drift cycle, vertical cracking developed along the interior edge of flange boundary elements and separation at the wall-foundation interface became apparent.
- During the 1.49% X-drift cycle, numerous No. 2 bars in the web and flanges had ruptured, significant cover spalling occurred in the corner boundary elements, and No. 4 bars in the East flange boundary element had begun buckling.
- During the second cycle at 2.25% X-drift, while approaching the negative peak displacement, a large number of No. 4 bars in the East flange boundary element ruptured leading to a drop in wall strength. Significant web sliding and some core crushing in corner boundary elements were observed.
- A final pushover was conducted. The final failure occurred at +3.52% X-drift as a result of severe buckling of No. 4 bars in the East flange boundary element and successive rupturing of No. 4 bars in West flange boundary element.

CWall6 was able to reach a maximum base moment of $0.95M_n$ and the maximum average shear stress demand was $4.26\sqrt{f'_c}A_{cv}$ psi. Loss of lateral strength was due to buckling-rupture of longitudinal reinforcement in corner boundary elements with secondary contributions from frame action, sliding along the web, and slipping/fracture of boundary element confining reinforcement. There was also notable out-of-plane shear demand on the flanges as a result of sliding and No. 2 bar fracture in the wall web. Fig. 5.1 shows images of CWall6 at the end of the test. Fig. 5.2 shows a plot of normalized shear force versus third story drift with the key performance limit states; each of the performance limit states are defined in the loading protocol in Fig. 5.3.

(a) West Flange (b) Web (c) East Flange

Figure 5.1: CWall6 failure images

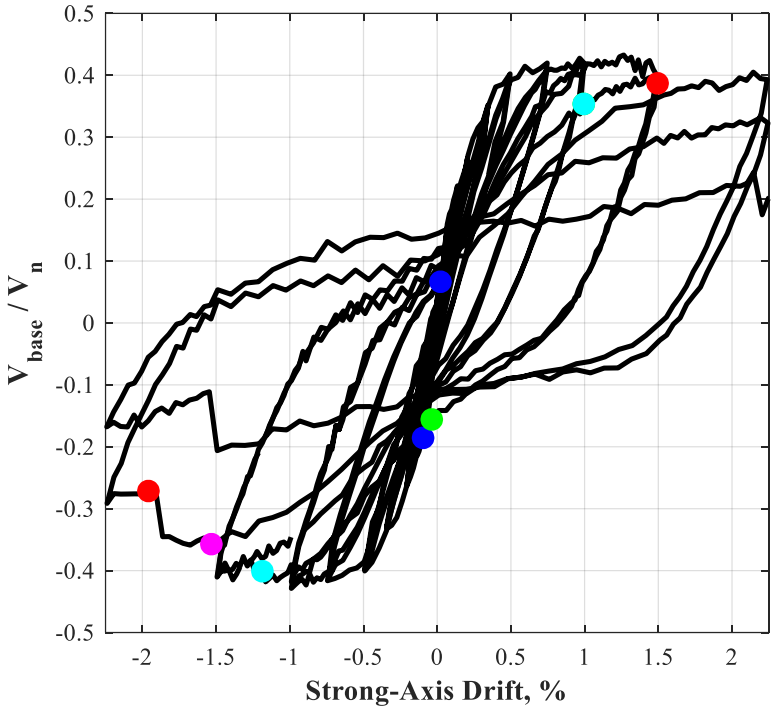

Figure 5.2: CWall6 Normalized Shear Force versus Third Story Drift for Strong-axis Loading
(Refer to Fig. 5.3 for damage states associated with each marker)

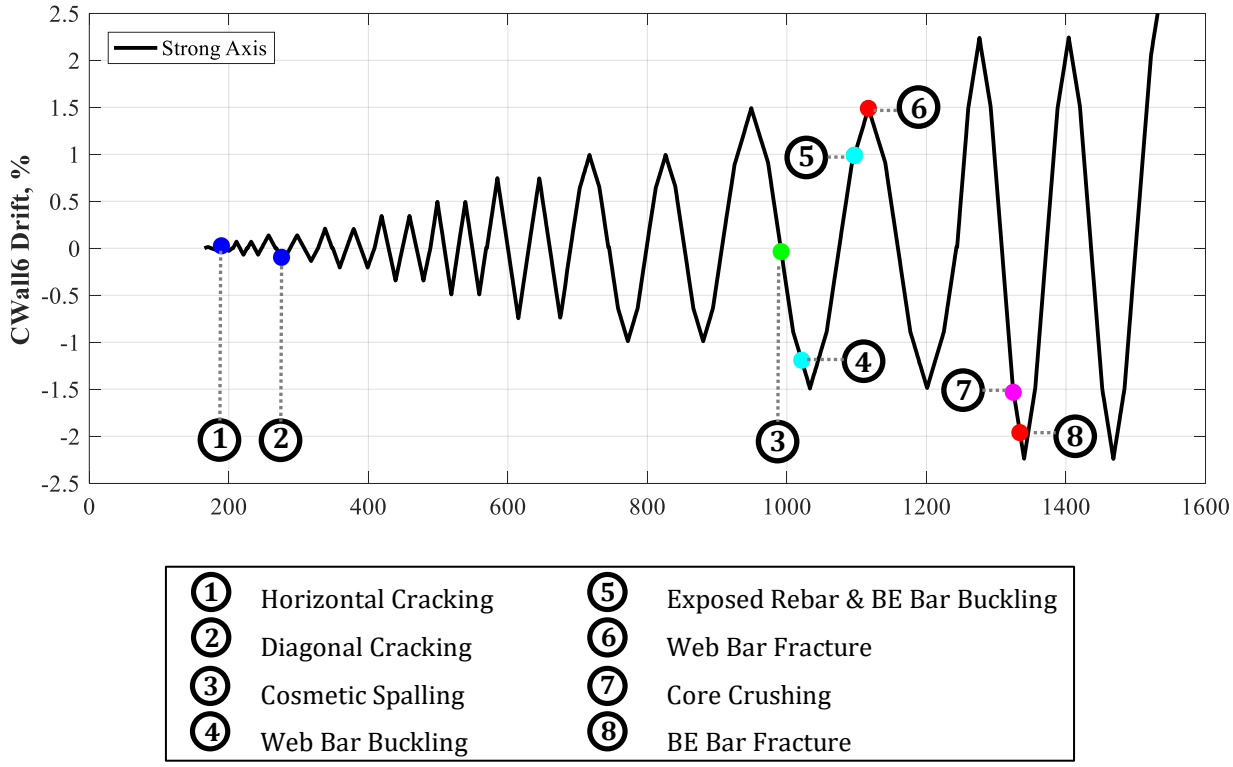

Figure 5.3: CWall6 Damage Limit States

5.3.2 CWall7 Test Results

The CWall7 test examined C-shaped wall behavior when subject to cruciform bi-directional loading and constant axial loading. It augments the existing data-set of isolated C-/U-Shaped wall tests summarized in Chapter 2 and 3 (IleXY from *Ile & Reynouard* [101] and TUA/TUB from *Beyer et al.* 2008 [34]) enabling researchers to further examine how bi-directional loading and specific design parameters effect non-planar wall performance. It should be noted for the following damage description that weak-axis positive/negative direction motion is defined as indicated in Fig. 4.16.

The damage progression for CWall7 is as follows:

- Flexural cracking initiated in the bottom two stories of the wall flanges at 0.03% X-drift, followed by diagonal shear cracking in the web at 0.07% X-drift. Y-direction loading consisted of reopening of these cracks, new horizontal and diagonal cracks due to weak-axis loading was first noted at +0.06% and +0.14% Y-drift, respectively.
- Strain gauges on longitudinal reinforcement indicated the yielding of multiple No. 4 bars in the bottom two floors of boundary elements in each direction and No. 2 bars in the web and flanges during the 0.35% X-drift (+0.42% and -0.63% Y) cycles. Separation at the wall-foundation interface also became apparent.
- During the 0.75% X (+2.25% and -1.49% Y) drift cycle, some No. 2 bar buckling was noted in the rear curtain of longitudinal reinforcement in the web, resulting in cover spalling. Additional spalling was observed in both flange toes about two feet above the footing.
- During the 1% X (+2% and -1.1 Y) drift cycles, numerous No. 2 bars in the web had ruptured, and No. 4 bars in the boundary element had begun buckling.
- During the X-direction pushover to 1.9% X drift (while maintaining +2% Y drift), approximately five No. 4 bars in the West flange boundary elements fractured. Loss of core confinement was extensive in corner boundary elements and buckling of longitudinal rebar in the East boundary elements was significant. There was one instance of hoop fracture in the Northeast corner boundary element.

CWall7 was able to reach a maximum base moment of $0.93M_n$ in the strong-axis direction, $0.88M_n$ for the positive weak-axis direction, and $1.0M_n$ for the negative weak-axis direction. The maximum average shear stress demand in the strong-axis direction was $3.98\sqrt{f_c'}A_{cv}$ psi, with stress demands in the positive weak-axis direction of $1.31\sqrt{f_c'}A_{cv}$ psi and negative weak-axis direction of $2.18\sqrt{f_c'}A_{cv}$ psi. Again, loss of lateral strength was attributable to buckling-rupture of longitudinal

reinforcement in corner boundary elements with secondary contributions from frame action, sliding along the web, and slipping/fracture of confinement reinforcement. As with CWall6, the sliding along the large separation that formed at the wall-footing interface resulted in considerable out-of-plane shear demand on the flanges and No. 2 bar fracture in the wall web. Images of the CWall7 after the +X-direction pushover failure can be seen in Fig. 5.4. A plot of normalized shear force versus third story drift for both X- and Y-direction (strong-axis and weak-axis) loading with the key performance limit states is shown in Fig. 5.5. Each of the performance limit states are defined in the loading protocol provided in Fig. 5.6.

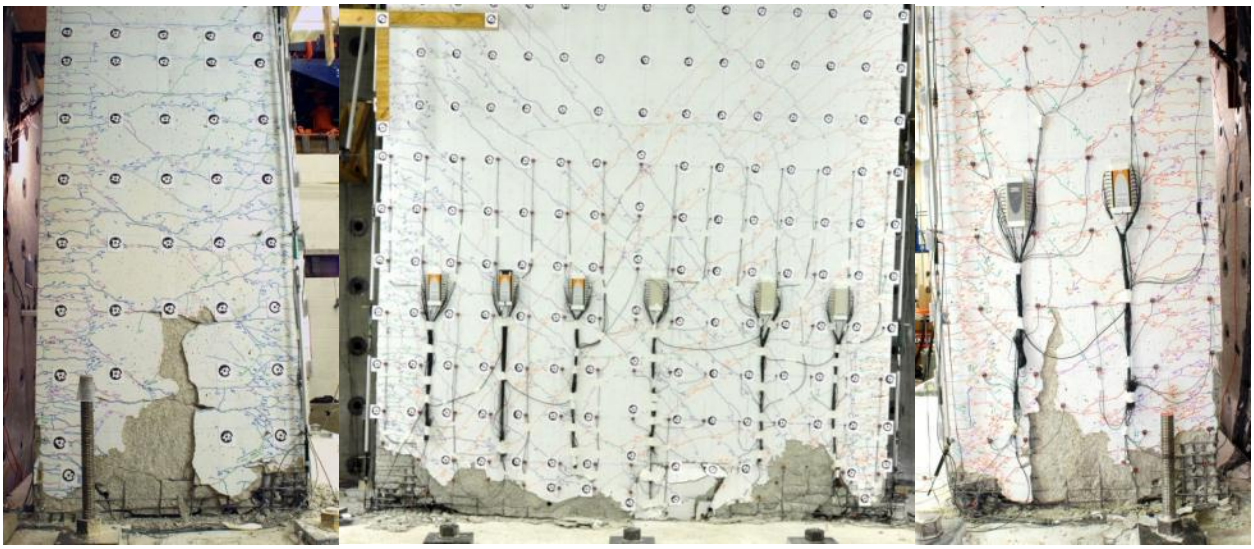

(a) West Flange (b) Web (c) East Flange

Figure 5.4: CWall7 failure images

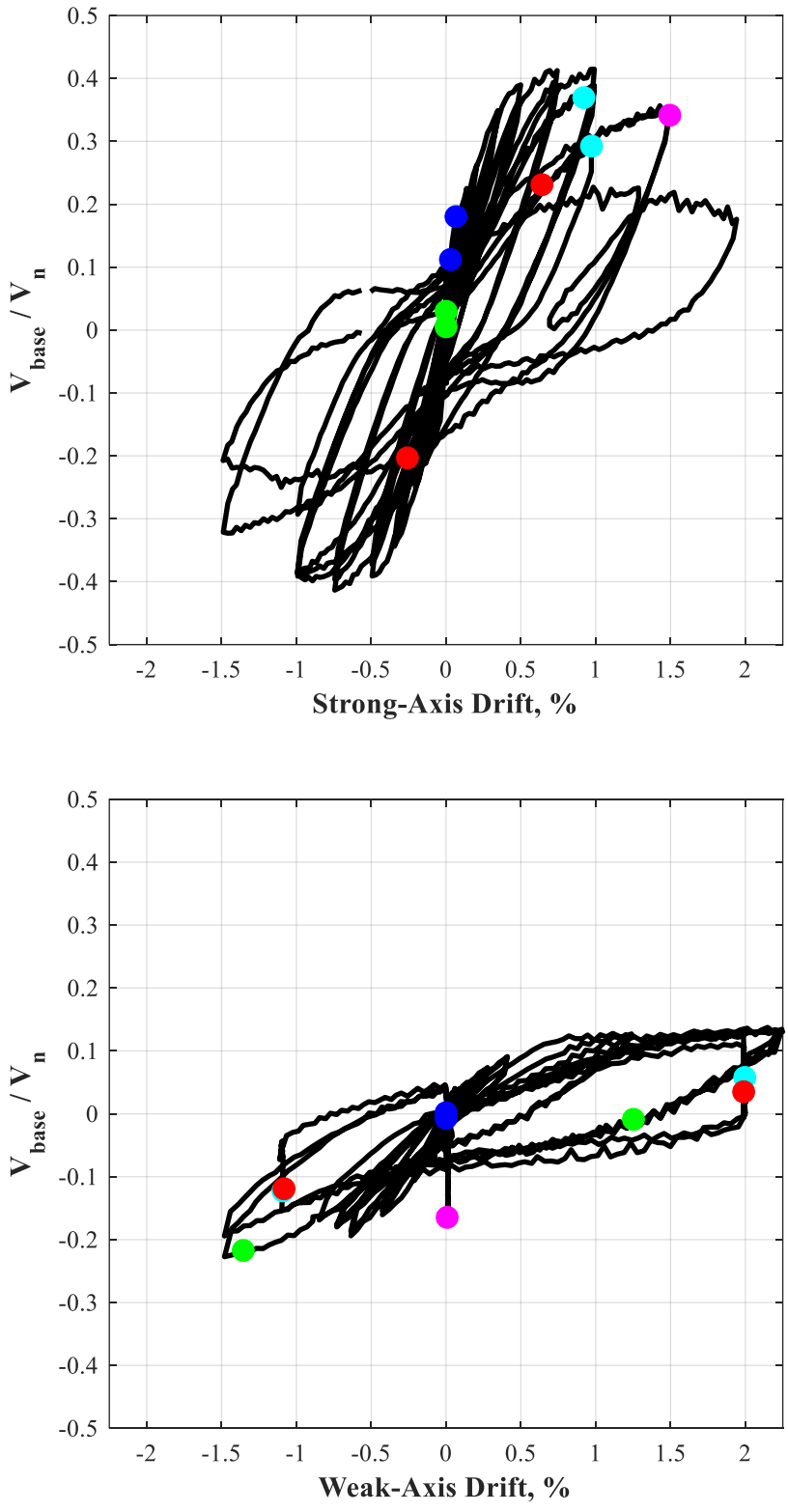

Figure 5.5: CWall7 Normalized Shear Force versus Third Story Drift: (Top) Strong-axis, (Bottom) Weak-axis
(Refer to Fig. 5.6 for damage states associated with each marker)

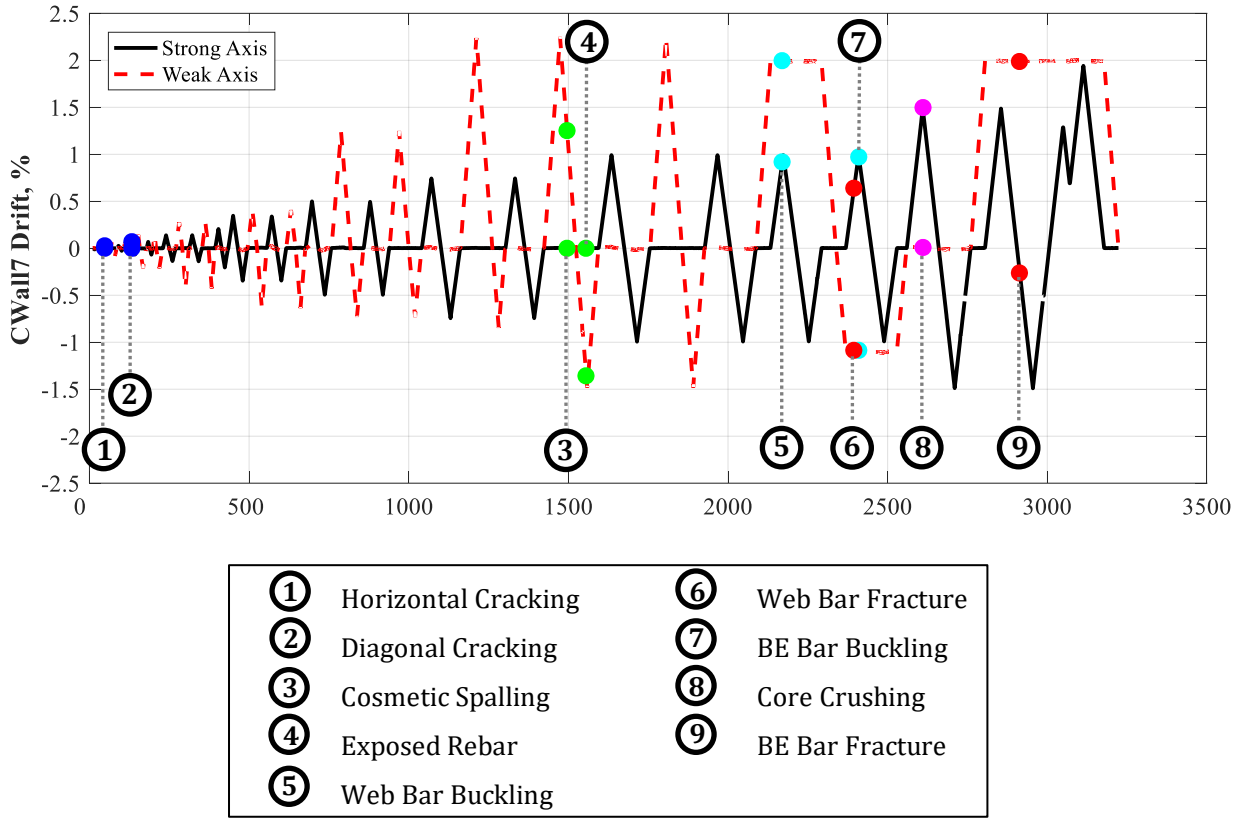

Figure 5.6: CWall7 Damage Limit States

5.3.3 CWall8 Test Results

The CWall8 test examined the behavior of a single wall pier in a coupled wall configuration subjected to cruciform bi-directional loading; as described in Chapter 4, the additional pier was simulated using a variable axial load. There have been prior tests examining coupling action in concrete walls, these have primarily consisted of planar wall piers (and infrequently walls with enlarged boundary elements as in *Ozselcuk* [142] and *Lequesne* [113]). The focus of these studies has been on the performance of varying coupling beam configurations and the influence of coupling on the response of the wall piers. At the time of the CWall8 test, the author was not aware of any other non-planar wall configuration that has been experimentally tested with simulated coupling action. This configuration is particularly critical to investigate since the use of coupled structural wall systems around service shafts is rather common. Consistent with CWall7, the following damage description the weak-axis positive/negative direction motion is defined as indicated in Fig. 4.16.

The observed progression of for CWall 8 was as follows:

- Flexural cracking initiated at 0.02% X-drift, followed by diagonal cracking at 0.06% X-drift. Y-direction loading consisted of reopening of these cracks, new horizontal and diagonal cracks due to weak-axis loading was first noted at +0.07% and +0.22% Y-drift, respectively.
- Strain gauges on longitudinal reinforcement indicated yielding first in No. 2 bars in the web prior to that in multiple No. 4 bars in boundary elements during the 0.35% X-drift cycle. Yielding in the boundary element was noted in the Y-direction during the 0.45% drift cycle.
- During the 0.75% X-drift (+1.11% and -0.28% Y) cycle, minor spalling was observed on the Southeast corner boundary element in a region where the cover had been patched.
- More significant vertical splitting cracks and spalling in corners and flanges were seen in the 1.5% X-drift (+1.9% and -1.9% Y) cycles. Additionally, bar buckling and rupture was observed in numerous No. 2 bars in the web and West flange. Out-of-plane shear demand on the flanges was significant enough to cause large regions of spalling near the footing.
- During the 1.78% X-drift (+1.9% and -1.9% Y) cycle, crushing and loss of confinement occurred in the corner boundary elements. The first negative Y cycle resulted in one No. 4 bar rupture, and the second cycle in approximately 10 No. 4 bar fractures.
- Additional cycles in the Y-direction (+1.62% and -1.9%) resulted in further loss of confinement and core crushing in corner boundary elements. Multiple No. 4 bars fractured in the East flange at -1.53% Y-drift and the specimen could no longer carry the full axial tension. The final positive Y-direction cycle ended in a minor compressive failure.

CWall8 was able to reach a maximum base moment of $0.91M_n$ in the strong-axis direction, 0.79 M_n for the positive weak-axis direction at a compressive axial load of 3320 kN (746 kips) and $0.84M_n$ for the negative weak-axis direction at a tensile axial load of 507 kN (114 kips). The maximum average shear stress demand in the strong-axis direction was $4.01\sqrt{f_c'}A_{cv}$ psi), with stress demands in the positive weak-axis direction of $4.07\sqrt{f_c'}A_{cv}$ psi and negative weak-axis direction of $2.76\sqrt{f_c'}A_{cv}$ psi. Again, the wall failure resulted from buckling- rupture of longitudinal No.4 reinforcement in the tension pier and a minor compressive failure in the compression pier with a reduction in axial and shear carrying capacity. Similar to the two previous walls, the sliding along wall-footing interface and out-of-plane shear demand on the flanges resulted in significant spalling as well as No. 2 bar fracture in the wall web. As a result, the secondary failure mechanisms included frame action, sliding along the web, and slipping/fracture of boundary element confining reinforcement. Fig. 5. 7 shows the wall damage at the end of the test. In Fig. 5.8 a plot of normalized

shear force versus third story drift is provided for both X- and Y-direction (strong-axis and weak-axis) loading with the key performance limit states. Each of the performance limit states are defined in the loading protocol provided in Fig. 5.9.

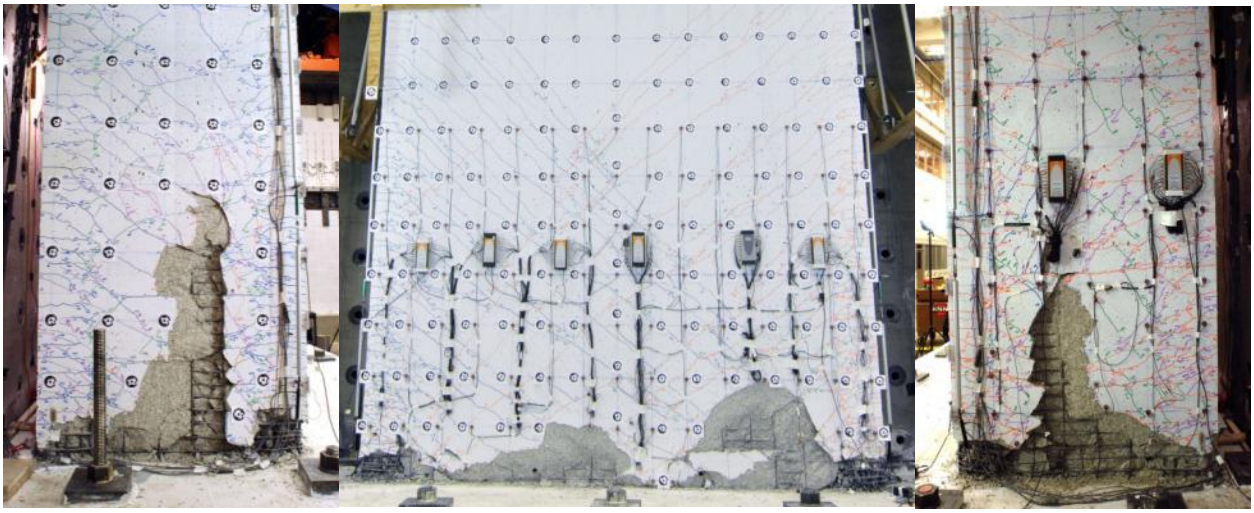

(a) West Flange (b) Web (c) East Flange

Figure 5.7: CWall8 failure images

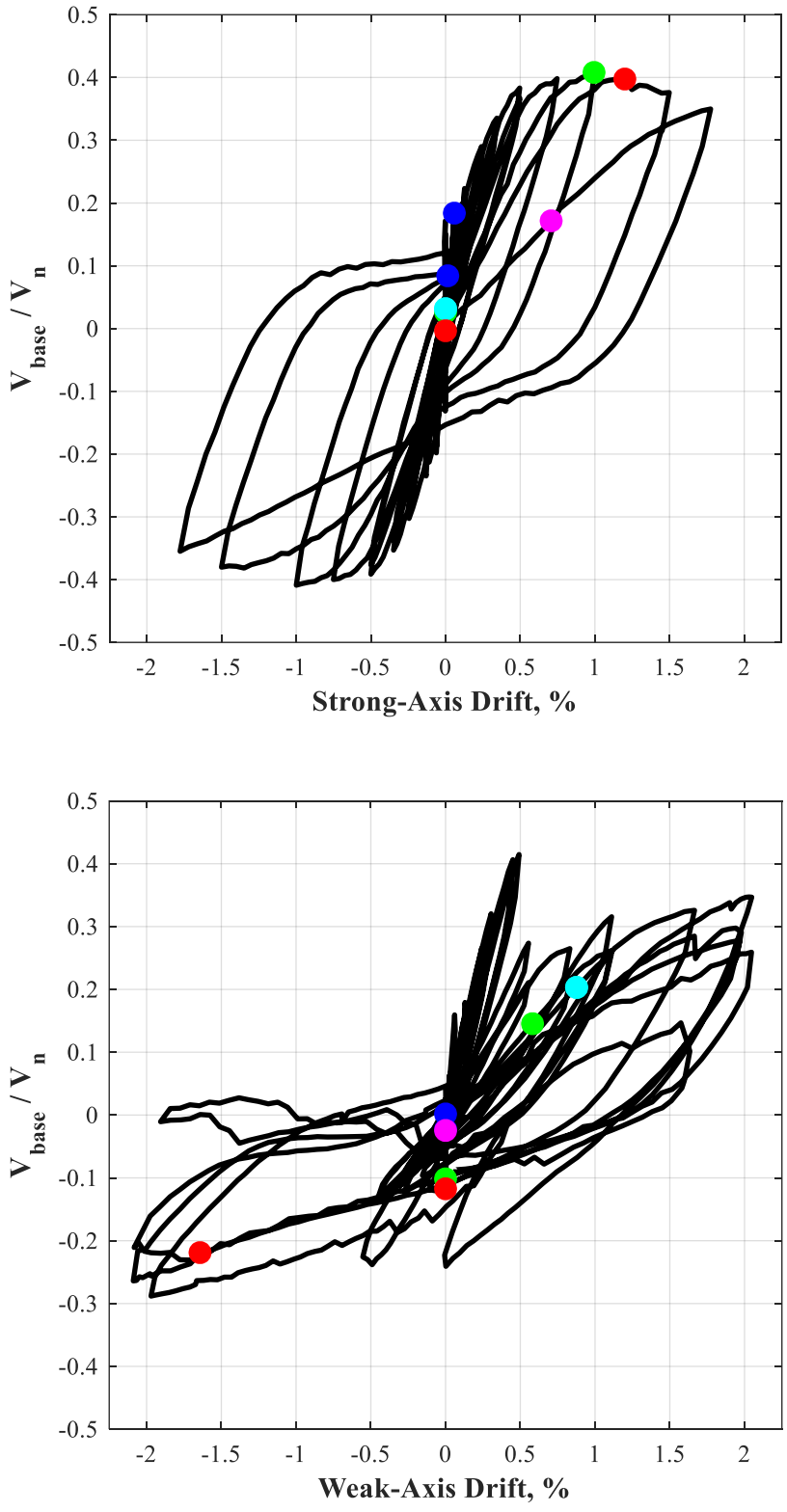

Figure 5.8: CWall8 Normalized Shear Force versus Third Story Drift: (Top) Strong-axis, (Bottom) Weak-axis
(Refer to Fig. 5.9 for damage states associated with each marker)

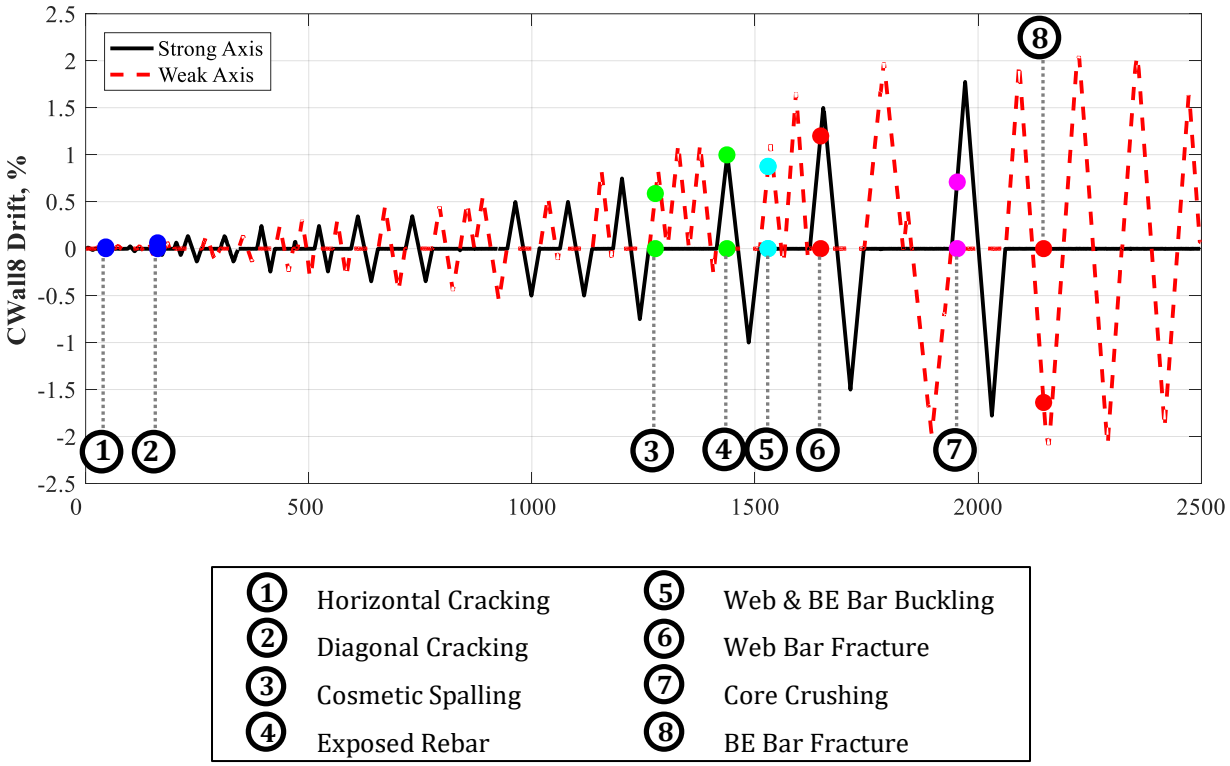

Figure 5.9: CWall8 Damage Limit States

5.4 *Summary of Experimental Results from C-Shaped Wall Tests*

This section examines the response of the C-Shaped walls that were subjected to varying loading conditions. The focus will be on the topics of: (i) similarities and differences in the damage progression and failure mechanisms; (ii) observed versus predicted capacities, (iii) onset of various limit states including cracking, spalling, buckling, crushing, and bar fracture, and (iv) the variations in the cyclic backbone curve in strong and weak-axis, where applicable for each wall.

5.4.1 Wall Damage/Failure Mechanism Comparison

***Note: Portions of Section 5.4.1 were taken from a sponsor report written for the Charles Pankow Foundation, titled "Summary of Large-Scale C-shaped Reinforced Concrete Wall Tests" (Behrouzi et al. [32] which is an update to Lowes et al. [119]). I was the primary author of content from both versions of the report which is presented below. ***

As indicated in the individual discussions of damage progression for the three wall specimens (Sections 5.3.1-5.3.3), the primary failure mechanism for all the wall tests were noted as buckling-rupture where significant strength loss was due to fracture of previously-buckled vertical No. 4 bars

in the boundary elements. Other common observations amongst the tests include: deterioration of the boundary elements, rupture of vertical No. 2 bars in the wall web primarily at a crack plane that formed at the wall-foundation interface, as well as web sliding along that crack plane. These damage types are discussed in further detail in this section.

5.4.1.1 Boundary Element Damage

For all of the test specimens, damage to the boundary elements at the end of the test was severe and included crushing of cover, loss of core integrity, and buckling-rupture of primary No. 4 flexural reinforcement, as well as yielding and, in some cases, rupture of transverse reinforcement. Across all tests, damage to the corner boundary elements initiated at lower drift levels and was more severe than for flange boundary elements.

In the corner boundary elements, compression damage initiated as vertical splitting cracks on both the web and flange faces, followed by spalling of cover concrete, and subsequent buckling of vertical No. 4 bars (Fig. 5.10). Multiple load reversals led to bar buckling followed by straightening, which resulted in stretching of confining reinforcement and loss of core confinement. Slip and fracture of the boundary element hoops eventually ensued. For all three tests, the bottom one to two hoops in the corner boundary elements were ruptured following failure.

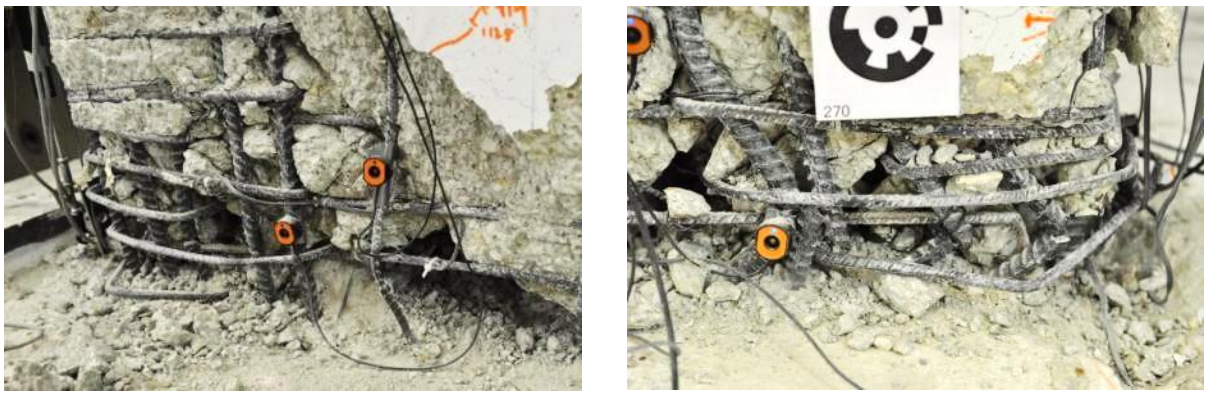

(a) West corner boundary element (b) East corner boundary element

Figure 5.10: CWall7 corner boundary element damage

For all three tests, the flange boundary elements at the ends of the flanges were not as severely damaged as the corner boundary elements. However, they did experience core crushing, buckling and rupture of vertical No. 4 bars, and yielding of transverse reinforcement. Damage to the flange boundary elements was most severe in the CWall6 test (Fig. 5.11). Four No. 4 bars fractured in the West flange boundary element that resulted in loss of load carrying capacity for the specimen (Fig.

5.11(a)), and the East flange boundary element experienced outward buckling of the vertical No. 4 bars and crushing of core concrete (Fig. 5.11(b)).

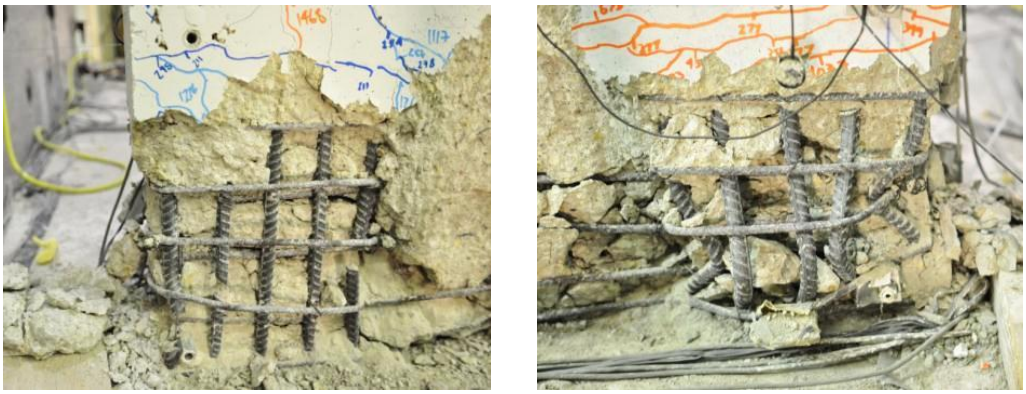

(a) West flange toe (b) East flange toe

Figure 5.11: CWall6 flange boundary element damage

5.4.1.2 Rupture of No. 2 Bars Along the Web and Flanges

For all three wall tests, the majority of vertical No. 2 bars in the web and flanges had fractured at the wall-foundation interface resulting in a large separation (i.e. wide crack) at this location. For the flanges, this separation was most pronounced when the wall was subjected to strong-axis, X-direction displacements; for CWall7 the measured separation of the East flange and footing exceeded 0.5-in (Fig. 5.12(a)). For the web of the C-shaped walls, the separation between the wall and footing was most pronounced when the wall was subjected to weak-axis, negative Y-direction displacements. For CWall8, displacement in the negative Y-direction was accompanied by application of a tensile axial loading, the resulting separation between the wall and footing exceeded 1-in (Fig. 5.12(b)).

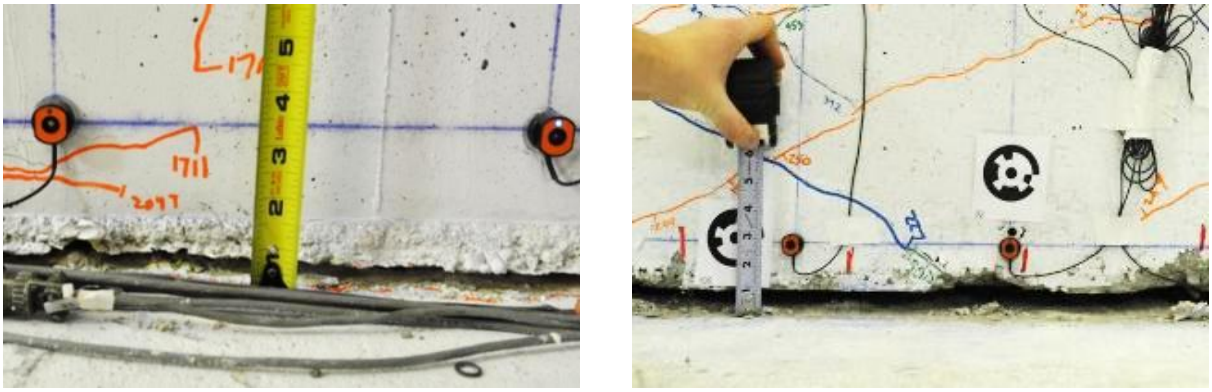

(a) CWall7 East flange base separation (b) CWall8 web separation

Figure 5.12: CWall7 & 8 Interface separation at base

The rupture of the vertical No. 2 bars was followed by outward buckling of the vertical and horizontal bars and cover spalling. However, for all of the tests, the interior concrete of the web remained largely intact throughout the test and maintained its compressive load carrying capacity. For CWall8, even after core crushing and complete loss of confinement in the boundary elements, the web was able to carry a large compressive load resulting from displacement in the +Y-direction with an additional axial load of up to 1000 kips (Fig. 5.13). The webs of CWall6 & 7 were also to remain largely intact (Fig. 5.1 and Fig. 5.4). However, the interior portion of the flanges did not remain intact due to effects of out-of-plane shear in the flanges that resulted from web sliding, discussed in the following section.

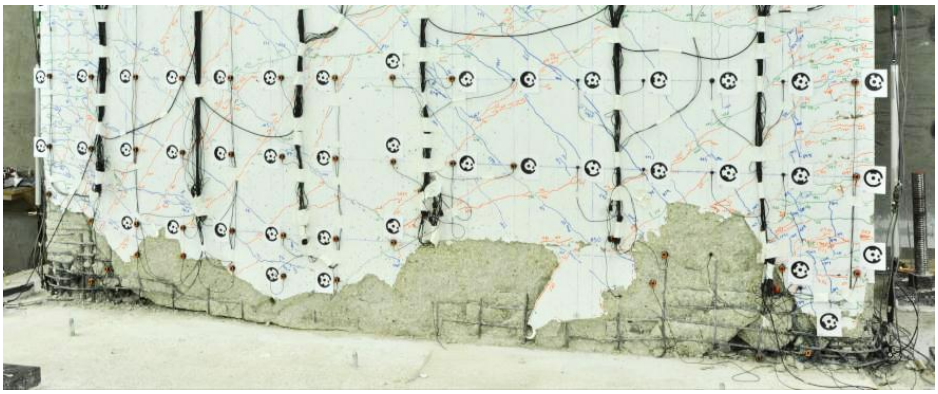

Figure 5.13: CWall8 largely intact web following failure

5.4.1.3 Web Sliding & Damage to Flanges

For large displacement demands in the X-direction, after a large number of vertical No. 2 bars in the wall web had fractured, sliding of the web along the wall-foundation interface became a significant portion of total wall displacement. Associated damage patterns observed in the wall tests included transfer of diagonal compression from the web to the flanges, extensive cyclic compressive/tensile demands on the boundary element longitudinal reinforcement, and separation between the corner boundary elements and the web.

Web sliding was resisted by flange boundary elements; this and the growing damage to the web resulted in the transfer of the web diagonal compressive forces being carried by the flanges. This demand on the flanges became significant enough that cover spalling, vertical bar buckling, and some loss of integrity of interior concrete was observed along both flanges between the corner and flange boundary elements extending from the wall base to a height of 2-3 feet (Fig. 5.14 and Fig. 5.15). Web sliding was also resisted by the boundary elements, both by intact cores and repeated cyclic action (buckling/straightening) of the vertical No. 4 bars. During cycles in the X-direction, these vertical No.

4 bars could be seen to bend in the direction of loading. For each wall test, web sliding was also considered to result in separation between the corner boundary element and the interior of the web. The larger drift demands in the uni-directional CWall6 test led to a more severe separation with a large inclined through opening in the web and the rupturing of horizontal reinforcing across this interface (Fig. 5.16 (a)). The separation was also present in CWall7 and 8 (Fig. 5.16(b)); however, it was not as pronounced as in CWall6.

(a) CWall6 (b) CWall7 (c) CWall8

Figure 5.14: CWall6,7,8 East flange out-of-plane shear damage

Figure 5.15: CWall8 East flange out-of-plane shear damage

(a) CWall6 (b) CWall8

Figure 5.16: CWall6 & 8 Boundary element and web separation

5.4.2 Demand/Capacity Ratio Comparison

The shear and moment strengths were calculated per *ACI 318-14* [18] to assess the demand-to-capacity ratios as summarized in Table 5.2 and 5.3. Given the geometry of the specimen, three capacities/demands can be compared: strong axis response as well as weak axis response in both positive and negative directions. Note that in this table the calculation for shear capacity of a C-shaped wall, V_n, the shear area is taken as the wall segment carrying in-plane lateral load. This means for strong-axis loading the shear area was taken as the area of the web, and for weak-axis loading the shear area is the area of the two flanges.

Table 5.2: Shear Demand/Capacity Ratio Comparisons for CWall6, CWall7, and CWall8

Wall No.	Shear Strength					
	Max shear stress demand, $V_u/A_{cv}\sqrt{f_c'}$			Shear Demand-to-Capacity, V_u/V_n		
						
CWall6	4.26			0.43		
CWall7	3.98	1.31	2.18	0.41	0.14	0.22
CWall8	4.01	4.07	2.76	0.41	0.41	0.28

Table 5.3: Flexural Demand/Capacity Ratio Comparisons for CWall6, CWall7, and CWall8

Wall No.	Flexural Strength					
	Max flexural demand, , k-ft			Shear Demand-to-Capacity, /*M*		
	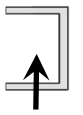	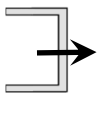	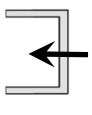	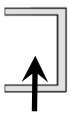	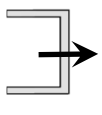	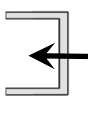
CWall6	6414			0.95		
CWall7	6426	1733	2538	0.93	0.88	1.00
CWall8	6421	2048 [A]	1717 [B]	0.91	0.79 [A]	0.84 [B]

[A] Axial Load = 746 kip compression

[B] Axial Load = 114 kip tension

5.4.3 Damage State Comparison

Table 5.4 presents the ***maximum historic*** third-story drift associated with various performance limit states; in other words, the maximum +/- X-drift, +Y, and –Y drift that the wall has been subject to up to the onset of a particular damage state. The maximum historic drift metric allows for a clear understanding of the demands each wall has experienced prior to a damage limit state. The ***actual*** point of onset for each damage state has been marked in Figs. 5.2-5.3, 5.5-5.6, and 5.8-5.9. The damage states include: horizontal (flexural) cracking, diagonal (shear) cracking, the initiation of cover (cosmetic) spalling, boundary element spalling that has resulted in exposed reinforcement, bar buckling/fracture in both the web (No. 2 bars) and the boundary element (No. 4 bars) vertical reinforcement, as well as core crushing in the confined boundary element. Note that the buckling/fracture of web (No. 2 bars) reinforcement can be difficult to assess as these can occur prior to spalling of cover concrete.

The results in Table 5.4 indicate that with respect to cracking, shear (diagonal) cracking initiated at slightly larger drifts in the strong-axis direction than flexural (horizontal) cracking. Observations for weak-axis cracking were as follows: (i) much larger drifts were required to initiate diagonal cracking than in the strong-axis direction, and (ii) a greater number of weak-axis diagonal cracks were observed in CWall8 compared to CWall7, which was attributed to the reduced point of inflection resulting from the simulated coupling in CWall8. For all wall tests, the strong-axis loading dictated the cracking and softening of the wall specimens. Relatively little new cracking was observed during weak-axis loading cycles, rather the horizontal and diagonal cracks initiated during strong-axis loading reopened in these weak-axis cycles.

For all damage limit states beyond cracking, the uni-directionally loaded wall (CWall6) had consistently higher strong-axis drifts than the bi-directionally loaded walls (CWall7 & 8). The progression of damage for CWall6 and CWall7 was essentially the same; however, CWall8 notably exhibited core crushing prior to boundary element bar fracture, rather than at concurrent drift levels as seen in CWall6 and CWall7. Between the bi-directionally loaded walls, where CWall7 had a comparatively high +Y-direction drift demands and CWall8 had significant variations in axial load, the strong-axis drift associated with the onset of damage states (including cracking) appear to be very similar. Collectively, these results suggest that walls subjected to bi-directional loading develop specific damage states at lower strong-axis drift demands than uni-directionally loaded walls.

Table 5.4: Maximum Historic Third-Story Drift for Damage Limit States

Damage State	CWall6	CWall7			CWall8		
	X	X	+Y	-Y	X	+Y	-Y
Horizontal Cracking	0.03%	0.03%	0.014%	0.014%	0.03%	0.014%	0.014%
Diagonal Cracking	0.14%	0.07%	0.06%	0.08%	0.07%	0.07%	0.07%
Cosmetic Spalling	1.49%	0.75%	2.25%	0.85%	0.75%	0.83%	0.55%
Exposed Rebar	1.49%	0.75%	2.25%	1.36%	1.00%	1.11%	0.55%
Web Bar Buckling	1.49%	1.00%	2.25%	1.49%	1.00%	1.11%	0.55%
Web Bar Fracture	1.49%	1.00%	2.25%	1.49%	1.20%	1.67%	0.55%
BE Bar Buckling	1.49%	1.00%	2.25%	1.49%	1.00%	1.11%	0.55%
BE Bar Fracture	2.25%	1.49%	2.25%	1.49%	1.78%	1.97%	1.97%
Core Crushing	2.25%	1.49%	2.25%	1.49%	1.49%	1.97%	1.97%

5.4.4 Cyclic Backbone Curve Comparison

Fig. 5.17 presents two cyclic backbone envelopes of normalized shear force versus third story drift, one for strong-axis (CWall6,7, & 8) and the other for weak-axis loading (CWall7 & 8 only). The global load-deformation response is an informative metric to assess the difference in behavior between the uni- and bi-directionally loaded C-shaped walls tested in this study.

The strong axis envelope shows nearly identical strength and stiffness performance of the walls up to $0.4V_n$ (or, 0.91-0.95M_n) at 0.75% X-drift, which indicates that the weak-axis loading has no significant effect on the strong-axis performance until after the peak capacity has been reached. Beyond 0.75% X-drift, the impact of weak-axis loading becomes apparent during the peak and post-peak inelastic response. The bi-directional tests exhibit a stiffness reduction in strong-axis response

as well as strength degradation and reduced ductility. Walls were able to maintain at least 80% of maximum strong-axis strength until: the first cycle at 2.25% X-drift for CWall6; the 1.5% X-drift cycle for CWall7; and the final 1.8% X-drift cycle for CWall8. The walls with constant axial load were able to maintain an axial load of $0.05A_g f'_c$ and moderate lateral load carrying capacities (40-45% of maximum strength) at relatively large drift demands (nearly 3.5% X-drift for CWall6 and 2% X-drift for CWall7).

The effect of weak-axis loading on strong-axis performance was most pronounced in CWall7 where an initial loss in capacity to about $0.31V_n$ (or, $0.68M_n$) occurred during the last 1% X-drift cycle while -1.1% Y-drift was maintained. The subsequent cycle at 1.5% X-drift shows an increase to $0.35V_n$ (or, $0.75M_n$) under strong-axis loading only.

Examination of the weak-axis response in Fig. 5.17 indicates that in that walls were able to reach $0.14\text{-}0.41V_n$ (or, $0.79 - 1.00M_n$). CWall8 appears to have an initially stiffer response in the weak-axis direction compared to CWall7. Bi-directionally loaded walls were able to maintain at least 80% of their maximum weak-axis flexural strength under loading until: the final +2.25% and -1.5% Y-drift cycle for CWall7; and the +2.05% and -2.09% Y-drift cycle for CWall8. In the final weak-axis direction cycle, CWall7 (with constant axial load) had only moderate strength degradation, while CWall8 (with simulated coupled action) had significant strength degradation.

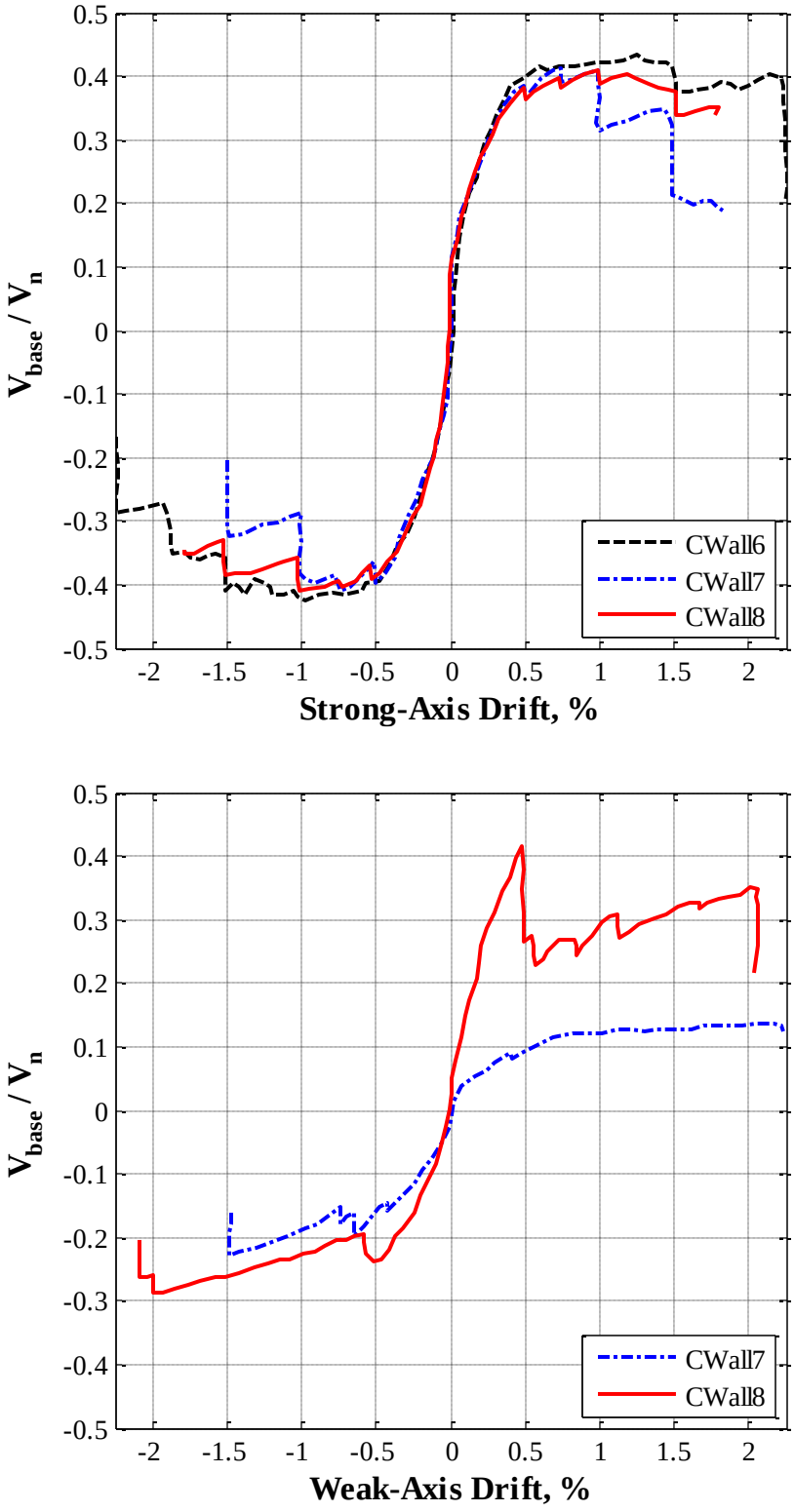

Figure 5.17: Comparison of Normalized Shear Force versus Third Story Drift Envelopes: (Top) Strong-axis, (Bottom) Weak-Axis

5.5 Analysis of Experimental Data from C-Shaped Wall Tests

5.5.1 Displacement Profiles

Displacement profiles for strong-axis cycle peaks were determined primarily using measurements from the Krypton system described in Section 4.8.4.2. These profiles were calculated by averaging the x-displacement data collected from the two center columns of LED sensors located on the wall web (refer to Fig. 4.27); when possible, these values were verified by displacements measured using string potentiometers. The displacement for the top of the wall was determined by a mathematical transformation of measurements taken from seven high-resolution linear potentiometers (refer to Fig. 4.23).

Fig. 5.18 shows the wall displacement profile at the first peak of the 0.50% X-drift cycle. This is prior to peak strength is achieved. The strain maps in Section 5.5.2 show that at the first positive 0.50% X-drift peak there were a number of locations where the measured tensile strain indicate that the vertical rebar was yielding; however, there were very few measurements suggesting steel strain hardening had begun. The displacement profiles for CWall6 and CWall7 are very similar with slightly higher displacements for CWall7 above the first story. The displacement profile for CWall8 seems to suggest that there was higher base slip already occurring at 0.5% X-drift compared to the other walls, possibly due to additional damage resulting combined bi-directional loading and coupling effects (varying axial load).

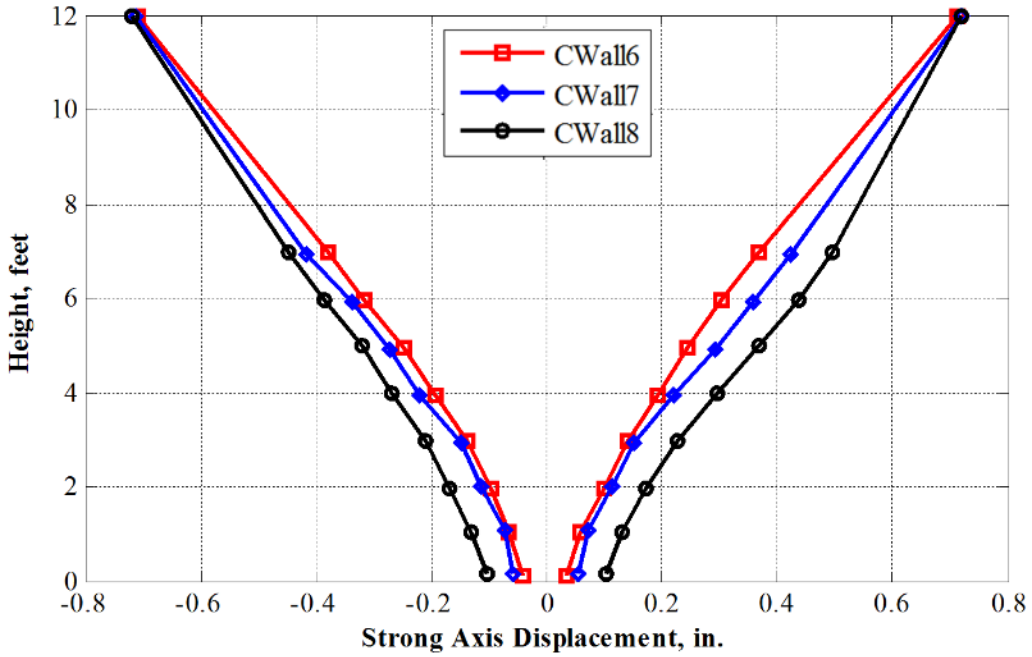

Figure 5.18: Displacement Profile at first +/- 0.5% X-drift Peaks

Fig. 5.19 shows the wall displacement profile at the first peak of the 1.00% X-drift cycle. At this drift level, the peak strength of both CWall7 and CWall8 had been achieved, and these specimens were just beginning their softening regime. CWall6 was nearing its peak strength. The strain maps in Section 5.5.2 show that at the first positive 1.00% X-drift peak a majority of steel strain gauges in the bottom two stories of the wall specimens indicated that vertical rebar had reached tensile yield. In CWall6 and CWall7, many of the first-story strain gauges in the web boundary elements and throughout the flange indicated that strain hardening had begun. Strain hardening had also begun in the first story of CWall8. At 1.0% X-drift, the displacement profiles for all the wall specimens are similar in nature; though CWall7 (bi-directionally loading) shows slightly higher base slip and displacements than CWall6 (uni-directionally loading), and CWall8 (bi-directionally loading with variable axial force) shows even greater base slip and displacement than CWall7.

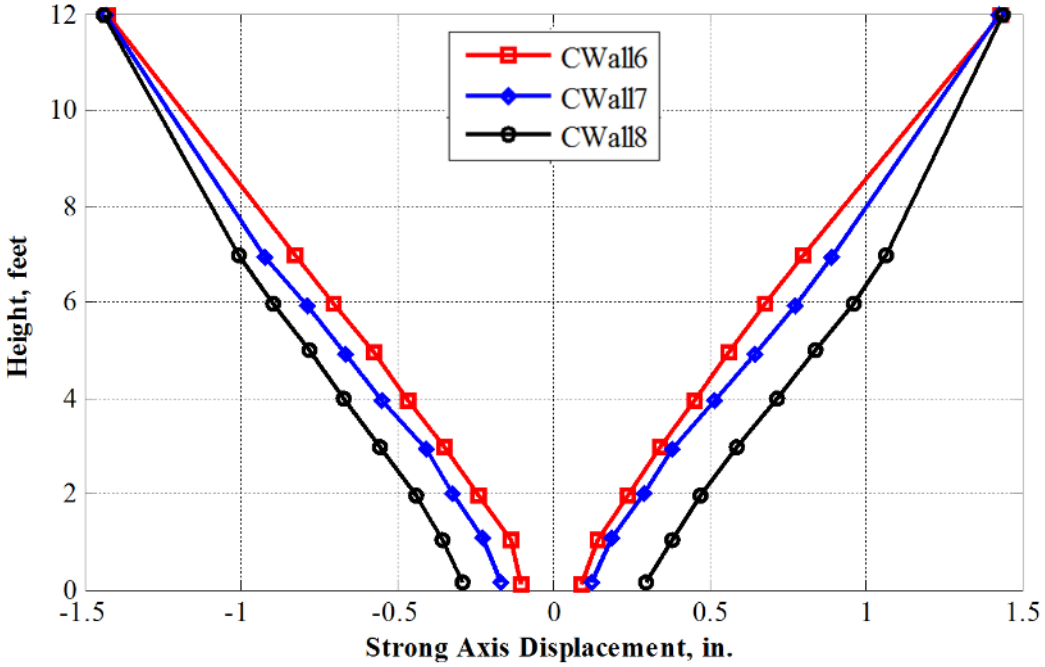

Figure 5.19: Displacement Profile at first +/- 1.0% X-drift Peaks

Fig. 5.20 shows the wall displacement profile at the first peak of the 1.50% X-drift cycle. At this drift level, both CWall7 and CWall8 have already experienced notable strength loss, while CWall6 has just begun softening. The strain maps in Section 5.5.2 indicate that tensile straining in the reinforcement at the first positive 1.5% X-drift peak is consistent with observations from 1.0% X-drift, with limited cases of additional strain hardening (locations vary per wall). The previous trend observed at 0.5% and 1.0% X-drift peaks, where CWall6, CWall7, and CWall8 had increasing base slip and displacements (in that order), does not hold. The data presented in Fig. 5.20 suggests that for CWall7 the high drift demands and "true" bi-directional loading cycles (where Y-drift is held

at +2% or -1% drift while cycling at +/-1% X-drift, as shown in Fig. 5.6) results in wall damage/deformation that exceeds of CWall8. This difference between CWall7 and CWall8 is more pronounced for +X-direction where the base slip is notably larger for CWall7.

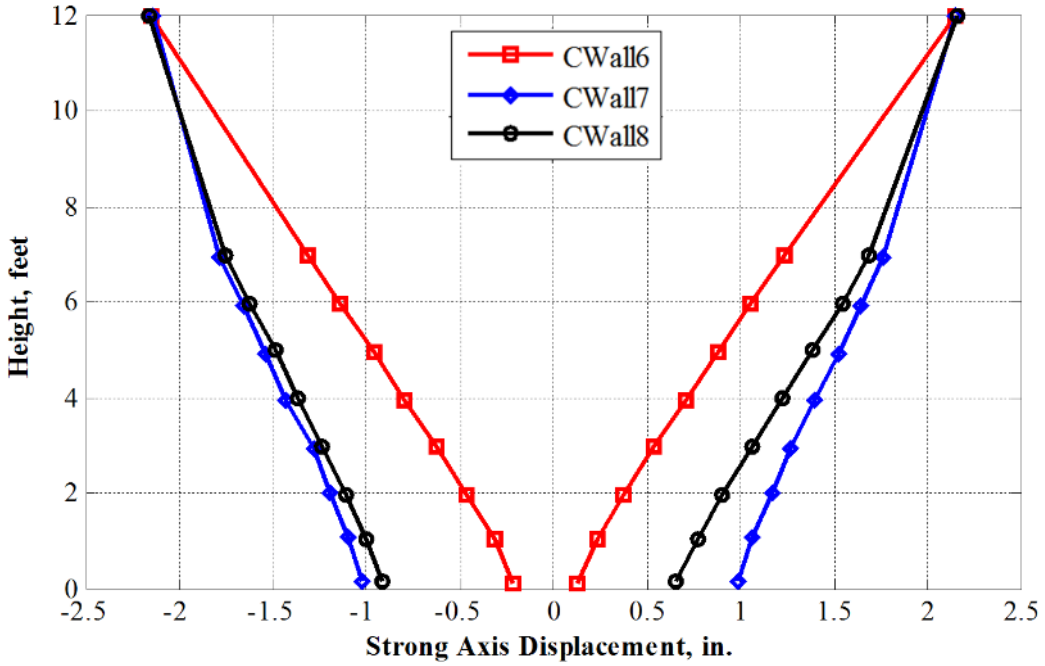

Figure 5.20: Displacement Profile at first +/- 1.5% X-drift Peaks

The deformation response between the uni- versus bi-directionally loaded C-shaped walls diverges at higher strong-axis drift demand levels, where bi-directionally loaded walls exhibit much greater deformations than uni-directionally loaded walls. In particular, the displacement profiles presented in Figs. 5.18-5.20 suggest that damage at the base of the wall is exacerbated by weak-axis loading, and indicates that this damage may be greater for walls with large weak-axis drift demands and "true" bi-directional loading compared to walls with a cruciform bi-directional loading with varying axial load.

Note: In Figs. 5.18-5.20 the displacement profiles vary between each of the wall specimens for all points up the height of the wall, except the third-story (top) displacement. This measured response occurs because the wall loading algorithm accurately controls the third-story displacement using the same configuration of seven high-resolution sensors that are used to calculate the top x-displacement for the displacement profiles.

5.5.2 Longitudinal Steel Reinforcement Strain Maps

Measured data from approximately 80 strain gauges on longitudinal reinforcement was analyzed to determine the degree of non-linear behavior in the steel for both tension and compression. The *Hoehler-Stanton* [90] cyclic stress-strain model for reinforcing steel was utilized to estimate steel stresses for the experimental strain history. These results were utilized to evaluate when certain thresholds were reached such as steel yield and strain hardening. A more detailed description of this process can be found in *Birely* [35]. Strain maps were created to qualitatively evaluate measured strains relative to the aforementioned thresholds at various drift levels throughout each C-shaped wall test (first positive peak at 0.5, 1.0, and 1.5% X-drift, as well as the end of test).

Figs. 5.21- 5.24 indicate the gauges that yield in tension ($+\varepsilon_y$ and $+\varepsilon_{sh}$), and Figs. 5.25- 5.28 shows those that yield in compression ($-\varepsilon_y$ and $-\varepsilon_{sh}$). On each map, strain gauge locations are marked with a black "x". Locations with open circles indicate initial yield strain ($\pm\varepsilon_y$), while closed circles represent strain hardening ($\pm\varepsilon_{sh}$) which suggests significant plastic deformation, finally, crosses show where yield stress ($\pm f_y$) was reached prior to/without reaching monotonic yield strain ($\pm\varepsilon_y$) due to cyclic loading. A red marker designates gauges that first reached yield strain in tension, where blue indicates compressive yield occurred first.

5.5.2.1 Tensile Response of Vertical Reinforcement

Figs. 5.21 -5.24 shows the tension yielding response of the C-shaped walls for the first positive peak at 0.5, 1.0, and 1.5% X-drift.

At 0.5% X-drift, all walls exhibit widespread tensile yielding of the vertical reinforcement at in the bottom two stories, and there are limited instances of strain hardening. Strain gauge measurements indicate that in most cases tensile yielding precedes compressive non-linear behavior.

At 1.0% X-drift, tensile strain hardening becomes more prevalent. For CWall 6 and CWall7, strain hardening has occurred in the first story boundary elements and across the flanges. CWall8 had a number of non-functional gauges up the height of the web boundary elements, but the available data suggests that the strain hardening behavior is similar in CWall8 as for CWall6 and CWall7.

At 1.5% X-drift, CWall6 exhibits additional tensile strain hardening in the first story of the east web boundary element; while CWall7 and CWall8 experience strain hardening at the toes of both the east and west flanges in the bottom two stories. There is essentially no observed change in the tensile strain yielding/strain hardening behavior between 1.5% X-drift and the end of the tests.

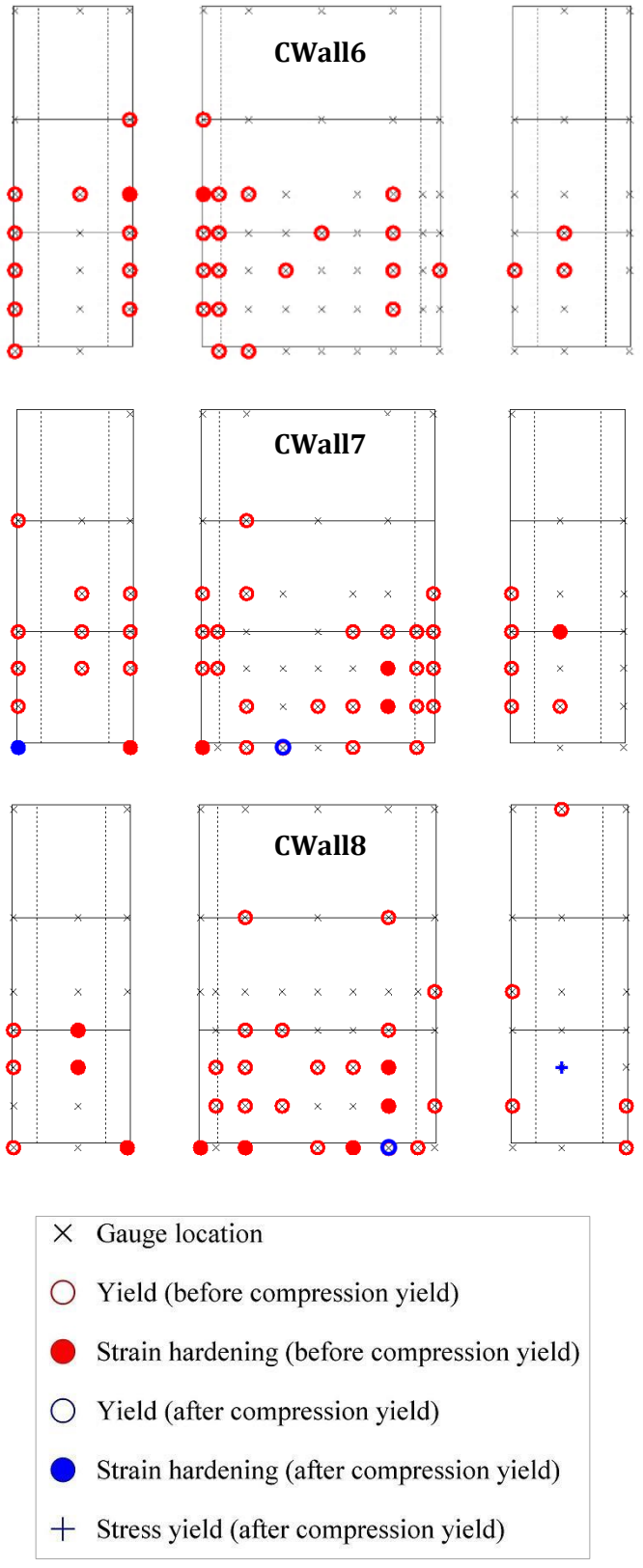

Figure 5.21: Tensile Yield for Vertical Reinforcement at First Positive Peak during 0.5% X-Drift Cycle

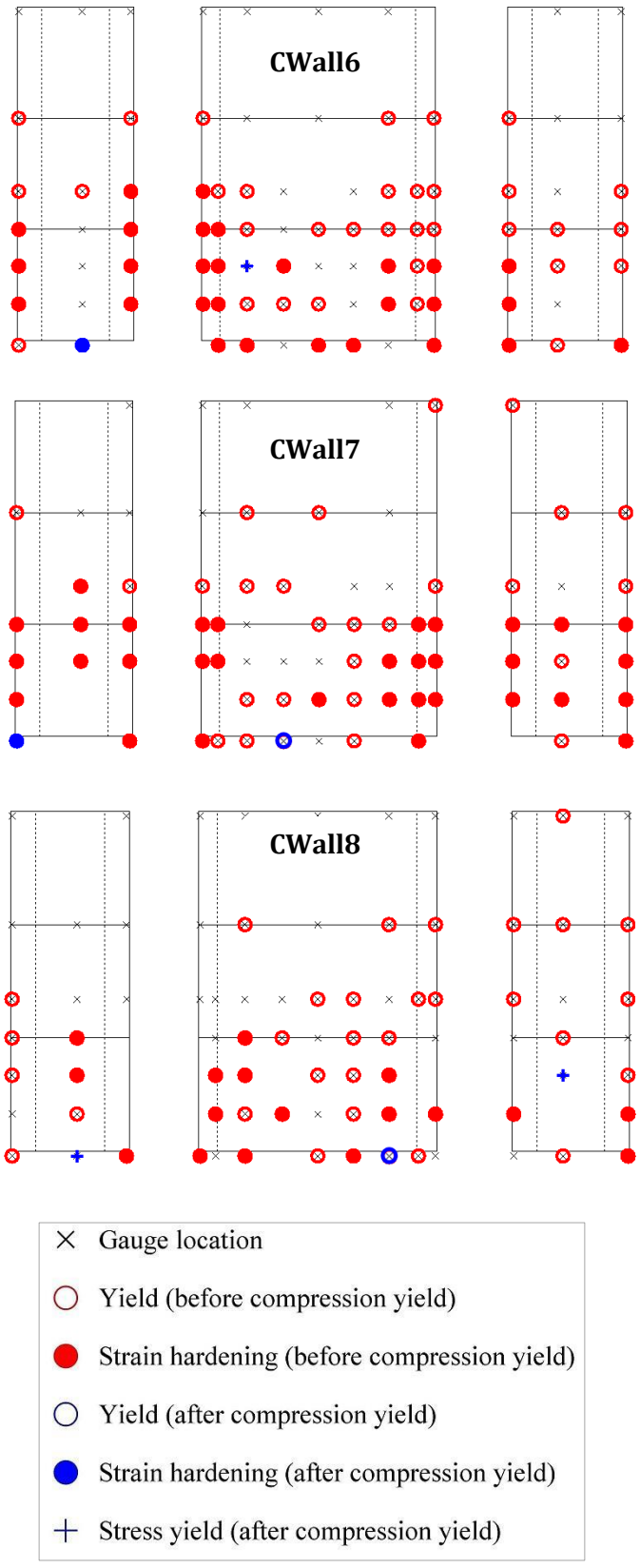

Figure 5.22: Tensile Yield for Vertical Reinforcement at First Positive Peak during 1.0% X-Drift Cycle

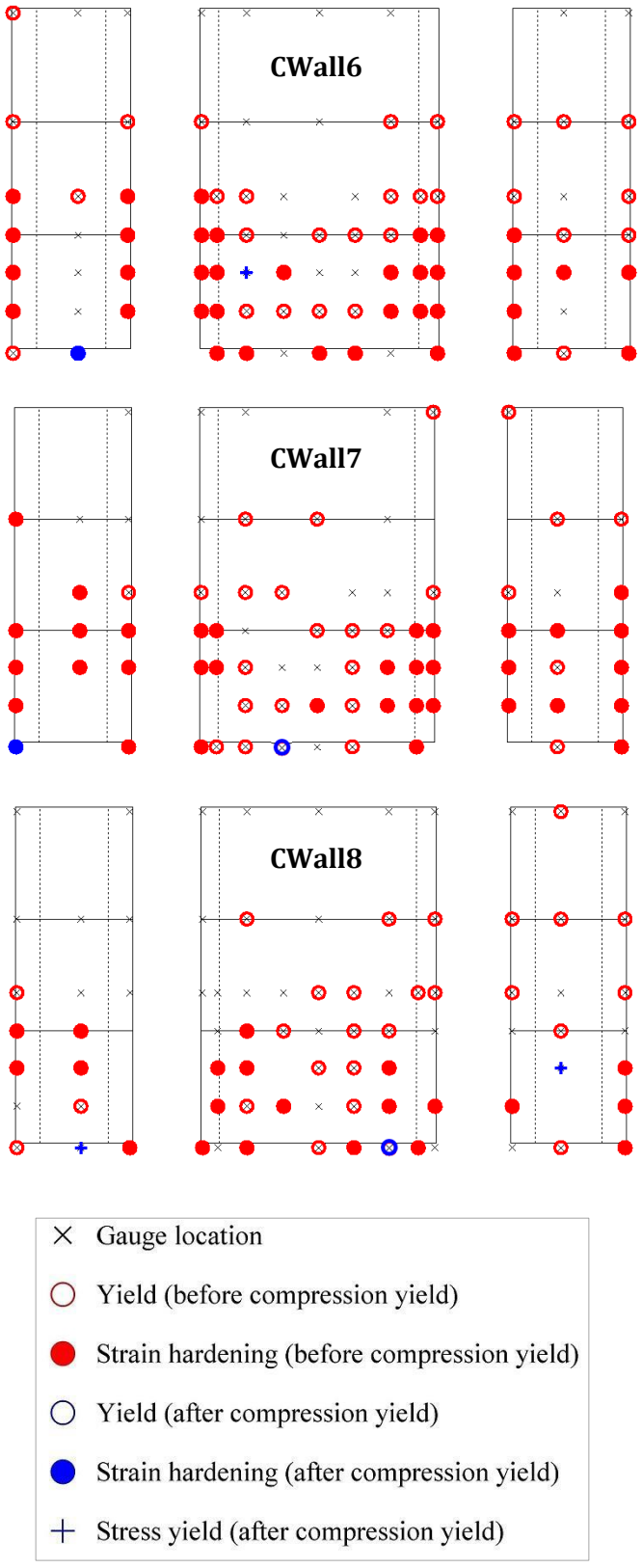

Figure 5.23: Tensile Yield for Vertical Reinforcement at First Positive Peak during 1.5% X-Drift Cycle

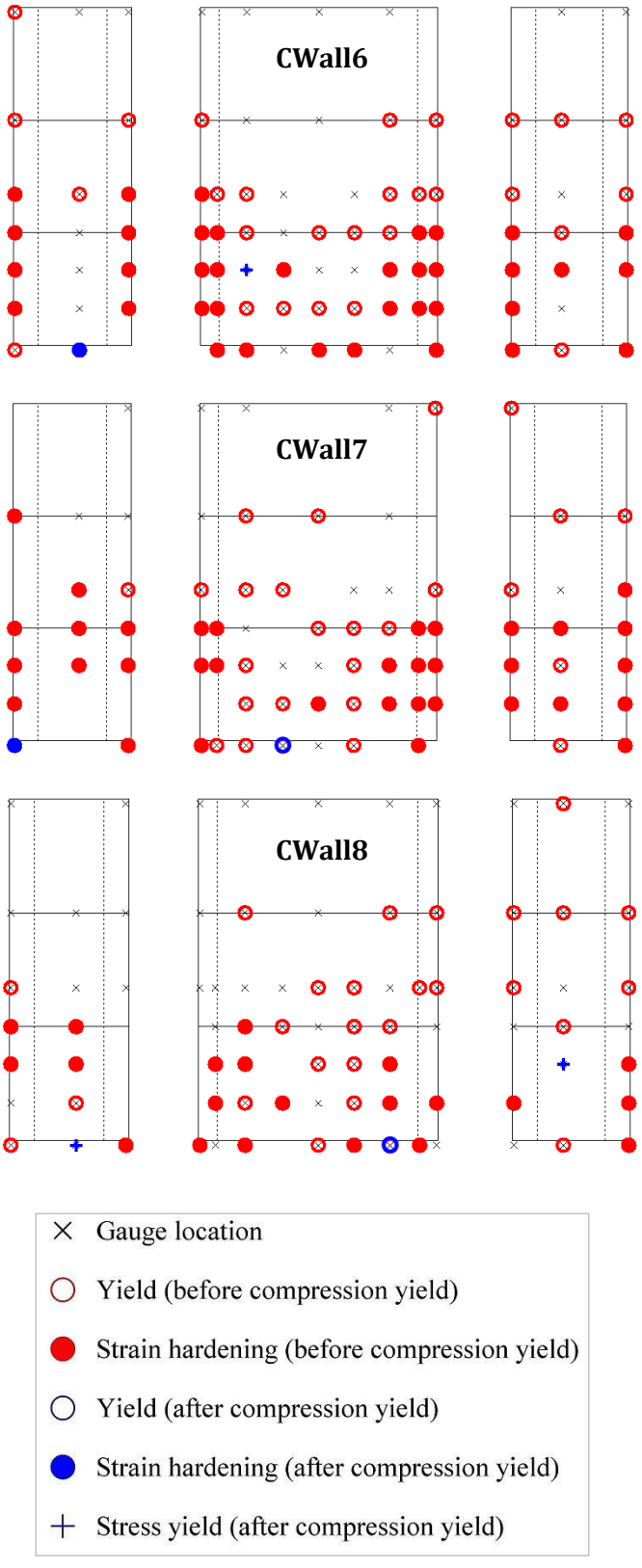

Figure 5.24: Tensile Yield for Vertical Reinforcement at End of Wall Tests

5.5.2.2 Compressive Response of Vertical Reinforcement

Figs. 5.25 -5.28 show the compression yielding response of the C-shaped walls for the first positive peak at 0.5, 1.0, and 1.5% X-drift.

At 0.5% X-drift, there are a very limited number of locations where strain measurements indicate the onset of non-linear compressive steel behavior prior to tensile yielding. Throughout the course of the tests, only one additional point for CWall6 at 1.0% X-drift is noted where non-linear compression precedes tensile response.

At 1.0% drift, the most common compressive response is ***stress*** yielding following tension yield. ***Compressive*** stress yielding occurs in the first story, for: CWall6 it is primarily in the web boundary elements, CWall7 is in the web/flange boundary elements, and CWall8 at locations concentrated near the base of the web. Compressive strain yielding occurs less frequently and can be observed in either at the base of the walls or in the lower portion of the flanges.

At 1.5% drift, compressive stress yielding occurs at additional locations in the bottom two stories of the walls, specifically in the web/flange boundary elements (CWall6, CWall7, and CWall8) and in the flange web (CWall6). Other notable observations include the fact that CWall6 and CWall7 very little compressive stress or strain yielding in the center of the wall web (even at the base), whereas CWall8 seems to have most of the non-linear compressive response across the base of the wall web.

Between 1.5% drift and the end of the test, only CWall6 experiences a measured change in compressive response with additional stress yielding occurring at the second story in both flange-toe boundary elements.

5.5.2.3 Summary of Tensile/Compressive Response of Vertical Reinforcement

The preceding descriptions provided in Sections 5.5.2.2 and 5.5.2.3 indicate that tensile yielding/plasticity tends to occur in the bottom two stories of the C-shaped wall specimens, and the onset of compressive stress/strain yielding comes after repeated cycles of loading and previous tensile yielding. A comparison of this response to the planar walls in *Birely* [35] shows that the C-shaped wall flanges carry a substantial portion of the compressive demand and failure via buckling-rupture (flexural-tension) failure, whereas the planar walls tend to exhibit more widespread non-linear compressive steel behavior in the boundary elements prior to tensile behavior and failure via crushing-buckling (flexural-compression mode).

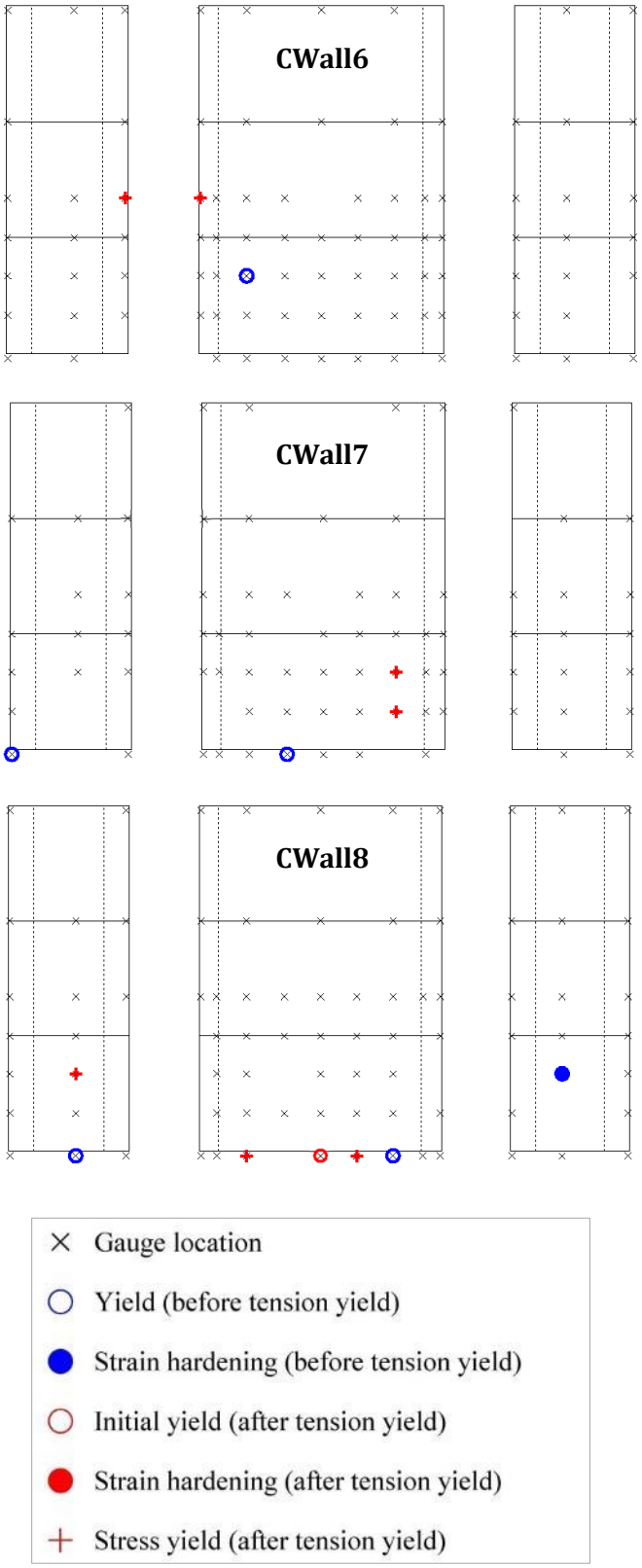

Figure 5.25: Compression Yield for Vertical Reinforcement at First Positive Peak during 0.5% X-Drift Cycle

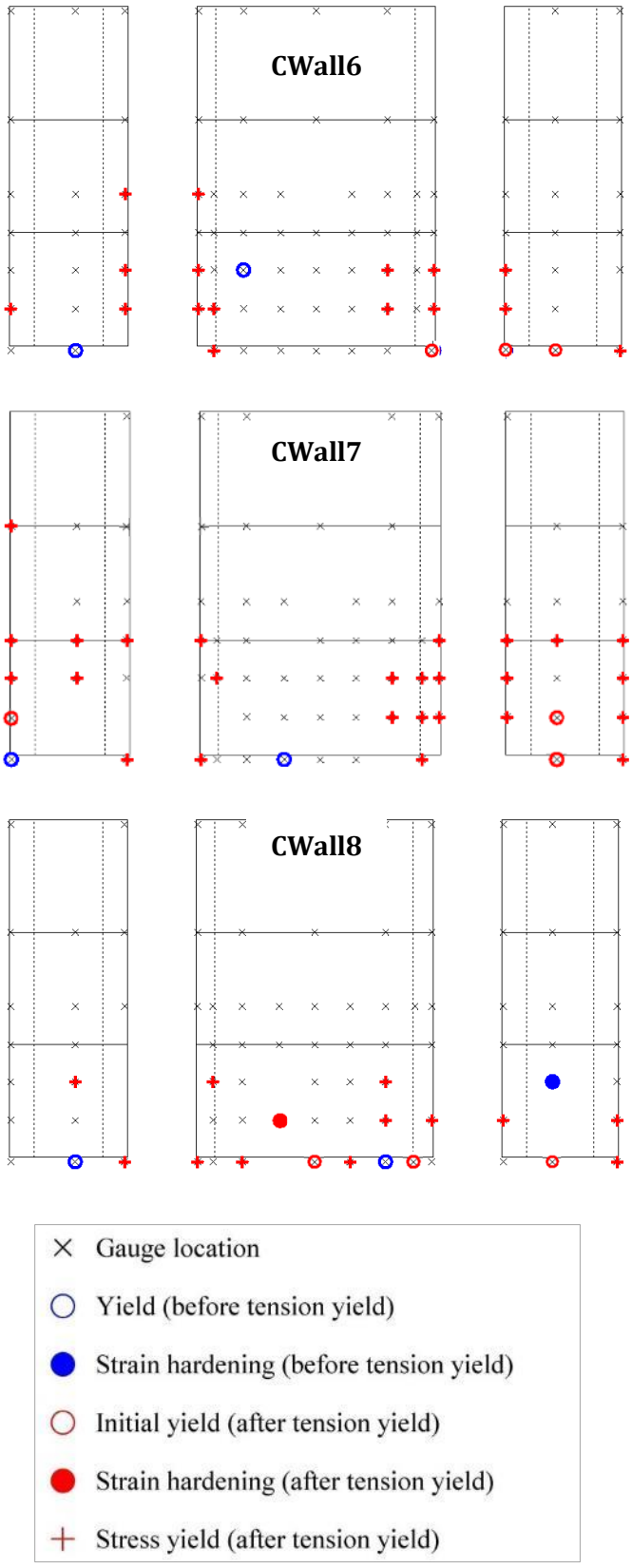

Figure 5.26: Compression Yield for Vertical Reinforcement at First Positive Peak during 1.0% X-Drift Cycle

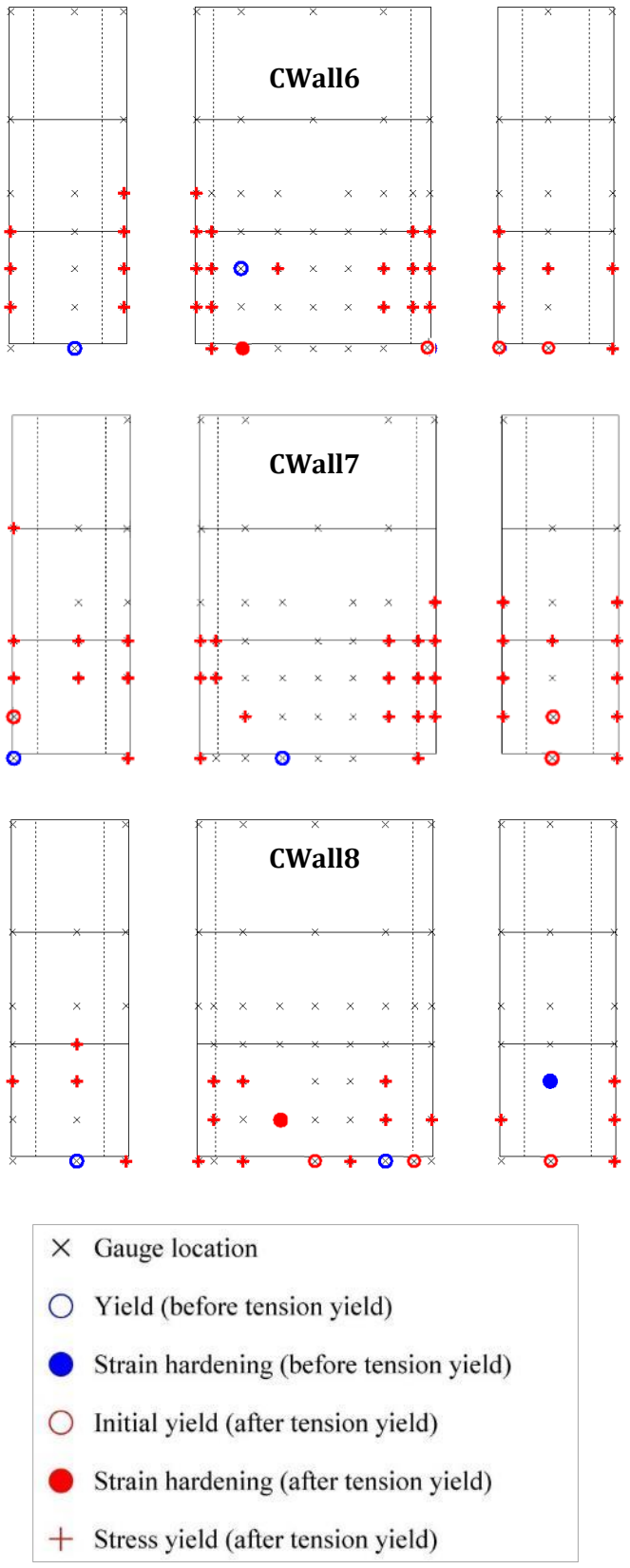

Figure 5.27: Compression Yield for Vertical Reinforcement at First Positive Peak during 1.5% X-Drift Cycle

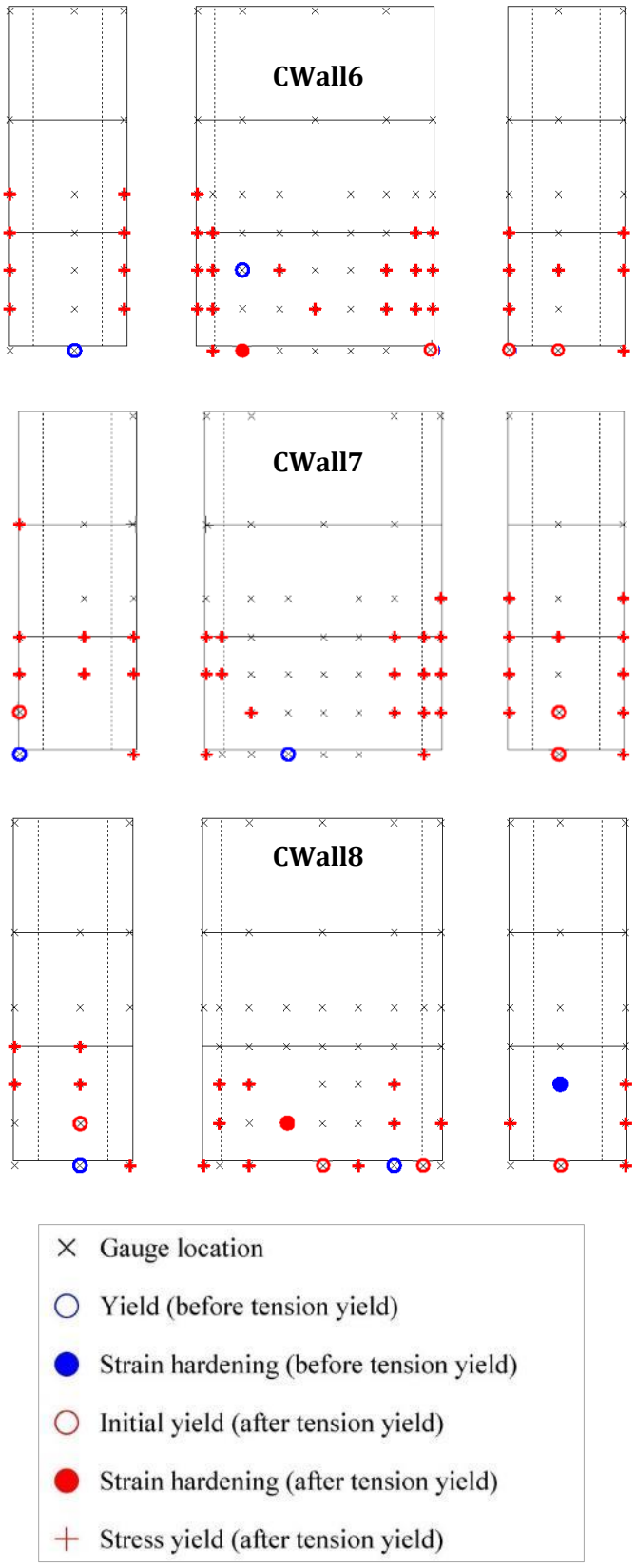

Figure 5.28: Compression Yield for Vertical Reinforcement at End of Wall Tests

5.5.3 Strain Fields

The high-resolution measurements collected using the Nikon Metrology/Krypton system enabled the calculation of average strain fields for the lower two floors of both the web and east flange. The LED targets were on a grid with approximately square regions, and therefore the in-plane displacement of each LED represented the deformation of the corner nodes in a four-node isoparametric quadrilateral finite element formulation. Strain fields were developed by calculating the strain at each of the nodes as described in *Birely* [35]. The remainder of this section summarizes observations on wall response that can be made via examination of vertical strain (ε_z), in-plane shear strain (γ_{xz}), as well as first and second principal strain ($\varepsilon_1$and ε_2). Figs. 5.29-5.32 include strain fields for each of the aforementioned types of strains at the positive peaks of the 0.5%, 1.0%, and 1.5% X-drift cycles. The strain fields provide a metric to assess C-shaped wall deformation resulting from different imposed loading.

Figs. 5.29 and 5.31, that illustrate the vertical and first principal (maximum tensile) strain fields, show that tension straining for all walls occurs predominantly at: (i) the base of the tension flange and adjacent wall web (most pronounced in CWall6), and (ii) along diagonal band(s) in the wall web that initiate at the second floor at the tension flange edge and extend towards the compression boundary element. By 1.0% X-drift for CWall6 and CWall8, the tensile strains in the tension region of the first-floor wall web are near or in access of the ultimate strain for the No. 2 steel rebar, suggesting bar rupture has occurred or is imminent.

For all walls, significant shear straining corresponds to the regions of the wall web that are in tension and at the first-story of the flange. There is also a vertical band of increased shear strain that develops at the second-floor along the outer edge of the corner boundary element of the compression flange. This band is first observed in CWall7 at 0.35% X-drift, which then spreads and increases in magnitude. For CWall6 and CWall8 this vertical band occurs at a later onset drift (1% and 1.5% X-drift, respectively), and the magnitude/extent of this high shear strain region is more limited. At these shear strain bands along the compression flange there is also relatively high tensile straining. This behavior likely results from the stiffness discontinuity due to the difference between the: (i) lightly reinforced wall web and the heavily-reinforced boundary element, as well as the transition from (ii) relatively thin wall web and the rather substantial flange. This particular response, where tensile straining was seen in the compression boundary element appears to be unique to flanged walls.

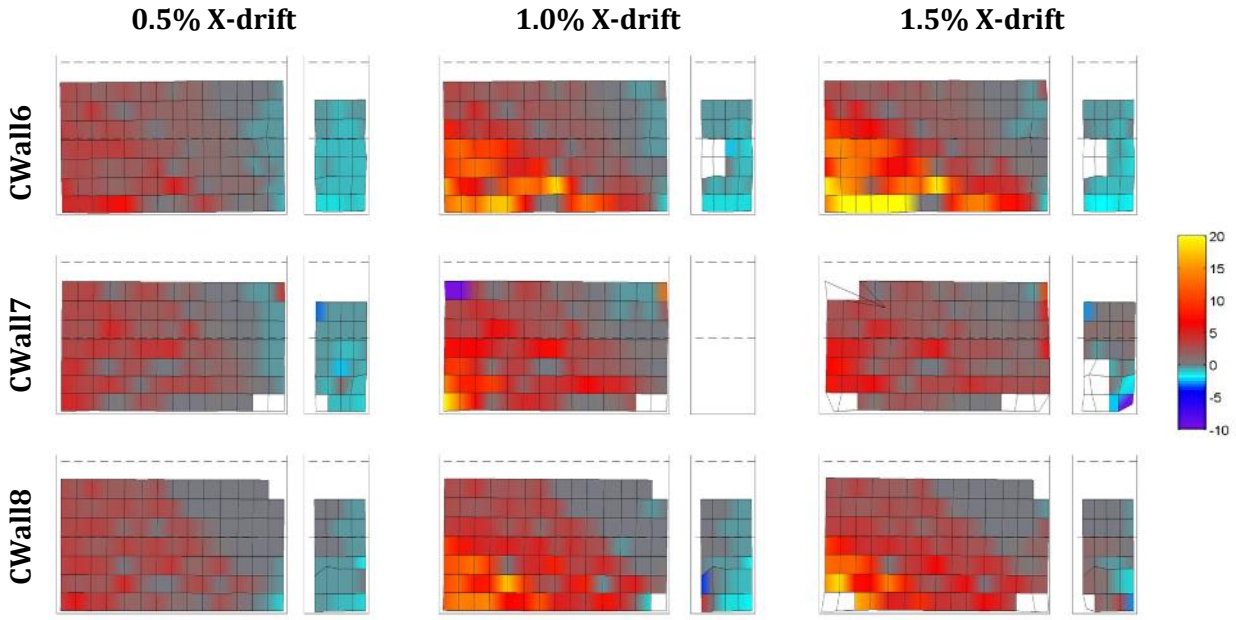

Figure 5.29: Vertical Strain Fields at 0.5%, 1.0%, and 1.5% X-drift peaks (units: millistrain)
Provided by Andrew Mock in preparation of [124]

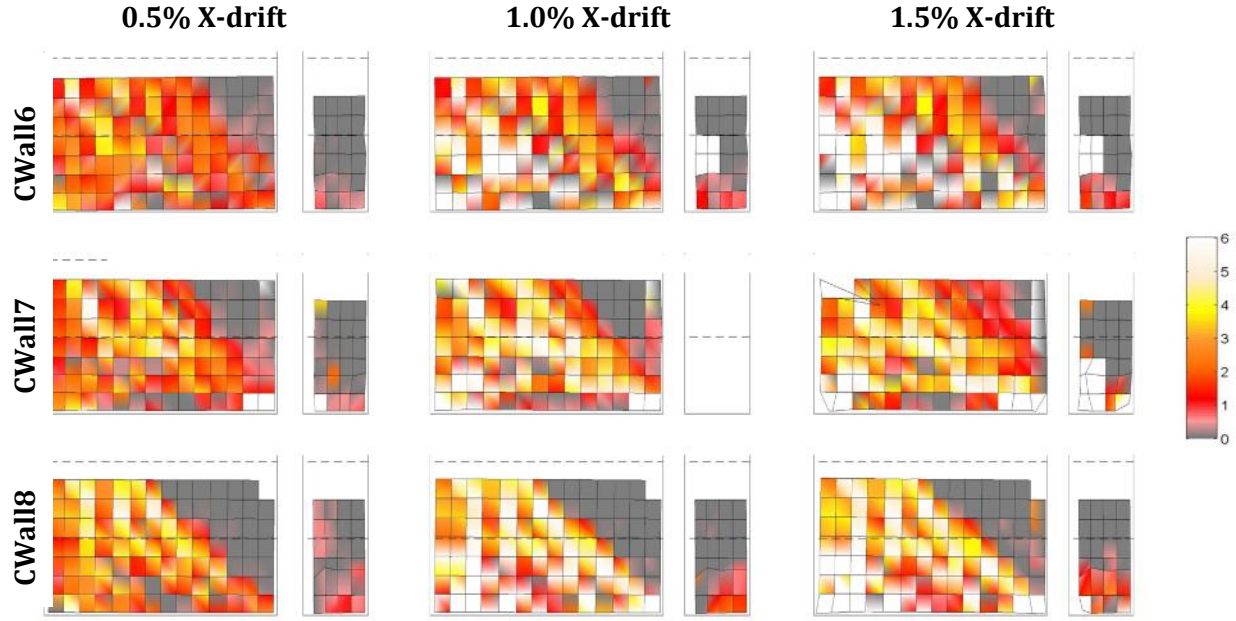

Figure 5.30: In-Plane Shear Strain Fields at 0.5%, 1.0%, and 1.5% X-drift peaks (units: millistrain)
Provided by Andrew Mock in preparation of [124]

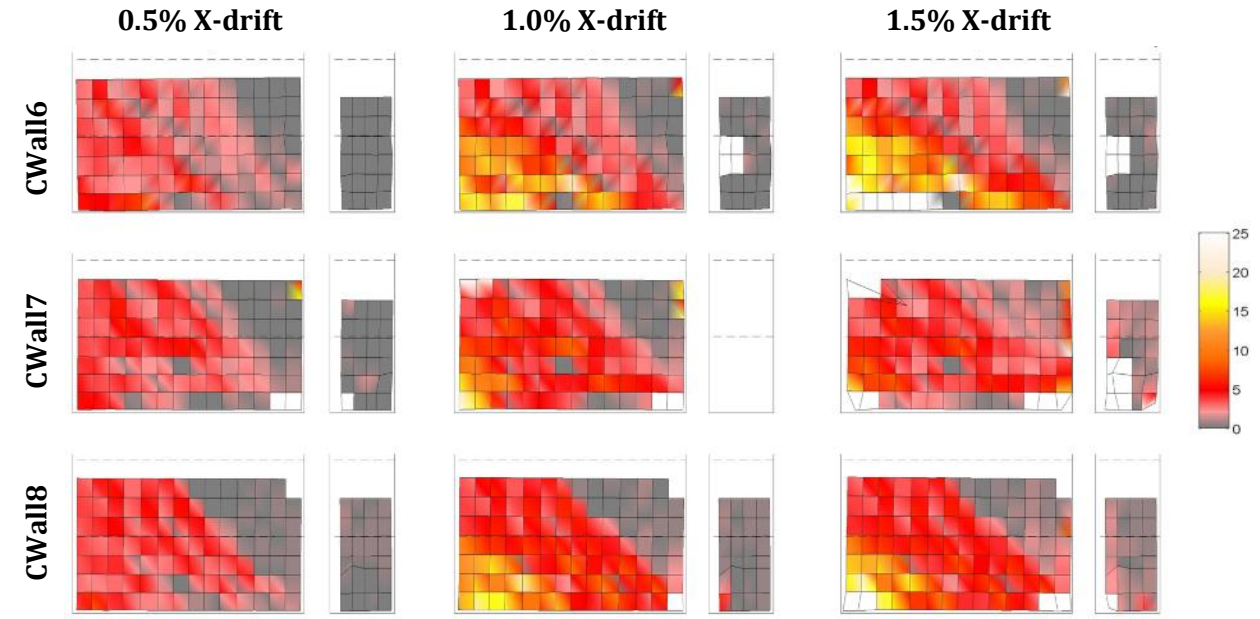

Figure 5.31: First Principal Strain Fields at 0.5%, 1.0%, and 1.5% X-drift peaks (units: millistrain)
Provided by Andrew Mock in preparation of [124]

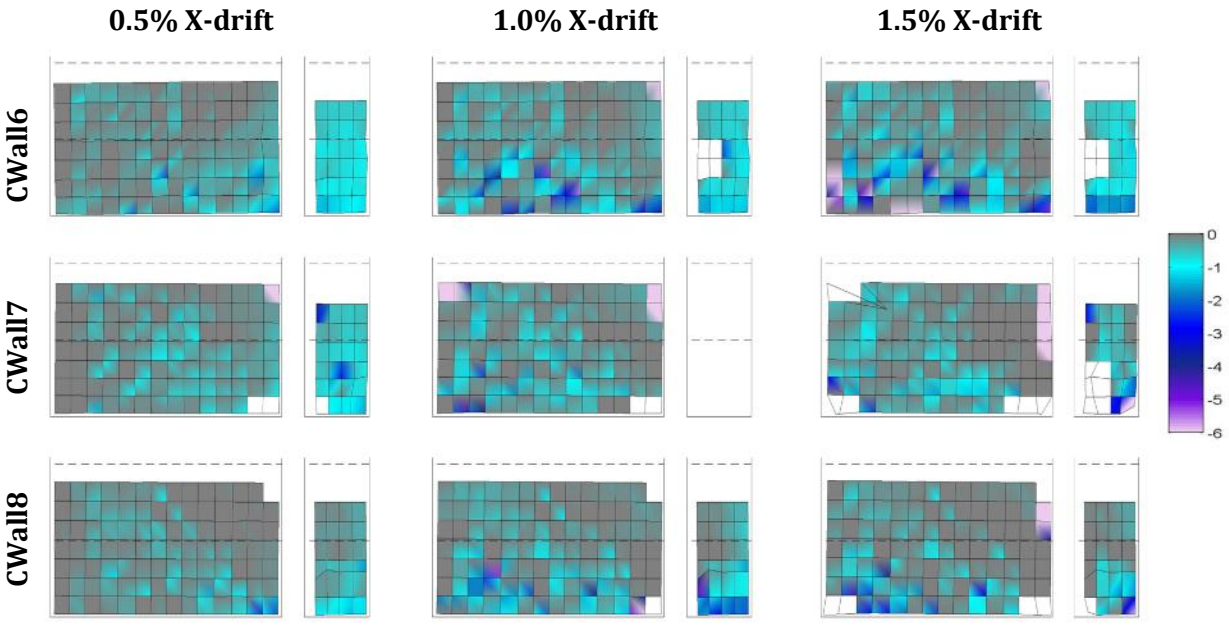

Figure 5.32: Second Principal Strain Fields at 0.5%, 1.0%, and 1.5% X-drift peaks (units: millistrain)
Provided by Andrew Mock in preparation of [124]

From the strain fields the following conclusions can be drawn for the C-shaped wall tests:

- The wall flanges contribute to carrying a rather significant portion of the compression demand thus reducing the demand on the wall web. As a result, the neutral axis depth is relatively narrow compared to a planar wall of similar design. Also the overall wall failure is tension-controlled (buckling-rupture mode) in contrast to the compression-controlled (crushing-buckling mode) walls described in *Birely* [35].
- There is significant shear demand in the wall web, particularly in tension regions. With increasingly drift level, the shear demand in the flange becomes more significant along the base of the wall and in the boundary elements. Shear straining in the flanges appears to have a more rapid onset and greater magnitude in the bi-directionally loaded walls.
- The stiffness discontinuity in transitioning from a lightly-reinforced web to boundary element/flange results in a region of tensile straining (and high shear straining) along the edge of the compression boundary element.

5.6 Conclusions

The three C-shaped wall tests described in Chapters 4 and 5 investigated the impact of non-planar wall response with respect to: (i) uni- versus bi-directional lateral loading and (ii) variable axial loading that occurs in wall piers in a coupled core wall system. To more fully understand the earthquake performance of C-shaped walls, test results including global load-deformation, damage, as well as localized and full-field deformation data were analyzed. The following summarizes the observations and conclusions of this work:

- The strong-axis drift capacity of the uni-directionally loaded wall was approximately -1.75% and +2.25%, while for the bi-directionally loaded walls it was at or slightly beyond 1.5% for both positive and negative loading. The bi-directionally loaded walls were able to sustain weak-axis drift demands in excess of 1.5%.
- Wall softening was more gradual for the uni-directionally loaded wall, while the bi-directionally loaded walls experienced rather sudden and substantial losses in strength. This (and the previous point) suggests that both strong-axis drift capacity and progression of strength loss can be impacted by weak-axis loading.
- For strong-axis bending, both uni- and bi-directionally loaded walls had essentially the same flexural strength (within 91-95% of nominal flexural strength calculated per *ACI 318-14* [18]) and were able to maintain a similar load-deformation response until 0.75% drift.

- The damage progression in all walls was similar. Yielding and fracture of a majority of No. 2 bars in the wall web led to significant sliding of wall web at wall-foundation interface; this sliding was resisted by cyclic (buckling/straightening) action of longitudinal reinforcement in the corner boundary elements and out-of-plane response of the wall flanges. Ultimately, the walls' boundary elements degraded due to crushing of confined concrete and buckling-rupture of longitudinal rebar which led to significant loss in lateral-load carrying capacity of the wall.
- Aside from the onset of horizontal and diagonal cracking, which occur at similar drifts, damage states occur at lower strong-axis drift demand levels for walls subject to bi-directional compared to uni-directional loading.
- For each of the C-shaped walls, strain gauge measurements indicate that compression yielding is limited and typically only occurs after repeated cycles of loading that have already resulted in tension strain yielding and hardening. This is distinct from planar walls described in *Birely* [35] where researchers noted that compression yielding often preceded tension yielding and the walls failed via a crushing-buckling mechanism (flexural-compression).
- Strain fields calculated from full-field measurements indicate that the walls' neutral axis is rather shallow. The wall flanges contribute to carrying a significant portion of the compression demand, such that the region and magnitude of compression demand on the wall web is limited. Also, shear straining is significant along diagonal bands in the wall web, at the base of the flanges, and at the web-boundary element transition at the wall corners. This corresponds to the base slip and out-of-plane shear damage to the flanges that was observed during experimental testing.

6 NON-LINEAR MODELLING OF STRUCTURAL WALLS USING 3D ELEMENTS: APPROACH AND CALIBRATION

This chapter provides a background for the modelling approach utilized in the parametric wall study described in Chapter 7. Section 6.1 consists of a brief discussion of the advantages of computational modelling and, in particular, the use of three-dimensional (3D) continuum modelling to further current understanding of structural wall response. Section 6.2 provides an introduction to ATENA, the non-linear 3D continuum-type finite element analysis software used for the study. Section 6.3 describes the finite element types and mesh generation and refinement. Sections 6.4 and 6.5 summarize the concrete and steel constitutive models. Section 6.6 provides information on the model validation process conducted by *Whitman* [173]. Section 6.7 provides details on how wall failure drift/rotation capacity and failure modes were determined. Section 6.8 discusses the development and calibration of the baseline wall model for the parametric study that is the focus of Chapter 7. Section 6.9 provides a summary for the modelling approach described in the chapter.

6.1 Benefits of 3D-Continuum Computational Wall Models

6.1.1 Role of Computational Wall Modelling

There is a great wealth of knowledge that can be acquired from in-the-field post-earthquake evaluation of walled buildings and from experimental testing of structural walls, as suggested by the work presented in earlier chapters. However, these sources of data can be insufficient to support modifications to design code provisions. Using field data and experimental testing, it is often difficult to isolate a particular design parameter, examine a large range of values for this parameter, and thereby establish correlation between the parameter and wall strength or deformability. The following sub-sections describe some of the shortcomings of field and experimental wall data on performance, and the role that computational modelling can play in addressing these shortcomings. Specifically, the benefits of using nonlinear finite element analysis with three-dimensional continuum-type elements is discussed.

6.1.1.1 Shortcomings of Data from Field Observation of Earthquake Damaged Walled Buildings

Chapter 2-3 and *Birely* [35] present the results of extensive investigation of the earthquake response of nonplanar and planar reinforced concrete walls, respectively. Both studies consider

laboratory data as well as field data collected following significant earthquakes. The following list of shortcomings for field data is based on these studies:

- ***Wall design parameters vary significantly for buildings in a region affected by a single earthquake; variability is greater still for geographically distributed buildings affected by different earthquakes.*** Wall designs differ due based on intended building use, engineer-of-record, contractor, year of design, prevailing code, etc. Wall response varies due to: interaction of structural walls with the rest of the lateral-load resisting or gravity system, unique site and earthquake properties, and interaction of different design parameters. Building response is complex, and it is difficult to isolate the impact of individual wall design parameters on this response. Thus, it is difficult to quantify the impact of a specific design parameter on wall response; typically, field data can be used only to link design variables with damage modes or potential for damage.

- ***Structural wall design details are often not readily available to researchers studying post-earthquake reconnaissance data.*** Typically, the field data collected as part of a post-earthquake reconnaissance effort comprises only images of wall damage, a building floorplan indicating the location/orientation of damaged walls, a brief description of observed damage, and a hypothesis as to the response mode and/or design variable that resulted in observed damage. Hypotheses about response and failure modes are often made quickly based on relatively little data. These findings may be the only discussion of wall damage that remains in the permanent record, without further detailed investigation to support these assessments. As a whole, the body of reconnaissance documents provides limited information by which to compare the impact of specific design parameters on wall response from a single or multiple earthquakes.

- ***Reconnaissance efforts usually focus on buildings with poor performance and include very few examples of good to excellent performance.*** In evaluating the impact of a specific wall design parameter, it is important to look at walls exhibiting the full range of response from poor to excellent. This more complete set of field data would enable researchers to establish correlations between the design parameter value and wall response, as well as set appropriate minimum thresholds for the design parameter. Together the correlations and minimum thresholds are important to modifying guidelines for wall design based on actual, field observations.

As a whole, reconnaissance data are a vital source of knowledge for engineers because they provide understanding of the behavior of real systems, which can only be approximated via experiment or computational modelling. The importance of reconnaissance data is appreciated by the design community and more recent reconnaissance efforts have worked to overcome some of the aforementioned shortcomings; a prime example being the *Recommendations for Seismic Design of Reinforced Concrete Wall Buildings Based on Studies of the 2010 Maule, Chile Earthquake* [135].

6.1.1.2 Shortcomings of Experimental Wall Data

Large-scale laboratory experiments can effectively approximate the in-field response of structural walls and provide data to inform the development of code provisions for wall design. However, there are a number of limitations that exist with laboratory experiments, including those associated with expense, schedule, and the current state of technology. These limitations relate to the application of lateral and axial load; consideration of boundary conditions; ability to examine a large range of values for a single design parameter; and the type, quality, and distribution of acquired data. Based on the review of structural wall experiments conducted in Chapter 2-3 the shortcomings of laboratory tests include:

- ***Large-scale wall tests are typically subject to lateral loading protocols that are not fully representative of seismic forces.*** Even advanced laboratories are typically only equipped to test large specimens with a quasi-static monotonic or cyclic lateral loading rather than a dynamic earthquake ground motion. Furthermore, lateral loading is typically applied uni-directionally, and only infrequently in a simplified bi-directional pattern. In a majority of tests, the load is applied at the top of the wall specimen in a manner that is intended to account for the full lateral load at the effective height of the prototype wall; there are a few instances where loads are applied at intermediate story heights. Finally, it is difficult to investigate walls subject to high shear demands due to the necessary capacity of the loading system.

- ***Most wall test specimens are subject to low and/or constant axial loads that are not representative of the combination of gravity load and vertical seismic forces.*** In most cases, the assigned axial load for the test specimen is based on the portion of the building's gravity load that the prototype wall would carry; the assigned values usually range from 0-$0.15A_g f'_c$. Other than the few tests where axial load was varied to capture effects of wall

coupling, monotonic or cyclic tests do not account for changes in axial load that would result from vertical ground motion.

- ***Realistic boundary conditions, resulting from wall interaction with other structural members or between soil and the structure, are not well captured by physical experiments.*** Many test specimens do not include slabs that, in an actual building, would connect to the walls and provide some degree of out-of-plane stiffness as well as transfer of diaphragm loads. Additionally, walls are typically constructed atop a large concrete foundation block which is post-tensioned to the laboratory strong floor; this does not allow for the partial fixity condition that would be observed with true soil-structure interaction.

- ***In an individual test program, or across multiple test programs, it is difficult to capture the impact of a large range of values for a single design parameter.*** Large-scale wall tests are both time intensive and costly, which explains why prior test programs often explore more than one design parameter at a time and wall sub-sets that do examine a single test parameter contain only three to five specimens. The limited number of values for a single design parameter results in only a few data points by which to assess that parameter. In reviewing the analyses of past wall experiments from Chapter 3 and *Birely* [35], it is important to be aware of the interaction between design variables and the fact that it is often difficult to isolate the effects of just one design parameter.

- ***There have been limitations in the amount, type, and quality of data acquired in wall experiments and the public availability of that data to other researchers.*** In addition to instrumentation time and cost, the level of technology has previously been an inhibitor in collecting high-resolution, full-field data necessary to understand localized damage progression and global wall response. Currently state-of-the art sensor and data acquisition systems allow for a multitude of high-resolution data to be captured, the difficulty is now the ability to effectively analyze and disseminate the data in a comprehensible manner.

6.1.1.3 Overcoming Shortcomings in Wall Data with Computational Modelling

Computational modeling can provide understanding of the seismic response of concrete structural walls. Models that provide high-fidelity, accurate simulation of wall behavior that are computationally efficient and numerically robust simulation can enable researchers to:

- ***Examine the impact on wall performance of a specific design parameter over a wide range of parameter values.*** It is often necessary to examine walls with a wide range of values for a given design parameter in order to establish code minimum/maximum(s) as well as design expressions.

- ***Conduct relatively efficient/inexpensive investigations.*** Assuming that the learning curve for a researcher implementing a non-linear FEM computational tool is as intensive as developing a command over experimental test methods, computational modelling is much more rapid and less costly. As an example, each ATENA simulation in the parametric wall study (details in Chapter 6 and 7) requires 2.5-4.0 hours of cpu time on a desktop computer, and with an annual investment of around $15,000 it is possible to run hundreds of robust computational simulations in the span of a year project. In comparison with laboratory testing, numerical simulation can be relatively fast and cost-effective.

- ***Apply loads with higher magnitude or greater complexity than what is physically possible using laboratory equipment***. High shear demands, variable axial loads, and/or multi-directional loading protocols – which are more representative of actual seismic forces – may be easier to achieve in computational models. (Some computational tools do pose difficulties with loading protocols with greater complexity based on how wall damage effects convergence.)

- ***Examine wall response using a comprehensive set of high-quality, full-field data.*** In the finite element analysis, displacement data are calculated at each node in the model. From this information an array of deformation metrics can be calculated (stress/strain, crack width/direction) or inferred (concrete crushing, steel yielding/buckling). Also, by increasing mesh refinement in the predicted plastic hinge zone, it is usually possible to investigate localized damage through failure. In many experimental tests, sensors near the wall's critical section are unable to provide viable data nearing the specimen failure as these sensors have been damaged or removed to avoid damage.

It is important to acknowledge that despite these benefits, the results of computational models should be regarded as a complement to field and laboratory data.

6.1.2 Advantages of 3D-Continuum Models over Other Approaches

Whitman [173] conducted an investigation into the strengths and weaknesses of common computational modelling approaches used for examining structural wall response. The statements presented in Section 6.1.2 are, for the most part, a summary of these findings.

6.1.2.1 Modelling Approaches with 2D Line Elements

Two-dimensional line elements refer to two-node beam-column elements with multiple nonlinear section models distributed along the length of the element (distributed plasticity element) or with nonlinear section models located at the element ends (lumped plasticity element). Typically, these elements employ fiber-type section models to simulate nonlinear flexural response and the interaction of axial and flexural response (P-M interaction). Elements may employ the assumption of a linear curvature field along the length of the element (displacement-based formulation) or the assumption of a linear moment field (force-based element formulation). These elements are computationally efficient and typically provide accurate prediction of strength for flexure-controlled components. For planar walls with moderate shear demands, these models can provide accurate and precise prediction of strength, stiffness, cyclic response and deformation capacity *Lehman et al.* [112]. Accurate prediction of deformation capacity is achieved using a material regularization method proposed by *Pugh* [148], *Lehman et al.* [112]. For walls with high shear demands or nonplanar configurations, stiffness and strength predictions may be poor.

Because line-element models are computationally efficient and provide accurate and precise simulation of response for walls that exhibit flexure-controlled response, these models are ideally suited for analysis of walled building response to earthquake loading. Using line-element models, many analyses of a walled building subjected to multiple ground motion records of varying intensity can be conducted in a short period of time. For the current study, that seeks to use analysis to investigate response mechanisms in walls with shear-flexure interaction, specific deficiencies in the line-element models that may result in poor prediction of response include the following:

- The nonlinear fiber section model employs the assumption that the vertical strain field distribution is linear across the section (i.e. plane sections remain plane). This can result in significant over-prediction of stiffness and strength for walls with high shear stress demands and/or nonplanar cross-sections for which a nonlinear shear strain distribution

on the cross section results in a highly nonlinear vertical strain field (i.e. for walls for which the plane-sections-plane assumption is not valid).

- Flexure and shear material responses are assumed to be uncoupled. Thus, high shear stress demand does not result in premature flexural failure, and high axial load does not result in premature shear failure.
- Typically, linear shear response is assumed. This can over predict shear stiffness in regions where cracking is significant due to flexural response and under predict stiffness in regions were flexural cracking is limited.
- The line-element modeling approach makes representation of 3-D geometry and 3-D loading difficult.

6.1.2.2 Modelling Approaches with 2D Shell and Membrane Elements

Other approaches to modeling structural walls include: 2D plane stress (i.e. membrane) elements, such those available in the VecTor2 software developed by the VecTor Analysis Group at the University of Toronto [174], and the layered shell elements in which the response of concrete "layers" are simulated using 2D constitutive models calibrated to represent the behavior of unconfined or confined concrete.

Major advantages of shell and membrane element models are the ability to simulate i) nonlinear vertical strain distributions on the wall cross section, and ii) flexure-shear interaction via a 2D material model. Shell and membrane element models can provide accurate prediction of stiffness, strength and deformation capacity [173]. Also, models developed with shell and member elements can be manipulated relatively easily to represent 3-D geometries and 3-D load patterns.

There are two major deficiencies with these element types:

- The user must define the response of confined and unconfined concrete, based on an assumption of confinement effectiveness. Thus, there is the potential to over or under predict deformation capacity if assumptions about confined concrete response are incorrect.
- Material regularization using concrete crushing energy and a mesh-dependent length is required to achieve accurate, mesh-objective simulation of deformation capacity. Material regularization is not supported in VecTor2, so VecTor2 analyses cannot provided accurate, mesh-objective simulation of deformation capacity [148].

6.1.2.3 Modelling Approaches with 3D-Continuum Type Elements

Finite element analysis (FEA) software that employs 3D-continuum type elements are computationally expensive; however, the additional computational time is accompanied by the following advantages:

- Simulates non-linear strain distribution on the wall cross section (i.e. does not assume plane sections remain plane).
- Simulates flexure-shear interaction at the material (and equilibrium) level; this results in accurate simulation of shear stiffness throughout the building as well as accurate simulation of the onset of strength loss due to a flexure-shear mechanism.
- Provides explicit simulation of the confined concrete, including expansion of concrete under compressive loading, activation of confining reinforcement to restrain concrete expansion, and increased strength and deformation capacity exhibited by confined concrete.
- Utilizes three-dimensional elements to represent three-dimensional geometry and three-dimensional loading.
- Can provide accurate prediction of stiffness, strength, deformation capacity and cyclic response; accurate simulation of deformation capacity requires material regularization.

There are a number of FEA software packages that include 3D solid elements and sophisticated 3D concrete constitutive models: ABAQUS, ADINA, ATENA, DIANA, LS-DYNA, and VecTor3. *Johnson* [104] provides a comprehensive review and comparison of most of these software packages, specifically for the purpose of modelling concrete structures; thus, a similar review is not presented here. *Whitman* [173] compares ABAQUS and ATENA for simulation of confined concrete prisms, representing confined boundary elements in concrete walls. Based on reviews by Johnson and Whitman, the ATENA software package was selected for the parametric wall study discussed in Chapter 7 as it has a number of capabilities with respect to modelling concrete structures; these capabilities are summarized in Section 6.2.

6.2 Brief Description of ATENA Software

ATENA is a nonlinear finite element analysis package developed by Červenka Consulting primarily for simulation of the nonlinear response of concrete structures. It enables realistic simulation of concrete structures by drawing on leading knowledge in concrete mechanics and computational methods. The toolset has been proven via numerous successful experimental validation case

studies and international prediction competitions. Between ATENA 2D and 3D, it is possible for a user to implement an array of:

- element geometries (truss, planar triangle/quadrilateral, 3D solid, shell, etc.);
- concrete constitutive models that can be easily implemented to appropriately capture fracture-plastic response (cracking, crushing, and crack closure);
- reinforcement constitutive models that can range from elastic to nonlinear hysteretic;
- reinforcement bond models when the use of perfect bond is inappropriate;
- complex spatial/temporal analyses for creep, durability, transport, or dynamics; and
- solution approaches for nonlinear equations which provide varying advantages in terms of efficiency and convergence based on the posed problem.

Furthermore, the graphical user interface provided in the ATENA pre- and post-processor enable rapid model generation and examination of a multitude of structural response metrics (crack propagation and strain/stress fields, among others). The advantages listed above serve as a strong motivator for academic researchers and industry practitioners to use the ATENA software package when faced with structural concrete challenges, as in the case with the current parametric study.

Note that the information provided in Sections 6.3-6.4 is in large part a condensed and simplified description of content that can be found in ATENA Program Documentation:

- Part 1- Theory (*Červenka et al.* [46]),
- Part 6- ATENA Input File Format (*Červenka & Jendele* [45]), and
- Part 11- Troubleshooting (*Pryl & Červenka* [147])

Therefore, references will only be provided for figures; textual citations will only be provided when other resources were utilized.

6.3 Overview of Finite Element Types & Meshing in ATENA

The simulation-based parametric study of concrete walls was conducted using ATENA 3D, employing three-dimensional solid elements to represent the concrete portion of the walls and two-dimensional truss elements to represent the embedded steel reinforcement. Both of these element types (2D truss and 3D solid) are described in the subsequent paragraphs. As a note, the simulations were conducted considering the effects of geometric non-linearity, with equilibrium requirements satisfied in the deformed configuration of the structure.

6.3.1 2D Truss Element

In the ATENA analyses, steel reinforcing bars in the wall can modeled using a two-dimensional truss element, classified in ATENA as CCIsoTruss <xx>. This truss element provides only axial stiffness and strength; This element includes two nodes and represents a linear displacement field with constant strain; Gaussian integration occurs at a single node at mid-length of the element. Fig. 6.1 shows the geometry and the interpolation/shape functions associated with CCIsoTruss<xx>.

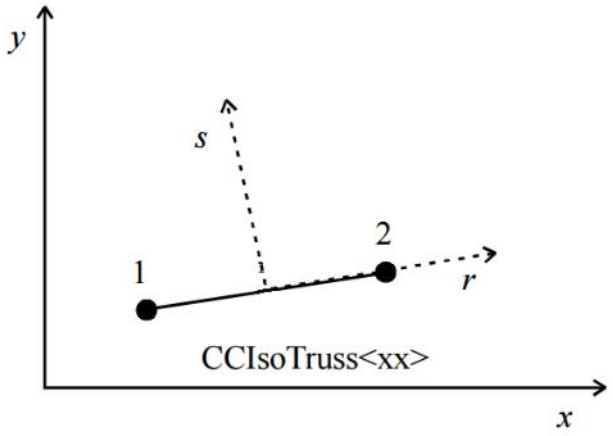

$$N_1 = \frac{1}{2}(1 - r)$$
$$N_2 = \frac{1}{2}(1 + r)$$

Figure 6.1: Geometry and Shape Functions for 2D Truss Element (modified from *Červenka et al.* [46])

As a further note, the mesh for the overall structural member is independent of the discrete embedded steel reinforcing bars. The mesh is generated based on the solid elements and subsequently the nodal displacements of the solid element mesh are linked to truss/bar nodes. In the case where the truss/bar node does not align with a solid element mesh node then standard interpolation is used to determine the displacement at the truss/bar node based on the displacements at adjacent solid element nodes.

6.3.2 3D Solid Hexahedron (Brick) Element

The solid volumes that make up the wall specimen, foundation, and loading cap of the walls in the parametric study were modelled using isoparametric 3D solid hexahedron (brick) elements classified as CCIsoBrick <xxxxxxxx>. These elements consist of eight nodes, where there are three translational degree-of-freedoms at each node. A linear interpolation scheme was selected such that Gaussian integration occurs at eight sampling points within the element. Fig. 6.2 provides the geometry and interpolation/shape functions for the CCIsoBrick <xxxxxxxx> element.

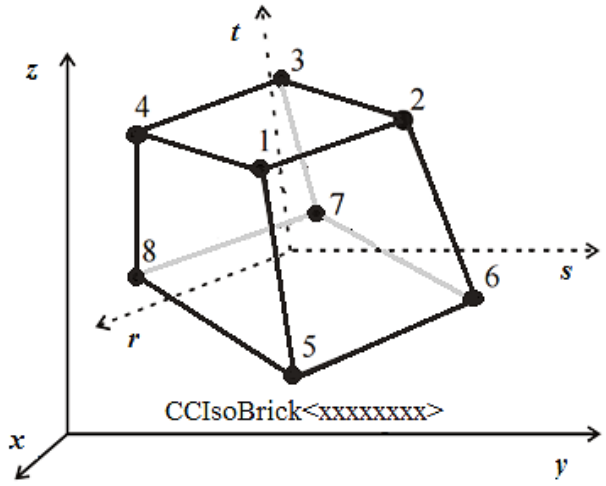

$$N_1 = \frac{1}{8}(1+r)(1+s)(1+t)$$
$$N_2 = \frac{1}{8}(1-r)(1+s)(1+t)$$
$$N_3 = \frac{1}{8}(1-r)(1-s)(1+t)$$
$$N_4 = \frac{1}{8}(1+r)(1-s)(1+t)$$
$$N_5 = \frac{1}{8}(1+r)(1+s)(1-t)$$
$$N_6 = \frac{1}{8}(1-r)(1+s)(1-t)$$
$$N_7 = \frac{1}{8}(1-r)(1-s)(1-t)$$
$$N_8 = \frac{1}{8}(1+r)(1-s)(1-t)$$

Figure 6.2: Geometry and Shape Functions for 3D Solid Hexahedron (Brick) Element (modified from *Červenka et al.* [46])

As an additional clarification for the modelling approach used in the parametric study, ATENA allows users to select a quadratic interpolation scheme for 3D brick elements that yields up to twenty integration points. However, given the agreement of the calibrated baseline model with experimental test data as shown in Section 6.6.2 and the number of wall simulations for the parametric study described in Chapter 7, eight integration points was deemed to provide sufficient solution accuracy for the associated computational economy.

6.3.3 Mesh Generation/Refinement

The finite element mesh for the overall wall sub-assembly is based on the size of the 3D solid elements; the presence of embedded discrete steel reinforcement does not impact node location or mesh generation. Each of the walls in the parametric study was sub-divided into seven macroelements (MEs). These MEs consist of the (#1) foundation, (#2-4) lower one-third of the wall (boundary elements and web), (#5-7) upper two-thirds of the wall (boundary elements and web), and (#8) loading cap (an elastic region that extends from the wall height to the effective height). Mesh refinement is executed via local mesh size specification; in other words, specifying the desired absolute or relative size of the elements for each of the MEs. The automatic mesh generator in ATENA uses this value as a guideline in dividing a given ME into 3D brick elements with equal dimensions. The absolute element size specified for MEs in the parametric wall study (as a ratio of element size-to-wall thickness, t_w) was as follows: (#1) foundation =1.33t_w, (#2-4) lower one-third of the boundary elements and web = 0.56t_w, (#5-7) upper two-thirds of the boundary elements and web = 0.89t_w, and (#8) loading cap = 1.33t_w. For the cantilever walls considered in this study, a fine mesh was used for the bottom portion of a wall where significant damage was expected to occur

and a coarser mesh was used above. Coarser meshes were using in elastic regions such as the foundation/loading cap. Fig. 6.3 is a sample wall from the parametric study that shows the wall sub-divided into seven MEs and the mesh refinement of each of these MEs.

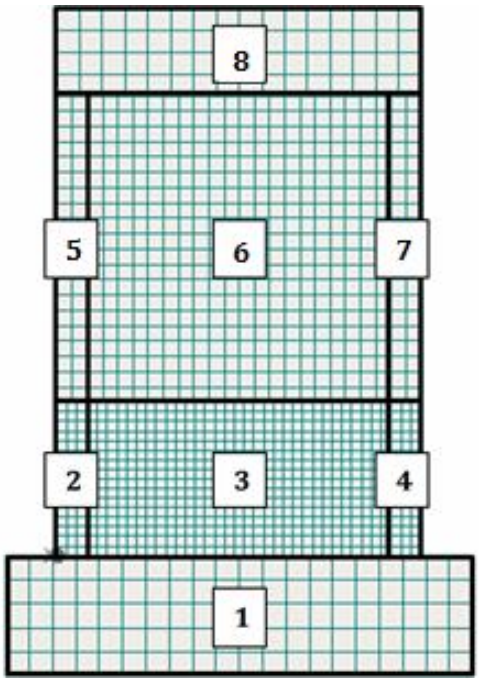

Figure 6.3: Mesh Refinement for Sample Wall from Parametric Study
(macroelements have numeric labels)

Note that for walls in the parametric study, nodes along the bottom surface of ME #1 are restrained in all directions and nodes along the top edge of ME #8 are restrained in the out-of-plane direction. Displacement is applied at the top of ME #8 corresponding to the effective height of the wall (h_{eff}), while loads are measured at the top of ME#7 at the height of the wall specimen (h_w).

6.4 Constitutive Model for Concrete in ATENA

In the parametric wall study, concrete was modelled in ATENA 3D using the constitutive model CC3DNonLinCementitious2 which combines a continuum damage model to simulate concrete cracking under tensile loading and a plasticity model to simulate concrete response under compressive loading. The models are combined per the strain decomposition method proposed by *de Borst* [49]: $\varepsilon_{tot} = \varepsilon_e + \varepsilon_f + \varepsilon_p$, where ε_e is elastic strain, ε_f is fracture strain and ε_p is plastic strain. The advantages of the CC3DNonLinCementitious2 material model include its ability to simulate three-dimensional stress states in concrete, to produce mesh-objective results, and to be

flexible in implementing either fixed or rotating crack approaches. The remainder of Section 6.4 includes details of this constitutive model related to tension, compression, and shear behavior of concrete. Fig. 6.4 provides the complete uni-axial concrete stress-strain curve with labels for each of the compression/tension behavior regions; this is intended to serve as a visual guide for the subsequent discussions in Sections 6.4.1-6.4.3.

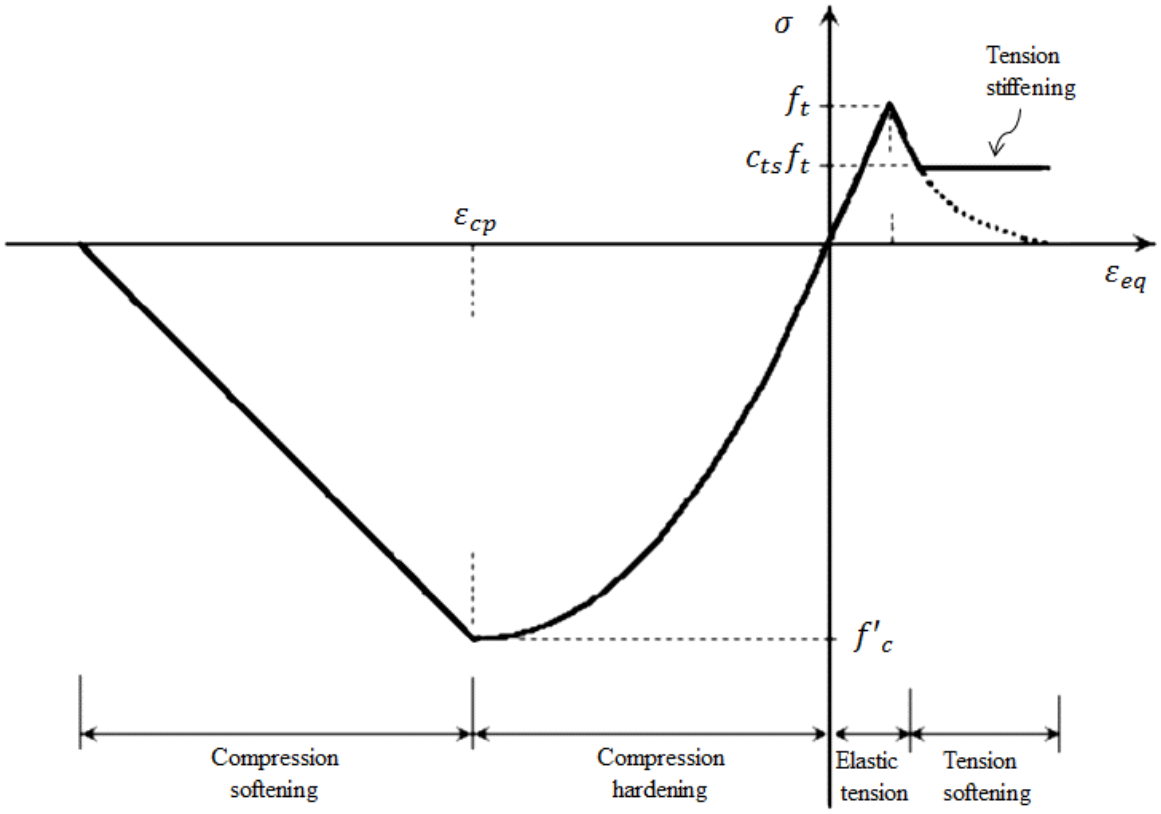

Figure 6.4: Concrete Compression/Tension Response (modified from *Červenka et al.* [46])

6.4.1 Concrete Tension Response

6.4.1.1 Elastic Tension Response: Rankine Fracture Model

The orthotropic smeared crack model in ATENA 3D utilizes the Rankine fracture model, which establishes a maximum (normal) stress criterion for the brittle fracture of concrete. A tension stress cut-off value, f_{ti} , based on a user-defined tensile concrete strength is associated with each of the principal material directions, *i*, such that if the stress that principal direction, $_i$, exceeds the cut-off then the concrete fractures. Therefore, in cases where the expression $_i - f_{ti} \leq 0$ is met, the stress state is within the 3D stress failure surface and the concrete exhibits a linear elastic response; otherwise, the concrete has fractured/cracked. In the parametric wall study, a fixed crack approach

was employed such that the crack direction is locked in the principal stress direction at initial cracking. This corresponds with the directions associated with principal stresses, $_i$, for assessing fracture using the Rankine criterion.

6.4.1.2 Tension Softening: Hordijk [91]

Following fracture, tension softening of concrete is modelled using either a linear or exponential curve to capture the loss in concrete tensile strength normal to a crack as the crack widens. In this study, an exponential tension softening curve from *Hordijk* [91] was used. The softening curve defines tension stress transferred across the crack versus crack with opening; the area under the curve is the concrete fracture energy. The stress vs. crack width opening curve is converted to stress vs. strain for use in the element via an element characteristic length, L_t, taken equal to the length of the element projected normal to the crack. The exponential tension softening curve per *Hordijk* [91] is shown in Fig. 6.5(a), note that the area under the curve is the specific fracture energy, G_f.

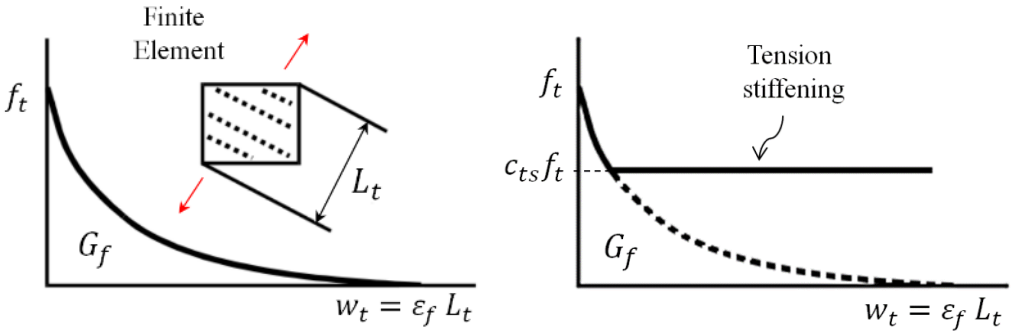

Figure 6.5: Concrete Exponential Tension Softening: (a) from *Hordijk* [91], (b) with Tension Stiffening (modified from *Červenka et al.* [46])

6.4.1.3 Tension Stiffening

In the post-cracking regime, intact concrete between cracks can carry some tensile force that is transferred from the steel reinforcement to the concrete via bond. This effect is referred to as tension stiffening and results in lower reinforcement strains (stiffening) in the uncracked concrete zones around reinforcement. In particular, heavily reinforced concrete structures are noted to exhibit tension stiffening since cracks do not fully develop and thus the concrete contributes to steel stiffness. This behavior can be accounted for in ATENA 3D by specifying a tension stiffening factor, c_{ts} , which defines a non-zero residual concrete tensile strength as a percentage of the user-specified concrete tensile strength, f_t. Fig. 6.5(b) illustrates the exponential tension softening curve with the inclusion of the tension stiffening factor. Tension stiffening was simulated in this study; the selection of the tension stiffening factor is described in Section 6.6.2.

6.4.2 Concrete Compression Response

The concrete compression formulation in the CC3DNonLinCementitious2 constitutive model employs the *Menétrey & William* [121] failure surface. The three-parameter *Menétrey & William* [121] failure surface definition enables the decoupling of concrete hardening and softening descriptions. The failure surface evolves during yielding/crushing based on the value of equivalent plastic strain, $\varepsilon_{eq,p}$, as a function of concrete compressive strength, f'_c, defined by the hardening/softening laws described in subsequent paragraphs.

The compression hardening/softening rules were developed using experimental data from testing by *van Mier* [168] of concrete cubes subjected to uniaxial loading. Concrete hardening is modelled by the non-linear (elliptical) stress versus equivalent plastic strain curve shown in Fig. 6.6(a). Both the onset of nonlinear behavior, f'_{c0}, and the plastic strain at compressive strength,ε_{cp} , are input parameters (where $f'_{c0} = 2f_t$ and $\varepsilon_{cp} = f'_c/E$). Concrete softening is defined by the linear stress versus compressive deformation relationship shown in Fig. 6.6(b). To achieve mesh-objective results, equivalent plastic strain, $\varepsilon_{eq,p}$ is related to compressive deformation via a mesh-dependent characteristic length, L_c, defined as the length of the element projected into the direction of minimal principal stresses (Fig. 6.6(b)). The critical compressive displacement, w_d, is a user-defined parameter; the ATENA user's manual provides a recommend range for w_d. For the current study, the $w_d$value used for all analyses was determined based on experimental data via a calibration process, the results of which are described in Section 6.6.2.

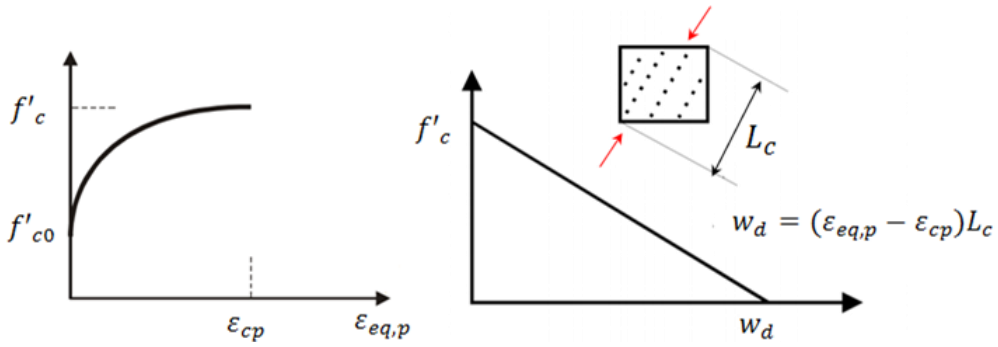

Figure 6.6: Concrete Compression Models based on *van Mier* [168]: (a) Hardening, (b) Softening (modified from *Červenka et al.* [46])

The final *Menétrey & William* [121] failure surface used to define the concrete compression response is calculated using a plastic potential function, $G_p(\ )$, which contains a coefficient term that is referred to as the return direction, β. The plastic potential function describes the variation in volumetric expansion. The return direction defines the amount of dilatancy, or the volumetric change, that the concrete experiences when loaded in compression. When $\beta < 0$ then the concrete

is contracting (decreasing in volume), if $\beta = 0$ then there is no volumetric change, and if $\beta > 0$ then concrete is dilating (increasing in volume). The return direction is a user-defined input, and was determined for the parametric wall study via a calibration process described in Section 6.6.2.

6.4.3 Other Considerations in Concrete Compression Model

6.4.3.1 Concrete Shear Response

The CC3DNonLinCementitious2 constitutive model simulates reduced shear strength, parallel to the crack surface, for cracked concrete using a modeling approach similar to that of the Modified Compression Field Theory proposed by *Vecchio and Collins* [169]. This approach is based on the assumption that shear transfer that occurs across concrete cracks is due primarily to aggregate interlock; as such, shear transfer capacity reduces once crack width opening exceeds the user provided maximum aggregate size, a_g. A user-defined shear stress coefficient, S_F , is utilized in the CC3DNonLinCementitious2 constitutive model to define the relationship between normal and shear crack stiffness. The shear factor is a user-defined input, and was determined for the parametric wall study via a calibration process described in Section 6.6.2.

6.5 Constitutive Model for Steel Reinforcement in ATENA

For the parametric wall study, steel reinforcement is modelled either as discrete truss elements (Section 6.3.1) or smeared reinforcement within a 3D brick element (Section 6.3.2) with composite material properties. Both cases were implemented using the same cyclic steel reinforcement constitutive model in ATENA 3D which is classified as CCCyclingReinforcement, additionally a perfect steel bond model was utilized for both discrete and smeared reinforcement.

A multi-linear steel hardening law was utilized to describe the stress-strain response of the steel including: elastic, yielding/hardening, and fracture states. The non-linear model from *Menegotto & Pinto* [120] is utilized to describe the uni-axial steel reinforcement response and has been extended in ATENA 3D to account for isotropic hardening provided in the user-defined steel hardening law. However, since the walls simulated in the parametric study were all monotonically loaded the non-linear description is not invoked and the steel response essentially follows the aforementioned multi-linear steel hardening law.

As a note, the 2D truss element with uni-axial stiffness in ATENA 3D does not precisely account for buckling the way that geometric non-linearity can be accounted for in other element types in the ATENA toolset. The user manual suggests disabling the steel constitutive model so that it is not

active in compression (i.e. the steel has no compressive strength). Despite the desire to model bar buckling in the parametric wall study, the suggested approach was not used as it was deemed too conservative given the significant compressive forces carried by the wall boundary elements which would result in premature wall failure. A consequence of the inability to appropriately model bar buckling in ATENA 3D is the difficulty identifying the onset of certain failure mechanisms.

6.6 Validation of ATENA 3D Modelling Approach by Whitman [173]

Whitman [173] conducted a study in ATENA 3D using experimental data from a set of 23 slender, planar walls subjected to cyclic lateral and constant axial loading and exhibiting primarily flexure-controlled failure mechanisms. The objective of the study was to develop a set of recommendations to achieve accurate simulation of concrete wall response using ATENA. The study addressed i) user-defined model parameters employed in the ATENA CC3DNonLinCementitious2 concrete constitutive model and ii) the relative quantity of discrete versus smeared reinforcement to be used in the boundary element and web regions of the wall.

6.6.1 Accuracy of Simulation Results for Planar Wall Models

The 23 reference specimens in this study represented a range of cross-sectional aspect ratios (6.0-21.1), axial load ratios (0-13.7%), normalized peak shear stresses ($1.10\text{-}7.00A_{cv}\sqrt{f_c'}$ with f_c' in psi), shear spans (1.5-3.1), shear capacity-to-demand ratios (0.23-0.91), boundary element classifications (ACI compliant vs non-compliant), and failure modes (shear-compression, crushing-buckling, and buckling-rupture). A summary of geometry and loading characteristics for these walls are included in Table 6.1.

Table 6.1: Geometry and Loading for Experimental Walls Simulated with ATENA 3D (*Whitman* [173])

Specimen	Author	CSAR	Shear Span	ALR	$V_{max}/A_{cv}(f'_c)^{0.5}$	V_b/V_n	ACI BE
		--	--	%	psi	--	--
WSH1	Dazio et al.	13.3	2.3	5.5	2.01	0.44	NBE
WSH2	Dazio et al.	13.3	2.3	6.3	2.27	0.53	NBE
WSH3	Dazio et al.	13.3	2.3	6.4	2.92	0.67	OBE
WSH4	Dazio et al.	13.3	2.3	6.3	2.77	0.62	NBE
WSH5	Dazio et al.	13.3	2.3	13.7	2.81	0.62	OBE
WSH6	Dazio et al.	13.3	2.3	11.4	3.58	0.83	NBE
W1	Liu	6.0	3.1	7.6	2.31	0.39	OBE
W2	Liu	6.0	3.1	3.5	1.67	0.33	NBE
PW4	Birely	20.0	2.0	12.2	4.63	0.88	SBE
RW1	Thomsen et al.	12.0	3.1	10.5	2.57	0.50	NBE
RW2	Thomsen et al.	12.0	3.1	9.2	2.65	0.52	NBE
S5*	Vallenas et al.	21.1	1.6	4.8	6.81	0.88	SBE
S6*	Vallenas et al.	21.1	1.6	4.8	6.42	0.83	SBE
WR20	Oh et al.	7.5	2.0	10.4	3.00	0.76	NBE
WR10	Oh et al.	7.5	2.0	9.8	2.87	0.64	OBE
WR0	Oh et al.	7.5	2.0	10.8	2.97	0.74	NBE
R1	Oesterle et al.	18.8	2.4	0.0	1.10	0.23	NBE
R2	Oesterle et al.	18.8	2.4	0.0	2.00	0.42	SBE
RW-A20-P10-S38	Tran	8.0	2.0	7.3	3.60	0.81	SBE
RW-A20-P10-S63	Tran	8.0	2.0	7.3	6.10	0.91	SBE
RW-A15-P10-S51	Tran	8.0	1.5	7.7	4.90	0.83	SBE
RW-A15-P10-S78	Tran	8.0	1.5	6.4	7.00	0.85	SBE
RW-A15-P2.5-S64	Tran	8.0	1.5	1.6	5.80	0.79	SBE
Mean		12.1	2.2	7.1	3.60	0.65	--
Maximum		21.1	3.1	13.7	7.00	0.91	--
Minimum		6.0	1.5	1.6	1.10	0.23	--
Standard Deviation		5.0	0.52	3.7	1.75	0.20	--
COV		0.41	0.24	0.52	0.49	0.31	--

Of the 23 ATENA 3D wall models, 20 of these were able to complete the simulation through to failure while the additional analyses terminated prior to failure due to numerical instability. The successful simulation results were compared to experimental data to assess accuracy with respect to stiffness, strength, and deformation predictions. Table 6.2 summarizes the accuracy of the model predictions where Δ_y is yield deformation (used to determine secant stiffness to yield), V_{max} is the normalized peak shear stress demand, and Δ_u is the deformation capacity

Table 6.2: Comparison of Simulated to Experimental Results for Wall Models in ATENA 3D (*Whitman* [173])

	Stiffness		Strength		Deformation		Failure Mode
	Exp. Δ_y %	Sim./ Exp. --	Exp. V_{max} kips	Sim./ Exp. --	Exp. Δ_u %	Sim./ Exp. --	--
WSH2	0.38	0.90	81.1	0.98	1.75	1.00	BR
WSH3	0.41	0.96	102.4	0.97	2.07	0.91	BR
WSH4	0.36	0.89	99.0	1.03	1.60	1.10	CB
WSH5	0.25	0.91	97.4	0.99	1.52	0.86	BR
WSH6	0.36	0.91	135.4	0.99	2.04	0.98	CB
W1	0.52	0.92	58.8	1.06	2.98	0.96	CB
W2	0.49	0.94	62.1	1.06	2.91	1.13	BR
PW4	0.41	0.76	218.0	1.08	1.01	1.87^{T}	CB
RW1	0.37	0.98	33.4	0.98	2.26	1.01	BR
RW2	0.35	0.94	35.7	0.91	2.35	0.93	CB
S6	0.41	0.93	194.3	0.98	1.65	0.96	CS
WR10	0.47*	0.56	96.7	1.04	2.82	0.98	CB
WR0	0.52*	0.50	95.4	1.04	2.14	0.99	CB
R1	0.15	1.81	27.4	0.93	2.52	1.12	BR
R2	0.34	0.95	50.4	0.92	3.25	1.01	BR
RW-A20-P10-S38	0.14	0.90	108.0	0.93	3.14	0.99	CB
RW-A20-P10-S63	0.55	0.88	166.9	0.97	3.00	1.09	CB
RW-A15-P10-S51	0.34	0.61	135.5	0.99	3.31	0.96	CB
RW-A15-P10-S78	0.40	0.87	193.2	1.05	3.00	0.92	CB

		Stiffness	Strength	Deformation
Total	Median	0.91	0.99	0.98
	COV	0.29	0.05	0.06
BR	Median	0.95	0.98	1.01
	COV	0.31	0.05	0.10
CB	Median	0.89	1.01	0.98
	COV	0.20	0.05	0.07

To summarize the prediction results presented in Table 6.2, *Whitman* [173] indicates that the ATENA 3D modelling approach was able to simulate:

- Secant stiffness to yield with an average error of -9.1% and coefficient of variation (C.O.V) of 0.29, with a much of uncertainty resulting from Specimen R1. Difference in stiffness was attributed to the fact that shrinkage cracking was not considered in the models.
- Strength with an average error of 0.9% and C.O.V. of 0.05.
- Deformation capacity with an average error of -1.3% and C.O.V. of 0.07.

The results from the planar wall modelling work conducted by *Whitman* [173] demonstrated that the necessary response metrics (yield drift, ultimate drift, and peak shear stress value) could be determined via this modelling approach with good accuracy. Furthermore, this research study included a model calibration portion conducted prior to the 23 wall simulations in order to determine the appropriate concrete parameter values and approach to modelling smeared versus discrete steel reinforcement. These details are summarized in Section

6.6.2 Summary of Model Calibration Recommendations from Whitman [173]

The outcomes of the first state of the *Whitman* [173] study led to the recommendations for modelling slender, planar structural walls in ATENA including: concrete parameters (Table 6.3) and (ii) discrete versus smeared reinforcement for various zones of the wall (Table 6.4). Where available the *Whitman* [173] recommendations are compared with the more general recommendations provided by Cervenka Consulting, developers of the ATENA software.

Table 6.3: Recommendations for Concrete Parameters in ATENA (adapted from *Whitman* [173])

Concrete Parameter	**Description**	**Recommended Value Ranges**	
		ATENA	Whitman (2015)
Plastic Deformation, w_d	Determines the plastic deformation capacity of concrete at zero compressive stress; enables material regularization in compression.	0.025 - 0.125	0.0425
Dilation Parameter, β	Determines the extent to which concrete dilates under inelastic compression loading.	0.0 -0.7	0.0, may increase up to 0.25
Shear Retention Factor, SF	Determines the shear stiffness of cracked concrete.	20 - 200	50
Tension Softening, c_{ts}	Determines the residual tensile strength of concrete.	0.00-0.05	0.00, may increase up to 0.01

Table 6.4: Recommendations for Reinforcement Modelling in ATENA (*Whitman* [173])

Reinforcement Type	Location	Recommended % Reinforcement	
		Discrete	Smeared
Vert. & Horiz. Reinf.	Bottom region of wall web	90%	10%
	Top region of wall web	90%	10%
Confinement Reinf.	Bottom region of boundary element	75%	25%*
	Top region of boundary element	0%	100%

"Bottom region" can refer to the first story of a three story specimen ($0.33h_w$), for example

*The smeared reinforcement should not exceed 0.20% gross

6.7 Determination of Wall Deformation Capacity and Failure Mode

This section describes how the deformation capacity (drift and hinge rotation) as well as failure mode were determined for the walls in the parametric study discussed in Chapter 7.

6.7.1 Introduction

When evaluating experimental wall tests, it is common for researchers to associate 20% strength loss with failure ($0.8V_{max}$), and for the deformation capacity to be taken as the drift and hinge rotation at the point when wall strength deteriorates to $0.8V_{max}$. The ATENA model does not simulate two important behaviors of cyclically-loaded walls that typically trigger the onset of strength loss: (i) rupture of previously buckled longitudinal reinforcing bars, and (ii) buckling of longitudinal reinforcing bars that occurs when crushing of concrete crushing around the bars leads transfer of compressive demands from the concrete to steel as well as loss of buckling restraint. Thus, in the parametric wall study, it was necessary to evaluate simulation results, specifically the stress-strain state of concrete in critical regions, to identify the point at which strength loss could be expected to occur rather than directly using strength loss indicated by the ATENA load-deformation response. Note that the approaches described in Sections 6.7.2 and 6.7.3 were implemented effectively in *Whitman* [173].

6.7.2 Determination of Drift Capacity

As discussed above, the ATENA model cannot provide accurate simulation a reinforcing steel strength loss due to buckling or fracture following buckling. Steel buckling or rupture following buckling can result in significant strength loss in walls and thus these mechanisms could be

expected to define the drift capacity of walls. Thus, in some cases, it is necessary to post-process ATENA results to identify the drift capacity of the wall as the point where significant strength loss could be expected due to steel buckling or rupture. The following criteria were used to determine "drift capacity" prior to the ATENA model simulating significant strength loss due to concrete crushing.

- **(Condition 1)** crushing in the compression boundary element at the location of large-diameter reinforcement. Here the assumptions are that 1) concrete crushing will result in stress transfer to reinforcing bars and reduction of steel restraint leading to bar buckling and 2) if large-diameter bars buckle this will lead to significant strength loss for the wall. Concrete is defined as crushed if the magnitude of the minimum principal stress drops to less than 30% of the historic maximum magnitude for the minimum principal stress. Condition 1 is indicated with a solid red circle marker in Fig. 6.7.

- **(Condition 2)** rupture of the large-diameter reinforcement in the tension boundary element nearest the extreme tension fiber. Here rupture is defined to occur when maximum tensile strain exceeds 33% of the measured fracture strain. Reduced strain capacity results from low-cycle fatigue: multiple tension-compression cycles with large local tensile strain demands due to buckling. Condition 2 is indicated with an open blue circle marker in Fig. 6.7.

- **(Condition 3)** onset of significant **simulated** strength loss, in excess of 20% of the peak wall strength ($\geq 0.2V_{max}$). Condition 3 is indicated with an open purple diamond marker in Fig. 6.7. Note that Condition 3 is the "onset" of significant strength loss, not the point after this strength loss has already occurred or "post-strength loss".

Fig. 6.7 (and Appendix B plots) shows the load-deformation plots for W5 (black line) and W5c (blue line) with each of the critical limit states noted. Additional markers indicate when the simulated base moment is approximately equal to the calculated nominal moment (open green circle); "post-strength loss" corresponding to the final strength loss of 20% has already occurred (solid purple diamond); and maximum shear strength (open gold star). The vertical red line indicates the drift associated with governing failure for each model. Due to uncertainty with determining failure due to bar buckling/fracture and concrete crushing in ATENA, the governing failure was always selected as the most conservative option out of Conditions 1, 2, and 3. Section 6.7.4 provides a more detailed discussion related to uncertainty with determining the onset and mode of failure.

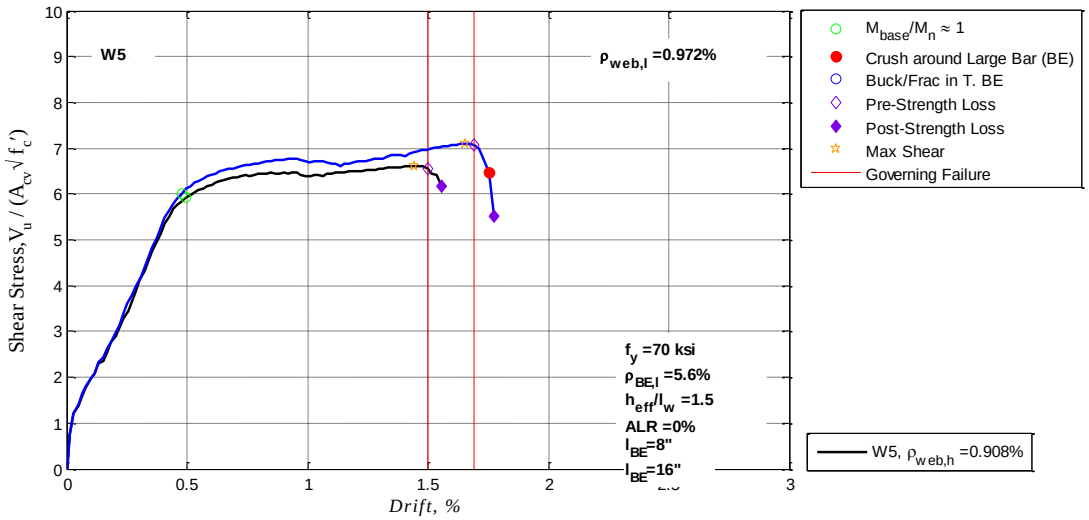

Figure 6.7: Load-Deformation Plot for Simulated Walls W5 and W5c with Critical Limit States

6.7.3 Determination of Failure Mode

Following the approach used by *Whitman* [173], the walls in the parametric study were categorized as exhibiting one of three failure modes: buckling-rupture (tension-controlled flexural failure), crushing-buckling (compression-controlled flexural failure), and shear-compression. The following criteria were used to determine failure mode:

- Failures are categorized as ***buckling-rupture*** if drift capacity is determined by Condition 2 above, or, if Condition 3 is met but buckling-rupture is the reason for the significant strength loss.
- Failures are categorized as ***crushing-buckling*** if drift capacity is determined by Condition 1 above and the concrete crushing (i) initiates at the outermost fiber of the compression boundary element, and (ii) is contained within the boundary element.
- Failures are categorized as ***shear-compression*** if Condition 1 is met and if loss of compressive strength: (i) initiates at the inner edge of the compression boundary element (interface between web and boundary element), and (ii) there is significant strength loss in the wall web as well as the boundary element. Additional characteristics of shear-compression failure include
    1. High minimum principal strain extending outside of the compression boundary element.

2. Minimum principal strain contours that have an elongated shape such that high minimum principal strain values cross the entire width of the compression boundary element.
3. High in-plane shear stress in web region, often in concentrated strut(s).
4. Loss of in-plane shear strength at the boundary element-web interface, often resulting in splitting of shear struts that form within in the web of the wall.

Differentiating between compression-buckling failure and compression-shear failure was the most challenging aspect of identifying wall failure modes. Data in Figs. 6.8-6.10 illustrate the difference between the compression-shear and compression-buckling failure modes. The data in these figures characterize the response of walls W2 and W17 from the parametric wall study discussed in Chapter 7; walls W2 and W17 exhibited compression-shear and compression-buckling failures, respectively.

Fig. 6.8 shows minimum principal stress contours for walls W2 and W17; these data indicate that there is loss in concrete compressive strength at the web-boundary element interface in W2 and the outermost fiber of the boundary element in W17.

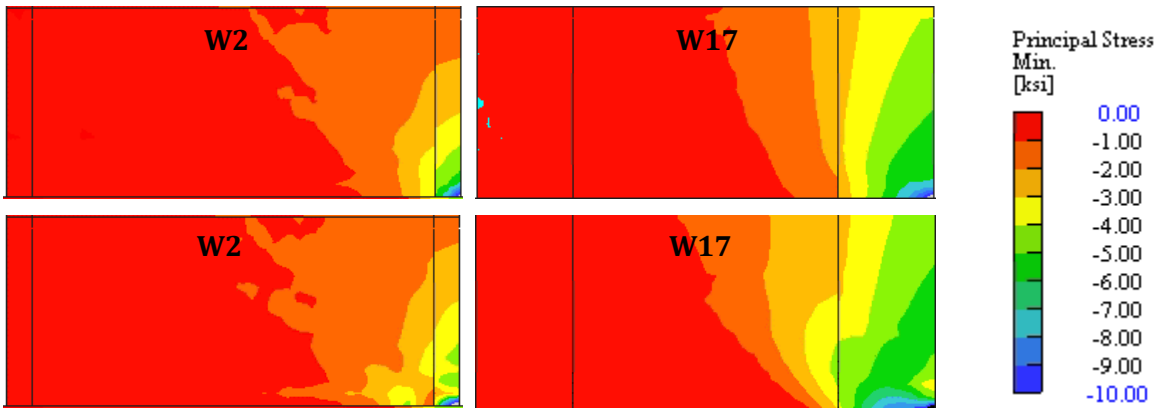

Figure 6.8: Comparison of Min. Principal Stress for SC (W2) and CB (W17) Failures: (Top) Mbase/Mn ≈ 1 and (Bottom) Halfway between Mbase/Mn ≈ 1 and Failure (Showing bottom of Wall at 33% of h_w and 100% of l_w)

Fig. 6.9 shows the minimum principal strain contours at the onset of failure for walls W2 and W17. At the failure point, high magnitudes of strain are seen across the entire compression boundary element and into the web for W2, while high magnitude strains are fully contained in the boundary element in W17.

Figure 6.9: Comparison of Min. Principal Strain for SC (W2) and CB (W17) Failures: At Failure Point (Showing bottom of Wall at 33% of h_w and 100% of l_w)

Fig. 6.10 shows the in-plane shear stress contours for walls W2 and W17. As the wall simulation progresses there is a loss in shear strength at the web-boundary element interface in W2. Though shear strength diminishes in the compression boundary element in W17, there is still considerable shear capacity at the web-boundary element interface at the failure point.

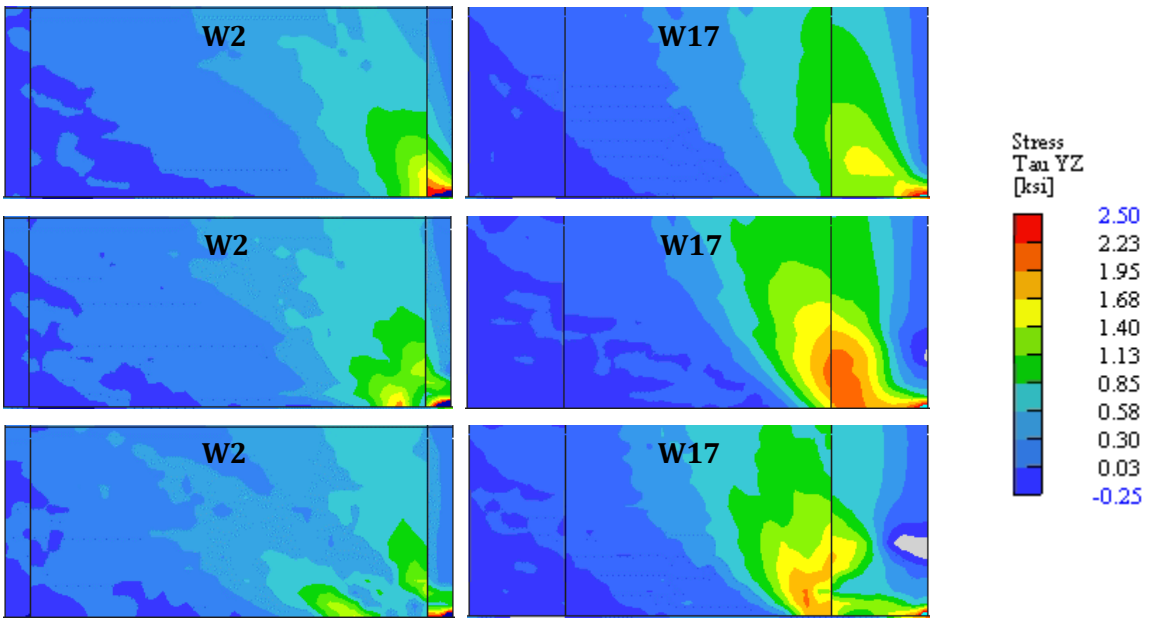

Figure 6.10: Comparison of Min. Principal Stress for SC (W2) and CB (W17) Failures:
(Top) Mbase/Mn ≈ 1, (Middle) Halfway between Mbase/Mn ≈ 1 and Failure, (Bottom) At Failure Point
(Showing bottom of Wall at 33% of h_w and 100% of l_w)

6.7.4 Uncertainty Related to Failure Determination

The metrics used for determining wall failure mode from ATENA analysis results are somewhat uncertain and subjective. Also, limited correlations could be made between failure mode and the wall design parameters investigated in Chapter 7. It is not clear that the lack of correlations is representative of realistic wall response, or an outcome of how failure mode was determined using model results.

Further research should be done to develop more definitive criteria for determining wall failure mode. This can be done by taking a large array of experimentally tested planar walls with clear failure modes to associate these failure modes with specific response characteristics observed from corresponding ATENA models. As an additional step, this investigation should also evaluate the appropriateness of the concrete crushing and steel buckling-rupture thresholds ($f_c \leq 0.3 f_{c,max}$ and $\varepsilon_t \geq 0.33\varepsilon_u$).

Greater certainty in failure mode classification and the onset of damage limit states is important in deriving meaningful results from a parametric study. Particularly in cases where only the baseline model can be compared to the response of an experimental test and the remainder of the walls represent a wide range of design parameter values.

6.8 Description of the Baseline Wall Model for Parametric Wall Study

A calibrated baseline model for the parametric study was generated using Specimen S6 from the *Vallenas et al.* [167] experimental test program. This planar slender structural wall was selected because it possessed the following characteristics:

(1) Specimen S6 was subjected to a relatively high shear demand, $6A_{cv}\sqrt{f_c'}$ with f_c' in psi and exhibited a compression-shear controlled failure [173]. One of the objectives of the study presented here is to examine how varying the horizontal and vertical web reinforcement ratios influences the occurrence of this undesirable, brittle failure mode.

(2) Specimen S6's design was compliant with current *ACI 318-14* [18]provisions for special structural walls, including distributed web reinforcement and boundary element detailing.

(3) Specimen S6 was one of eight experimental tests used by *Whitman* [173] to develop recommendations for modelling slender structural walls using ATENA 3D, the non-linear finite element analysis tool selected for this parametric study. The recommendations that are adopted from *Whitman* [173] for this parametric study are discussed in Section 6.6.2.

6.8.1 Details on Specimen S6 from Vallenas et al. [167]

Specimen S6 (Fig 6.11) is a three-story rectangular wall specimen that represents the lower portion of a seven-story prototype wall, and can be considered a 3:8 scale specimen. The wall has an approximate wall thickness of 4.5-in, length of 95-in, and height of 120-in which results in a cross-sectional aspect ratio (CSAR) of 21.1. The end zones of the wall have concentrated flexural and transverse reinforcement; though the wall specimen was designed in accordance with *UBC 1973* [94], the boundary element dimensions and reinforcing details meet current requirements of *ACI 318-14* [18]. Details for steel reinforcement and concrete properties of the Specimen S6 are summarized in Tables 6.5 and 6.6, respectively. The specimen was subjected to cyclic lateral loading (such that the effective height, h_{eff}, of the wall was 152-in) and a constant axial loading of $0.048A_g f_c'$. Additional details on the experimental test program can be found in *Wang et al.* [171] and *Vallenas et al.* [167].

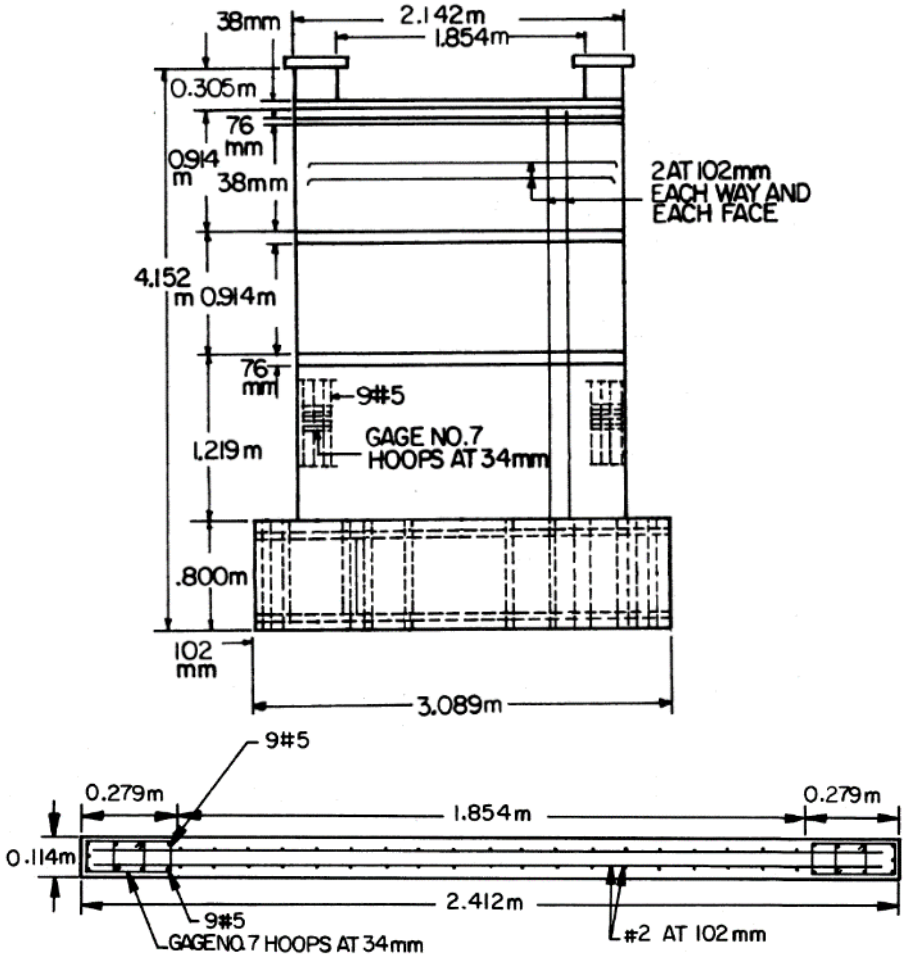

Figure 6.11: Test Specimen Geometry and Reinforcement Details for Specimen S6 of Vallenas et al. [167]

Table 6.5: Summary of Specimen S6 Steel Reinforcement Properties and Ratios

Reinforcement Type	Bar Size	Bar Area (in^2)	f_y (ksi)	ε_y (in/in)	f_u (ksi)	ε_u (in/in)	ρ (%)
Confine Hoops & Ties	Gage #7	0.025	63.8	0.0022	69.5	0.019	1.17
Web Horiz/Vert Reinf.	#2	0.049	73.5	0.0025	105.9	0.120	0.54/0.54
BE Vert Reinf.	#4	0.31	69.9	0.0024	99.6	0.150	5.63

Table 6.6: Summary of Specimen S6 Concrete Properties

f_c' (psi)	f_r* (psi)	E_c* (ksi)	G* (ksi)
5033	532.1	4044	1685

* Calculated using $f_r = 7.5\sqrt{f_c'}\ (\ si),\ E_c = 57000\sqrt{f_c'}\ (psi), G = \frac{E_c}{2(1+\nu)}\ (psi)$

6.8.2 Calibration of the Baseline Model

6.8.2.1 Baseline Model Calibration using Whitman [173] *Recommendations*

The recommendations of *Whitman* [173] were used to create a baseline model of Specimen S6; model parameters included w_d = 0.0425, β=0.0, SF=50, and c_{ts}=0.01 and the discrete/ smeared reinforcement distributions consistent with Table 6.3. As an additional verification step to examine if the selected parameter values were appropriate, a set of models with varying w_d, β, SF, and c_{ts} values were also conducted. In most cases, the values were selected to span the full range recommended by Cervenka Consulting (column three in Table 6.3). The simulation matrix is summarized in columns 1-4 of Table 6.7, where the first row represents the baseline model with *Whitman* [173] recommendations. Fig. 6.12(a-d) shows the positive portion of the load-deformation curve from the experimental test of Specimen S6 ("Exp Results") as well as computational results from the ATENA baseline model ("S6-1") and comparison to models with the varying concrete parameters. The peak shear stress and drift capacity for the baseline model and each of the models with varying concrete parameters is summarized in Table 6.7.

Table 6.7: Comparison of Results for Baseline Model and Models with Varying Concrete Parameters

Model Concrete Parameters				Positive Direction Loading				Negative Direction Loading				Average Error	
				Strength		Deformation		Strength		Deformation		Strength	Deformation
w_d	β	SF	c_{ts}	Sim. V_{max}	Sim./ Exp.	Sim. Λ	Sim./ Exp.	Sim. V_{max}	Sim./ Exp.	Sim. Λ	Sim./ Exp.	% Error	% Error
0.0425	0	50	0.0100	6.12	1.005	1.59	1.026	6.12	0.981	1.59	0.969	1.2	2.8
0.0250	0	50	0.0100	6.02	0.988	1.30	0.840	6.02	0.965	1.30	0.794	2.3	18.3
0.0750	0	50	0.0100	6.28	1.030	1.69	1.087	6.28	1.006	1.69	1.027	1.8	5.7
0.1000	0	50	0.0100	6.37	1.046	1.70	1.094	6.37	1.021	1.70	1.034	3.4	6.4
0.1250	0	50	0.0100	6.47	1.062	1.93	1.245	6.47	1.037	1.93	1.176	4.9	21.1
0.0425	0.125	50	0.0100	6.17	1.012	1.28	0.826	6.17	0.988	1.28	0.780	1.2	19.7
0.0425	0.250	50	0.0100	6.23	1.023	1.14	0.736	6.23	0.999	1.14	0.695	1.2	28.4
0.0425	0.500	50	0.0100	6.21	1.019	0.97	0.625	6.21	0.995	0.97	0.591	1.2	39.2
0.0425	0.700	50	0.0100	6.16	1.011	0.72	0.463	6.16	0.987	0.72	0.437	1.2	55.0
0.0425	0	20	0.0100	6.04	0.991	1.72	1.110	6.04	0.967	1.72	1.049	2.1	8.0
0.0425	0	80	0.0100	6.23	1.023	1.52	0.976	6.23	0.998	1.52	0.923	1.2	5.1
0.0425	0	160	0.0100	6.35	1.042	1.41	0.909	6.35	1.017	1.41	0.859	3.0	11.6
0.0425	0	200	0.0100	6.41	1.053	1.30	0.839	6.41	1.028	1.30	0.793	4.0	18.4
0.0425	0	50	0.0000	5.90	0.969	1.29	0.830	5.90	0.946	1.29	0.784	4.2	19.3
0.0425	0	50	0.0025	5.96	0.979	1.49	0.960	5.96	0.955	1.49	0.907	3.3	6.7
0.0425	0	50	0.0050	6.06	0.994	1.45	0.937	6.06	0.970	1.45	0.886	1.8	8.8
0.0425	0	50	0.0075	6.07	0.996	1.45	0.937	6.07	0.972	1.45	0.886	1.6	8.8

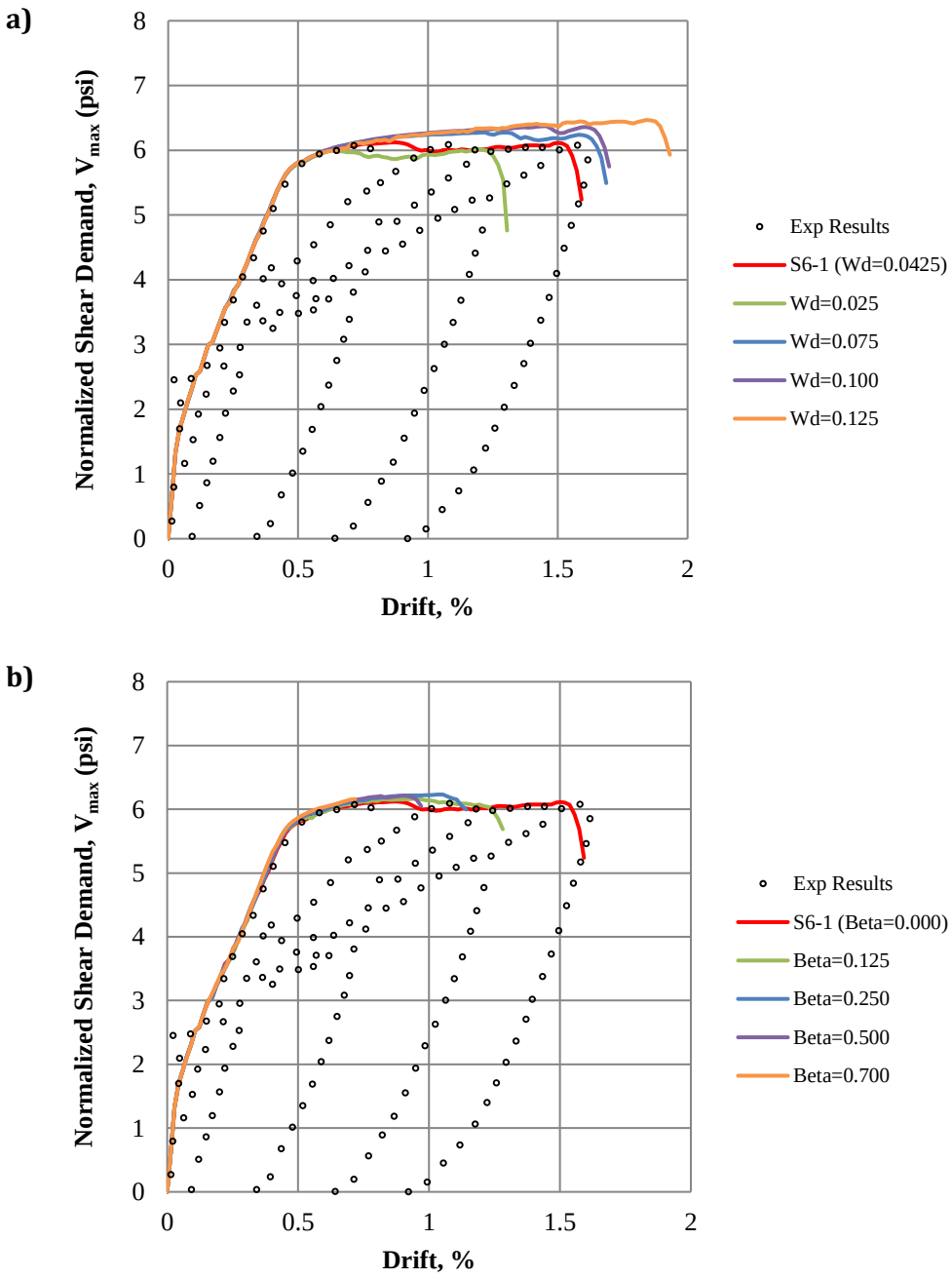

Figure 6.12: Comparison of Specimen S6 Baseline Model and Models with Varying Concrete Parameters

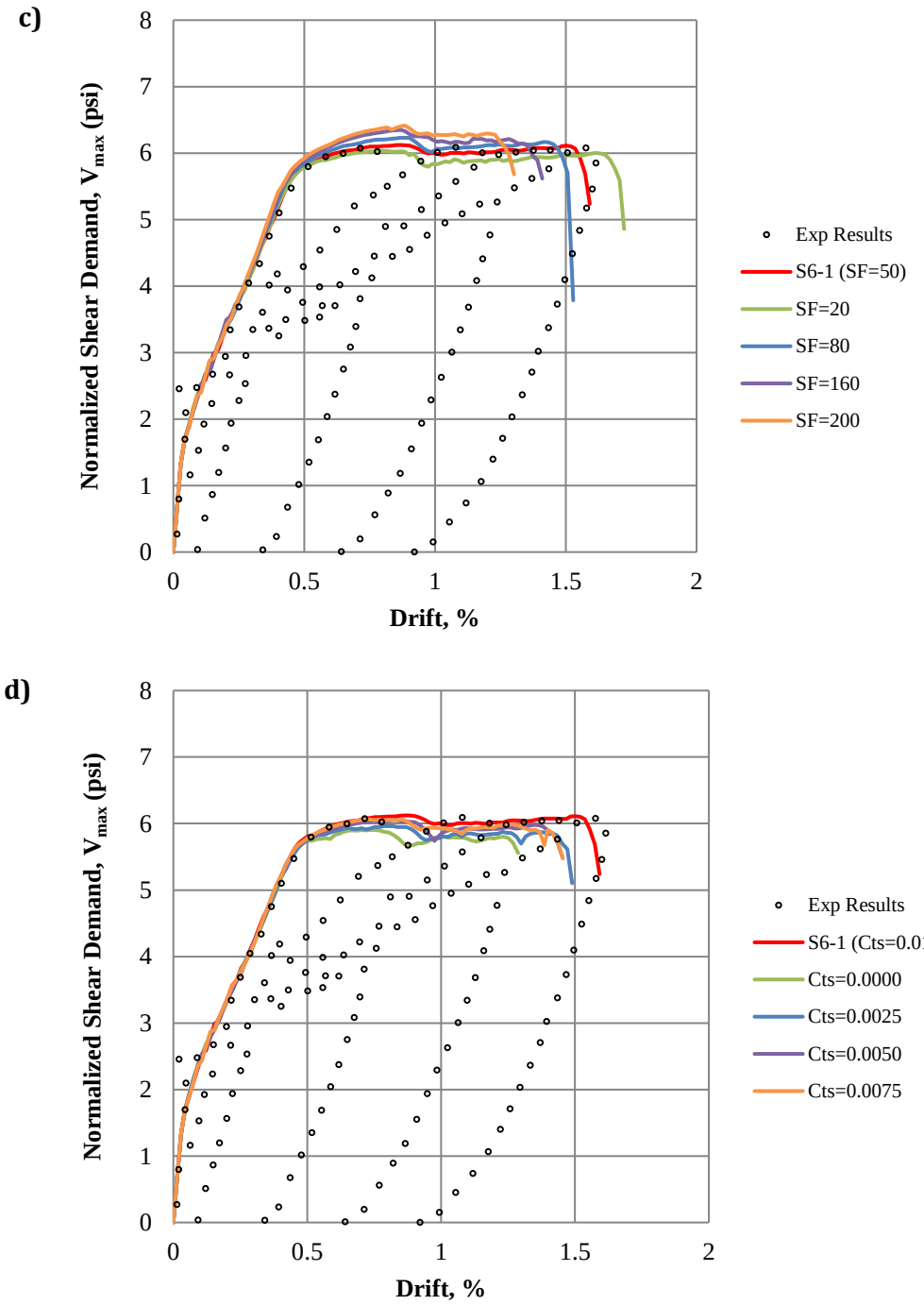

Figure 6.12 cont'd: Comparison of Specimen S6 Baseline Model and Models with Varying Concrete Parameters

Varying the model parameters has no impact on stiffness to yield, minimal impact on strength and significant impact on drift capacity. The initial stiffness is nearly identical for all models shown in Fig. 6.12(a-d). The only notable increases in peak strength result from increasing SF, with more minor effects seen with increasing c_{ts}. These increases are consistent with the impact of the SF and

c_{ts} parameters on concrete material response, as increasing SF increases shear stress transfer on the crack surface for a given shear strain demand and increasing c_{ts} increases residual concrete tensile strength. Modification of the concrete parameters has a significant impact on drift capacity; increasing w_d and decreasing β and SF result in large gains in drift capacity. Again these results are consistent with the impact of the parameters on concrete material response. Increasing w_d results in increased compressive strain capacity for concrete, which could be expected to increase wall drift capacity and concrete crushing determines the onset of strength loss of most planar concrete walls. Decreasing SF results in less shear stress transfer on a crack surface at a given shear strain demand, since shear and flexural compressive stresses combine to produce concrete crushing, reduced shear stress demand could be expected to increase the drift at onset of strength loss. Finally, decreasing β results in less expansion of crushing concrete, lower 3D compressive demands and delay in concrete crushing. Based on the experimentally measured peak shear stress and drift capacity for the positive and negative direction loading directions (Table 6.7), the baseline model provides the best prediction for the range of concrete parameter values investigated. These findings indicate that the *Whitman* [173] recommendations of w_d = 0.0425, β=0.0, SF=50, and c_{ts}=0.01 for calibrating the concrete model parameters are appropriate for use with Specimen S6 and can be implemented in the parametric study described in the remainder of Chapter 7.

6.8.2.2 Specimen S6 Baseline Model and Comparison to ACI Compliant Model

Boundary element detailing for Specimen S6 actually exceed *ACI 318-14* [18] requirements for special concrete walls. To achieve a compliant special boundary element, the boundary element length, l_{be}, could be reduced from 11-in to 8.5-in, and the vertical spacing of the confinement reinforcement, *s*, could be increased from 1.34-in to 1.4-in. An additional model was generated to examine the effect of these modifications on wall response. The load-deformation response of the experiment ("S6 Test Data"), baseline Specimen S6 model ("S6-1"), and the modified model ("S6-2") are shown in Fig. 6.13.

The load-deformation response shows that while the modified model (l_{be}=8.5-in and *s*=1.4-in) predicts stiffness and strength that are nearly identical to those predicted using the baseline model (l_{be}=11-in and *s*=1.34-in), but that the modified model predicts a drift capacity that is 12% less than that predicted using the baseline model. Results of the "S6-2" model are relevant to the simulation wall matrix presented in Section 7.3.1, since all the walls were designed to meet the minimum requirements of *ACI 318-14* [18] for special boundary elements.

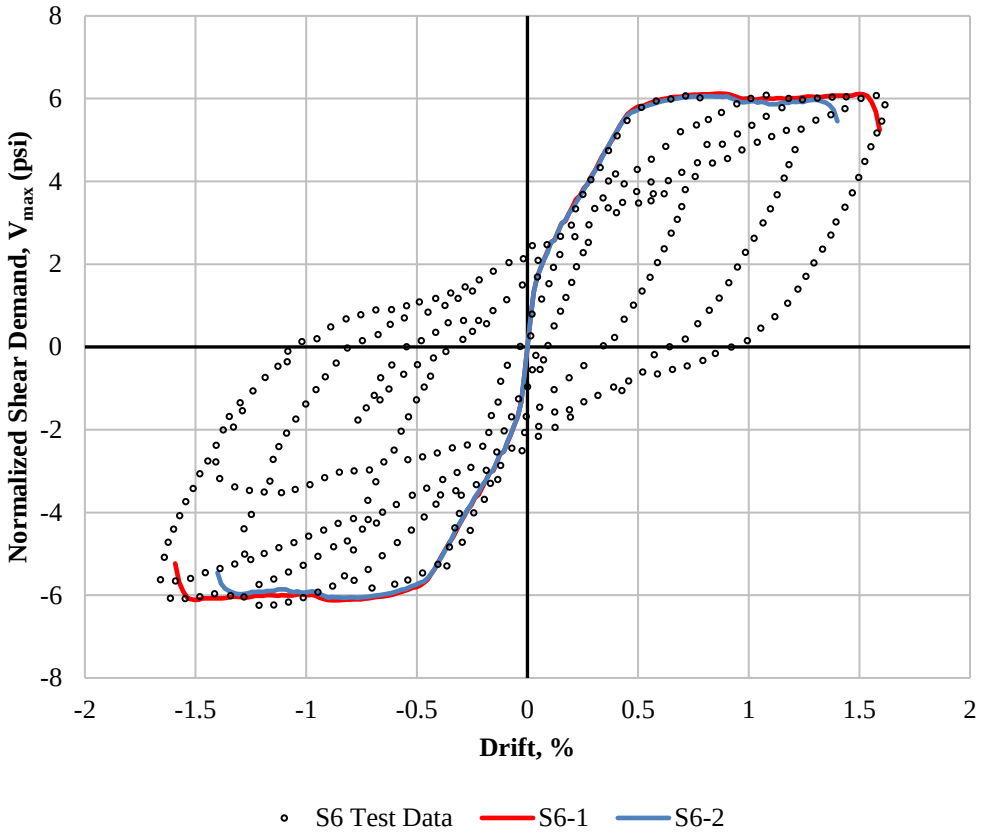

Figure 6.13: Comparison of Specimen S6 Baseline Model to Model with ACI Compliant Boundary Element

6.9 Summary

Computational modelling can complement field observations and experimental testing to further understanding of the earthquake performance of structural walls. Computational modelling is particularly advantageous as it provides a means of examining the impact of specific wall design parameters over a large design space and is relatively inexpensive compared with experimental testing. In particular, nonlinear analysis to investigate the behavior of wall behavior can employ line-element models as well as two- and three-dimensional continuum modeling. Three-dimensional continuum modeling was chosen for this study as this particular type of model can account for a non-linear strain distribution; provide accurate predictions of strength, stiffness, and drift; and capture localized damage.

Previous research by *Whitman* [173] showed that the 3D continuum analysis employing the ATENA software platform and the concrete constitutive models available in this platform provides accurate simulation of the stiffness, strength and deformation capacity of planar walls subjected to lateral

loading exhibiting flexure and flexure-shear failure mechanisms. The modeling approach and material model parameters recommended by Whitman are reviewed. Because the ATENA software does not does not support simulation strength loss in reinforcing steel due to buckling or premature fracture following buckling, for some wall configurations onset of strength loss is not simulated. For these walls, identification of the *expected* drift at onset of strength loss (i.e. the drift capacity) due to non-simulated failure modes requires post-processing of simulation data. Rules used to classify wall failure mode (buckling-rupture, crushing-buckling, and shear-compression) and the expected onset of strength loss are presented. These classifications rules are based on assessments of: (i) tensile strain in longitudinal reinforcement, (ii) location in the compression zone where there are significant reductions in minimum principal stress and/or high values for minimum principal strain, and (iii) the presence of high in-plane shear stresses in the web (struts) or loss of shear capacity at the web-boundary element interface.

The Chapter concludes with a discussion of the specimen used as the baseline configuration in the parameter study presented in Chapter 7. Comparison of simulation and response data for this specimen, shows that the modeling recommendations developed by Whitman result in accurate simulation of stiffness, strength and deformation capacity of the specimen. For this specimen, strength loss due to crushing of concrete at the web-boundary element interface is simulate; thus, the specimen is classified as exhibiting a flexure-shear failure mode. An investigation of the sensitivity of simulation results to variation calibrated model parameters (i.e. model parameters that are not defined by commonly employed material tests) shows that the stiffness is independent of these parameters, that strength is minimally affected by these parameters and that drift capacity is significantly affected by variation in these parameters. Given that recommended values for model parameters were determined using a moderately large data set (planar wall specimens) and results in accurate simulation o response for wall specimen S6; these recommended values were employed for the parameter study presented in Chapter 7.

A few of the major challenges encountered in the computational wall study conducted using ATENA (described in Chapter 7) relate to:

- Consideration of bar buckling, since ATENA does not adequately model this steel material behavior, and determination of whether bar buckling results in failure prior to the strength-loss indicated by model output. This can introduce uncertainty into simulation data and the conclusions based on that data.

- Determination of failure mode using available deformation metrics; and assessment of whether damage limit states of concrete crushing, bar buckling, or bar rupture result in failure prior to the strength-loss indicated by model output

Other researchers have noted concerns with numerical robustness of ATENA, particularly challenges with convergence in cases where there is: (i) excessive shear damage to a lightly-reinforced wall web, (ii) cyclic and/or multi-directional lateral loading. However, these convergence issues were not observed in the parametric study of planar, monotonically-loaded structural walls in this study. More investigation will be necessary to address these modelling challenges.

7 PARAMETRIC STUDY OF WALL WEB REINFORCEMENT RATIOS

7.1 Introduction

7.1.1 Major Research Impetuses for Parametric Study

The research impetuses for this parametric study on wall web reinforcement are: (i) the damage sustained by lightly reinforced concrete walls, both in the field and experimentally (including the C-shaped walls described in Chapters 4-5), that suggest early web reinforcement fracture, and (ii) the limited existing experimental test data related to the response of slender walls with varying vertical and/or horizontal web reinforcement ratios.

In terms of earthquake response of reinforced concrete walls, *Sritharan et al.* [159] indicates that walls designed to minimum vertical web reinforcement requirements are vulnerable to brittle failures due to fracture of tensile longitudinal reinforcement after the onset of flexural cracking. Furthermore, inelastic deformations are concentrated at very few rather than distributed cracks which results in a limited plastic hinge length that can negatively impact wall ductility. Poor wall response attributed to limited longitudinal reinforcement was observed in the Canterbury, NZ events (2010-2011) as reported by *Kam et al.* [105] and *Bull* [41] as well as several failures in the Llolleo, Chile (1985) that were noted by *Wood et al.* [177].

With respect to availability of experimental test data that examines minimum vertical web reinforcement ratios, *Sritharan et al.* [159] indicates that previous wall tests predominately consist of squat, shear-dominated walls (in reference to work by *Greifenhagen and Lestuzzi* [84]; *Hildalgo et al.* [89]; and *Wood* [175]) rather than slender, flexural-dominated walls. *Birely* [35] also notes that there are limited slender wall tests that examine horizontal web reinforcement ratios, and identifies only two relevant test programs from an extensive literature review of slender wall tests (*Pilakoutas and Elnashai* [146] and *Oesterle et al.* [140, 141]). Of these, *Pilakoutas and Elnashai* [146] has boundary element reinforcement ratios ($\rho_{be} \geq 6.9\%$) that are not representative of modern wall design. In the literature review presented in Chapter 2, only one additional slender wall test program was identified that examined vertical and horizontal web reinforcement ratios in C-shaped walls (*Sittipunt & Wood* [158]). However, researchers suggested that the C-shaped wall response was not necessarily a result of vertical or horizontal web reinforcement ratios, but other factors. This results in very few slender wall tests that directly examine either vertical and/or horizontal web reinforcement ratios. Most other wall tests (summarized in *Birely* [35] and Chapter 2) are designed such that horizontal reinforcement ratio meets the shear demand, but does not

consider the impact of web reinforcement on wall ductility. A major objective of this parametric study was to examine the influence that web reinforcement has on deformation and ductility, in addition to previously studied effects of web reinforcement on strength.

7.1.2 Brief History of ACI 318 Requirements related to Web Reinforcement and Shear Design

The parametric study discussed in the remainder of Chapter 7 focuses on vertical and horizontal reinforcement ratios. Therefore, it is important to examine the historic arc of relevant *ACI 318* code provisions and related code commentary to understand how and why the requirements for vertical and horizontal web reinforcement ratios have evolved, as well as where there may be a need for further investigation of wall response associated with these design parameters.

At present, the minimum distributed ***web*** (or shear) reinforcement ratio for special structural walls in both the vertical and horizontal directions is 0.0025, and has been since the introduction of seismic design provisions for walls in *ACI318-71* [4]. Unassociated with specific seismic design provisions, the 0.0025 value first appeared in the *1910 NACU Standard* [127] as the minimum ***total*** reinforcement ratio required for a wall. The only notable exceptions that occur between 1910 [127] and 1971 [4] for the ***total*** reinforcement ratio are in 1920 [1] (where no explicit minimum reinforcement ratio was provided for walls), as well as 1956 [2] and 1963 [3] (where vertical reinforcement ratio minimum was reduced to 0.0015, though the horizontal ratio remained 0.0025). This historic timeline shows that the minimum web reinforcement ratio values used today are rooted in pre-seismic requirements from over a hundred years ago.

The shear design requirements have also evolved very little over time since the formal inclusion of seismic provisions in *ACI 318-71* [4]. Originally shear capacity was calculated $\phi V_n = \phi(V_c + V_s)$ where $V_c = 2\sqrt{f_c'}bd$ and $V_s = (A_{v,h}f_y d/s_2)$. This changed in *ACI 318-83* [7] when the code became more consistent with the current approach of calculating $V_n = A_{cv}(\alpha_c \lambda \sqrt{f_c'} + \rho_{v,h} f_y)$, where $h_w/l_w \leq 1.5 \rightarrow \alpha_c = 3.0$, $h_w/l_w \geq 2.0 \rightarrow \alpha_c = 2.0$, and varied linearly in between these values. The maximum shear limit on an individual wall has been $V_n \leq 10A_{cv}\sqrt{f_c'}$ since *ACI 318-71* [4]. Note that there were some changes in language or variable designations in these expressions, but the intent of these code provisions have not changed for the last 30-40 years.

Also relevant to the shear design of walls are the changes to the reduction factor used in the expression $\phi V_n \geq V_u$. From *ACI 318-71* [4] to *ACI 318-77* [5], the shear reduction factor was 0.85 irrespective of whether walls were shear or flexure-dominated; in *ACI 318-83* [7] an additional

reduction factor of 0.6 was added for shear-dominated walls. In *ACI 318-02* [13] the general shear reduction factor was decreased from 0.85 to 0.75 and the 0.6 factor was maintained for shear-dominated walls. The *ACI 318-02* [13] reduction factors still apply in the current *ACI 318-14* [18] code.

7.1.3 Summary of Research Approach

The objective of the parametric study described in Chapter 7 is to investigate the impact that vertical and horizontal web reinforcement have on the deformation capacity and ductility of slender reinforced concrete walls subject to varying shear stress demands. A non-linear finite modelling approach with three-dimensional elements was employed for this study in order to capture the effects of shear-flexure interaction observed in slender walls. Planar walls, rather than C-shaped walls described in the experimental portion of this research (Chapters 4 and 5), were selected for this study since:

- Walls with a simple planar configuration do not exhibit the shear lag effects observed in the flanges of non-planar walls. These shear lag effects would likely obfuscate the impacts of varying the web reinforcement ratios.
- The C-shaped walls tested as part of this study are subject to relatively low shear stress demands ($\leq 4.3A_{cv}\sqrt{f'_c}$), and it was necessary to calibrate the non-linear model with an experimentally tested wall subject to a high shear stress demand. This was deemed necessary as the parametric study was specifically evaluating response for walls with a shear stress demand range of $4.5 - 9.0A_{cv}\sqrt{f'_c}$.

Chapter 6 has already detailed the non-linear modelling procedure used in the ATENA 3D software tool to conduct this parametric study; the justification for selecting the *Vallenas et al* [167] Specimen S6 planar wall test to generate a baseline model; important specimen details from Specimen S6 necessary to develop the baseline model; and a description of the process for calibrating the model against experimental test data.

The remainder of Chapter 7 discusses the design and response of the walls that were simulated to investigate the impact of web reinforcement ratios at different shear stress demand levels. Section 7.2 describes the design criteria and procedure used to design the walls in the simulation matrix. Section 7.3 provides details on the specific design parameters and deformation/strength response for each of the simulated walls. Section 7.4 examines the model results to assess the impact that various design parameters have on wall deformation and ductility. Section 7.5 discusses the

potential implications of the findings from Section 7.4 on the engineer's design of a wall to achieve specific deformation capacity or ductility targets for a slender planar wall with a given shear stress demand. Section 7.6 summarizes the findings of the wall web reinforcement study.

7.2 Design of Walls in Parametric Study

The slender concrete walls in the parametric study were designed to explore the impact of varying levels of vertical and horizontal web reinforcement for different shear stress demand levels (4.5, 6.0, and $9.0A_{cv}\sqrt{f'_c}$). As shear stress demand increases, slender walls have been noted to exhibit limited drift capacity/ductility and fail via brittle mechanisms (*Whitman* [173]). The current parametric study is particularly relevant as there have been proposals in the Subcommittee ACI 318-H to increase the current nominal shear capacity limit, V_n, beyond $10A_{cv}\sqrt{f'_c}$ for an individual wall such that the allowable shear demand limit, V_u, would be in excess of $7.5A_{cv}\sqrt{f'_c}$ (*Lehman* [109, 110]).

The primary interest in the study is evaluating the potential deformation and ductility gains for walls with moderate-to-high shear stress demands when designed in excess of the minimum web reinforcement ratios: (i) ≥ 0.0025 for both vertical and horizontal steel, and (ii) $V_u/V_n \leq 0.75$ for horizontal steel. The resulting vertical and horizontal reinforcement ratios in the parametric wall study range from 0.25% to approximately 1.0%; the upper bound was set so that designs did not significantly exceed the 0.25% minimum.

The walls in the parametric study are designed based upon the overall geometry and boundary element reinforcement properties of the Specimen S6 model from *Vallenas et al*. [167]. Specimen S6 model has a cross-sectional aspect ratio (CSAR) of 21.1; therefore, all the walls in the parametric study have a CSAR akin to a 30-foot-long wall that is 18 inches thick. Furthermore, the walls in the study were designed for two different boundary element length scenarios: the *ACI 318-14* [18] compliant length and a length approximately equal to the neutral axis depth. The effect of this design variable was investigated in response to a recent wall simulation study by *Whitman* [173] which concluded that increasing the boundary element length beyond the ACI minimum led to improved response for walls subject to high shear stress demands.

7.2.1 Procedure to Achieve Target Peak Shear Stress Demands

7.2.1.1 Variation in Design Parameters to Achieve Target Peak Shear Stress Demands

Four primary parameters were varied to achieve the target peak shear stresses of 4.5, 6.0, and $9.0A_{cv}\sqrt{f'_c}$ for the wall data set, these included: steel strength (f_y, ksi), area of concentrated vertical reinforcement in the wall end zones ($A_{conc,l}$, in^2), shear span ratio (h_{eff}/l_w), and axial load ratio (ALR, %). Note that the selection of these values are intended to drive shear demand up and are not necessarily representative of modern wall design.

- Steel strength (f_y, ksi): the same steel strength was used for all reinforcement types in an individual wall model. The design values were f_y = 70 ksi and f_y = 80 ksi.
- Area of concentrated vertical reinforcement in wall end zones ($A_{conc,l}$, in^2): the baseline Specimen S6 model had nine bars with a total reinforcement area of 2.79 in^2 in each of the wall end zones. The location and number of bars in the baseline model was maintained for all walls in the simulation wall matrix; however, the bar area was modified so a single wall end zone had a total reinforcement area of 2.79in^2 and 3.24in^2.
- Shear span ratio (h_{eff}/l_w): ratio defined by the vertical height above the wall base where the lateral load is applied, divided by the wall length. The baseline Specimen S6 model had an h_{eff}/l_w =1.6 , the parametric study employed shear span ratios, h_{eff}/l_w, of 1.5 and 2.0.
- Axial load ratio (ALR, %): used to determine the distributed line load, kip/in, applied to the top of the wall. The baseline Specimen S6 model had an ALR =4.8%; the parametric study includes ALR values of: 0, 5, 10, 15, and 20%.

As a point of clarification for the preceding descriptions:

- "Wall end zone" is a designation used in this study that refers to the original Specimen S6 boundary element length of 11-in. For the simulation wall matrix, it is used to describe the 11-in. regions at the wall corners that contain heavy longitudinal reinforcement.
- The boundary element length is a designation used in this study that refers to the region with confining reinforcement (seismic hoops and ties). The boundary element length varies throughout the simulation wall matrix based on the minimum ACI boundary element length requirements or the neutral axis depth.
- The "wall end zone" and boundary element length are typically different values.

7.2.1.2 Procedure to Determine Design Parameter Values to Meet Target Shear Stress Demands

The approach for flexural/shear design of the walls in the parametric study is outlined in the flowchart shown in Fig. 7.1. The remainder of this section will elaborate on the various steps in the flowchart. As a note: these steps apply for both ACI compliant and "extended" boundary element wall designs; except for Steps 7 and 8 which are modified to allow for a boundary element length equal to the neutral axis depth, *c*.

Step 1: Set target peak shear stress as $V_{max} = 4.5, 6.0, \quad 9.0A_{cv}\sqrt{f'_c}$.

Steps 2-4: Select appropriate values for parameters (f_y, $A_{conc,l}$, h_{eff}/l_w, ALR) described in Section 7.2.1.2 to achieve the desired peak shear stress demand. Note that f_y and $A_{conc,l}$ are selected in combination, the designs employ two options: f_y=70 ksi and $A_{conc,l}$ = 2.79in^2 (OR) f_y=80 ksi and $A_{conc,l}$ = 3.24in^2.

Steps 5: Calculate the vertical reinforcement ratio, $\rho_{web,l}$ needed to achieve the nominal moment $M_n = V_{max}h_{eff}$ where V_{max}, h_{eff}, and parameters from Steps 1-3 have already been selected. Below are pertinent details related wall material properties, geometry, and reinforcement configuration, as well as underlying assumptions in the iterative solution process necessary to determine $\rho_{web,l}$ from the nominal moment calculation approach described in *ACI 318-14* [18] Section 22.2:

- Material Properties:
  - Concrete Properties:
    - Compression strength, f_c'=5000 psi
    - Maximum concrete compression strain, ε_{cu} =0.003
    - Tensile strength neglected
    - Stress-strain relationship given by equivalent rectangular stress distribution in accordance with *ACI 318-14* [18] Section 22.2
  - Steel Strength:
    - All reinforcing bars in the walls are assigned the same material properties based on the parameter selection from Step 1, f_y= 70 ksi or 80 ksi
    - Stress-strain relationship given by elastic-perfectly plastic response in accordance with *ACI 318-14* [18] Section 20.2.2.1-2.

- Geometry and Reinforcement Configuration:
    - Cross-sectional dimensions: wall length, l_w = 95-in and wall thickness, t_w = 4.5-in.
    - Location of concentrated vertical reinforcement in wall end zones: each end zone has four layers of reinforcement where the outermost layer contains three bars and all others contain two bars (for a total of nine bars). Measured from the edge of the wall these reinforcement layers are located at 1, 4, 7, and 10-in.
    - Location of web vertical/horizontal reinforcement: 4-in on center spacing.

- Nominal Moment Calculation
    - Calculation approach uses a plane-sections-remain-plane (PSRP) with linear strain distribution and is consistent with *ACI 318-14* [18] Section 22.2.
    - The contribution of vertical web steel is considered in the nominal moment calculation.

Step 6: Eliminate wall designs if the calculated value for vertical web reinforcement ratio, $\rho_{web,l}$, from Step 5 does not meet the bounds of 0.25-1.00%. These bounds were set since the parametric study is intended to investigate the minimum web reinforcement ratio required by *ACI 318-14* [18] Section 18.10.2.1 of 0.25%, .

Step 7: Calculate the boundary element length, l_{be}, using *ACI 318-14* [18] Section 18.10.6.4 which requires at least the maximum of $c - 0.1l_w$ and $c/2$. The neutral axis depth, *c*, is determined through the PRSP approach outlined in Steps 4-5 and the calculated l_{be}value is rounded up to the nearest 0.5-in.

Step 8: Eliminate wall designs if the calculated value for boundary element-to-wall length, l_{be}/l_w, exceeds 0.25. The objective of the parametric study is to examine the effect of ***web*** reinforcement; therefore, the l_{be}/l_w limit ensures that at least 50% of the wall cross-section is unconfined web.

Step 9: Select the desired shear demand-to-capacity ratio, V_u/V_n, for the wall design (0.5, 0.75, 1.00, or 1.25). Use the target peak shear stress (selected in Step 1 of $V_{max} = 4.5, 6.0, \quad 9.0A_{cv}\sqrt{f'_c}$), as V_u. Calculate the corresponding nominal shear capacity of the wall, V_n.

Step 10: Calculate the horizontal reinforcement ratio, $\rho_{web,h}$ based on the nominal shear strength, V_n, from Step 9 and the *ACI 318-14* [18] Section 18.10.4.1 expression $V_n = A_{cv}(\alpha_c\lambda\sqrt{f_c}' + \rho_{web,h}f_y)$, where $h_w/l_w \leq 1.5 \rightarrow \alpha_c = 3.0$, $h_w/l_w \geq 2.0 \rightarrow \alpha_c = 2.0$, and linear relationship in between.

Step 11: Eliminate wall designs if the calculated value for horizontal web reinforcement ratio, $\rho_{web,h}$, from Step 10 does not meet the bounds of 0.25-1.00% (approximately). These bounds were set since the parametric study is intended to investigate the minimum web reinforcement ratio required by *ACI 318-14* [18] Section 18.10.2.1 of 0.25%.

Step 12: Walls that meet the criteria of Steps 1-11 are included in the simulation matrix for the parametric study.

7.2.1.3 Boundary Element Design Procedure

The next stage in the design process was determining the total area and vertical/horizontal spacing of transverse reinforcement to confine the wall boundary element (based on the boundary element length already determined in Step 7 of the procedure described in Section 7.2.1.2). The total area of transverse reinforcement in each direction, $A_{sh,i}$, was calculated using *ACI 318-14* [18] Table 18.10.6.4(f) for rectilinear hoops with cross-ties as:

$$A_{sh,i} \geq ma \begin{cases} 0.3sb_{c,i}\left(\frac{A_g}{A_{ch}} - 1\right)\frac{f_c'}{f_{yt}} \\ 0.09sb_{c,i}\frac{f_c'}{f_{yt}} \end{cases}$$

where the gross area of the boundary element, A_g, is calculated as the length multiplied by the width of the boundary element ($= l_{be}b_{be}$). This is distinct from the area of the confined core, A_{ch}, measured to the outside edges of the reinforcement (=$b_{c1}b_{c2}$, where $b_{c,i}$ refers to the dimension of the confined core for each direction).

The vertical spacing of the transverse reinforcement, *s*, is determined using *ACI 318-14* [18] Section 18.7.5.3 which requires that the spacing not be greater than the minimum of: (i) b/3, (ii) $6d_b$ for the smallest longitudinal bar, and (iii) 4 $in \leq 4 + \left(\frac{14-h_x}{3}\right) \leq 6$ i*n*. The horizontal spacing, h_x, is specified in *ACI 318-14* [18] Section 18.10.6.4(e) as less than or equal to the minimum of 2b/3 or 14 inches. In these expressions, *b* is the wall thickness. Note that for vertical/horizontal transverse reinforcement spacing the *ACI 318-14* [18] values are for a full-scale wall specimen, which can be assumed to correspond to a wall thickness of 12-in; therefore, these provisions were adapted for a wall thickness of 4.5-in (3:8 scale specimen) for the design of walls in the parametric study.

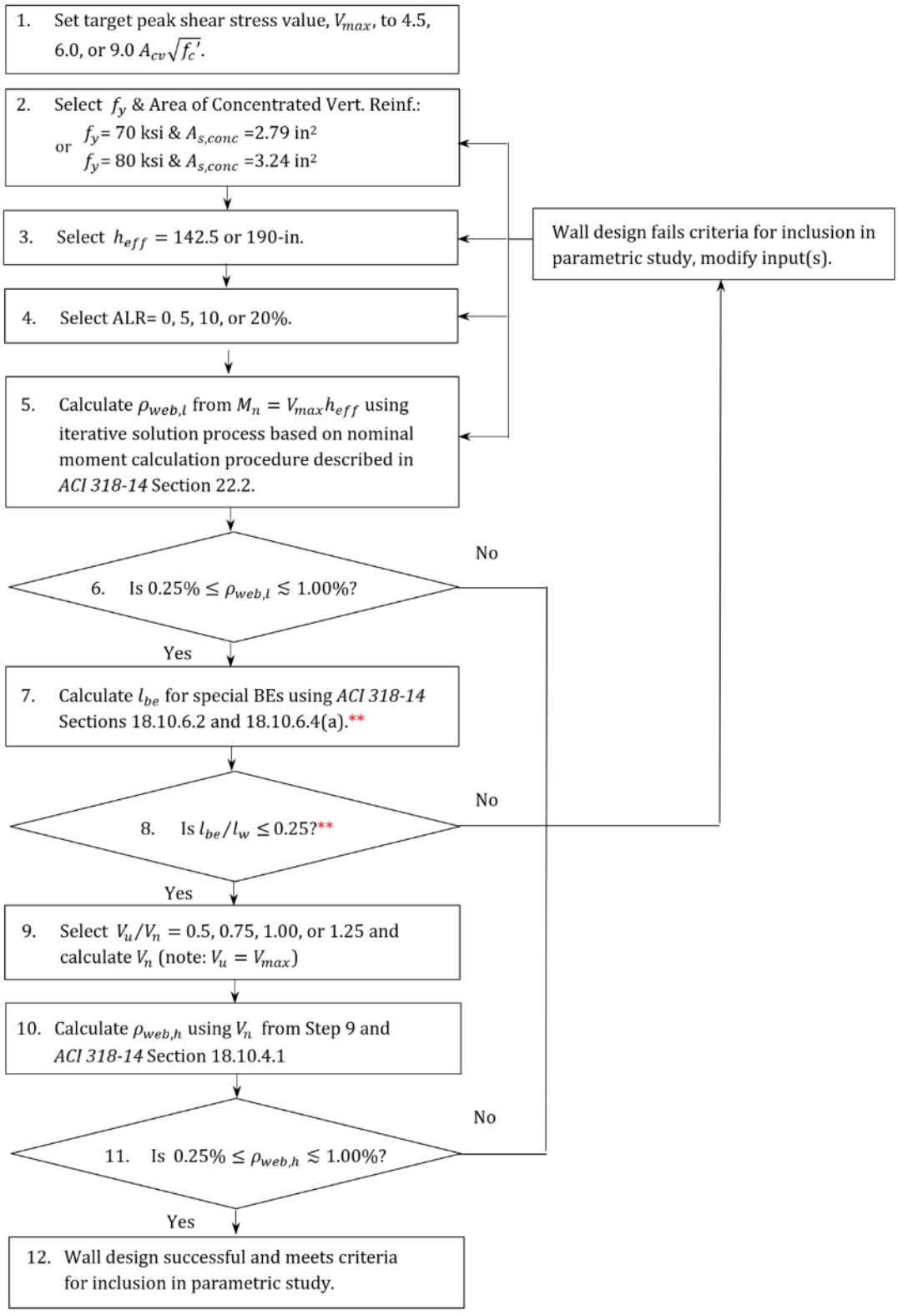

**These steps are modified for walls with BE length equal to neutral axis depth

Figure 7.1: Flowchart for Flexure/Shear Design of Walls in Parametric Study

7.3 Details and Summary of Results for Simulated Walls

7.3.1 Simulated Walls with ACI 318-14 [18] *Compliant Boundary Elements*

7.3.1.1 Design Details

Table 7.1 includes details on all 45 walls with *ACI318-14* [18] compliant boundary elements included in the parametric study; these wall specimens are assigned names W1-W42 (and W28*,W31*, and W34*). Figs. 7.2 and 7.3 summarize the distribution of wall parameters per target peak shear stress demand ($V_{max} = 4.5, 6.0, \quad 9.0 A_{cv}\sqrt{f'_c}$) represented by the simulation wall matrix, including:

- Target shear stress demand: design peak shear stress demand (V_{max}) and design shear capacity-to-demand ratios (V_u/V_n);
- Selected parameter values for shear drivers: combination of steel strength (f_y) and concentrated vertical reinforcement in the wall end zone ($A_{conc,l}$), effective height (h_{eff}), axial load ratio (ALR);
- Resulting steel reinforcement ratios: boundary element vertical reinforcement ratio ($\rho_{BE,l}$); vertical ($\rho_{web,l}$), horizontal ($\rho_{web,h}$), and horizontal-to-vertical ($\rho_{web,h}/\rho_{web,l}$) web reinforcement ratios; as well as
- Resulting boundary element details: boundary element length-to-neutral axis depth (l_{be}/c) and boundary element length-to-wall length (l_{be}/l_w) ratios.

7.3.1.2 Results Summary

Table 7.2 summarizes the strength/deformation response and failure mode of each ACI compliant boundary element wall described in Section 7.3.1.1 using the procedure described in Chapter 6. In this table drift, (%), is calculated as the horizontal displacement measured at the wall height divided by the wall height, $(\%) = \frac{\Delta_{horiz}}{h_w}$. Hinge rotation, θ, is determined at the top of the predicted plastic hinge height (half the length of the wall, $\frac{l_w}{2}$). Hinge rotation is calculated as the difference between the vertical displacements at the right and left side of the wall at the top of the plastic hinge, divided by the length of the wall, such that $\theta = \frac{\Delta_{vert,left} - \Delta_{vert,right}}{l_w}$. The ductility calculations (displacement and rotation) are consistent with the 75% Method presented in Section 3.1.1.2.2; also, used to determine yield for experimentally tested wall specimens.

Table 7.1: Design Details for Simulated Wall Models with ACI Compliant Boundary Elements

Wall No.	Targets		Selected Parameter Values					Resulting Parameter Values					
								Reinforcement Ratios				BE Details	
	V_{max}	V_u/V_n	f_y	$A_{conc,l}$	h_{eff}	$\frac{h_{eff}}{l_w}$	ALR	$\rho_{BE,l}$	$\rho_{web,l}$	$\rho_{web,h}$	$\frac{\rho_{web,h}}{\rho_{web,l}}$	$\frac{l_{be}}{c}$	$\frac{l_{be}}{l_w}$
	-	-	ksi	in^2	in	-	%	%	%	%	-	-	-
W1	4.54	0.75	70	2.79	142.5	1.50	0	6.26	0.25	0.31	1.23	0.56	0.06
W2	4.54	0.50	70	2.79	142.5	1.50	0	6.26	0.25	0.61	2.45	0.56	0.06
W3	6.00	1.00	70	2.79	142.5	1.50	0	6.03	0.97	0.30	0.31	0.51	0.08
W4	6.00	0.75	70	2.79	142.5	1.50	0	6.03	0.97	0.51	0.52	0.51	0.08
W5	6.00	0.50	70	2.79	142.5	1.50	0	6.03	0.97	0.91	0.93	0.51	0.08
W6	6.00	1.00	70	2.79	142.5	1.50	5	5.67	0.52	0.30	0.59	0.51	0.09
W7	6.00	0.75	70	2.79	142.5	1.50	5	5.67	0.52	0.50	0.97	0.51	0.09
W8	6.00	0.50	70	2.79	142.5	1.50	5	5.67	0.52	0.91	1.75	0.51	0.09
W9	4.50	1.00	70	2.79	190.0	2.00	0	6.03	0.97	0.25	0.26	0.51	0.08
W10	4.50	0.75	70	2.79	190.0	2.00	0	6.03	0.97	0.40	0.42	0.51	0.08
W11	4.50	0.50	70	2.79	190.0	2.00	0	6.03	0.97	0.71	0.73	0.51	0.08
W12	4.50	1.00	70	2.79	190.0	2.00	5	5.67	0.52	0.25	0.48	0.51	0.09
W13	4.50	0.75	70	2.79	190.0	2.00	5	5.67	0.52	0.41	0.78	0.51	0.09
W14	4.50	0.50	70	2.79	190.0	2.00	5	5.67	0.52	0.71	1.35	0.51	0.09
W15	6.00	1.25	70	2.79	190.0	2.00	15	3.66	0.93	0.28	0.30	0.68	0.21
W16	6.00	1.00	70	2.79	190.0	2.00	15	3.66	0.93	0.40	0.44	0.68	0.21
W17	6.00	0.75	70	2.79	190.0	2.00	15	3.66	0.93	0.61	0.65	0.68	0.21
W18	6.00	0.50	70	2.79	190.0	2.00	15	3.66	0.93	1.01	1.09	0.68	0.21
W19	6.00	1.25	70	2.79	190.0	2.00	20	2.96	0.50	0.28	0.57	0.71	0.24
W20	6.00	1.00	70	2.79	190.0	2.00	20	2.96	0.50	0.40	0.81	0.71	0.24
W21	6.00	0.75	70	2.79	190.0	2.00	20	2.96	0.50	0.61	1.21	0.71	0.24
W22	6.00	0.50	70	2.79	190.0	2.00	20	2.96	0.50	1.01	2.02	0.71	0.24
W23	6.00	1.00	80	3.24	142.5	1.50	0	6.67	0.31	0.27	0.86	0.50	0.06
W24	6.00	0.75	80	3.24	142.5	1.50	0	6.67	0.31	0.44	1.44	0.50	0.06
W25	6.00	0.50	80	3.24	142.5	1.50	0	6.67	0.31	0.80	2.58	0.50	0.06
W26	9.00	1.25	80	3.24	142.5	1.50	10	4.49	1.09	0.37	0.34	0.66	0.19
W27	9.00	1.00	80	3.24	142.5	1.50	10	4.49	1.09	0.53	0.48	0.66	0.19
W28	9.00	0.75	80	3.24	142.5	1.50	10	4.49	1.09	0.80	0.73	0.66	0.19
W28*	9.00	0.50	80	3.24	142.5	1.50	10	4.49	1.09	1.33	1.21	0.66	0.19
W29	9.00	1.25	80	3.24	142.5	1.50	15	3.93	0.71	0.37	0.52	0.69	0.22
W30	9.00	1.00	80	3.24	142.5	1.50	15	3.93	0.71	0.53	0.75	0.69	0.22
W31	9.00	0.75	80	3.24	142.5	1.50	15	3.93	0.71	0.80	1.12	0.69	0.22
W31*	9.00	0.50	80	3.24	142.5	1.50	15	3.93	0.71	1.33	1.86	0.69	0.22
W32	9.00	1.25	80	3.24	142.5	1.50	20	3.26	0.32	0.37	1.15	0.72	0.25
W33	9.00	1.00	80	3.24	142.5	1.50	20	3.26	0.32	0.53	1.65	0.72	0.25
W34	9.00	0.75	80	3.24	142.5	1.50	20	3.26	0.32	0.80	2.47	0.72	0.25
W34*	9.00	0.50	80	3.24	142.5	1.50	20	3.26	0.32	1.33	4.11	0.72	0.25
W35	4.50	0.75	80	3.24	190.0	2.00	0	6.67	0.31	0.35	1.15	0.51	0.06
W36	4.50	0.50	80	3.24	190.0	2.00	0	6.67	0.31	0.62	2.02	0.51	0.06
W37	6.00	1.00	80	3.24	190.0	2.00	5	6.29	0.87	0.35	0.41	0.56	0.13
W38	6.00	0.75	80	3.24	190.0	2.00	5	6.29	0.87	0.53	0.61	0.56	0.13
W39	6.00	0.50	80	3.24	190.0	2.00	5	6.29	0.87	0.88	1.02	0.56	0.13
W40	6.00	1.00	80	3.24	190.0	2.00	10	5.47	0.47	0.35	0.76	0.59	0.14
W41	6.00	0.75	80	3.24	190.0	2.00	10	5.47	0.47	0.53	1.13	0.59	0.14
W42	6.00	0.50	80	3.24	190.0	2.00	10	5.47	0.47	0.88	1.89	0.59	0.14

* Only modelled with ACI Compliant boundary element length.

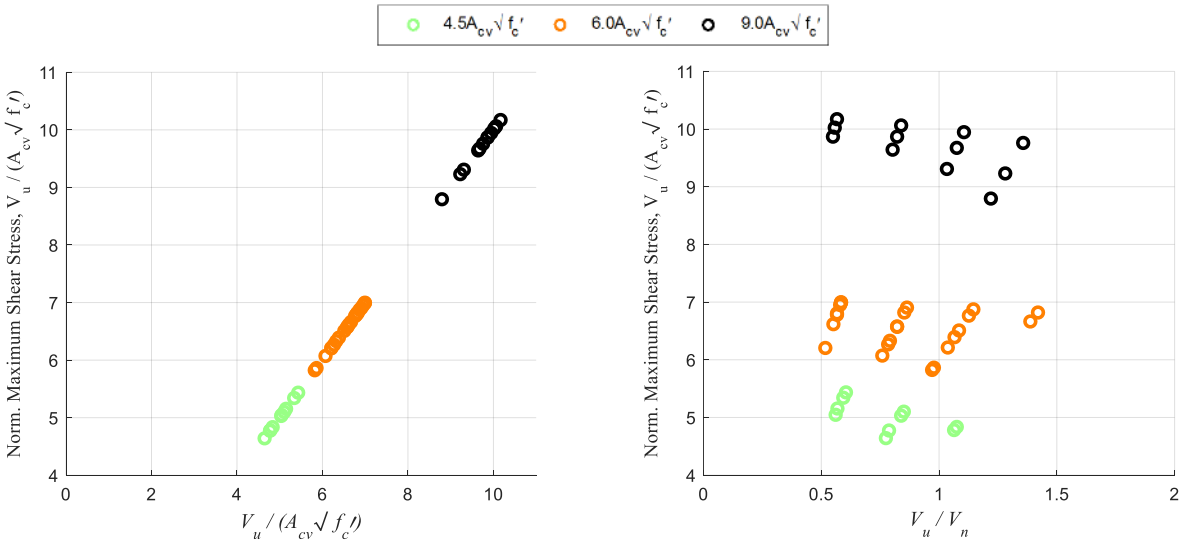

(a) Target Parameters

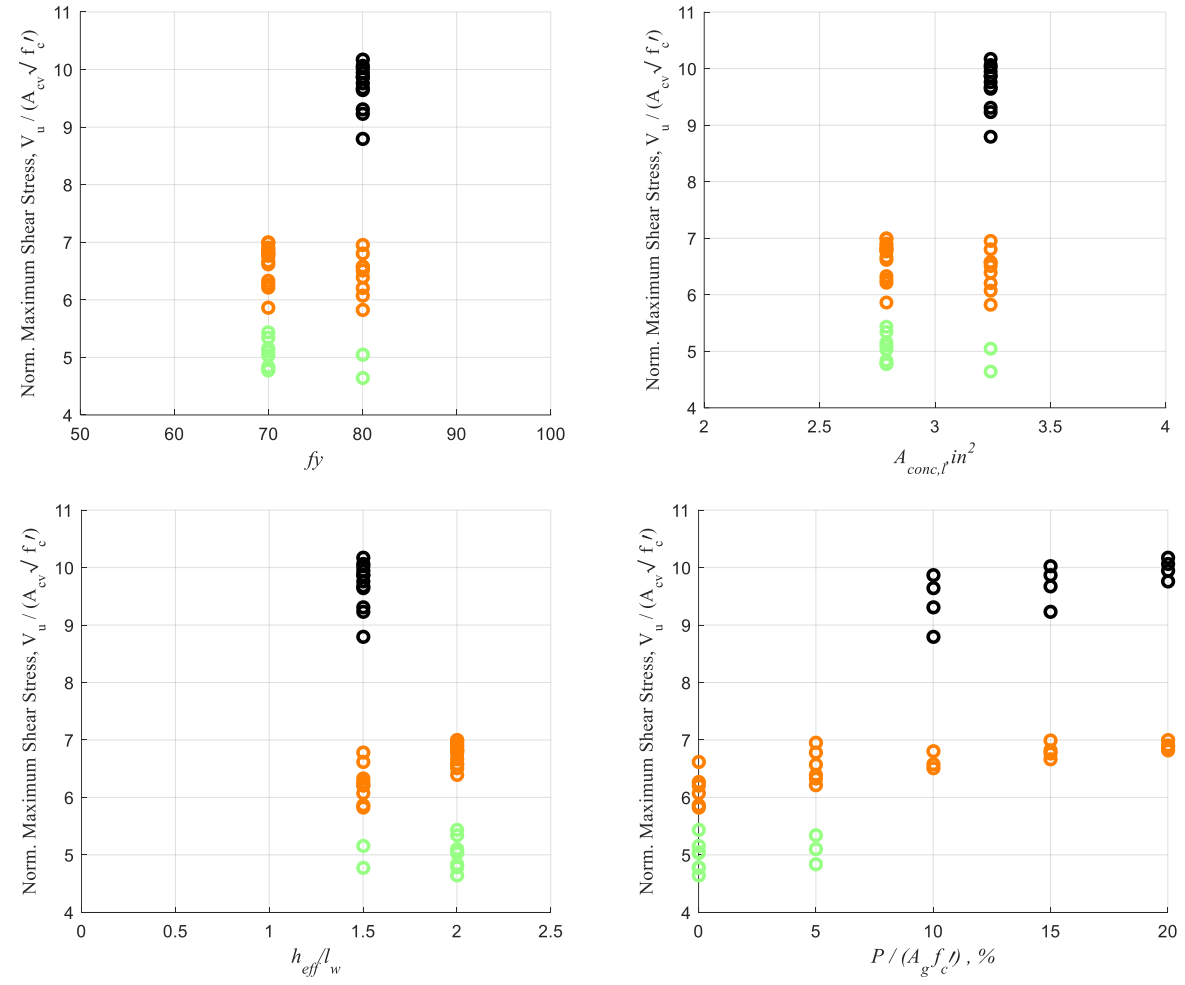

(b) Selected Parameter Values

Figure 7.2: Distribution of Target and Selected Parameter Values for the Simulation Wall Matrix Classified Based on Shear Stress Demand Level

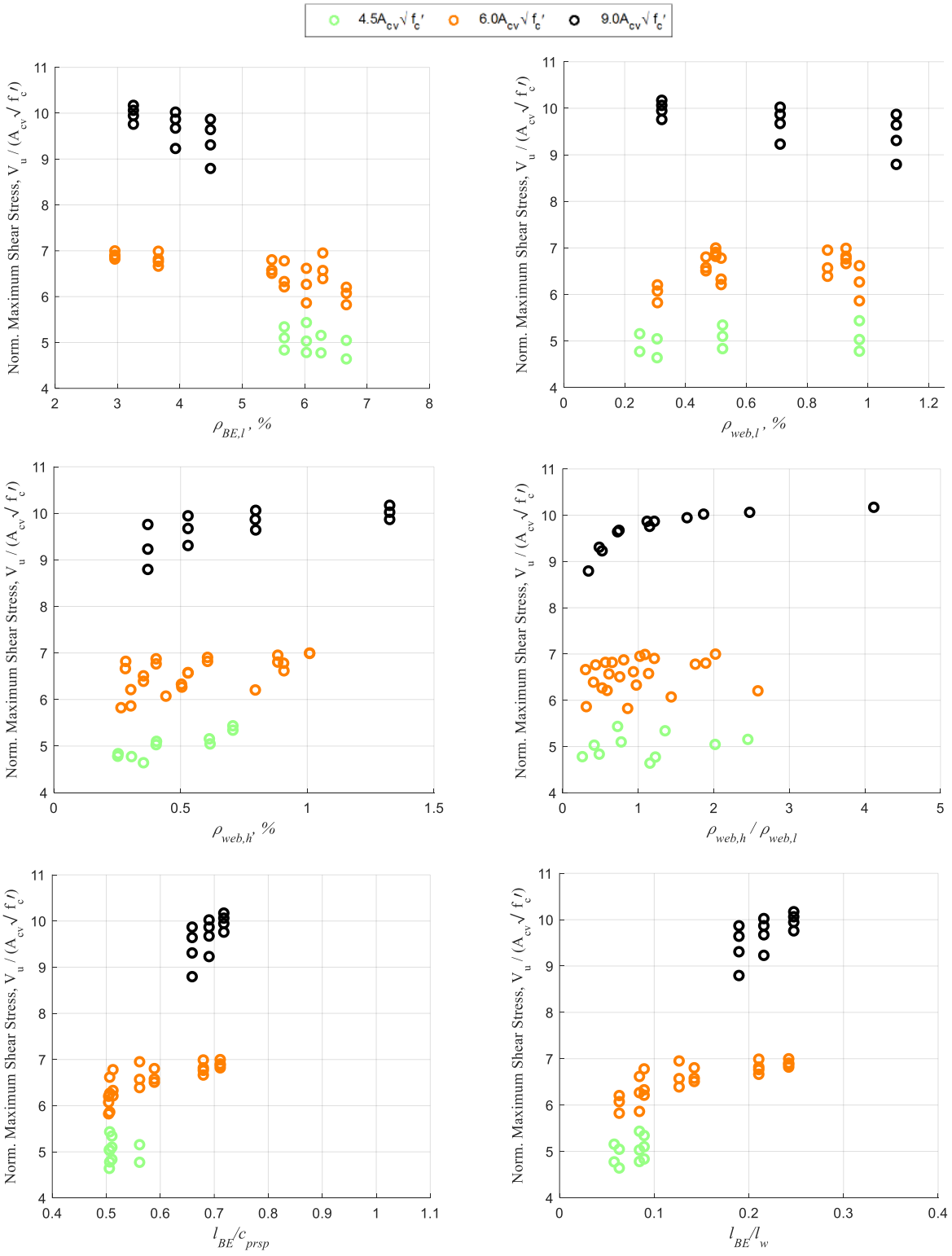

Figure 7.3: ACI Compliant Walls:
Distribution of Resulting Parameter Values for the Simulation Wall Matrix
Classified Based on Shear Stress Demand Level

Table 7.2: Results for Simulated Walls with ACI Compliant Boundary Elements

Wall No.	Shear Response		Drift		Hinge Rotation		Failure Mode
	$V_u/A_{cv}\sqrt{f'_c}$	V_u/V_n	Δ_u %	Δ_u/Δ_y	θ_u rad	θ_u/θ_y	
W1	4.77	0.79	0.99	2.24	0.006	3.08	SC
W2	5.15	0.57	1.75	3.83	0.013	5.33	SC
W3	5.86	0.98	0.70	1.42	0.003	1.50	SC
W4	6.27	0.78	0.99	2.00	0.006	2.54	SC
W5	6.62	0.55	1.50	3.01	0.011	4.19	SC
W6	6.21	1.04	0.70	1.49	0.004	1.78	SC
W7	6.33	0.79	1.15	2.53	0.008	3.45	SC
W8	6.78	0.57	1.72	3.59	0.013	5.09	BR
W9	4.78	1.06	1.34	2.76	0.008	3.33	SC
W10	5.03	0.84	1.82	3.70	0.013	4.57	SC
W11	5.43	0.60	2.19	4.11	0.017	5.10	BR
W12	4.84	1.07	1.56	3.62	0.010	4.64	SC
W13	5.10	0.85	2.08	4.63	0.015	5.95	SC
W14	5.34	0.59	2.23	4.70	0.017	5.94	BR
W15	6.67	1.39	1.24	2.79	0.009	3.50	SC
W16	6.76	1.13	1.04	2.34	0.008	2.96	CB
W17	6.82	0.85	1.37	3.10	0.011	4.12	CB
W18	6.99	0.58	1.59	3.58	0.013	4.78	CB
W19	6.82	1.42	1.35	3.39	0.010	4.32	SC
W20	6.87	1.15	1.41	3.56	0.011	4.67	CB
W21	6.91	0.86	1.45	3.66	0.012	4.87	CB
W22	7.00	0.58	1.90	4.76	0.016	6.50	CB
W23	5.82	0.97	0.62	1.16	0.003	1.21	SC
W24	6.08	0.76	0.73	1.41	0.004	1.74	SC
W25	6.21	0.52	0.98	1.96	0.007	2.68	SC
W26	8.79	1.22	0.78	1.45	0.004	1.47	SC
W27	9.31	1.03	0.90	1.61	0.005	1.80	SC
W28	9.64	0.80	1.16	2.09	0.007	2.60	SC
W28*	9.87	0.55	1.62	2.94	0.012	3.95	SC
W29	9.23	1.28	0.86	1.65	0.005	1.80	SC
W30	9.67	1.07	0.94	1.78	0.006	2.09	SC
W31	9.87	0.82	1.16	2.19	0.008	2.80	SC
W31*	10.02	0.56	1.54	2.99	0.011	4.05	SC
W32	9.76	1.36	0.76	1.54	0.004	1.65	CB
W33	9.95	1.11	1.12	2.26	0.007	2.81	SC
W34	10.06	0.84	1.27	2.59	0.009	3.38	SC
W34*	10.17	0.57	1.09	2.29	0.008	2.90	SC
W35	4.64	0.77	1.21	2.54	0.008	3.43	SC
W36	5.04	0.56	1.78	3.50	0.013	4.63	SC
W37	6.39	1.06	1.36	2.55	0.009	3.29	SC
W38	6.57	0.82	1.68	3.13	0.012	4.25	SC
W39	6.95	0.58	2.43	4.37	0.019	5.95	BR
W40	6.51	1.09	1.79	3.58	0.013	4.87	SC
W41	6.58	0.82	1.66	3.37	0.013	4.62	SC
W42	6.80	0.57	1.97	3.92	0.016	5.36	SC

* Only modelled with ACI Compliant boundary element length.

7.3.2 Simulated Walls with "Extended" Boundary Elements

7.3.2.1 Design Details

Each of the walls with ACI compliant boundary element length (W1-W42, but not W28*, W30*, and W34*) described in Table 7.1 were re-designed for an "extended" boundary element of length at least equal to the neutral axis depth, *c*. Walls with "extended" boundary elements are assigned names W1c-W42c, and these walls have identical target/selected parameters as their ACI compliant counterparts. Variations can be seen for "extended" boundary element walls in:

- Resulting steel reinforcement ratios: boundary element vertical reinforcement ratio ($\rho_{BE,l}$); as well as
- Resulting boundary element details: boundary element length-to-neutral axis depth (l_{be}/c) and boundary element length-to-wall length (l_{be}/l_w) ratios.

Table 7.3 includes details on the design variations between the ACI compliant and "extended" boundary element wall designs. Fig. 7.4 presents the distribution of these design variations per target peak shear stress demand ($V_{max} = 4.5, 6.0, \quad 9.0 A_{cv}\sqrt{f'_c}$).

7.3.1.2 Results Summary

Table 7.4 summarizes the strength/deformation response and failure mode of each "extended" boundary element wall described in Section 7.3.2.1 using the procedure described in Chapter 6. Calculations for drift, hinge rotation, and ductility values are described in Section 7.3.1.2.

Note that Table 7.4 does not include failure mode, since analysis of previously simulated walls with ACI compliant boundary elements indicated that: (i) assessment of failure modes in ATENA 3D were informed by qualitative rules-of-thumb that may not be representative of true failure mode (this approach was taken due to limitations in ATENA 3D software to assess various damage limit states including bar buckling and concrete crushing prior to significant strength loss), and (ii) categorization of walls by failure mode to evaluate the impact of various design parameters was not informative as it yielded limited, if any, correlations.

Through the process of examining walls with ACI compliant boundary element length, it was decided that failure mode would not be used for walls with "extended" boundary element as categorizing walls by normalized peak shear stress demand was far more effective in examining the impact of various design parameters.

Table 7.3: Design Details for Walls with ACI Compliant vs. "Extended" Boundary Element Length

Original BE Details				Extended BE Details			
Wall No.	$\rho_{BE,l}$ %	$\frac{l_{be}}{c}$ -	$\frac{l_{be}}{l_w}$ -	Wall No.	$\rho_{BE,l}$ %	$\frac{l_{be}}{c}$ -	$\frac{l_{be}}{l_w}$ -
W1	6.26	0.56	0.06	W1c	5.90	1.07	0.11
W2	6.26	0.56	0.06	W2c	5.90	1.07	0.11
W3	6.03	0.51	0.08	W3c	4.36	1.01	0.17
W4	6.03	0.51	0.08	W4c	4.36	1.01	0.17
W5	6.03	0.51	0.08	W5c	4.36	1.01	0.17
W6	5.67	0.51	0.09	W6c	3.89	1.02	0.18
W7	5.67	0.51	0.09	W7c	3.89	1.02	0.18
W8	5.67	0.51	0.09	W8c	3.89	1.02	0.18
W9	6.03	0.51	0.08	W9c	4.36	1.01	0.17
W10	6.03	0.51	0.08	W10c	4.36	1.01	0.17
W11	6.03	0.51	0.08	W11c	4.36	1.01	0.17
W12	5.67	0.51	0.09	W12c	3.89	1.02	0.18
W13	5.67	0.51	0.09	W13c	3.89	1.02	0.18
W14	5.67	0.51	0.09	W14c	3.89	1.02	0.18
W15	3.66	0.68	0.21	W15c	2.73	1.00	0.31
W16	3.66	0.68	0.21	W16c	2.73	1.00	0.31
W17	3.66	0.68	0.21	W17c	2.73	1.00	0.31
W18	3.66	0.68	0.21	W18c	2.73	1.00	0.31
W19	2.96	0.71	0.24	W19c	2.22	1.00	0.34
W20	2.96	0.71	0.24	W20c	2.22	1.00	0.34
W21	2.96	0.71	0.24	W21c	2.22	1.00	0.34
W22	2.96	0.71	0.24	W22c	2.22	1.00	0.34
W23	6.67	0.50	0.06	W23c	6.10	1.01	0.13
W24	6.67	0.50	0.06	W24c	6.10	1.01	0.13
W25	6.67	0.50	0.06	W25c	6.10	1.01	0.13
W26	4.49	0.66	0.19	W26c	3.35	1.02	0.29
W27	4.49	0.66	0.19	W27c	3.35	1.02	0.29
W28	4.49	0.66	0.19	W28c	3.35	1.02	0.29
W29	3.93	0.69	0.22	W29c	2.87	1.01	0.32
W30	3.93	0.69	0.22	W30c	2.87	1.01	0.32
W31	3.93	0.69	0.22	W31c	2.87	1.01	0.32
W32	3.26	0.72	0.25	W32c	2.42	1.01	0.35
W33	3.26	0.72	0.25	W33c	2.42	1.01	0.35
W34	3.26	0.72	0.25	W34c	2.42	1.01	0.35
W35	6.67	0.51	0.06	W35c	6.10	1.01	0.13
W36	6.67	0.51	0.06	W36c	6.10	1.01	0.13
W37	6.29	0.56	0.13	W37c	3.83	1.01	0.23
W38	6.29	0.56	0.13	W38c	3.83	1.01	0.23
W39	6.29	0.56	0.13	W39c	3.83	1.01	0.23
W40	5.47	0.59	0.14	W40c	3.37	1.00	0.24
W41	5.47	0.59	0.14	W41c	3.37	1.00	0.24
W42	5.47	0.59	0.14	W42c	3.37	1.00	0.24

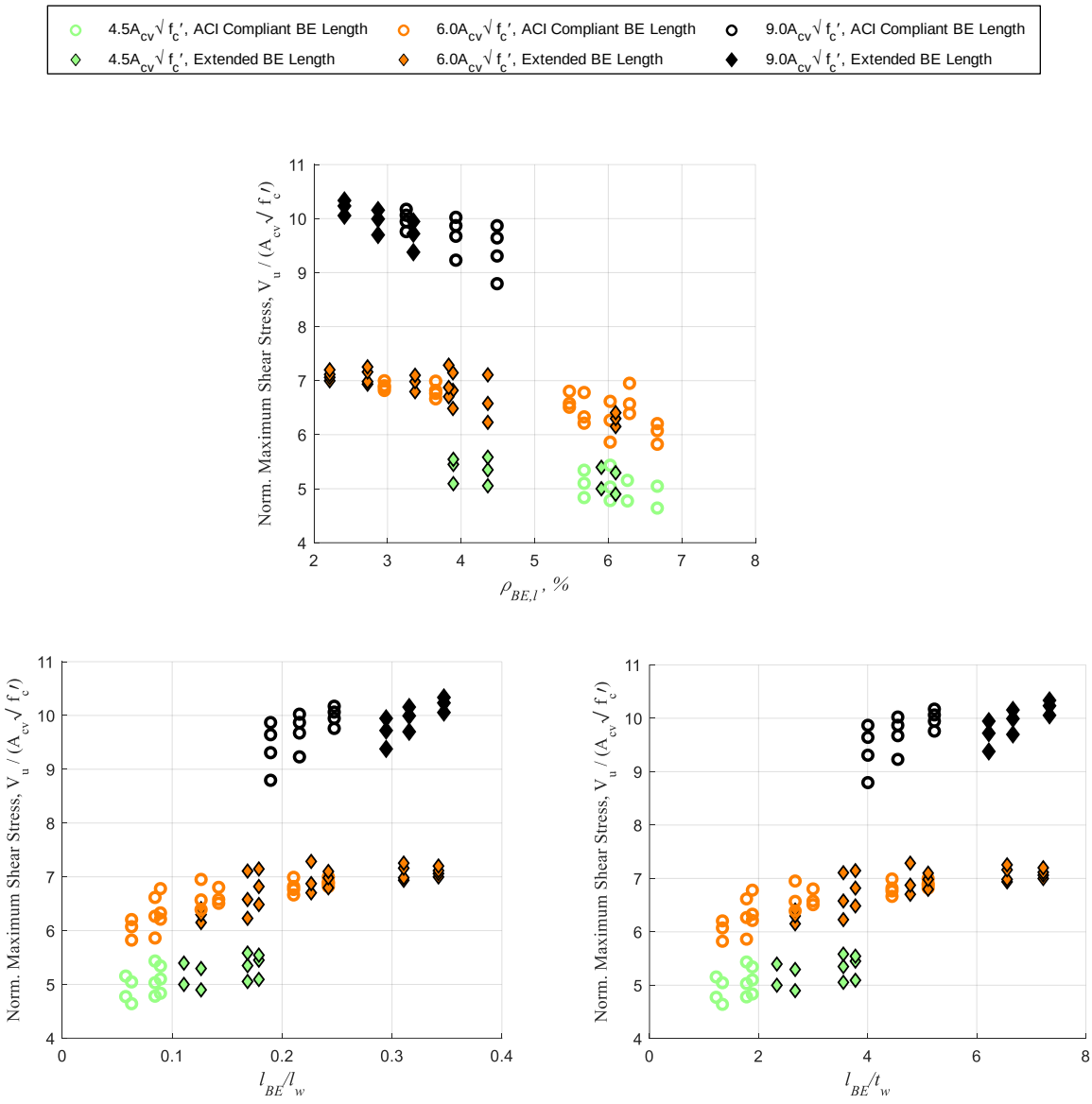

Figure 7.4: ACI Compliant vs. "Extended" Boundary Element Walls:
Distribution of Resulting Parameter Values for the Simulation Wall Matrix
Classified Based on Shear Stress Demand Level

Table 7.4: Results for Simulated Walls with "Extended" Boundary Elements

Wall No.	Shear Response		Drift		Hinge Rotation	
	$V_u/A_{cv}\sqrt{f'_c}$	V_u/V_n	Δ_u %	Δ_u/Δ_y	θ_u rad	θ_u/θ_y
W1c	5.00	0.83	0.91	2.04	0.006	2.78
W2c	5.40	0.59	1.80	3.83	0.013	5.34
W3c	6.23	1.04	0.65	1.30	0.003	1.43
W4c	6.58	0.82	1.08	2.14	0.007	2.75
W5c	7.10	0.59	1.69	3.21	0.013	4.44
W6c	6.48	1.08	0.87	1.83	0.005	2.23
W7c	6.82	0.85	1.64	3.40	0.012	4.85
W8c	7.14	0.60	1.75	3.49	0.013	4.77
W9c	5.05	1.12	1.58	3.20	0.011	3.94
W10c	5.35	0.89	2.08	4.01	0.015	4.96
W11c	5.58	0.62	2.08	3.72	0.016	4.54
W12c	5.10	1.13	1.82	4.07	0.013	5.21
W13c	5.45	0.91	2.64	5.46	0.019	6.83
W14c	5.55	0.62	1.89	4.01	0.014	4.98
W15c	6.93	1.44	1.45	3.15	0.011	4.10
W16c	6.98	1.16	1.37	2.96	0.011	3.92
W17c	7.16	0.89	2.19	4.67	0.018	6.37
W18c	7.26	0.61	2.08	4.47	0.018	6.04
W19c	6.99	1.46	1.57	3.84	0.012	5.06
W20c	7.06	1.18	1.89	4.63	0.016	6.25
W21c	7.12	0.89	1.81	4.39	0.015	5.98
W22c	7.20	0.60	1.94	4.69	0.017	6.42
W23c	6.15	1.03	0.63	1.18	0.003	1.27
W24c	6.30	0.79	0.70	1.34	0.004	1.59
W25c	6.41	0.53	0.89	1.76	0.006	2.34
W26c	9.38	1.30	0.67	1.21	0.003	1.26
W27c	9.72	1.08	0.97	1.72	0.006	1.99
W28c	9.95	0.83	0.82	1.47	0.005	1.72
W29c	9.69	1.35	0.84	1.57	0.005	1.74
W30c	10.00	1.11	1.03	1.90	0.006	2.29
W31c	10.16	0.85	1.28	2.40	0.009	3.08
W32c	10.05	1.40	0.79	1.56	0.005	1.72
W33c	10.23	1.14	1.00	1.97	0.007	2.42
W34c	10.33	0.86	1.33	2.62	0.010	3.43
W35c	4.90	0.82	1.40	2.84	0.010	4.01
W36c	5.29	0.59	2.03	3.90	0.015	5.17
W37c	6.71	1.12	1.49	2.72	0.010	3.47
W38c	6.87	0.86	1.83	3.31	0.014	4.36
W39c	7.29	0.61	2.45	4.28	0.020	5.69
W40c	6.79	1.13	1.74	3.41	0.013	4.61
W41c	6.98	0.87	2.12	4.10	0.017	5.68
W42c	7.10	0.59	2.13	4.15	0.017	5.71

7.3.3 Comparison of Simulated Walls with ACI Compliant and "Extended" Boundary Elements

7.3.3.1 Results Summary

Table 7.5 compares the deformation, ductility, and strength response between walls with ACI Compliant and "extended" boundary element lengths. The calculated values in the table are percent differences, where positive values indicate that the wall with the "extended" boundary element had better performance for a given response metric than its counterpart wall with an ACI compliant boundary element length.

Fig. 7.5 is a graphical representation of the data in Table 7.5 where walls are classified based on specific shear stress demand level of 4.5, 6.0, $9.0A_{cv}\sqrt{f'_c}$. This figure indicates that "extended" boundary element walls generally have a better response for all deformation, ductility, and strength metrics than walls with an ACI compliant boundary element length. Increasing the length of the boundary element to the full neutral axis appears to have modest benefits in terms of drift and hinge rotation capacity at an average of 8-10% improvement, and more modest displacement ductility and hinge rotation ductility benefits at an average of 5-5.6%.

For the deformation and ductility metrics, it appears that walls subject to high shear stress demands, particularly $9.0A_{cv}\sqrt{f'_c}$, are less predictable in their response possibly due to the brittle nature of these walls. This can be observed in the rare, but large, negative percent differences when increasing the boundary element length. If walls subject to high shear stress demands are excluded from the data set, then increasing the boundary element length results in more significant benefits in terms of drift and hinge rotation capacity with an average of 11-13% improvement, as well as increased ductility and hinge rotation ductility benefits at an average of 8-8.5%.

The difference in maximum shear stress and shear demand-to-capacity for ACI compliant versus "extended" boundary element walls is small at an average of <5%, but consistent across the entire set of simulated walls.

Table 7.5: Difference in Response for Walls with ACI Compliant vs. "Extended" Boundary Element Length

Wall No.	Shear Response		Drift		Hinge Rotation	
	$V_u/A_{cv}\sqrt{f'_c}$	V_u/V_n	Δ_u %	Δ_u/Δ_y	θ_u rad	θ_u/θ_y
W1 to W1c	4.64	4.64	-8.35	-8.97	-7.11	-10.44
W2 to W2c	4.62	4.62	2.82	0.08	2.97	0.35
W3 to W3c	6.10	6.10	-7.00	-9.07	0.73	-4.14
W4 to W4c	4.85	4.85	8.49	6.77	11.32	7.85
W5 to W5c	7.08	7.08	12.10	6.44	14.26	5.66
W6 to W6c	4.26	4.26	21.88	20.33	25.33	22.44
W7 to W7c	7.48	7.48	35.52	29.32	41.51	33.65
W8 to W8c	5.20	5.20	1.80	-2.82	0.44	-6.59
W9 to W9c	5.51	5.51	16.80	14.78	21.86	16.70
W10 to W10c	6.07	6.07	13.27	8.27	15.77	8.10
W11 to W11c	2.66	2.66	-4.98	-10.15	-3.52	-11.79
W12 to W12c	5.18	5.18	15.89	11.61	18.04	11.68
W13 to W13c	6.51	6.51	23.62	16.43	25.46	13.79
W14 to W14c	3.79	3.79	-16.80	-15.96	-18.15	-17.51
W15 to W15c	3.95	3.95	16.11	12.10	21.31	15.92
W16 to W16c	3.17	3.17	27.76	23.36	33.09	27.84
W17 to W17c	4.86	4.86	46.05	40.32	50.12	42.79
W18 to W18c	3.69	3.69	26.46	22.00	28.55	23.31
W19 to W19c	2.51	2.51	14.75	12.36	18.41	15.77
W20 to W20c	2.65	2.65	29.17	26.05	32.64	29.02
W21 to W21c	2.98	2.98	22.02	18.14	24.34	20.33
W22 to W22c	2.92	2.92	1.72	-1.32	1.94	-1.17
W23 to W23c	5.49	5.49	2.53	1.98	6.36	4.24
W24 to W24c	3.61	3.61	-5.15	-5.28	-7.19	-8.89
W25 to W25c	3.20	3.20	-9.48	-10.77	-13.21	-13.48
W26 to W26c	6.45	6.45	-14.99	-17.63	-9.27	-15.72
W27 to W27c	4.39	4.39	7.20	6.75	13.47	9.73
W28 to W28c	3.10	3.10	-34.01	-34.71	-37.80	-40.50
W29 to W29c	4.92	4.92	-3.11	-5.36	1.70	-3.22
W30 to W30c	3.27	3.27	8.85	6.57	13.13	9.37
W31 to W31c	2.93	2.93	10.16	8.88	12.62	9.63
W32 to W32c	2.92	2.92	3.98	1.23	8.60	4.05
W33 to W33c	2.85	2.85	-10.87	-13.57	-10.52	-14.72
W34 to W34c	2.68	2.68	3.98	1.24	5.53	1.37
W35 to W35c	5.32	5.32	14.69	11.09	17.54	15.46
W36 to W36c	4.88	4.88	12.80	10.89	14.16	11.10
W37 to W37c	4.83	4.83	9.24	6.36	12.37	5.28
W38 to W38c	4.45	4.45	8.47	5.32	10.00	2.63
W39 to W39c	4.79	4.79	1.13	-2.18	1.24	-4.42
W40 to W40c	4.25	4.25	-2.91	-5.09	-1.64	-5.43
W41 to W41c	5.94	5.94	24.32	19.51	26.78	20.63
W42 to W42c	4.22	4.22	8.14	5.57	9.66	6.32

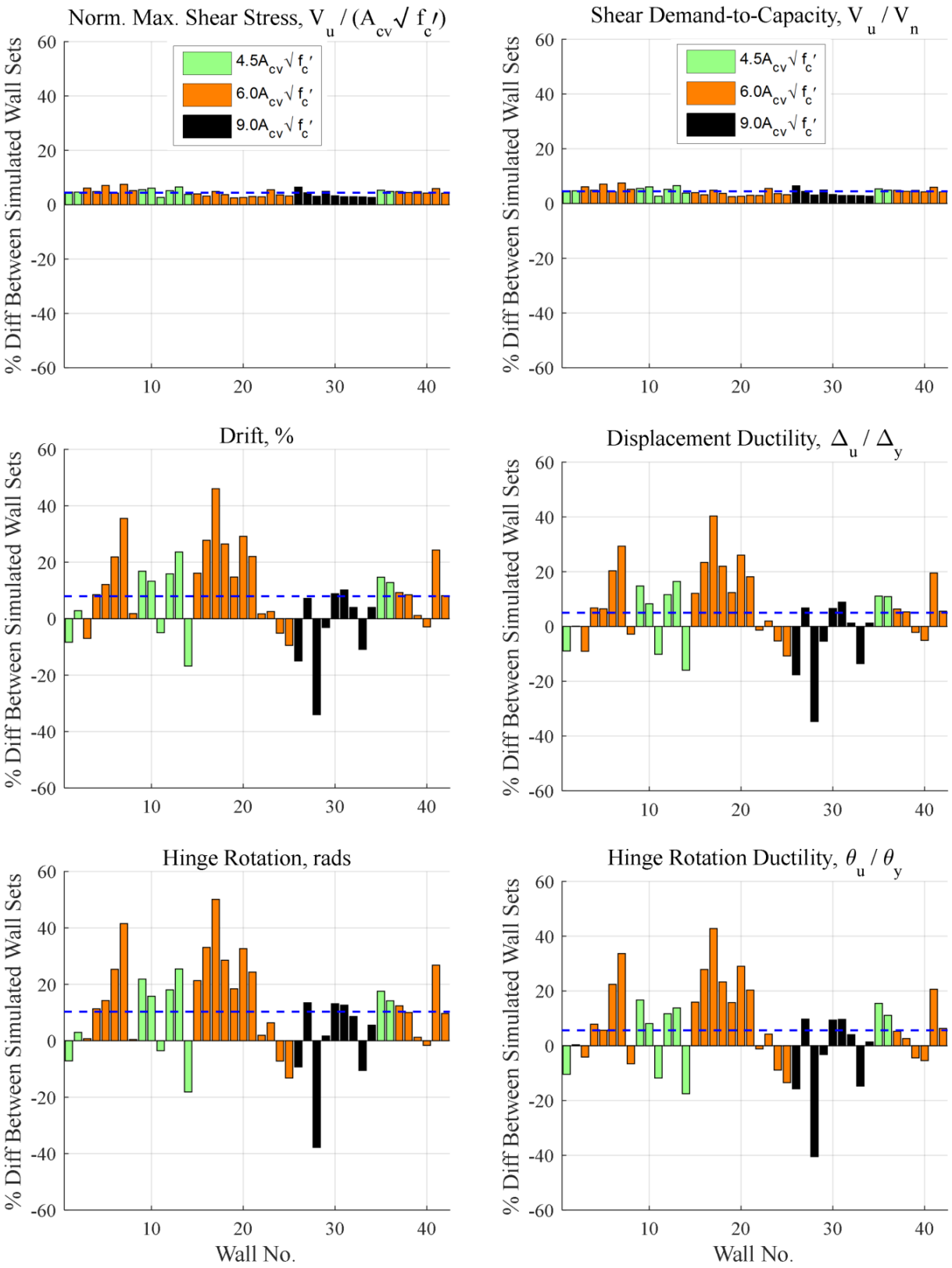

Figure 7.5: Difference in Response for Walls with ACI Compliant vs. "Extended" Boundary Element Length (Dashed blue line indicates average percent difference for 42 walls in the simulation)

7.4 Impact of Wall Design Parameters on Deformation and Ductility

This section investigates the impact that various wall design parameters have in terms of deformation and ductility. These assessments are based on simulations of slender planar walls with a cross-sectional aspect ratio of approximately 20, which would be equivalent to a wall that is 30 feet long and 18 inches thick. Each of the figures in Sections 7.4.1-7.4.7 summarizes model results for an individual design parameter by categorizing walls based on: (i) the shear stress demand level ($4.5, 6.0, \quad 9.0A_{cv}\sqrt{f'_c}$) and (ii) whether the boundary element length is minimally ACI compliant or "extended" to the full neutral axis depth. Section 7.4.8 includes cumulative probability distribution functions (CDFs) to further explore the impact of each of these design parameters individually, and to examine the interaction between the boundary element length and a selection of these design parameters.

7.4.1 Impact of Shear Demand

7.4.1.1 Shear Stress Demand

Shear stress demand, $V_u/A_{cv}\sqrt{f'_c}$, is the most influential parameter that was investigated in the parametric study. Fig. 7.6 indicates that increasing shear stress has a significant negative impact on wall deformation/ductility. The figure indicates that as shear stress demand increases, the average and maximum observed displacement ductility values decrease. Furthermore, walls with high shear stress demand $9.0A_{cv}\sqrt{f'_c}$ exhibit a very narrow band of response, as indicated by comparatively its smaller standard deviation values, compared to walls subject to lower shear stress demands.

7.4.1.2 Shear Demand-to-Capacity Ratio

The data in Fig. 7.7 indicates that for ACI compliant walls, deformation/ductility improves as the shear demand-to-capacity ratio, V_u/V_n, decreases. In particular, it appears that walls subject to high shear stress demands of $9.0A_{cv}\sqrt{f'_c}$ and with shear design that is more conservative than the code of $V_u/V_n < 0.75$ exhibit improved drift/rotation capacity and displacement/rotational ductility. These results are an initial indicator that engineers who intend to design walls with high shear demands should consider using a lower V_u/V_n value to avoid a brittle reponse.

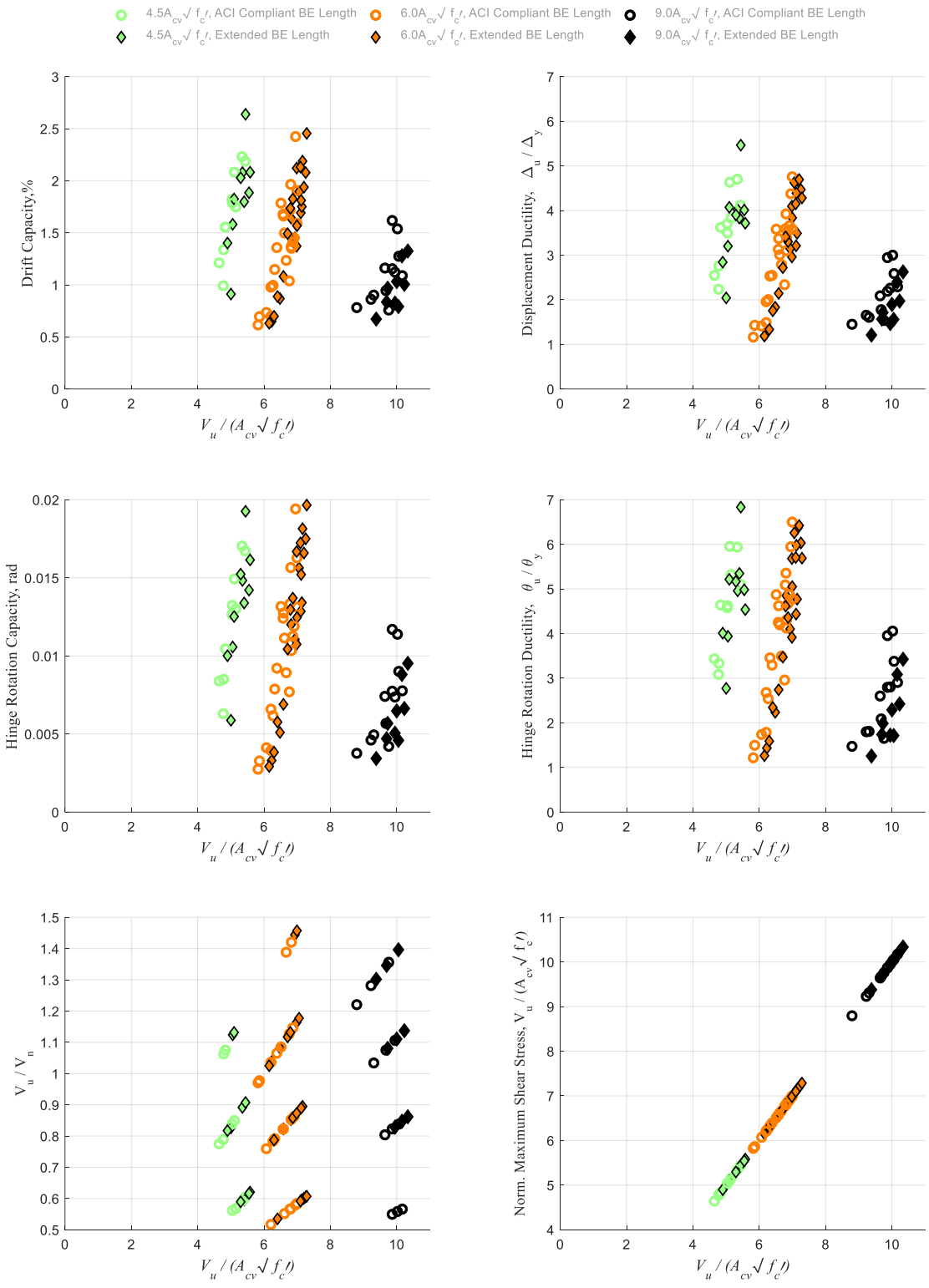

Figure 7.6: Relationship between Maximum Shear Stress Demand and Wall Response:
(Top) Drift and Displacement Ductility;
(Middle) Hinge Rotation Capacity and Rotational Ductility;
(Bottom) Shear Demand-to-Capacity and Maximum Shear Stress Demand

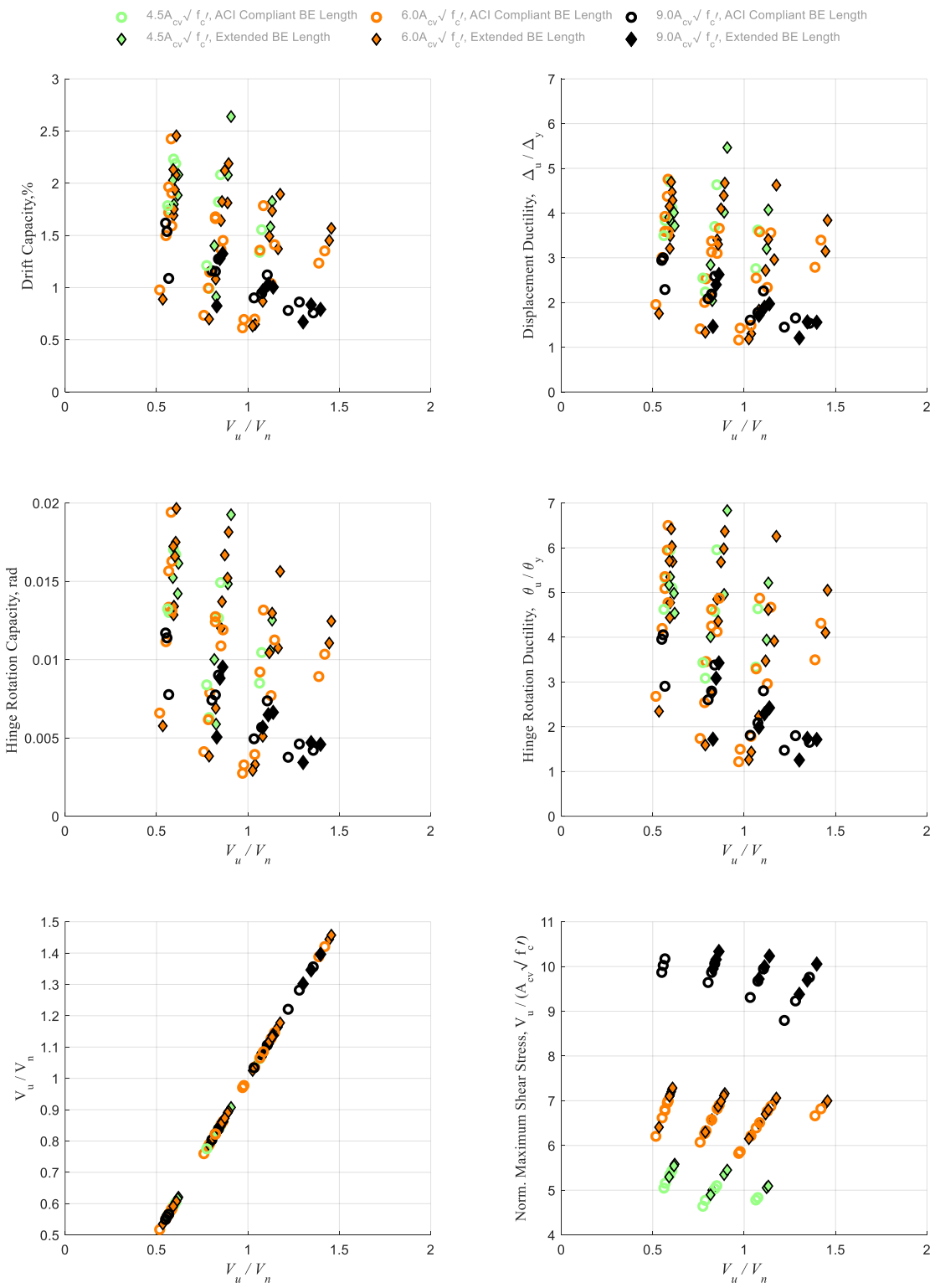

Figure 7.7: Relationship between Shear Demand-to-Capacity Ratio and Wall Response:
(Top) Drift and Displacement Ductility;
(Middle) Hinge Rotation Capacity and Rotational Ductility;
(Bottom) Shear Demand-to-Capacity and Maximum Shear Stress Demand

7.4.2 Impact of Vertical Web Reinforcement

One of the major objectives in the parametric study was to assess the *ACI 318-14* [18] minimum for vertical web reinforcement. Fig. 7.8 indicates that there is no clear, significant relationship between vertical web reinforcement ratio, $\rho_{web,l}$, and deformation or ductility.

7.4.3 Impact of Horizontal Web Reinforcement

Another objective of the parametric study was to examine the *ACI 318-14* [18] minimum for horizontal web reinforcement. Fig. 7.9 indicates that:

- There is a significant positive correlation between horizontal web reinforcement ratio, $\rho_{web,h}$, and deformation/ductility. Increasing $\rho_{web,h}$ leads to the greatest deformation/ ductility improvements for walls with low shear stress demands ($4.5A_{cv}\sqrt{f'_c}$) compared to those with high shear stress demands ($9.0A_{cv}\sqrt{f'_c}$).
- For most walls (low-to-moderate shear stress demands), the deformation/ductility response can be further improved by combining an increased $\rho_{web,h}$ and extending the boundary element length. However, as discussed in Section 7.3.3.1, walls with high shear stress demands do not demonstrate a consistent improved response for increased boundary element length. Walls with high shear stress demands in particular exhibit more predictable, though modest, performance gains from increasing $\rho_{web,h}$ alone.
- Overall, there is a significant negative correlation between $\rho_{web,h}$ and the shear demand-to-capacity ratio, V_u/V_n. For a specific V_u/V_n ***design*** value, walls with higher $\rho_{web,h}$ exhibit a higher ***observed*** V_u/V_n. This response is most notable in walls with moderate shear stress demands; though, this observation may be a product of the fact that these walls have a greater distribution of $\rho_{web,h}$ for each V_u/V_n ***design*** value.

These results suggest that there is a deformation capacity/ductility incentive to including additional horizontal web reinforcement, aside from the shear strength improvements associated with the provision in *ACI 318-14* [18]. Deformation/ ductility benefits from increasing $\rho_{web,h}$ are most pronounced in walls designed for lower shear stress demands, yet critical gains are still observed in walls with high shear stresses where it is possible to use additional horizontal reinforcement to increase displacement ductility to over 2. Therefore, these findings are relevant to design engineers irrespective of whether they intend to design a wall with low, moderate, or high shear stress demand.

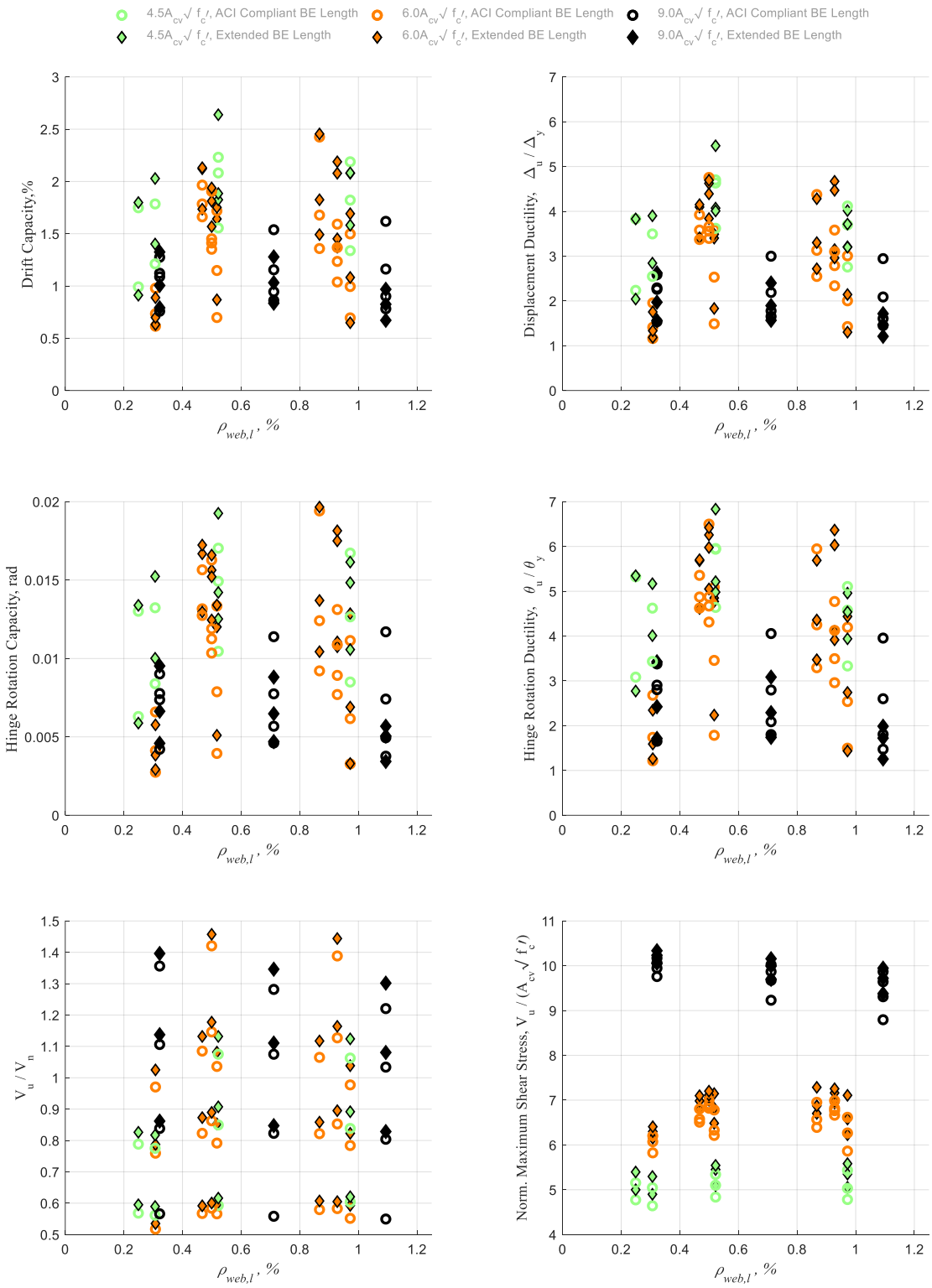

Figure 7.8: Relationship between Vertical Web Reinforcement Ratio and Wall Response:
(Top) Drift and Displacement Ductility;
(Middle) Hinge Rotation Capacity and Rotational Ductility;
(Bottom) Shear Demand-to-Capacity and Maximum Shear Stress Demand

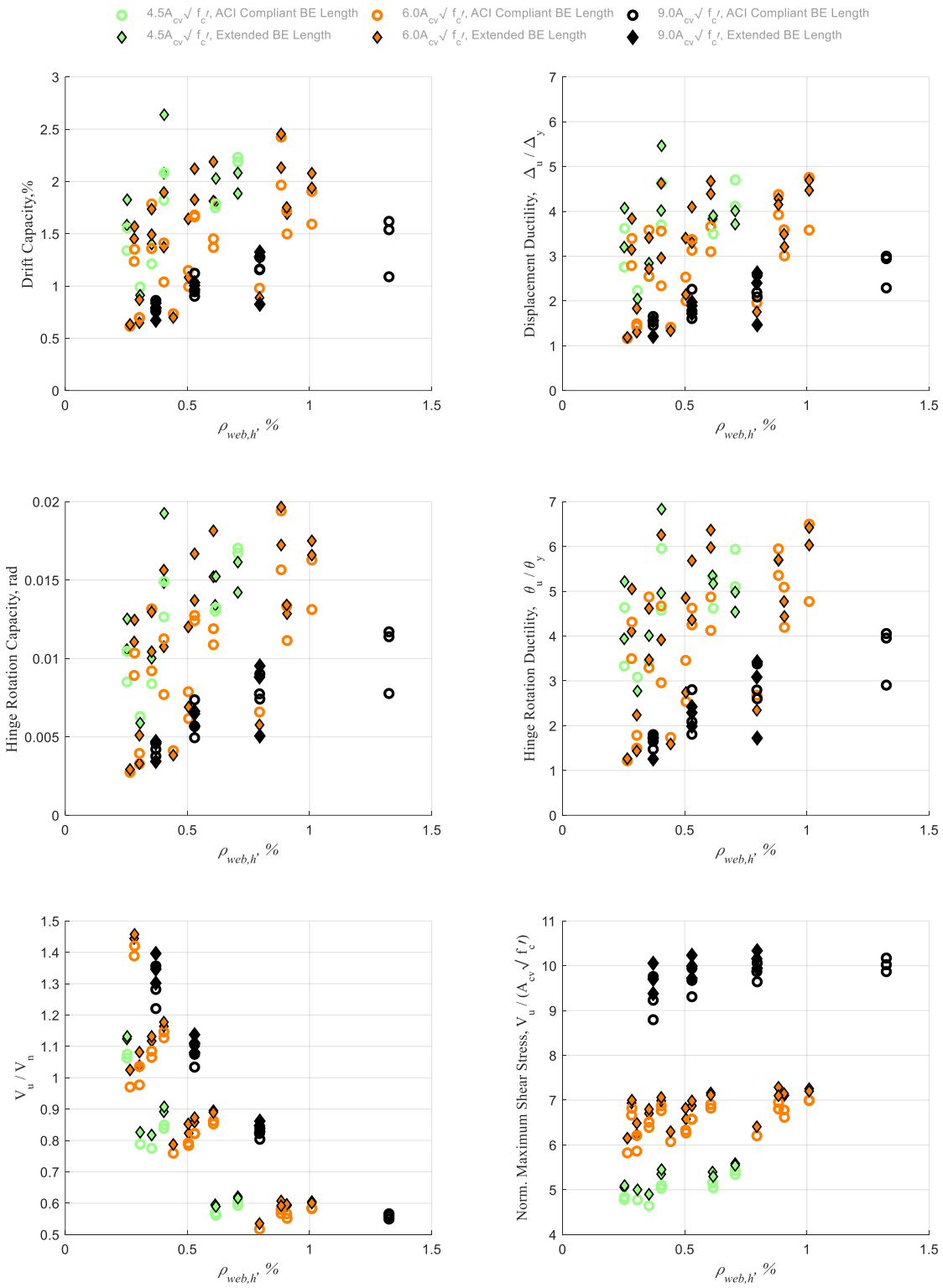

Figure 7.9: Relationship between Horizontal Web Reinforcement Ratio and Wall Response:
(Top) Drift and Displacement Ductility;
(Middle) Hinge Rotation Capacity and Rotational Ductility;
(Bottom) Shear Demand-to-Capacity and Maximum Shear Stress Demand

7.4.4 Impact of Horizontal-to-Vertical Web Reinforcement Ratio

After investigating vertical and horizontal web reinforcement as independent design parameters, the ratio between the two was examined via the horizontal-to-vertical web reinforcement ratio, $\rho_{web,h} / \rho_{web,l}$. The data in Fig. 7.10 indicates that:

- There is a significant negative correlation between $\rho_{web,h} / \rho_{web,l}$ and the shear demand-to-capacity ratio, V_u/V_n. This correlation appears to be primarily driven by the $\rho_{web,h}$ value.
- When considering walls with design shear stress of 4.5, 6.0, $9.0A_{cv}\sqrt{f'_c}$ separately:
  - Walls with low-moderate shear stresses (4.5 $6.0A_{cv}\sqrt{f'_c}$) do not exhibit any significant correlations for the deformation capacity/ductility metrics. However, if walls with low axial load ratio (ALR = 0%) and low vertical web reinforcement ($\rho_{web,l} \leq 0.35\%$) are removed, then these walls have a significant positive correlation for all deformation capacity/ductility metrics.
  - In general, walls with a high design shear stress ($9.0A_{cv}\sqrt{f'_c}$) exhibit an improved deformation capacity/ductility with increasing $\rho_{web,h} / \rho_{web,l}$. However, more walls with $\rho_{web,h} / \rho_{web,l} > 2.5$ need to be simulated to investigate the results observed with $\rho_{web,h} / \rho_{web,l} \approx 4$.
- For most walls (low-to-moderate shear stress demands), the deformation/ductility response can be further improved by combining an increased $\rho_{web,h} / \rho_{web,l}$ and extending the boundary element length. The most common cases where this does not apply are the walls that exhibit low axial load ratio (ALR = 0%) and low vertical web reinforcement ($\rho_{web,l} \leq 0.35\%$). Walls with high shear stress demands typically exhibit modest deformation/ductility improvements from increasing $\rho_{web,h} / \rho_{web,l}$ alone.

These results suggest that deformation capacity/ductility can be improved in walls with: (i) low-moderate design shear stress by increasing only $\rho_{web,h} / \rho_{web,l}$ (OR) increasing both $\rho_{web,h} / \rho_{web,l}$ and extending the boundary element (for walls when ALR > 0% and $\rho_{web,l} \geq 0.35\%$), and (ii) high design shear stress by increasing only $\rho_{web,h} / \rho_{web,l}$. Similar to the impact of increasing $\rho_{web,h}$, the greatest deformation/ductility benefits from $\rho_{web,h} / \rho_{web,l}$ are observed in walls subject to lower shear stress demands (excluding walls with ALR = 0% and $\rho_{web,l} \leq 0.35\%$).

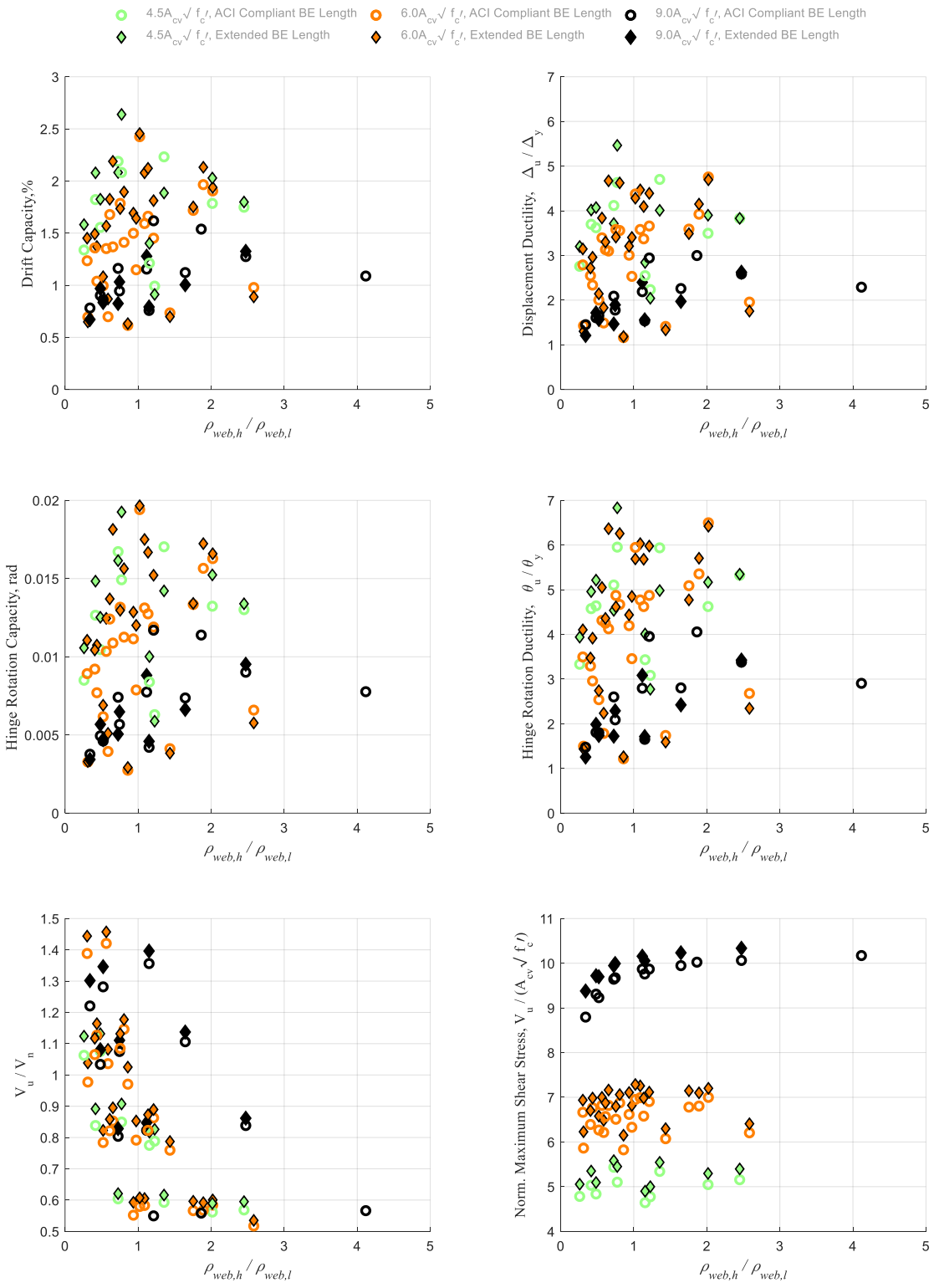

Figure 7.10: Relationship between Horizontal-to-Vertical Web Reinforcement Ratio and Wall Response:
(Top) Drift and Displacement Ductility;
(Middle) Hinge Rotation Capacity and Rotational Ductility;
(Bottom) Shear Demand-to-Capacity and Maximum Shear Stress Demand

7.4.5 Impact of Excess Horizontal Reinforcement

Results from the investigation of horizontal web reinforcement in Section 7.4.3 suggested that there is a deformation capacity/ductility incentive to providing additional ("excess") horizontal reinforcement, $\rho_{web,h\ (excess)}$, beyond what was required by *ACI 318-14* [18] to meet the shear demand . The calculation for the ***required*** horizontal web reinforcement to meet the observed shear demand $\rho_{web,h\ (req)}$ and the associated $\rho_{web,h\ (excess)}$ is presented in Fig. 7.11. In this calculation, $\rho_{web,h\ (prov)}$ is the amount of horizontal web reinforcement ***provided*** in the wall design.

$\phi V_n \geq V_u$, for the following calculation ϕ-factor is excluded

$$V_n = A_{cv}\left(\alpha_c\sqrt{f_c'} + \rho_{web,h\ (req)} f_y\right) \geq V_u$$

$$\rho_{web,h\ (req)}\ (\%) = 100 \times [V_u - A_{cv}\alpha_c\sqrt{f_c'}]/A_{cv}f_y$$

$$\rho_{web,h\ (excess)}\ (\%) = \rho_{web,h\ (prov)}\ (\%) - \rho_{web,h\ (req)}\ (\%)$$

Figure 7.11: Calculation Procedure for "Excess" Horizontal Reinforcement

Note that in these calculations when $\rho_{web,h\ (excess)}$ is a negative value (or, $\rho_{web,h\ (prov)}/\rho_{web,h\ (req)}$ is less than one), then the amount of horizontal web reinforcement provided in the design does not meet the amount required to carry the observed shear demand. Thus, the wall is non-compliant.

The data in Figs. 7.12 and 7.13 indicates that:

- There is positive correlation for both $\rho_{web,h\ (excess)}$ and $\rho_{web,h\ (prov)}/\rho_{web,h\ (req)}$ with all of the deformation capacity/ductility metrics. Also, these parameters have a significant negative correlation with V_u/V_n.
- For most walls, the extending the boundary element leads to improved deformation/ductility response; refer to discussion in Sections 7.4.3 and 7.4.4.

Similar to the findings in Section 7.4.3, the results for $\rho_{web,h\ (excess)}$ and $\rho_{web,h\ (prov)}/\rho_{web,h\ (req)}$ suggest that providing excess horizontal web reinforcement improves deformation response.

Results seem to indicate that walls with low-moderate shear stress demands (4.5 $6.0A_{cv}\sqrt{f'_c}$) that have $\rho_{web,h\ (excess)} \geq 0.25\%$ and $\rho_{web,h\ (prov)}/\rho_{web,h\ (req)} \gtrapprox 2.0$ are able to achieve displacement ductility in excess of 3. The data is more limited for walls with high shear stress demand ($9.0A_{cv}\sqrt{f'_c}$), but it appears that it is at least necessary to have $\rho_{web,h\ (excess)} \geq 0.25\%$ and $\rho_{web,h\ (prov)}/\rho_{web,h\ (req)} \gtrapprox 1.25$ to approach a displacement ductility of 2.

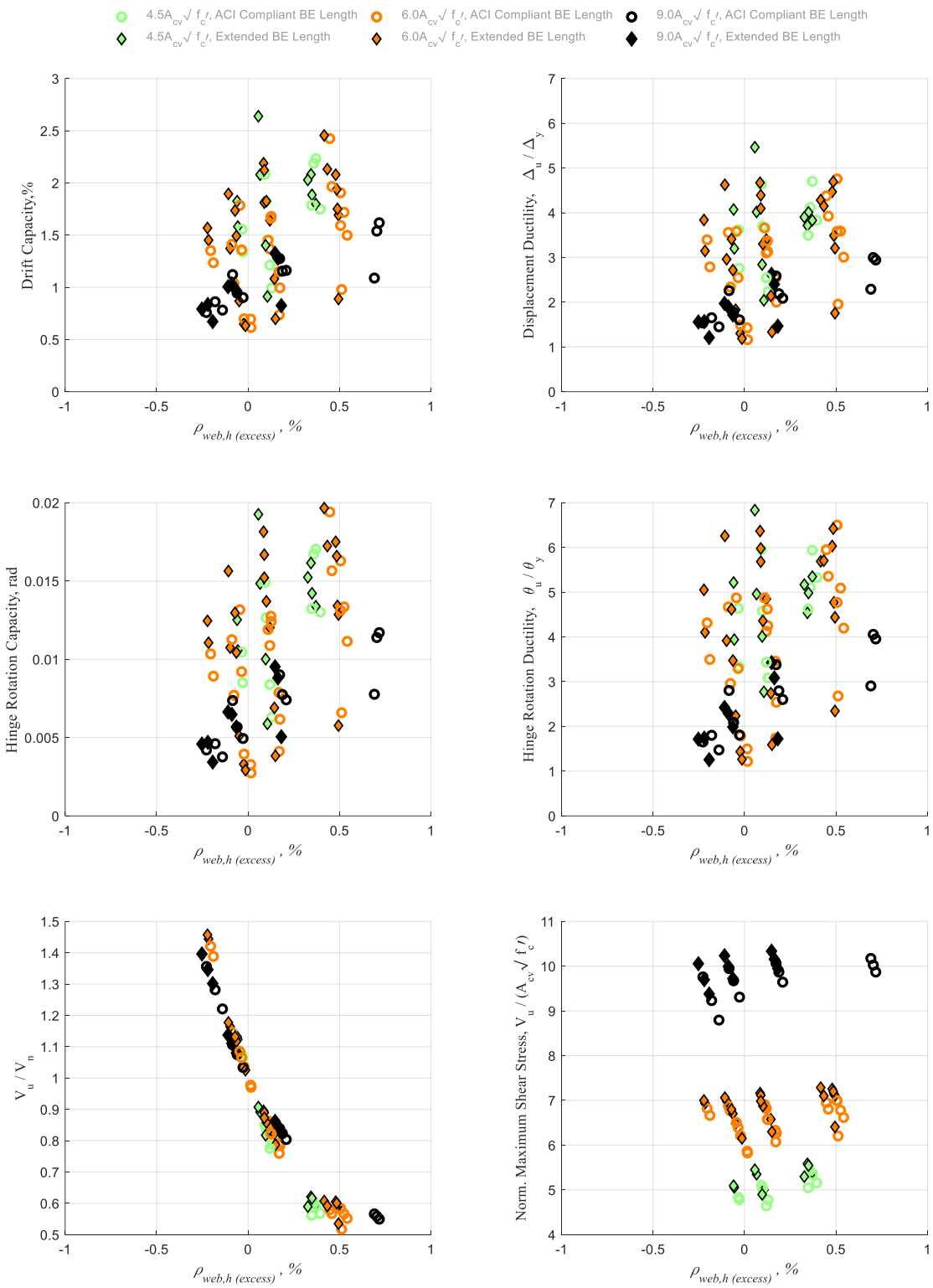

Figure 7.12: Relationship between Excess Horizontal Web Reinforcement Ratio and Wall Response:
(Top) Drift and Displacement Ductility;
(Middle) Hinge Rotation Capacity and Rotational Ductility;
(Bottom) Shear Demand-to-Capacity and Maximum Shear Stress Demand

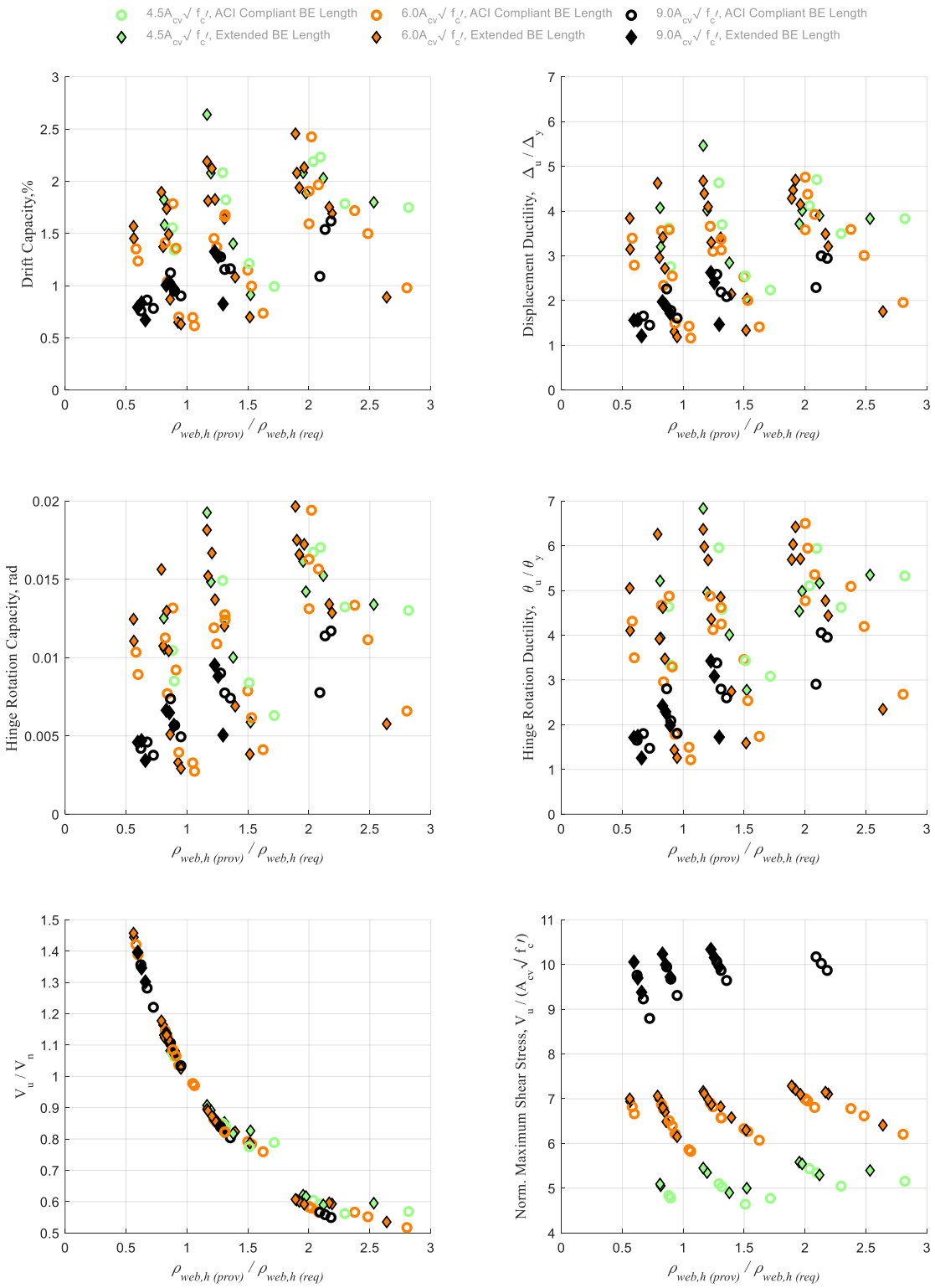

Figure 7.13: Relationship between Prov'd-to-Req'd Horizontal Web Reinforcement Ratio and Wall Response:
(Top) Drift and Displacement Ductility;
(Middle) Hinge Rotation Capacity and Rotational Ductility;
(Bottom) Shear Demand-to-Capacity and Maximum Shear Stress Demand

7.4.6 Impact of Boundary Element Length

In order to study the impact of boundary element length,l_{BE}, on wall deformation/ductility, the walls were first designed with a l_{BE} value that was minimally compliant with *ACI 318-14* [18] provisions for special structural walls and then "extended" to the full neutral axis depth.

The ACI compliant walls have l_{BE} / c_{psrp} values from 0.5 to 0.72, where walls with moderate shear stress demand ($6.0A_{cv}\sqrt{f'_c}$) represent this full range. Walls with $4.5A_{cv}\sqrt{f'_c}$ are at the lower end of the range with l_{BE} / c_{psrp} values of 0.50 to 0.56 and walls with $9.0A_{cv}\sqrt{f'_c}$ are at the higher end of the range at 0.66 to 0.72. Therefore, the conclusions related to the impact of ACI compliant boundary element length are limited to walls with $6.0A_{cv}\sqrt{f'_c}$. For these walls, Fig. 7.14 indicates that there is a positive correlation between l_{BE} / c_{psrp} and deformation/ductility.

A majority of walls with "extended" boundary element length have l_{BE} / c_{psrp} values between 1.0-1.02 (only two walls fall outside this range at 1.07). The data in Fig. 7.14 suggests that only increasing the boundary element length, from ACI compliant to the full neutral axis depth, is insufficient to achieve significant improved deformation/ductility particularly for walls with high shear stress demands.

7.4.7 Impact of Axial Load Ratio

In the simulation wall matrix, axial load ratio (ALR) was one of the selected parameters utilized to achieve the target shear demand. A consequence of this design approach, which can be seen in the distributions presented in Fig. 7.2(b) and Fig. 7.15, is that walls with low shear stress demand ($4.5A_{cv}\sqrt{f'_c}$) do not have moderate to high ALR values, and walls with high shear demand ($9.0A_{cv}\sqrt{f'_c}$) do not have low ALR values. Therefore, the conclusions related to the impact of ALR are limited to walls with moderate shear demand ($6.0A_{cv}\sqrt{f'_c}$) since they represent the full range of ALR design values examined for this study. Fig. 7.15 illustrates that on average, moderate shear demand walls exhibit higher ductilities as axial load ratio increases; this is particularly notable in walls with an ALR greater than 5%. For these walls an improvement in ductility is also observed as a result of extending the boundary element length, though this benefit seems to correspond only to walls with an applied axial load ratio (rather than ALR=0%). Additional investigations would be necessary to investigate upper-bound ALR value where the compression demand becomes detrimental, leading to brittle failures, rather than exhibiting the deformation/ductility improvements seen in this parametric study.

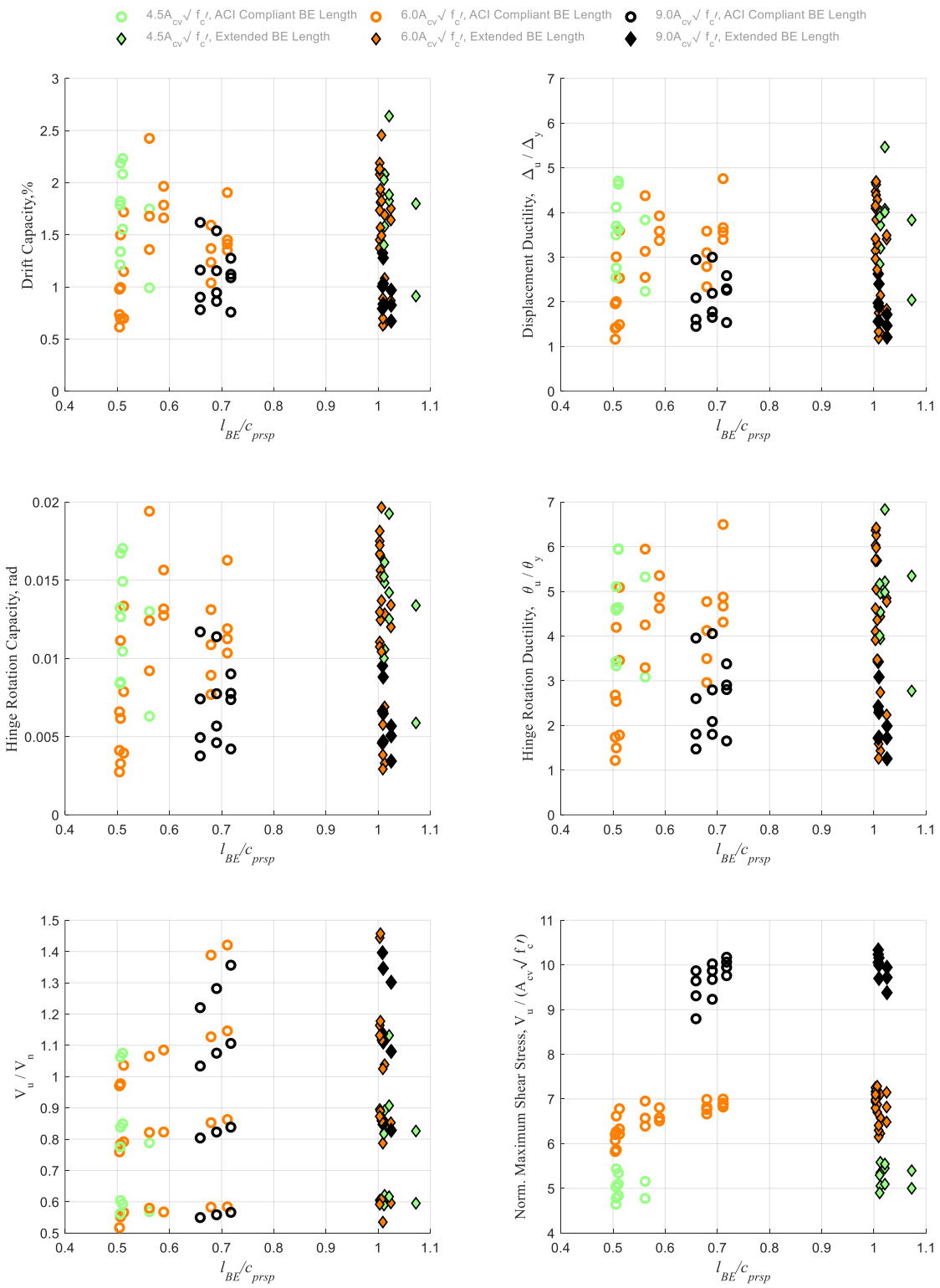

Figure 7.14: Relationship between Boundary Element Length-to-Neutral Axis Depth Ratio and Wall Response:
(Top) Drift and Displacement Ductility;
(Middle) Hinge Rotation Capacity and Rotational Ductility;
(Bottom) Shear Demand-to-Capacity and Maximum Shear Stress Demand

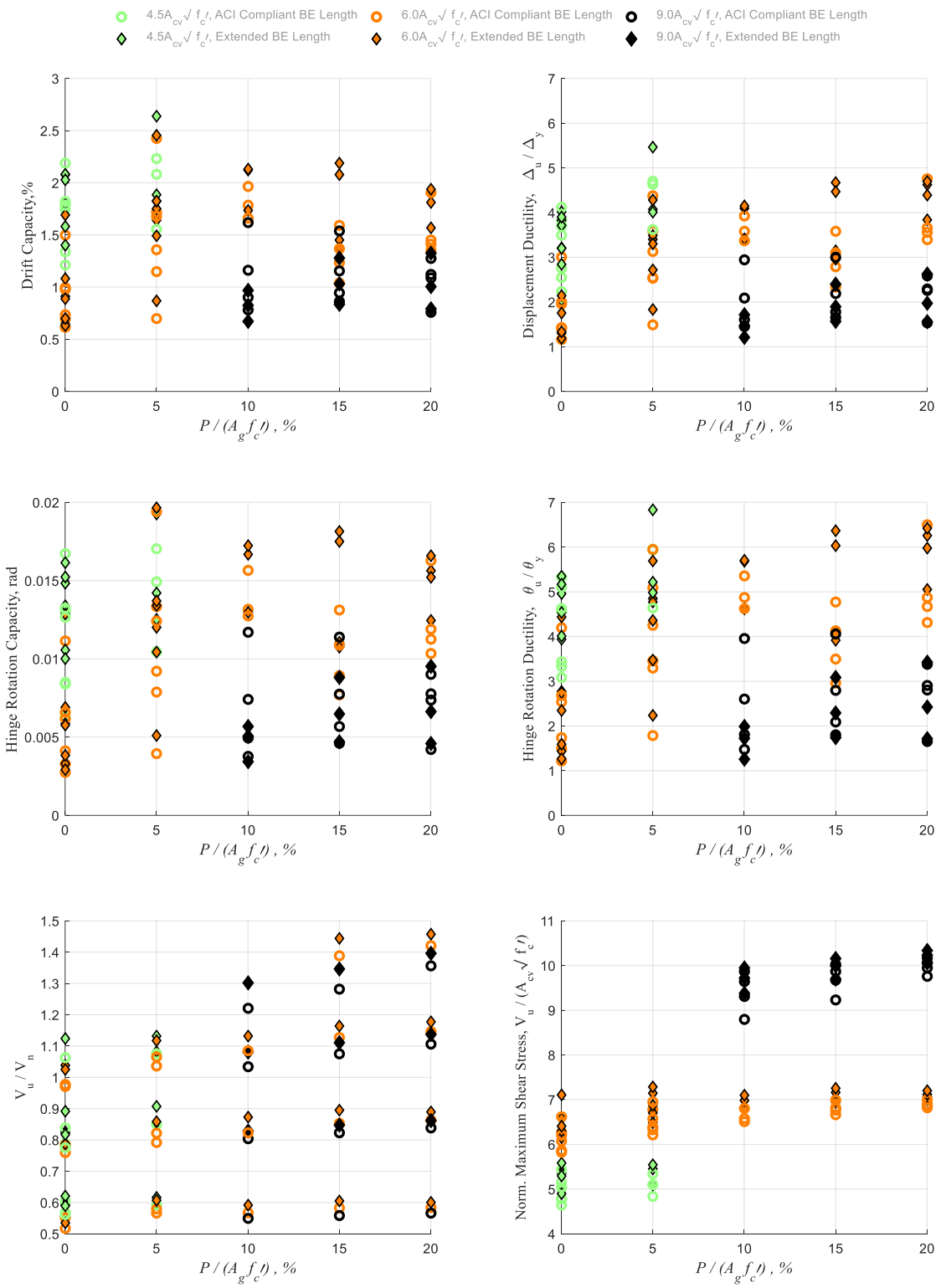

Figure 7.15: Relationship between Axial Load Ratio and Wall Response:
(Top) Drift and Displacement Ductility;
(Middle) Hinge Rotation Capacity and Rotational Ductility;
(Bottom) Shear Demand-to-Capacity and Maximum Shear Stress Demand

7.4.8 Examination of Cumulative Distribution Functions (CDFs) for Individual Wall Parameters

7.4.8.1 Introduction

Performance-based earthquake engineering of walls requires damage-prediction models such as cumulative probability functions (CDFs). The CDFs included this section define the likelihood of wall failure (as defined in Chapter 6), for a given displacement ductility level or drift capacity. As an example, the stepwise CDF for displacement ductility is calculated as:

$$P\left(\left| \Delta_u/\Delta_{M_n} = \ _u/\ _{M_n,j} \right)_{observed} = \frac{\text{number of failures when } \Delta\ /\Delta_{M_n} = \Delta\ /\Delta_{M_n,j}}{\text{number of total wall specimens}} \quad \text{(Eq. 7.1)}$$

The smoothed CDF for displacement ductility are calculated by the lognormal cumulative probability as shown below, and where the sample mean equals $\mu+\frac{\sigma^2}{2}$ and median equals μ:

$$P = F(\ |\ ,\ ) = \frac{1}{\sigma\sqrt{2\pi}} \int_0^x \frac{e^{-\frac{(\ln(t)-\mu)^2}{2\sigma^2}}}{t} dt \quad \text{(Eq. 7.2)}$$

These functions are used to develop the CDF plots found in the remainder of Section 7.4.8.

7.4.8.2 Discussion of Cumulative Distribution Functions

In general, the CDFs presented in Figs. 7.17-7.18 and Appendix C serve to reinforce conclusions from Sections 7.4.1 and 7.4.3-7.4.7 regarding the impact that individual design parameters have on wall deformation/ductility. Of the three most significant parameters in the two will be examined in the remainder of Section 7.4.8.2: (i) normalized shear stress demand and (ii) shear demand-to-capacity ratio. The third is boundary element length, which was examined in detail in Section 7.3.3.

Shear stress demand significantly influences the deformation/ductility of the simulated walls. Fig. 7.16 shows walls with shear stresses $< 8.0A_{cv}\sqrt{f'_c}$ have considerably higher drift capacity and displacement ductility than those $\geq 8.0A_{cv}\sqrt{f'_c}$. This suggests that, when possible, engineers should attempt to limit the shear stress to levels lower than this threshold to avoid brittle failures.

Wall designs with lower shear demand-to-capacity ratios, V_u/V_n, lead to improved deformation/ ductility. Fig. 7.17 shows considerable improvements in walls where $V_u/V_n < 0.75$ (current ACI requirements for shear strength). This response is noteworthy for walls with high shear stress demands, as it is suggests that providing additional horizontal reinforcement can be an approach to improving deformation/ductility in walls that tend to be brittle.

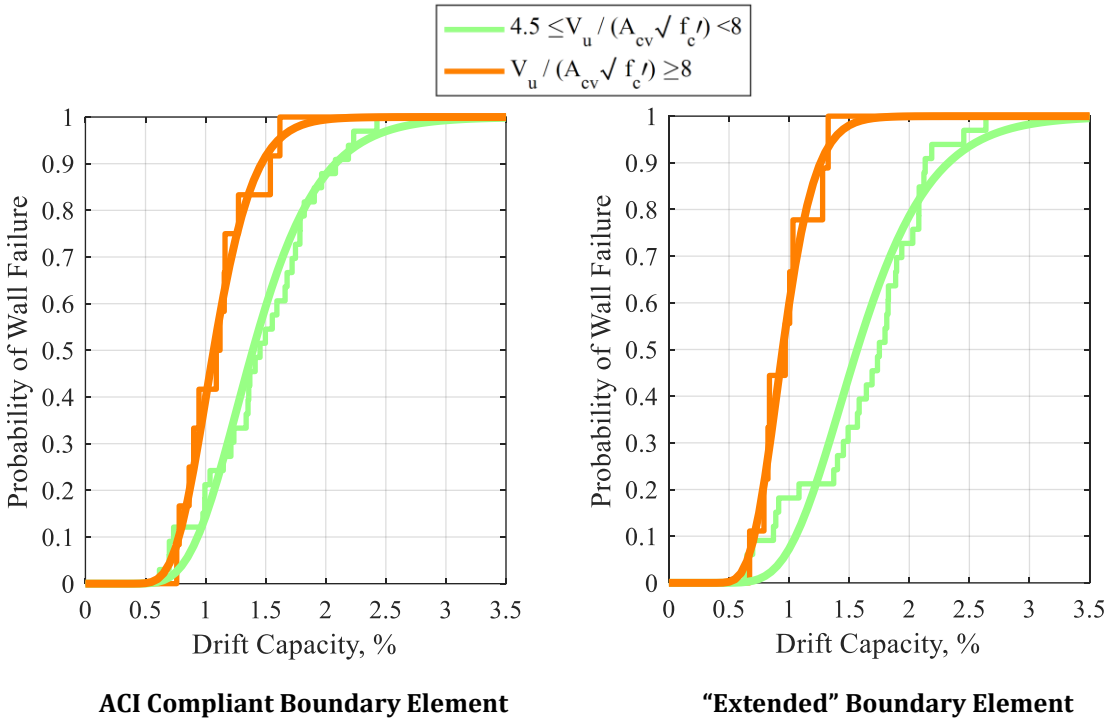

(a) Drift Capacity

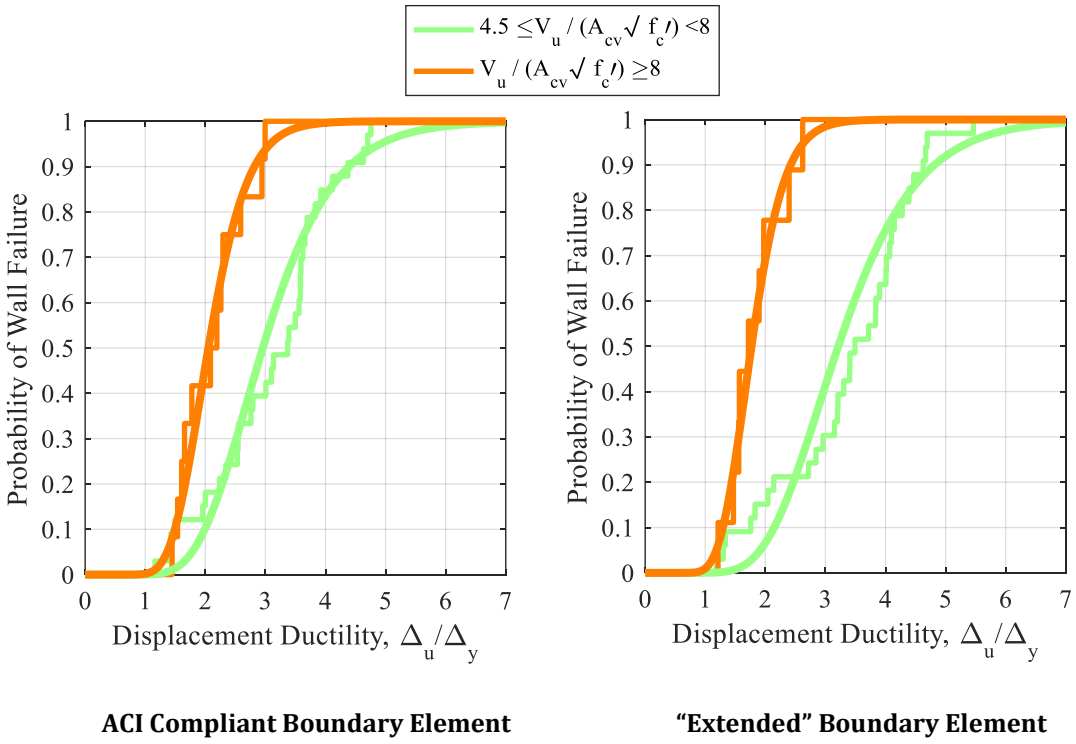

(b) Displacement Ductility

Figure 7.16: Cumulative Distribution Functions for Peak Shear Stress Demand

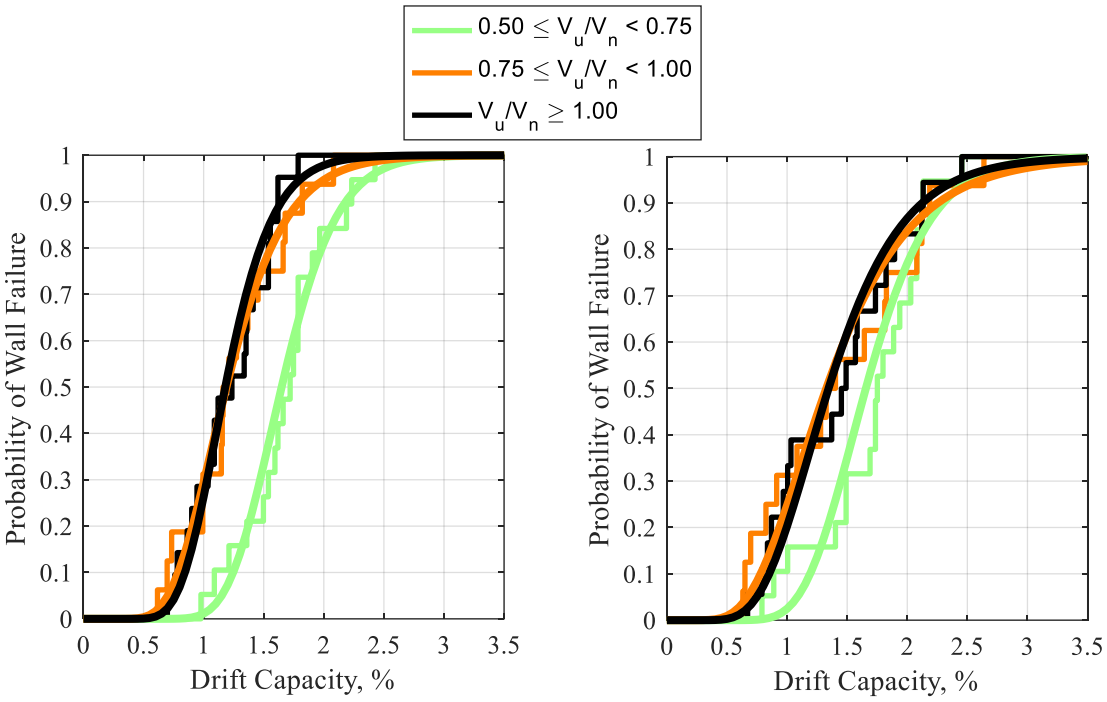

(a) Drift Capacity

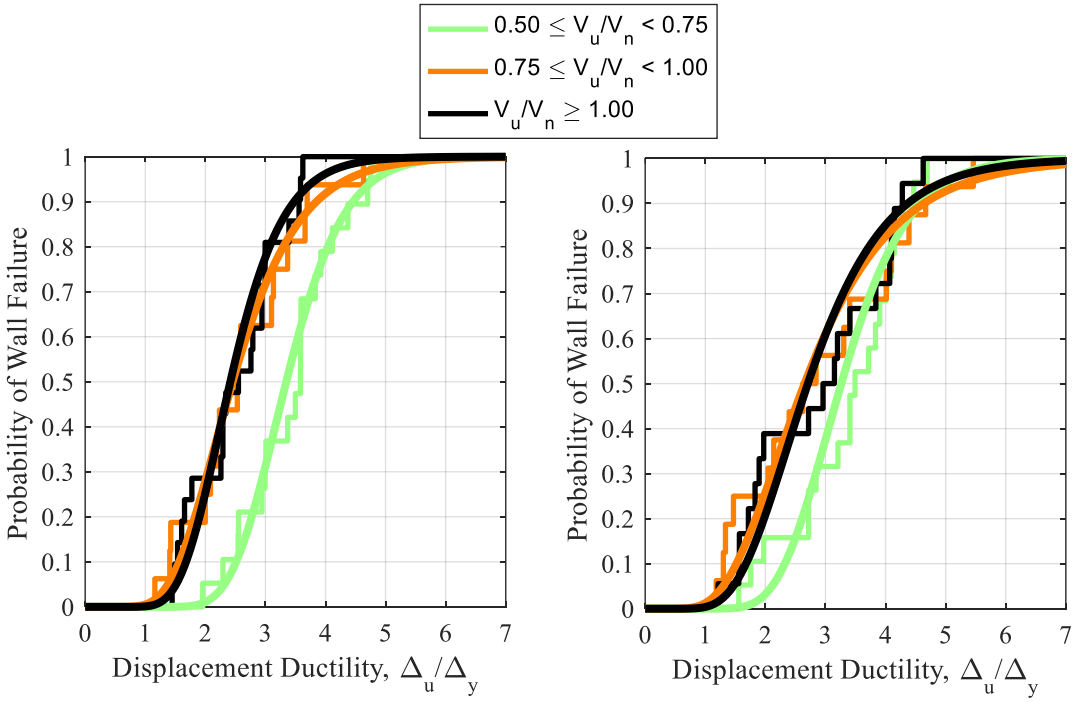

(b) Displacement Ductility

Figure 7.17: Cumulative Distribution Functions for Shear Demand-to-Capacity Ratio

The following statements are reference to the CDFs provided in the Appendix C:

- Examining the full set of walls with ACI compliant boundary elements it is possible to observe that increasing $\rho_{web,h}$, $\rho_{web,h}$ / $\rho_{web,l}$, $\rho_{web,h\ (excess)}$, and $\rho_{web,h\ (prov)}/\rho_{web,h\ (req)}$, as well as decreasing V_u/V_n leads to higher wall ductility.
- Specifically, designs with $\rho_{web,h} \geq 0.50\%$, $\rho_{web,h\ (excess)} \geq 0.25\%$, and $V_u/V_n < 0.75$ show a marked improvement of walls with other design values for these parameters.
- The full set of "extended" boundary element walls show the same trends as the ACI compliant walls.

7.5 Comparison of Parametric Study Results to Experimental Data

Birely [35] assembled a comprehensive slender shear wall dataset consisting of 72 walls of which 43 were rectangular/planar in cross-section. In order to compare these planar walls to the simulated walls conducted in Chapter 7 only walls with shear stress demands in excess of $4.0A_{cv}\sqrt{f'_c}$ were utilized, amounting to 19 walls. 14 of these 19 walls (74%) had no applied axial load. Table 7.7 presents a limited selection of design and response data from *Birely* [35] that is relevant to assessing the results of the parametric wall study.

Table 7.7: Experimental Data for Planar Walls Subjected to Shear Stress Demands $\geq 4.0A_{cv}\sqrt{f'_c}$ (Excerpted from *Birely* [35])

Researcher	Specimen	ALR	$\rho_{tot,h}$, %	Drift Capacity, %	$V_u/A_{cv}\sqrt{f_c'}$	V_u/V_n
Khalil et al	C1	0.07	0.27	2.6	5.9	1.14
Lefas	SW21	0	0.82	1.6	6.2	0.57
	SW22	0.12	0.82	1.2	7.2	0.68
	SW23	0.21	0.82	1	8.3	0.8
	SW24	0	0.82	1.4	5.8	0.54
	SW25	0.21	0.82	0.8	7.1	0.67
	SW26	0	0.41	1.6	7.1	0.99
	SW30	0	0.36	1.6	6.8	1.03
	SW31	0	0.36	1.7	6.2	0.99
	SW32	0	0.36	1.9	4.9	0.89
	SW33	0	0.36	1.9	5.2	0.91
Pilakoutas & Elnashai	SW4	0	0.39	2	5.7	0.92
	SW5	0	0.35	0.8	7	1.4
	SW6	0	0.35	1.8	5.8	1.24
	SW7	0	0.39	1.8	7.5	1.15
	SW8	0	0.42	2.2	4.7	0.94
	SW9	0	0.60	2.2	5.3	0.79
Shiu	C1	0	0.37	2.9	4.3	0.69
Tupper	W3	0.10	0.73	2.9	4.3	0.48

There is a limited experimental data to make an assessment of the simulated wall results. The most compelling relationship confirming modelling results is the negative correlation between shear stress demand and drift capacity. For horizontal reinforcement ratio and shear demand-to-capacity, the correlation is not as clear; $\rho_{web,h}$ may exhibit a weak positive correlation with drift capacity and V_u/V_n would exhibit a strong negative correlation with drift capacity if the Lefas SW21-25 tests were removed (as response may be impacted by high vertical web reinforcement ratios of 2.49%).

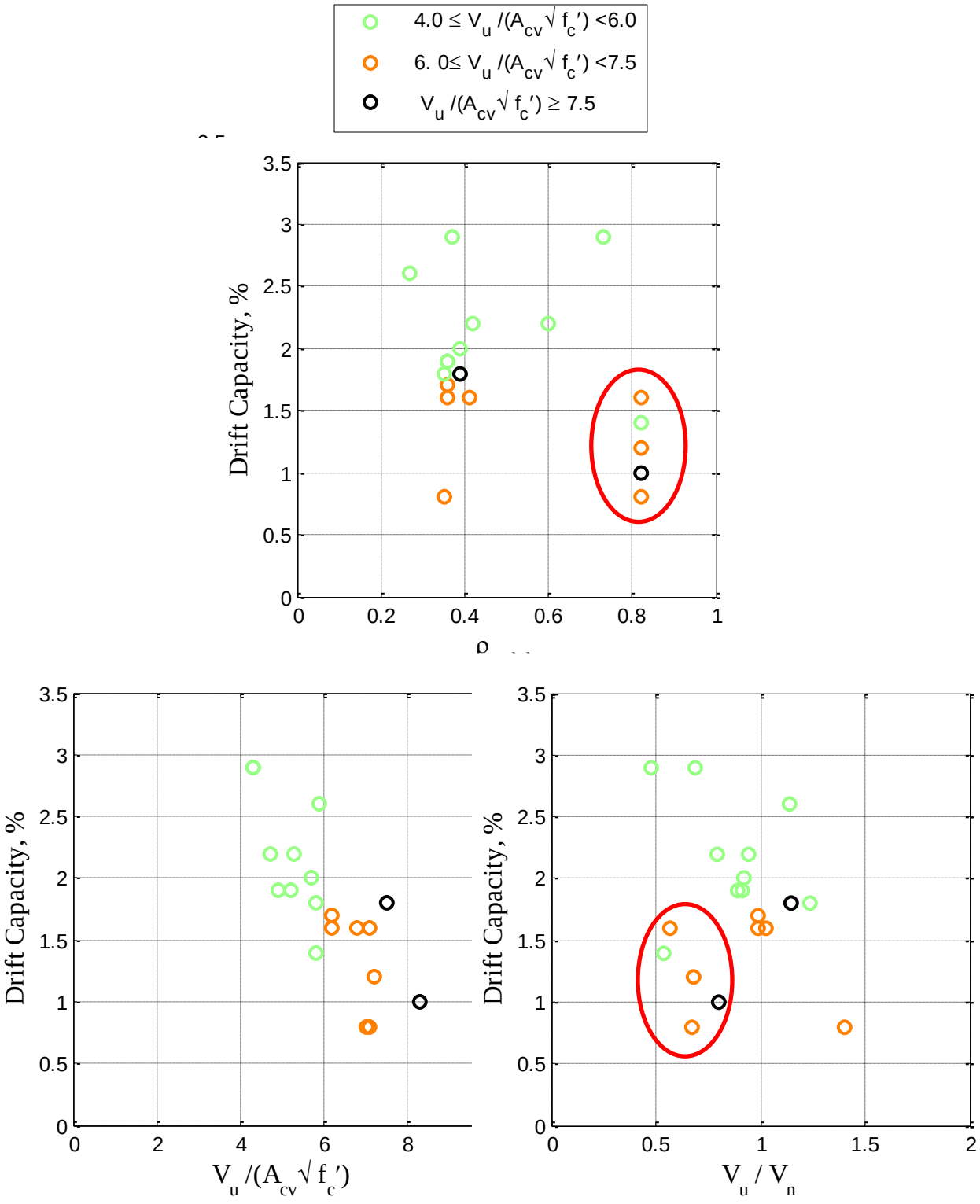

Figure 7.18: Experimental Data for Planar Walls Subjected to Shear Stress Demands ≥ $4.0A_{cv}\sqrt{f'_c}$
(Top): Horizontal Web Reinforcement Ratio,
(Bottom Left) Shear Stress Demand, (Bottom Right) Shear Demand-to-Capacity Ratio

Note: Red circle encloses Lefas SW21-SW25 that may exhibit response outside of the trend.

7.6 Summary of Wall Web Reinforcement Study

7.6.1 Discussion of Parametric Study Results

A parametric study was conducted to investigate the impact of vertical and/or horizontal reinforcement ratios on deformation/ductility response of slender, planar walls subjected to varying levels of shear stress demand: 4.5, 6.0, and $9.0A_{cv}\sqrt{f'_c}$. These walls were originally designed with boundary element lengths that were minimally compliant with *ACI 318-14* [18], these walls were then re-designed with an "extended" boundary element length approximately equal to the neutral axis depth. The investigation of the ACI compliant and "extended" boundary element lengths was carried out to see what additional deformation/ductility benefit this design change would have on walls, particularly those with high shear stress demands that tend to exhibit lower ductility and more commonly exhibit brittle failures.

The following conclusions correspond to slender, planar walls with a cross-sectional aspect ratio (CSAR) of approximately 20 that were modelled in the parametric study:

Parameters with Significant Impact

- ***Normalized Shear Stress Demand:*** There is a strong negative correlation between shear stress demand and deformation/ ductility, consistent with the experimental wall test data from *Birely* [35]. Walls modelled in the study that have a low-moderate shear stress demand ($< 8.0A_{cv}\sqrt{f'_c}$) appear to have very similar ductility. This observed ductility is significantly higher than walls subject to high shear stress demands ($> 8.0A_{cv}\sqrt{f'_c}$).
- ***Shear Demand-to-Capacity Ratio:*** As shear demand-to-capacity ratio, is reduced, wall deformation/ductility improves. This is a particularly important observation for walls with high shear stress demands ($9.0A_{cv}\sqrt{f'_c}$) where a more conservative shear design can be carried out to achieve improved deformation/ductility for walls that tend to be brittle.
- ***Boundary Element Length:*** Increasing the boundary element length from the ACI minimum to the full neutral axis depth is most effective for walls with low-moderate shear stress demands. Beyond a certain threshold, $8.0A_{cv}\sqrt{f'_c}$, there does not seem to be much benefit in extending the boundary element of walls. The results of this study supports a measure being balloted in ACI318 by *Lehman & Lowes* [110] whereby the boundary element length, l_{be}, is calculated as at least the maximum of $c - 0.1l_w$ and $c/2 \ \leq \ \frac{V}{8.0A_{cv}\sqrt{f'_c}} * c \leq c$.

Variables Associated with Parameters of Significant Impact

- ***Horizontal Web Reinforcement Ratio***: There is a positive correlation between horizontal web reinforcement and deformation/ ductility. The most significant performance gains from increasing $\rho_{web,h}$ appear to be in walls with lower shear stress demands, though modifying this design parameter in walls with high shear stress demands can result in displacement ductility values of 2.0 or greater.
    - The fragility curves indicate that for both ACI compliant and "Extended" boundary element walls of all shear demand levels $\rho_{web,h} \geq 0.50\%$ results in a clear improvement over other designs.
- ***"Excess" Horizontal Web Reinforcement Ratio***: There is a positive correlation between "excess" reinforcement ratio and deformation/ ductility ("excess" refers to additional reinforcement beyond what is required by *ACI 318-14* [18] to meet the shear demand).
    - For both ACI compliant and "Extended" boundary element walls designs $\rho_{web,h\ (excess)} \geq 0.25\%$ and $\rho_{web,h\ (prov)}/\rho_{web,h\ (req)} \gtrsim 1.25 - 1.50$ are generally able to achieve a displacement ductility of greater than 2.0.
- ***Horizontal-to-Vertical Web Reinforcement Ratio***: There is a positive correlation between horizontal-to-vertical web reinforcement ratio and deformation/ductility for walls with low-moderate shear stress demands (excluding ALR > 0% and $\rho_{web,l} \geq 0.35\%$) and for walls with high shear stress demands.
    - For both ACI compliant and "Extended" boundary element walls designs of all shear demand levels $\rho_{web,h}\ /\ \rho_{web,l} \gtrsim 0.75\%$ are generally able to achieve a displacement ductility of greater than 2.0 (excluding the aforementioned group of walls).

Parameters with Modest to No Impact

- ***Axial Load Ratio:*** There appears to be a positive correlation between axial load ratio and deformation/ductility for walls with moderate shear stress demands (low and high shear stress demands did not have sufficient distribution of ALR to ascertain a correlation). This conclusion is based only on ALR values less than or equal to 20%.
- ***Vertical Web Reinforcement Ratio:*** This parameter does not appear to impact wall deformation/ductility.

7.6.2 Discussion of Comparison of Parametric Study Results to Experimental Test Data

An effort was made to compare modelling results to experimentally tested slender, planar walls with shear stress demand ratios greater than $4.0A_{cv}\sqrt{f'_c}$. There are very few tests that met the desired criteria; however, the experimental results reaffirmed shear stress demand as the most influential parameter. The experimental data exhibits a strong negative correlation between shear stress demand and drift capacity. Correlations with other parameters are not as clear due to the data points associated with walls with very heavy vertical web reinforcement which is not representative of modern design. Without these data points the experimental data (reduced to 14 walls) seems to indicate a weak positive relationship where increased horizontal web reinforcement resulted in higher drift capacity, and a strong negative relationship where decreasing shear demand-to-capacity ratio also results in higher drift capacity.

7.6.3 Conclusion Related to Wall Web Reinforcement Design

The primary design recommendations resulting from this study to achieve adequate wall ductility for walls with varying shear demand are:

1. Design for a normalized shear stress demand ($V_u/A_{cv}\sqrt{f'_c}$) less than 8.0, when possible.
2. Select a shear demand-to-capacity ratio (V_u/V_n) between 0.50-0.75, particularly for walls where ductility is a concern and/or walls with high shear stress demands.
3. Extend boundary element length (l_{be}) accounting for normalized shear stress demand by taking l_{be} as at least the maximum of $c - 0.1l_w$ and $c/2 \leq \frac{V}{8.0A_{cv}\sqrt{f'_c}} * c \leq c$.

8 SUMMARY, CONCLUSIONS, AND FUTURE WORK

8.1 Summary of Research Study

8.1.1 Research Impetus

Damage to reinforced concrete shear walls in recent earthquakes exceeded expectations. Walls were observed to have severe crushing over part or all of their length, lateral instabilities, and, in some cases, walled buildings have collapsed. Many reinforced concrete buildings in seismic regions employ reinforced concrete shear walls as part of the lateral force resisting system and these walls often have non-planar cross-sectional geometries. To date, the majority of experimental tests on slender concrete walls have been conducted on planar walls which have been subject to low normalized shear stress demands. Recent research has indicated that (i) shear can reduce the ductility of slender walls, and (ii) non-planar (flanged) wall response is distinct from that of planar walls. A research study was undertaken to study these phenomena in seismic-resisting walls and develop new design recommendations to mitigate damage at low drifts and improve their deformability.

8.1.2 Research Approach and Objectives

The research was conducted in two primary phases. First, an experimental program was developed to study the response of C-shaped walls, with a specific focus on the impact of bi-directional loading. The experimental results were combined with prior tests on flanged (non-planar) walls to better understand the performance of this category of walls. The second phase of the program investigated the impact of the normalized shear stress demand and web reinforcement on wall performance, in particular deformation and ductility.

It is postulated that reduced normalized shear stress demand and increased horizontal reinforcement ratios (beyond that required to meet the required shear capacity) can increase the ductility of walls; however, none of the previous experimental programs have explicitly studied these parameters. Therefore, a high-resolution non-linear finite element modeling procedure was utilized, which has been validated previously as part of a companion research study. The validation used walls tests with a range of geometries, normalized shear stress demands, and reinforcement ratios. That study found that the cross-sectional aspect ratio (CSAR), or l_w/t_w, impacted the performance of the walls, and most tests have been conducted on lower ratios. As such, this

parametric study was founded on one of the test walls with a CSAR of ~20 which better simulated geometries of walls in modern building construction (a CSAR of 20 equates to a bay with 25 ft column spacing and a 15 in thick wall), with a parameterization of the normalized shear stress demand and web reinforcement ratios. These results were used to develop recommendations for design related to the web reinforcement ratios. This is a significant advancement since the web reinforcement ratios have remained unchanged throughout the history of the *ACI 318*. In addition, the study considered the impact of the confined length as a function of the normalized shear stress demand; the results indicated that larger normalized shear stress demands result in higher values of the minimum principal strains across the compressive region of the wall, thus requiring a longer confined length. These results have been expressed as an equation for adoption by *ACI 318*.

8.2 Conclusions of Research Study

8.2.1 Experimental Test Program on C-Shaped Walls

8.2.1.1 Overview of C-Shaped Wall Test Results

The experimental test program (Phase 3 of the NSF-funded UW-UIUC "Complex Walls Project") consisted of three nominally identical C-shaped walls that were subjected to different patterns of loading: (i) uni-directional, (ii) bi-directional (cruciform pattern), and (iii) bi-directional (cruciform pattern) with variation in axial load and to simulate wall coupling. The primary objective was to investigate the difference in deformation at key damage states, drift capacity/ductility, and strength associated with uni-directional versus bi-directional loading.

Damage Progression/Failure: Each of the walls failed due to buckling-rupture (flexural-tension mechanism). The damage progression was similar for each wall and was as follows: (1) formation of crack plane at or near the wall-foundation interface, (2) spalling of concrete in the web of the wall, (3) buckling followed by fracture of vertical reinforcement in the unconfined web of the wall, (4) spalling of the unconfined region between flange boundary elements (BEs), (5) buckling of the longitudinal bars in the BE, (6) opening and plastic deformation of the confining reinforcement, and (7) BE longitudinal bar fracture. Comparison of deformations corresponding to each of these damage states indicates that, other than horizontal and diagonal cracking, the damage states occurred at lower strong-axis drift levels for the bi-directionally loaded walls than the wall subjected to uni-directional loading.

Drift Capacity/Ductility: The strong-axis drift capacity and displacement ductility is higher for uni-directionally loaded wall. The uni-directionally loaded wall had a strong-axis drift capacity of slightly beyond -1.75% and +2.25% and had an average displacement ductility of 5.5. Both bi-directionally loaded walls had strong-axis drift capacities that were nearly 1.5% for both positive and negative loading directions. The wall with only bi-directional loading had an average strong-axis displacement ductility of 3.5, while the wall with bi-directional loading and coupling had a strong-axis ductility of 4.9. In this discussion, the drift capacity is associated with a loss of 20% strength in the strong-axis loading direction.

Strength: Both uni- and bi-directionally loaded walls have nearly identical flexural strength and stiffness up to 0.75% strong-axis drift, which nearly coincides with the peak flexural strength of the walls between 0.91-0.95M_n (or, shear strength 0.40-0.43V_n). While these walls do not exhibit substantial strength gain past yield, yet they are able to sustain additional deformation beyond nominal curvature. There are critical implications of the fact that these walls do not meet the nominal flexural strength as design engineers often make the assumptions that shear walls have flexural overstrength.

8.2.1.2 Comparison to Planar Wall Results

This section compares the C-Shaped walls to the planar walls that made up Phase 1 of the "Complex Walls Project" which tested 4 planar walls. These planar wall tests studied the impact of normalized shear stress demand and longitudinal bar configuration (distribution and splices) on their seismic response; details on these experiments can be found in *Birely* [35] and *Hart* [87].

Damage Progression/Failure: Only one of the planar wall subjected to a lower shear demand (approximately 2.5$A_{cv}\sqrt{f'_c}$ psi) exhibited bar fracture of previously buckled vertical BE bars. The other planar walls in the test program exhibited extensive core damage and significant bar buckling; such that damage was largely dominated by a flexural-compression response. The pattern of the concrete damage was dependent on the longitudinal bar distribution and the presence of bar splices. The C-shaped walls in the current test program exhibit a more ductile failure mode despite higher shear demands; this may be a product of the compression strength redundancy of the flanges.

Drift Capacity/Ductility: The four planar walls in the test program achieved drift capacities between 1.0-1.5%. The uni-directional C-shaped wall appears to have significantly capacity than the planar walls in the "Complex Walls Project".

Strength: All the planar walls in the "Complex Walls Project" were able to reach their nominal moment capacity and had a peak flexural strength ranging from 1.02-1.16M_n. The shear force was equal to 0.75V_n to 1.07V_n (note that this was the intent of the horizontal web reinforcement design and was not a study parameter of that test program). In contrast to the current wall study, these planar walls were all able to reach or exceed the nominal flexural strength.

8.2.2 Examination of Prior Flanged Wall Experiments

To further examine the behavior of slender non-planar walls, tests from fourteen additional experimental programs were evaluated. The objective was to assess the impact that various design parameters have on wall response based on wall shape, symmetric versus asymmetric loading, and uni- versus bi-directional loading. The particular response metrics that were investigated include: drift capacity, and displacement ductility. Maximum normalized shear stress and shear demand-to-capacity were also evaluated.

General observations about non-planar wall behavior based on the experimental database:

- **Loading of Asymmetric versus Symmetric Wall Cross Sections:** In an average sense, loading of walls in a symmetric direction results in a higher displacement ductility compared to loading of walls in an asymmetric direction.
- **Uni- versus Bi-directional Loading:** Walls, irrespective of uni- or bi-directional loading conditions, exhibit very similar drift capacity and displacement ductility.

However, these conclusions do not apply to each individual wall shape in the experimental database, as specific wall types tend to exhibit its own deformation/ ductility trend with respect to loading in a symmetric versus asymmetric direction and uni- versus bi-directional loading. When considering loading direction in design refer to specific data in Chapter 3 for each wall shape.

Observations related to specific design parameters:

- **Normalized shear stress Demand & Shear Demand-to-Capacity Ratio:** Considering the walls with buckling-rupture and shear-compression failures, increasing the magnitude of V_u/V_n and $V_u/A_{cv}\sqrt{f'_c}$ leads to decreased wall ductility. Walls that fail via crushing-buckling tend to have low wall ductility values irrespective of the magnitude of V_u/V_n and $V_u/A_{cv}\sqrt{f'_c}$. A limited group of walls exhibit a positive correlation between V_u/V_n and $V_u/A_{cv}\sqrt{f'_c}$ with respect to deformation/ductility; these are C-/U and I-shaped cross-sections loaded in a symmetric direction that fail via buckling-rupture. This may have to do

with the ability for shear demand to effectively transfer from the damaged web to flange and boundary elements which enables the wall to maintain its lateral strength at higher drift demands.

- **Wall Geometry:** Increasing the web cross-sectional aspect ratio (l_w/t_w) results in lower drift capacity and displacement ductility for C-/U-shaped walls (irrespective of loading direction) or walls with buckling-rupture failures. The flange cross-sectional aspect ratio (l_f/t_f) did not exhibit any clear trends with respect to wall deformability across the wall shape, failure modes, and loading.
- **Boundary Element Geometry:** For C-,U-,I-Shaped walls loaded parallel to the web, increasing the length of the corner boundary element into the web, $l_{w,BE-w}$, led to improved drift capacity and ductility. Increasing the slenderness of the flange-end boundary element ($l_{f,BE}/t_f$) at the stem tip for the T-shaped walls leads to lower drift capacity and is often associated with instability failures in this wall type.
- **Reinforcement Ratios:** For the overall non-planar wall dataset, increasing the ratio of confinement in the boundary element ($\rho_{BE,conf}$) leads to improvements in drift capacity. Increasing the vertical reinforcement ratio in the boundary element or the total vertical/ horizontal reinforcement ($\rho_{BE,l}, \rho_{tot,l}, \rho_{tot,h}$), results in reduced drift capacity and displacement ductility. This is largely due to the fact that increasing $\rho_{BE,l}, \rho_{tot,l}$ can drive up shear demand.
- **Shear Span Ratios:** Increasing the web shear span ratio (h_{eff}/l_w) results in reduced drift capacity for walls with buckling-rupture and shear-compression failures, as well as uni-directionally loaded walls. This negative correlation also applies to displacement ductility for buckling-rupture failures, symmetric cross sections and bi-directionally loaded walls. Increasing the flange shear span ratio (h_{eff}/l_f) appears to have a negative impact on drift capacity for the overall wall data set and bi-directionally loaded walls. However, these assessments are made on a rather narrow range of shear span values.
- **Axial Load Ratio:** There appears to be no correlation between magnitude of constant axial load ratio and wall deformability/ductility based on the non-planar wall data set.

8.2.3 Computational Parametric Wall Study

8.2.3.1 Overview of Parametric Wall Study Results

Damage to the unconfined web of the flanged C-shaped walls tested as part of this research was substantial. There are also various cases from previous non-planar wall experiments and in-field performance that show similar web damage where there is moderate-to-widespread fracture of vertical/horizontal web bars as well as severe concrete degradation near the wall critical section. In addition, study of the prior tests indicates that the V_u/V_n ratio impacts the ductility of the wall where walls with lower V_u/V_n values result in higher ductility values. These performance metrics suggests that increasing minimum web steel content required by *ACI318* may positively impact performance and deserves study.

A parametric study was conducted to investigate the impact of these parameters on the deformation capacity of seismically detailed walls, specifically vertical and horizontal web reinforcement as well as normalized shear stress demand. The investigation was conducted using an experimentally-validated, high-resolution finite modelling approach. In addition to examining the influence of web reinforcement, the study also investigates the effects of extending the boundary element length from the ACI 318 minimum to the full neutral axis depth. The parametric study was founded on an experimentally-tested planar wall to: (i) isolate the impact of web reinforcement and avoid the influence of shear lag that occurs in flanged walls, and (ii) calibrate the baseline model using a wall that was subject to high normalized shear stress demands. The following discussion summarizes the major findings with respect to shear response, vertical and horizontal web reinforcement, boundary element length, and axial load ratio.

Shear Response

- Increasing normalized shear stress demand ($V_u/A_{cv}\sqrt{f'_c}$ psi) leads to reduced deformation capacity. Walls with low-moderate normalized shear stress demand (less than $8.0A_{cv}\sqrt{f'_c}$ psi) appear to have very similar ductility, which is significantly higher than walls subject to normalized shear stress demands in excess of $8.0A_{cv}\sqrt{f'_c}$ (psi).
- Walls designed with lower shear demand-to-capacity ratios (V_u/V_n) exhibit an increase in deformation capacity. Employing V_u/V_n=0.5-0.75 (such that additional horizontal reinforcement is provided beyond what is required by *ACI318* for shear strength) increases the displacement ductility of walls to values in excess of 2.0, even for relatively brittle walls subject to high shear stress demands.

Vertical & Horizontal Web Reinforcement

- Vertical web reinforcement can increase the normalized shear stress demand. Prior work by *Whitman* [173] demonstrated that the strain distribution of walls with higher CSAR values and/or moderate to high normalized shear stress demands is highly nonlinear, and approximately uniform in the tensile region. As such, the web reinforcement is more highly stressed than a cross-sectional analysis assuming linear-strain distribution would predict. This can result in a higher normalized shear stress demand, which can decrease the deformability of the wall.
- An increase in horizontal web reinforcement ($\rho_{web,h}$) leads to improved deformation capacity where the most significant increases were in walls with normalized shear stress demands between 4.5 and $8A_{cv}\sqrt{f'_c}$ (psi). However, walls with higher normalized shear stress demands did exhibit improved deformation capacities for lower values of V_u/V_n.
- Increasing horizontal-to-vertical web reinforcement ratio leads to higher deformation capacity/ductility for walls with low-moderate normalized shear stress demands (excluding ALR $> 0\%$ and $\rho_{web,l} \geq 0.35\%$) and for walls with high normalized shear stress demands.

Boundary Element Length

- Extending the boundary element from the ACI minimum length to the full neutral axis depth increases the drift capacity of walls subjected to normalized shear stress demands less than $8.0A_{cv}\sqrt{f'_c}$ (psi).

Axial Load Ratio

- An increase in axial load ratio (ALR) leads to improved deformation capacity for walls with moderate normalized shear stress demands (walls with low and high normalized shear stress demands in the parametric study did not have sufficient distribution of ALR to ascertain a correlation). Note that the examined ALR values range from 0-20%; higher values may have a negative impact on wall deformation capacity.

8.2.3.2 Comparison to Planar Wall Experimental Database

Birely [35] conducted four planar wall tests and also assembled a comprehensive slender shear wall dataset including 43 additional slender planar walls. Of these walls, those with stress demands in excess of $4.0A_{cv}\sqrt{f'_c}$ (psi) were examined to assess the results of the parametric wall study (19

walls in the data set). It is important to note that none of the walls were subjected to normalized shear stress demands greater than $8.3A_{cv}\sqrt{f'_c}$ (psi), and the walls tended to have low CSAR values, generally between 6.58 and 10 with only one wall with a higher CSAR at 18.75. Both of these parameters (normalized shear stress demand and CSAR) were shown to significantly impact the deformation capacity of the walls.

The experimental data set also showed an inverse relationship between normalized shear stress and deformation capacity (shear stress demand negatively impacts wall response), confirming the conclusions of the parametric study. Other items that were investigated include horizontal web reinforcement and shear demand-to-capacity ratios. Excluding a set of walls from a test program that high vertical web reinforcement ($\rho_{web,l}$=2.49%), the experimental data showed that decreasing the shear demand-to-capacity (aV_u/V_n) ratio results in higher deformation capacity.

8.2.3.3 Design Recommendations Based on Study Results

Specific recommendations related to wall design based on the results of this study include:

1. Design for a normalized shear stress demand ($V_u/A_{cv}\sqrt{f'_c}$) less than 8.0 (when possible, and particularly for walls expected to sustain large drifts).
2. Select a shear demand-to-capacity ratio (V_u/V_n) between 0.50-0.75, particularly for walls where ductility is a concern and/or walls with high shear stress demands.
3. Extend boundary element length (l_{be}) accounting for normalized shear stress demand by taking l_{be} as at least the maximum of $c - 0.1l_w$ and $c/2 \leq \frac{V}{8.0A_{cv}\sqrt{f'_c}} * c \leq c$.

8.3 Future Work

The future research needs are assessed for experimental testing, computational modelling, and collecting/curating earthquake reconnaissance data of walls in high seismic regions.

8.3.1 Experimental Testing

- Most tests have focused on lower normalized shear stress demands and lower CSAR values. The parametric study indicates that these parameters influence performance. In addition, there appears to be a benefit of higher axial stresses for larger normalized shear stress demands. A systematic testing program studying these parameters is needed.
- The majority of tests have focused on planar walls. Additional testing focusing on flanged walls, in particular studying higher high normalized shear stress demands and asymmetric

cross section (e.g., an asymmetric I where the two flanges have different lengths and different axial capacities).

- Most studies have used flanges that are equal to or less than the ACI effective flange width. Evaluation of effective flange width for strength and stiffness would be beneficial.
- A standard set of bi-directional loading protocols that effectively assess the performance of various wall cross-sections is needed. It is difficult to make a true comparison of wall response between different tests when the specimens have been subjected to different load histories, even if they may have similar strong-axis drift capacities. In addition, a set of reference walls subjected to uni-directional loading is required.
- With the advent of new, non-contact instrumentation, there is an increasing volume of data. A new post-processing/visualization tool that enables structural wall researchers to import large-volume, high-resolution data would be greatly beneficial. This tool should have a robust 3-D graphical user interface where users can examine their undeformed specimen and subsequently view cracking/damage progression via overlaid test photographs. Furthermore, this program should have a data structure that enables associations between the sensor data with the sensor's metadata including sensor type, calibration value, location; as well as data time step with images or crack maps. Users should be able to plot or conduct calculations on multiple streams of raw sensor data. A prototype tool, ExVis, may serve as the foundation for this next-generation tool [108, 129].

8.3.2 Computational Modelling

8.3.2.1 Non-linear Modelling of Walls with ATENA 3D

In terms of the use of ATENA 3D, additional efforts are needed to accurately determine the occurrence of failure and the associated failure mode for structural wall models.

- Damage Limit State Indicator to facilitate assessment of damage limit states including cover spalling, core concrete crushing and steel reinforcement yield/fracture/buckling.
- Model to simulate bar buckling. ATENA 3D does not have an adequate method to simulate bar buckling. The company suggests deactivating the steel reinforcement response in compression to account for buckling. In experimental tests, ductile boundary element reinforcement can sustain rather large, repeated cycles of compressive/tensile demands before buckling. Therefore, this approach will not simulate ductile walls.

- There are convergence issues when walls with low amounts and/or wide spacing of web reinforcement are subject to cyclic loading and the wall web has experienced significant inclined cracking. Additional work is necessary to resolve the stated issue.

8.3.2.2 Computational Parametric Wall Studies

This research built upon a prior study by Whitman [173]. Both studies focused on planar walls. Recommended parameters for additional study include:

- Symmetric flanged walls
- T-Shaped walls
- Coupled walls
- Walls with openings

8.3.3 Closing Remarks

There has been considerable progress in the last code cycle (ACI 318-14) to updating special structural wall provisions specifically with respect to boundary element provisions based on observations in the recent Chile and New Zealand earthquakes. This momentum should continue with work related to other wall provisions that either have not changed in many years, as with the web reinforcement ratio, or sections where the code has been essentially silent, such as non-planar walls. The author believes that it is the continued pursuit of the three branches of research: experimental testing, computational modelling, and in-field reconnaissance will help the earthquake engineering field have a more complete understanding of the seismic performance of structural walls, and consequently, a safer reinforced concrete building inventory.

9 REFERENCES

[1] ACI, ACI Standard Specifications No. 23: Standard Building Regulations for the Use of Reinforced Concrete. 1920: American Concrete Institute.

[2] ACI, Building Code Requirements for Reinforced Concrete (ACI 318-56). 1956: American Concrete Institute.

[3] ACI, Building Code Requirements for Reinforced Concrete (ACI 318-63). 1963: American Concrete Institute.

[4] ACI, Building Code Requirements for Reinforced Concrete (ACI 318-71). 1971: American Concrete Institute.

[5] ACI, Building Code Requirements for Reinforced Concrete (ACI 318-77). 1977: American Concrete Institute.

[6] ACI, Commentary on Building Code Requirements for Reinforced Concrete (ACI 318R-77). 1977: American Concrete Institute.

[7] ACI, Building Code Requirements for Reinforced Concrete (ACI 318-83). 1983: American Concrete Institute.

[8] ACI, Commentary on Building Code Requirements for Reinforced Concrete (ACI 318R-83). 1983: American Concrete Institute.

[9] ACI, Building Code Requirements for Reinforced Concrete (ACI 318-89) and Commentary (ACI 318R-89). 1989: American Concrete Institute.

[10] ACI, Building Code Requirements for Reinforced Concrete (ACI 318-89) and Commentary (ACI 318R-89) (Revised 1992). 1992: American Concrete Institute.

[11] ACI, Building Code Requirements for Structural Concrete (ACI 318-95) and Commentary (ACI 318R-95). 1995: American Concrete Institute.

[12] ACI, Building Code Requirements for Structural Concrete (ACI 318-99) and Commentary (ACI 318R-99). 1999: American Concrete Institute.

[13] ACI, Building Code Requirements for Structural Concrete (ACI 318-02) and Commentary (ACI 318R-02). 2002: American Concrete Institute.

[14] ACI, Building Code Requirements for Structural Concrete (ACI 318-05) and Commentary (ACI 318R-05). 2005: American Concrete Institute.

[15] ACI, Building Code Requirements for Structural Concrete (ACI 318-08) and Commentary. 2008: American Concrete Institute.

[16] ACI, Building Code Requirements for Structural Concrete (ACI 318-11) and Commentary. 2011: American Concrete Institute.

[17] ACI American Concrete Institute Releases the Reorganized ACI 318-14. 2014.

[18] ACI, Building Code Requirements for Structural Concrete (ACI 318-14) and Commentary (ACI 318R-14). 2014: American Concrete Institute.

[19] AIJ, Preliminary Reconnaissance Report of the 2011 Tohoku-Chicho Taiheiyo-Oki Earthquake. 2012, Architectural Institute of Japan.

[20] ASCE, FEMA 356: Prestandard and Commentary for the Seismic Rehabilitation of Buildings. 2000, American Society of Civil Engineers.

[21] ASCE, Minimum Design Loads for Buildings and Other Structures (ASCE/SEI 7-05). 2005: American Society of Civil Engineers.

[22] ASCE, Seismic Rehabilitation of Existing Buildings (ASCE/SEI 41-06). 2006: American Society of Civil Engineers.

[23] ASCE, Minimum Design Loads for Buildings and Other Structures (ASCE/SEI 7-10). 2010: American Society of Civil Engineers.

[24] ASTM, ASTM A706/A706M-09 Standard Specification for Deformed and Plain Low-Alloy Steel Bars for Concrete Reinforcement. 2009, ASTM International.

[25] ASTM, ASTM C78/C78M-10: Standard Test Method for Flexural Strength of Concrete (Using Simple Beam with Third-Point Loading). 2010, ASTM International.

[26] ASTM, ASTM C39/C39M-12a: Standard Test Method for Compressive Strength of Cylindrical Concrete Specimens. 2012, ASTM International.

[27] ATC, ATC-40: Seismic Evaluation and Retrofit of Concrete Buildings Volume 1. 1996, Applied Technology Council.

[28] ATC, FEMA 273: NEHRP Guidelines for the Seismic Rehabilitation of Buildings. 1997, Applied Technology Council.

[29] ATC, FEMA 445/ATC-58: Next-Generation Performance-Based Seismic Design Guidelines. 2006, Applied Technology Council.

[30] ATC, FEMA 445: Next-Generation Performance-Based Seismic Design Guidelines: Program Plan for New and Existing Buildings. 2006, Applied Technology Council.

[31] Bal, I.E., et al., On the Seismic Response of School Buildings in Van: A Closer Look to the Collapsed Gedikbulak School. 2013.

[32] Behrouzi, A., et al., Summary of Large-Scale C-shaped Reinforced Concrete Wall Tests. 2015, Charles Pankow Foundation.

[33] Behrouzi, A., et al., Summary of Large-Scale Nonplanar Reinforced Concrete Wall Tests. 2015, Charles Pankow Foundation.

[34] Beyer, K., A. Dazio, and M.J.N. Priestly, Quasi-Static Cyclic Tests of Two U-Shaped Reinforced Concrete Walls. Journal of Earthquake Engineering, 2008. 12(7): p. 1023-1053.

[35] Birely, A.C., Seismic Performance of Slender Reinforced Concrete Structural Walls. 2012, University of Washington.

[36] Bonelli, P., 2010 Chile Earthquake - Explanation of Structural Damage in Reinforced Concrete Buildings (Spanish). 2010, Vimeo.

[37] Bonelli, P., et al., Improvements from the Seismic Design of Reinforced Concrete Walls in Chile and Suggestions for the Refinement of Other Seismic Code Provisions, in 2012 New Zealand Society for Earthquake Engineering Conference. 2012.

[38] BRI, Summary of the Field Survey and Research on “The 2011 off-the-Pacific Coast of Tohoku Earthquake” (the Great East Japan Earthquake). 2011, National Institute for Land and Infrastructure Management in Japan (Building Research Institute).

[39] Brown, P., Probabilistic Earthquake Damage Predictions for Reinforced Concrete Buildings Components. 2008, University of Washington.

[40] Brueggen, B.L., Performance of T-Shaped Reinforced Concrete Structural Walls under Multi-Directional Loading. 2009, University of Minnesota.

[41] Bull, D., The Performance of Concrete Structures in the Canterbury Earthquakes: Lessons to be Learned & Future of Concrete Buildings. 2012, American Concrete Institute.

[42] Butcher, G., et al., The September 1985 Mexico earthquakes: Final report of the New Zealand reconnaissance team. Bulletin of the New Zealand Society for Earthquake Engineering, 1988. 21(1).

[43] CEN, ENV 1998: Eurocode 8: Design Provisions for Earthquake Resistance of Structures 1994: European Committee for Standardization.

[44] CEN, preEN 1998: Eurocode 8: Design Provisions for Earthquake Resistance of Structures. 2003: European Committee for Standardization.

[45] Cervenka, J. and L. Jendele, ATENA Program Documentation, Part 6: ATENA Input File Format. 2016: Cervenka Consulting s.r.o.

[46] Cervenka, V., L. Jendele, and J. Cervenka, ATENA Program Documentation, Part 1: Theory. 2016: Cervenka Consulting s.r.o.

[47] Choi, C.-S., et al., Evaluation of Deformation Capacity for RC T-Shaped Cantilever Walls. Journal of Earthquake Engineering, 2004. 8(3): p. 397-414.

[48] Constantin, R. and K. Beyer, Modelling of Reinforced Concrete Core Walls Under Bi-direction Loading, in 15th World Conference on Earthquake Engineering. 2012.

[49] de Borst, R., Non-linear Analysis of Frictional Materials. 1986, Delft University of Technology.

[50] Degenblog Degenkolb Engineer Takes Park in EERI Chile Recon Trip. 2010.

[51] Dogangun, A., Performance of reinforced concrete buildings during the May 1, 2003 Bingol Earthquake in Turkey. Engineering Structures, 2004. 26: p. 841-856.

[52] Dunning Thorton Consultants, Report on the Structural Performance of the Hotel Grand Chancellor in the Earthquake of 22 February 2011. 2011, New Zealand Department of Building and Housing.

[53] EEFIT, The Mexican Earthquake of 19th September 1985: A Field Report by EEFIT. 1986, The Institution of Structural Engineers.

[54] EEFIT, The San Salvador Earthquake of 10 October 1986: A Field Report by EEFIT. 1987, The Institution of Structural Engineers.

[55] EEFIT, The Chilean Earthquake of 3 March 1985: A Field Report by EEFIT. 1988, The Institution of Structural Engineers.

[56] EEFIT, The Hyogo-Ken Nanbu (Kobe) Earthquake of 17 January 1995: A Field Report by EEFIT. 1997, The Institution of Structural Engineers.

[57] EEFIT, The Kocaeli, Turkey Earthquake of 17 August 1999: A Field Report by EEFIT. 2003, The Institution of Structural Engineers.

[58] EEFIT, The Mw 8.8 Maule Chile Earthquake of 27th February 2010: A Preliminary Field Report by EEFIT. 2010, The Institution of Structural Engineers.

[59] EEFIT, The Mw 9.0 Tohoku Earthquake and Tsunami of 11th March 2011: A Field Report by EEFIT. 2011, The Institution of Structural Engineers.

[60] EERI, The San Salvador Earthquake of October 10, 1986. Earthquake Spectra, 1987. 3(3): p. 413-634.

[61] EERI, Armenia Earthquake: Report of the Soviet Earthquake Investigation Team on the Armenian Earthquake of December, 1988. 1989, Earthquake Engineering Research Institute.

[62] EERI, Armenian Earthquake of December 7, 1988: Reconnaissance Report. Earthquake Spectra, 1989. 5(S1): p. 1-175.

[63] EERI, Loma Prieta Earthquake October 17, 1989: Preliminary Reconnaissance Report. 1989, Earthquake Engineering Research Institute.

[64] EERI, Mexico Earthquake of September 19, 1985. Earthquake Spectra, 1989. 5(1): p. 1-298.

[65] EERI, Erzincan, Turkey Earthquake of March 13, 1992. 1993, Earthquake Engineering Research Institute.

[66] EERI, Erzincan, Turkey Earthquake of March 13, 1992: Reconnaissance Report. Earthquake Spectra, 1993. 9(S1): p. 1-210.

[67] EERI, The Guam Earthquake of August 8, 1993. 1993, Earthquake Engineering Research Institute.

[68] EERI, Guam Earthquake of August 8, 1993: Reconnaissance Report. Earthquake Spectra, 1995. 11(S3): p. 1-175.

[69] EERI, Northridge, California 1994 Earthquake: Reconnaissance Report. Earthquake Spectra, 1996. 12(S1): p. 1-278.

[70] EERI, The July 9, 1997, Cariaco, Eastern Venezuela Earthquake. 1997, Earthquake Engineering Research Institute.

[71] EERI, The Chi-Chi, Taiwan Earthquake of September 21, 1999. 1999, Earthquake Engineering Research Institute.

[72] EERI, Kocaeli, Turkey Earthquake of August 17, 1999: Reconnaissance Report. Earthquake Spectra, 2000. 16(S1): p. 1-461.

[73] EERI, Chi-Chi, Taiwan Earthquake of September 21, 1999: Reconnaissance Report. Earthquake Spectra, 2001. 17(S1): p. 1-183.

[74] EERI Chile Earthquake Clearinghouse: Observations on Building Damage from Francisco Medina. 2010.

[75] EERI, The Mw 8.8 Chile Earthquake of February 27, 2010. 2010, Earthquake Engineering Research Institute.

[76] EERI, The M6.3 Christchurch, New Zealand Earthquake of February 22, 2011. 2011, Earthquake Engineering Research Institute.

[77] EERI, The Mw 7.1 Ercis-Van, Turkey Earthquake of October 23, 2011. 2012, Earthquake Engineering Research Institute.

[78] EERI, Performance of Engineered Structures in the Mw 9.0 Tohoku, Japan Earthquake of March 11, 2011. 2012, Earthquake Engineering Research Institute.

[79] EERI, Concrete Buildings Damaged in Earthquakes: A Collection of Case Studies. 2013, Earthquake Engineering Research Institute. <http://db.concretecoalition.org/list>

[80] EERI, Learning from Earthquakes Reconnaissance Archive. 2016, Earthquake Engineering Research Institute. <https://www.eeri.org/projects/learning-from-earthquakes-lfe/lfe-reconnaissance-archive/>

[81] EQE Engineering, The October 17, 1989 Loma Prieta Earthquake. 1989, EQE Engineering.

[82] Erdik, M., et al., May 01, 2003 Bingol (Turkey) Earthquake. Kandilla Observatory and Earthquake Research Institute at Bogazici University.

[83] Filiatrault, A., et al., Reconnaissance Report of the February 28, 2011 Nisqually (Seattle-Olympia) Earthquake. 2011, University of California - San Diego.

[84] Greifenhagen, C. and P. Lestuzzi, Static Cyclic Tests on Lightly Reinforced Concrete Shear Walls. Engineering Structures, 2005. 27(11): p. 1703-1712.

[85] Gulec, C.K., A.S. Whittaker, and J.D. Hooper, Fragility functions for low aspect ratio reinforced concrete walls. Engineering Structures, 2010. 32: p. 2894-2901.

[86] Ha, S.-S., et al., Experimental Investigation on the Structural Performance of RC T-shaped Walls with Different Confinement Effects. Architectural Institute of Korea Journal of Structural Engineering, 2002. 18(3): p. 39-45.

[87] Hart, C.R., Cracking of Reinforced Concrete Structural Walls Subjected to Cyclic Loading. 2012, University of Illinois at Urbana-Champaign.

[88] Herrick, C.K., An Analysis of Local Out-of-Plane Buckling of Ductile Reinforced Structural Walls Due to In-Plane Loading. 2013, North Carolina State University.

[89] Hidalgo, P.A., C.A. Ledezma, and R.M. Jorden, Seismic Behavior of Squat Reinforced Concrete Shear Walls. Earthquake Spectra, 2002. 18(2): p. 287-308.

[90] Hoehler, M.S. and J.F. Stanton, Simple Phenomenological Model for Reinforcing Steel under Arbitrary Load. Journal of Structural Engineering, 2006. 132: p. 1061-1069.

[91] Hordijk, D.A., Local Approach to Fatigue of Concrete. 1991, Delft University of Technology.

[92] Hosaka, G., H, Funaki, H, Hosoya, and H. Imai., Experimental Study on Structural Performance of RC Shear Wall with L Shaped Section, in 14th World Conference on Earthquake Engineering. 2008.

[93] Hu, G.-L., Shear Wall Test R09 (conducted in 2004) in SLDRCE Database on Static Tests of Structural Members and Joint Assemblies. 2008: State Key Laboratory of Disaster Reduction in Civil Engineering, Tongji University, China.

[94] ICBO, Uniform Building Code (UBC-1973). 1973: International Conference of Building Officials.

[95] ICBO, Uniform Building Code (UBC-1991). 1991: International Conference of Building Officials.

[96] ICBO, Uniform Building Code (UBC-1994). 1994: International Conference of Building Officials.

[97] ICBO, Uniform Building Code (UBC-1997). 1997: International Conference of Building Officials.

[98] ICC, Uniform Building Code, 1997. 1997: International Code Council.

[99] ICC, International Building Code 2003 (IBC-2003). 2003: International Code Council.

[100] Ignacio Rosas, M., Structural Damage - Edificio Emerald - Paz Contractors - Irarrazaval 2931 (Spanish). 2010, Youtube.

[101] Ile, N. and J.M. Reynouard, Behaviour of U-Shaped Walls Subjected to Uniaxial and Biaxial Cyclic Lateral Loading. Journal of Earthquake Engineering, 2005. 9(1): p. 67-94.

[102] Inada, K., et al., Seismic Performance of RC L-Shaped Core Structural Walls, in 14th World Conference on Earthquake Engineering. 2008.

[103] Jenning, P.C.e., Engineering Features of the San Fernando Earthquake of February 9, 1971. 1971: California Institute of Technology.

[104] Johnson, S., Comparison of Nonlinear Finite Element Modeling Tools for Structural Concrete. 2006, University of Illinois at Urbana-Champaign.

[105] Kam, W.Y., S. Pampanin, and K. Elwood, Seismic Performance of Reinforced Concrete Buildings in the 22 February Christchurch (Lyttelton) Earthquake. Bulletin of the New Zealand Society for Earthquake Engineering, 2011. 44(4).

[106] Kaplan, H., et al., May 1, 2003 Turkey - Bingol earthquake: damage in reinforced concrete structures. Engineering Failure Analysis, 2004. 11: p. 271-291.

[107] Kono, S., K. Sakamoto, and M. Sakashita, Simulation of Seismic Load Resistance of Core-Walls for Tall Buildings. Applied Mechanics and Materials, 2011. 82: p. 386-391.

[108] Kuchma, D., ExVis Tool and Case Study Implementation for the Visualization, Fusion, and Analysis of Experimental Test Data on Concrete Structural Walls. 2012: NEES Project Warehouse.

[109] Lehman, D., Personal Communication. 2016.

[110] Lehman, D. and L. Lowes, Ballot Proposal: ACI 318 Subcommittee Change Submittal for Shear Wall Boundary Element Length. 2016, American Concrete Institute.

[111] Lehman, D., et al., Seismic Behavior of a Modern Concrete Coupled Wall. Journal of Structural Engineering, 2013. 139: p. 1371-1381.

[112] Lehman, D.E., et al., Nonlinear Analysis Methods for Flexural Seismic Reinforced Concrete Walls, in 2nd ATC-SEI Conference on Improving the Seismic Performance of Existing Buildings and Other Structures. 2015, American Society of Civil Engineers.

[113] Lequesne, R.D., J.K. Wight, and G.J. Parra-Montesinos, Seismic Detailing and Behavior of Coupled-Wall Systems with High-Performance Fiber-Reinforced Concrete, in 9th US National and 10th Canadian Conf. on Earthquake Engineering. 2010.

[114] Loh, C.-H. and C.-Y. Tsay, Response for the Earthquake Engineering Research Community to the Chi-Chi (Taiwan) Earthquake. Earthquake Spectra, 2001. 17(4): p. 635-656.

[115] Lowes, L., Chi-Chi Reconnaissance Images.

[116] Lowes, L., et al., Performance-Based Seismic Design of Concrete Walls. 2015, Charles Pankow Foundation. <http://www.pankowfoundation.org/grants.cfm>

[117] Lowes, L., et al., Behavior, Analysis and Design of Complex Wall Systems. 2014: NEEShub. <https://nees.org/warehouse/project/104>

[118] Lowes, L.N., et al., Planar Wall Test Program Summary Document. 2011, University of Washington.

[119] Lowes, L.N., et al., Large Scale Testing of C-Shaped Reinforced Concrete Walls. 2013, Charles Pankow Foundation.

[120] Menegotto, M. and P.E. Pinto, Method of Analysis for Cyclically Loaded R.C. Plane Frames Including Changes in Geometry and Non-Elastic Behavior of Elements under Combined

Normal Force and Bending. 1973, International Association for Bridge and Structural Engineering.

[121] Menetrey, P. and K.J. William, Triaxial failure criterion for concrete and its generalization. ACI Structural Journal, 1995. 92(3): p. 311-318.

[122] Mitchell, D., et al., Damage to concrete structures due to the January 17, 1995, Hyogo-Ken Nanbu (Kobe) earthquake. Canadian Journal of Civil Engineering, 1996. 23: p. 757-770.

[123] Mitchell, D., et al., Damage to concrete structures due to the 1994 Northridge earthquake. Canadian Journal of Civil Engineering, 1995. 22: p. 361-377.

[124] Mock, A.W., Modeling the Response of Structural Concrete to Cyclic Loadings. 2017, University of Illinois at Urbana-Champaign.

[125] Moehle, J.P. Recommendations from 2 June 2010 Meeting on the 27 February 2010 Chile Earthquake: Implications for U.S. Building Codes and Standards. in Meeting of ASCE, NIST, and PEER Center. 2010.

[126] NACU, NACU Report of 1908: Report of the Committee on Laws and Ordinances. 1908: National Association of Cement Users.

[127] NACU, Standard Building Regulations for the Use of Reinforced Concrete (Standard No. 4). 1910: National Association of Cement Users.

[128] Nakachi, T., T. Toda, and K. Tabata, Experimental Study on Deformation Capacity of Reinforced Concrete Core Walls after Flexural Yielding, in 11th World Conference on Earthquake Engineering. 1996.

[129] NCHRP, NCHRP Report 579. Application of LRFD Bridge Design Specifications to High-Strength Structural Concrete: Shear Provisions. 2007, Transportation Research Board of the National Academies (National Cooperative Highway Research Program).

[130] NECG, The Nisqually Earthquake of 28 February 2011: Preliminary Reconnaissance Report. 2011, Nisqually Earthquake Clearinghouse Group at the University of Washington - Seattle.

[131] NISEE, The Earthquake Engineering Online Archive. 2016, National Information Service for Earthquake Engineering. <https://nisee.berkeley.edu/elibrary/>

[132] NIST, The January 17, 1995 Hyogoken-Nanbu (Kobe) Earthquake: Performance of Structures, Lifelines, and Fire Protection Systems. 1996, National Institute of Standards and Technology.

[133] NIST, Comparison of U.S. and Chilean Building Code Requirements and Seismic Design Practice 1985-2010 (NIST GCR 12-917-18). 2012, National Institute of Standards and Technology.

[134] NIST, Seismic Design of Cast-in-Place Concrete Special Structural Walls and Coupling Beams: A Guide for Practicing Engineers (NIST GCR 11-917-11REV-1). 2012, National Institute of Standards and Technology.

[135] NIST, Recommendations for Seismic Design of Reinforced Concrete Wall Buildings Based on Studies of the 2010 Maule, Chile Earthquake (NIST GCR 14-917-25). 2014, National Institute of Standards and Technology.

[136] NOAA-NGDC, The Significant Earthquake Database. 2016, National Oceanic and Atmospheric Administration - National Geophysical Data Center. <http://www.ngdc.noaa.gov/nndc/struts/form?t=101650&s=1&d=1>

[137] NRC-DoES, The Great Alaska Earthquake of 1964. 1973, National Academy of Sciences (National Research Council - Division of Earth Sciences).

[138] NZS, NZS 3101:1982, Code of Practice for Design of Concrete Structures. 1982: Standards Association of New Zealand

[139] OECD, School Safety and Security: Keeping Schools Safe in Earthquakes. 2004: Organisation for Economic Cooperation and Development.

[140] Oesterle, R.G., et al., Earthquake Resistant Structural Walls - Tests of Isolated Walls - Phase II. 1979, Construction Technology Laboratories of the Portland Cement Association.

[141] Oesterle, R.G., et al., Earthquake Resistant Structural Walls - Tests of Isolated Walls. 1976, Construction Technology Laboratories of the Portland Cement Association.

[142] Ozselcuk, A.R., Experimental and Analytical Studies of Coupled Wall Structures. 1989, University of California - Berkeley.

[143] Paulay, T. and W.J. Goodsir, The Ductility of Structural Walls. Bulletin of the New Zealand Society for Earthquake Engineering, 1985. 18(3).

[144] Pegon, P., et al., U-shaped walls: Quasi-static test in the X and Y directions - Test report, TMR-ICONS-TOPIC5. 2000, Joint Research Centre - Ispra.

[145] Pegon, P., et al., U-shaped walls: Quasi-static test in the X direction - Test report, TMR-ICONS-TOPIC5. 2000, Joint Research Centre - Ispra.

[146] Pilakoutas, K. and A. Elnashai, Cyclic Behavior of Reinforced Concrete Cantilever Walls, Part I: Experimental Results. ACI Structural Journal, 1995. 92(3): p. 271-281.

[147] Pryl, D. and J. Cervenka, ATENA Program Documentation, Part 11: Troubleshooting Manual. 2016: Cervenka Consulting s.r.o.

[148] Pugh, J.S., Numerical Simulation of Walls and Seismic Design Recommendations for Walled Buildings. 2012, University of Washington.

[149] Ramos, P.V., Municipality may support actions of residents of effected buildings (Spanish). 2010, El Mercurio de Valparaiso.

[150] Raschke, M., et al., The Cariaco (Northern Venezuela) Earthquake of 09 July 1997: Reconnaissance. 1997, German Task Force for Earthquakes.

[151] Reynouard, J.-M. and M.N. Fardis, Shear wall structures, CAFEEL-ECOEST. 2001, Laboratorio Nacional de Engenharia Civil, Lisbon, Portugal.

[152] Riddell, R., S.L. Wood, and J.C. De La Llera, The 1985 Chile Earthquake: Structural Characteristics and Damage Statistics for the Building Inventory in Vina del Mar. 1987, University of Illinois at Urbana-Champaign.

[153] Saatcioglu, M. and M. Bruneau, The 1992 Erzincan Earthquake. Concrete International, 1994. 16(9): p. 52-56.

[154] Saatcioglu, M., et al., The August 17, 1999, Kocaeli (Turkey) earthquake - damage to structures. Canadian Journal of Civil Engineering, 2001. 28: p. 715-737.

[155] Sezen, H., et al., Structural Engineering Reconnaissance of the August 17, 1999 Earthquake: Kocaeli (Izmit), Turkey. 2000, Pacific Earthquake Engineering Research Center.

[156] Sezen, H., et al., Performance of reinforced concrete buildings during the August 17, 1999 Kocaeli, turkey earthquake, and seismic design and construction practise in Turkey. Engineering Structures, 2003. 25: p. 13-114.

[157] Shouzhong, J., Shear Wall Test R03 (conducted in 2002) in SLDRCE Database on Static Tests of Structural Members and Joint Assemblies. 2008: State Key Laboratory of Disaster Reduction in Civil Engineering, Tongji University, China.

[158] Sittipunt, C. and S.L. Wood, Finite Element Analysis of Reinforced Concrete Shear Walls. 1993, University of Illinois at Urbana-Champaign.

[159] Sritharan, S., et al., Understanding Poor Seismic Performance of Concrete Walls and Design Implications. Earthquake Spectra, 2014. 30(1): p. 307-334.

[160] Standards, C.N., GB 50010-2002: Code for Design of Concrete Structures (English). 2002: China Architecture & Building Press.

[161] Thomsen, J.H. and J.W. Wallace, Displacement-Based Design of Reinforced Concrete Structural Walls: An Experimental Investigation of Walls with Rectangular and T-Shaped Cross-Sections. 1995, Clarkson University.

[162] Thomsen, J.H. and J.W. Wallace, Displacement-Based Design of Slender Reinforced Concrete Structural Walls - Experimental Verification. Journal of Structural Engineering, 2004. 130(4): p. 618-630.

[163] Turgeon, J., The Seismic Performance of Coupled Reinforced Concrete Walls. 2011, University of Washington.

[164] USDOC, An Investigation of the Miyagi-ken-oki, Japan, Earthquake of June 12, 1978. 1980, U.S. Department of Commerce National Bureau of Standards.

[165] USGS, The San Fernando, California earthquake of February 9, 1971: a preliminary report. 1971, U.S. Geological Survey and the National oceanic and Atmospheric Administration.

[166] USGS, USGS Earthquake Hazards Program: Earthquake Photo Collections. 2016, U.S. Geological Survey.

[167] Vallenas, J.M., V.V. Bertero, and E.P. Popov, Hysteretic Behavior of Reinforced Concrete Structural Walls. 1979, Earthquake Engineering Research Center Report.

[168] van Mier, J.G.M., Multi-axial Strain-softening of Concrete, Part I: Fracture. Materials and Structures, 1986. 19(3): p. 179-190.

[169] Vecchio, F.J. and M.P. Collins, Modified Compression-Field Theory for Reinforced Concrete Beams Subjected to Shear. ACI Journal Proceedings, 1986. 83(2): p. 219-231.

[170] Wallace, J., Behavior, Design, and Modeling of Structural Walls and Coupling Beams - Lessons from Recent Laboratory Tests and Earthquakes. International Journal of Concrete Structures and Materials, 2012. 6(1): p. 3-18.

[171] Wang, T.Y., V.V. Bertero, and E.P. Popov, Hysteretic Behavior of Reinforced Concrete Framed Walls. 1979, Earthquake Engineering Research Center Report.

[172] Welt, T.S., Detailing for Compression in Reinforced Concrete Wall Boundary Elements: Experiments, Simulations, and Design Recommendations. 2015, University of Illinois at Urbana-Champaign.

[173] Whitman, Z.J., Investigation of Seismic Failure Modes in Flexural Concrete Walls using Finite Element Analysis. 2015, University of Washington.

[174] Wong, P.S., H. Trommels, and F.J. Vecchio, VecTor2 & FormWorks User's Manual. 2013: VecTor Analysis Group - University of Toronto.

[175] Wood, S.L., Minimum Tensile Reinforcement Requirements in Walls. ACI Structural Journal, 1989. 86(5): p. 582-591.

[176] Wood, S.L., Performance of Reinforced Concrete Buildings During the 1985 Chile Earthquake: Implications for the Design of Structural Walls. Earthquake Spectra, 1991. 7(4): p. 1-298.

[177] Wood, S.L., J.K. Wight, and J.P. Moehle, The 1985 Chile Earthquake: Observations on Earthquake-Resistant Construction in Vina del Mar. 1987, University of Illinois at Urbana-Champaign.

[178] Wyllie, L.A., Lessons from the Armenian Earthquake. Concrete International, 1989: p. 21-26.

APPENDIX A. DRIFT CAPACITY AND DISPLACEMENT DUCTILITY PLOTS FOR EXPERIMENTALLY TESTED NON-PLANAR WALLS

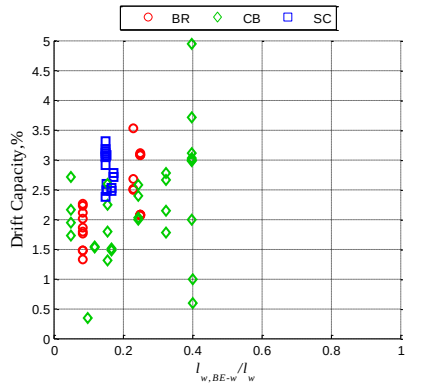

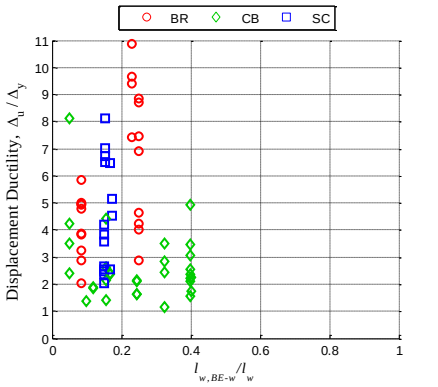

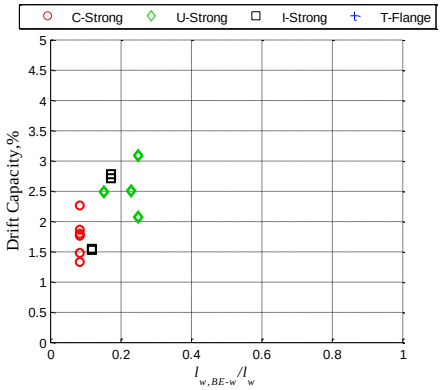

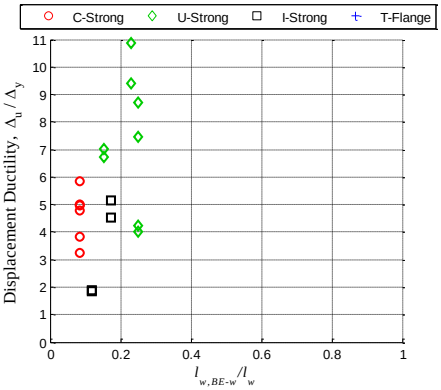

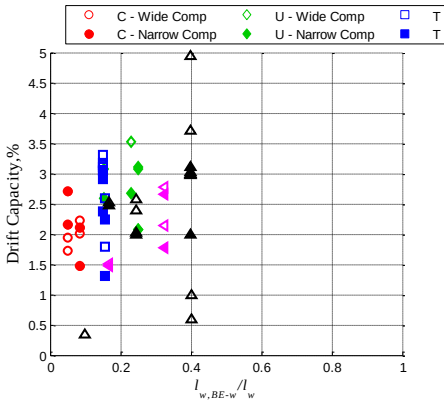

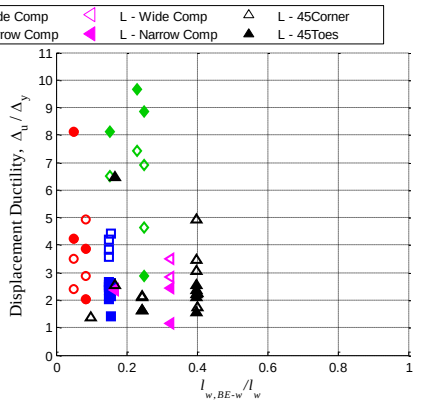

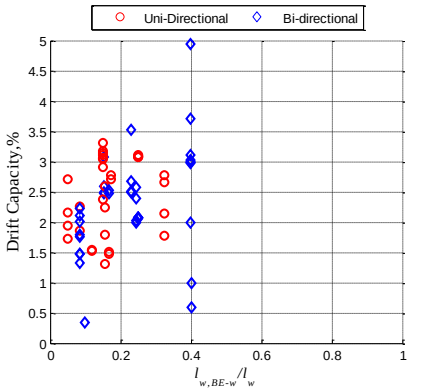

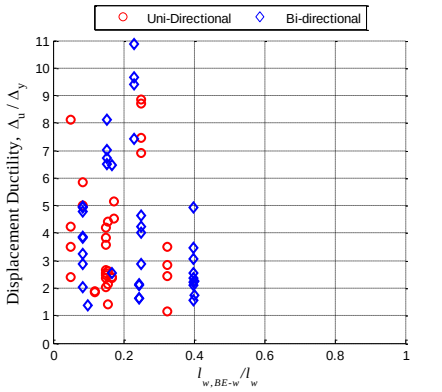

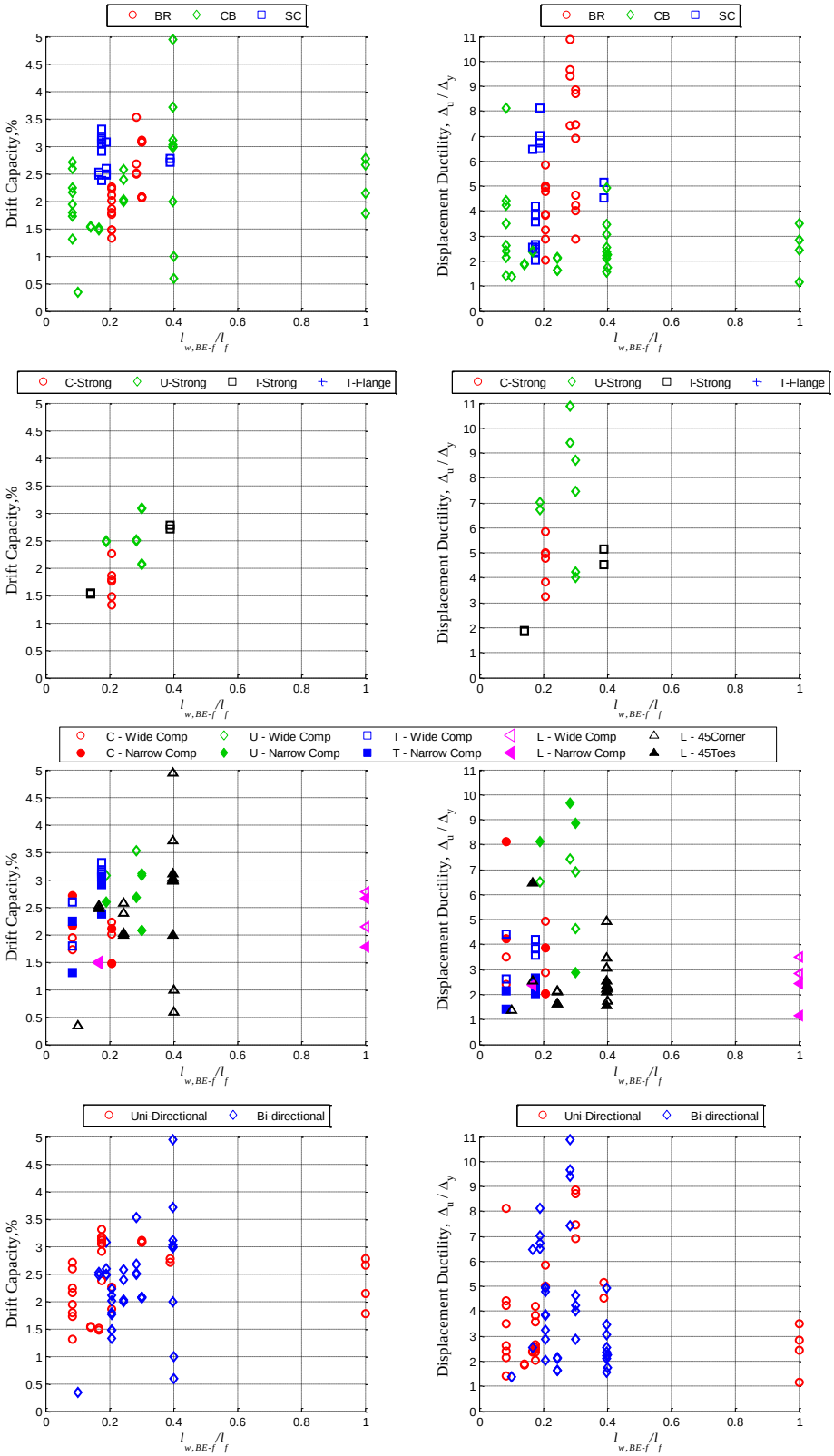
BR
CB
SC
C-Strong
U-Strong
I-Strong
T-Flange
C - Wide Comp
C - Narrow Comp
U - Wide Comp
U - Narrow Comp
T - Wide Comp
T - Narrow Comp
L - Wide Comp
L - Narrow Comp
L - 45Corner
L - 45Toes
Uni-Directional
Bi-directional
Drift Capacity,%
Displacement Ductility, Δ_u / Δ_y
$l_{w,BE\text{-}f} / l_f$

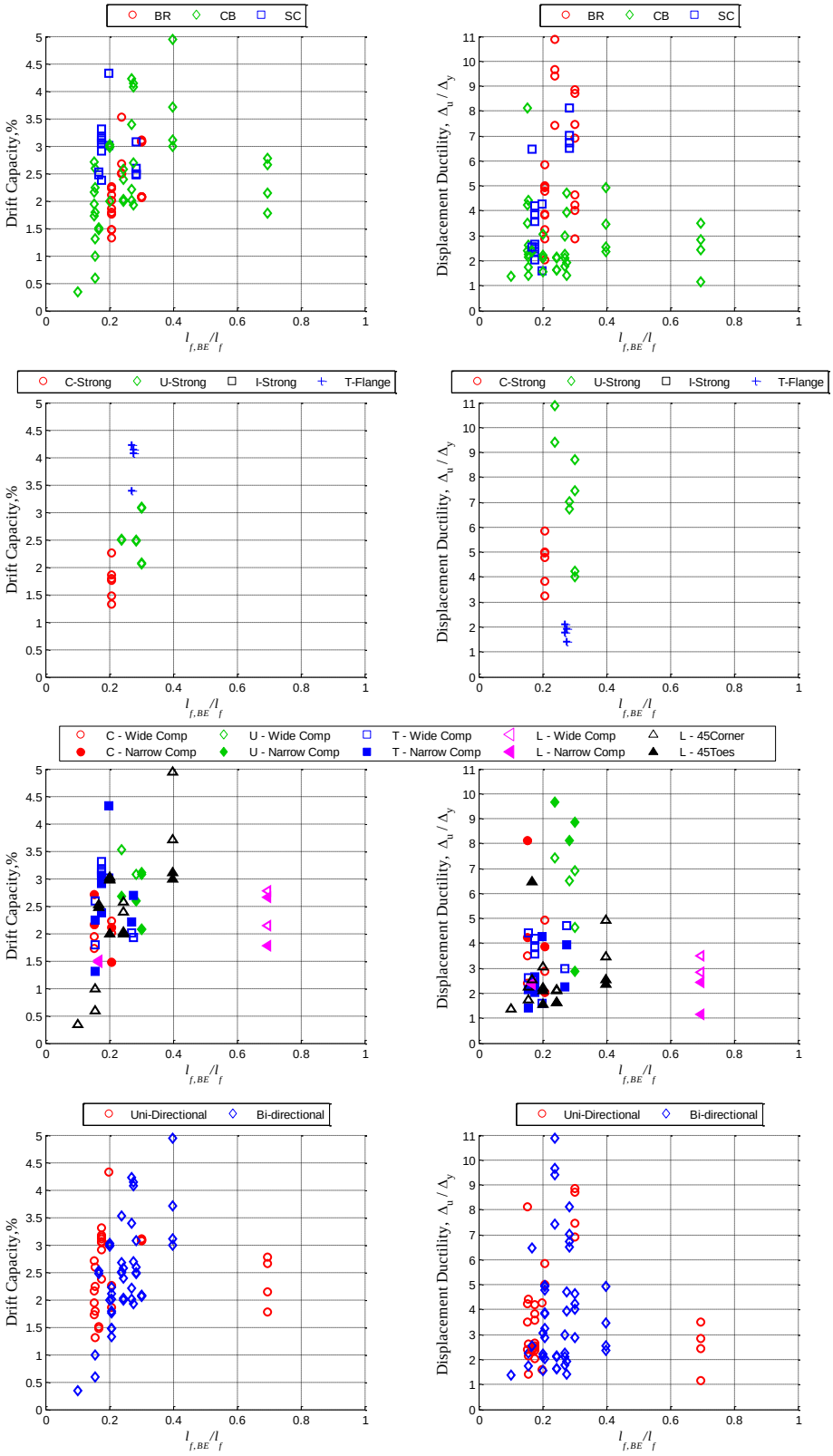
BR
CB
SC
Drift Capacity,%
Displacement Ductility, Δ_u / Δ_y
$l_{f,BE}/l_f$
C-Strong
U-Strong
I-Strong
T-Flange
C - Wide Comp
C - Narrow Comp
U - Wide Comp
U - Narrow Comp
T - Wide Comp
T - Narrow Comp
L - Wide Comp
L - Narrow Comp
L - 45Corner
L - 45Toes
Uni-Directional
Bi-directional

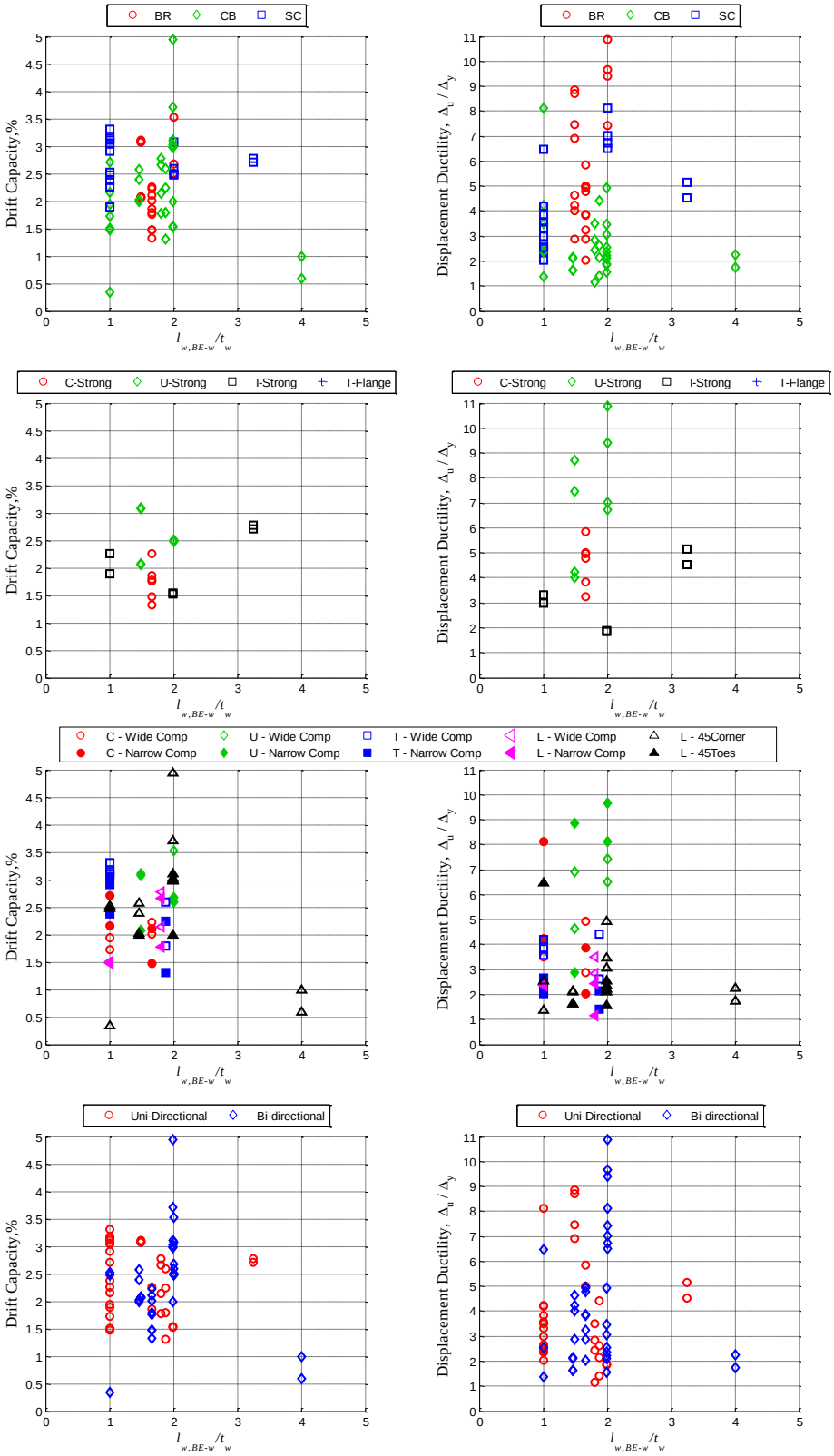
BR
CB
SC
Drift Capacity,%
Displacement Ductility, Δ_u / Δ_y
$l_{w,BE\text{-}w} / t_w$
C-Strong
U-Strong
I-Strong
T-Flange
C - Wide Comp
C - Narrow Comp
U - Wide Comp
U - Narrow Comp
T - Wide Comp
T - Narrow Comp
L - Wide Comp
L - Narrow Comp
L - 45Corner
L - 45Toes
Uni-Directional
Bi-directional

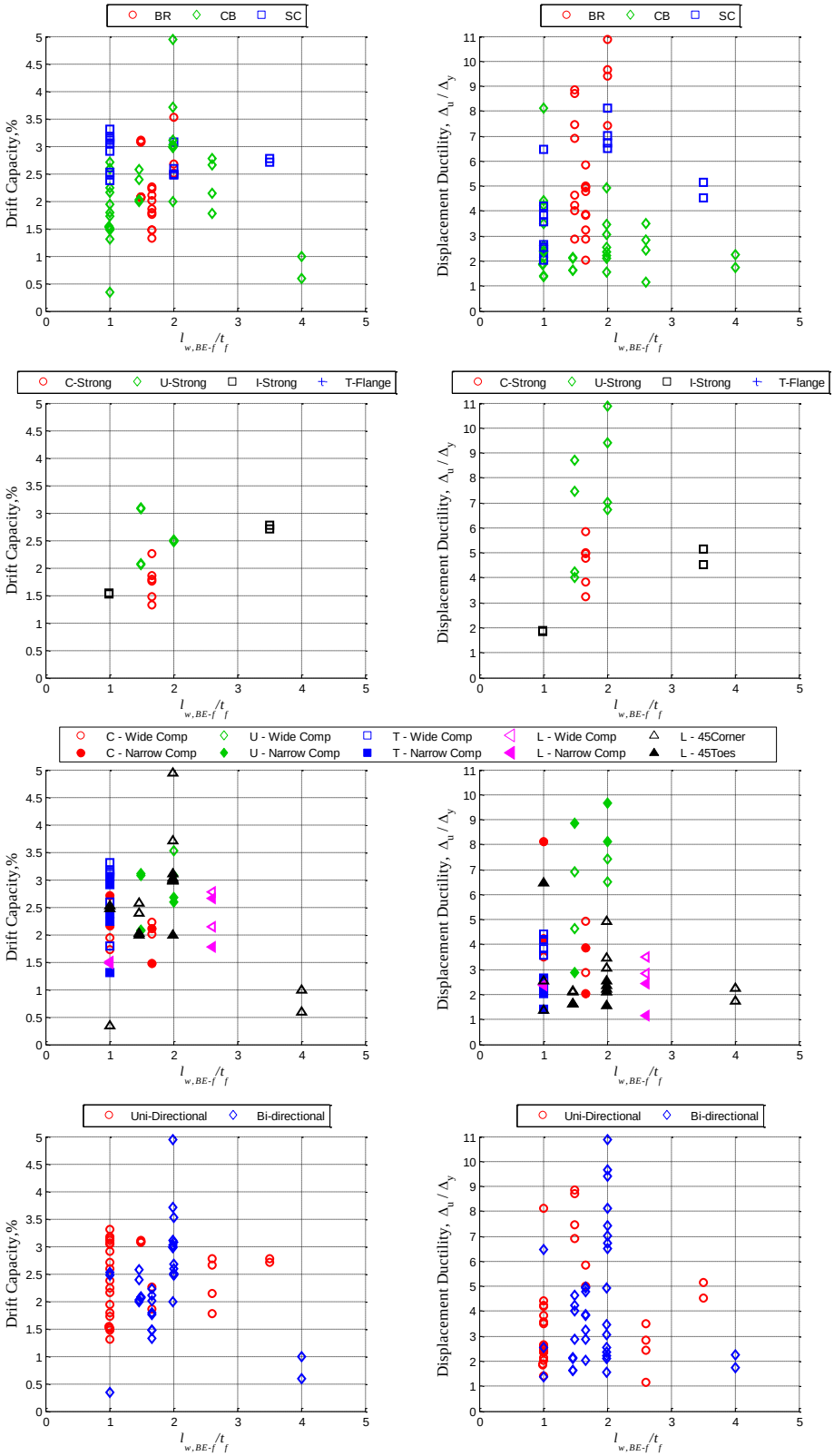
BR
CB
SC
Drift Capacity,%
Displacement Ductility, Δ_u / Δ_y
$l_{w,BE\text{-}f}/t_f$
C-Strong
U-Strong
I-Strong
T-Flange
C - Wide Comp
C - Narrow Comp
U - Wide Comp
U - Narrow Comp
T - Wide Comp
T - Narrow Comp
L - Wide Comp
L - Narrow Comp
L - 45Corner
L - 45Toes
Uni-Directional
Bi-directional

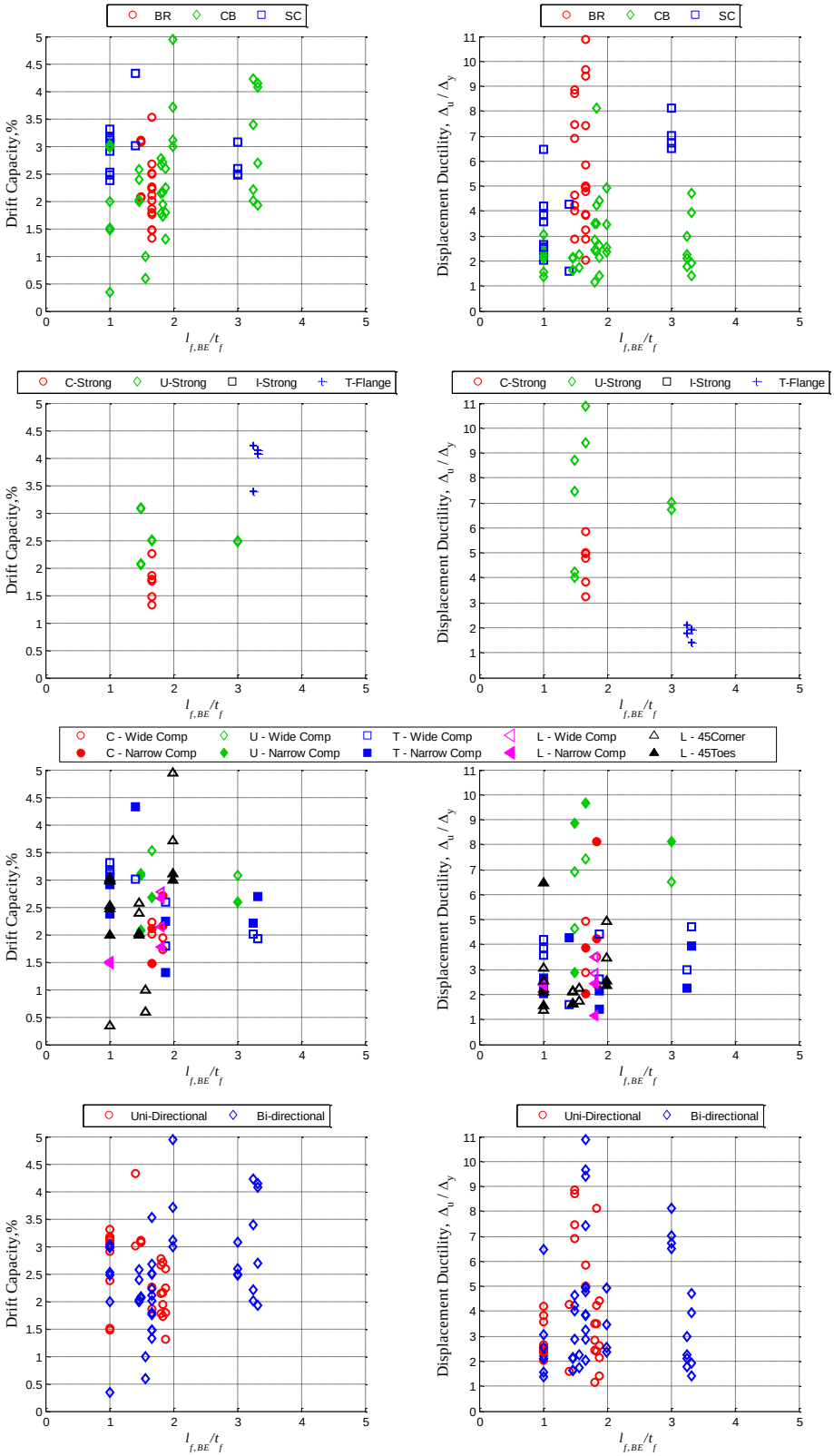
BR
CB
SC
Drift Capacity,%
Displacement Ductility, Δ_u / Δ_y
$l_{f,BE}/t_f$
C-Strong
U-Strong
I-Strong
T-Flange
C - Wide Comp
C - Narrow Comp
U - Wide Comp
U - Narrow Comp
T - Wide Comp
T - Narrow Comp
L - Wide Comp
L - Narrow Comp
L - 45Corner
L - 45Toes
Uni-Directional
Bi-directional

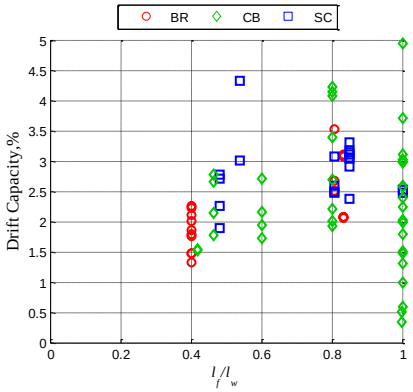
BR
CB
SC
Drift Capacity,%
l_f/l_w

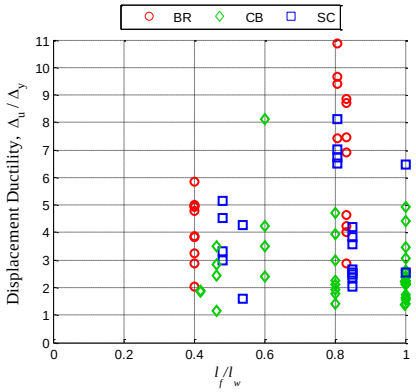
BR
CB
SC
Displacement Ductility, Δ_u/Δ_y
l_f/l_w

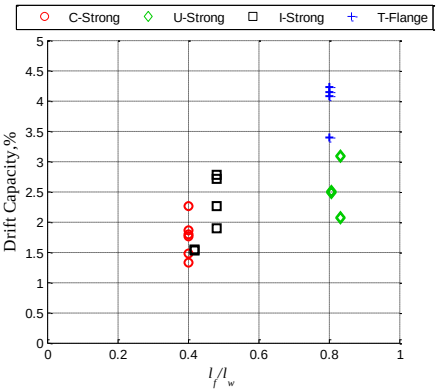
C-Strong
U-Strong
I-Strong
T-Flange
Drift Capacity,%
l_f/l_w

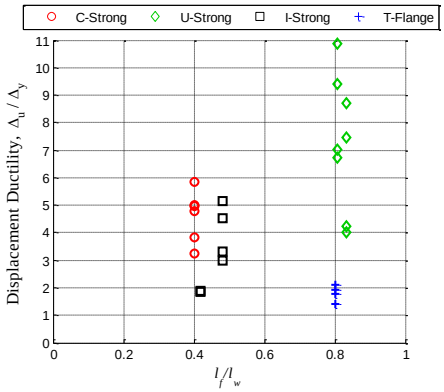
C-Strong
U-Strong
I-Strong
T-Flange
Displacement Ductility, Δ_u/Δ_y
l_f/l_w

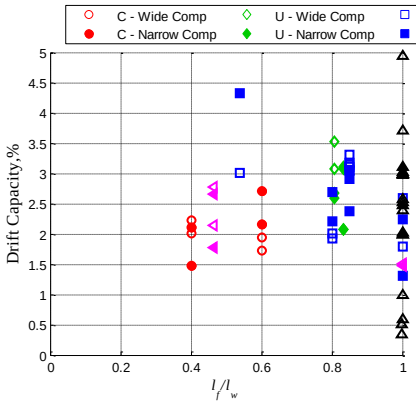
C - Wide Comp
C - Narrow Comp
U - Wide Comp
U - Narrow Comp
T - Wide Comp
T - Narrow Comp
L - Wide Comp
L - Narrow Comp
L - 45Corner
L - 45Toes
Drift Capacity,%
l_f/l_w

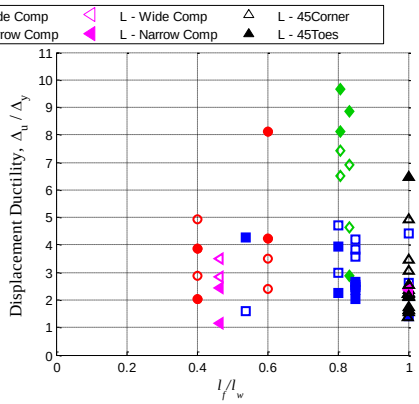
Displacement Ductility, Δ_u/Δ_y
l_f/l_w

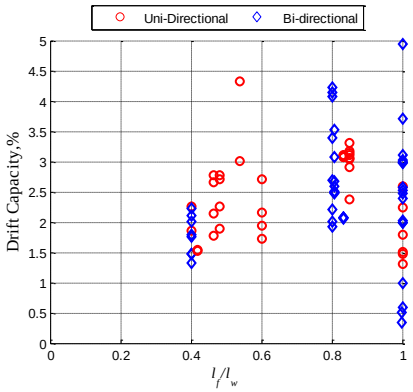
Uni-Directional
Bi-directional
Drift Capacity,%
l_f/l_w

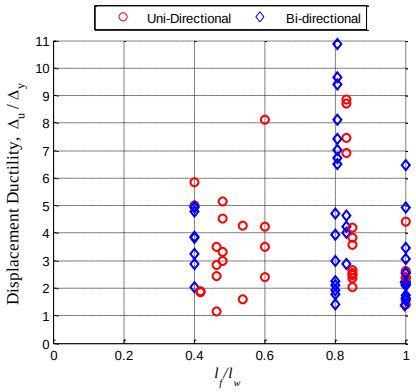
Uni-Directional
Bi-directional
Displacement Ductility, Δ_u/Δ_y
l_f/l_w

APPENDIX B. LOAD-DEFORMATION PLOTS FOR SIMULATED WALLS WITH ACI COMPLIANT AND EXTENDED BOUNDARY ELEMENTS

Note: In the following load-deformation plots the solid black line corresponds to W# and the solid blue line corresponds to W#c. As an example the first plot is for wall models W1 and W1c where the original, ACI compliant boundary element length is 5.5" and the extended boundary element length is 10.5". All other design parameters for the walls is consistent.

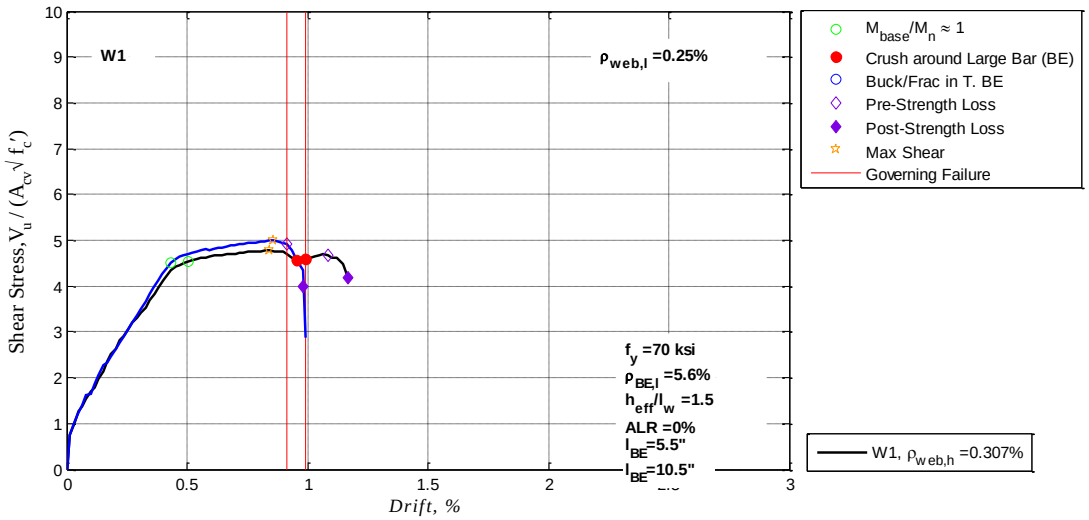

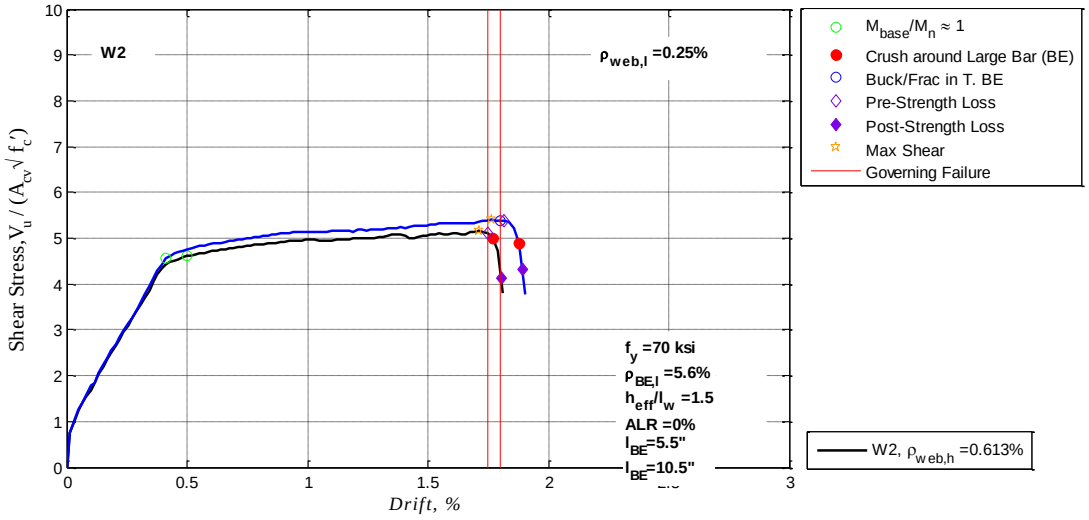

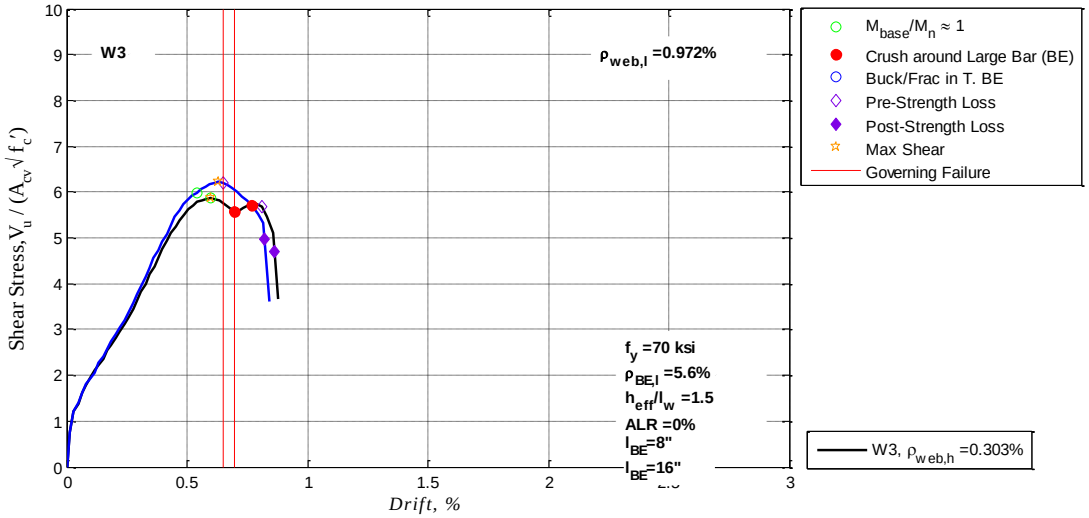
W3
ρweb,l =0.972%
fy =70 ksi
ρBE,l =5.6%
heff/lw =1.5
ALR =0%
lBE=8"
lBE=16"
Mbase/Mn ≈ 1
Crush around Large Bar (BE)
Buck/Frac in T. BE
Pre-Strength Loss
Post-Strength Loss
Max Shear
Governing Failure
W3, ρweb,h =0.303%
Shear Stress, Vu / (Acv √f'c)
Drift, %

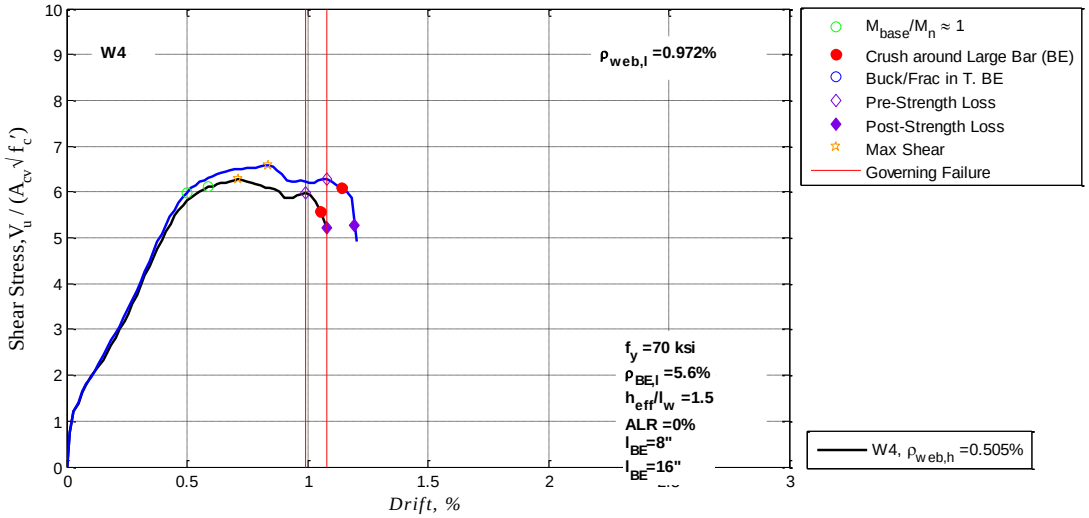
W4
ρweb,l =0.972%
fy =70 ksi
ρBE,l =5.6%
heff/lw =1.5
ALR =0%
lBE=8"
lBE=16"
Mbase/Mn ≈ 1
Crush around Large Bar (BE)
Buck/Frac in T. BE
Pre-Strength Loss
Post-Strength Loss
Max Shear
Governing Failure
W4, ρweb,h =0.505%
Shear Stress, Vu / (Acv √f'c)
Drift, %

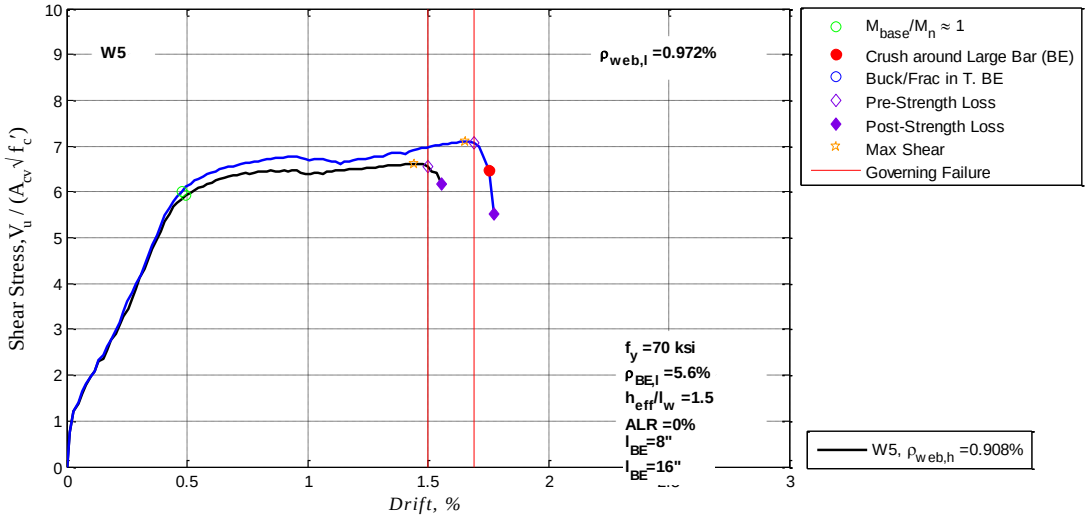
W5
ρweb,l =0.972%
fy =70 ksi
ρBE,l =5.6%
heff/lw =1.5
ALR =0%
lBE=8"
lBE=16"
Mbase/Mn ≈ 1
Crush around Large Bar (BE)
Buck/Frac in T. BE
Pre-Strength Loss
Post-Strength Loss
Max Shear
Governing Failure
W5, ρweb,h =0.908%
Shear Stress, Vu / (Acv √f'c)
Drift, %

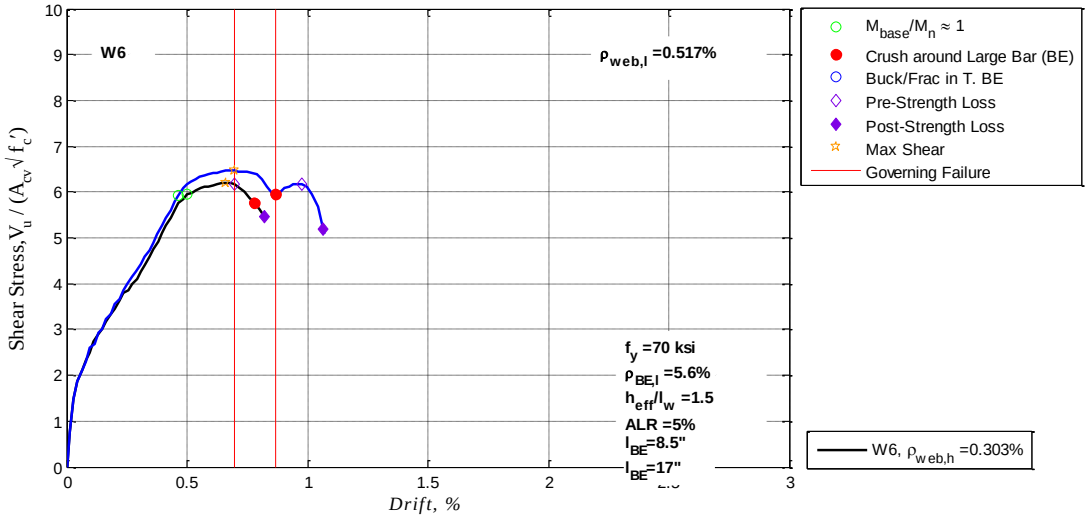
W6
ρweb,l =0.517%
fy =70 ksi
ρBE,l =5.6%
heff/lw =1.5
ALR =5%
lBE=8.5"
lBE=17"
Mbase/Mn ≈ 1
Crush around Large Bar (BE)
Buck/Frac in T. BE
Pre-Strength Loss
Post-Strength Loss
Max Shear
Governing Failure
W6, ρweb,h =0.303%
Shear Stress, Vu / (Acv √f'c)
Drift, %

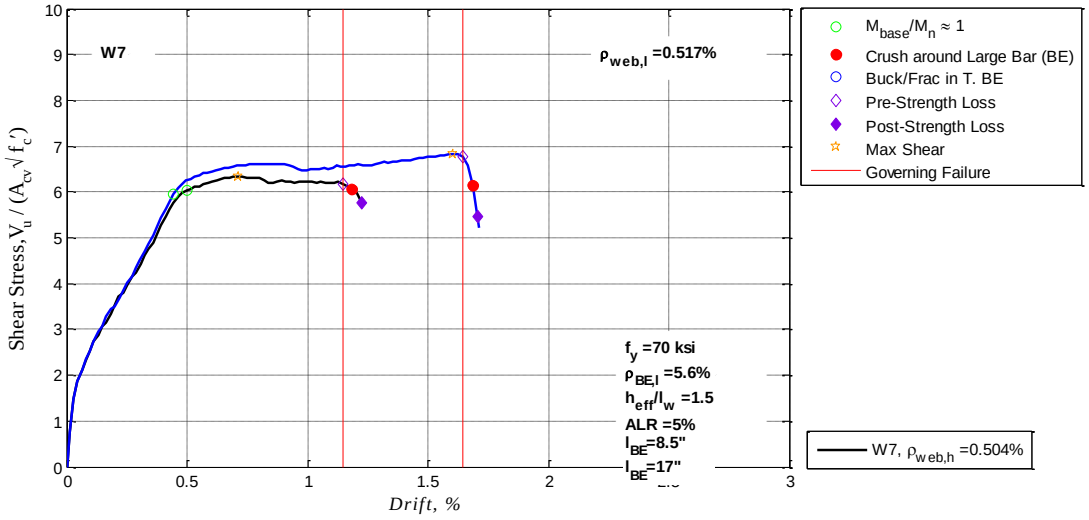
W7
ρweb,l =0.517%
fy =70 ksi
ρBE,l =5.6%
heff/lw =1.5
ALR =5%
lBE=8.5"
lBE=17"
Mbase/Mn ≈ 1
Crush around Large Bar (BE)
Buck/Frac in T. BE
Pre-Strength Loss
Post-Strength Loss
Max Shear
Governing Failure
W7, ρweb,h =0.504%
Shear Stress, Vu / (Acv √f'c)
Drift, %

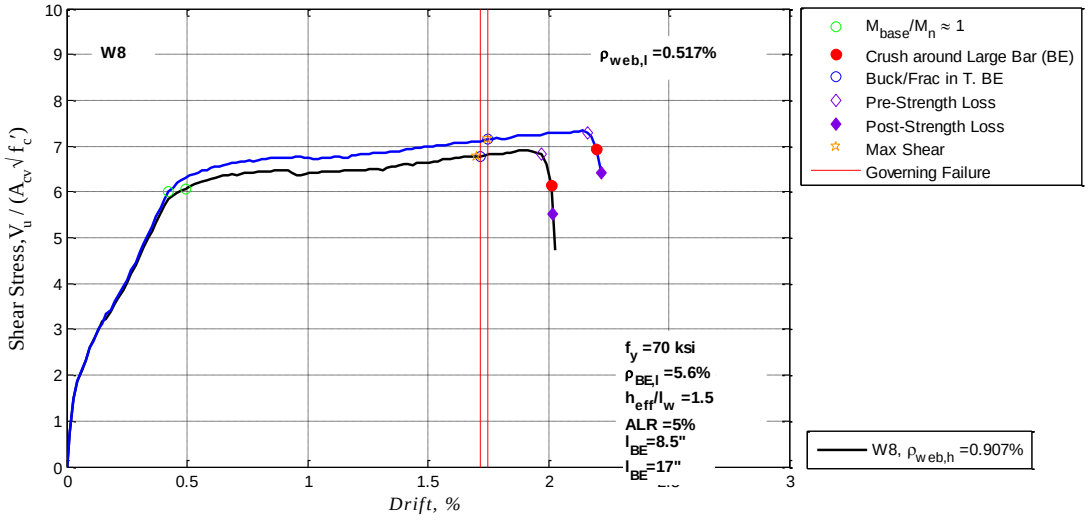
W8
ρweb,l =0.517%
fy =70 ksi
ρBE,l =5.6%
heff/lw =1.5
ALR =5%
lBE=8.5"
lBE=17"
Mbase/Mn ≈ 1
Crush around Large Bar (BE)
Buck/Frac in T. BE
Pre-Strength Loss
Post-Strength Loss
Max Shear
Governing Failure
W8, ρweb,h =0.907%
Shear Stress, Vu / (Acv √f'c)
Drift, %

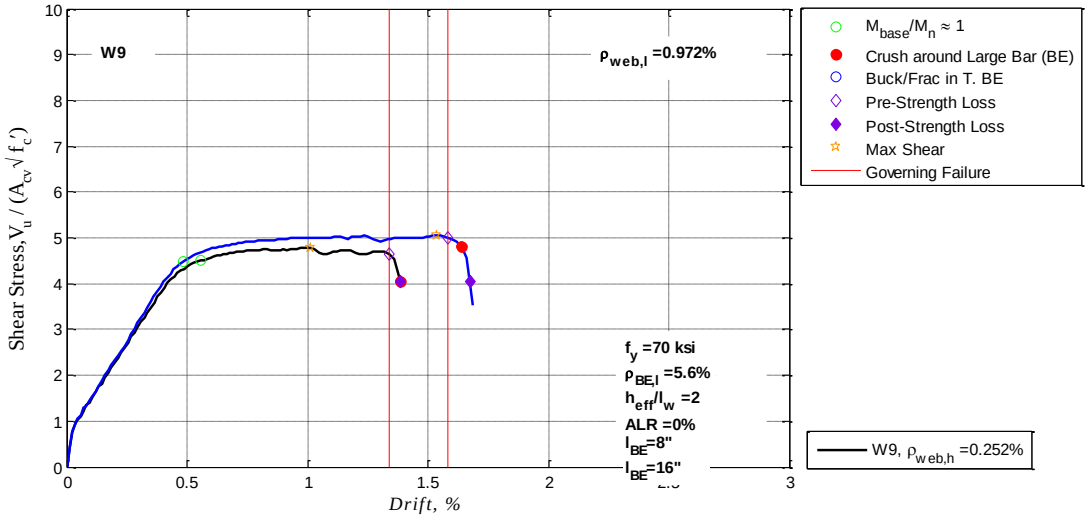
W9
ρweb,l =0.972%
fy =70 ksi
ρBE,l =5.6%
heff/lw =2
ALR =0%
lBE=8"
lBE=16"
Mbase/Mn ≈ 1
Crush around Large Bar (BE)
Buck/Frac in T. BE
Pre-Strength Loss
Post-Strength Loss
Max Shear
Governing Failure
W9, ρweb,h =0.252%
Shear Stress, Vu / (Acv √f'c)
Drift, %

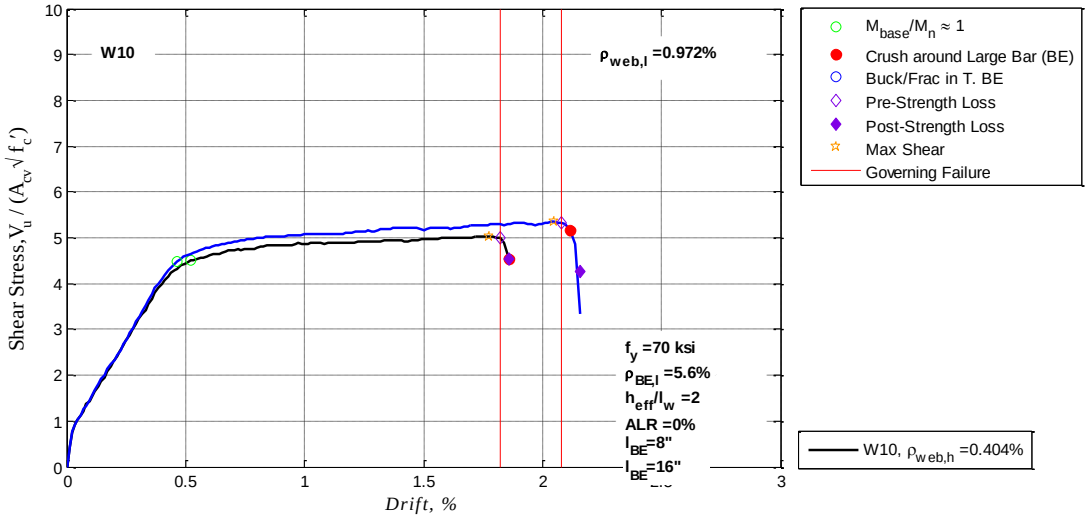
W10
ρweb,l =0.972%
fy =70 ksi
ρBE,l =5.6%
heff/lw =2
ALR =0%
lBE=8"
lBE=16"
Mbase/Mn ≈ 1
Crush around Large Bar (BE)
Buck/Frac in T. BE
Pre-Strength Loss
Post-Strength Loss
Max Shear
Governing Failure
W10, ρweb,h =0.404%
Shear Stress, Vu / (Acv √f'c)
Drift, %

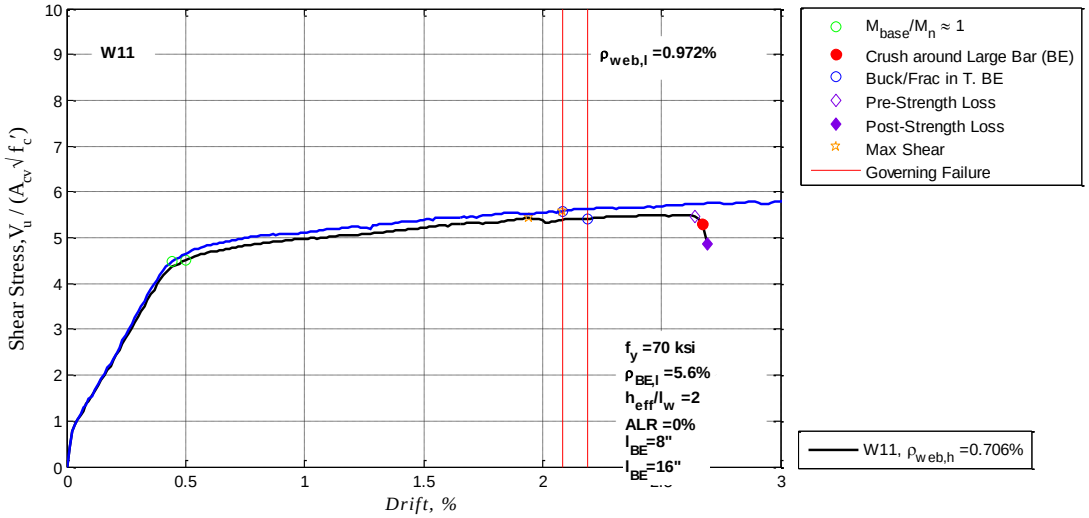
W11
ρweb,l =0.972%
fy =70 ksi
ρBE,l =5.6%
heff/lw =2
ALR =0%
lBE=8"
lBE=16"
Mbase/Mn ≈ 1
Crush around Large Bar (BE)
Buck/Frac in T. BE
Pre-Strength Loss
Post-Strength Loss
Max Shear
Governing Failure
W11, ρweb,h =0.706%
Shear Stress, Vu / (Acv √f'c)
Drift, %

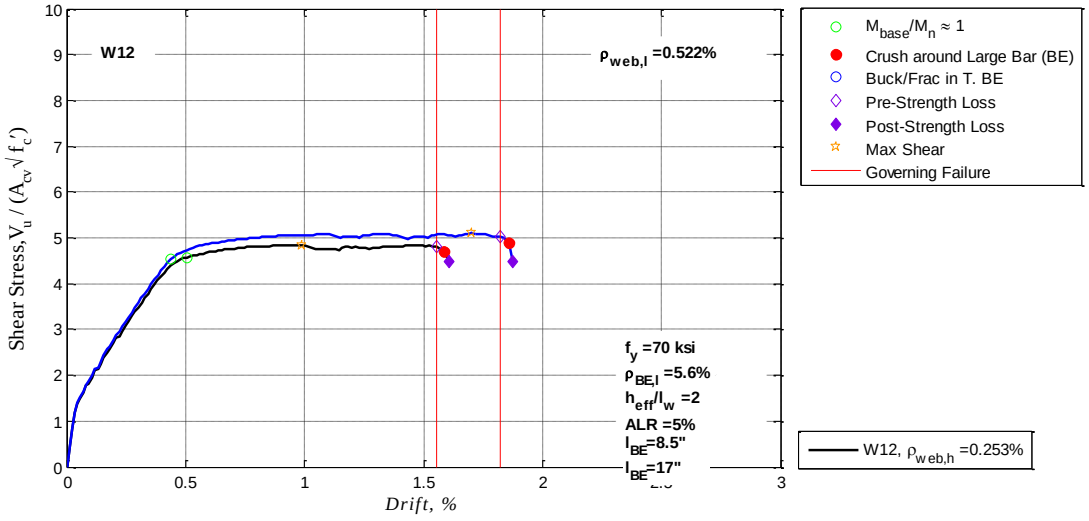
W12
ρweb,l =0.522%
fy =70 ksi
ρBE,l =5.6%
heff/lw =2
ALR =5%
lBE=8.5"
lBE=17"
Mbase/Mn ≈ 1
Crush around Large Bar (BE)
Buck/Frac in T. BE
Pre-Strength Loss
Post-Strength Loss
Max Shear
Governing Failure
W12, ρweb,h =0.253%
Shear Stress, Vu / (Acv √f'c)
Drift, %

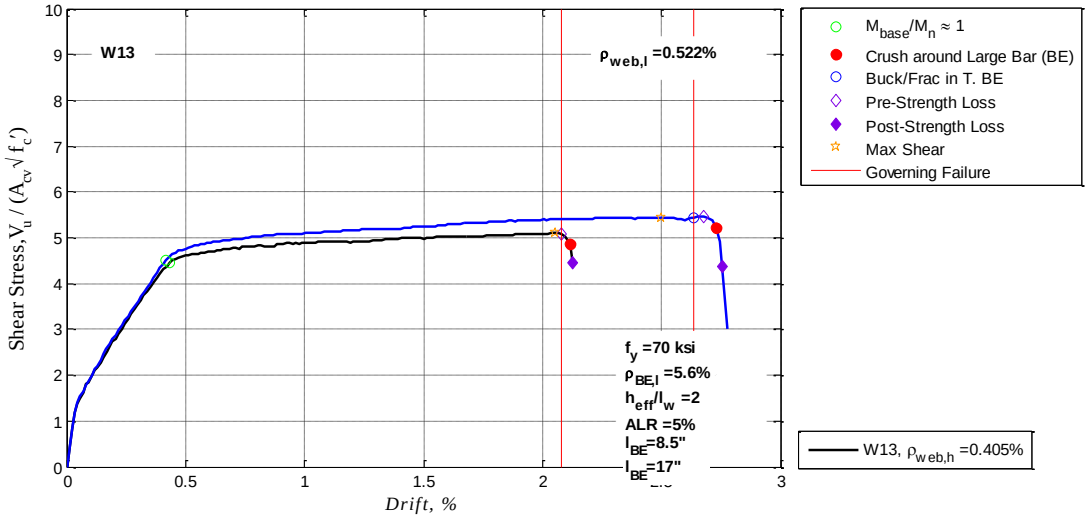
W13
ρweb,l =0.522%
fy =70 ksi
ρBE,l =5.6%
heff/lw =2
ALR =5%
lBE=8.5"
lBE=17"
Mbase/Mn ≈ 1
Crush around Large Bar (BE)
Buck/Frac in T. BE
Pre-Strength Loss
Post-Strength Loss
Max Shear
Governing Failure
W13, ρweb,h =0.405%
Shear Stress, Vu / (Acv √f'c)
Drift, %

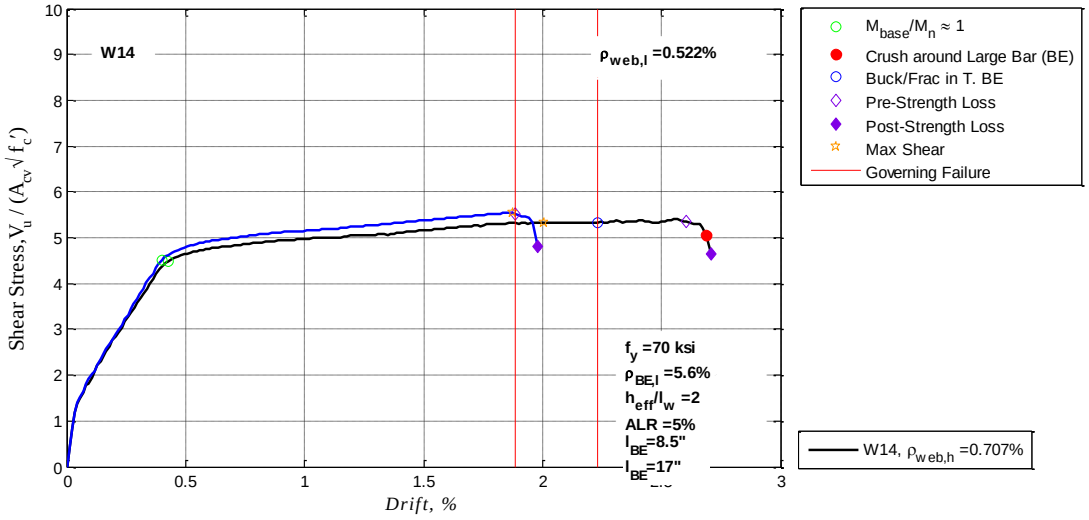
W14
ρweb,l =0.522%
fy =70 ksi
ρBE,l =5.6%
heff/lw =2
ALR =5%
lBE=8.5"
lBE=17"
Mbase/Mn ≈ 1
Crush around Large Bar (BE)
Buck/Frac in T. BE
Pre-Strength Loss
Post-Strength Loss
Max Shear
Governing Failure
W14, ρweb,h =0.707%
Shear Stress, Vu / (Acv √f'c)
Drift, %

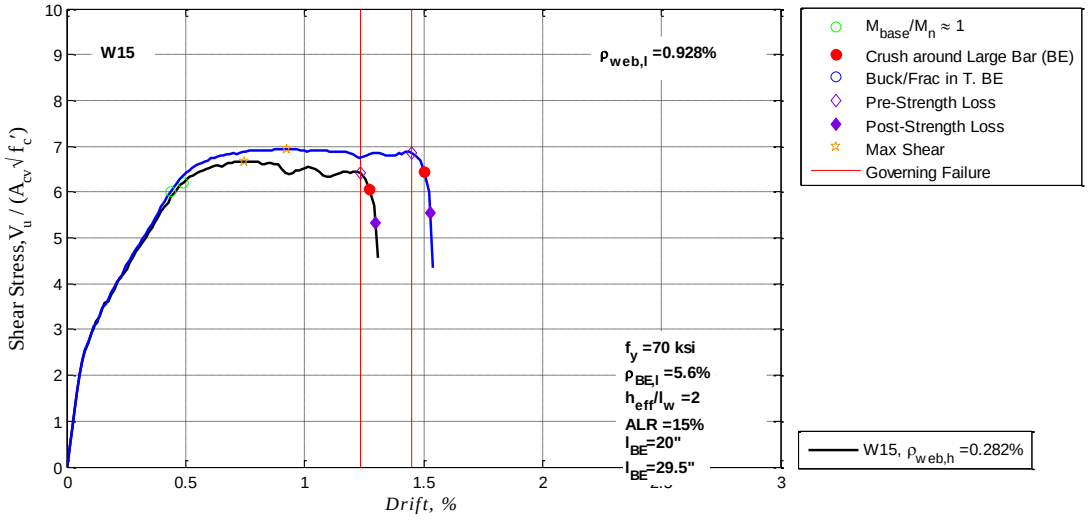
W15
ρweb,l =0.928%
fy =70 ksi
ρBE,l =5.6%
heff/lw =2
ALR =15%
lBE=20"
lBE=29.5"
Mbase/Mn ≈ 1
Crush around Large Bar (BE)
Buck/Frac in T. BE
Pre-Strength Loss
Post-Strength Loss
Max Shear
Governing Failure
W15, ρweb,h =0.282%
Shear Stress, Vu / (Acv √f'c)
Drift, %

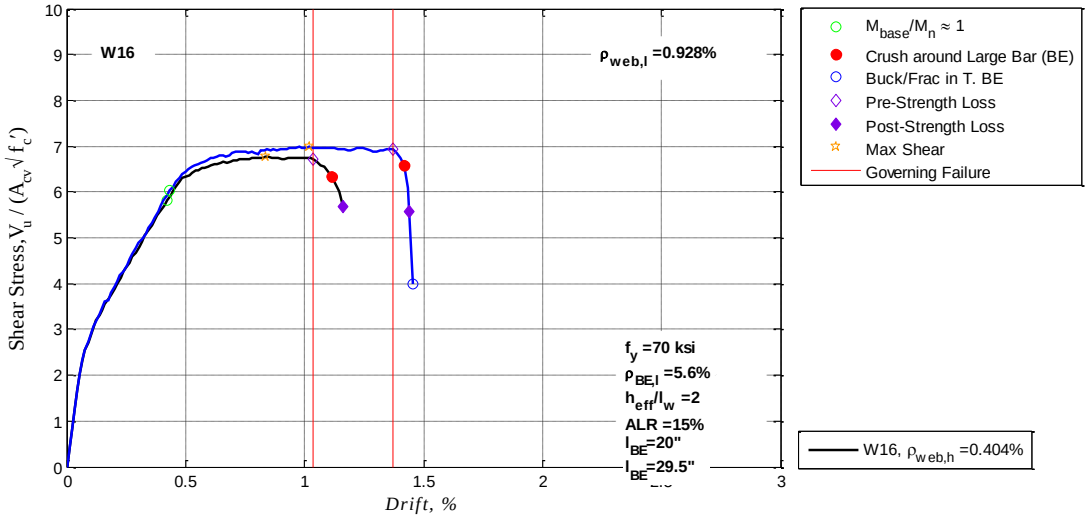
W16
ρweb,l =0.928%
fy =70 ksi
ρBE,l =5.6%
heff/lw =2
ALR =15%
lBE=20"
lBE=29.5"
Mbase/Mn ≈ 1
Crush around Large Bar (BE)
Buck/Frac in T. BE
Pre-Strength Loss
Post-Strength Loss
Max Shear
Governing Failure
W16, ρweb,h =0.404%
Shear Stress, Vu / (Acv √f'c)
Drift, %

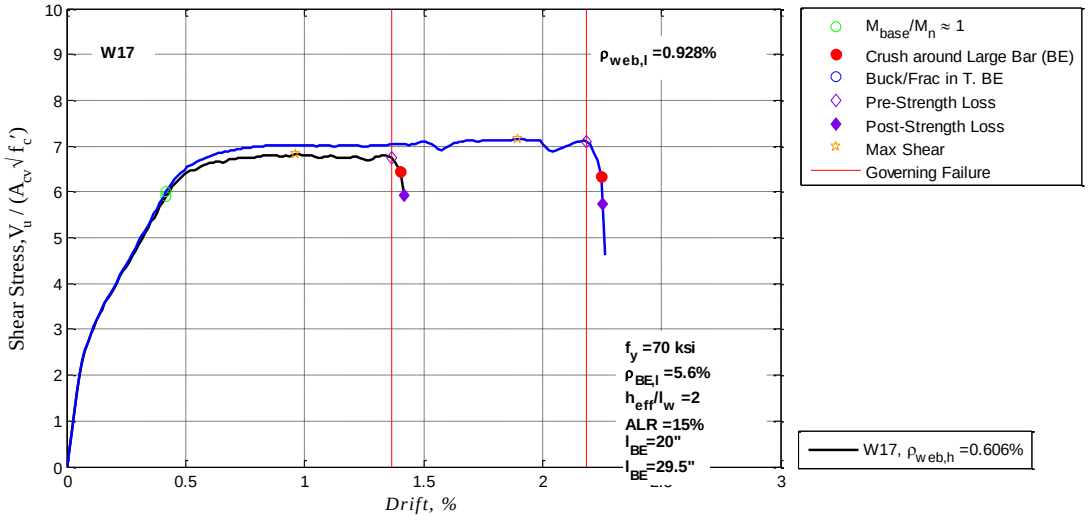
W17
ρweb,l =0.928%
fy =70 ksi
ρBE,l =5.6%
heff/lw =2
ALR =15%
lBE=20"
lBE=29.5"
Mbase/Mn ≈ 1
Crush around Large Bar (BE)
Buck/Frac in T. BE
Pre-Strength Loss
Post-Strength Loss
Max Shear
Governing Failure
W17, ρweb,h =0.606%
Shear Stress, Vu / (Acv √f'c)
Drift, %

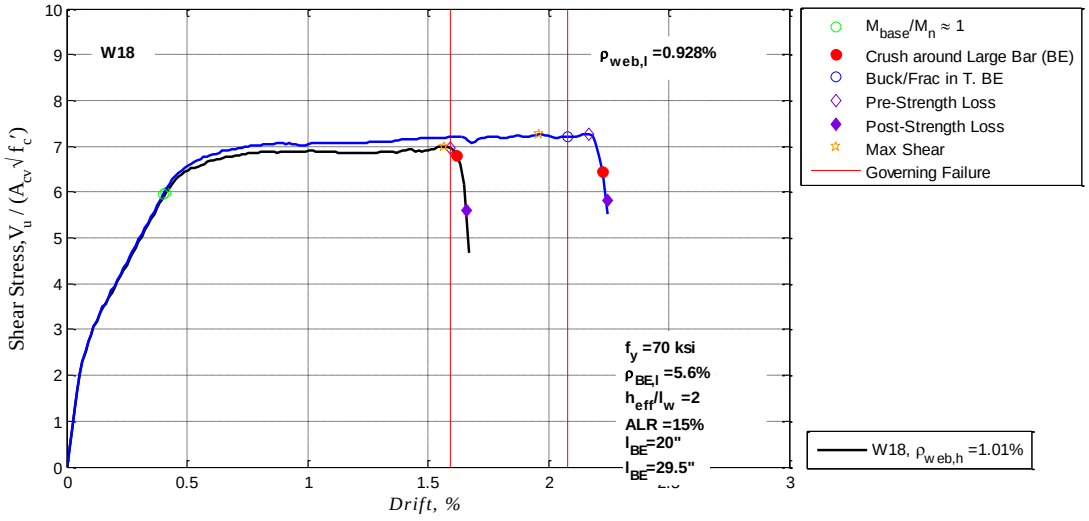
W18
ρweb,l =0.928%
fy =70 ksi
ρBE,l =5.6%
heff/lw =2
ALR =15%
lBE=20"
lBE=29.5"
Mbase/Mn ≈ 1
Crush around Large Bar (BE)
Buck/Frac in T. BE
Pre-Strength Loss
Post-Strength Loss
Max Shear
Governing Failure
W18, ρweb,h =1.01%
Shear Stress, Vu / (Acv √f'c)
Drift, %

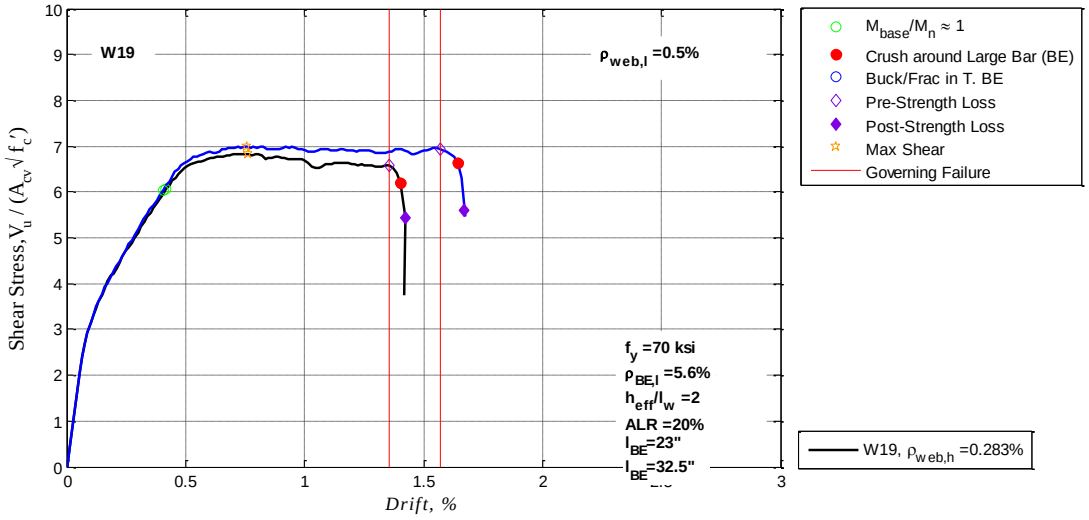
W19
ρweb,l =0.5%
fy =70 ksi
ρBE,l =5.6%
heff/lw =2
ALR =20%
lBE=23"
lBE=32.5"
Mbase/Mn ≈ 1
Crush around Large Bar (BE)
Buck/Frac in T. BE
Pre-Strength Loss
Post-Strength Loss
Max Shear
Governing Failure
W19, ρweb,h =0.283%
Shear Stress, Vu / (Acv √f'c)
Drift, %

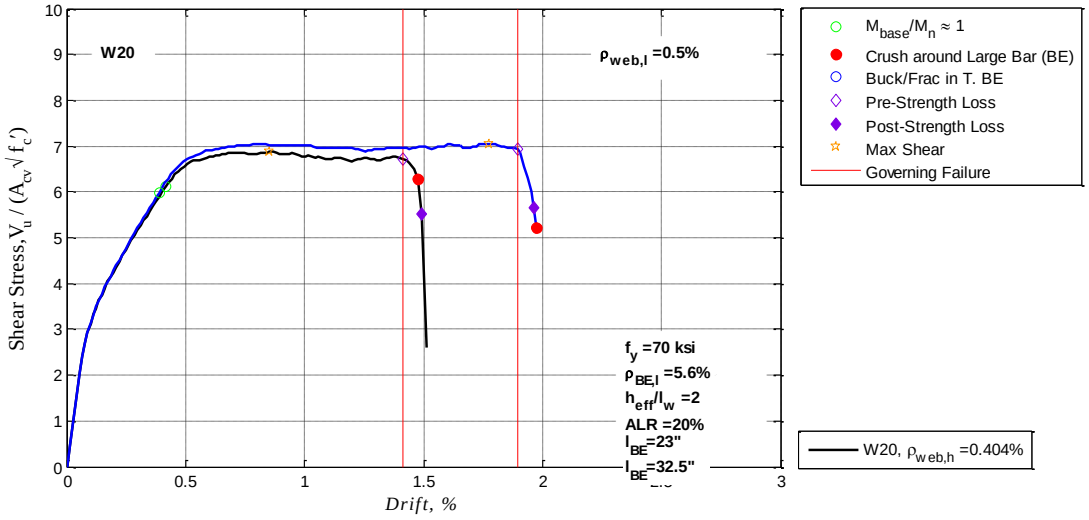
W20
ρweb,l =0.5%
fy =70 ksi
ρBE,l =5.6%
heff/lw =2
ALR =20%
lBE=23"
lBE=32.5"
Mbase/Mn ≈ 1
Crush around Large Bar (BE)
Buck/Frac in T. BE
Pre-Strength Loss
Post-Strength Loss
Max Shear
Governing Failure
W20, ρweb,h =0.404%
Shear Stress, Vu / (Acv √f'c)
Drift, %

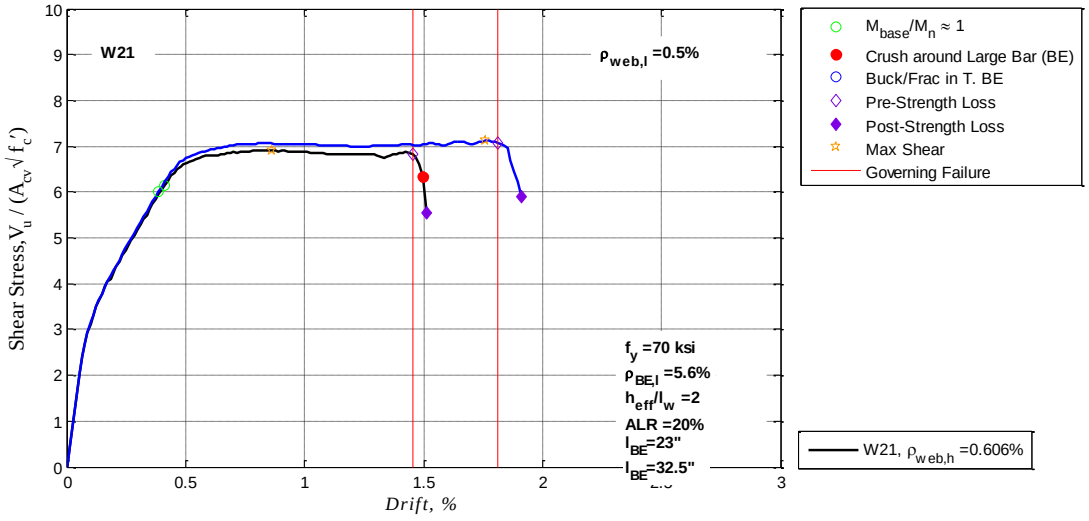
W21
ρweb,l =0.5%
fy =70 ksi
ρBE,l =5.6%
heff/lw =2
ALR =20%
lBE=23"
lBE=32.5"
Mbase/Mn ≈ 1
Crush around Large Bar (BE)
Buck/Frac in T. BE
Pre-Strength Loss
Post-Strength Loss
Max Shear
Governing Failure
W21, ρweb,h =0.606%
Shear Stress, Vu / (Acv √f'c)
Drift, %

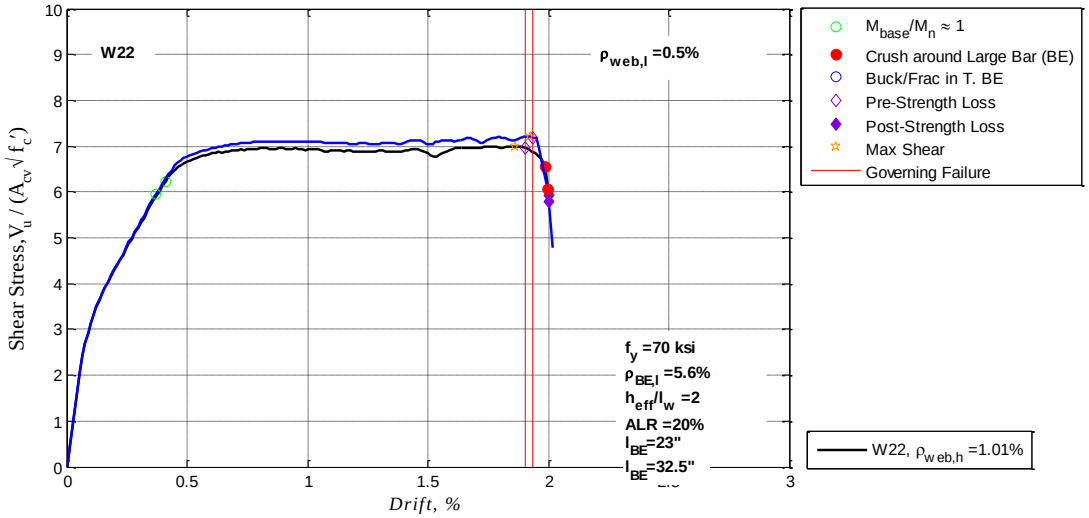
W22
ρweb,l =0.5%
fy =70 ksi
ρBE,l =5.6%
heff/lw =2
ALR =20%
lBE=23"
lBE=32.5"
Mbase/Mn ≈ 1
Crush around Large Bar (BE)
Buck/Frac in T. BE
Pre-Strength Loss
Post-Strength Loss
Max Shear
Governing Failure
W22, ρweb,h =1.01%
Shear Stress, Vu / (Acv √f'c)
Drift, %

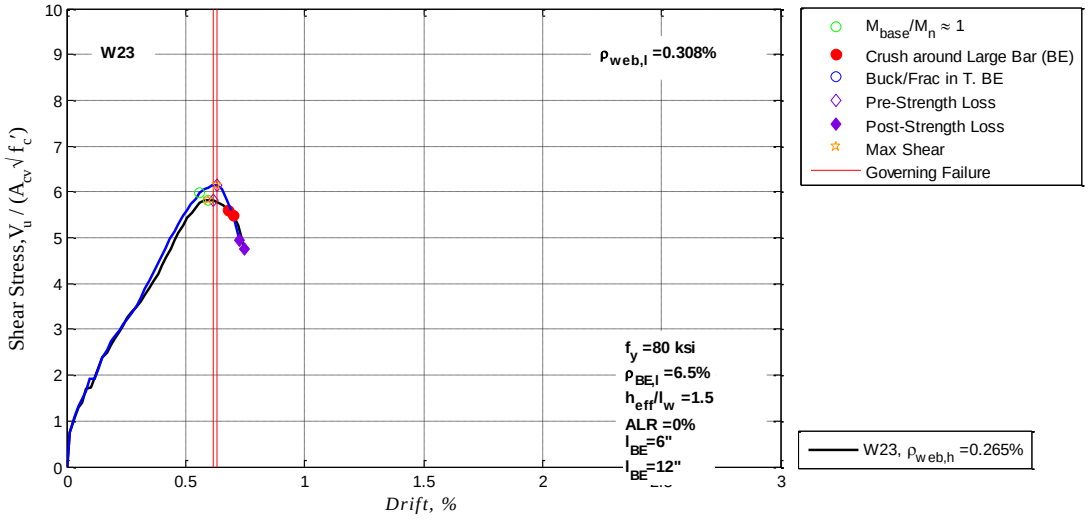
W23
ρweb,l =0.308%
fy =80 ksi
ρBE,l =6.5%
heff/lw =1.5
ALR =0%
lBE=6"
lBE=12"
Mbase/Mn ≈ 1
Crush around Large Bar (BE)
Buck/Frac in T. BE
Pre-Strength Loss
Post-Strength Loss
Max Shear
Governing Failure
W23, ρweb,h =0.265%
Shear Stress, Vu / (Acv √f'c)
Drift, %

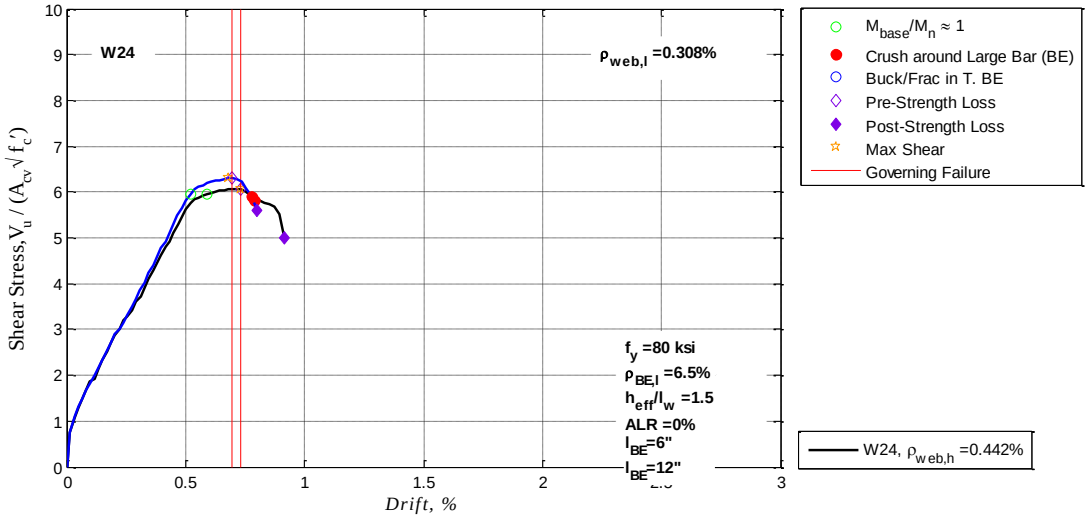
W24
$\rho_{web,l}$ =0.308%
f_y =80 ksi
$\rho_{BE,l}$ =6.5%
h_{eff}/l_w =1.5
ALR =0%
l_{BE}=6"
l_{BE}=12"
Shear Stress, $V_u / (A_{cv}\sqrt{f_c'})$
Drift, %
$M_{base}/M_n \approx 1$
Crush around Large Bar (BE)
Buck/Frac in T. BE
Pre-Strength Loss
Post-Strength Loss
Max Shear
Governing Failure
W24, $\rho_{web,h}$ =0.442%

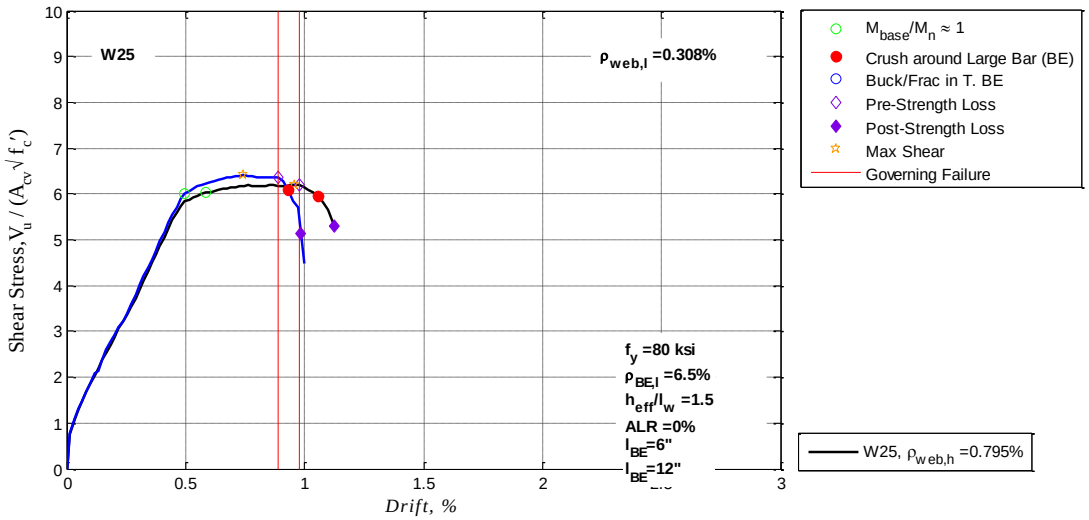
W25
$\rho_{web,l}$ =0.308%
f_y =80 ksi
$\rho_{BE,l}$ =6.5%
h_{eff}/l_w =1.5
ALR =0%
l_{BE}=6"
l_{BE}=12"
Shear Stress, $V_u / (A_{cv}\sqrt{f_c'})$
Drift, %
$M_{base}/M_n \approx 1$
Crush around Large Bar (BE)
Buck/Frac in T. BE
Pre-Strength Loss
Post-Strength Loss
Max Shear
Governing Failure
W25, $\rho_{web,h}$ =0.795%

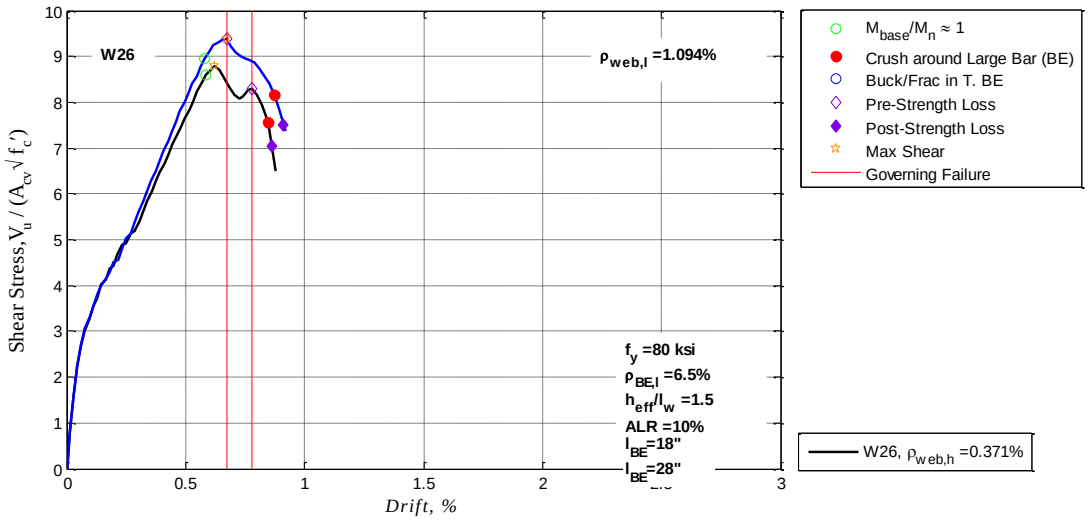
W26
$\rho_{web,l}$ =1.094%
f_y =80 ksi
$\rho_{BE,l}$ =6.5%
h_{eff}/l_w =1.5
ALR =10%
l_{BE}=18"
l_{BE}=28"
Shear Stress, $V_u / (A_{cv}\sqrt{f_c'})$
Drift, %
$M_{base}/M_n \approx 1$
Crush around Large Bar (BE)
Buck/Frac in T. BE
Pre-Strength Loss
Post-Strength Loss
Max Shear
Governing Failure
W26, $\rho_{web,h}$ =0.371%

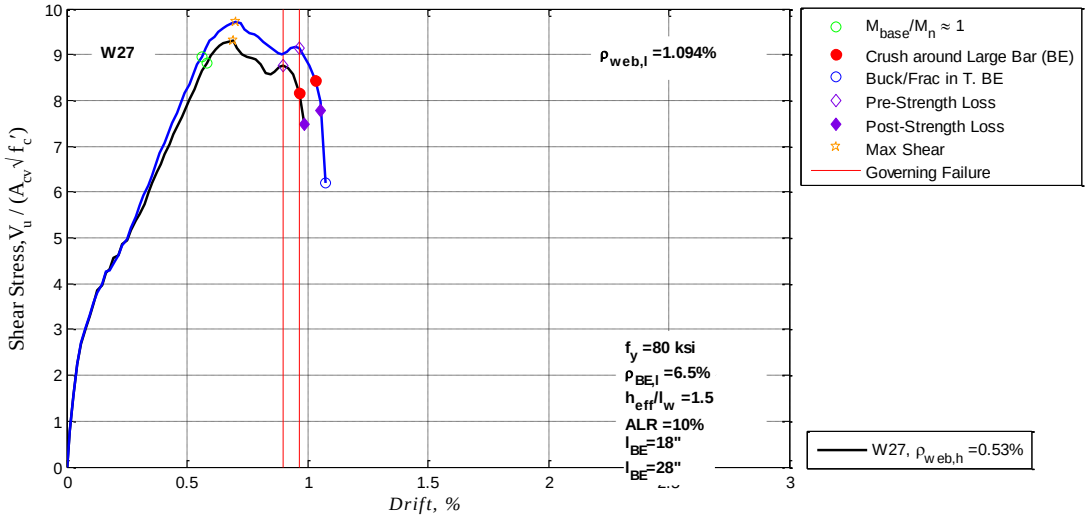
W27
ρweb,l =1.094%
fy =80 ksi
ρBE,l =6.5%
heff/lw =1.5
ALR =10%
lBE=18"
lBE=28"
Mbase/Mn ≈ 1
Crush around Large Bar (BE)
Buck/Frac in T. BE
Pre-Strength Loss
Post-Strength Loss
Max Shear
Governing Failure
W27, ρweb,h =0.53%
Shear Stress, Vu / (Acv √f'c)
Drift, %

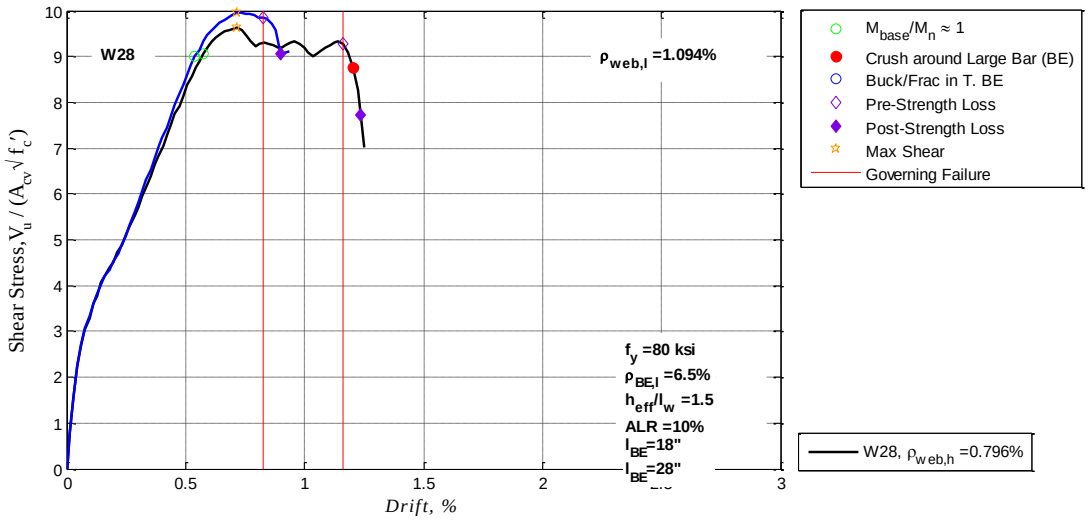
W28
ρweb,l =1.094%
fy =80 ksi
ρBE,l =6.5%
heff/lw =1.5
ALR =10%
lBE=18"
lBE=28"
Mbase/Mn ≈ 1
Crush around Large Bar (BE)
Buck/Frac in T. BE
Pre-Strength Loss
Post-Strength Loss
Max Shear
Governing Failure
W28, ρweb,h =0.796%
Shear Stress, Vu / (Acv √f'c)
Drift, %

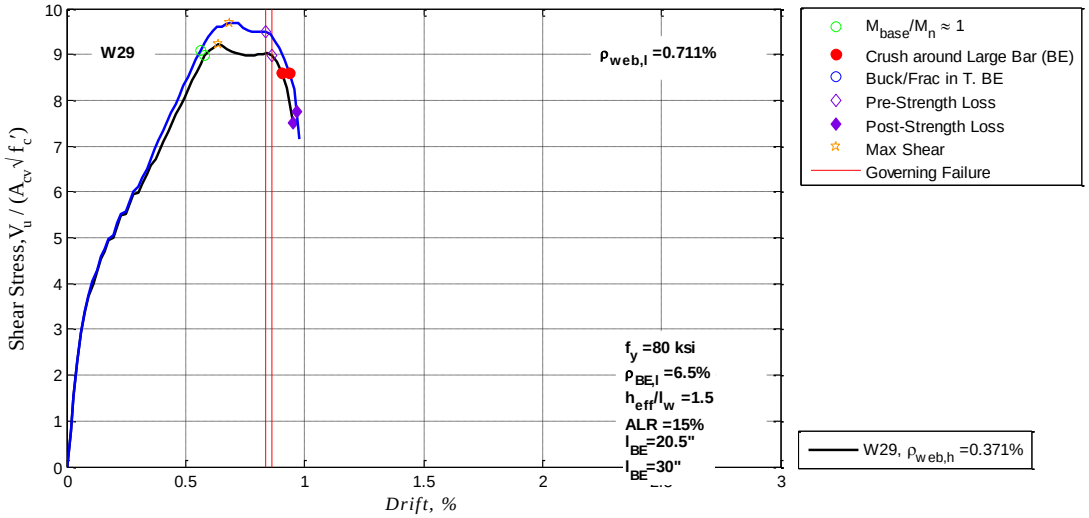
W29
ρweb,l =0.711%
fy =80 ksi
ρBE,l =6.5%
heff/lw =1.5
ALR =15%
lBE=20.5"
lBE=30"
Mbase/Mn ≈ 1
Crush around Large Bar (BE)
Buck/Frac in T. BE
Pre-Strength Loss
Post-Strength Loss
Max Shear
Governing Failure
W29, ρweb,h =0.371%
Shear Stress, Vu / (Acv √f'c)
Drift, %

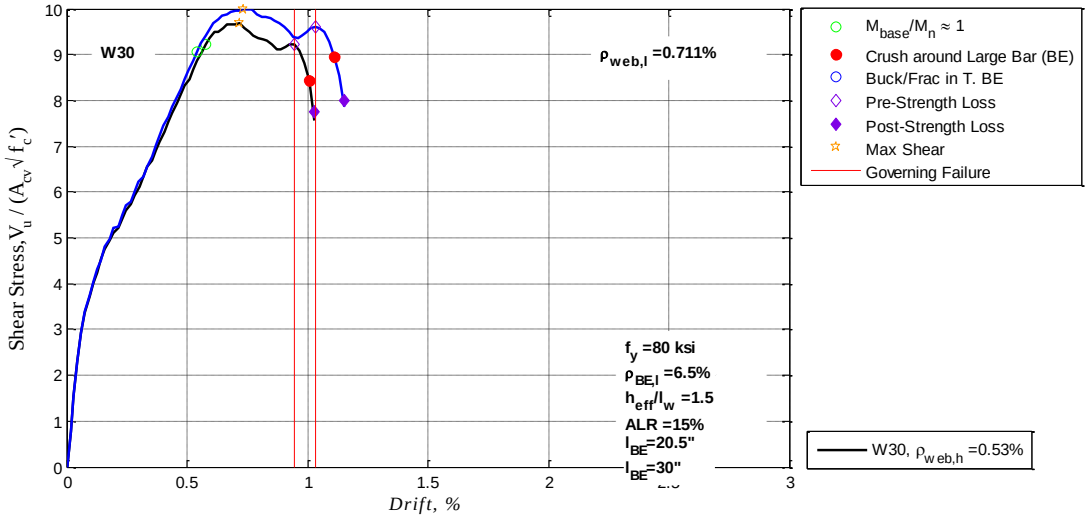
W30
ρweb,l =0.711%
fy =80 ksi
ρBE,l =6.5%
heff/lw =1.5
ALR =15%
lBE=20.5"
lBE=30"
Mbase/Mn ≈ 1
Crush around Large Bar (BE)
Buck/Frac in T. BE
Pre-Strength Loss
Post-Strength Loss
Max Shear
Governing Failure
W30, ρweb,h =0.53%
Shear Stress, Vu / (Acv √f'c)
Drift, %

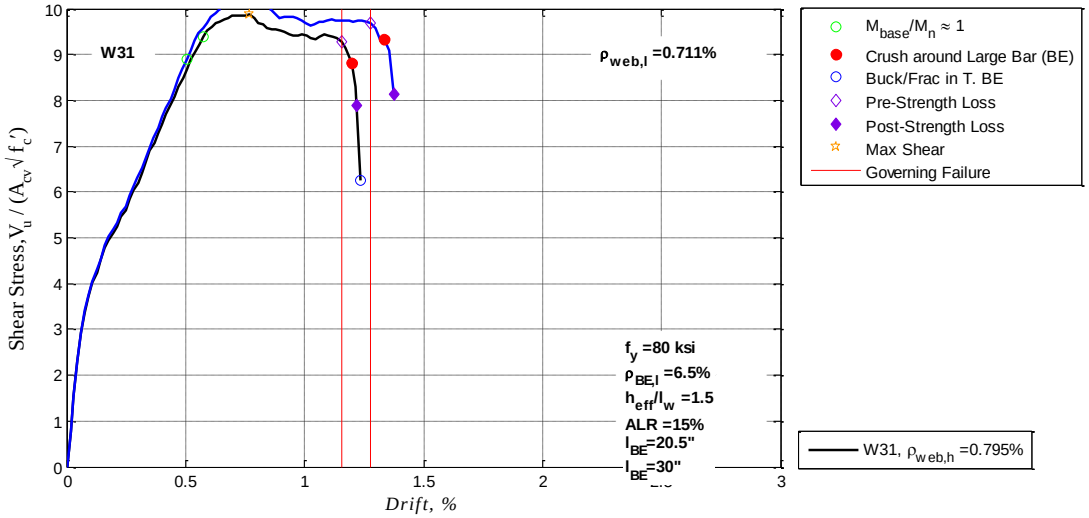
W31
ρweb,l =0.711%
fy =80 ksi
ρBE,l =6.5%
heff/lw =1.5
ALR =15%
lBE=20.5"
lBE=30"
Mbase/Mn ≈ 1
Crush around Large Bar (BE)
Buck/Frac in T. BE
Pre-Strength Loss
Post-Strength Loss
Max Shear
Governing Failure
W31, ρweb,h =0.795%
Shear Stress, Vu / (Acv √f'c)
Drift, %

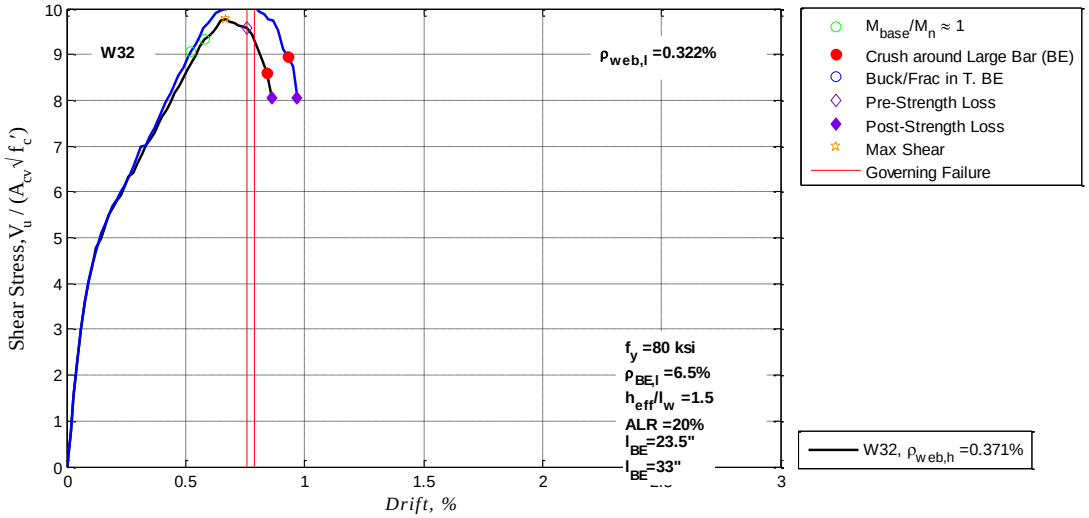
W32
ρweb,l =0.322%
fy =80 ksi
ρBE,l =6.5%
heff/lw =1.5
ALR =20%
lBE=23.5"
lBE=33"
Mbase/Mn ≈ 1
Crush around Large Bar (BE)
Buck/Frac in T. BE
Pre-Strength Loss
Post-Strength Loss
Max Shear
Governing Failure
W32, ρweb,h =0.371%
Shear Stress, Vu / (Acv √f'c)
Drift, %

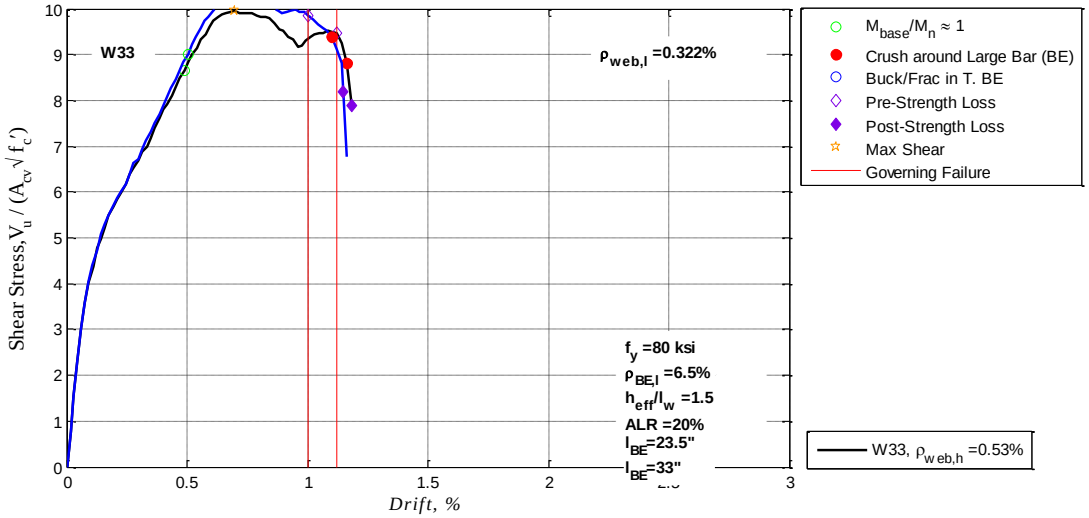
W33
ρweb,l =0.322%
fy =80 ksi
ρBE,l =6.5%
heff/lw =1.5
ALR =20%
lBE=23.5"
lBE=33"
Mbase/Mn ≈ 1
Crush around Large Bar (BE)
Buck/Frac in T. BE
Pre-Strength Loss
Post-Strength Loss
Max Shear
Governing Failure
W33, ρweb,h =0.53%
Shear Stress, Vu / (Acv √f'c)
Drift, %

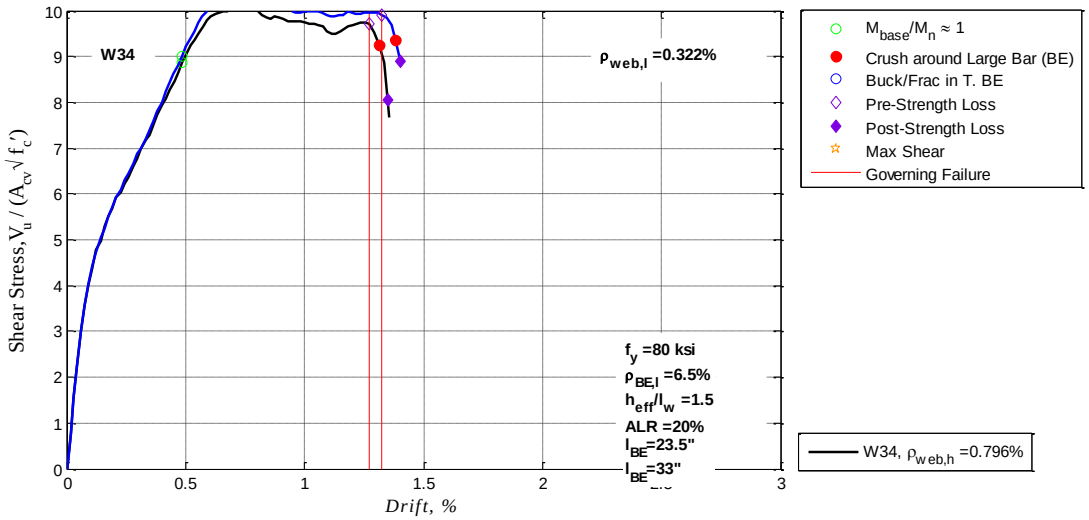
W34
ρweb,l =0.322%
fy =80 ksi
ρBE,l =6.5%
heff/lw =1.5
ALR =20%
lBE=23.5"
lBE=33"
Mbase/Mn ≈ 1
Crush around Large Bar (BE)
Buck/Frac in T. BE
Pre-Strength Loss
Post-Strength Loss
Max Shear
Governing Failure
W34, ρweb,h =0.796%
Shear Stress, Vu / (Acv √f'c)
Drift, %

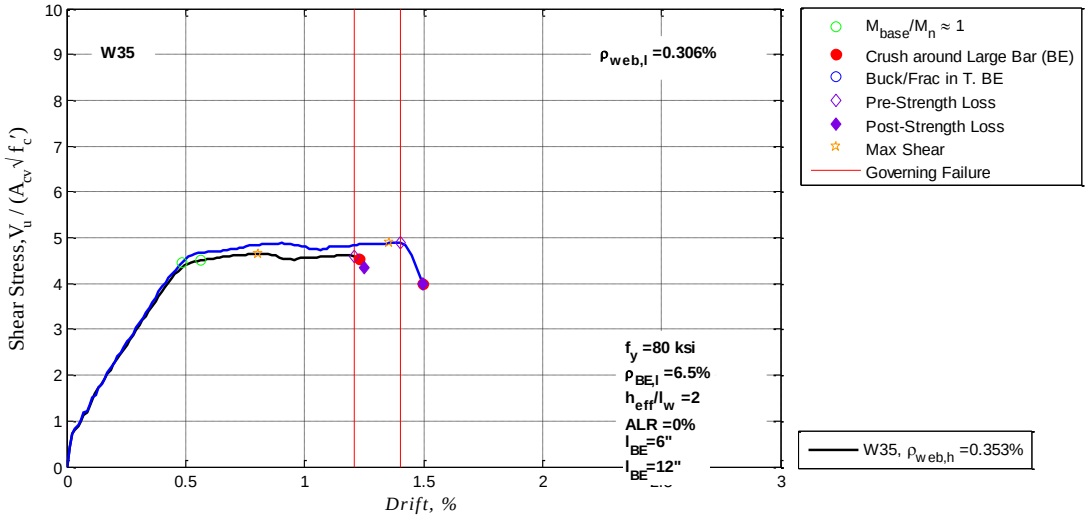
W35
ρweb,l =0.306%
fy =80 ksi
ρBE,l =6.5%
heff/lw =2
ALR =0%
lBE=6"
lBE=12"
Mbase/Mn ≈ 1
Crush around Large Bar (BE)
Buck/Frac in T. BE
Pre-Strength Loss
Post-Strength Loss
Max Shear
Governing Failure
W35, ρweb,h =0.353%
Shear Stress, Vu / (Acv √f'c)
Drift, %

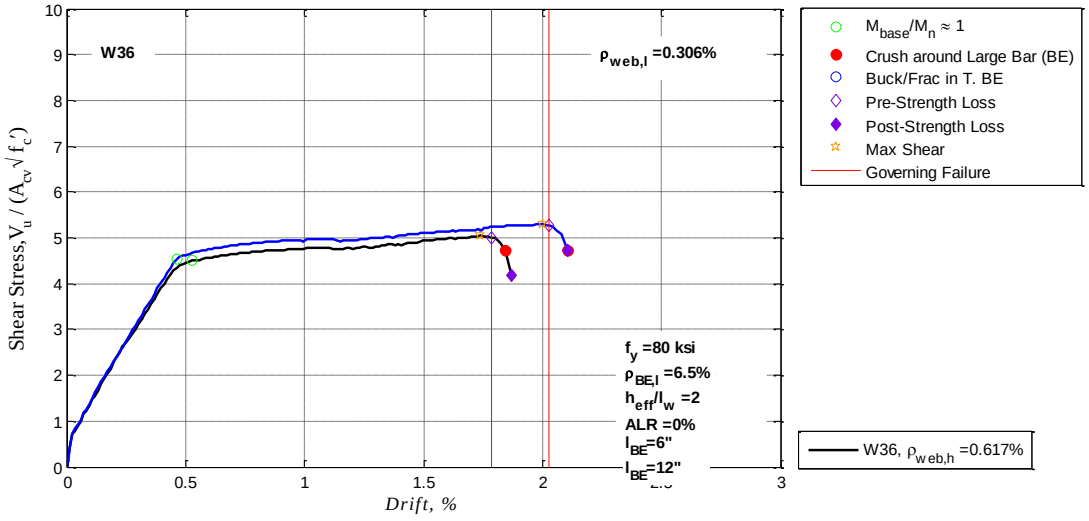
W36
ρweb,l =0.306%
fy =80 ksi
ρBE,l =6.5%
heff/lw =2
ALR =0%
lBE=6"
lBE=12"
Mbase/Mn ≈ 1
Crush around Large Bar (BE)
Buck/Frac in T. BE
Pre-Strength Loss
Post-Strength Loss
Max Shear
Governing Failure
W36, ρweb,h =0.617%
Shear Stress, Vu / (Acv √f'c)
Drift, %

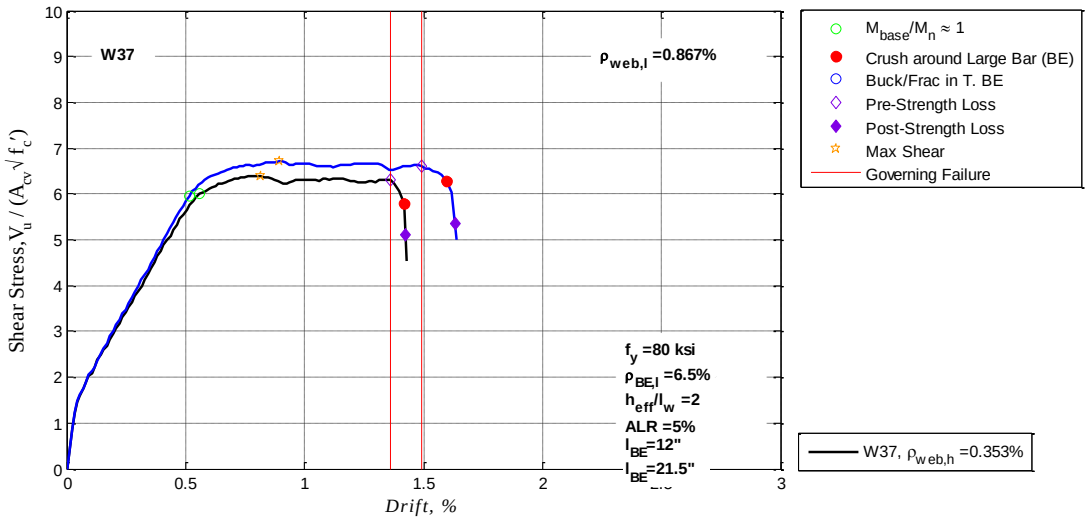
W37
ρweb,l =0.867%
fy =80 ksi
ρBE,l =6.5%
heff/lw =2
ALR =5%
lBE=12"
lBE=21.5"
Mbase/Mn ≈ 1
Crush around Large Bar (BE)
Buck/Frac in T. BE
Pre-Strength Loss
Post-Strength Loss
Max Shear
Governing Failure
W37, ρweb,h =0.353%
Shear Stress, Vu / (Acv √f'c)
Drift, %

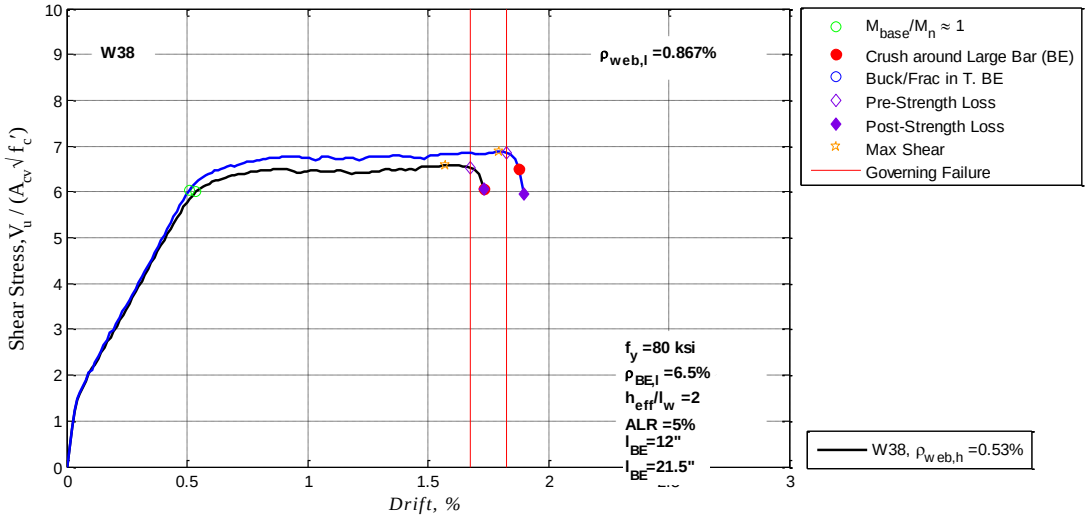
W38
ρweb,l =0.867%
fy =80 ksi
ρBE,l =6.5%
heff/lw =2
ALR =5%
lBE=12"
lBE=21.5"
Mbase/Mn ≈ 1
Crush around Large Bar (BE)
Buck/Frac in T. BE
Pre-Strength Loss
Post-Strength Loss
Max Shear
Governing Failure
W38, ρweb,h =0.53%
Shear Stress, Vu / (Acv √f'c)
Drift, %

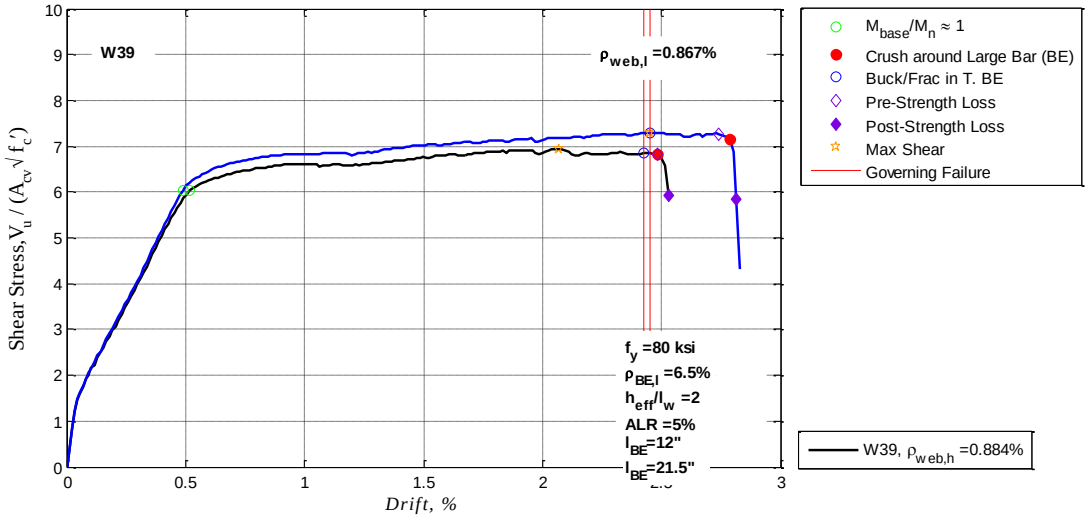
W39
$\rho_{web,l}$ =0.867%
f_y =80 ksi
$\rho_{BE,l}$ =6.5%
h_{eff}/l_w =2
ALR =5%
l_{BE}=12"
l_{BE}=21.5"
Shear Stress, $V_u / (A_{cv}\sqrt{f'_c})$
Drift, %
$M_{base}/M_n \approx 1$
Crush around Large Bar (BE)
Buck/Frac in T. BE
Pre-Strength Loss
Post-Strength Loss
Max Shear
Governing Failure
W39, $\rho_{web,h}$ =0.884%

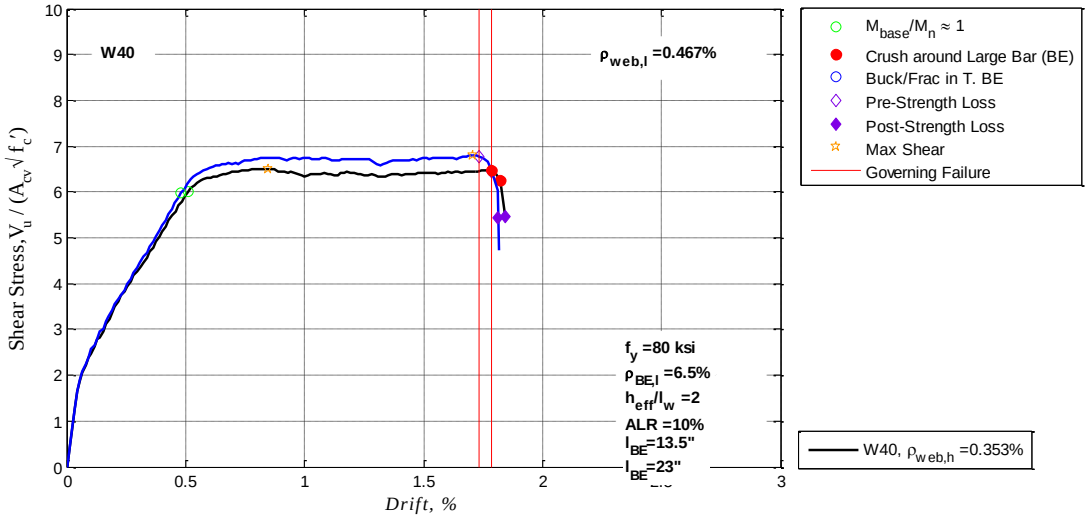
W40
$\rho_{web,l}$ =0.467%
f_y =80 ksi
$\rho_{BE,l}$ =6.5%
h_{eff}/l_w =2
ALR =10%
l_{BE}=13.5"
l_{BE}=23"
Shear Stress, $V_u / (A_{cv}\sqrt{f'_c})$
Drift, %
$M_{base}/M_n \approx 1$
Crush around Large Bar (BE)
Buck/Frac in T. BE
Pre-Strength Loss
Post-Strength Loss
Max Shear
Governing Failure
W40, $\rho_{web,h}$ =0.353%

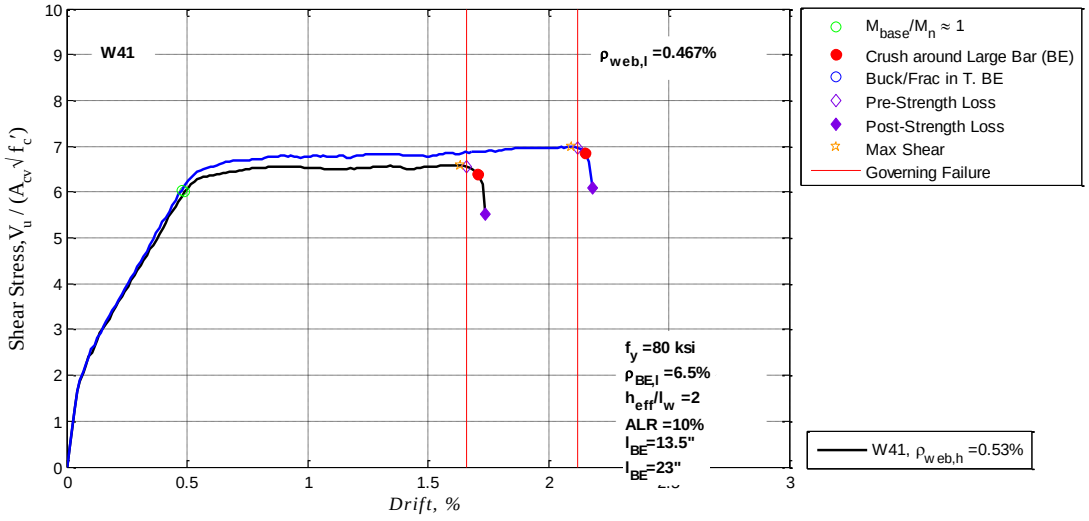
W41
$\rho_{web,l}$ =0.467%
f_y =80 ksi
$\rho_{BE,l}$ =6.5%
h_{eff}/l_w =2
ALR =10%
l_{BE}=13.5"
l_{BE}=23"
Shear Stress, $V_u / (A_{cv}\sqrt{f'_c})$
Drift, %
$M_{base}/M_n \approx 1$
Crush around Large Bar (BE)
Buck/Frac in T. BE
Pre-Strength Loss
Post-Strength Loss
Max Shear
Governing Failure
W41, $\rho_{web,h}$ =0.53%

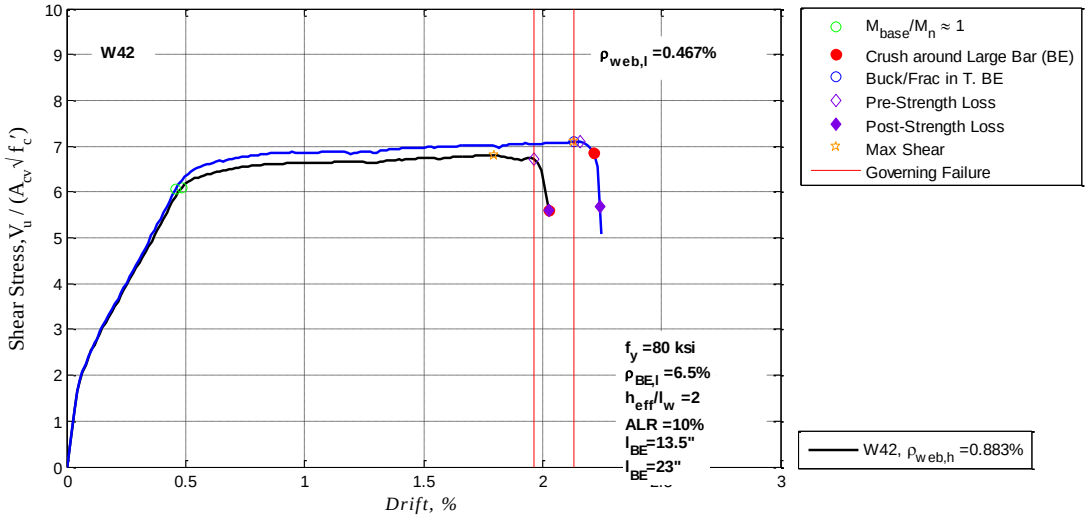
W42
$\rho_{web,l}$ =0.467%
f_y =80 ksi
$\rho_{BE,l}$ =6.5%
h_{eff}/l_w =2
ALR =10%
l_{BE}=13.5"
l_{BE}=23"
Shear Stress, $V_u / (A_{cv}\sqrt{f'_c})$
Drift, %
$M_{base}/M_n \approx 1$
Crush around Large Bar (BE)
Buck/Frac in T. BE
Pre-Strength Loss
Post-Strength Loss
Max Shear
Governing Failure
W42, $\rho_{web,h}$ =0.883%

APPENDIX C. CUMULATIVE DISTRIBUTION PLOTS FOR SIMULATED WALLS WITH ACI & EXTENDED BOUNDARY ELEMENTS

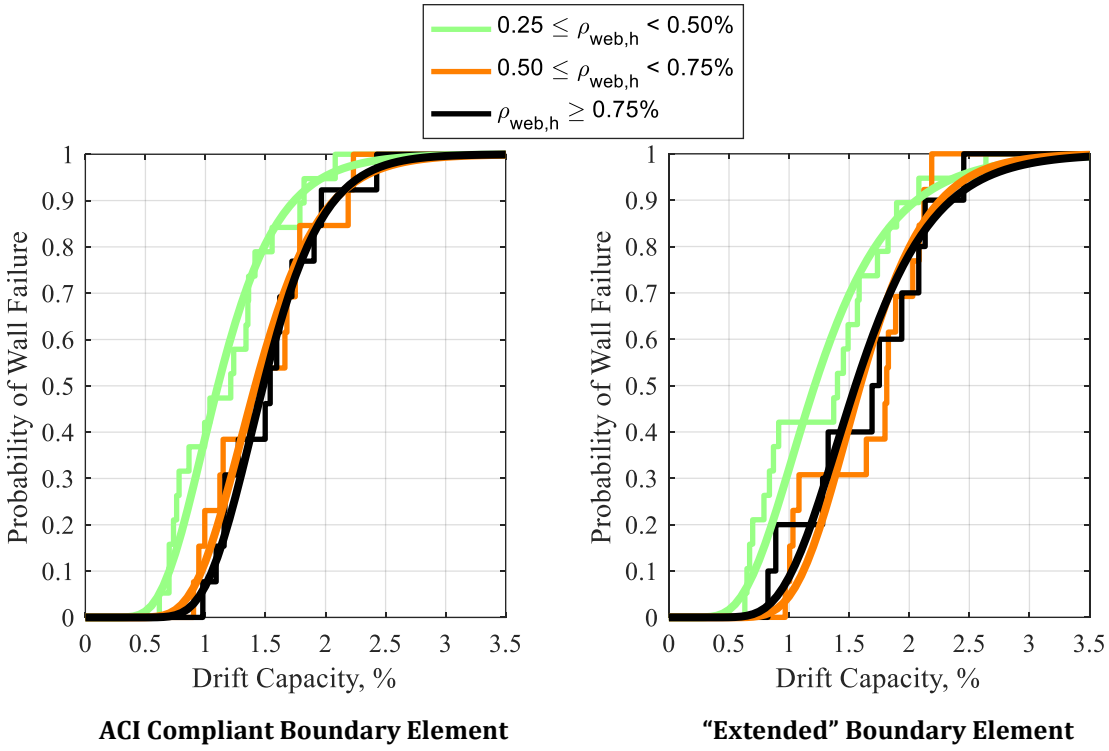

(a) Drift Capacity

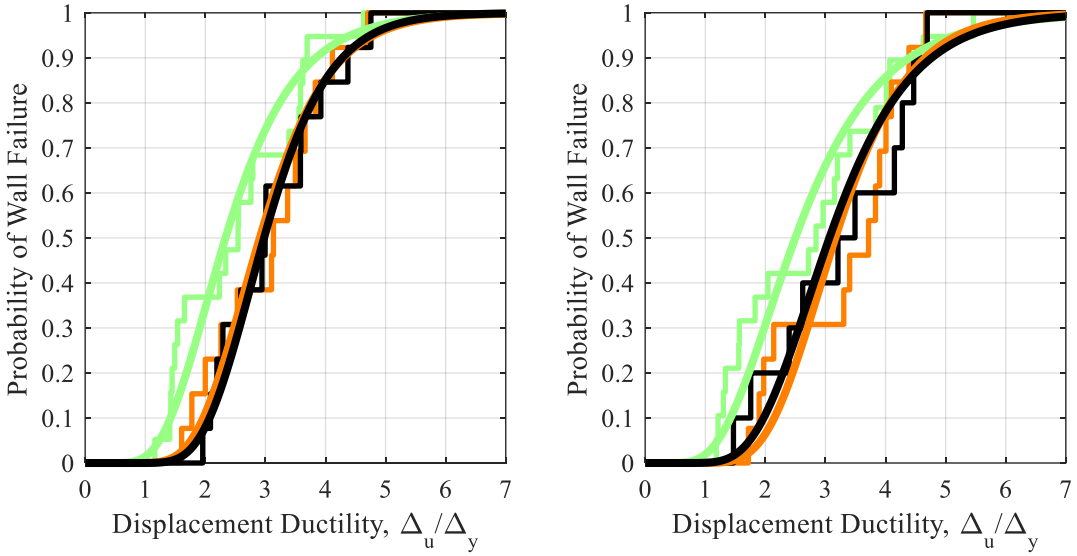

(b) Displacement Ductility

Cumulative Distribution Functions for Horizontal Web Reinforcement Ratio

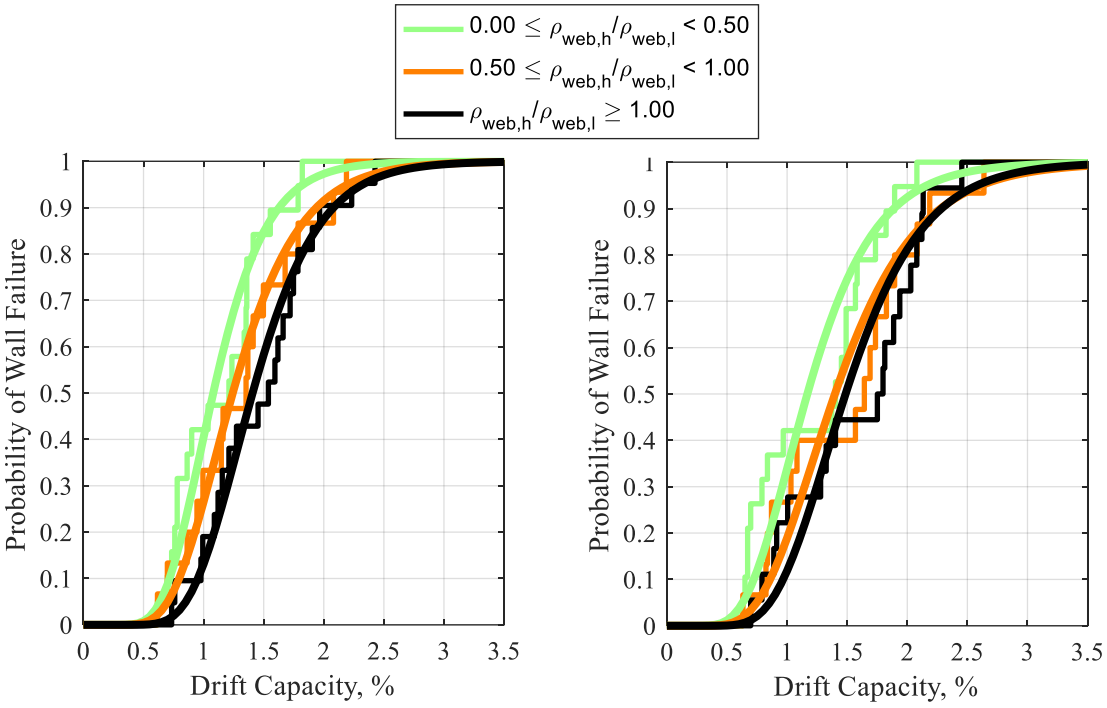

ACI Compliant Boundary Element **"Extended" Boundary Element**

(a) Drift Capacity

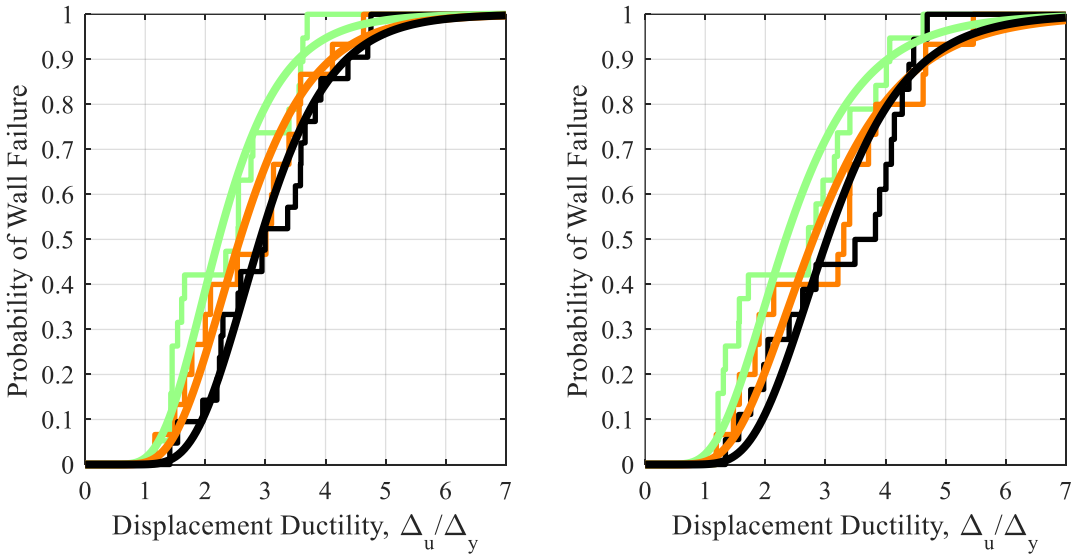

ACI Compliant Boundary Element **"Extended" Boundary Element**

(b) Displacement Ductility

Cumulative Distribution Functions for Horizontal-to-Vertical Web Reinforcement Ratio

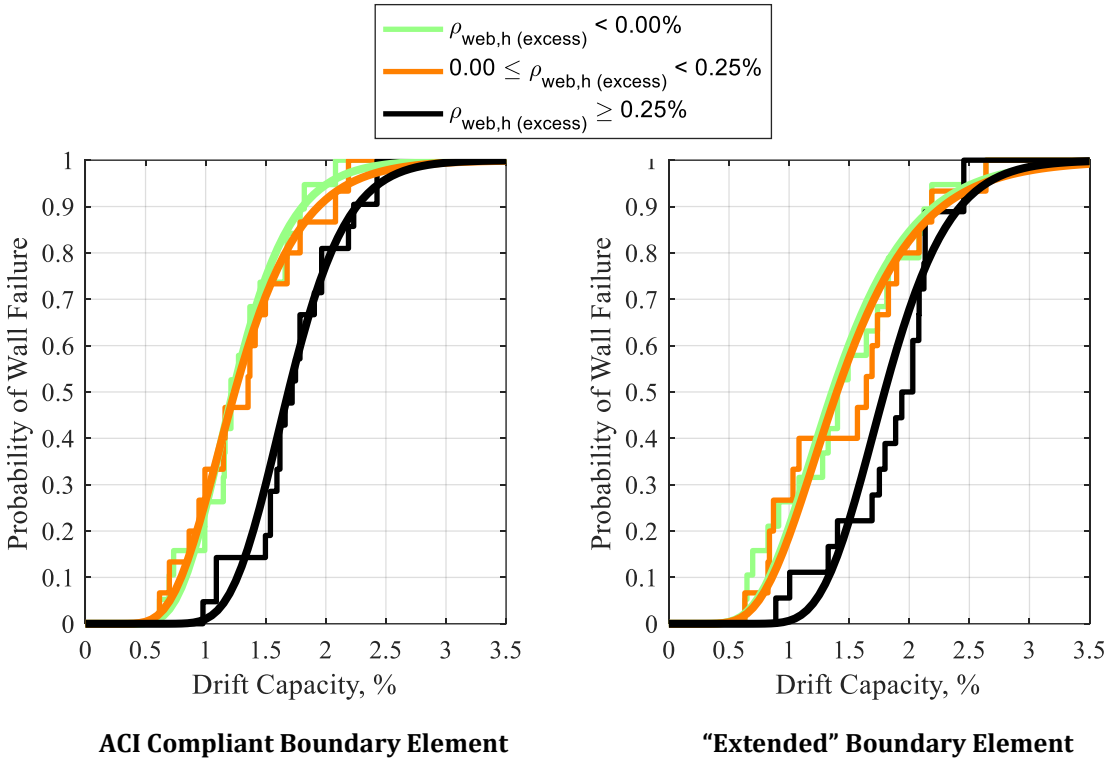

ACI Compliant Boundary Element **"Extended" Boundary Element**

(a) Drift Capacity

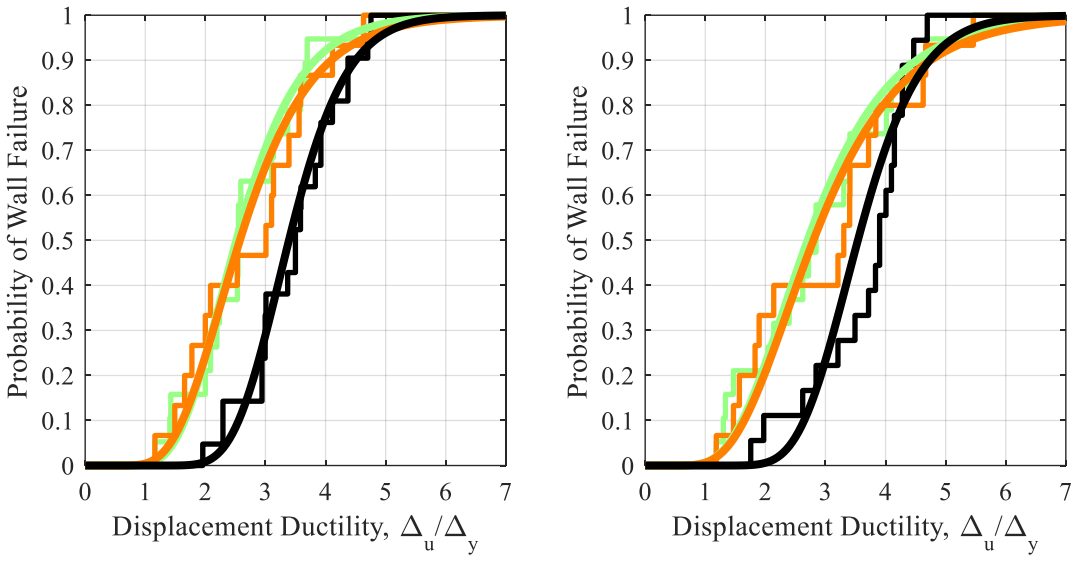

ACI Compliant Boundary Element **"Extended" Boundary Element**

(b) Displacement Ductility

Cumulative Distribution Functions for "Excess" Horizontal Web Reinforcement Ratio

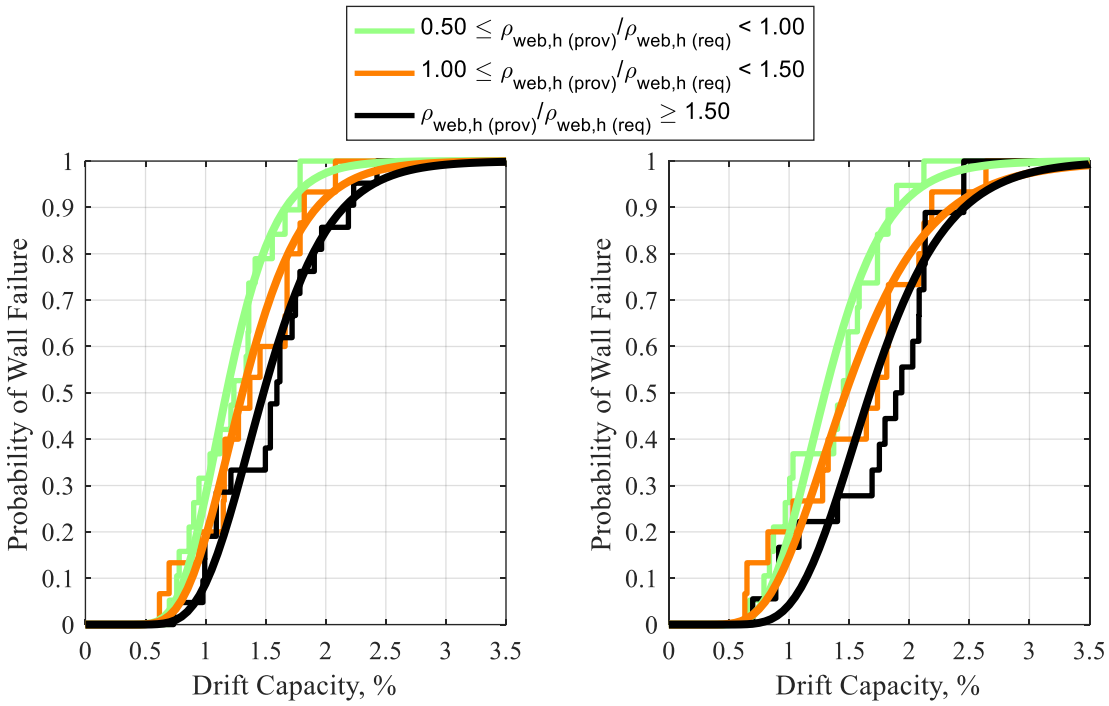

(a) Drift Capacity

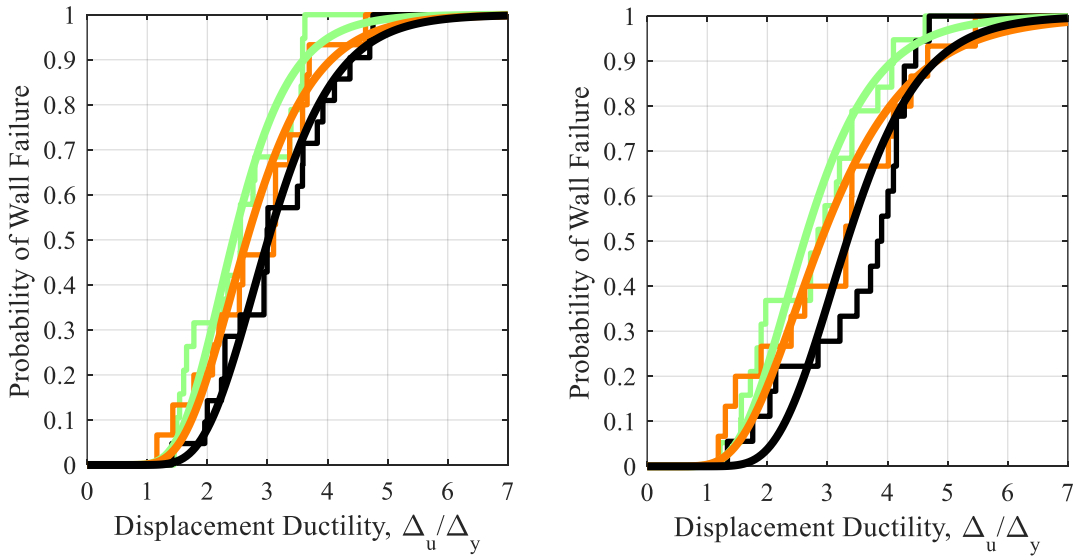

(b) Displacement Ductility

Cumulative Distribution Functions for Provided-to-Required Horizontal Web Reinforcement

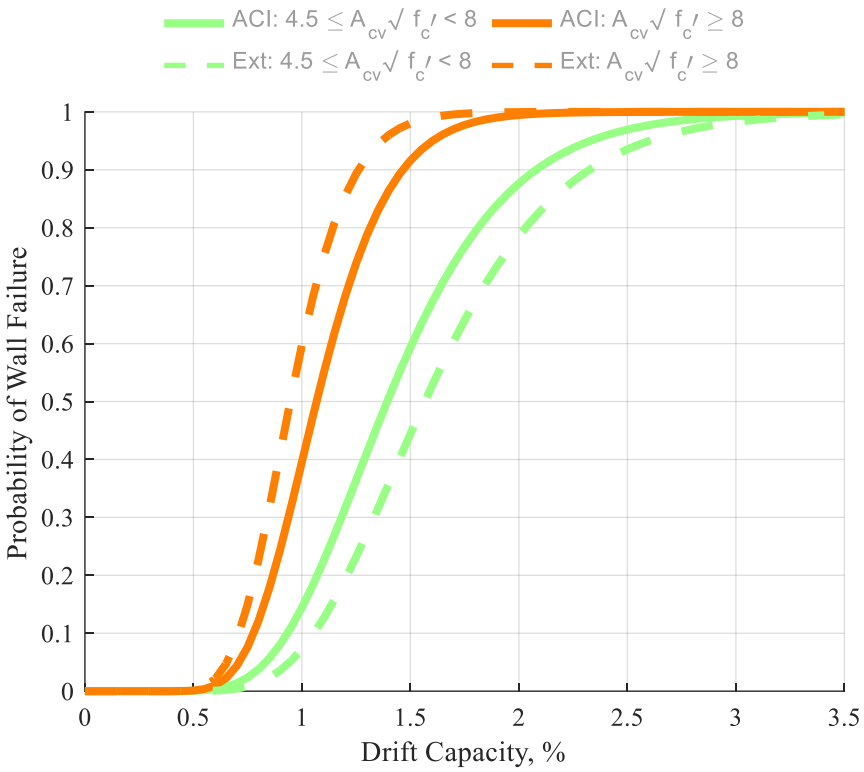

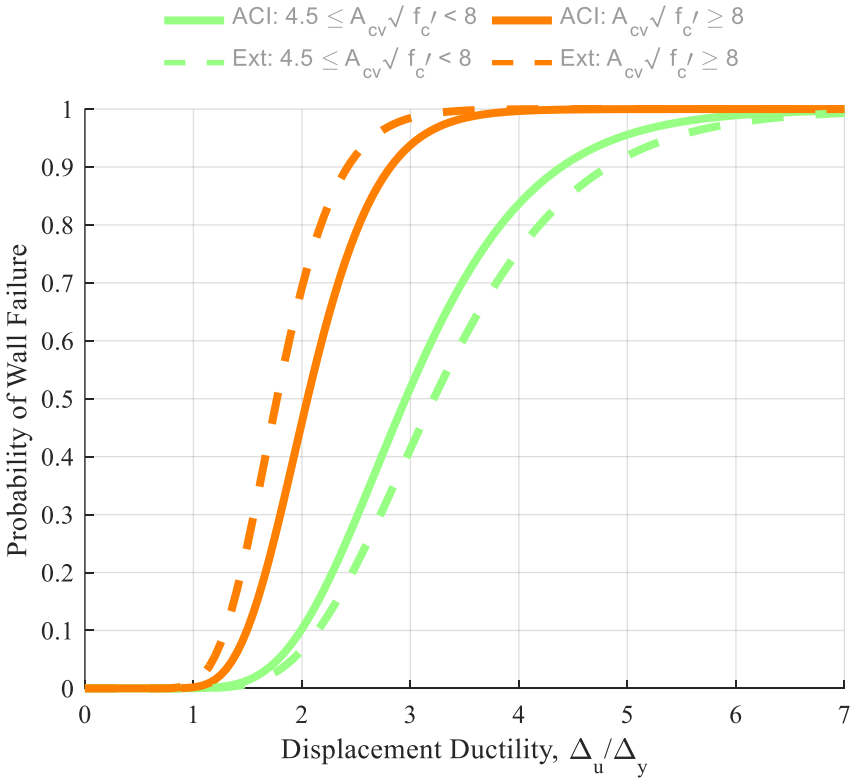

Cumulative Distribution Functions for Peak Shear Stress Demand
(ACI Compliant Boundary Element –solid line, Extended Boundary Element – dashed line)

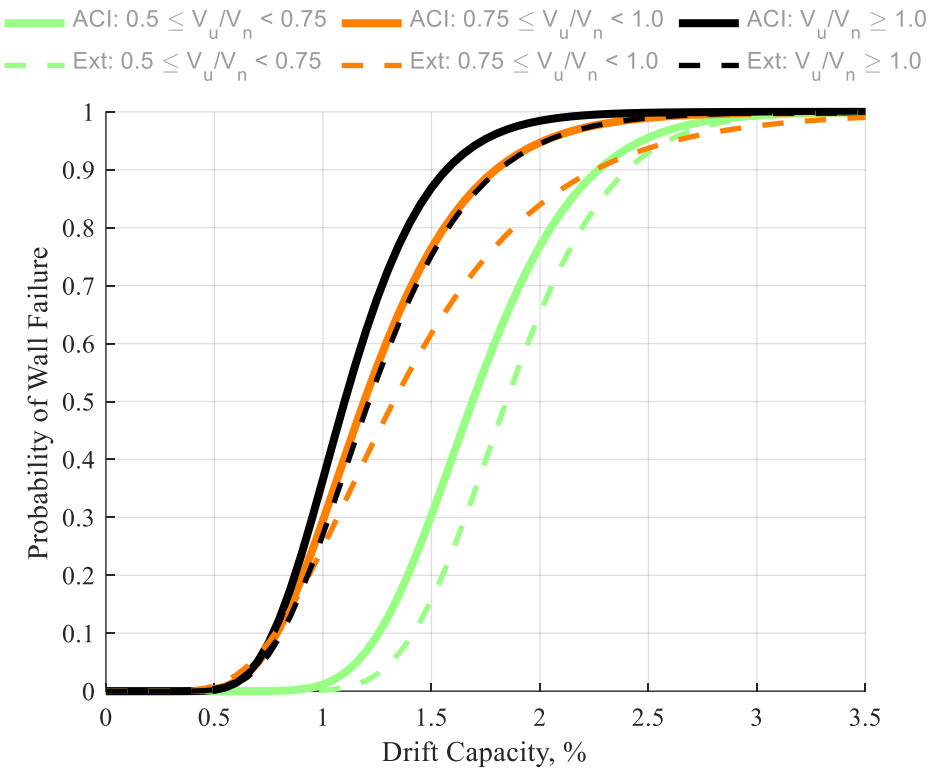

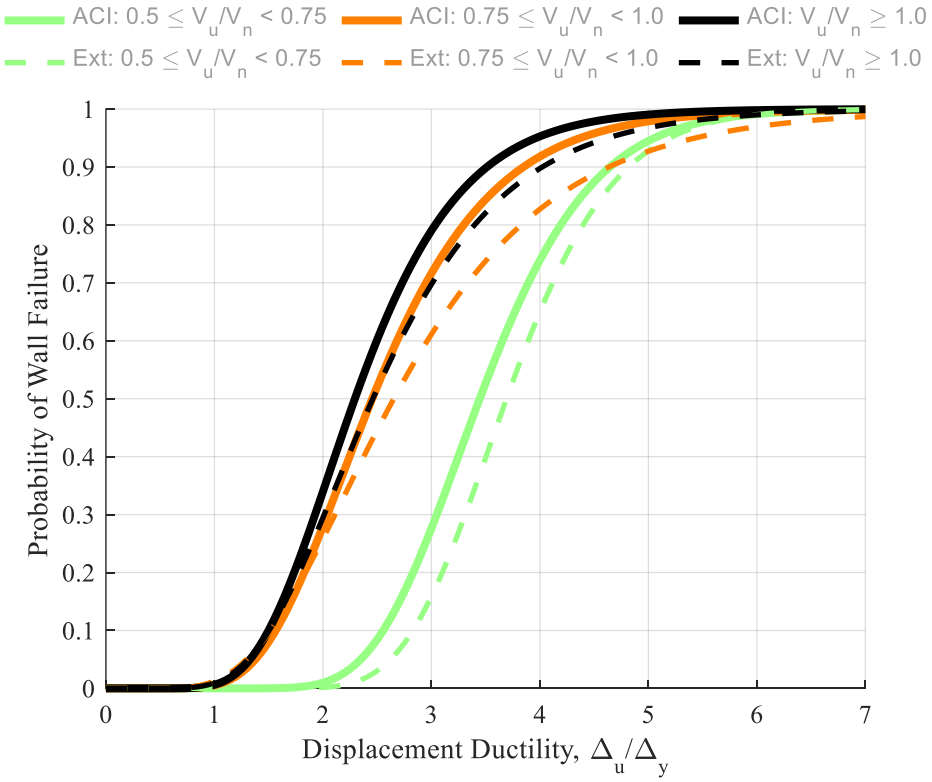

Cumulative Distribution Functions for Shear Demand-to-Capacity Ratios
(ACI Compliant Boundary Element –solid line, Extended Boundary Element – dashed line)